TOPICS IN CURRENT CHEMISTRY 286

Volume Editor T. Carlomagno

Tubulin-Binding Agents

Synthetic, Structural and Mechanistic Insights

Springer

286

Topics in Current Chemistry

Topics in Current Chemistry

Recently Published and Forthcoming Volumes

Tubulin-Binding Agents:
Synthetic, Structural and Mechanistic Insights
Volume Editor: Carlomagno, T.
Vol. 286, 2009

STM and AFM Studies on (Bio)molecular Systems: Unravelling the Nanoworld
Volume Editor: Samorì, P.
Vol. 285, 2008

Amplification of Chirality
Volume Editor: Soai, K.
Vol. 284, 2008

Anthracycline Chemistry and Biology II
Mode of Action, Clinical Aspects and New Drugs
Volume Editor: Krohn, K.
Vol. 283, 2008

Anthracycline Chemistry and Biology I
Biological Occurence and Biosynthesis, Synthesis and Chemistry
Volume Editor: Krohn, K.
Vol. 282, 2008

Photochemistry and Photophysics of Coordination Compounds II
Volume Editors: Balzani, V., Campagna, S.
Vol. 281, 2007

Photochemistry and Photophysics of Coordination Compounds I
Volume Editors: Balzani, V., Campagna, S.
Vol. 280, 2007

Metal Catalyzed Reductive C–C Bond Formation
A Departure from Preformed Organometallic Reagents
Volume Editor: Krische, M. J.
Vol. 279, 2007

Combinatorial Chemistry on Solid Supports
Volume Editor: Bräse, S.
Vol. 278, 2007

Creative Chemical Sensor Systems
Volume Editor: Schrader, T.
Vol. 277, 2007

In situ NMR Methods in Catalysis
Volume Editors: Bargon, J., Kuhn, L. T.
Vol. 276, 2007

Sulfur-Mediated Rearrangements II
Volume Editor: Schaumann, E.
Vol. 275, 2007

Sulfur-Mediated Rearrangements I
Volume Editor: Schaumann, E.
Vol. 274, 2007

Bioactive Conformation II
Volume Editor: Peters, T.
Vol. 273, 2007

Bioactive Conformation I
Volume Editor: Peters, T.
Vol. 272, 2007

Tubulin-Binding Agents

Synthetic, Structural and Mechanistic Insights

Volume Editor: Teresa Carlomagno

With Contributions by

K.-H. Altmann · J.M. Andreu · A. Cormier · C. Griesinger
A. Dorléans · J.F. Díaz · B. Gigant · G.J. Florence
F. Manetti · J. Jiménez-Barbero · J.H. Nettles
C.N. Kuzniewski · Kenneth H. Downing · M. Knossow
M. Botta · M. Magnani · B. Pfeiffer · I. Paterson
R.B.G. Ravelli · S. Forli · V.M. Sánchez-Pedregal
C. Wullschleger

Springer

The series *Topics in Current Chemistry* presents critical reviews of the present and future trends in modern chemical research. The scope of coverage includes all areas of chemical science including the interfaces with related disciplines such as biology, medicine and materials science. The goal of each thematic volume is to give the nonspecialist reader, whether at the university or in industry, a comprehensive overview of an area where new insights are emerging that are of interest to a larger scientific audience.

As a rule, contributions are specially commissioned. The editors and publishers will, however, always be pleased to receive suggestions and supplementary information. Papers are accepted for *Topics in Current Chemistry* in English.

In references *Topics in Current Chemistry* is abbreviated Top Curr Chem and is cited as a journal. Visit the TCC content at springerlink.com

Topics in Current Chemistry e-ISSN 1436-5049
ISBN 978-3-540-69036-8 e-ISBN 978-3-540-69039-9
DOI 10.1007/978-3-540-69039-9
Springer Dordrecht Heidelberg London New York

Library of Congress Control Number: 2009926058

Cover design: WMX Design GmbH, Heidelberg, Germany

Printed on acid-free paper

Springer is part of Springer Science+Business Media (www.springer.com)

Volume Editor

Dr. Teresa Carlomagno

The European Molecular Biology Laboratory
(EMBL)
Meyerhofstrasse 1
69117 Heidelberg
Germany
teresa.carlomagno@embl.de

Editorial Board

Topics in Current Chemistry Also Available Electronically

For all customers who have a standing order to Topics in Current Chemistry, we offer the electronic version via SpringerLink free of charge. Please contact your librarian who can receive a password or free access to the full articles by registering at:

springerlink.com

If you do not have a subscription, you can still view the tables of contents of the volumes and the abstract of each article by going to the SpringerLink Homepage, clicking on "Browse by Online Libraries", then "Chemical Sciences", and finally choose Topics in Current Chemistry.

You will find information about the

– Editorial Board
– Aims and Scope
– Instructions for Authors
– Sample Contribution

at springer.com using the search function.

Color figures are published in full color within the electronic version on SpringerLink.

Preface

The multifaceted conformational properties of tubulin have represented a challenge for mechanistic and structural studies of the protein for the past 20 years. The conformational equilibrium between the dimeric and polymeric form of tubulin can be controlled by different solvents (H_2O, D_2O, DMSO), cofactors (divalent ions, as for example Mg^{2+}, GTP/GDP), or small molecules. Alternatively, depending on the environment and concentration, tubulin can assemble in rings, protofilaments sheets, or even amorphous aggregates. Small organic molecules bind to tubulin at several, often flexible, sites, usually stabilizing the protein in one conformational form. All in all, the large number of structural entities that tubulin can build, together with the easy inter-conversion among them as a response to external conditions, underlies an intrinsic flexibility of the protein and an amazing capacity of rearranging the tertiary interaction network of well-defined structural domains.

In this book we review the current knowledge of the mechanistic and structural aspects of the conformation switches triggered in tubulin by small organic molecules. Despite years of research by many groups around the world, the structural basis of the mechanisms of action of many tubulin binders is still unknown. Mapping of a consistent pharmacophore at specific tubulin interaction sites is tricky, due to the fact that each binding pocket in tubulin can accommodate molecules with very diverse chemical scaffolds. The case of the microtubules stabilizing agent Epothilone (Chapters 1, 3, 4, and 5) is exemplary: despite the presence of activity data for hundreds of derivatives, no consensus has been reached either for the bioactive conformation or for the binding mode to the protein, with two contradicting models having been proposed by Nuclear Magnetic Resonance spectroscopy (NMR, Chapter 4) and Electron Microscopy (EM, Chapter 5) studies. This contradiction might reflect the different tubulin structural forms used in the two studies or might be indicative of a constitutive problem encountered in the endeavour to describe the structural properties of a very flexible complex.

Tubulin binders are usually large and complex natural products. The difficulties and challenges encountered in the chemical synthesis of these molecules and their derivatives, with the goal of building solid structure-activity relationship (SAR) datasets, are described in the first and second chapters of the book.

The first chapter focuses on the total synthesis of macrolide-based microtubules stabilizing agents and on SAR data thereof, which have not been covered in other

reviews. The SAR data are discussed in light of the structural information available for each agent.

The second chapter focuses on the total synthesis of the marine sponge-derived polyketide discodermolide. A comprehensive survey of the synthetic chemistry efforts of several groups over a 14-year period is provided together with a comparison of the different approaches.

The third chapter describes a comprehensive study of the mechanisms of activity of microtubules stabilizing drugs. Thermodynamic, kinetic, structural and functional data on microtubules stabilizing drugs are discussed in an interdisciplinary manner to generate a "time-resolved" picture of the interaction of the drugs with different tubulin forms.

The fourth and fifth chapters review the efforts and achievements made in the characterization of the structure of the complexes of tubulin with microtubules stabilizing agents by NMR (Chapter 4) and EM (Chapter 5). Especially evident is the discrepancy of the results obtained for epothilones, where the two techniques deliver radically different structures of the bound drug. Both NMR and EM models are, however, able to explain a consistent set of SAR data. The authors of the two chapters discuss critically the advantages and limitations of each methodology.

The sixth chapter reviews the structural studies of complexes of tubulin with microtubules destabilizing agents performed by X-ray crystallography. The intelligent use of a complex of two tubulin dimers and the stathmin-like domain of the RB3 protein allows crystallization of the proteins in presence of microtubules destabilizing agents. A mechanistic model for the activity of microtubules destabilizing agents is provided on the basis of the structural results.

The last chapter is a comprehensive overview of the efforts made to understand the pharmacophore of both microtubules stabilizing and destabilizing agents by molecular modelling techniques. In the absence of converging structural information, modelling is a viable technique to study the feasibility of ligand bound conformations and pharmacophore models, bearing in mind the intrinsic problems associated with the structural flexibility of the binding site(s).

The broad range of techniques used by the authors of the book to investigate the mechanisms of the conformational control exerted on tubulin by small organic molecules is representative of the complexity of the problem. I hope that you will enjoy reading this book: those of you who are actively working in the field of tubulin-binding agents may find useful insights into the mechanisms of tubulin-binding drugs and inspiration for new experiments; those of you who are not concerned about tubulin-binding agents will appreciate this survey of the joined effort of many scientists with different expertise around the world to address the intriguing and difficult problem of conformational control in tubulin.

Spring 2009 Teresa Carlomagno

Contents

Top Curr Chem (2009) 286: 1–72
DOI: 10.1007/128_2008_9

Published online: 13 March 2009

Macrolide-Based Microtubule-Stabilizing Agents – Chemistry and Structure–Activity Relationships

B. Pfeiffer, C.N. Kuzniewski, C. Wullschleger, and K.-H. Altmann

Abstract This article provides an overview on the chemistry and structure–activity relationships of macrolide-based microtubule-stabilizing agents. The primary focus will be on the total synthesis or examples thereof, but a brief summary of the current state of knowledge on the structure–activity relationships of epothilones, laulimalide, dictyostatin, and peloruside A will also be given. This macrolide class of compounds, over the last decade, has become the subject of growing interest due to their ability to inhibit human cancer cell proliferation through a taxol-like mechanism of action.

Keywords Anticancer, Dictyostatin, Epothilone, Laulimalide, Macrolide, Peloruside A

Contents

B. Pfeiffer, C.N. Kuzniewski, C. Wullschleger, and K.-H. Altmann (✉)
ETH Zürich, Department of Chemistry and Applied Biosciences, Institute of Pharmaceutical Sciences, HCI H405, Wolfgang-Pauli-Str. 10 CH-8093 Zürich, Switzerland
e-mail: karl-heinz.altmann@pharma.ethz.ch

Abbreviations

9-BBN	9-borabicyclo[3.3.1]nonane
Ac	acetyl
acac	acetylacetonate
AIBN	2,2'-azobisisobutyronitrile
Ar	aryl
Bn	benzyl
Boc	*tert*-butoxycarbonyl
BOM	benzyloxymethyl
cat	catalytic
CBS	Corey-Bakshi-Shibata
Cp	cyclopentadienyl
CSA	camphorsulfonic acid
CuTC	copper(I) thiophenecarboxylate
dba	dibenzylidene acetone
DCC	*N,N*-dicyclohexylcarbodiimide
DDQ	2,3-dichloro-5,6-dicyano-1,4-benzoquinone
de	diastereomeric excess
DEAD	diethyl azodicarboxylate
DET	diethyl tartrate
DIAD	diisopropyl azodicarboxylate
DIBALH	diisobutylaluminum hydride
DIP	diisopinocampheyl
DMA	*N,N*-dimethyl acetamide
DMAP	4-(dimethylamino)pyridine
DMB	3,4-dimethoxybenzyl
DMDO	3,3-dimethyldioxirane
DME	1,2-dimethoxyethane
DMF	*N,N*-dimethylformamide
DMP	Dess-Martin periodinane
DMSO	dimethyl sulfoxide
Dppf	1,1'-ferrocenylbis(diphenyl-phosphine)
dr	diastereomeric ratio
EBTHI	ethylenebis(tetrahydroindenyl)
EDCI	1-ethyl-3-(3-dimethylaminopropyl)carbodiimide monohydrochloride
EDTA	ethylenediaminetetraacetic acid
ee	enantiomeric excess
Epo	epothilone
equiv	equivalent(s)
HBTU	*O*-benzotriazolyl-*N,N,N',N'*-tetramethyl-uronium-hexafluoro-phosphate
HMPA	hexamethylphosphoric triamide
HOBt	*N*-hydroxybenzotriazole
HWE	Horner-Wadsworth-Emmons
Ipc	isopinocampheyl

KHMDS	potassium hexamethyldisilazide
LDA	lithium diisopropylamide
LHMDS	lithium hexamethyldisilazide
m-CPBA	*m*-chloroperoxybenzoic acid
MOM	methoxymethyl
Ms	methanesulfonyl (mesyl)
NaHMDS	sodium hexamethyldisilazide
NIS	*N*-iodosuccinimide
NMO	*N*-methyl morpholine
NMP	1-methyl-2-pyrrolidinone
PDC	pyridinium dichromate
PMB	4-methoxybenzyl
PPTS	pyridinium *p*-toluenesulfonate
Py	pyridine
RCM	ring-closing metathesis
Red-Al	sodium bis(2-methoxyethoxy)aluminium hydride
rt	room temperature
TBAF	tetrabutylammonium fluoride
TBS	*tert*-butyldimethylsilyl
TBDPS	*tert*-butyldiphenylsilyl
TEMPO	2,2,6,6-tetramethyl-1-piperidinyloxy
TES	triethylsilyl
Tf	trifluoromethanesulfonyl (triflyl)
TFA	trifluoroacetic acid
THF	tetrahydrofuran
THP	tetrahydropyran-2-yl
TIPS	triisopropylsilyl
TMS	trimethylsilyl
TMSE	2-(trimethylsilyl)ethyl
Tol	4-methylphenyl
Tr	triphenylmethyl
Tris	2,4,6-triisopropylbenzenesulfonyl
Troc	2,2,2-trichloroethyloxycarbonyl
Ts	tosyl, 4-toluenesulfonyl

1 Introduction

Macrolides – highly oxygenated and stereochemically elaborate polyketides with a macrocyclic lactone as a core structure [1] – have attracted a great deal of interest over the last decades, either for their structural complexity, as challenging and interesting targets for synthetic chemists, or due to their bioactivity and enormous potential as drug leads or future drugs, for instance as antibiotics (for reviews on macrolide antibiotics see [2, 3], or on tumor therapy [4, 5]). Among this chemically interesting structural class of compounds, some demonstrate very potent cancer cell inhibitory activity and therefore might represent promising lead structures for new

chemotherapeutic agents. For most of these macrolides the modulation of the dynamics of the two major cytoskeletal proteins, tubulin and actin, are considered to be their predominant modes of action. In the following article we will focus on four groups of macrolide-based microtubule-interacting agents that are derived from the natural products epothilone A (**1**) and B (**2**), laulimalide (**3**), dictyostatin (**4**), and peloruside A (**5**).

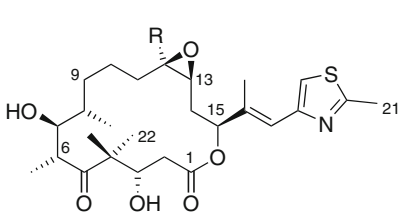

R = H: epothilone A (**1**)
R = Me: epothilone B (**2**)

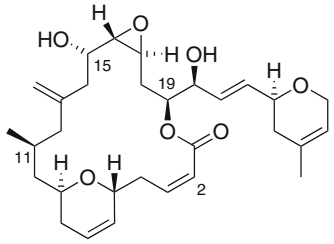

laulimalide (**3**)

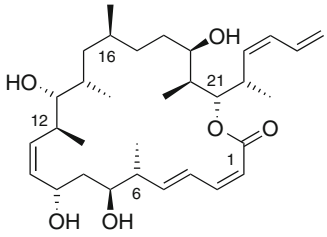

dictyostatin (**4**)

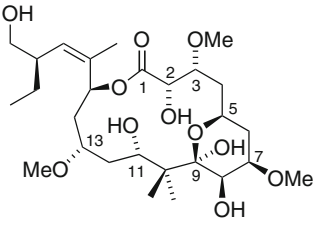

(+)–peloruside A (**5**)

Among these four groups of compounds, the epothilones have received the most attention so far (for a recent review on the chemistry and biology of epothilone see [6, 7]). They were isolated from the cellulose-degrading myxobacterium *Sorangium cellulosum* Soce90 as part of a joint research effort between the groups of Reichenbach and Höfle at the Gesellschaft für Biotechnologische Forschung[1] in Braunschweig, Germany, in the late 1980s [7–9]. Today at least seven epothilone-derived agents have entered clinical evaluation in humans as potential anticancer drugs with one derivative obtaining FDA approval last year for the treatment of breast cancer [7, 10]. In contrast to epothilones, laulimalide, dictyostatin, and peloruside A are all of marine origin and were isolated from a variety of sponges, or organisms associated with them [4–12]. These natural products act on the tubulin/microtubule system in a similar way as the previously discovered microtubule-stabilizing agent taxol (paclitaxel, Taxol®)[2] [11–15].

[1] Now Helmholtz Centre for Infection Research.

[2] The name Taxol® is a protected trademark of Bristol-Myers Squibb and it refers to the drug paclitaxel in its final clinical formulation. Paclitaxel is identical with the compound "taxol" as it was first reported in the scientific literature in 1971 by Wani et al. [12]. As this occurred long before the drug Taxol® was introduced to the market we prefer to maintain the name taxol for the compound throughout this article. This should not be considered as an infringement of the BMS trademark.

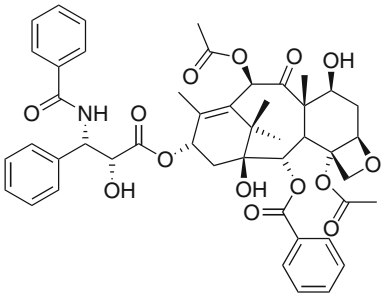

taxol

Taxol was the first compound identified to act on tubulin as a so-called microtubule-stabilizing agent and is arguably one of the most important anticancer drugs brought into the clinic in the last two decades [16]. Taxol is a complex diterpene and was first isolated in 1971 from the bark of the Pacific yew *Taxus brevifolia* by Wani et al. [17]. After evaluation by the National Cancer Institute it was prioritized for preclinical development in 1977. Horwitz et al. [18, 19] in 1979 discovered the – at that time – unique mechanism of action, which involves the stabilization of microtubules under otherwise destabilizing conditions [16]. At the same time microtubule-stabilizing agents are able to promote the polymerization of soluble tubulin into microtubules or microtubule-like polymeric structures in the absence of factors that are normally required to initiate and sustain the polymerization process [20–24]. At the cellular level the effect of microtubule-stabilizing agents on microtubule dynamics leads to cell cycle arrest in mitosis and triggers cell death through apoptosis [20–24]. Mitotic arrest is associated with anomalous spindle formation, thus clearly associating inhibition of cell proliferation with disturbance of microtubule functionality. It is often assumed that apoptosis induced by microtubule-stabilizing agents is a direct consequence of G2/M *arrest*, which in turn would be a prerequisite for growth inhibition and cell death. However, Horwitz and co-workers in a series of recent experiments elegantly demonstrated that the situation is certainly more complex [25, 26]. Thus, the treatment of human cancer cells with low concentrations of microtubule-stabilizing drugs can lead to mitotic slippage (i.e. aberrant mitosis after formation of multipolar spindles) and subsequent cell cycle arrest in G1. Apoptosis then occurs from this arrested G1 state. On the other hand, higher drug concentrations lead to a protracted mitotic block from which the cells eventually exit without division, thus forming tetraploid G1 cells [26], which will then undergo apoptosis. Based on these results it is clear that *entry* of cells into mitosis is a fundamental prerequisite for cell killing by microtubule-stabilizing agents, but that apoptosis does not necessarily occur from a G2/M arrested state.

2 Epothilones

As indicated above, epothilones are microtubule-stabilizing agents that were discovered by Höfle and Reichenbach at the "Gesellschaft für Biotechnologische Forschung (GBF)" in Braunschweig, Germany in 1987. In a screen for antifungal agents Höfle

and Reichenbach identified epothilone A (Epo A) and B (Epo B) as bioactive components from extracts of the cellulose-degrading myxobacterium *Sorangium cellulosum* Soce90, collected along the Zambezi river in southern Africa [7–9]. Although the activity of epothilones against human cancer cells was known for several years before, it was not until 1995 that Bollag et al. identified these compounds as being microtubule-stabilizing agents with a "taxol-like" mechanism of action [13]. Interestingly, epothilones offer some distinct advantages over taxol, which makes them extremely valuable lead structures for further development into anticancer drugs. Their low susceptibility to P-glycoprotein (Pgp)-mediated drug efflux let epothilones retain near to full activity against Pgp-overexpressing, taxol-resistant cell lines [13, 27–29]. In addition, they are unaffected by certain tubulin mutations that render taxanes inactive and they also show better water-solubility. They can thus be administered without the use of problematic formulation vehicles such as Cremophor EL® (polyethoxylated castor oil), which are believed to be responsible for negative side effects in taxane treatment [16].

2.1 Synthesis of Natural Epothilones

After publication of the absolute configuration of Epo A and B in 1996 [30], the first total syntheses were presented by the groups of Danishefsky, Nicolaou, and Schinzer in a matter of months [31–40]. First generation approaches to the synthesis of epothilones made use of three different types of macrocyclization reactions (Fig. 1), namely RCM (ring closing metathesis) for the formation of a C12–C13 double bond (**A**), macrolactonization (**B**), or the formation of the C2–C3 bond through intramolecular aldol reaction (**C**). This was then usually followed by deprotection of the hydroxyl functionalities and epoxidation of the double bond

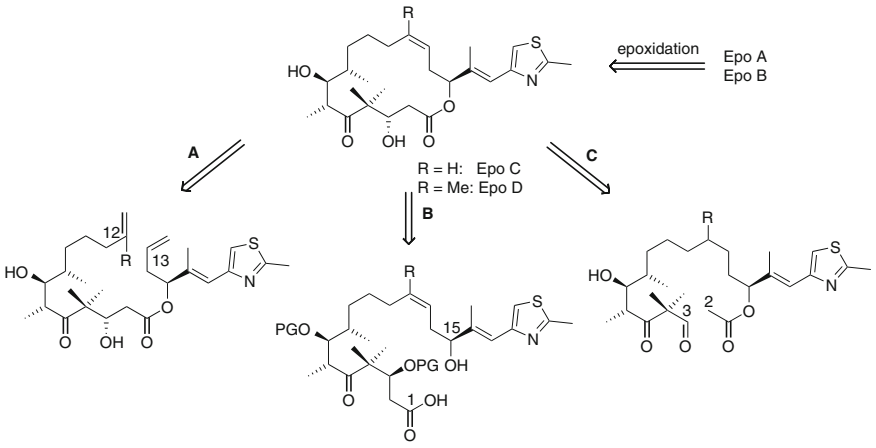

Fig. 1 First-generation strategies for the total synthesis of epothilones (PG = protecting group)

between C12 and C13. In a second synthesis of Epo A by Nicolaou et al. [34] (Scheme 1), the dianion of carboxylic acid **6** reacted with α-chiral aldehyde **7** to yield aldol product **8** as the major isomer (dr = 2:1). Esterification of acid **8** with side chain fragment **9** yielded RCM precursor **10** in 45% overall yield from **6**. Subsequent RCM then furnished a mixture of **11** (50%) and its *E*-isomer (35%). After chromatographic separation and TBS-deprotection with CH_2Cl_2/TFA the unsaturated **12** was finally epoxidized with *m*-CPBA in CH_2Cl_2 to afford Epo A (**1**) in 55% yield.

Recent syntheses have been exploiting several other methods to build up the macrocycle. In Mulzer's second generation synthesis the epoxide moiety is introduced at an earlier stage before the macrocycle is closed [41, 42], while RCM of an already epoxidized substrate was shown by Sun and Sinha [43] to be yet another option. Numerous other approaches have been explored in the syntheses of a host of closely related epothilone analogs, where RCM between C9 and C10 as well as C10–C11 have been employed to close the macrocycle and generate unsaturated derivatives, which could in turn be reduced to the saturated compounds [44, 45]. Forming the C12–C13 bond via alkyne metathesis has been another very inventive

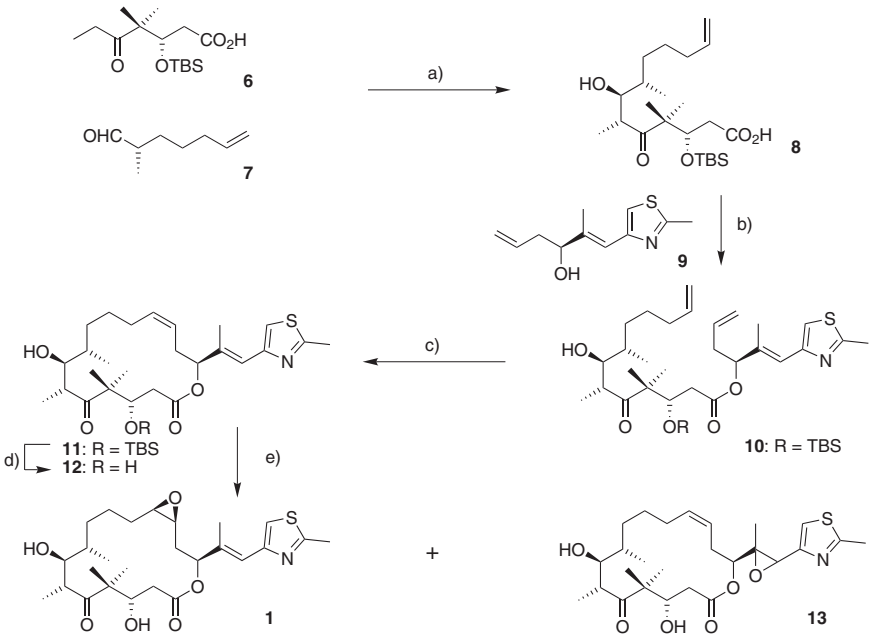

Scheme 1 **a** 2.2 equiv LDA, THF −78 → −40 °C, 0.5 h. then 1.2 equiv of **7** in THF −78 → −40 °C, 0.5 h. **b** 2.0 equiv **9**, 1.5 equiv DCC, 1.5 equiv DMAP, toluene, 25 °C, 12 h. **5** (45% overall yield from **6**) and (6*S*,7*R*)-diastereomer of **10** (25% overall yield from **6**). **c** **10** (0.006 M in CH_2Cl_2) 15 mol% Grubbs first generation catalyst, 25 °C, 8 h, 50% plus *trans*-isomer of **11** (35%) **d** TFA (20 vol%), CH_2Cl_2, 0 °C, 4 h, 98%. **e** 1.1 equiv *m*-CPBA, benzene, 0 °C. 20 h, **1** (55%) and 12α,13α-epoxide (20%) plus regioisomeric epoxide **13** (20%) [32]

strategy to control elegantly *E/Z*-selectivity of the double bond between C12 and C13. This strategy devised by Fürstner et al. paves the way to the required *Z*-selectivity between C12 and C13, which can be achieved by catalytic reduction of the triple bond [46, 47].

2.2 C12–C13 Modifications

A large part of the early work on the epothilone SAR was focused on structural variations around the epoxide moiety of the natural compounds. One of the most important results that emerged from those early studies was the fact that "deoxyepothilones" (Epo C and D) possess potent biological activity similar to that of the epoxide containing compounds [36, 40, 48–50]. Although Epo C and Epo D can also be isolated from the fermentation broths of myxobacteria [51] it was only because of their availability as synthetic intermediates on the way to Epo A and B that their favorable in vitro pharmacological profiles became obvious. The IC_{50}s of Epo D for human cancer cell growth inhibition are in the low nanomolar range and it retains full activity against Pgp-overexpressing multidrug-resistant cells. Intrigued by its promising properties after in vitro profiling, extensive in vivo studies were conducted by the Sloan Kettering group showing that compound **14** (Epo D) is a highly effective antitumor agent [52, 53] in mouse models of human cancer. **14** has entered clinical trials in humans, but the clinical development of the compound was recently terminated [54–56]. At the same time the BMS group was able to demonstrate that access to the deoxyEpos is also possible via semisynthesis [57]. The efficient deoxygenation protocols they developed for Epo A as well as Epo B allow a one step transformation of these compounds into the respective deoxy-congeners Epo C and D (Scheme 2).

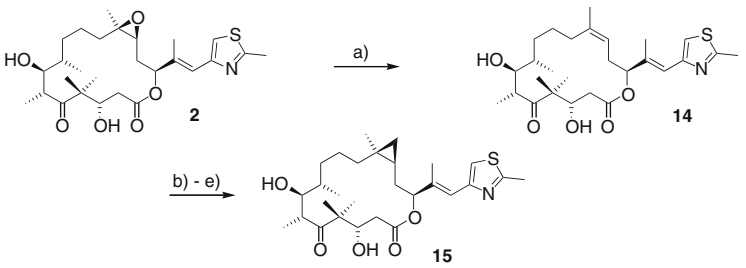

Scheme 2 **a** WCl_6, *n*-BuLi, 78%. **b** TBS-OTf, 2,6-lutidine, CH_2Cl_2, 0 °C. **c** Benzyltriethylammonium chloride, 50% NaOH (aq), $CHBr_3$, 45 °C (ca. 30%). **d** Bu_3SnH, AIBN, 70 °C. **e** 20% TFA/CH_2Cl_2, −15 °C [57]

At the same time, the Danishefsky group, who did not have access to biologically produced Epo B, continuously improved their synthetic strategy towards Epo D. The aim of these efforts at that time was to deliver sufficient material for extensive in vivo studies and eventual clinical trials, which required a concise and scalable synthesis of **14**. Selectivity-enhancing elements of a new macrolactonization-based approach (Scheme 3) were an improved aldol reaction for the formation of C6–C7 bond (dr = 5.5:1) and a highly selective reduction of a keto-group using Noyori methodology to introduce the chiral center at C3 [58, 59].

This strategy was also applied to the synthesis of Epo F (21-hydroxy-Epo B), but was accompanied by unexpected side reactions in the Noyori reduction step [60]. As a consequence, the Danishefsky group developed an alternative protocol to establish the chiral center at C3, which relied on aldol chemistry developed by Duthaler and co-workers (Scheme 4). This methodology could be successfully employed to elongate aldehyde **23** with *tert*-butyl acetate to provide the desired aldol product with >20:1 selectivity. This aldol product could then be elaborated into the Suzuki-Miyaura precursor **24** and ultimately into dEpo F (**25**).

Apart from giving improved access to the natural products Epo B and Epo D, Nicolaou's second generation approach to epothilones was also optimized for the production of C26-modified analogs of Epo B. Epo C and D (produced by semisynthesis) have also served as precursors for cyclopropyl epothilones such as **15** (Scheme 2). The IC_{50} value of **15** against the human colon carcinoma cell line HCT-116 is 1.4 nM, compared to 4.4 nM and 0.8 nM for Epo A (**1**) and Epo B (**2**),

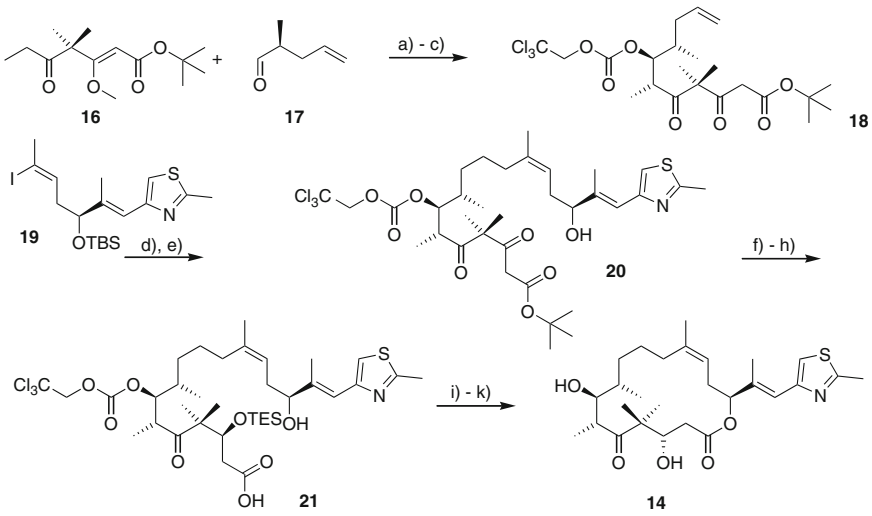

Scheme 3 **a** LDA, -120 °C, 50–60%. **b** Troc-Cl, py, 0 °C. **c** *p*-TsOH, acetone, 87% (two steps). **d** 9-BBN; Cs_2CO_3, $Pd(dppf)_2Cl_2$, Ph_3As, DMF, water, ca. 75%. **e** 0.5 M HCl–MeOH, 85%. **f** $[RuCl_2((R)\text{-BINAP})_2][Et_3N]$, H_2, 1200 psi, MeOH, HCl, 82–88% (de >95%). **g** TES-OTf, 2,6-lutidine, −78 °C → rt. **h** 0.1 M HCl–MeOH, 70–77% (two steps). **i** 2,4,6-$Cl_3C_6H_2C(O)Cl$, Et_3N, DMAP, 78%. **j** SmI_2 (cat) NiI_2, −78 °C, 90–95%. **k** HF·py, 0 °C, 98% [247]

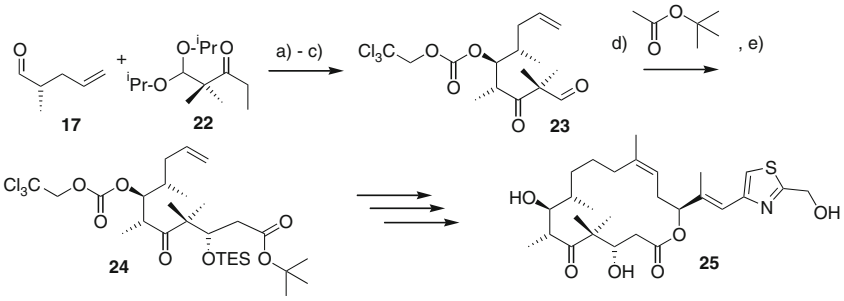

Scheme 4 **a** LDA, −78 °C, 85%, dr = 4:1. **b** TrocCl, py, CH_2Cl_2, 0°C, 99%. **c** THF/water (cat) TsOH, 88%. **d** $CpTiCl(OR)_2$ (R = 1,2:5,6-di-*O*-isopropylidene-α-l-glucofuranos-3-*O*-yl), THF, −78 °C, 89%, dr >20:1. **e** TESCl, imidazole, DMF, 96% [248]

respectively [57]. This finding indicates that the epoxide ring of the natural epothilones rather than acting as a hydrogen bond acceptor or a reactive electrophile merely serves to stabilize the proper bioactive conformation of the macrolactone ring.

Apart from deoxy and cyclopropyl analogs of epothilones an additional very potent class of analogs are derived from the non-natural 12,13-*trans* analog of Epo A, which was first obtained as a side product in the synthesis of epothilones. *Trans*-Epo A (**36**) was first reported to be virtually equipotent with Epo A on an ovarian (1A9) and breast cancer (MCF-7) cell line by Nicolaou et al. [38], but the stereochemistry of the active epoxide isomer remained unassigned. To address this question and also to provide a synthetic basis for the development of additional analogs with a *trans*-epoxide moiety the group at Novartis (Altmann and co-workers, now at the ETH Zürich) devised a stereoselective synthesis of *trans*-Epo A (Scheme 5) [61]. The key steps of this synthesis are a highly stereoselective aldol reaction between Schinzer ketone **26** and aldehyde **27** (>20:1 selectivity) and the B-alkyl Suzuki coupling between olefin **29** and *trans*-vinyl iodide **30** to produce **31** in 61% yield. While the elaboration of compound **32** into *trans*-deoxy Epo A (**34**) was straightforward (38% over four steps), the final stereo- and regioselective epoxidation was rather problematic. Although selectivity in this step was good (8:1–10:1), employing catalyst **35** [62, 63], the product could only be obtained in low yield (27% for an 8:1 mixture of isomers, 54% based on recovered starting material, 11% of the desired isomer after HPLC-purification). In this context it should be mentioned that the aldol reaction between aldehyde **7** (Scheme 1) and Schinzer ketone **26** provides an epothilone A precursor with excellent selectivity (dr = 24:1).

(12*S*, 13*S*)-*trans*-Epo A (**36**) is a strong inducer of tubulin polymerization in vitro and exhibits potent antiproliferative activity, whereas its (12*R*,13*R*)-isomer is at least 500-fold less active. **36** in fact shows slightly higher growth inhibitory activity than Epo A and this rank order of activity was observed over a wide range of human cancer cell lines (e.g. IC_{50}-values against the human epidermoid carcinoma cell

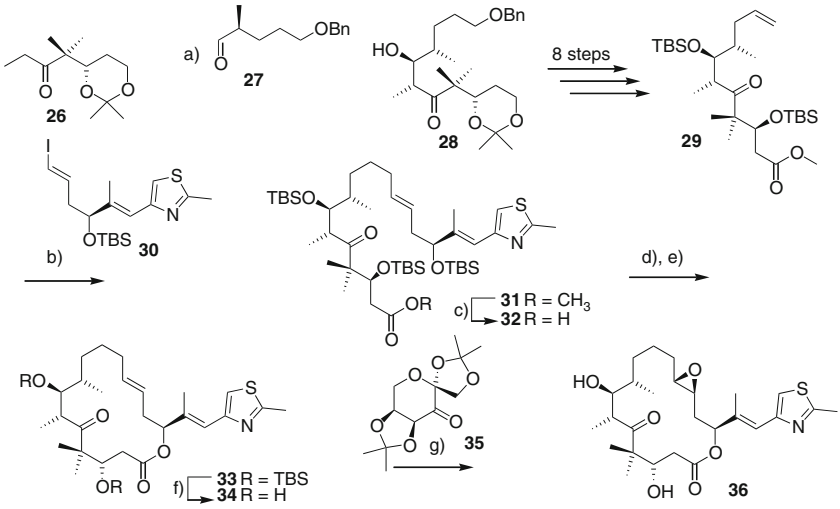

Scheme 5 **a** LDA, THF, −78 °C, 82% **b** (1) Olefin **29**, 9-BBN, THF, rt; (2) Cs_2CO_3, $PdCl_2(dppf)_2$, Ph_3As, vinyl iodide **30**, DMF, −10 °C→ rt, 63%. **c** LiOH (6 equiv), *i*-PrOH/water 4:1, 50 °C, 85%. **d** TBAF, THF, 64%. **e** 2,4,6-$Cl_3C_6H_2C(O)Cl$, Et_3N, DMAP, THF/toluene, 61%. **f** TFA/CH_2Cl_2, 91%. **g** Oxone®, **35** (30 mol%) (cat) Bu_4NHSO_4, K_2CO_3, CH_3CN/DME/0.05 M $Na_2B_4O_7 \cdot 10\ H_2O$ in 4×10^{-4} M Na_2EDTA 2:1:2, rt, 1 h, 27% (dr ca.8:1; 50% recovered starting material) [61]

lines KB-31/KB-8511 are 2.0/1.8 nM for Epo A (**1**) and 1.0/0.8 nM for **36**, respectively) [61].

After the assignment of the absolute configuration of the epoxide moiety in *trans*-Epo A (**36**), Nicolaou et al. developed a convergent approach for the synthesis of a series of side chain modified *trans*-cyclopropyl Epo A analogs [64]. Given the poor yields obtained in the direct cyclopropanation of Epo C and D [57], Nicolaou's synthesis relied on the early stereoselective introduction of the cyclopropane moiety (Scheme 6) via Charette cyclopropanation. The side chain was introduced as a single building block in a Nozaki-Hiyama-Kishi coupling. Although the stereogenic center at C15 was still undefined at that point, subsequent oxidation with DMP and stereoselective reduction furnished the desired configuration, thus leading to the aldol precursor **47**. Ketone **48** effected high aldol selectivity, which led to essentially one isomer (as determined by ^{1}H-NMR spectroscopy). The *trans*-cyclopropyl-Epo A derivatives synthesized in this manner, including a number of pyridine-based analogs, all showed highly potent biological activity, which in some cases was even comparable with that of Epo B.

A fundamentally different approach for substituting the C12–C13 region with other functionalities is the disruption of the polyketide backbone by the introduction of an amide bond as a polar isostere for the *cis* double bond in the deoxy epothilone series [65, 67]. While these amide-based analogs proved to be virtually inactive [65, 67], 12-aza-analogs with higher activity could be obtained by removal of the C13 keto group of the amide moiety and substitution of N12 with alkyl- or

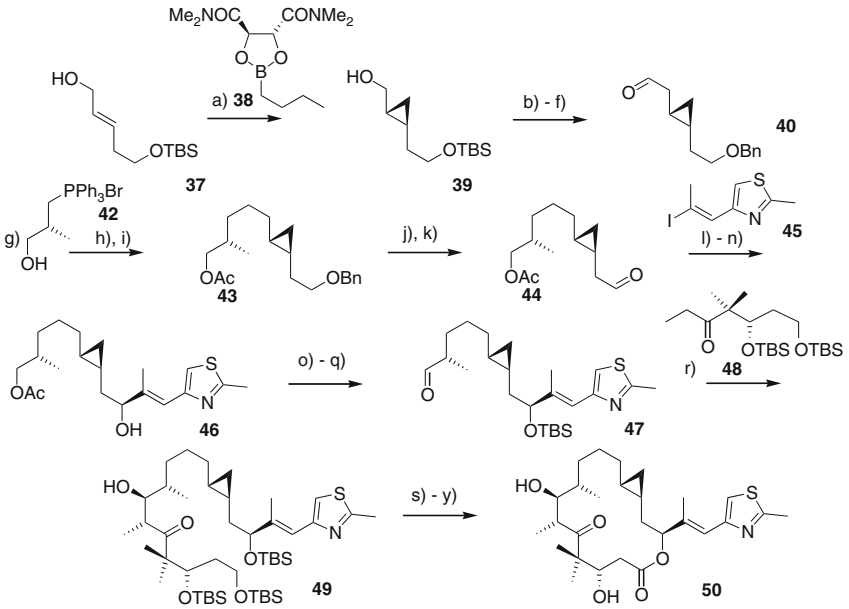

Scheme 6 **a** DME, Et_2Zn, CH_2I_2, CH_2Cl_2, 98% (ee >90%). **b** Et_3N, SO_3·py, CH_2Cl_2/DMSO 4:1, 0 °C. **c** $MeOCH_2PPh_3Cl$, NaHMDS, THF, –40 °C → 25 °C, 81% (two steps). **d** TBAF, THF, 25 °C. **e** NaH, BnBr, THF/DMF 5:1, 0 °C → 25 °C. **f** (cat) HCl, acetone/water 9:1, 50 °C. **g** NaHMDS, TMSCl, THF, 58% (four steps). **h** $(NCO_2K)_2$, HOAc, MeOH, py, 25 °C. **i** Ac_2O, Et_3N, DMAP, CH_2Cl_2, 0 °C. **j** 20% $Pd(OH)_2$/C, H_2 (1 atm), EtOAc/EtOH 1:1 25 °C, 98% (three steps). **k** DMP, CH_2Cl_2, 0 °C → 25 °C. **l** $CrCl_2$, (cat) $NiCl_2$, DMSO, 25 °C, 91% (two steps). **m** DMP, CH_2Cl_2, 0 °C → 25 °C, 83%. **n** (–)-DIPCl, Et_2O, –15 °C → 25 °C, 84%. **o** TBS-OTf, 2,6-lutidine, CH_2Cl_2, –78 °C, 91–100%. **p** DIBAL, CH_2Cl_2, –78 °C, 93–96%. **q** DMP, CH_2Cl_2, 25 °C. **r** LDA, THF, –78 °C, 4 min, 70%. **s** TBS-OTf, 2,6-lutidine, CH_2Cl_2, –25 °C → 25 °C, 94%. **t** HF·py, py, 0 °C → 25 °C. **u** DMP, $NaHCO_3$, CH_2Cl_2, 25 °C. **v** $NaClO_2$, 2-methyl-2-butene, NaH_2PO_4, *t*-BuOH/water 4:1, 25 °C, **w** TBAF, THF, 25 °C. **x** 2,4,6-$Cl_3C_6H_2C(O)Cl$, Et_3N, THF, 0 °C, then DMAP, toluene, 75 °C, 53% (five steps). **y** 25% TFA in CH_2Cl_2, 25 °C, 73% [64, 94, 95]

alkoxycarbonyl groups. This kind of modification leads to analogs in which the carbonyl oxygen atoms of the N-substituent might adopt the role of the epoxide oxygen in natural epothilones (Scheme 7).

The "azathilones" **54** thus obtained can retain significant antiproliferative activity against human cancer cells, with IC_{50} values <100 nM in the most favorable cases investigated so far (compounds **54a**, **54c** and **54f**) [65, 66]. In particular, *tert*-butyl carbamate **54a** proved to be only 15-fold less active than Epo A against the human cervix carcinoma cell line KB-31 (IC_{50} ~30 nM vs 2.1 nM for Epo A), making it roughly equipotent with Epo C. Activity against Pgp-overexpressing cell lines is somewhat compromised for all of these "azathilone" derivatives, which probably mirrors a general trend observed for more polar epothilone analogs to show higher susceptibility to Pgp efflux.

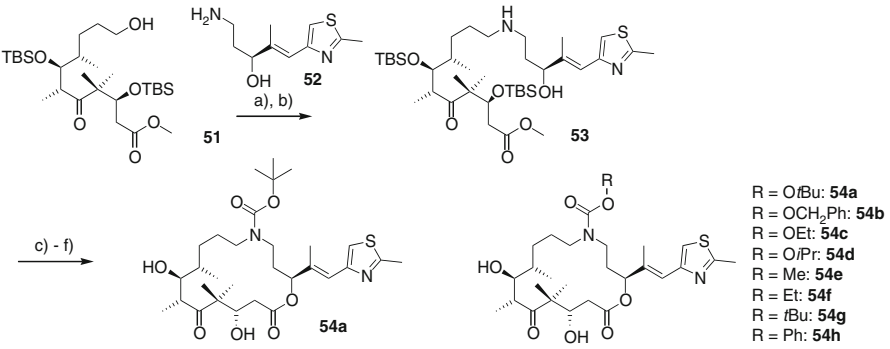

Scheme 7 **a** Ms-Cl, Et_3N, CH_2Cl_2, 0 °C, 1 h, 91%. **b** **52**, MeOH, 70 °C, 24 h, 30%. **c** Boc_2O, Et_3N, CH_2Cl_2, rt, 2 h, 49%. **d** LiOH (6 equiv), *i*-PrOH/water 4:1, 55 °C, 16 h, 83%. **e** (1) 2,4,6-$Cl_3C_6H_2C(O)Cl$, Et_3N, THF, 0 °C, 15 min; (2) dilute with toluene, add to solution of DMAP in toluene, 75 °C, 3 h, 90%. **f** HF·py, THF, rt, 17 h, 22% [65, 97]

2.3 C9–C11 Modifications

Another structural sub-domain of the epothilone scaffold, where structural modification has led to interesting effects on the antiproliferative activity of the resulting analogs, is the C9–C11 trimethylene segment. Initial efforts towards derivatization in this region were focused on changes in ring-size by introducing and removing methylene units in the C9–C11 segment (e.g. **55** and **56**) [50, 68]. All of these initial analogs showed substantially decreased activity. Also investigated was the stabilization of the purported bioactive conformation in this region, based on pharmacophore modeling. The design of such analogs (e.g. **57**) originated from the basic hypothesis that the C9–C11 region represents the site of highest conformational mobility in the epothilone macrocycle, implying that the introduction of appropriate conformational constraints in this part of the structure should lead to analogs with improved biological activity [69, 70]. However, compound **57** proved to be completely inactive. The reasons for the loss in activity can only be speculated about; they might be due to the incompatibility of the bulky phenylene moiety with the spatial requirements of the tubulin binding site.

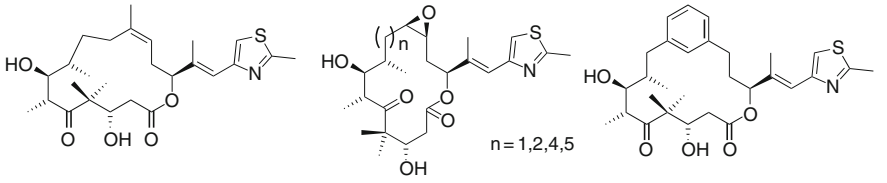

In contrast to these disappointing findings, more recent studies have shown that other types of modifications in the C9–C11 region are well tolerated. In particular, the introduction of *trans*-double bonds between C9 and C10 or C10 and C11, respectively, has proven to be an attractive approach to enhance antiproliferative activity in vitro as well as in vivo. The pharmacological profiles of these didehydro compounds in some cases were found to be superior to those of their saturated congeners Epo B and D. Access to this class of epothilones is possible either via isolation from the fermentation products of bacterial strains [71, 72] or by total chemical synthesis as demonstrated by the Danishefsky group [45, 73–78].

Thus, the unsaturated compound Epo 490 (**58**) was first isolated as a minor fermentation product from a strain of *Myxococcus xanthus* which had been genetically modified such as to express the epothilone polyketide synthase from *Sorangium cellulosum*. After further engineering of the (Epo D producing) respective *Myxococcus* strain and deactivation of an enoyl reductase, which is responsible for the reduction of the C10–C11 *trans*-double bond, it was possible to obtain a strain which produces Epo 490 (**58**) as the major product [79]. The activity of this Epo analog is only three- to fourfold lower than that of Epo D against a variety of human cancer cell lines [79].

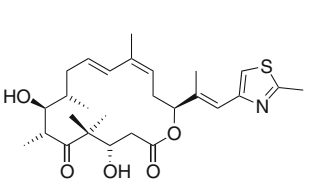

epothilone 490 (**58**)

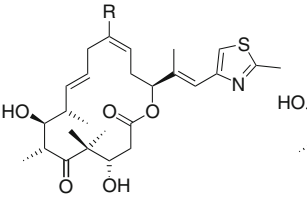

R = Me: **59**
R = CF_3: **60**

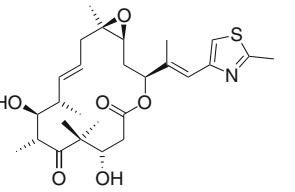

61

The corresponding Epo C derived doubly unsaturated compound Epo 475 (without the methyl group at C12) had previously been isolated from the cultures of myxobacterium *Sorangium cellulosum* by Höfle and Reichenbach and had been proven to possess potent antiproliferative activity against a mouse fibroblast cell line [51]. The total synthesis of Epo 490 has been reported by Danishefsky et al. based on their second generation synthesis of Epo D and employing RCM for ring-closing between C10 and C11. While exhibiting potent in vitro cytotoxicity, in vivo experiments gave disappointing results. There was practically no observable effect on xenograft tumors in mice and further investigation showed that the overall pharmacokinetic properties were unfavorable [45, 73, 80].

Subsequent research by the Sloan-Kettering group showed that Epo 490 was not the only interesting epothilone analog with unsaturation between C9 and C11. In fact they discovered what they called a "highly promising family of second generation epothilones". Building on the macrocycle formation through RCM between C9 and C10, they were able to provide *trans*-9,10-didehydro-analogs of Epo D and B (e.g. **59**, **61**) (Scheme 8) [44, 45, 76].

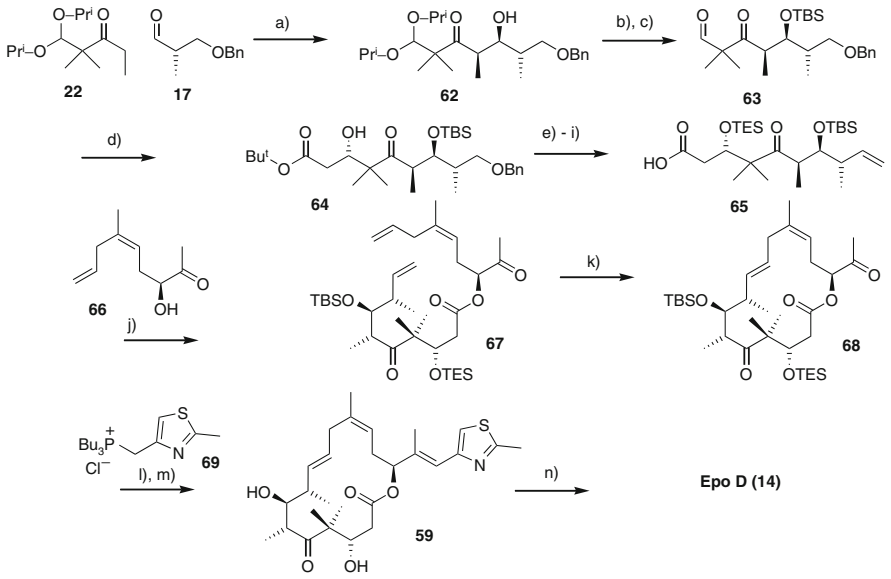

Scheme 8 **a** LDA, THF, −90 °C (78% based on aldehyde). **b** TBS-OTf, 2,6-lutidine, CH_2Cl_2, −40 → −20 °C, 97%. **c** (cat) *p*-TsOH/water, THF/water (4:1), 64 °C, 98% (two steps, 95%). **d** *tert*-butyl acetate, LDA, $CpTiCl(OR)_2$ (*R* = 1,2:5,6-di-*O*-isopropylidene-α-l-glucofuranos-3-*O*-yl), Et_2O, −78 °C, 86% (dr >20:1). **e** TESCl, imidazole, DMF, 0 °C → rt, 98%. **f** H_2, Pd/C (10%), EtOH, 83%. **g** TPAP, NMO, CH_2Cl_2, 95%. **h** $MePPh_3I$, *n*-BuLi, THF, −78 → −5 °C, 78% (four steps, 60%). **i** TES-OTf, 2,6-lutidine, CH_2Cl_2, 0 °C → rt. **j** EDCI, DMAP, CH_2Cl_2, **65**, 0 °C → rt (81% two steps). **k** Grubb second generation catalyst, toluene, 110 °C, 20 min, 78%. **l** KHMDS, **69**, THF, −78 → −20 °C, 76%. **m** HF·py, THF, 97% (two steps, 74%). **n** $TrisNHNH_2$, Et_3N, $ClCH_2CH_2Cl$, 50 °C, 91% [76]

The two compounds were superior to the parent epothilones D and B in cellular proliferation assays and thus represented highly promising candidates for further investigation and development. In light of these findings an optimized synthetic route to 9,10-didehydro analogs was developed by Danishefsky and co-workers [76]. While their first synthesis of C9–C10 unsaturated epothilones was hampered by selectivity problems in the RCM step (extrusion of the thiazole side chain), they were able to carry out *E*-selective RCM with a ketone precursor **67**. This allowed for a late introduction of the thiazole side chain, thus preventing the RCM problems. Other crucial steps of this sequence are two aldol reactions to furnish the stereocenters at C6/C7 and C3 respectively. The first of these reactions uses chiral pool derived aldehyde **17** and ketone **22**, whose aldol reaction gave the desired diastereomer in a 85:15 ratio. As expected the Duthaler aldol reaction [81] of **63** with *tert*-butyl acetate provided the desired aldol product with excellent selectivity (>20:1). The RCM reaction with triene **67** eventually furnished **68** with high *E*-selectivity, which could then be converted into the respective 9,10-didehydro-analog of Epo D (**59**) and also Epo D (**14**) itself. Biological evaluation of **59** and **61** showed that the in vitro antiproliferative activity of both these compounds was improved compared to Epo D and B (IC_{50}: 0.9 nM for **59** vs 3.6 nM for Epo D (**14**)

[45, 76, 78]. This improved activity can be accounted for by considering recent spectroscopic findings, which hint at *anti*-periplanar conformations around the C9–C10 and C10–C11 bonds in the tubulin-bound structure of epothilones [82]. Further evidence, which corroborates this hypothesis is the decreased activity of the *cis*-9,10-didehydro-Epo D, which is ~30-fold less active than Epo D [83]. (Note that the compound assumed to be *trans* in [83] was later found to be the *cis*-isomer [84].) Apart from the promising in vitro results initial experiments also hinted at improved in vivo activity of **59** and **61** over Epo D and B, respectively. Both compounds have shown to exhibit potent antitumor activity in the human breast cancer model MX-1, where the effect of **59** has been ascribed to the combined effects of enhanced antiproliferative activity and plasma stability in rodents [76, 80]. Although the development of **59** as a potential drug candidate might be hampered by the fact that in these experiments **59** was associated with significant toxicity [44] the compound is now being evaluated in the clinical setting (phase I clinical trials as KOS-1584).

One remarkable extension of this work and probably the most promising result generated in the context of 9,10-didehydro epothilones is the discovery of the extremely favorable pharmacological profile of "fludelone"(**60**), the C26-trifluoro analog of **59**. Synthesized based on the same strategic principles (Scheme 8) as with **59**, this fluoro analog exhibits a remarkably broad therapeutic index in in vivo xenograft models. In contrast to **59**, fludelone could be administered at higher doses because of its excellent tolerability and in MX-1 xenografts effected complete tumor disappearance without relapse [44]. Another advantage of fludelone seems to be the high oral bioavailability. Because of its excellent antitumor effects in vivo (the observed in vitro activity is somewhat smaller than for its non-fluorinated parent compound **59**) fludelone might eventually be recognized as a major milestone in epothilone-based anticancer drug discovery.

2.4 C1–C6 Modifications

The clinically most relevant modification of the epothilone macrocycle so far has been the replacement of the lactone oxygen by a nitrogen to produce Epo B lactam **71** (Scheme 9) [85]. This modification was reportedly designed in order to overcome

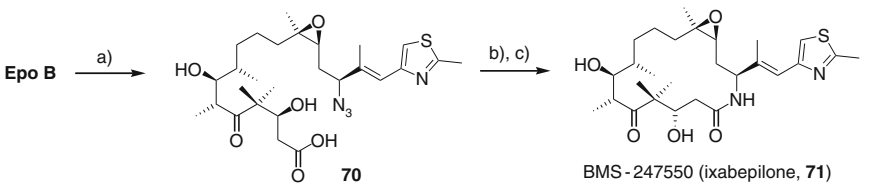

Scheme 9 **a** $[Pd(PPh_3)_4]$, NaN_3, 45 °C, 60–70%. **b** Me_3P, 71%. **c** EDCI, HOBt, 65% [85]

the limited plasma stability of Epo B in rodents [85]. However, despite its limited plasma stability, Epo B exhibits very potent antitumor activity in mice and its deoxy analog Epo D has been found to be significantly more stable in human than in rodent plasma [15, 86, 87], this indicating that lactone-based macrocycles (including Epo B itself) may not be metabolically unstable in humans. This observation is corroborated by the fact that Epo B has entered phase III clinical trials. A semisynthetic approach to BMS-247550 (**71**) has been developed (Scheme 9) by the BMS group which exploits the fact that the ester at C1 is allylic in nature, thus rendering it easily cleavable by Pd-catalysis [85]. Reaction of Epo B (**2**) with NaN_3 in the presence of $[Pd(PPh_3)_4]$ proceeds with complete retention of configuration at C15 and without affecting the remaining functionalities of the molecule to provide **70**. The azide group could then be reduced to the amine, which was cyclized to yield the macrolactam. In addition to this three step semisynthetic approach, the Danishefsky group has also devised a synthetic strategy towards epothilone lactams [88]. BMS-247550 (**71**) is a potent inducer of tubulin polymerization, but its antiproliferative activity is about one order of magnitude lower than that of Epo B [85, 89]. In addition, the compound shows significantly reduced activity against multidrug-resistant cancer cell lines, thus indicating that **71** is a substrate for the Pgp-efflux pump [89]. In October of 2007 BMS-247550 (Ixempra®, ixabepilone, **71**) then was the very first epothilone-derived compound to obtain FDA approval for the use in patients with metastatic or locally advanced breast cancer [10].

Other intriguing structural modifications in the C1–C6 domain are connected to variations at C3. Initially the hydroxyl group attached to C3 had been proposed to be a site for hydrogen bonding with the carbonyl group at C1, which might lead to stabilization of the proper bioactive conformation by acting as a conformational constraint. More detailed investigations and the synthesis of 3-deoxy-3-cyano derivatives **73a** and **73b** clearly showed that this conformational constraint is not mandatory for activity [90]. While intramolecular H-bonding with the carbonyl group at C1 is not possible any more in these cyano analogs, they nevertheless exhibit potent antiproliferative activity. Thus **73a** is only twofold less potent than Epo A against the human colon carcinoma cell line HCT-116.

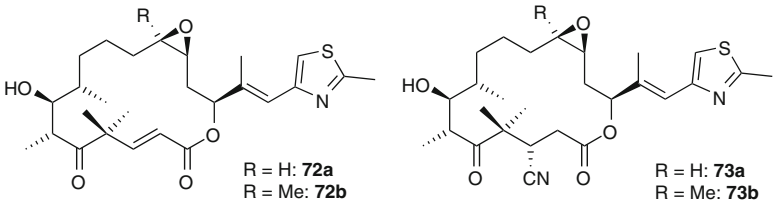

Interestingly, the corresponding 3-*R*-isomers of **73** no longer show any significant activity, neither in the tubulin polymerization assay nor in experiments with the human colon carcinoma cell line HCT-116 [90]. In the case of 3-deoxy-2,3-didehydro-Epo B (**72b**), the decrease in activity was similar to that of **73b**. It was fourfold less active than Epo B.

Analogs with a saturated C2–C3 bond, i.e. without any bond conformational constraint between C2 and C3, have recently been investigated by Altmann and co-workers as part of a more comprehensive program directed at the development of hypermodified epothilone analogs and, ultimately, of new scaffolds for microtubule inhibition. The overall synthetic strategy for the production of these analogs had been previously developed for the synthesis of *trans*-Epo A as well as a family of new side chain modified epothilone analogs (Scheme 5) [61, 91].

The western half of the molecule was obtained by aldol reaction between ketoester **74** and α-chiral aldehyde **27**. Subsequent Suzuki-Miyaura coupling to form the C11–C12 bond, saponification and cleavage of the TES-protecting group yielded the precursor for macrocyclization **77**. Yamaguchi macrolactonization was followed by protecting group removal and provided 3-deoxyEpo D. The desired target epothilone **78** was obtained after selective (9:1) epoxidation with the $MeReO_3$/H_2O_2/water system (Scheme 10). The IC_{50} values for inhibition of human cancer cell growth for 3-deoxyEpo B (**78**) are still in the nanomolar range as could be demonstrated with the human cervix carcinoma cell lines KB-31 and KB-8511. (**78**; IC_{50} [nM]: KB-31: 7.4; KB-8511: 4.0. Epo B (**2**); IC_{50} [nM]: KB-31: 0.29 KB-8511: 0.22). These results are clear evidence for the fact that a hard conformational constraint around the C2–C3 bond is not necessary for potent biological activity.

In the context of the Altmann group's efforts to develop epothilone analogs with a heteroatom-interrupted polyketide backbone, 4-aza analogs of Epo D (**83**) (Scheme 11) were investigated. As in many other cases, analog design was based on the NMR-derived bioactive conformation of tubulin bound Epo A [82]. In the solution phase NMR-structure of Epo A as reported by Carlomagno et al. the conformation about the C4–C5 bond is *syn*-periplanar and it appeared possible to efficiently mimic this geometry by introduction of an amide bond between N4 and C5. Modeling studies also indicated that a *cis*-amide bond in this position should allow the replacement

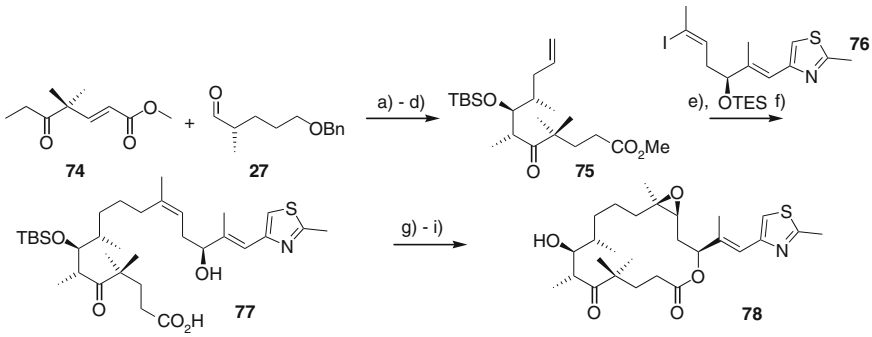

Scheme 10 **a** LDA, −78 °C, 58%. **b** TBS-OTf, 2,6-lutidine, −10 °C, 82%. **c** H_2, Pd/C, MeOH, 97%. **d** *o*-NO_2-(C_6H_4)SeCN, Bu_3P, $NaHCO_3$, H_2O_2, rt, 69%. **e** (1) 9-BBN, THF, rt; (2) **76**, Cs_2CO_3 [$PdCl_2(dppf)_2$], Ph_3As, DMF, −10 °C rt, 55%. **f** LiOH, *i*-PrOH/water (4:1), 60 °C, 98%. **g** 2,4,6-$Cl_3C_6H_2C(O)Cl$, Et_3N, THF, 0 °C. **h** HF·py, THF, rt, 90% (2:1 mixture of isomers at C15). **i** $MeReO_3$, H_2O_2/py/water, rt, 72% (9:1 mixture of epoxide isomers) [91]

of the C1–C4 segment by various β-amino acids and thus give access to a large variety of analogs without major distortion of the bioactive conformation of the C5–O16 segment. Structures of type **83** would thus be attractive targets for a combinatorial chemistry approach starting from the C21–C5 fragment **81**, which can easily be coupled to various β-amino acids. The synthetic route [92] to this precursor **81** comprises a stereoselective aldol reaction between acyl oxazolidinone **78** and chiral aldehyde **27**. The desired aldol product **79** could be isolated in 90% yield as a single isomer and was subsequently transformed into iodide **80**, which underwent smooth Negishi coupling with vinyl iodide **19**. After cleavage of the chiral auxiliary with LiOH in THF the key building block **81** was available for analog synthesis with β-amino acids. Coupling of acid **81** with racemic *N*-methyl-β-alanine (**82**) followed by selective removal of the TBS-protecting group from O15, Yamaguchi macrolactonization, and finally cleavage of the O7 TBS group gave a mixture of the target compounds, which could be easily separated at this stage to provide **83a** and **83b** as single isomers (Scheme 11).

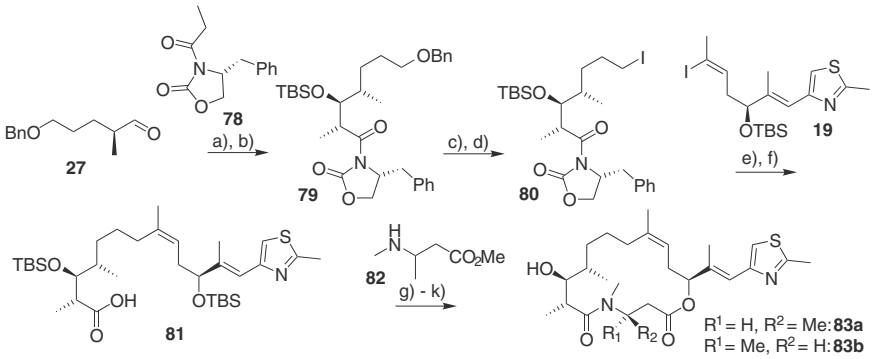

Scheme 11 **a** **78**, Bu_2BOTf, Et_3N, CH_2Cl_2, 0 °C, 1 h; then addition of **27**, −78 °C, 3 h, 90%. **b** TBS-OTf, 2,6-lutidine, 0 °C → rt, 4 h, 91%. **c** H_2, Pd/C (10%), MeOH, rt, 6 h, 82%. **d** (1) MsCl, Et_3N, 0 °C, 30 min; (2) NaI, acetone, 50 °C, 3 h, 81% (two steps). **e** (1) Zn-Cu, 1,2-dibromoethane, TMSCl, DMA, TMS-OTf; (2) **19** [$Pd(PPh_3)_4$], benzene, 65 °C, 71%. **f** LiOH, H_2O_2, THF/water (4:1), rt, 3 h; 70%. **g** **82**, HBTU, *i*-Pr_2EtN, DMF, rt,3 h, 72%. **h** TBAF, HOAc, rt, 6 h, 65%. **i** LiOH, THF/water (7:1), rt, 6 h, 64%. **j** 2,4,6-$Cl_3C_6H_2C(O)Cl$, Et_3N, THF, rt, 30 min; then DMAP, toluene, rt, 1.5 h, 90%. **k** (1) HF·py, MeCN, rt, 6 h, 86%; (2) flash chromatography, **83a**: 30%; **83b**: 30% [92]

Although the compounds of type **83** that have been synthesized so far lack any significant tubulin polymerizing or antiproliferative activity [92], it has to be noted that only few building blocks have been investigated as potential C1–C4 replacements in this pilot study.

2.5 Side-Chain Modifications

The structural sub-domain that has been modified most extensively for SAR studies on epothilone analogs is the unsaturated heterocycle-bearing side-chain. A highly efficient strategy for the synthesis of such analogs (e.g. **86**) has been developed

by Nicolaou and co-workers and involved the coupling between stannanes of type **85** and vinyl iodide **84** as the key intermediate (Scheme 12) [93–95].

The synthesis of key vinyl iodide **84** involves an early asymmetric Brown allylation of aldehyde **87** to establish the stereocenter at C15 (Scheme 13). Subsequent Wittig reaction between **88** and ylide **89** then furnished the northern part of the epothilone scaffold. After functional group manipulations, aldehyde **90** was used in the highly selective aldol coupling (dr >10:1) with the lithium enolate of **48**.

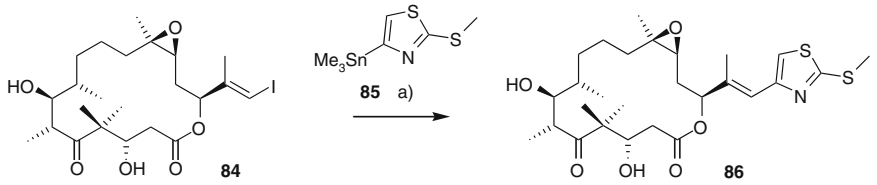

Scheme 12 **a** **85** $[Pd_2(dba)_3]\cdot CHCl_3$, CuI, $AsPh_3$, 25 °C, 72% [96]

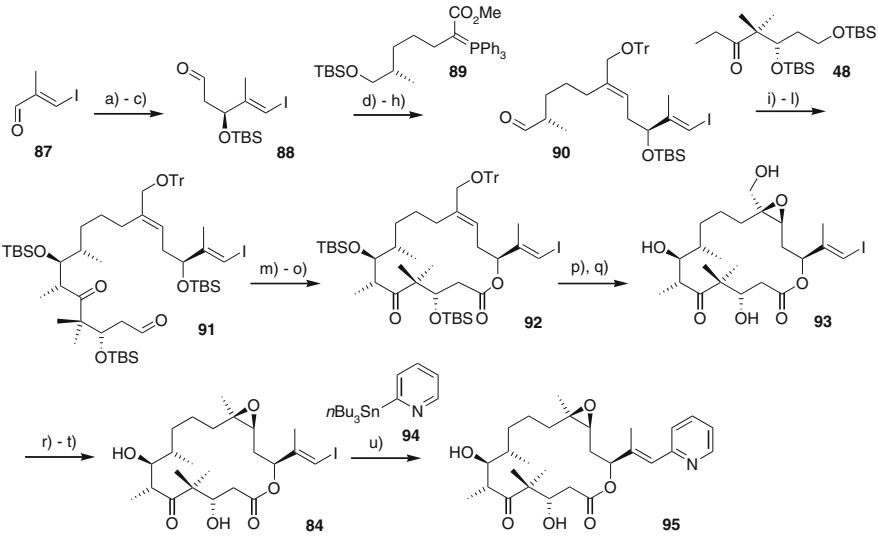

Scheme 13 **a** (+)-Ipc_2B (allyl), Et_2O, −100 °C, 91% **b** TBSCl, imidazole, DMF, 0 °C → 25 °C, 84%. **c** (1) OsO_4, NMO, THF/*t*-BuOH/water (5:5:1), 0 °C → 25 °C, 89%; (2) $NaIO_4$, MeOH/water (2:1), 0 °C, 0.5 h, 92%. **d** **89**, benzene, reflux, 92%. **e** DIBAL, THF, −78 °C, 71%. **f** TrCl, DMAP, DMF, 80 °C, 94%. **g** HF·py, py/THF, 0 °C, 67%. **h** SO_3·py, Et_3N, DMSO/CH_2Cl_2 (1:1), 0 °C, 98% (crude). **i** LDA, THF, −78 °C → −40 °C; **90**, THF, −78 °C; AcOH, −78 °C → 0 °C, 74%. **j** TBSOTf, 2,6-lutidine, CH_2Cl_2, 20 °C → 0 °C, 90%. **k** HF·py, py/THF, 0 °C, 84%. **l** $(COCl)_2$, DMSO, Et_3N, CH_2Cl_2, −78 °C → 0 °C, 98%. **m** $NaClO_2$, 2-methyl-2-butene, NaH_2PO_4, *t*-BuOH/water (9:2), 25 °C, 100%. **n** TBAF, THF, 0 °C → 25 °C, 95%. **o** Et_3N, 2,4,6-$Cl_3C_6H_2C(O)Cl$, DMAP, THF, 84%. **p** HF·py (25% v/v), THF, 0 °C → 25 °C, 86%. **q** (+)-diethyl-(L)-tartrate $[Ti(i\text{-}PrO)_4]$, *t*-BuOOH, CH_2Cl_2, M.S. (4 Å), −30 °C, 2 h, 67%. **r** TsCl, Et_3N, DMAP, CH_2Cl_2, 0 °C → 25 °C. **s** NaI, acetone, 25 °C, 75% (two steps). **t** $NaBH_3CN$, DMPU, 45 °C, 70%. **u** **94** $[PdCl_2(MeCN)_2]$, DMF, 25 °C, 66% [93, 94, 97, 208–210]

Cleavage of the primary TBS-ether in the resulting aldol product followed by oxidation of the primary hydroxyl group then yielded aldehyde **91**. The carboxylic acid was generated with $NaClO_2$ and underwent smooth Yamaguchi macrolactonization to provide fully protected macrolactone **92**. After deprotection at O-26 the free allylic hydroxyl group then allowed stereoselective installment of the epoxide moiety through directed Sharpless asymmetric epoxidation. Due to the lability of the epoxide moiety reduction at C26 was carried out by transforming **93** to the iodide followed by reduction with $NaBH_3CN$. Remarkably, virtually all of the stereochemical issues that were associated with the earlier syntheses were solved by this approach. The double bond between C12 and C13 is formed with high *E*-selectivity; likewise the selectivity of the aldol reaction is high and selective epoxidation of the allylic alcohol obtained by removal of the trityl group from **92** is achieved by applying Sharpless' conditions. A particularly remarkable aspect of this route is the stability of the vinyl iodide moiety attached to C15, which proved to be sufficiently resistant to all reaction conditions it was exposed to in the course of macrocycle construction. With this central intermediate in hand it was now possible to attach various side-chains via Stille-type coupling of **84** with the respective aromatic stannanes (e.g. **94**). This provides rapid access to a large number of side-chain modified analogs.

SAR studies on side-chain-modified epothilone analogs have shown that substituents at the 2-position of the thiazole moiety were well tolerated as long as these functionalities are sufficiently small [49, 89, 96–100]. Analogs such as **95** [101, 102] have been found to exhibit enhanced potencies. One of the most important findings for side-chain-modified epothilones is the fact that a nitrogen atom in the heterocycle has to be located in the *ortho*-position to the vinyl linker. Thus, studies by the TSRI and Novartis groups on pyridine analogs **96** and **97**, in which the nitrogen atom was moved to the *meta*- and *para*-positions, have demonstrated that these compounds exhibit considerably lower activity than **95** [94].

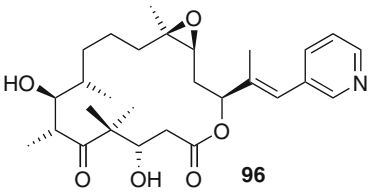

96

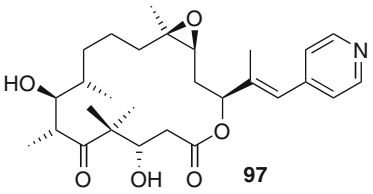

97

This finding also shows that potent biological activity is not confined to five-membered ring analogs as long as the proper position of the nitrogen atom within the heterocycle is conserved. The distinct drop in activity that is observed when the nitrogen atom is in *meta*- or *para*-position can be accounted for by the available structural information on tubulin bound Epo A. In a complex between a two-dimensional tubulin polymer sheet and Epo A the thiazole nitrogen atom was found to be involved in a hydrogen bond with His 227 of β-tubulin [103]. However, recent work by Altmann and co-workers on epothilone analogs related to **95** shows that the correlation between nitrogen positioning and tubulin-polymerization activity might be

more complex. As will be discussed in more detail below, their data indicate that the position of the side chain nitrogen atom in these analogs, while important for cellular activity, may not be crucial for the interaction of epothilones with the tubulin/microtubule system. This conclusion is in line with the binding model of Carlomagno and co-workers [104], which does not invoke a hydrogen bond between the thiazole nitrogen and βHis227, but rather involves a π–π-stacking interaction between the thiazole and the imidazole rings. This assumption is further supported by the potent activity of a phenyl-based analog of Epo B (replacement of the thiazole moiety by a simple phenyl ring), where the hydrogen bonding capability of the side chain has been abrogated [67].

As indicated above, Nicolaou and co-workers have also prepared a number of side-chain-modified cyclopropyl analogs of epothilone, whose synthesis is explained in Scheme 14 for pyridine derivative **110** [96]. Therein the stereoselective introduction of the cyclopropyl moiety was achieved early on by applying Charette conditions on the geraniol isomer nerol (**98**), yielding cyclopropane **99** in 80% yield with 95% ee [105]. After protection of the hydroxyl group, ozonolysis and reductive workup monoprotected diol **100** was obtained. Transformation to the iodide **101** followed by Enders asymmetric alkylation with (–)-SAMP hydrazone (**102**) proceeded with 87% yield. Subsequent cleavage of the auxiliary provided aldehyde **104**, which then underwent selective aldol reaction (dr >14:1) with ketone **48** to form alcohol **105**.

Alcohol **105** was then converted over several steps, including a Wittig based homologation, to the key aldehyde **106**. Key intermediate **106** then can be coupled to various vinyl iodides (e.g. **107**) using Nozaki–Hiyama–Kishi conditions [106, 107]. Subsequent deprotection yields seco acid **108** as a 1:1 mixture of the two C15-epimers. Yamaguchi macrolactonization of **108** leads to the 1:1 mixture of the resulting diastereoisomers. Chromatographic separation led to the desired isomer **109** which, after final deprotection, provides the cyclopropyl epothilone analog **110**.

Vinyl iodide **84** (Scheme 13) has also served as an intermediate for Nicolaou's synthesis of 20-desmethyl-20-methylsulfanyl-Epo B (**86**; ABJ879) [108], a compound which had also been prepared by the Novartis group by means of semisynthesis [108]. ABJ879 induces tubulin polymerization in vitro with slightly higher potency than Epo B and taxol and it shows markedly higher antiproliferative activity. The average IC_{50} value for growth inhibition across a panel of drug-sensitive human cancer cell lines has been reported as 0.9 nM for ABJ879 vs 0.24 nM for Epo B and 4.7 nM for taxol [108]. Activity against cancer cells over expressing the Pgp efflux pump is fully retained like it is the case for Epo B. Due to these intriguing properties ABJ879 has entered phase I clinical trials as a potential follow-up compound for EPO906 [108], but the clinical development of the compound has recently been terminated. Building on their established "vinyl iodide strategy" the Nicolaou group subsequently expanded their work on side-chain-modified epothilone analogs to a series of new, mainly five-membered, heterocycles with differing positions and numbers of nitrogen atoms (e.g. **111**) [93]. As an additional potency

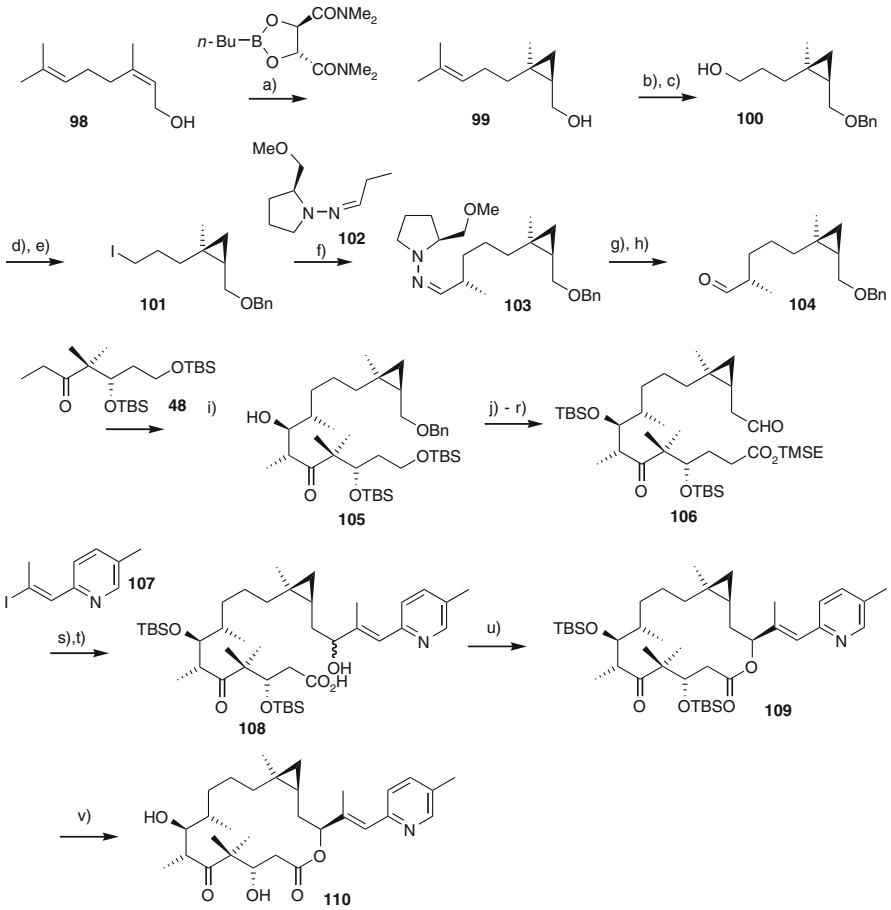

Scheme 14 **a** 80% yield, 95% ee. **b** NaH, BnBr, DMF, 0 → 25 °C, 12 h, 100%. **c** O_3, CH_2Cl_2/MeOH (4:1), −78 °C; then $NaBH_4$, −78 → 25 °C, 1 h, 83%. **d** MsCl, Et_3N, CH_2Cl_2, 25 °C, 1 h. **e** NaI, acetone, 25 °C, 12 h (91% for two steps). **f** LDA, **102**, THF, 0 °C, 6 h; then **101**, −98 → −10 °C, 14 h, 87%. **g** MeI, reflux, 3 h. **h** HCl (3 M)/pentane (1:1), 25 °C, 3 h (91% for two steps). **i** LDA, **48**, THF/Et_2O (1:1), −78 °C, 1 h; then −40 °C, 0.5 h; then **104** at −78 °C, 5 min, 80%. **j** TBS-OTf, 2,6-lutidine, CH_2Cl_2, −20 °C, 1 h. **k** HF·py, py/THF (1:2), 0 °C, 8 h (86% for two steps). **l** $(COCl)_2$, DMSO, CH_2Cl_2, −78 °C, 5 min, 20 min; then Et_3N, −78–0 °C. **m** $NaClO_2$, NaH_2PO_4, 2-methyl-2-butene, *t*-BuOH/THF/water (4:2:1), 25 °C, 1 h. **n** TMSE-OH, EDCI, DMAP, DMF, 25 °C, 12 h (73% for three steps). **o** $Pd(OH)_2$/C (10 wt%; 10%), H_2, EtOH/EtOAc (1:1), 25 °C, 2 h, 89%. **p** $(COCl)_2$, DMSO, CH_2Cl_2, −78 °C, 5 min, 20 min; then Et_3N, −78 → 0 °C, 99%. **q** $MeOCH_2PPh_3Cl$, *n*-BuLi, THF, 0 °C, 1 h, −78 → 0 °C, 2 h, 79%. **r** PPTS, dioxane/water (9:1), 70 °C, 12 h, 81%. **s** $CrCl_2$, $NiCl_2$, 4-*t*-BuPy, **107**, DMSO, 25 °C, 24 h. **t** TBAF, THF, 25 °C, 2 h, 42% yield for two steps. **u** Et_3N, 2,4,6-trichlorobenzoyl chloride, **108**, THF, 0 °C, 1 h; then DMAP, toluene, 75 °C, 3 h, 33%. **v** TFA/CH_2Cl_2 (20% v/v), 25 °C, 3 h, 48% [109, 164]

enhancing functionality lipophilic substituents such as methyl and methylthio groups were attached to the heterocycles, which was based on the good results obtained with **86**.

The SAR data generated from these experiments with functionalized imidazole, pyrazole, triazole and tetrazole rings [93] provided new insights into the effects of side-chain modifications and hint at the importance of the electron density in the heterocycle for high antiproliferative activity. Surprisingly, the imidazole-based analog **112** was associated with a substantial loss in activity, despite the fact that its side-chain is part of the eleutherobin and sarcodyctin scaffolds, both potent natural product microtubule inhibitors. Triazole as the side-chain heterocycle led to an equally disappointing activity profile, while tetrazole-based analog **113** proved almost equally potent as Epo B. The fact that the analogous 2-substituted thiazole derivative is about 100-fold less active than **113** highlights the important role that electron density distribution in the ring plays in tubulin affinity.

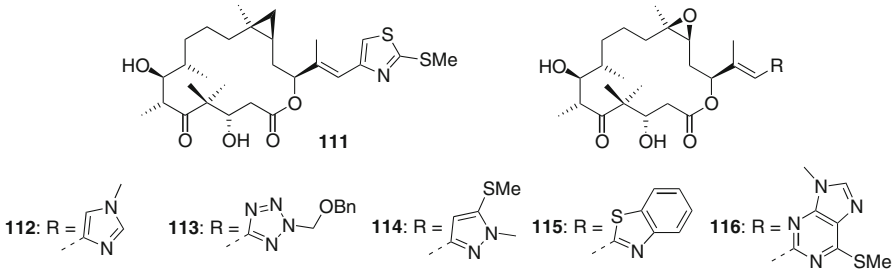

The most active variant of these side-chain-modified epothilone analogs is compound **114**, which incorporates a pyrazole ring and at the same time both of the above mentioned potency enhancing functional groups (methyl, methyl thio). With its striking activity profile, **114** is one of the most potent epothilones that have been synthesized to date [93]. Thus, the compound exhibits a remarkable 17-fold increase in activity against both the 1A9 parental and the 1A9/A8 EpoA-resistant cell lines and an even more impressive 78-fold increase in potency against the taxol resistant 1A9/PTX10 cell line, relative to the potency of naturally Epo B. Apart from these monocyclic side-chain structures Nicolaou's recent study [93] also included analog **115** and purine substituted analogs (e.g. **116**) as representatives of a class of extended side-chain epothilones, which were designed to probe the effect of additional rings and the ability of the tubulin receptor pocket to accommodate bulkier substituents [93]. A series of bicyclic aromatic thiazole replacements was synthesized, again based on the Pd-catalyzed cross coupling approach depicted in Scheme 13. These benzothiazole- (e.g. **115**) and purine-based (e.g. **116**) analogs exhibit remarkable cytotoxicity across a broad range of cell lines (e.g. IC_{50}-values against the human epidermoid carcinoma cell lines KB-31/KB-8511 are 0.21 nM/0.08 nM for **115** and 0.36 nM/6.21 nM for **116**) [93]. Both **115** and **116** show higher activity than Epo B, with benzothiazole analog **115** being significantly more active than Epo B in many of the cell lines that were investigated. These findings suggest that additional steric bulk in the epothilone side-chain is well tolerated as long as it is located in the northeastern quadrant of the structure. Increased susceptibility to

Pgp efflux as observed for **116** mirrors the findings of the Altmann group, which indicate that dimethyl benzimidazole-based side-chains (see below) make the respective epothilone analogs substrates for the Pgp-efflux pump. Interestingly these results are not in line with the substantial loss in biological activity, which has been reported for analogs incorporating bulky substituents at the 2-position of the thiazole in Epo B [89, 100].

In the course of attempts to rationally design Epo B analogs that surpass the activity of the parent compound, the outstanding biological profiles of cyclopropyl epothilones were considered to be viable targets and the combination with other activity-enhancing features seemed very promising. This led to the synthesis of cyclopropyl-based *trans*-analogs of Epo A and B with modified side-chains, based on strategies depicted in Schemes 6 and 13 (employing geraniol instead of nerol as a starting material) [64, 96]. For *trans*-cyclopropyl Epo A analogs the access to a small library was possible employing different heteroarylated vinyl iodides such as **45** and **117–119**.

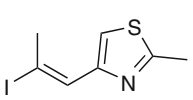

45

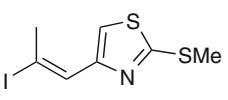

117

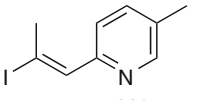

118

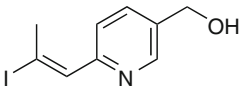

119

One major conclusion that can be drawn from these studies is that *trans*-cyclopropyl epothilones do not uniformly show increased activity. In fact *trans*-cyclopropane analogs of Epo B show significantly decreased activities [109] compared to the corresponding *trans*-Epo A derivatives or the *cis*-cyclopropyl-Epo B's. As anticipated, the potency enhancing methylsulfanyl substituent in the thiazole side-chain led to the analog with highest activity **111**. This cyclopropane analog of ABJ879 (**86**) binds to stabilized microtubules with 27.4-fold greater affinity than Epo B and has been found to be a more potent antiproliferative agent in vitro than either Epo B or, in some cases, ABJ879 (**86**). Its high antiproliferative activity is believed to be the result of a synergistic effect of the *cis*-cyclopropane moiety and the methylsulfanyl substituent. Experiments with sterically more demanding alkylsulfanyl substituents (SCH_2CH_3, $S(CH_2)_2CH_3$, SCH_2CF_3, SCH_2-furane) show markedly diminished activity relative to Epo B, thus underlining that steric bulk beyond the heterocyclic side-chain has to be confined to the northeastern quadrant of the molecule to preserve high biological activity.

While all of the above side-chain modifications aim at the variation of the heterocyclic moiety alone, the group at Novartis (Altmann and co-workers now at ETH Zürich) has designed a different type of side-chain modification, which comprises the entire side-chain structure. By taking into account the results of solution NMR studies, this design aimed at mimicking the side-chain conformations in the bioactive (i.e. tubulin-bound) structure of epothilones, which is characterized by a transoid arrangement of the C16–C17 double bond [102, 110]. In a first series analogs of Epo B and D were synthezised, in which the natural (2-(2-methyl-thiazol-4-yl)-1-methyl)-ethenyl side-chain was replaced by a number

of benzo-fused aromatic heterocycles. Synthetic access to these analogs relied on the same general strategy as the one that had been developed for the synthesis of *trans*-Epo A in the same group [61].

Thus, as exemplified in Scheme 15 for quinoline-based analogs **123a** and **124a** [110], one of the key steps in the construction of the macrocycle was the Suzuki–Miyaura coupling of vinyl iodide **121** with the C1–C11 fragment **120** to form the C11–C12 bond. After ester hydrolysis and TBS-deprotection the obtained seco-acid **122** was cyclized in a Yamaguchi-type macrolactonization to yield the respective 12,13-deoxy compounds **123a**, which could then be epoxidized with the $MeReO_3/H_2O_2$ system [111]. This yielded **123a** with approx. 6:1 selectivity in 37% yield after HPLC purification. For the benzothiazole analog **124b** epoxidation was accomplished with dimethyldioxirane at –50 °C.

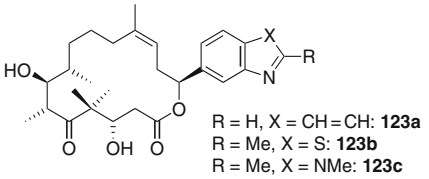

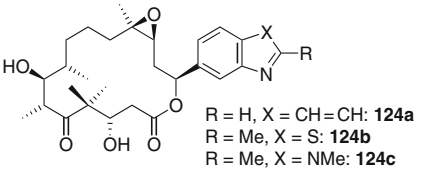

The in vitro antiproliferative effects of these Epo B and Epo D analogs are generally higher than those of the corresponding parent epothilones, with the activity increase being more pronounced for the Epo D congeners **123a–c**. The reason for this activity differential between deoxy analogs and epoxides is not clear since further studies of similar compounds have revealed a very complex picture of the effects of

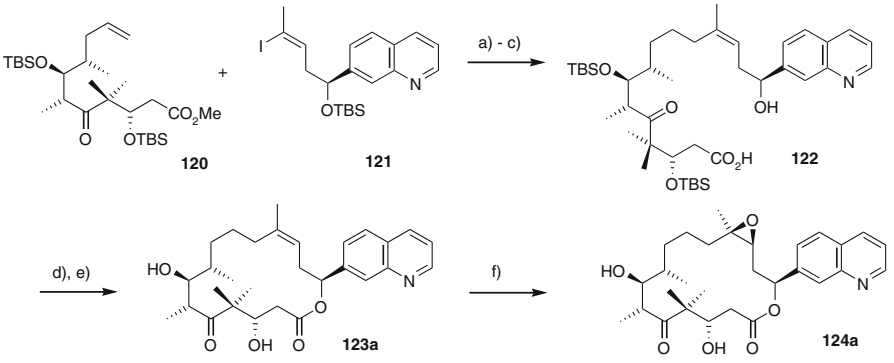

Scheme 15 **a** (1) olefin **120** 9-BBN, THF, rt, 4 h; (2) **121** Cs_2CO_3 [$PdCl_2(dppf)_2$], Ph_3As, DMF, –10 °C-rt, 16 h, 90%. **b** LiOH, *i*PrOH/water (4:1), 50 °C, 7 h, 84%. **c** TBAF, THF, rt, 18 h, 84%. **d** (1) 2,4,6-$Cl_3C_6H_2C(O)Cl$, Et_3N, THF, 0 °C, 15 min; (2) dilution with toluene, addition to a solution of DMAP in toluene, 75 °C, 3 h, 70%. **e** HF·py, THF, rt, 17 h, 73%. **f** (1) $MeReO_3$, H_2O_2, py/CH_2Cl_2, rt, 17 h; (2) H_2, Ra-Ni, EtOH, rt, 37% [110]

these rigidified side-chain modifications. Thus it may be assumed that the enhancement in cellular activity of **123a–c** is not related to more efficient interactions with the microtubule system (this point is discussed in more detail below).

In an extensive lead optimization program directed at the improvement of the therapeutic window of epothilones without compromising their high activity the group at Schering AG equally identified the side-chain at C15 (in addition to the C6 position of the molecule) as one of the key positions for the tuning of tolerability and efficacy. This research has led to the identification of a C6-allylated analog of compound **124b**, ZK-Epo (sagopilone), which was chosen for clinical development from about 350 active analogs on the basis of its promising preclinical profile [112]. Currently ZK-Epo is being evaluated in Phase II clinical studies and thus represents the first fully synthetic epothilone analog in clinical development. The synthesis of ZK-Epo (Scheme 16) [112] is based on a convergent approach, which includes the early Wittig coupling of fragments **125** and **126** to form the C12–C13 double bond unselectively in a ratio of 1:1 (after separation the *E*-isomer was subsequently converted to a *E/Z*-mixture by photochemical isomerization). Selective aldol reaction between aldehyde **127** and the C1–C6 fragment **128** furnished the macrolactonization precursor **130**, which was cyclized via Yamaguchi reaction and, after TBS-protecting group removal, epoxidized with DMDO at –78 °C to yield ZK-Epo

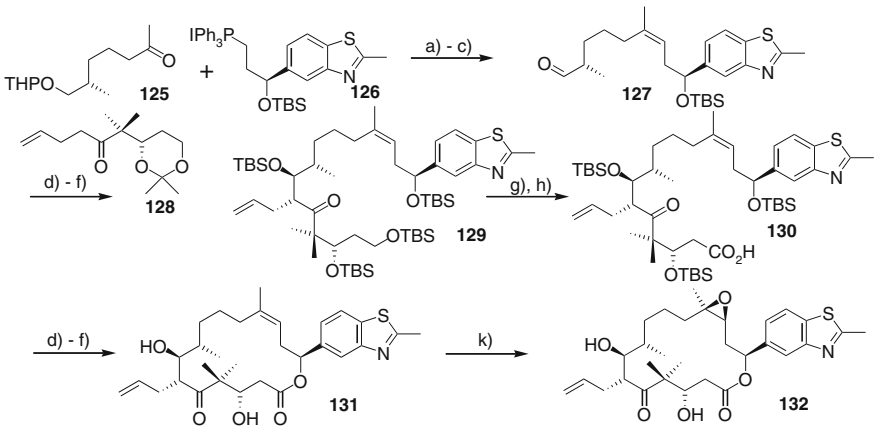

Scheme 16 **a** NaHMDS, THF, 0 °C → rt, 83% (1:1 mixture of *Z*- and *E*-isomers). **b** (cat) *p*-TsOH, EtOH, rt, 43% (86% for mixture of *Z*- and *E*-isomers). **c** $(COCl)_2$, DMSO, CH_2Cl_2, –78 °C; then Et_3N, –78 °C → 0 °C, crude. **d** **128**, LDA, $ZnCl_2$, THF, –70 °C, 64%. **e** (cat) *p*-TsOH, EtOH, rt, 97%. **f** TBDMS-OTf, 2,6-lutidine, CH_2Cl_2, –70 °C → 0 °C, 96%. **g** CSA, CH_2Cl_2, MeOH, rt, 80%. **h** (1) $(COCl)_2$, DMSO, CH_2Cl_2, –78 °C; then Et_3N, –78 °C → 0 °C, crude; (2) $NaOCl_2$, NaH_2PO_4, 2-methyl-2-butene, THF/water/*t*-BuOH, 0 °C → 15 °C, 85%. **i** (1) TBAF, THF, rt, crude; (2) 2,4,6-$Cl_3C_6H_2C(O)Cl$, Et_3N, THF, 0 °C, 60%. **j** HF·py, hexafluorosilicic acid, THF, rt, 87%. **k** DMDO, acetone/CH_2Cl_2, –78 °C, 71% + 10% β-epoxide [112]

(**132**). The in vitro biological properties of ZK-Epo are reported to be superior to those of Epo B, one major advantage over Epo B being the lower resistance factors in experiments with multidrug-resistant cancer cells [112]. The compound also showed significant antitumor activity in a number of mouse xenograft models without inducing any profound body weight loss. However it should be noted that no tumor regressions were observed at these nontoxic doses.

Because of the apparent generality of the potency-enhancing properties of the rigidified side-chains discussed above [93–95, 110], Altmann and co-workers carried out a more comprehensive program on the effects of this type of modification in various epothilone scaffolds. Synthesis of dimethyl benzimidazole-based analogs of Epo A, *trans* Epo A, Epo C and *trans* Epo C revealed that the favorable effect that is connected with this more rigid side-chain is not confined to analogs of Epo B [113–115]. All of the above analogs are potent inducers of tubulin polymerization and possess more potent antiproliferative activity against drug sensitive cancer cells than the respective parent compound. In particular, **134** is one of the few Epo A-derived compounds that have Epo B-like antiproliferative activity against drug sensitive cancer cells. The solubility properties connected with the benzimidazole analogs are the most favorable in aqueous medium of the analogs with bicyclic heterocycles in their side-chains. Interestingly this enhanced polarity is also connected to lower cellular activity of these compounds against MDR cell lines [91, 113]. A similar effect was also observed for lactam analogs of epothilones (see above).

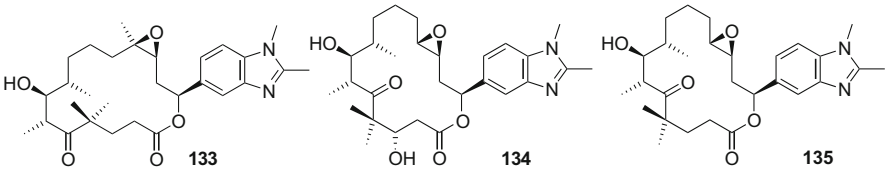

To counteract this undesired effect, 3-deoxy analogs of the Epo A-derived as well as the *trans* Epo A-derived benzimidazole based scaffolds **133** and **135** were synthesized and screened for their activity profiles. Although loss of the 3-hydroxy functionality is associated with (a limited) drop in potency, the promoting effect of the side-chain can almost completely compensate for this decrease. It has to be noted that in spite of significant structural deviations from the original product lead, the activity of **135** (IC_{50} [nM]: KB-31: 3.16 ± 0.55; KB-8511: 7.60 ± 2.44) is still similar to that of Epo A, Epo D and taxol. It might thus be considered the first representative of a new structural class of microtubule stabilizers, whose overall pharmacological profile may be distinct from that of Epo A and B and more closely related analogs.

To overcome the increased Pgp-susceptibility Altmann and co-workers replaced the polar epoxide functionality by the more lipophilic cyclopropane moiety, which led to the syntheses of cyclopropane analogs **136** and **137** [113].

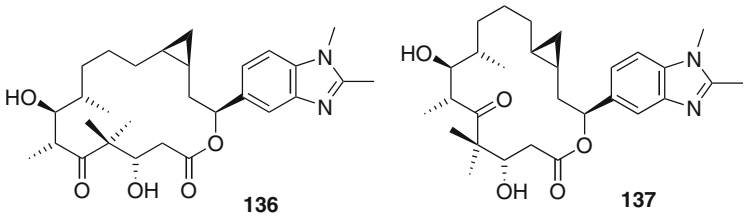

Compound **137** was synthesized according to Scheme 17. This comprised a key Suzuki-Miyaura coupling between **138** and **139**. Using precursor **140** with the unnatural (*R*)-configuration at C15 instead of the natural (*S*)-configuration, it was possible to effect highly selective directed cyclopropanation. This necessitated macrolactonization to be conducted under Mitsunobu conditions to introduce the correct (*S*)-stereocenter at C15. Analog **136** was obtained in an analogous way [113].

Since cyclopropanation of the unsaturated precursor of **137** proved to be extremely difficult under a number of different reaction conditions and produced only 1:1 mixtures at best, the substrate-directed method with **140** was favored, even if the Mitsunobu esterification was somewhat lower yielding than the usual Yamaguchi esterification. The cyclopropane-based analogs **136** and **137** retain high potency against drug-sensitive KB-31 cells and also show full activity against the multidrug-resistant cell line KB-8511. This illustrates impressively how the polarity adjustment through introduction of an isosteric cyclopropane ring instead of the epoxide moiety can efficiently eliminate susceptibility to Pgp related drug efflux.

In light of the highly favorable properties of benzimidazole-based epothilone analogs it seemed interesting to probe the effect of a rigidified side-chain moiety in combination with one of the above mentioned "azathilones" (Scheme 7) [66]. Although not as active as the parent polyketide-based epothilones, some of

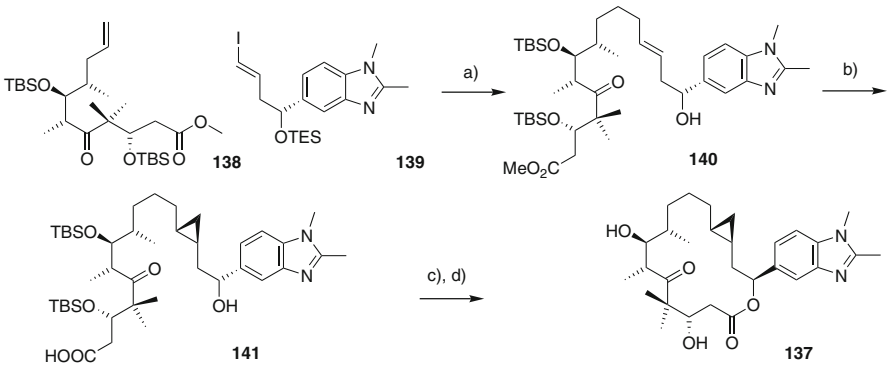

Scheme 17 **a** Ref. [114]. **b** (1) Et_2Zn, CH_2I_2, TFA, −13 °C, 30 min; (2) **140**, −13 °C, 20 min, 77%; (3) LiOH, *i*-PrOH/water (4:1), 60 °C, 3 h, 91%. **c** PPh_3, DIAD, toluene, −13 °C, 90 min, 46% (65% based on recovered starting material). **d** HF·py, MeCN, rt, 2 h, 42% (after HPLC purification, 83% crude)

these compounds had proven to be interesting chemotypes with activities in the region of ~30 nM for compound **54a**, making it roughly equipotent with Epo C. Thus, the Altmann group has devised synthetic routes towards "azathilone" analogs of type **148**, which include bicyclic aromatic moieties connected to C15 [66] (Scheme 18).

Starting from Schinzer ketone **26**, highly selective aldol coupling with PMB-protected aldehyde **142** yielded, after TBS-protection, **143**. Subsequent reductive PMB cleavage, oxidation, Wittig olefination and final elaboration of C1 to the carboxylic acid furnished the esterification precursor **144**. Following esterification of **144** with alcohol **145**, RCM-based ring closure of **146** was achieved with complete *E*-selectivity in the presence of Grubbs second generation catalyst. Subsequent

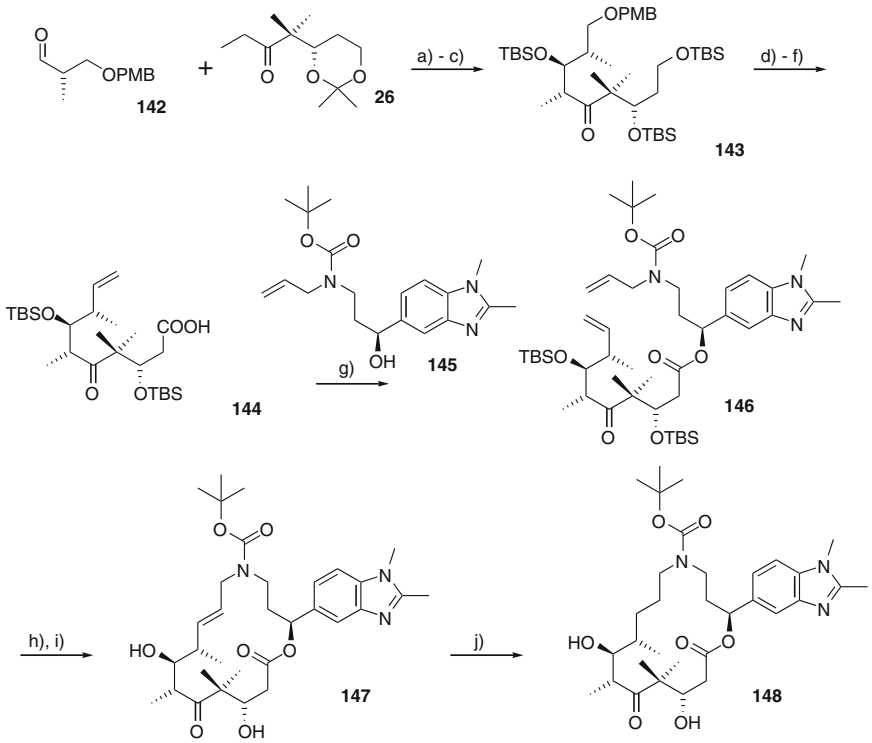

Scheme 18 **a 26**, LDA, -78 °C, 5 h, then addition of **142**, -90 °C, 75 min, 76%, dr 8:1. **b** PPTS, MeOH, rt, 20 h, 86%. **c** 1. TBS-OTf, 2,6-lutidine, −78 °C → rt, 1.5 h; 2. flash chromatography; 76%. **d** (1) H_2/Pd-C, MeOH, RT, 20 h; (2) TPAP, NMO, 4-Å MS, CH_2Cl_2, rt, 1 h; 3. $MePPh_3Br$, LiHMDS, THF, 0 °C, 1.5 h, 79% (three steps). **e** CSA (1.0 equiv), CH_2Cl_2/MeOH 1:1, 0 °C, 1 h, 87%. **f** PDC (11 equiv), DMF, rt, 64 h, 85%. **g** **145**, DCC (1.2 equiv), DMAP (0.3 equiv), CH_2Cl_2, 0 °C, 15 min, rt, 15 h, 60%. **h** Grubbs second (0.15 equiv, incremental addition), CH_2Cl_2, reflux, 8 h, 85%. **i** HF·py, py/THF, rt, 4 h, 70%. **j** KO_2C-N = N-CO_2K (excess), AcOH, CH_2Cl_2, 31%, pure **148** obtained through purification by preparative HPLC

TBS-deprotection yielded the unsaturated "azathilone" **147**, which could be transformed into saturated **148** using in situ generated diimide to reduce the double bond between C9 and C10. Although compounds **148** and its unsaturated precursor **147** could be generated via this RCM-based synthetic strategy, the low yielding double bond reduction was an unfavorable drawback (Scheme 18).

As a consequence, and in order to enable the preparation of sufficient quantities of material for eventual in vivo experiments, a more efficient synthesis was required. Since initial in vitro biological profiling of C9–C10 unsaturated analog **147** had proven to be disappointing (see below), the new approach (Scheme 19) did not comprise RCM chemistry but rather relied on macrolactonization of saturated seco acid **152**. The latter was constructed by reductive amination of aldehyde **151** with amine **150**, followed by selective cleavage of the primary TBS-protecting group. After oxidation to the acid, selective removal of the TBS-protecting group at C15 and Yamaguchi-type macrolactonization, compound **148** could be obtained by

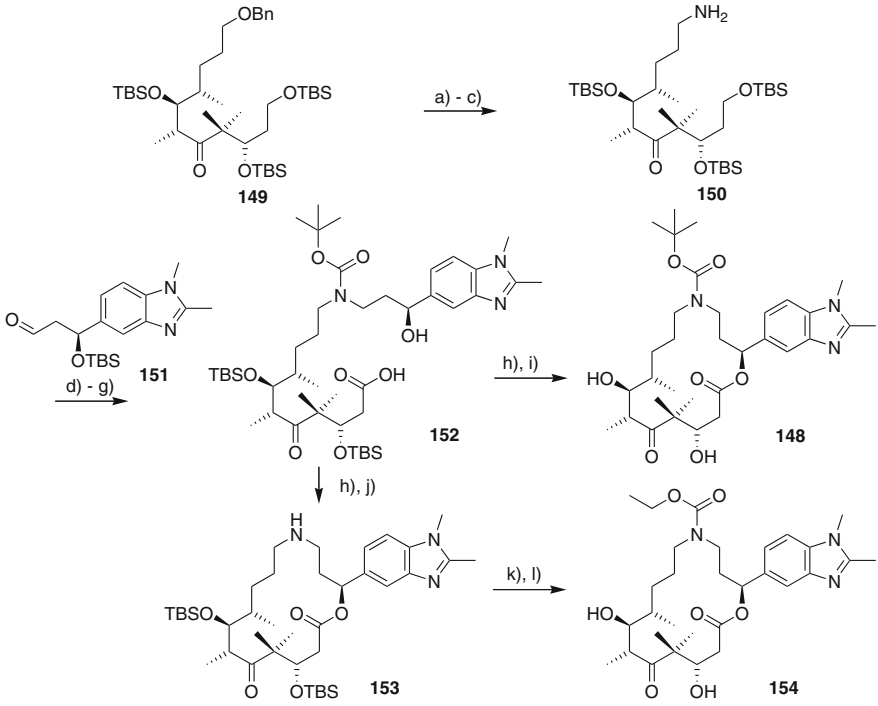

Scheme 19 **a** H_2/Pd-C, EtOAc, rt, 62 h, 86%. **b** HN_3, DEAD, PPh_3, THF, 0 °C, 25 min, rt, 30 min, 96%. **c** H_2/Pd-C, MeOH, rt, 3 h, 92%. **d** (1) **151** (1.1 equiv), $NaBH(OAc)_3$ (1.6 equiv), AcOH (2.0 equiv), 4-Å MS, rt, 2.5 h; 2) Boc_2O, Et_3N, THF, 0 °C, 45 min, 60% (two steps). **e** CSA (1.1 equiv), CH_2Cl_2/MeOH 1:1, 0 °C, 3 h, 80%. **f** PDC (15 equiv), DMF, rt, 24 h, 50%. **g** TBAF (6 equiv), THF, rt, 24 h. **h** 2,4,6-$Cl_3C_6H_2C(O)Cl$, Et_3N, THF, 0 °C, 20 min, then diluted with toluene and added to a solution of DMAP in toluene, 75 °C, 1 h, 44% (two steps). **i** HF·py, py/THF, rt, 2.5 h, then preparative HPLC, 40%. **j** $ZnBr_2$ (4.0 equiv), CH_2Cl_2, rt, 2.5 h, quant. **k** $CH_3CH_2OC(O)Cl$, Et_3N, THF, 0 °C, 30 min. **l** HF·py, py/THF, rt, 3.5 h, then preparative HPLC, 32% (two steps) [66, 99]

simultaneous HF·pyridine deprotection at O3 and O7. Stunningly, the biological activity of **148**, was comparable with Epo A (**148**: IC_{50} [nM]: A549 (lung): 1.9; HCT-116 (colon): 1.6; PC-3M (prostate): 2.3; KB-31 (cervix): 0.34; Epo A: IC_{50} [nM]: A549 (lung): 3.2; HCT-116 (colon): 2.2; PC-3M (prostate): 3.4; KB-31 (cervix): 2.15) [66]. This constitutes a >60-fold increase compared with thiazolyl vinyl derivative **54a**. Against the background of 2- to 15-fold increased in vitro activity for polyketide-derived benzimidazole-containing epothilone analogs, these numbers are highly impressive and hint at the potential of azathilones for further tuning of their potency. Surprisingly, unsaturated compound **147** showed significantly lower potency than **148**, which is in marked contrast to the results previously obtained for 9,10-unsaturated analogs of Epo B and D (see above).

Recent SAR studies on the position of the nitrogen atom in the heterocycle in bicyclic side-chain derivatives by the Altmann group have shed new light on the interesting relationship between the position of the nitrogen atom in the heterocycle and biological activity [115]. While previous studies by the Nicolaou/Altmann groups with simple pyridine-substituted side-chains (see above) had suggested a requirement for the positioning of the nitrogen atom in a position *ortho* to the attachment point to the vinyl linker, the recent studies by Altmann and co-workers with bicyclic side-chains (compounds **123b**, **155**, **156**) indicate these correlations to be much more complex. Thus, while both isomers within compound pairs **123b/155** and **123a/156** exhibit virtually identical effects on tubulin polymerization, they show very different antiproliferative activities. On the other hand, the isomers **123b** and **123a**, with a "natural" *meta* positioning of the nitrogen atom relative to the connection between the macrolactone and the side-chain, are >50-fold more potent than their respective isomers **155** and **156** in cellular proliferation assays [115].

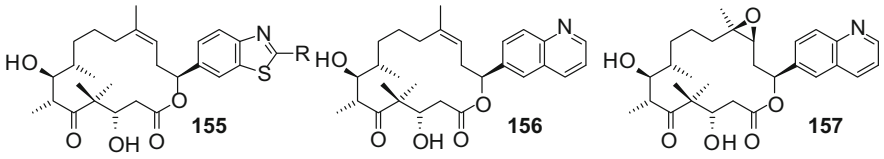

Based on this differential one may assume that nitrogen positioning in the heterocyclic side-chain of these compounds is of significant importance for cellular activity but does not profoundly impact the interactions with the tubulin target. On the other hand, no activity differential was observed for epoxide-containing analogs **124a** and **157**, either at the level of tubulin polymerization in vitro or at the level of cancer cell growth inhibition. These findings clearly illustrate that factors other than tubulin-polymerizing activity must have a pronounced impact on the cellular activity of Epo D analogs **123b/155** and **123a/156**. As indicated above, these data appear to favor the Epo A binding model of Carlomagno [104] over the EC-derived model [103], as the former does not invoke a specific hydrogen bond between the thiazole nitrogen in epothilones and βHis227. However, specific structural data for the complexes of the above analogs with tubulin/microtubules will be required, in order to confirm (or reject) this assumption.

Another group of side-chain modified epothilone analogs has recently been reported by the group at Kosan [116]. In these analogs the vinyl linker between the macrolide and the aromatic heterocycle was removed and a (2-substituted) thiazol-4-yl moiety was directly attached to C15 [116]. Since the direct attachment of the thiazole ring to the macrocycle had already been reported by Danishefsky [50] to lead to a significant loss in activity, the side-chain modification was combined with the potency-enhancing 9,10-dehydro modification of the macrolactone ring. Since direct attachment of the thiazole to C15 leads to a repositioning of the vital thiazole nitrogen atom, aromatic heterocyclic extensions were introduced in the 2-position of the thiazole ring. The aim of these biaryl analogs was to reestablish the interaction between His227 and a basic nitrogen atom (in this case the nitrogen atom of the aromatic extensions) that has been suggested to be required for high-affinity tubulin binding of natural epothilones [103]. Remarkably the activity loss observed by Danishefsky [50] could be compensated for to some extent by introduction of these extensions in compounds **158**–**161**, which show IC_{50} values against the human breast cancer cell line MCF-7 of 40, 52, 34, and 38 nM respectively. Although still 50-fold less active than natural epothilones, there is significant room for further modifications of these compounds, which might lead to still more potent congeners of this class.

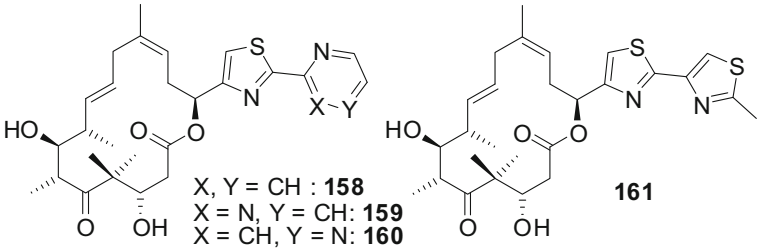

In a very recent publication, Tillekeratne et al. [117] reported the synthesis of two constrained Epo D analogs **162** and **163**. By introducing a methylene bridge between C14 and C17 the mobility of the aromatic side-chain was reduced while the flexibility of the C1–C8 region of the macrolactone was preserved. Analog **163** showed high cellular antiproliferation activity in leukemia cell lines (**163**: GI_{50} [nM]: CCRF-CEM: 2.7; SR: 2.9) while being virtually inactive on breast (MCF-7) and ovarian (SK-OV-3) cancer cell lines normally associated with epothilone antiproliferative activity. In spite of this interesting cellular profile it remains to be seen what effect these analogs have on tubulin-polymerization.

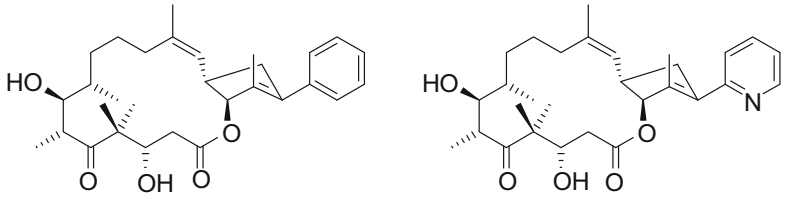

3 Laulimalide

In 1988 Crews and co-workers [118] isolated a cytotoxic macrolide from the sponge *Cacospongia mycofijiensis* and elucidated its structure by NMR. The compound was named fijianolide B (**3**). The same compound was discovered in an independent investigation by Moore, Scheuer and co-workers [119] of the Indonesian sponge *Hyatella* sp. and the nudibranch *Chromodoris lochi*, which was found grazing on that sponge. The compound was termed laulimalide (**3**) by Moore and Scheuer and this is the name commonly used today. Laulimalide was subsequently also reisolated from the Okinawan sponge *Fasciospongia rimosa* and from a sponge in the genus *Dactylospongia* [120, 121]. In all these cases a structural variant of laulimalide (**3**), the rearrangement product isolaulimalide (fijianolide A, **3A**) was also obtained from the corresponding crude extracts. The rearrangement of laulimalide (**3**) to isolaulimalide (**3A**) readily takes place in an acidic environment. Laulimalide was rapidly identified as a potent antiproliferative agent [11, 118, 119, 122] but, as has been the case for other microtubule-stabilizing agents, it took several years before its molecular target was identified as the tubulin/microtubule system [11].

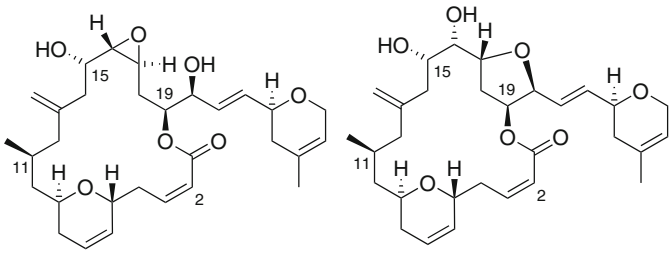

laulimalide (**3**) isolaulimalide (**3A**)

3 leads to notably longer microtubules than those induced by taxol despite its somewhat lower potency for the induction of tubulin polymerization (EC_{50} values of 4.32 μM and 1.44 μM for **3** and taxol, respectively) [11]. Laulimalide was also found to inhibit the growth of the human ovarian cancer cell line SKOV-3 with an IC_{50} of 11.5 nM which is six times less potent than taxol (IC_{50}: 1.7 nM). It was, however, found to be 800-fold more potent than taxol against the multidrug-resistant SKVLB line. These findings were confirmed in a subsequent study by Pryor et al. [122], who also established that **3** did not bind to the taxol site on β-tubulin, which has been confirmed by some recent studies [123–125]. In a subsequent study, Hamel and co-workers showed that laulimalide and taxol not only occupy different binding sites on tubulin but also induce tubulin polymerization in a highly synergistic fashion [123]. Remarkably, similar synergistic effects were also observed for combinations of laulimalide with epothilone A or discodermolide, while no such synergy occurred for any combination of drugs that are known to share the taxol site (taxol, discodermolide, epothilone A/B). However, no synergistic effects between laulimalide and taxol had originally been reported to occur at the cellular

level [122]. In a more recent finding by Mooberry and co-workers it was demonstrated that laulimalide acts synergistically with both taxol or 2-methoxy-estradiol (2-ME) in the growth inhibition of A549 lung or MDA-MB-435 breast carcinoma cells and the same is true for two synthetic laulimalide analogs [126]. Most recently, laulimalide has also been reported to inhibit human umbilical vein endothelial cell (HUVEC) tubule formation and vascular endothelial growth factor (VEGF)-induced HUVEC migration [127], both of which are key components of the angiogenic process.

With the elucidation of the absolute configuration of laulimalide (**3**) [128], synthetic work towards the total synthesis of **3** started immediately [129-156, 166], and further intensified when laulimalide was identified as a microtubule-stabilizing agent [11]. As a result of these efforts, 11 total syntheses from various research groups have been reported at this point in time (for an excellent review on the chemistry of laulimalide up to 2003 see [129]).

The first total synthesis of laulimalide was successfully completed by Gosh and Wang [146] in 2000, who later refined their synthesis [147-148]. The synthesis based on the assembly of the two building blocks **165** and **166** by Julia olefination, elaboration of the coupling product **164** into laulimalide (**3**) via HWE-based ring closure and Sharpless epoxidation (Scheme 20).

The synthesis of fragment **165** proceeded through lactone **167** (obtained in seven steps starting from Roche ester), which was converted first to chiral alcohol **168** and

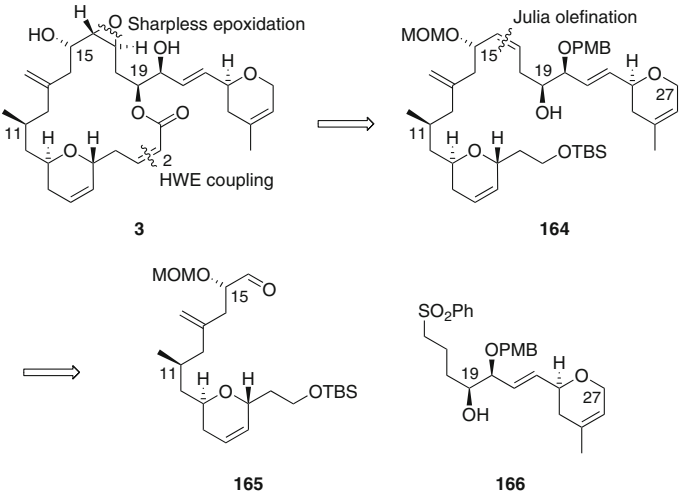

Scheme 20 Gosh's improved retrosynthesis [147, 148]

then to iodide **169** in six steps with moderate overall yield of 37%. **169** was then used to alkylate α-phenylsulfonyl-lactone **171** to give intermediate **170** as a 4.2:1 mixture of diastereoisomers. Over three steps the *exo*-methylene group at C13 was introduced, leading to intermediate **172** in good 72% overall yield. Some protective group manipulations and a Swern oxidation provided the key aldehyde **165** (Scheme 21) [146].

The synthesis of the building block **166** (Scheme 22) started from glycidyl ether **173** which was converted to the homoallylic ether **174** which could be converted smoothly to the dihydropyran **175** with Grubbs first-generation Ru catalyst. After deprotection of **175** and oxidation of the resulting primary alcohol, Corey-Fuchs chemistry led to the dibromo olefin **176**. The alkynyl anion derived from **176** was then coupled with aldehyde **177**, however only with low stereoselectivity (*syn/anti*= 1.8:1). **177** itself was accessible through a four step synthesis starting also from **173**. Oxidation of **178** followed by reduction with L-selectride delivered the pure *syn*-diol **179**. Subsequent selective reduction of the triple bond to *E*-geometry and a PMB protection group shift furnished building block **166** with an overall yield of 42% from **179** (Scheme 22) [146].

Coupling of the two fragments **165** and **166** by Julia chemistry involved lithiation of **166** and treatment of the resulting dianion with aldehyde **165** (Scheme 20).

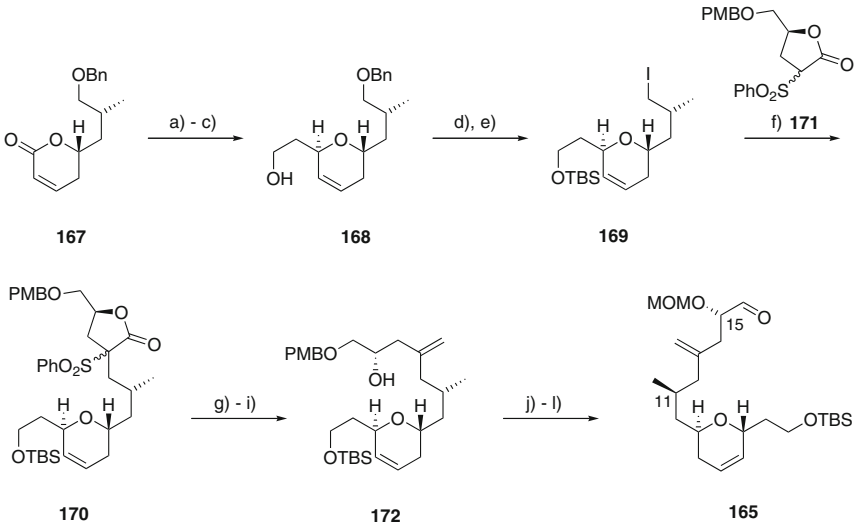

Scheme 21 **a** DIBAL-H, –78 °C then CSA, EtOH, 23 °C. **b** montmorillonite K-10, CH_2 = CHOTBS, 23°C. **c** $NaBH_4$, MeOH, 0 °C, 54%. **d** TBSCl, imidazole, DMF, 23 °C, 75%. **e** (1) Li, NH_3, 95%; (2) I_2, PPh_3, imidazole, 96%. **f** **171**, NaH, DMF, 0 °C then iodide **169**, 60 °C, 89%. **g** Red-Al, THF, 0 °C. **h** PhCOCl, Et_3N (cat) DMAP. **i** Na(Hg), Na_2HPO_4, MeOH, –20 °C → 23 °C, 72%. **j** MOMCl, *i*-Pr_2NEt, 23 °C. **k** DDQ, pH 7 buffer, 23 °C, 81%. **l** DMSO, $(COCl)_2$, *i*-Pr_2NEt, –60 °C, 85%

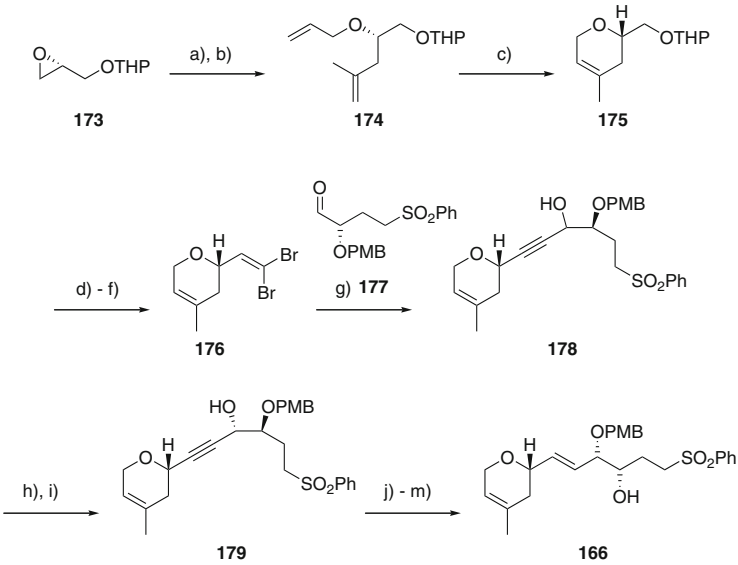

Scheme 22 **a** Isopropenyl magnesium bromide, CuCN (10 mol%), THF, −78 °C → 23 °C, 94%. **b** KH (cat) 18-Crown-6, allyl bromide, THF, 0 °C → 23 °C, 100%. **c** Grubbs first (2 mol%), CH_2Cl_2, 23 °C. **d** CSA, MeOH, 81%. **e** $(COCl)_2$, DMSO, Et_3N, CH_2Cl_2, −78 °C → 0 °C. **f** CBr_4, PPh_3, CH_2Cl_2, 0 °C → 23 °C, 67%. **g** *n*-BuLi, −78 °C, 1 h and 23 °C, 1 h then **177**, −78 °C, 64%. **h** Dess-Martin, CH_2Cl_2, 23 °C, 81%. **i** L-selectride, THF, −78 °C, 87%. **j** Red-Al, THF, −20 °C, 81%. **k** CF_3CO_2H, CH_2Cl_2, 23 °C. **l** *p*-MeO-Ph-$CH(OMe)_2$, CSA, CH_2Cl_2, 23 °C, 71%. **m** DIBAL-H, CH_2Cl_2, −78 °C, 74%

Peracylation and Na/Hg exposure furnished a 3.4:1 mixture of olefination products, from which the desired isomer **180** could be separated in reasonable yield (34%). After acylation of **180** with *bis*(2,2,2-trifluoroethyl)phosphonoacetic acid under Yamaguchi conditions, followed by TBS deprotection and oxidation, ring closure was finally achieved through a Still-Gennari modified HWE olefination, which led to a 1:2 mixture of *Z/E* macrolactones in 84% combined yields. UV irradiation of the *E*-isomer led to an overall improvement for the yield of the *Z*-isomer **181** from 28 to 47%. Finally the fully protected **181** was converted to laulimalide (**3**) with an overall yield of 22% over three steps, including the regioselective Sharpless epoxidation of the C16–C17 double bond, providing the first synthetic sample of laulimalide (Scheme 23) [146].

Following the first total synthesis a number of alternative approaches to laulimalide were reported in close succession 1 year later by the groups of Mulzer

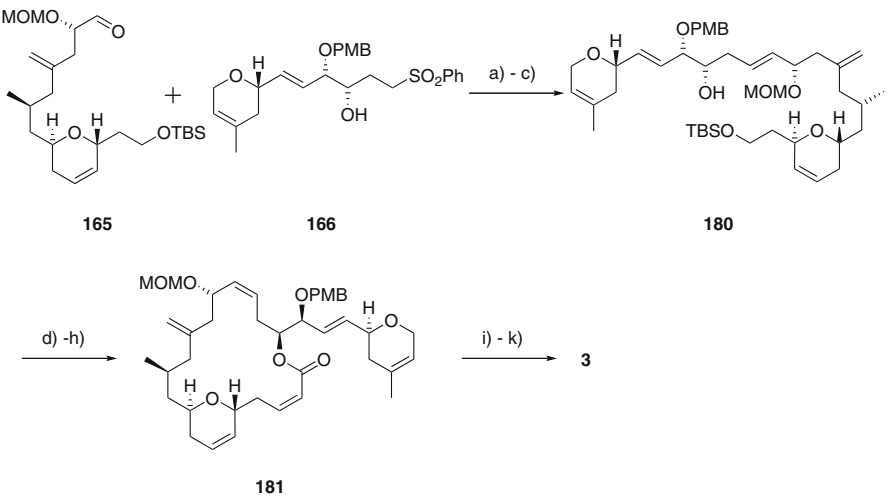

Scheme 23 **a** **166**, *n*-BuLi, −78 °C, 15 min, then **165**, −78 °C → −40 °C, 2 h. **b** Ac_2O, Et_3N (cat) DMAP. **c** Na(Hg), Na_2HPO_4, MeOH, −20 °C → 23 °C, 34%. **d** $(CF_3CH_2O)_2P(O)CH_2CO_2H$, $Cl_3C_6H_2COCl$, *i*-Pr_2NEt, DMAP. **e** AcOH/THF/water (3:1:1), 23 °C, 99%. **f** DMP, CH_2Cl_2, 23 °C, 79%. **g** K_2CO_3, 18-Crown-6, −20 °C → 0 °C, 84%. **h** *hν*, Et_2O, 50 min, 66%. **i** PPTS, *t*-BuOH, 84 °C, 45%. **j** Ti(O*i*-Pr)$_4$, (+)-DET, *t*-BuOOH, −20 °C. **k** DDQ, pH 7, 23 °C, 48%

[149–151] and Paterson [153]. One of Mulzer's three approaches was a fully stereoselective [150] synthesis which will be discussed below. Retrosynthetically, macrocyclization was to be achieved through intramolecular allyl transfer in seco intermediate **183**. The latter, which includes the entire carbon skeleton of laulimalide, was envisioned to be formed by a Still-Gennari modified HWE olefination between **184** and **185** (Scheme 24).

The building block **184** was synthesized starting from the commercially available ethyl hydrogen (*R*)-3-methylglutarate **186** (Scheme 25) and transformed to the homoallylic alcohol **187** by reduction, oxidation, asymmetric Brown allylation [139, 152, 158–160] and dimethyl amide formation. The dihydropyran moiety was elaborated by RCM after transketalization of **187** with acrolein diethylacetal. The stereoselective introduction of the two carbon side-chain at C5 was achieved by reaction of the RCM product (a cyclic acetal) with TBS vinyl ether. The resulting aldehyde was reduced and the alcohol protected as a TES ether to give amide **188**. The latter was subsequently converted to the methyl ketone **189** in high yields (90%). Treatment of **189** with $PhNTf_2$ [161, 162] provided the enoltriflate as a single regioisomer which was coupled with trimethylsilyl methylmagnesium chloride under Kumada conditions [163, 164] to afford allylsilane **190** in excellent yield. Final removal of the TES group and subsequent oxidation led to the C3–C14 fragment **184** (Scheme 25).

The phosphonoacetate building block was easily derived from a previously reported C15–C27 fragment [136]. Thus, TBDPS protected intermediate **192**,

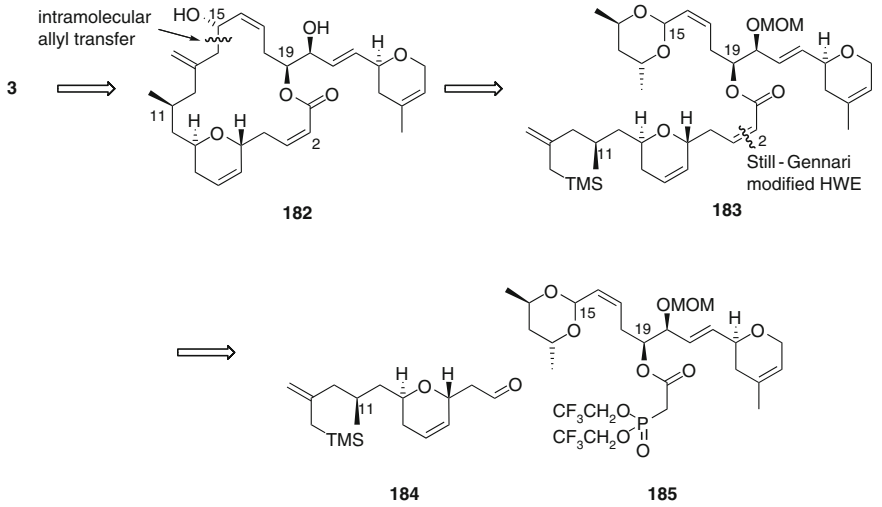

Scheme 24 Retrosynthetic analysis of Mulzer and Enev [150]

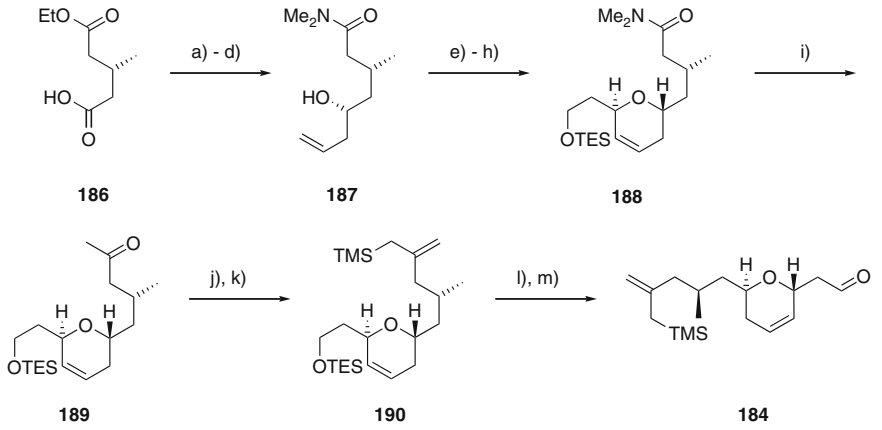

Scheme 25 **a** $BH_3{\cdot}Me_2S$, 99%. **b** DMP oxidation, 96%. **c** (–)-Ipc_2B-allyl, 87%. **d** Me_2NH, EtOH, 98%. **e** Acrolein-diethylacetal, TsOH, toluene, 92%. **f** 4 mol% Grubbs catalyst, CH_2Cl_2, 87%. **g** CH_2 = CHOTBS, $LiClO_4$, 92%. **h** (1) $NaBH_4$, MeOH, 0 °C, 99%; (2) TESCl, py, 92%. **i** MeLi, Et_2O, −75 °C, 90%. **j** KHMDS, $C_6H_5NTf_2$, THF, 80%. **k** 5 mol% $Pd(PPh_3)_4$, LiCl (5 equiv), $TMSCH_2MgBr$ (2 equiv), Et_2O, 96%. **l** K_2CO_3, MeOH, 0 °C, 98%. **m** DMP oxidation 90%

which is accessible in two steps with 91% yield from the glycidyl ether **191**, was first converted over three steps into the alcohol **193** and subsequently into methyl ester **194**. The latter was converted into a β-oxophosphonate by reaction with dimethyl methylphosphonate, which was then reacted with aldehyde **195** to yield *E*-enone **196**, thereby introducing the C21–C22 double bond of **3**. Reduction of the

enone under Luche conditions [165] followed by MOM protection of the alcohol formed and THP deprotection led to propargylic alcohol **197** with the correct stereochemistry at C20. **197** was converted to intermediate **198** by stereoselective reduction of the triple bond, oxidation of the resulting *E*-allylic alcohol and subsequent acetalization with commercially available (*R,R*)-(+)-pentane-2,4-diol. The synthesis of building block **185** was completed by TBDPS deprotection and subsequent acylation with *bis*(2,2,2-trifluoroethoxy)-phosphinylacetyl chloride (Scheme 26).

Fragment assembly (Scheme 27) involved the treatment of deprotonated **185** with aldehyde **184** at −78 °C, carefully avoiding excess of base. Under these reaction conditions **199**, comprising the complete laulimalide skeleton, was obtained as a single isomer in 85% yield. The latter cyclized through an intramolecular Hosomi-Sakurai reaction providing macrolactone **200** in an excellent yield (85%).

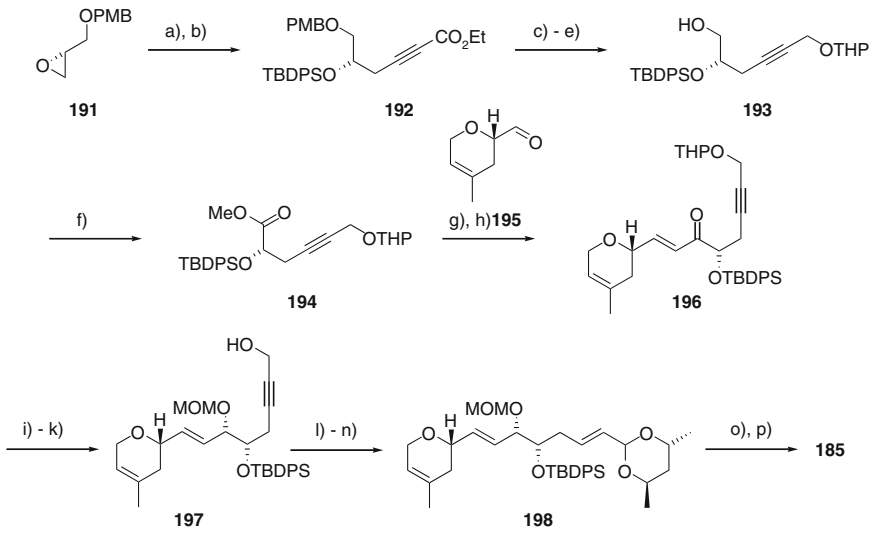

Scheme 26 **a** Ethyl propiolate, *n*-BuLi, $BF_3{\cdot}OEt_2$ (each 3 equiv), then **191**, THF, 30 min, −78 °C, 100%. **b** TBDPSCl (1.3 equiv), imidazole, DMF, 5 h, 100%. **c** DIBALH (2.2 equiv), CH_2Cl_2, 1 h, −78 °C, 91%. **d** Dihydropyran, TsOH, 20 min, 96%. **e** DDQ (1.2 equiv), CH_2Cl_2/water (20:1), 30 min, 97%. **f** (1) $SO_3{\cdot}$pyr, TEA, CH_2Cl_2, 30 min; (2) $NaClO_2$ (3 equiv), KH_2PO_4, 2,3-dimethylbut-2-ene:*t*-BuOH (1:1), 1 h; (3) CH_2N_2, Et_2O, 80%. **g** Dimethyl methylphosphonate (2.5 equiv), *n*-BuLi, then **194**, THF, 3 h, −78 °C, 91%. **h** *n*-BuLi then water, then **195**, THF/Et_2O (1:1), 0 °C → rt, 2 h, 80%. **i** $NaBH_4$ (1.0 equiv), $CeCl_3$, MeOH, 5 min, 67% (plus 20% mixed regioisomers). **j** MOMCl (20 equiv), DIPEA, DMF, 3 h, 90%. **k** 2.5% HCl (aq.), MeOH, 0 °C → rt, 30 min, 100%. **l** Red-Al® (1.2 equiv), Et_2O, rt, 24 h, 84%. **m** DMP oxidation, 96%. **n** (*R,R*)-(+)-2,4-pentanediol (1.8 equiv), montmorillonite K-10, toluene, 98%. **o** TBAF, THF, 82%. **p** $(CF_3CH_2O)_2P(O)CH_2COCl$ (1.6 equiv), DMAP, −78 °C → 0 °C, 98%

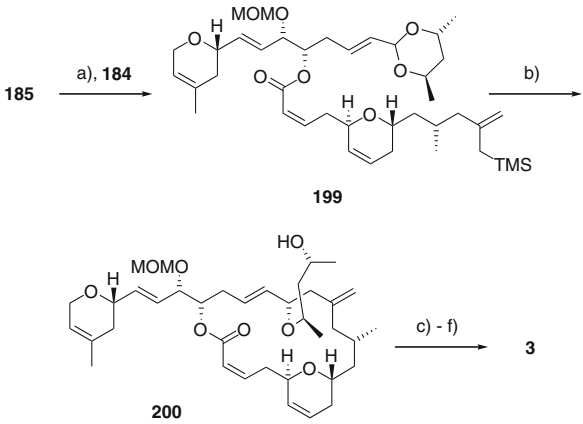

Scheme 27 **a** KHMDS, –78 °C, 40 min, then **184**, 1.2 equiv, 20 min, 82%. **b** $EtAlCl_2$ (2 equiv), –50 °C → 0 °C, 82%. **c** DMP oxidation, 90%. **d** TsOH, $CHCl_3$, 80%. **e** Me_2BBr, –78 °C, 20 min, 96%. **f** (+)-DIPT, *t*-BuOOH, Ti(O-*i*-Pr)$_4$, CH_2Cl_2, -20 °C, 2 h, 70%

Removal of the γ-hydroxy ether at C15, MOM deprotection, and finally Sharpless epoxidation then gave the desired laulimalide (**3**).

In a more recent approach to the total synthesis of laulimalide (**3**), Uenishi et al. [166] involved a Sakurai-Hosomi coupling of fragments **201** and **202** and Yamaguchi macrolactonization for ring closure (Scheme 28). The synthesis also features a new approach to the construction of the dihydropyran moiety.

Fragment **201** was prepared by first coupling building blocks **203** and **204** through a HWE olefination followed by diastereoselective reduction of the keto group to the β-alcohol **205** in reasonable yield (56% in two steps). Mitsunobu-based esterification of **205** with benzoic acid yielded (under inversion) a 1:1 mixture of C21 and C23 benzoates **206**, which after TBDPS cleavage was subjected to Pd^0-catalyzed intramolecular *O*-allylation to furnish **208** together with the unreacted benzoate **207** which only underwent Pd^0-catalysed intramolecular *O*-allylation after ester cleavage and subjection to $[PdCl_2(CH_3CN)_2]$. After cleavage of the acetonide, oxidation of the PMB ether led to **209**. TBS protection at C20 followed by reductive benzylidene acetal opening, oxidation of the primary alcohol and Wittig olefination of the resulting aldehyde provided ester **210** in a reasonable yield (66% over four steps). Ester reduction and final Dess-Martin oxidation gave the desired fragment **201** with excellent yield (92% over two steps) (Scheme 29).

Fragment **202** was synthesized starting from the homoallylic alcohol **211** which was converted to allylic alcohol **212** via TBS protection, osmylation and subsequent diol cleavage, and Ni/Cr-promoted coupling [167, 168] of the

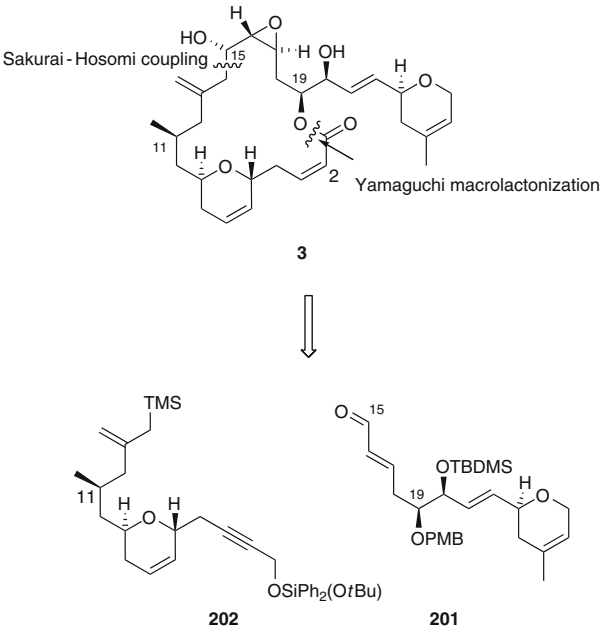

Scheme 28 Retrosynthetic analysis of (−)-laulimalide (**3**) by Uenishi et al. [166]

resulting aldehyde with (*E*)-4-benzoyloxy-1-iodo-1-butene. Dess-Martin oxidation, followed by enantioselective reduction and TBS deprotection then led to the diol **213** which was subjected to Pd^{II}-catalyzed ring formation to give the desired pyran **214** exclusively (Scheme 30) (for 5-endo-trig cyclization in dihydrofuran synthesis see [169]).

Cleavage of the benzoate ester in **214**, oxidation of the resulting alcohol to the corresponding aldehyde, homologation of the latter to the 1,1-dibromoalkene **215**, debromination with *n*-BuLi and reaction of the resulting lithioalkyne with paraformaldehyde, and finally protection of the resulting propargylic alcohol furnished **216**. PMB removal followed by Dess-Martin oxidation and dibromo olefination led to intermediate **217** in 68% yield. 1,1-Dibromo-1-alkene **217** was subsequently crosscoupled in high yield (86%) with TMS-CH_2MgCl and finally treated with PPTS to provide fragment **202**.

The two fragments **201** and **202** were then assembled through a Sakurai-Hosomi reaction promoted by $SnCl_4$. The reaction resulted in a mixture of diastereomeric alcohols which by an oxidation, stereoselective reduction cascade was converted into the single diastereomer **218** (Scheme 31). After silylation of **218** the propargylic hydroxyl group was deprotected chemoselectively and the resulting primary alcohol was converted to the seco acid **219** in three steps. Yamaguchi macrolactonization, global silyl deprotection and partial reduction of the C2–C3 triple bond afforded

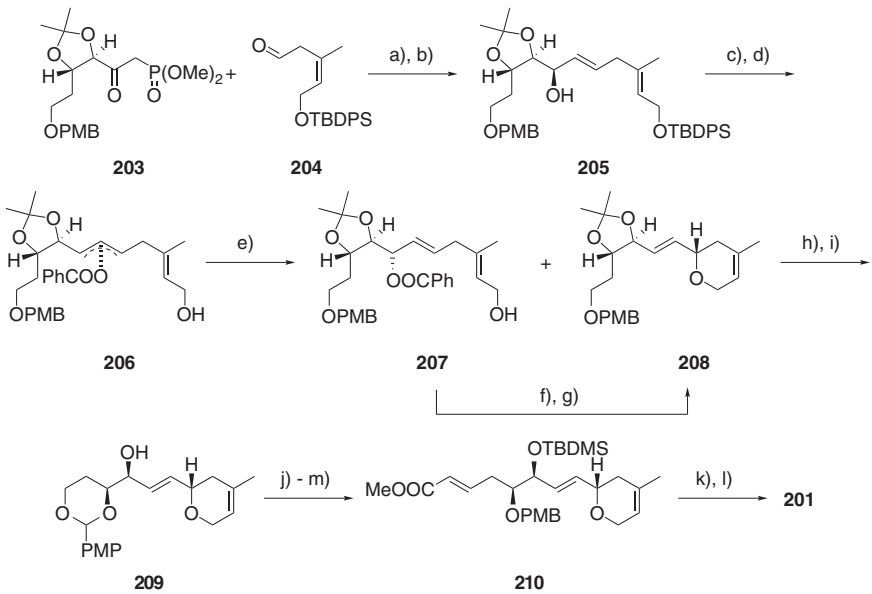

Scheme 29 **a** K_2CO_3 THF/water (1:1), rt, 70%. **b** $NaBH_4$, $CeCl_3 \cdot 7\ H_2O$, MeOH, -78 °C → rt, 80%. **c** DEAD, Ph_3P, PhCOOH, benzene, rt, 81%. **d** TBAF, THF, rt, 86%. **e** $[Pd_2(dba)_3]$ (20 mol%), neocuproine, toluene, rt, 89% (based on recovered **207**). **f** K_2CO_3, MeOH, rt, 97%. **g** $[PdCl_2(CH_3CN)_2]$ (10 mol%), THF, 0 °C, 89%. **h** HCl, MeOH, rt, 89%. **i** DDQ, molecular sieves (4 Å), CH_2Cl_2, 0 °C, 87%. **j** TBSCl, imidazole, DMF, rt, 90%. **k** DIBAL-H, CH_2Cl_2, −78 °C, 83%. **l** DMP, 96%. **m** $Ph_3PCHCOOMe$, benzene, rt, 92%; **210** → **201**: (**k**) 98%; (**l**) 94%

desoxylaulimalide **220** which was finally converted to laulimalide (**3**) via Sharpless epoxidation.

Following the development of laulimalide chemistry, various non-natural [152, 170–176] and natural [177] analogs have been reported over the course of the past few years. As for epothilone, it was shown for laulimalide (**3**) that the C16–C17 epoxide moiety seems not to be an absolute requirement for the induction of tubulin polymerization and cytotoxic activity [122, 152, 170, 171]. The synthetic intermediate **220** (Scheme 31) incorporating a *trans*-C16–C17 double bond still showed tubulin-polymerization activity and had an IC_{50} for MCF-7 cells of 89 nM (**3**: 3.8 nM) [152]. On the other hand, isolaulimalide and natural analogs thereof have lost most of the activity of laulimalide [11, 177]. A similar loss of activity can be observed when replacing the C2–C3 double bond by a triple bond or a *trans*-double bond [152, 171].

Acylation or methylation of the C20-hydroxyl group did result in a 100-(resp. 200-)fold loss of activity, while acylation of the hydroxyl group at C15 only led to ca. a ten-fold decrease in activity compared to **3** [172]. However, these analogs still show potent antiproliferative activity with IC_{50}s in the 30–300 nM range.

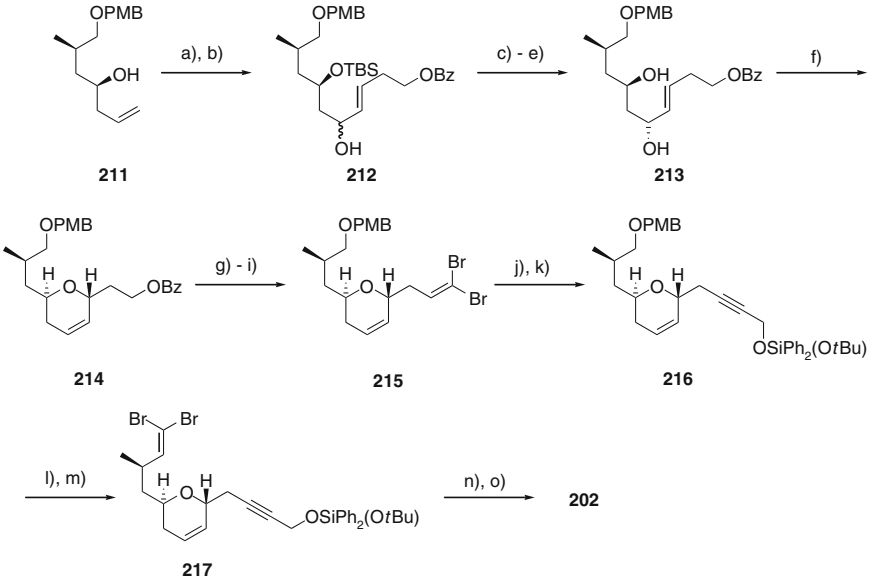

Scheme 30 **a** TBSCl, imidazole, DMF, rt, 97%. **b** (1) (cat) OsO_4, NMO, THF/water (5:1), rt; (2) $NaIO_4$, THF/water (5:1); (3) (*E*)-4-benzyloxy-1-iodo-1-butene, $NiCl_2$/(cat) $CrCl_2$, DMSO, rt, 75%. **c** DMP, 91%. **d** BH_3. THF complex (*S*)-CBS, THF, −40 °C, 99% (dr >97:3). **e** TBAF, THF, rt, 85%. **f** $[PdCl_2(CH_3CN)_2]$ (15 mol%), benzoquinone, THF, −5 °C, 60%. **g** K_2CO_3, MeOH, rt, 92%. **h** DMP, 90%. **i** CBr_4, PPh_3, CH_2Cl_2, 0 °C, 94%. **j** *n*-BuLi, THF, −78 °C; then $(HCHO)_n$, −78 °C → 0 °C, 83%. **k** (O*t*-Bu)Ph_2SiCl, Et_3N, CH_2Cl_2, rt, 99%. **l** DDQ, CH_2Cl_2/buffer (pH 7) (10:1), rt, 87%. **m** (1) DMP; (2) CBr_4, PPh_3, CH_2Cl_2, 0 °C, 78%. **n** (cat) $Pd(OAc)_2$, PPh_3, Me_3SiCH_2MgCl, THF, 50 °C, 86%. **o** PPTS, THF/CH_3CN (9:1), rt, 99%

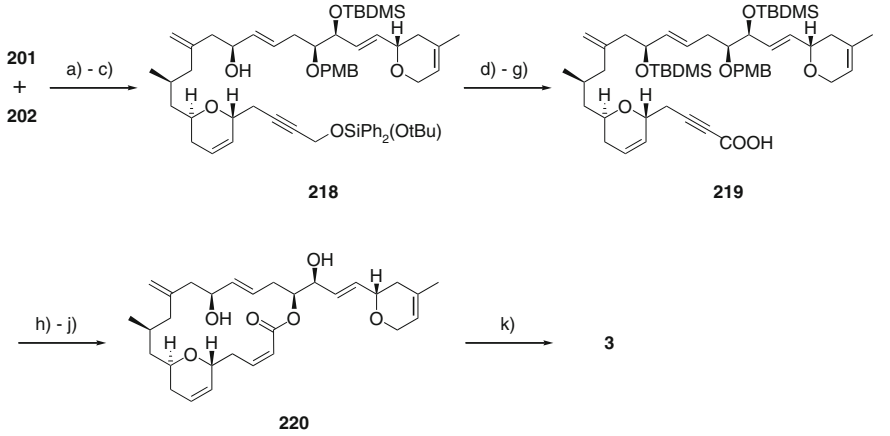

Scheme 31 **a** $SnCl_4$, CH_2Cl_2, −78 °C, 86%. **b** DMP, 86%. **c** BH_3. THF complex (*R*)-CBS, THF, −40 °C, 92%. **d** TBSCl, imidazole, DMF, rt, 95%. **e** K_2CO_3, MeOH/THF (3:1), rt, 93%. **f** (1) DMP; (2) DDQ, CH_2Cl_2/buffer (pH 7) (2:1), 0 °C, 80%. **g** $NaClO_2$, 2-methyl-2-butene, NaH_2PO_4, THF/*t*-BuOH (1:2), 0 °C, 98%. **h** Yamaguchi lactonization, 88%. **i** HF·py, CH_3CN, rt, quant. **j** Lindlar cat, H_2, quinoline, EtOAc/1-hexene (1:1), rt, 77%. **k** Sharpless epoxidation conditions (+)-diisopropyl tartrate, 80%

Particularly interesting is the finding that the removal of the methyl group at C11 only causes a 10- to 20-fold [175, 176] loss in antiproliferative activity (**3**: IC_{50} (MDA-MB-435) = 5.7 ± 0.6 nM; **221**: IC_{50} (MDA-MB-435) = 49.0 ± 2.3 nM; [176]). Also, 11-desmethyllaulimalide (**221**) retains significant tubulin polymerizing activity in vitro [175], thus providing an interesting starting point for the design and evaluation of simplified laulimalide analogs.

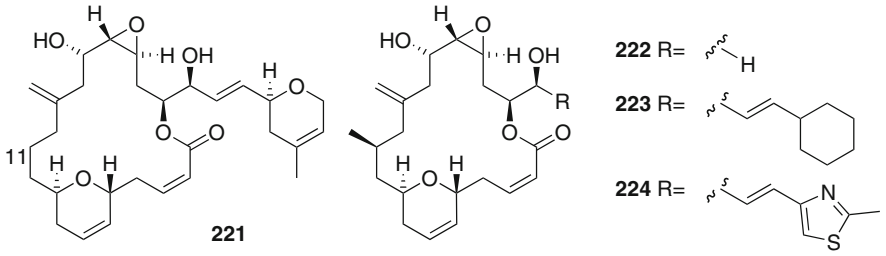

Side-chain modifications such as those reported by Paterson et al. [175] (e.g. **222–224**) while still exhibiting tubulin-polymerizing activity seem to have lost their cytotoxic activity almost completely. Similar observations regarding cytotoxicity were made by Mooberry, Crews and co-workers for side-chain-modified analogs recently isolated from natural sources [177].

As for other microtubule-stabilizing agents, attempts have been made to determine the conformation of laulimalide in solution. Paterson et al. have investigated the conformation of **3** and **221** in MeOH-d_4 solution by ^{1}H-NMR and constrained MD simulations and found similar conformations, resembling the X-ray structure of laulimalide [128], for both **3** and its analog **221** [178]. A combination of NMR experiments and NAMFIS deconvolution analysis of laulimalide (**3**) in DMSO-d_6 by Thepchatri et al. has led to somewhat different conclusions. They identified five major structural families in conformational equilibrium [179], one of which closely resembles the solid-state structure of **3** [128]. However, almost 40% of the low energy structures are distinctly different from the solid-state conformation. Likewise the findings of Thepchatri et al. [179] regarding the flexibility of the C12–C20 region are not congruent with Paterson's results, which had suggested this region to be rather rigid. It remains to be seen how these conformational proposals will compare to the tubulin-bound conformation once this becomes available.

4 Dictyostatin

Like laulimalide (**3**), dictyostatin (**4**, also called dictyostatin-1) is a microtubule-stabilizing polyketide of marine origin. It was first isolated in 1994 by Pettit et al. from a sponge of the genus *Spongia* sp., collected off the coast of the Maldives in

the Indian Ocean [180]. Dictyostatin was found to inhibit the growth of murine P388 lymphocytic leukemia cells at sub-nanomolar concentrations (ED_{50} approx. 0.7 nM). However, synthetic efforts following this interesting finding, were hampered by the fact that the complete absolute configuration of dictyostatin (**4**) remained unassigned.

While the exact configuration at C16 and C19 was yet unknown, Curran, Day and co-workers in 2002 [181] recognized the notable structural similarities between **4** and the dictyostatin-like linear polyketide discodermolide **225**[3], which had been isolated some years earlier from the deep-water Caribbean sponge *Discodermia dissoluta* [182]. The notion of the structural similarity of discodermolide and dictyostatin has recently been re-enforced by conformational studies by Sánchez-Pedregal et al. [104].

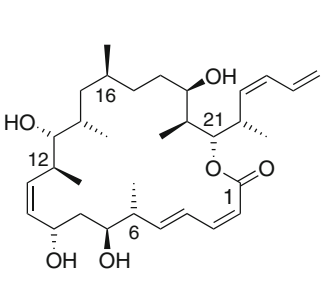

dictyostatin (**4**)

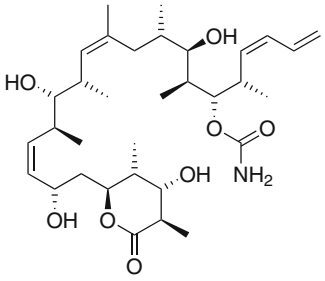

discodermolide (**225**)

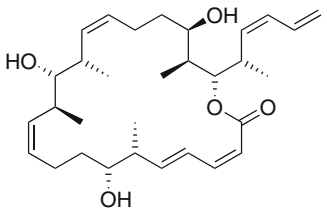

226

Reflecting their interest in discodermolide analogs Curran and co-workers prepared dictyostatin-discodermolide hybrids such as **226**, which showed a significant ability to displace taxol from microtubules, thus providing a first hint at **4**'s potential microtubule-stabilizing properties [181]. It was not, however, until almost a decade later that dictyostatin was unambiguously established as a microtubule-stabilizing agent [14]. In 2003, Wright and co-workers reported the re-isolation of dictyostatin from a sponge of the family *Corallistidae* in the Caribbean and showed that it potently induced tubulin polymerization in vitro and further showed other typical features of compounds interfering with microtubule dynamics such as bundling of

[3]The chemistry of discodermolide is discussed in another chapter of this volume by I. Paterson.

interphase microtubules, cell cycle block in G2/M with anomalous spindle formation, and the induction of apoptosis [14]. Dictyostatin was found to inhibit the growth of human cancer cells even more potently than taxol and, even more importantly, to retain most of its activity in multidrug-resistant cell lines [14]. Two subsequent studies not only confirmed these findings, but also showed dictyostatin to have an equal if not higher potency than discodermolide to promote tubulin polymerization and to stabilize microtubules [123–125, 183]. Competition of dictyostatin for microtubule binding has been shown with taxol [123–125, 183], epothilone B [183], and discodermolide [183], suggesting that **4** binds to the taxol binding site on the β-subunit of tubulin. The re-isolation of dictyostatin [14] has also led to the complete stereochemical determination of dictyostatin (**4**) [184], applying Murata's method of *J*-based configuration analysis [185] in combination with extensive NOESY experiments [184].

With the absolute configuration at hand it was only a matter of time until the first total synthesis of dictyostatin was to be accomplished. Paterson et al. [186] as well as Curran and co-workers [187] succeeded almost simultaneously. Up until today four total syntheses from four different research groups have been reported [186–189] and several partial syntheses indicate that additional total syntheses of **4** will be reported in the near future [190–194].

Apart from the recent total synthesis of Phillips and co-workers [188], which used an intramolecular Still-Gennari-modified HWE olefination to connect C2 and C3, all successful attempts for the synthesis of dictyostatin so far are based on the use of the Yamaguchi protocol for closure of the macrolactone ring [186, 187, 189].

As stated above, the first total synthesis of dictyostatin was accomplished by Paterson et al. [186] employing Yamaguchi macrolactonization as well as Still-Gennari modified HWE olefination and a Stille coupling as key steps (Scheme 32). All three reactions represent possible modes of ring closure and this approach offers considerable synthetic flexibility in the synthesis. The strategy further relied on a late-stage stereoselective reduction of the enone **227**, controlled by the conformation of the macrocycle. The construction of the northern half of **227** (i.e. **228**) was based on the coupling of two building blocks derived from a common precursor **231** by HWE olefination. The southern half was subsequently elaborated through attachment of the C4–C10 subunit (**229**) by Still-Gennari-HWE olefination and through Stille coupling for the C1–C3 subunit (**230**) (Scheme 32).

The synthesis of the northern half **228** as shown in Scheme 33 started with the conversion of the common precursor **231** (which is available on a multigram scale in five steps from Roche ester [195]) into the iodide **232** over three steps followed by alkylation of the Myers propionamide **233** [196] yielding **234** with excellent diastereoselectivity (dr = 19:1; 88% yield). The reductive removal of the pseudoephedrine auxiliary and subsequent oxidation with Dess-Martin periodinane provided aldehyde **235** (83% yield over two steps), which was then coupled to **236** by HWE olefination yielding enone **237** in excellent yield (92%). **236** is accessible from **231** in nine steps [195, 197, 198]. The conversion of enone **237** to the triol **238** involved conjugate reduction using Stryker's reagent ($[Ph_3PCuH]_6$) followed by

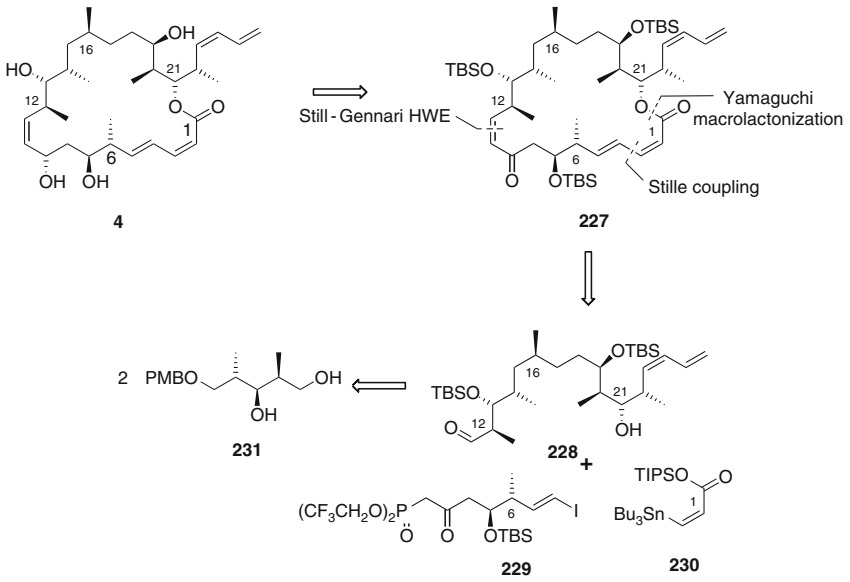

Scheme 32 Retrosynthetic analysis for dictyostatin by Paterson et al. [186]

oxidative removal of the two PMB protecting groups and 1,3-*syn*-selective reduction, which again proceeded with excellent diastereoselectivity (dr >20:1). A final three-step sequence involving protecting group manipulations and a final oxidation-step furnished the required C11–C26 building block **228**.

The choice of the specific C4–C10 subunit **229** was guided by concerns about the epimerizable center at C12 in **228**, which should be addressed by the use of the mild Still-Gennari modified HWE to link **228** and **229**. The required phosphonate **229** was prepared starting from alcohol **239** (Scheme 34). Silyl ether formation, ozonolysis and Takai methylenation provided *E*-vinyl iodide **240**. After selective cleavage of the primary TBS-ether, oxidation of the resulting alcohol afforded acid **241** which was converted to **229** using the Ghosez reagent ($Me_2C = C(Cl)NMe_2$) [199]. **228** and **229** were then readily coupled with a selectivity of 5:1 for the desired *Z*-enone **242**. The dictyostatin backbone **243** was then finally assembled through a copper-mediated, Liebeskind-type Stille coupling [200] of **242** with *Z*-alkenyl stannane **230**. TIPS removal and Yamaguchi macrolactonization yielded enone **227** which, after Luche reduction and subsequent global deprotection, provided dictyostatin (**4**) in 3.8% overall yield (Scheme 34).

Compared to the synthesis of Paterson et al. [186], Curran and co-workers envisaged a synthesis with stereochemical flexibility as a key design element, reflecting the uncertainties existing at the time with regard to the absolute configuration (Scheme 35). In addition, the design of a less convergent strategy was preferred to

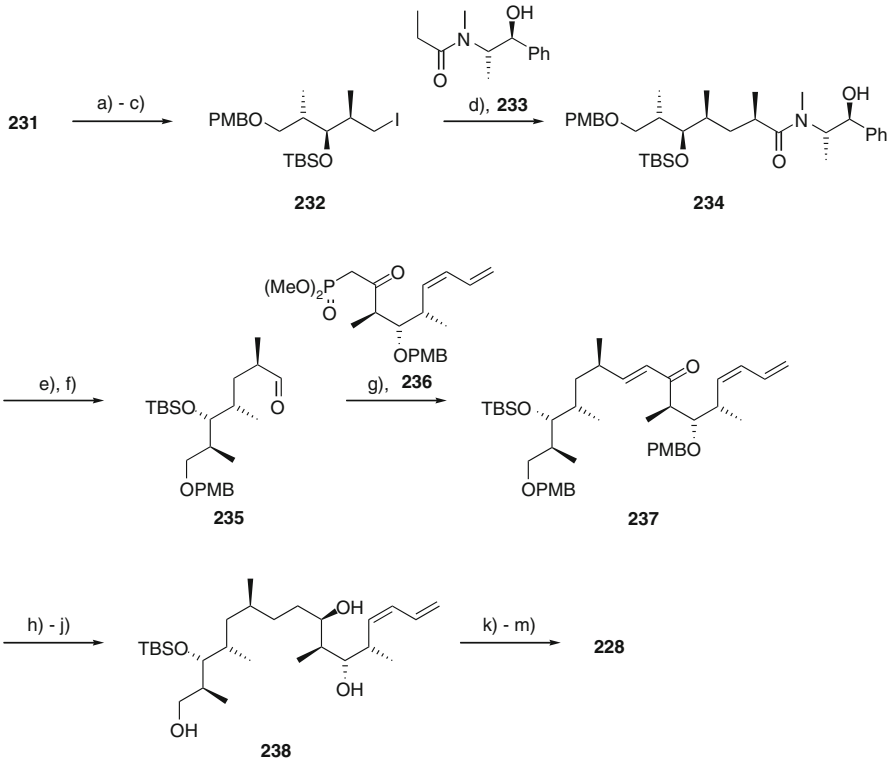

Scheme 33 **a** TBS-OTf, 2,6-lutidine, CH_2Cl_2, 0 °C → rt, 15 min, 100%. **b** *p*-TsOH, THF/water, 24 h, 93%. **c** PPh_3, I_2, imidazole, toluene, 0 °C, 15 min, 86%. **d** (1) **233**, LiCl, LDA, THF, -78 °C → rt; (2) **232**, THF, 0 °C → rt, 18 h, 88%, dr 19:1. **e** (1) LDA, BH_3NH_3, THF, 0 °C; (2) **234**, THF, 0 °C → rt, 18 h. **f** DMP, $NaHCO_3$, CH_2Cl_2, 0 °C, 2 h, 79% over two steps. **g** (1) **236**, $Ba(OH)_2 \cdot 8H_2O$, THF, 1 h; (2) **235**, 40:1 THF/water, 20 h, 92%. **h** $[Ph_3PCuH]_6$, toluene/water rt, 2 h. **i** DDQ, pH 7 buffer, CH_2Cl_2, 0 °C, 6 h. **j** $Zn(BH_4)_2$, Et_2O, −30 °C, 2 h, 66% over three steps. **k** TBS-OTf, 2,6-lutidine, −78 °C → 0 °C, 30 min, 91%. **l** TBAF, AcOH, THF, rt, 24 h, 100%. **m** TEMPO, $PhI(OAc)_2$, CH_2Cl_2, rt, 18 h

facilitate the subsequent preparation of analogs. This was to be accomplished by introducing both diene moieties after the coupling of all fragments [187].

The key intermediate **244** was to be assembled from the three main fragments **245**, **246** and **247**, whose synthesis had been accomplished previously in the context of the synthesis of discodermolide (**225**) [23, 201–205] (Scheme 35).

The building blocks were assembled by metalation of fragment **245** and the following addition of the Weinreb amide **247** to form an alkyne ketone (Scheme 36). The latter was asymmetrically reduced according to Noyori [206, 207] followed by Lindlar hydrogenation to yield **248** as a single isomer. TBS protection of the newly formed hydroxyl group, followed by cleavage of the primary TBS-ether and subsequent oxidation of the alcohol gave an aldehyde, whose HWE coupling with **246** led to the key intermediate **244**. After the reduction of the conjugated double bond in **244**

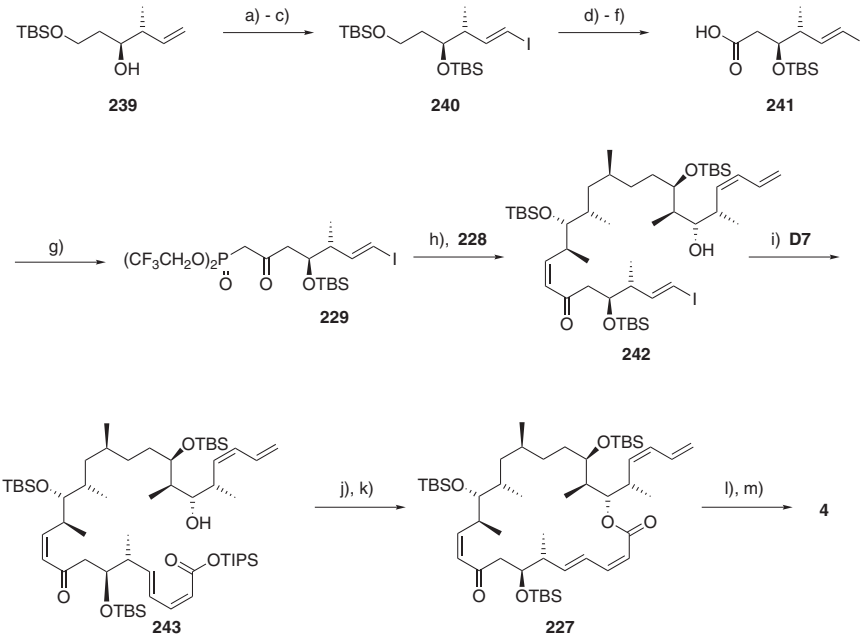

Scheme 34 **a** TBS-OTf, 2,6-lutidine, CH_2Cl_2, −78 °C, 30 min. **b** (1) O_3, CH_2Cl_2, −78 °C; (2) Ph_3P, −78 °C → rt, 2 h. **c** $CrCl_2$, CHI_3, THF, dioxane, 0 °C, 18 h, 71% over three steps. **d** TBAF, AcOH, THF, rt, 14 h. **e** DMP, py/CH_2Cl_2, rt, 3 h. **f** $NaClO_2$, NaH_2PO_4, 10:1 *t*-BuOH/water, 0 °C, 2 h, 74% over three steps. **g** (1) Me_2C = C(Cl)NMe_2, CH_2Cl_2, rt, 15 min; (2) $(F_3CCH_2O)_2P(O)CH_2Li$, THF, −100 °C, 1 h, 57%. **h** **228**, K_2CO_3 (10 equiv), 18-crown-6 (25 equiv), toluene, rt, 48 h, 77%, *Z*/*E*= 5:1. **i** **230**, CuTC, NMP, rt, 1 h. **j** KF, THF, MeOH, rt, 2 h, 83% over two steps. **k** 2,4,6-$Cl_3C_6H_2C(O)Cl$, NEt_3, DMAP, toluene, 60 °C, 2 h, 77%. **l** $NaBH_4$, $CeCl_3 \cdot 7\,H_2O$, EtOH, −30 °C, 70%. **m** HCl (3 N), MeOH, rt, 6 h, 87%

the ketone was reduced with $NaBH_4$, resulting in a mixture of two epimers with a ratio of 2.4:1 (in favor of the desired alcohol). Following TBS protection and PMP acetal opening the terminal diene was introduced using similar procedures (Nozaki-Hiyama reaction followed by Peterson-type *syn*-elimination) as described in the synthesis of discodermolide [198] to give **249**. Detritylation of **249** followed by oxidation and Still-Gennari olefination [208] gave fully protected seco acid **250**. PMB removal, saponification of the methyl ester, Yamaguchi lactonization, and final deprotection then provided **4** in 1% overall yield (Scheme 36).

The most recent total synthesis of dictyostatin by O'Neil and Phillips, while using some of the concepts already implemented in previous approaches, also introduced novel strategies for assembling **4** (Scheme 37) [188]. Thus, the formation of an intermediate macrocycle by RCM was applied to form the C10–C11 bond of dictyostatin. RCM precursor was **253** assembled from building blocks **251** and **252** by ester bond formation under Yamaguchi conditions. The RCM gave selectively the desired *Z*-

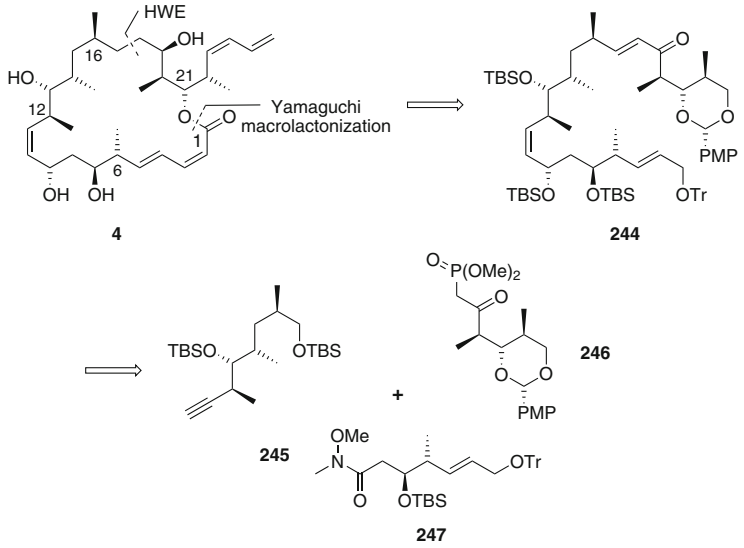

Scheme 35 Retrosynthetic analysis for dictyostatin by Curran and co-workers [187]

isomer **254**, which was then converted to **255** in five steps, involving, apart from protecting group manipulations, the reduction of lactone **254**, olefination of the resulting aldehyde with (carboethoxy)-methylentriphenylphosphorane and subsequent reduction to the allylic alcohol. Like Paterson et al. [186] and Curran and coworkers [187], the C17–C18 connection was formed by applying HWE olefination to access an α,β-unsaturated ketone **256** at C19, which was then elaborated into the saturated alcohol **257** (in analogy to the reduction of Paterson's intermediate **237** (Scheme 33) [186] and likewise achieving excellent diastereoselectivity in ketone reduction step (dr > 20/1)). Protecting group manipulations and acylation under Yamaguchi conditions led to precursor **258**, which was used in an intramolecular Still-Gennari olefination (*Z*/*E*= 6.1:1) for ring closure providing, after final deprotection, dictyostatin (**4**) (Scheme 37) [188].

The synthesis by Ramachandran et al. [189] is based on forming 8 of the 11 stereocenters of dictyostatin during the synthesis of the building blocks by pinene-mediated crotylborations [209] and another two by Myers alkylation [196] and the use of Roche ester as a starting material. To assemble the various building blocks Ramachandran et al., similar to Paterson et al. [186], first linked the C11–C17 subunit **259** by Julia olefination with the C18–C23 subunit **260** forming the northern half **261** of dictyostatin. The latter was elaborated into **262**, which connected with the C1–C9 subunit **263** by substrate-controlled vinyl zincate addition [210]. The desired epimer **264** was obtained as a single isomer, which could be converted into dictyostatin (**4**) in five steps, including Yamaguchi macrolactonization for ring closure (Scheme 38) [211].

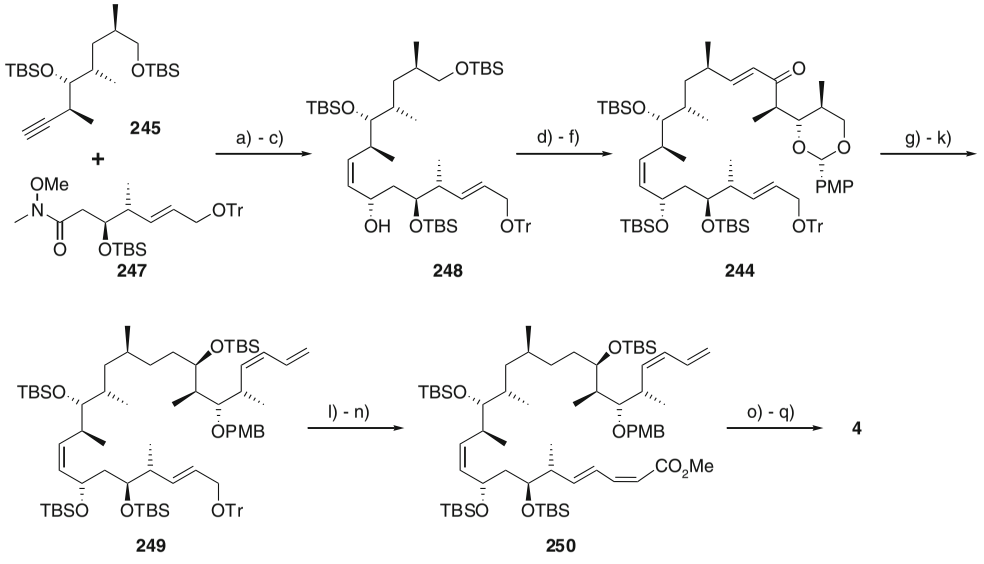

Scheme 36 **a** *n*-BuLi, THF, 93%. **b** *S*,*S* Noyori catalyst (20 mol%), *i*-PrOH, 79%. **c** Lindlar catalyst, H_2 (balloon), toluene, 91%. **d** TBS-OTf, 2,6-lutidine, CH_2Cl_2, 99%. **e** HF/py, py, THF, 0 °C, 1 day, 67%. **f** (1) DMP oxidation; (2) $Ba(OH)_2$, **246**, THF/water, 80% (two steps). **g** $NiCl_2$, $NaBH_4$, MeOH/THF, 76%. **h** $NaBH_4$, MeOH/THF, 70% (β), 29% (α). **i** TBS-OTf, 2,6-lutidine, CH_2Cl_2, 99%. **j** DIBALH, CH_2Cl_2, 88%. **k** (1) DMP oxidation; (2) CH_2 = CHCH(TMS) Br, $CrCl_2$, THF; (3) NaH, THF, 89% (three steps). **l** $ZnBr_2$, CH_2Cl_2/MeOH, 69%. **m** (1) DMP oxidation; (2) $(CF_3CH_2O)_2P(O)CH_2CO_2Me$, KHMDS, 18-crown-6, THF, 86% (two steps). **n** DDQ, CH_2Cl_2/water, 88%. **o** KOH (1 N), EtOH/THF. **p** 2,4,6-$Cl_3C_6H_2C(O)Cl$, Et_3N, THF then DMAP (10 equiv), toluene, 78% (two steps). **q** HCl/MeOH (3 N), THF, 55%

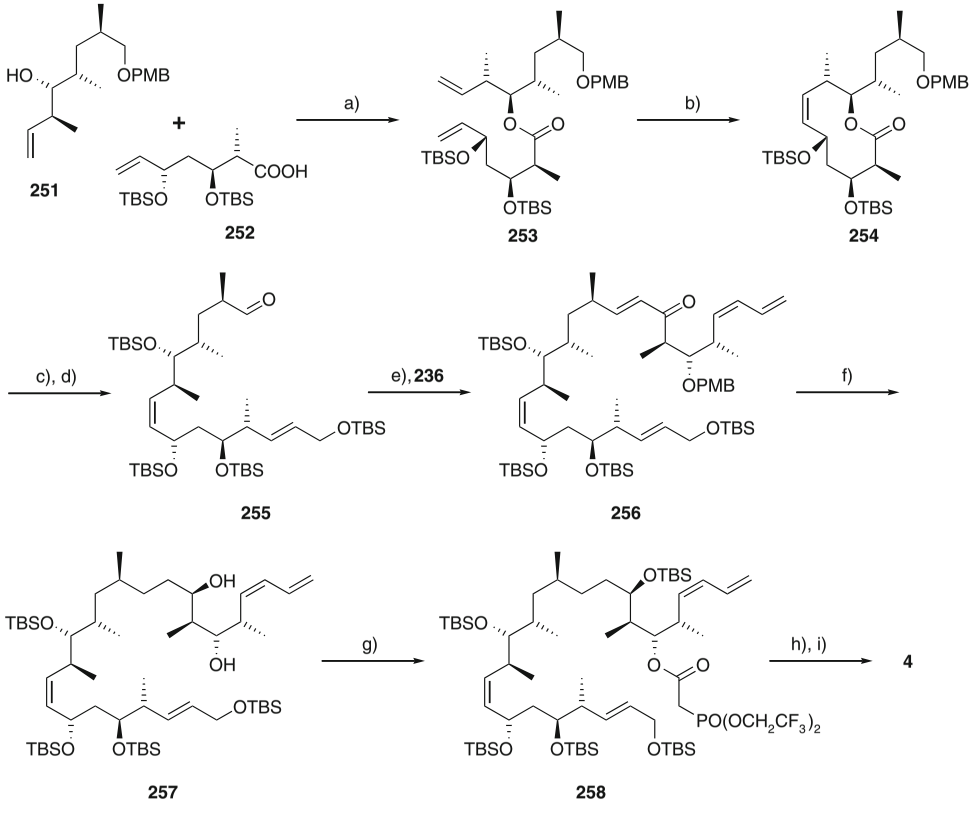

Scheme 37 **a** 2,4,6-$Cl_3C_6H_2C(O)Cl$, Et_3N, DMAP, toluene, 90%. **b** 15 mol% of Grubbs II, toluene, 110 °C, 76%. **c** DIBAL-H, CH_2Cl_2 then Ph_3PCHCO_2Et, 73%. **d** (1) DIBAL-H then TBS-OTf, 2,6-lutidine; (2) DDQ, CH_2Cl_2, pH = 7 buffer; (3) DMP, CH_2Cl_2 (60% over three steps). **e** **236**, $Ba(OH)_2$, THF/water, 80%. **f** (1) $[Ph_3P{\cdot}CuH]_6$, PhH; (2) DDQ, CH_2Cl_2/water, 0 °C (82% over two steps); (3) $Zn(BH_4)_2$, Et_2O, 88%. **g** (1) TBS-OTf, CH_2Cl_2, 2,6-lutidine, 89%; (2) $(CF_3CH_2O)_2P(O)CH_2CO_2H$, 2,4,6-$Cl_3C_6H_2C(O)Cl$, Et_3N, DMAP, toluene, 93%. **h** (1) AcOH, THF/water, 78%; (2) DMP, CH_2Cl_2; (3) K_2CO_3, 18-c-6, toluene, rt, 85% (two steps, 74% of desired diastereoisomer). **i** HF·py, THF, 40 h, 67%

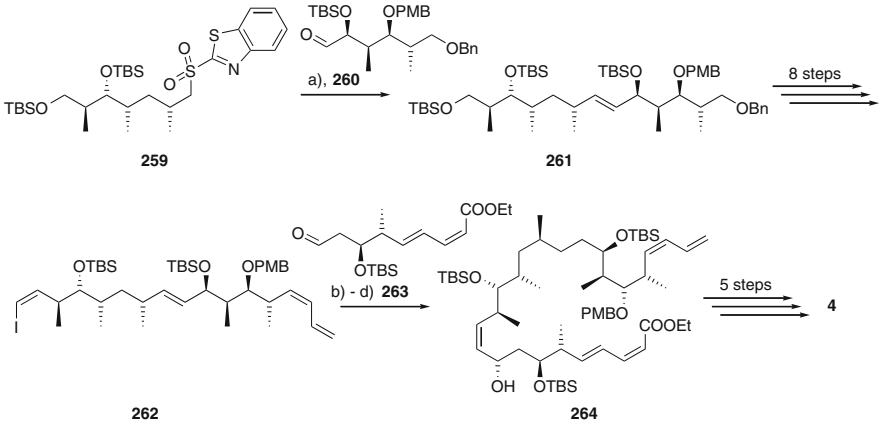

Scheme 38 Assembly of subunits by Ramachandran et al. [189]: **a** NaHMDS, DMF, **260**, 80%; **b** *t*-BuLi; **c** Me_2Zn; **d** **263**, 80%

As indicated above, early work by Curran and co-workers [181] had shown that dictyostatin–discodermolide hybrid **226** showed measurable displacement of taxol from microtubules, but was a significantly less potent growth inhibitor than **225** [181]. The concept of dictyostatin–discodermolide hybrids has recently been revived by Paterson et al. [212] who have prepared hybrid structure **265**.

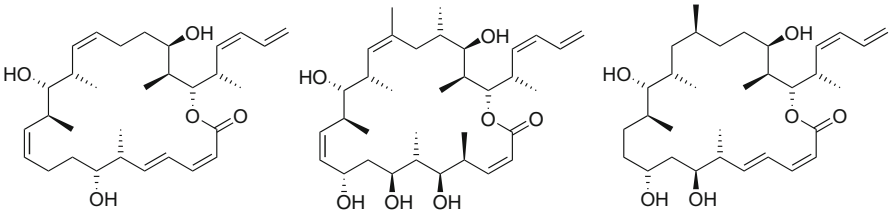

In comparison to **226**, **265** relies heavily on the incorporation of the full C2–C24 linear sequence of discodermolide (**225**) and on restraining of **265** in a conformation resembling the X-ray structure [213] and the bioactive conformation [104] of **225** through the cyclization of **265** via the (*Z*)-enoate of dictyostatin [212]. **265** showed significant antiproliferative activity against all cancer cell lines (GI_{50} [μM]: MDA-MB231: 0.208; A549: 0.399; HT29: 0.170) with respect to **225** (GI_{50} [μM]: MDA-MB231: 0.029; A549: 0.020; HT29: 0.015) [212] and

this encouraging result will certainly fuel further efforts in the field of dictyostatin-discodermolide hybrids.

In the process of establishing their total synthesis of dictyostatin [187], Curran and co-workers also prepared several stereoisomers of **4** [214–216]. Of these, *bis-epi*-diastereomer (6*S*,7*R*)-dictyostatin (GI_{50} [nM]: 1A9/Ptx22: 123 ± 25) was less active compared to dictyostatin (6*R*,7*S*; GI_{50} [nM]: 1A9/Ptx22: 3.4 ± 0.7) itself, but the individual mono-epimers retained ((6*R*,7*R*)-dictyostatin (GI_{50} [nM]: 1A9/Ptx22: 4.7 ± 0.6)), or even showed increased potency ((6*S*,7*S*)-dictyostatin (GI_{50} [nM]: 1A9/Ptx22: 0.81 ± 0.17)) [215–217]. On the other hand, the inversion of configuration at C16 led to a significant loss of activity (16-*epi*-dictyostatin (GI_{50} [nM]: 1A9: 61 ± 6), dictyostatin (GI_{50} [nM]: 1A9: 0.69 ± 0.8)). Removal of the methyl group attached to C16 was reported by Curran and co-workers not to cause any loss in antiproliferative potency (GI_{50} [nM]: 1A9: 0.41 ± 0.52) [214–216]. In contradiction to these findings, Paterson et al. reported 16-normethyldictyostatin (IC_{50} [nM]: AsPC-1: 170 ± 19) to be significantly less active when compared to dictyostatin in the cell lines investigated in their study (IC_{50} [nM]: AsPC-1: 9.0 ± 5.6) [214].

The activity of 19-*epi*-dictyostatin (GI_{50} [nM]: 1A9: 21 ± 14) on the other hand, has been reported by Curran and co-workers to be lower than dictyostatin [215]. While a C15–C16 alkene moiety seems to be tolerated to some extent, all C2–C3-*E*-dictyostatin derivatives investigated so far are characterized by a complete loss of activity; however, most of these data stem from dictyostatin derivatives incorporating multiple modifications, thus making it difficult to assess the contribution of each individual structural change to changes in biological activity [214, 215]. More recent work by Paterson et al. [218] has addressed the effects of modifications at C9 more thoroughly. Thus, while the conversion of **4** to 9-*epi*-dictyostatin (IC_{50} [nM]: AsPC-1: 410 ± 200) leads to a substantial drop of activity in all cell lines investigated compared to dictyostatin (IC_{50} [nM]: AsPC-1: 9.0 ± 5.6), 9-methoxy-dictyostation (IC_{50} [nM]: AsPC-1: 31 ± 9.2) remains very potent.

In a most recent study, Paterson et al. investigated the dictyostatin analog **266** [219]. 10,11-Dihydrodictyostatin (**266**) was hereby found to show similar cytotoxicity to taxol while being 2–3 times more active than discodermolide (**225**) but losing 5- to 12-fold in activity compared to **4**. However, in common with discodermolide, the dictyostatin analog **266** showed significantly reduced activity against taxol-resistant cell lines (e.g. NCI/ADR). Paterson et al. concluded from their data that the C10–C11 double bond of **4** does not seem to contribute significantly to the cytotoxic activity of dictyostatin (**4**) while, in accordance with results from saturated discodermolide analogs [182, 213], it seems to be important for dictyostatin not being a substrate for the Pgp efflux pump [219].

In summary, our understanding of the structure–activity relationships for dictyostatin is still in its early stages, but it is beyond doubt that more data will emerge in the near future, as dictyostatin represents another interesting lead structure for anticancer drug discovery.

5 Peloruside A

Peloruside A (**5**) is a polyoxygenated, polyketide-based 16-membered macrolide, that was first isolated from the New Zealand marine sponge *Mycale hentscheli* by Northcote and co-workers in 2000 [220]. While the structure of **5** and its relative configuration had been determined by a variety of spectroscopic methods, mainly by different NMR-techniques [220], the absolute configuration of the compound was recently determined by De Brabander and co-workers by means of total synthesis [221]. Based on De Brabander's work the absolute configuration of peloruside A (**5**) is opposite to that originally proposed by Northcote and co-workers [220].

As first shown by Miller and co-workers, peloruside A has potent paclitaxel-like microtubule-stabilizing activity and is cytotoxic at nanomolar concentrations [15]. In addition, **5** was shown by Miller and co-workers to arrest the cell cycle in the G2/M phase and to induce apoptosis in human cancer cells. Subsequent studies have revealed the compound to be less susceptible than taxol to multidrug resistance arising from overexpression of the Pgp efflux pump and most probably not to bind to the taxoid binding site on β-tubulin [222]. This latter conclusion arises from several lines of evidence. E.g. **5** is not affected by mutations that affect the taxol binding to β-tubulin and the binding of **5** to crosslinked microtubules is not inhibited in the presence of a fluorescent taxol analog (Flutax-2). In addition, laulimalide (**3**) is able to displace peloruside A (**5**) from microtubules, thus indicating that **5** and laulimalide (**3**) may compete for the same or overlapping binding sites. Recent spectroscopic and computational work suggest the microtubule binding site of peloruside A to be located on α- rather than on β-tubulin [223, 224]. While the binding site of peloruside A on microtubules is as yet unknown, its tubulin-bound conformation has recently been determined by NMR-spectroscopy and the data show that the tetrahydropyran (THP) ring assumes a chair-like conformation [224]. Recent work has also demonstrated that peloruside A acts synergistically with a number of taxoid site agents on tubulin assembly; by contrast none of the taxoid site compounds showed any synergism with each other [225]. Likewise, synergistic effects were observed between peloruside A and either taxol or epothilone A in cell proliferation assays [226].

While several stereoselective syntheses of fragments of peloruside A (**5**) have been reported [227–237], only two total syntheses of this natural product have been successfully completed so far, one by De Brabander [221] and one by Taylor [228, 237].

Since only the relative configuration of peloruside A was known at the outset of their efforts, the first total synthesis by De Brabander and co-workers led to *ent*-peloruside A [221]. In contrast, the retrosynthetic analysis shown in Scheme 39 is based on the by now established absolute configuration.

De Brabander's approach [221] involved an aldol reaction of aldehyde **267** with the methyl ketone **268** and macrolactonization as key steps in the synthesis. **267** was to be constructed by aldol reaction of aldehyde **269** with the enolate of **270**. Taylor and co-workers' approach involved aldol reaction between **271** and **272** with subsequent macrolactonization [228, 237].

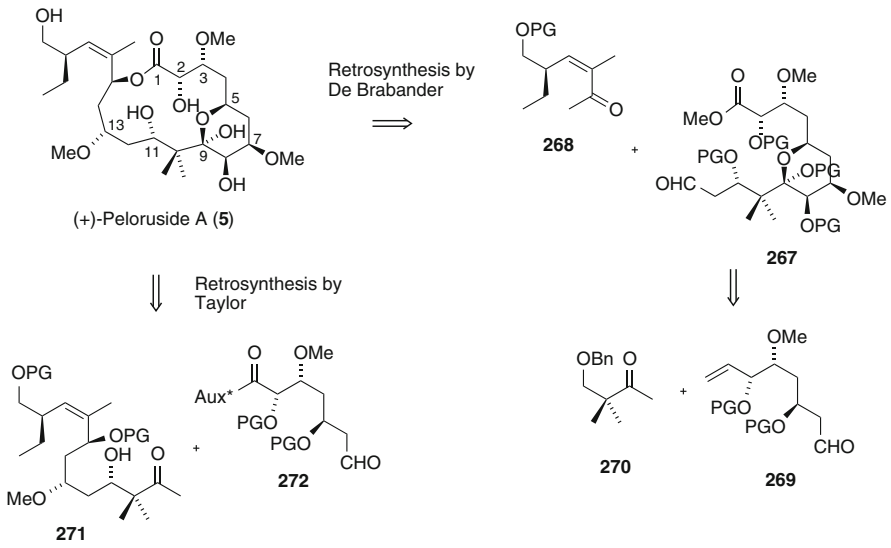

Scheme 39 Retrosynthetic approaches for the total syntheses of peloruside A (**5**)

The synthesis of building block **268** commences with the Zr-catalyzed enantioselective ethylmagnesation reaction of dihydrofuran to provide homoallylic alcohol **273** [238]. The latter was acylated with methacryloyl chloride followed by ring-closing olefin metathesis (RCM) with second generation Grubbs catalyst [239, 240], to furnish the α,β-unsaturated δ-lactone **275**. Treatment of **275** with methyllithium and subsequent protection of the primary hydroxyl group as a TBS-ether finally gave the desired building block **276** (Scheme 40).

Building block **269** was prepared via the chiral homoallylic alcohol **277** obtained by Brown asymmetric allylation from 3-(*p*-methoxybenzyloxy)propanal [241]. Subsequent protection of the secondary hydroxyl group as TES-ether followed by dihydroxylation of the terminal double bond and diol cleavage gave aldehyde **278**, which was submitted to highly stereoselective Brown allylation with (*Z*)-alkoxyallylborane **279** at low temperature (dr >10:1). The resulting homoallylic alcohol was methylated with MeI/NaH to give **280**. Oxidative debenzylation with DDQ, oxidation of the resulting primary alcohol to the aldehyde, aldol reaction with methyl ketone **270** and subsequent Dess-Martin oxidation then led to β-diketone **281**. Cleavage of the silyl ether in acidic toluene furnished dihydro-4-pyranone **282**, which was reduced diastereoselectively and in high yield to the corresponding dihydro-4-pyranol by Luche reduction. Subsequent hydroxy directed epoxidation with *m*-CPBA in MeOH and in situ methanolysis produced the glycoside **283** as a single product. Subsequent regioselective methylation of the equatorial OH-group and proximate silylation of the axial OH-group led to **284** in 75% yield. This was followed by oxidative transformation of the double bond to a carboxyl group and

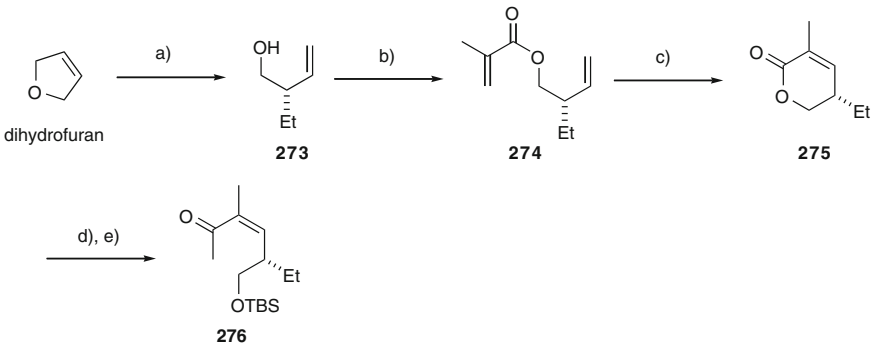

Scheme 40 **a** 0.8 equiv of EtMgBr, 0.4 mol% (*S*)-(EBTHI)-Zr-binol, THF, 99% ee. **b** $CH_2CMeC(O)Cl$, *i*-Pr_2NEt, DMAP, CH_2Cl_2, 75%. **c** RCM, 10 mol% Grubbs second, CH_2Cl_2 (0.0025 M), 17 h reflux (50–70% + 20% dimer derived from **274**. **d** MeLi, THF, -78 °C or $TMSCH_2Li$, pentane, -78 °C. **e** TBSCl, imidazole, DMAP, DMF (52–63% from **275**)

esterification of the acid with diazomethane to provide methyl ester **285**. Debenzylation of **285** by hydrogenolysis, oxidation of the primary alcohol to the aldehyde and a highly efficient allyl transfer reaction with allyldiethylborane provided homoallylic alcohol **286** as a single diastereoisomer. The latter was converted to the corresponding (2-naphthyl)-methylidene acetal (which allowed the assignment of the stereochemical outcome at C11 by NOE analysis) followed by consecutive treatment with OsO_4 and $NaIO_4$ to furnish aldehyde **287** (Scheme 41).

Mukaiyama-type aldol reaction of aldehyde **287** with the enol silane derived from methyl ketone **276** afforded almost exclusively (80%, dr 14:1) the unexpected 1,3-*syn*-β-hydroxy ketone, contrary to prior reports by Evans and co-workers [242], although this was not immediately recognized (Scheme 42). Methylation of the aldol product (to give **288**) followed by CBS-reduction, ester hydrolysis and macrolactonization gave **290** in 40–50% yield. At this point, a series of NOE correlations between H11, H13, and H15 revealed the undesired (*S*)-configuration of the stereocenter at C13 (Scheme 42).

In order to adjust the configuration at C13, homoallylic alcohol **286** was converted to the β-hydroxy aldehyde and treated with the enolborinate derived from **276** which gave a separable 2:1 mixture of C13-epimers **291a** and **291b** (Scheme 43). At this stage, the absolute stereochemical outcome of the reaction was left unresolved and both epimers were advanced individually. Surprisingly, methylation of these two compounds **291a** and **291b** occurred with hydrolysis to the C9 hemiketals, but the hydroxyl group at C11 remained unaffected. Asymmetric reduction of enones **292a** and **292b** with $BH_3 \cdot SMe_2$ and (*S*)- and (*R*)-*B*-Me-CBS-oxazaborolidine, respectively, followed by saponification gave the carboxylic acids **293a/b** and **294a/b** (Scheme 43).

Remarkably, epimers **293b** and **294b**, when treated with PPh_3 and diisopropylazodicarboxylate either individually or as an equimolar mixture were converted to macrolactone **295** (Scheme 44). According to De Brabander these findings consti-

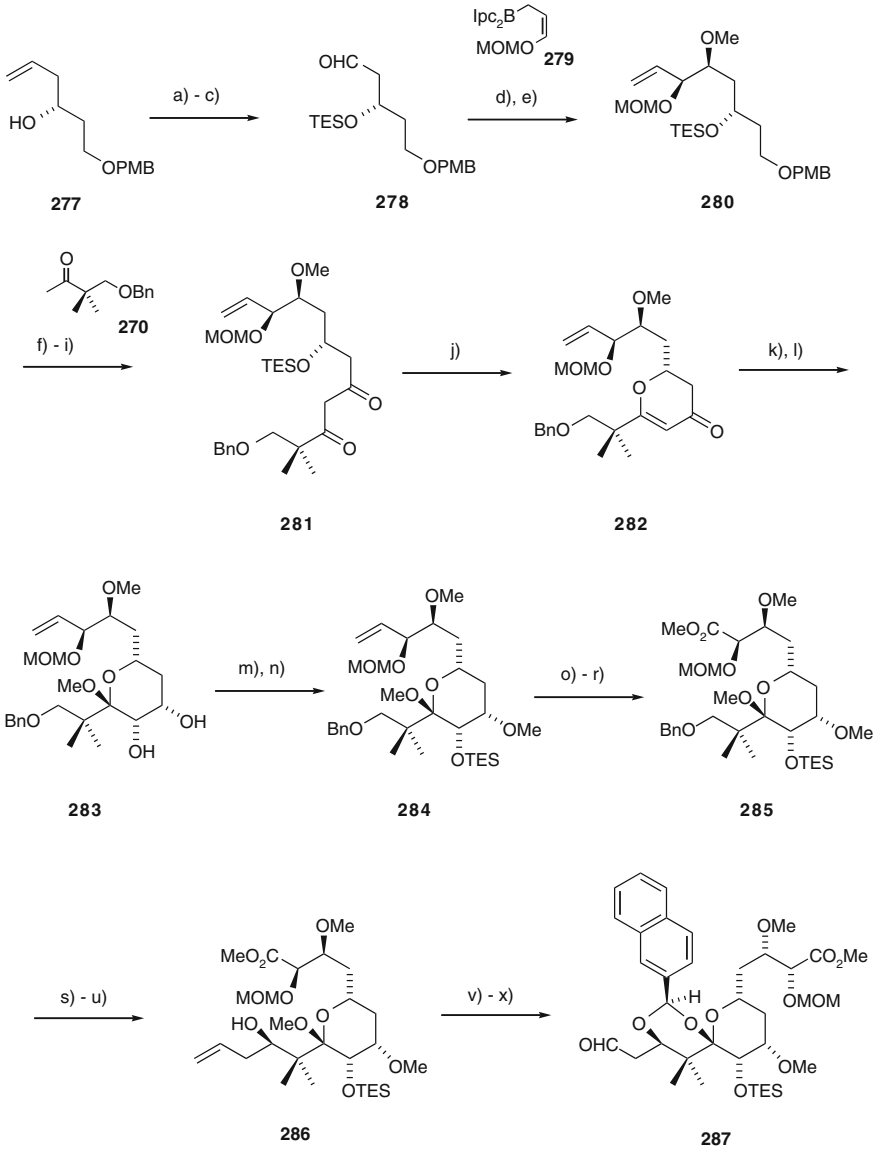

Scheme 41 **a** TES-OTf, 2,6-lutidine, CH_2Cl_2, 97%. **b** (cat) OsO_4, NMO, acetone/water. **c** $Pb(OAc)_4$, py, CH_2Cl_2 (78% from **277**). **d** **279**, *s*-BuLi, THF, −78 °C, 15 min, then (+)-Ipc_2BOMe, then **278**, −95 °C, 3 h; 30% H_2O_2, NaOH, 16 h, rt, 91%. **e** NaH, MeI, DMF, −5 °C, 89%. **f** DDQ, CH_2Cl_2/water, 0 °C, 88%. **g** py·SO_3, Et_3N, DMSO, CH_2Cl_2, 0 °C, 87%. **h** **270**, LDA, THF, −78 °C, 94%. **i** DMP, CH_2Cl_2, −10 °C, 81%. **j** *p*-TsOH, toluene, rt, 92%. **k** $NaBH_4$, $CeCl_3.7\ H_2O$, MeOH, −30 °C. **l** *m*CPBA, $NaHCO_3$, CH_2Cl_2/MeOH, 0 °C, 72% over two steps. **m** *t*-BuOK, MeI, THF, 0 °C. **n** TES-OTf, 2,6-lutidine, CH_2Cl_2, 75% over two steps. **o** (cat) OsO_4, NMO, acetone/water. **p** $Pb(OAc)_4$, py, CH_2Cl_2. **q** $NaClO_2$, NaH_2PO_4, 2-Me-2-butene, *t*-BuOH/water. **r** CH_2N_2, Et_2O, 0 °C, 80% from **284**. **s** H_2, Pd/C (10%), MeOH, quant. **t** py.SO_3, Et_3N, DMSO, CH_2Cl_2, 0 °C, 90%. **u** Allyl-BEt_2, Et_2O, −10 °C, 94%. **v** TES-OTf, 2-naphthaldehyde, −78 °C, then 2,6-lutidine, TES-OTf, 0 °C, 81%. **w** (cat) OsO_4, NMO, acetone/water. **x** $NaIO_4$ on silicagel, CH_2Cl_2, 76% from **286**

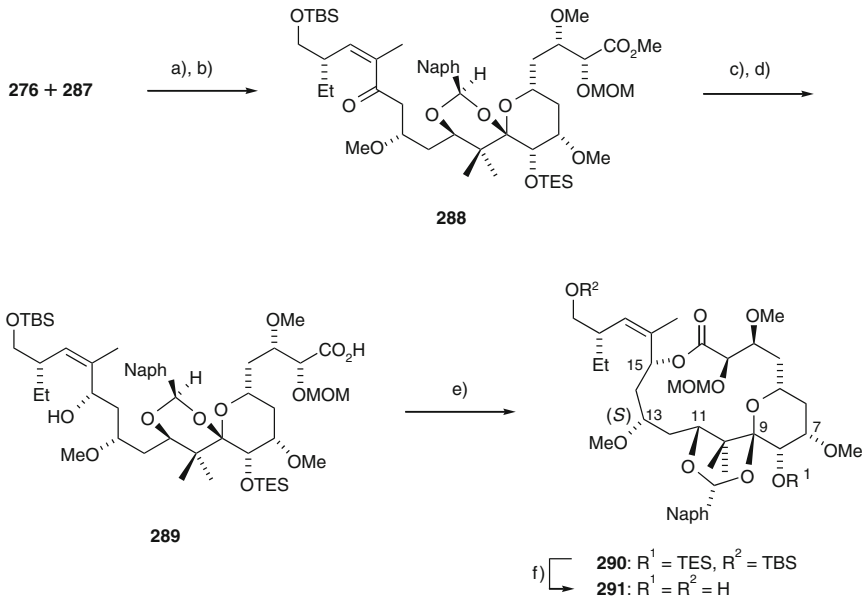

Scheme 42 **a** Enolsilane derived from **276** (TMS-OTf, Et_3N, CH_2Cl_2, –10 °C), then **287** CH_2Cl_2, –78 °C, $BF_3{\cdot}Et_2O$, 2 h, 80% dr 14:1. **b** Me_3OBF_4, 1,8-bis(dimethlyamino)naphthalene, CH_2Cl_2, rt, 92%. **c** (*S*)-B-Me-CBS, $BH_3{\cdot}SMe_2$, CH_2Cl_2, –30 °C, 83% dr 13:1. **d** 0.3 N aq. LiOH, THF, rt, quant. **e** PPh_3, DIAD, THF, rt, 40–50%. **f** 48% aq. HF, MeCN/water, rt, 88%

tute the first observation of a configuration-dependent mechanistic switch for a Mitsunobu lactonization which in the case of **293b**, as suggested by De Brabander [221], would proceed via the usual alkoxyphosphonium intermediate (leading to inversion at C15), while an acyloxyphosphonium intermediate would be formed from **294b** (leading to retention of configuration at C15). On the other hand, Mitsunobu lactonization of **294a** followed by simultaneous cleavage of the MOM and silyl protecting groups in aqueous HCl furnished the desired peloruside A. The latter was formed from the major aldol isomer and proved to be *ent*-(–)-peloruside A. Thus, the absolute configuration of the natural peloruside A is opposite to that originally proposed for this compound by Northcote and co-workers [220] (Scheme 44).

The total synthesis of peloruside A (**5**) reported by Taylor and co-workers [228, 237] departs from the readily available (*R*)-oxazolidinone **296**, which was diastereoselectively alkylated with BOMCl and titanium tetrachloride [243] (Scheme 45). Exchange of the protecting groups and reductive removal of the chiral auxiliary with $LiBH_4$ gave chiral alcohol **297**. Oxidation to the corresponding aldehyde followed by Still-Gennari olefination [208] furnished the (*Z*)-trisubstituted alkene **298** as the only isomer. Ester reduction, oxidation of the primary hydroxyl group to the aldehyde, and Brown asymmetric allylation provided alcohol **299** (77%, dr 97:3). Because of difficulties in the purification of **299**, an alternative access to **299** was developed that involved non-selective Grignard allylation. However, the resulting 1:1 mixture of diaster-

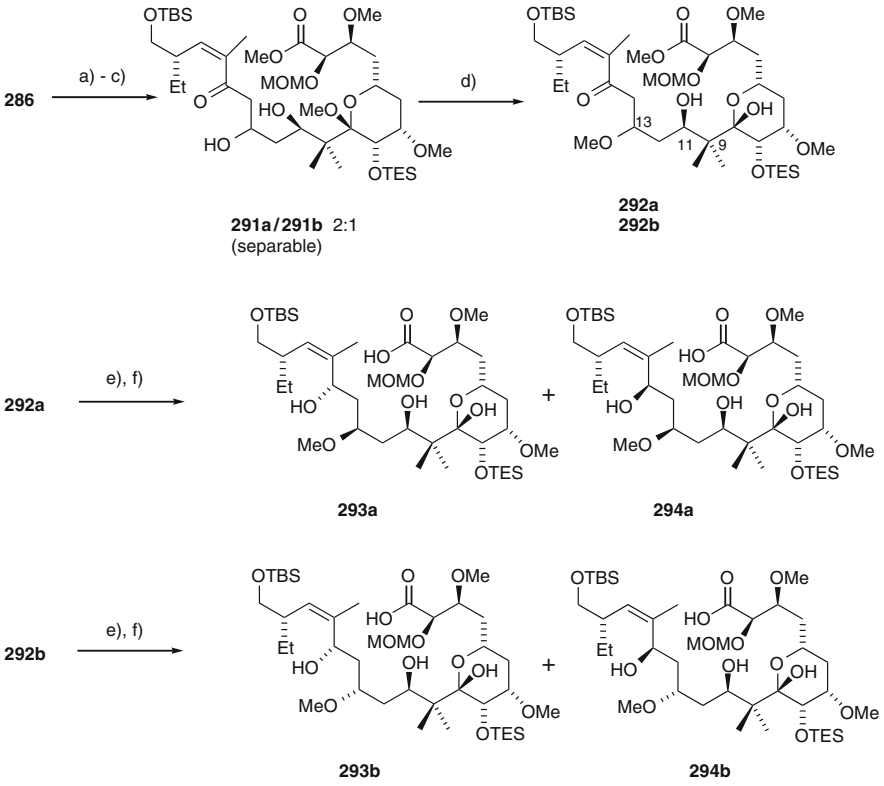

Scheme 43 **a** (cat) OsO_4, NMO, acetone/water. **b** $Pb(OAc)_4$, py, CH_2Cl_2, 95% from **286**. **c** **276**, *i*-Pr_2NEt, Et_2BOTf, CH_2Cl_2, 87% dr 2:1. **d** Me_3OBF_4, 2,6-di-*tert*-butyl-4-methylpyridine, CH_2Cl_2, 85%. **e** (*R*)- or (*S*)-*B*-Me-CBS, $BH_3{\cdot}SMe_2$, CH_2Cl_2, 80–94%. **f** 0.3 N aq. LiOH, THF, rt, quant

eoisomers was easily separable by flash chromatography and the undesired isomer could be converted to the desired product through Mitsunobu inversion (78% yield based on the intermediate aldehyde). Alcohol **299** was then protected as a *tert*-butyl carbonate and subsequent NIS-mediated electrophilic cyclization of this homoallylic carbonate [244, 245] furnished the cyclic iodocarbonate **300**, which exhibited the desired 1,3-*syn* relationship. Treatment of the *tert*-butyl carbonate with either I_2 or IBr instead of NIS only gave complex mixtures of products. Exposure of **300** to basic methanol gave a *syn*-epoxy alcohol that was converted to *syn*-epoxy ether **301** by reaction with TBS–Cl. Epoxide opening with the lithium anion of 1,3-dithiane followed by methylation of the hydroxyl group and subsequent removal of the dithiane then led to aldehyde **302**, which was further elaborated into methyl ketone **304** via 1,3-*anti* Mukaiyama aldol addition of enol silane **303** in 91% yield (dr = 8:1) followed by MOM-protection of the resulting hydroxyl group (Scheme 45).

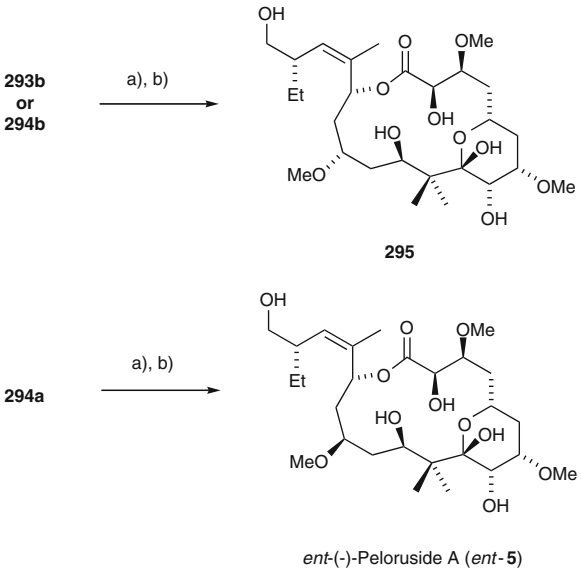

Scheme 44 **a** PPh_3, DIAD, THF (0.05 M), rt, 47% from **293b** or **294b**, 69% from **294a**; **b** 4 N HCl, THF, rt, **295**: 65%, *ent*-**5**: 65%

The construction of Taylor's fragment **272** (Scheme 39) started from commercially available (*S*)-glycidyl tosylate **305**, whose treatment with lithiated 1,3-dithiane followed by copper-catalyzed vinyl-Grignard addition, reaction of the resulting homoallylic alcohol with TES–Cl, and removal of the dithiane moiety led to aldehyde **306** (Scheme 46). This aldehyde underwent diastereoselective aldol addition to oxazolidinone **307**, thus furnishing **308** as a single isomer. **308** was elaborated into **309** by methylation with Meerwein's salt followed by PMB → MOM protecting group exchange and finally oxidative cleavage of the terminal double bond with ozone. The PMB → MOM exchange was required, as the aldol reaction with MOM-protected oxazolidinone analog to **308** failed (Scheme 46).

Aldol reaction of aldehyde **309** and the Li-enolate derived from methyl ketone **304** gave a diastereoisomeric mixture that was oxidized by Dess-Martin periodinane to the β-diketone (Scheme 47). Upon cleavage of the TES ether at C5 with *p*-TsOH the dihydropyranone derivative **310** was formed spontaneously through an intramolecular condensation reaction as described by De Brabander [221] (Scheme 41). Desilylation of **310** followed by regioselective reprotection of the primary hydroxyl group gave a carboxy protected seco acid; treatment of this intermediate with aqueous LiOH revealed the free seco acid which was cyclized under Yamaguchi conditions [211] to furnish lactone **311**. Stereoselective Luche reduction [246] at low temperature fol-

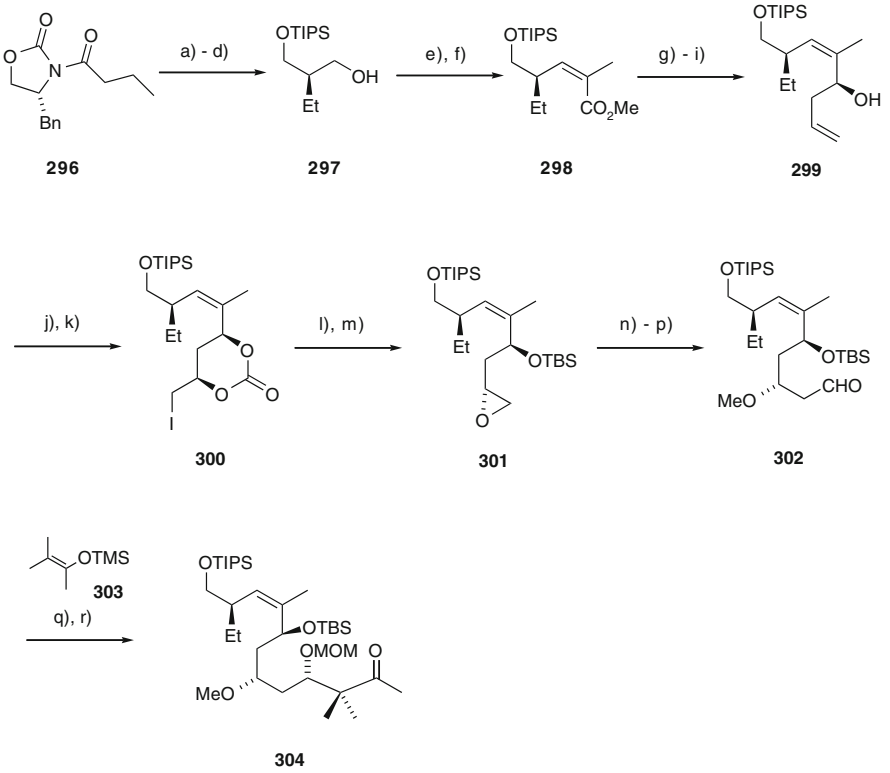

Scheme 45 **a** $TiCl_4$, Et_3N, BOMCl, CH_2Cl_2, 0 °C, 2 h, 80%. **b** H_2 (1 atm), Pd/C, EtOH, 3 d, rt. **c** TIPSCl, DMAP, Et_3N, CH_2Cl_2, 5 h, rt, 95%. **d** $LiBH_4$, H_2O, Et_2O, THF, 5 h, rt, 82%. **e** DMP, py, CH_2Cl_2, 1 h, 0 °C. **f** 18-crown-6, bis(2,2,2-trifluoroethyl)-1-(methoxycarbonyl) ethyl-phosphonate, KHMDS, THF, 1 h, −78 °C. **g** DIBAL-H, CH_2Cl_2, −78 °C, 90%. **h** DMP, py, CH_2Cl_2, 1 h, 0 °C. **i** (+)-Ipc_2allylborane, pentane, 1 h, −100 °C, 75% over two steps. **j** *n*-BuLi, Boc-on, 4 h, 0 °C, 91%. **k** NIS, MeCN, 12 h, 0 °C, 92%. **l** K_2CO_3, MeOH, 86%. **m** TBSCl, imidazole, DMAP, DMF, 12 h, rt, 92%. **n** 1,3-dithiane, *n*-BuLi, THF, HMPA, 85%. **o** *t*-BuOK, MeI. **p** MeI, Na_2CO_3, MeCN/H_2O 9:1, 1.5 h, reflux, 90%. **q** enol silane **303**, $BF_3{\cdot}Et_2O$, 30 min, −78 °C, 91% dr 8:1. **r** MOM–Cl, 88%

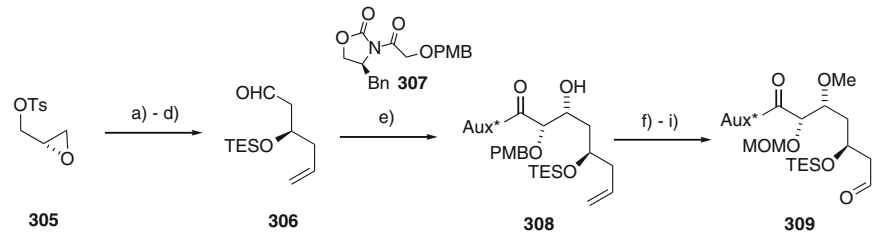

Scheme 46 **a** 1,3-Dithiane, *n*-BuLi, THF, 4 h, −78 °C. **b** CH_2=CHMgBr, CuI, THF, 40 min, −40 °C; 65%. **c** TESCl, imidazole, DMAP, DMF, 12 h, rt, 92%. **d** MeI, $CaCO_3$, MeCN/water 9:1, 2.5 h, 45 °C. **e** Oxazolidinone **307**, Bu_2BOTf, Et_3N, toluene, 2.5 h, −30 °C; 61% over two steps. **f** Me_3OBF_4, proton sponge, 15 h, rt. **g** DDQ, water, CH_2Cl_2, 2 h, rt. **h** MOMCl, *i*-Pr_2NEt, CH_2Cl_2, 15, rt, 62% over three steps. **i** O_3, PPh_3, py, CH_2Cl_2, −78 °C, 91%

lowed by treatment with *m*-CPBA in CH_2Cl_2 yielded triol **312** with concomitant loss of the C11-MOM protecting group. Regioselective methylation of the less hindered equatorial hydroxyl group and final global deprotection gave (+)-peloruside A (**5**) (Scheme 47).

No comprehensive structure–activity-relationships have so far been elaborated for this natural product. As an exception the $NaBH_4$ reduction product **313** has been described by Hood and co-workers [15]. This derivative was proved to be less active than peloruside A (**5**) with an IC_{50} (HL-60) value of 221 ± 24 nM (*vs* 7 ± 4 nM for peloruside A).

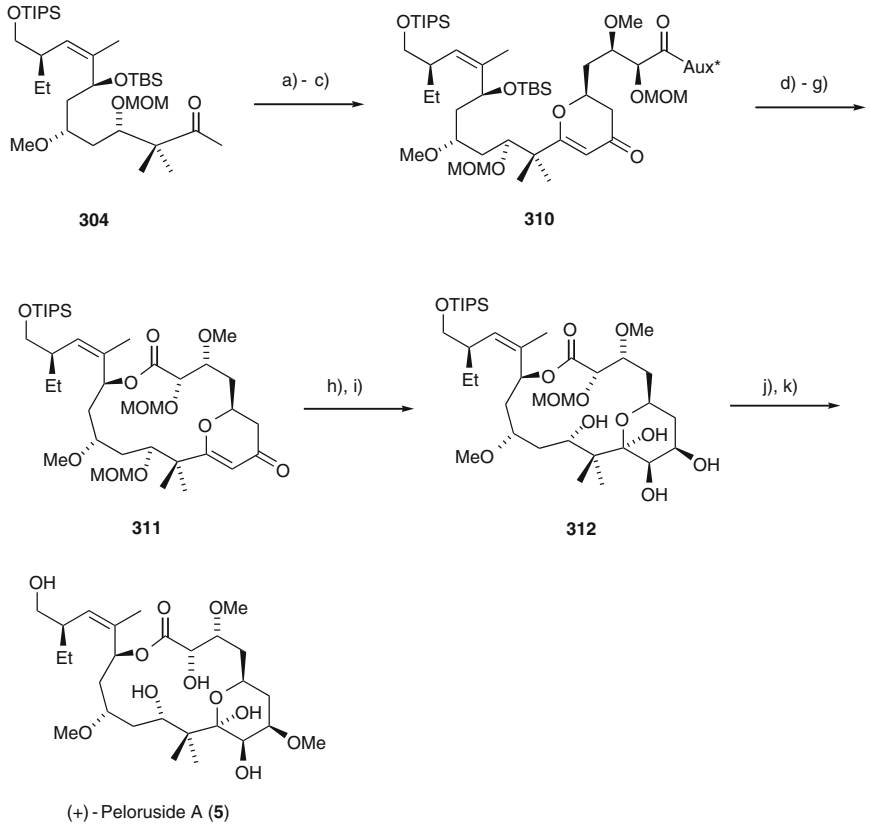

Scheme 47 **a** LDA, **309**, −78 °C. **b** DMP, py, CH_2Cl_2, 4 h, 0 °C, 85%. **c** *p*-TsOH, toluene, 3 h, 45 °C, 60%. **d** HF·py, MeCN/water 5:1, 15 h, rt. **e** TIPSCl, imidazole, DMAP, CH_2Cl_2, 10 h, rt, 60% over two steps. **f** LiOH, H_2O, THF, 40 min, 0 °C. **g** 2,4,6-$Cl_3C_6H_2C(O)Cl$, Et_3N, toluene, DMAP, 6 h, 90 °C; 51% over two steps. **h** $NaBH_4$, $CeCl_3.7H_2O$, MeOH, 40 min, −60 °C. **i** *m*-CPBA, $NaHCO_3$, CH_2Cl_2, 30 min, −30 °C, aqu. work-up, 52% over two steps. **j** Me_3OBF_4, 2,6-di-*tert*-butyl pyridine, 0 °C. **k** 4 N HCl, THF, 3 h, 0 °C, 43% over two steps

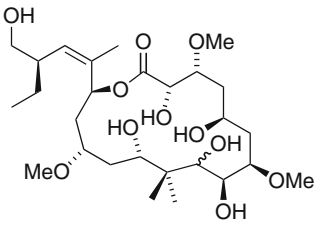

313

6 Conclusions and Outlook

The stabilization of cellular microtubules is a clinically relevant mechanistic principle which underlies the therapeutic effects of two of the world's most important anticancer drugs, taxol (Taxol®) and docetaxel (Taxotere®). In addition, a third microtubule stabilizer, the Epo B lactam BMS-247550 (Ixabepilone, Ixempra®) has recently been approved by the FDA for clinical treatment of human cancer. Apart from these clinically approved agents, a significant number of microtubule stabilizers are currently undergoing clinical trials in humans.

Until the discovery of the tubulin-polymerizing activity of epothilones in 1995, a taxol-like structure was considered a precondition for microtubule-stabilizing compounds. However, the last decade has witnessed the emergence of a significant number of new and structurally diverse microtubule-stabilizing natural products, which do not bear any structural resemblance with taxol and of which four are based on polyketide-derived macrolactone core structures. While all these macrolide based microtubule-stabilizing agents share the ability to induce tubulin polymerization, differences exist between individual agents with regard to their interaction with tubulin. In particular, they do not all bind to a common microtubule binding site and this is likely the reason for synergistic effects that have been observed at the levels of tubulin polymerization in vitro, inhibition of cancer cell proliferation in vitro, and the suppression of tumor growth in vivo for some specific combinations of these agents, either between themselves or with taxol.

In the light of their potential medical relevance, it is not surprising that significant efforts have been made to develop and refine the synthetic organic chemistry of macrolide-based microtubule-stabilizing agents and total syntheses have been accomplished for every one of them. Given the fact that compound supply is usually limited for natural products of marine origin, total synthesis often is an important enabling technology for the comprehensive pharmacological profiling of new natural product leads. In addition, and equally important, the chemistry developed for these total syntheses also provides a basis for the generation of fully synthetic analogs for SAR studies, in spite of the complexity of these natural product leads. In this context it should be emphasized that many structural analogs of natural products are only accessible through total synthesis. Thus, together with semisynthesis (which, however, requires the availability of significant amounts of a natural product as starting material), total synthesis provides the basis for the elucidation of comprehensive struc-

ture–activity relationships. Last but not least, the continuous improvement of existing synthetic methods can also serve as the means for the provision of material for clinical studies, as is the case for ZK-Epo (sagopilone).

Nature has proven to be the most efficient provider of new microtubule-stabilizing agents by far with the majority of macrolide-based agents originating from marine organisms. As this resource is still far from exhaustive exploitation, new potent macrolide-based microtubule stabilizers will undoubtedly continue to emerge in the future, which can serve as leads for the development of new anticancer drugs.

References

1. Woodward RB (1957) Angew Chem 69:50
2. Omura S (1984) Macrolide antibiotics, Academic, Orlando
3. Ishibashi M, Omura S (eds) (2002) Macrolide antibiotics. Academic, San Diego, p 57
4. Mooberry SL (2007) Methods Mol Med 137:289
5. Altmann K-H, Gertsch J (2007) Nat Prod Rep 2:327
6. Altmann KH, Pfeiffer B, Arseniyadis S, Pratt BA, Nicolaou KC (2007) Chem Med Chem 2:396
7. Höfle G, Reichenbach H (2005) In: Cragg GM, Kingston DG, Newman DJ (eds) Anticancer agents from natural products. CRC, Boca Raton, p 413
8. Höfle G, Bedorf N, Gerth K, Reichenbach H (1993) German Patent Disclosure, DE4138042 120:52841
9. Gerth K, Bedorf G, Höfle H, Irschik H, Reichenbach H (1996) J Antibiot 49:460
10. DiFrancesco C (2007) FDA Press-release from October 22, 2007
11. Mooberry SL, Tien G, Hernandez AH, Plubrukarn A, Davidson BS (1999) Cancer Res 59:653
12. Yeung KS, Paterson I (2005) Chem Rev 105:4237
13. Bollag DM, McQueney PA, Zhu J, Hensens O, Koupal L, Liesch J, Goetz M, Lazarides E, Woods CM (1995) Cancer Res 55:2325
14. Isbrucker RA, Cummins J, Pomponi A, Longley RE, Wright AE (2003) Biochem Pharmacol 66:75
15. Hood KA, West LM, Rouwé B, Northcote PT, Berridge MV, Wakefield J St, Miller JH (2002) Cancer Res 62:3356
16. Rowinsky EK (1997) Annu Rev Med 48:353
17. Wani MC, Taylor HL, Wall ME, Coggon P, McPhail AT (1971) J Am Chem Soc 93:2325
18. Schiff PB, Fant J, Horwitz SB (1979) Nature 277:665
19. Schiff PB, Horwitz SB (1980) Proc Natl Acad Sci USA 77:1561
20. He L, Orr GA, Horwitz SB (2001) Drug discovery today 6:1153
21. Altmann K-H (2001) Curr Opin Chem Biol 5:424
22. Jordan MA (2002) Curr Med Chem: Anti-Cancer Agents 2:1
23. Myles DC (2002) Ann Rep Med Chem 37:125
24. Jordan MA, Wilson L (2004) Nat Rev Cancer 4:253
25. Chen JGC, Horwitz SB (2002) Cancer Res 14:1935
26. Chen JGC, Yang CPHY, Cammer M, Horwitz SB (2003) Cancer Res 15:7891
27. Altmann K-H, Wartmann M, O'Reilly T (2000) BBA Rev Cancer 1470:M79
28. Kowalski RJ, Giannakakou P, Hamel E (1997) J Biol Chem 272:2534
29. Wolff A, Technau A, Brandner G (1997) Intl J Oncol 11:123
30. Höfle GH, Bedorf N, Steinmetz H, Schomburg D, Gerth K, Reichenbach H (1996) Angew Chem Int Ed Engl 35:1567

31. Nicolaou KC, He Y, Vourloumis D, Vallberg H, Yang Z (1996) Angew Chem Int Ed 35:2399
32. Meng DF, Bertinato P, Balog A, Su DS, Kamenecka T, Sorensen EJ, Danishefsky SJ (1996) Angew Chem Int Ed 35:2801
33. Balog A, Bertinato P, Su DS, Meng DF, Sorensen E, Danishefsky SJ, Zheng YH, Chou TC, He LE, Horwitz SB (1997) Tetrahedron Lett 38:4529
34. Yang Z, He Y, Vourloumis D, Vallberg H, Nicolaou KC (1997) Angew Chem Int Ed 36:166
35. Nicolaou KC, He Y, Vourloumis D, Vallberg H, Roschangar F, Sarabia F, Ninkovic S, Yang Z, Trujillo JI (1997) J Am Chem Soc 119:7960
36. Nicolaou KC, Ninkovic S, Sarabia F, Vourloumis D, He Y, Vallberg H, Finlay MRV, Yang Z (1997) J Am Chem Soc 119:7974
37. Nicolaou KC, Sarabia F, Ninkovic S, Yang Z (1997) Angew Chem Int Ed 36:525
38. Nicolaou KC, Winssinger N, Pastor J, Ninkovic S, Sarabia F, He Y, Vourloumis D, Yang Z, Li T, Giannakakou P, Hamel E (1997) Nature 387:268
39. Schinzer D, Limberg A, Bauer A, Bohm OM, Cordes M (1997) Angew Chem Int Ed Engl 36:523
40. Su DS, Meng DF, Bertinato P, Balog A, Sorensen EJ, Danishefsky SJ, Zheng YH, Chou TC, He LF, Horwitz SB (1997) Angew Chem Int Ed Engl 36:757
41. Martin HJ, Drescher M, Mulzer J (2000) Angew Chem Int Ed 39:581
42. Martin HJ, Pojarliev P, Kahlig H, Mulzer J (2001) Chem Eur J 7:2261
43. Sun J, Sinha SC (2002) Angew Chem Int Ed 41:1381
44. Rivkin A, Chou TC, Danishefsky SJ (2005) Angew Chem Int Ed 44:2838
45. Rivkin A, Yoshimura F, Gabarda AE, Cho YS, Chou TC, Dong HJ, Danishefsky SJ (2004) J Am Chem Soc 126:10913
46. Fürstner A, Mathes C, Grela K (2001) Chem Commun 1057
47. Fürstner A, Mathes C, Lehmann CW (2001) Chem Eur J 7:5299
48. Meng DF, Su DS, Balog A, Bertinato P, Sorensen EJ, Danishefsky SJ, Zheng YH, Chou TC, He LF, Horwitz SB (1997) J Am Chem Soc 119:2733
49. Nicolaou KC, Vourloumis D, Li TH, Pastor J, Winssinger N, He Y, Ninkovic S, Sarabia F, Vallberg H, Roschangar F, King NP, Finlay MRV, Giannakakou P, Verdier-Pinard P, Hamel E (1997) Angew Chem Int Ed 36:2097
50. Su DS, Balog A, Meng DF, Bertinato P, Danishefsky SJ, Zheng YH, Chou TC, He LF, Horwitz SB (1997) Angew Chem Int Ed Engl 36:2093
51. Hardt IH, Steinmetz H, Gerth K, Sasse F, Reichenbach H, Höfle G (2000) J Nat Prod 64:847
52. Chou TC, Zhang XG, Balog A, Su DS, Meng DF, Savin K, Bertino JR, Danishefsky SJ (1998) Proc Natl Acad Sci USA 95:9642
53. Chou TC, Zhang XG, Harris CR, Kuduk SD, Balog A, Savin KA, Bertino JR, Danishefsky SJ (1998) Proc Natl Acad Sci USA 95:15798
54. Holen K, Hannah A, Zhou YQ, Cropp G, Johnson R, Volkman J, Binger K, Alberti D, Wilding G (2003) Clin Cancer Res 9:6133S
55. Spriggs D, Dupont J, Pezzulli S, Larkin J, Cropp G, Johnson R, Hannah AL (2003) Clin Cancer Res 9:6129S
56. Kolman A (2005) Curr Opin Invest Drugs 6:657
57. Johnson J, Kim SH, Bifano M, DiMarco J, Fairchild C, Gougoutas J, Lee F, Long B, Tokarski J, Vite G (2000) Org Lett 2:1537
58. Harris CR, Danishefsky SJ (1999) J Org Chem 64:8434
59. Mulzer J, Martin HJ, Berger M (1999) J Heterocycl Chem 36:1421
60. Lee CB, Chou TC, Zhang XG, Wang ZG, Kuduk SD, Chappell MD, Stachel SJ, Danishefsky SJ (2000) J Org Chem 65:6525
61. Altmann K-H, Bold G, Caravatti G, Denni D, Florsheimer A, Schmidt A, Rihs G, Wartmann M (2002) Helv Chim Acta 85:4086
62. Tu Y, Wang ZX, Shi Y (1996) J Am Chem Soc 118:9806
63. Wang ZX, Tu Y, Frohn M, Zhang JR, Shi Y (1997) J Am Chem Soc 119:11224

64. Nicolaou KC, Namoto K, Ritzen A, Ulven T, Shoji M, Li J, D'Amico G, Liotta D, French CT, Wartmann M, Altmann K-H, Giannakakou P (2001) J Am Chem Soc 123:9313
65. Altmann K-H, Florsheimer A, Bold G, Caravatti G, Wartmann M (2004) Chimia 58:686
66. Feyen F, Gertsch J, Wartmann M, Altmann K-H (2006) Angew Chem Int Ed 45:5880
67. Altmann K-H, Blommers MJJ, Caravatti G, Flörsheimer A, Nicolaou KC, O'Reilly T, Schmidt A, Schinzer D, Wartmann M (2001) In: Ojima I, Vite G, Altmann K-H (eds) ACS Symposium Vol. Series 796. American Chemical Society, Washington DC, p 112
68. Nicolaou KC, Sarabia F, Ninkovic S, Finlay MRV, Boddy CNC (1998) Angew Chem Int Ed 37:81
69. Altmann K-H, Bold G, Caravatti G, End N, Florsheimer A, Guagnano V, O'Reilly T, Wartmann M (2000) Chimia 54:612
70. End N, Furet P, van Campenhout N, Wartmann M, Altmann K-H (2004) Chem Biodiversity 1:1771
71. Hardt IH, Steinmetz H, Gerth K, Sasse F, Reichenbach H, Höfle G (2001) J Nat Prod 64:847
72. Starks CM, Zhou YQ, Liu FH, Licari PJ (2003) J Nat Prod 66:1313
73. Biswas K, Lin H, Njardarson JT, Chappell MD, Chou TC, Guan YB, Tong WP, He LF, Horwitz SB, Danishefsky SJ (2002) J Am Chem Soc 124:9825
74. Rivkin A, Biswas K, Chou TC, Danishefsky SJ (2002) Org Lett 4:4081
75. Rivkin A, Njardarson JT, Biswas K, Chou TC, Danishefsky SJ (2002) J Org Chem 67:7737
76. Rivkin A, Yoshimura F, Gabarda AE, Chou TC, Dong HJ, Tong WP, Danishefsky SJ (2003) J Am Chem Soc 125:2899
77. Yoshimura F, Rivkin A, Gabarda AE, Chou TC, Dong HJ, Sukenick G, Morel FF, Taylor RE, Danishefsky SJ (2003) Angew Chem Int Ed 42:2518
78. Rivkin A, Cho YS, Gabarda AE, Yoshimura F, Danishefsky SJ (2004) J Nat Prod 67:139
79. Arslanian RL, Tang L, Blough S, Ma W, Qiu RG, Katz L, Carney JR (2002) J Nat Prod 65:1061
80. Chou TC, Dong HJ, Rivkin A, Yoshimura F, Gabarda AE, Cho YS, Tong WP, Danishefsky SJ (2003) Angew Chem Int Ed 42:4761
81. Duthaler RO, Herold P, Lottenbach W, Oertle K, Riediker M (1989) Angew Chem Int Ed Engl 28:495
82. Carlomagno T, Blommers MJJ, Meiler J, Jahnke W, Schupp T, Petersen F, Schinzer D, Altmann K-H, Griesinger C (2003) Angew Chem Int Ed 42:2511
83. White JD, Carter RG, Sundermann KF, Wartmann M (2001) J Am Chem Soc 123:5407
84. White JD, Carter RG, Sundermann KF, Wartmann M (2003) J Am Chem Soc 125:3190
85. Borzilleri RM, Zheng XP, Schmidt RJ, Johnson JA, Kim SH, DiMarco JD, Fairchild CR, Gougoutas JZ, Lee FYF, Long BH, Vite GD (2000) J Am Chem Soc 122:8890
86. Rothermel J, Wartmann M, Chen TL, Hohneker J (2003) Semin Oncol 30:51
87. Pietras K, Stumm M, Hubert M, Buchdunger E, Rubin K, Heldin CH, McSheehy P, Wartmann M, Ostman A (2003) Clin Cancer Res 9:3779
88. Stachel SJ, Lee CB, Spassova M, Chappell MD, Bornmann WG, Danishefsky SJ, Chou TC, Guan YB (2001) J Org Chem 66:4369
89. Wartmann M, Altmann K-H (2002) Curr Med Chem Anticancer Agents 2:123–148.
90. Regueiro-Ren A, Leavitt K, Kim SH, Höfle G, Kiffe M, Gougoutas JZ, DiMarco JD, Lee FYF, Fairchild CR, Long BH, Vite GD (2002) Org Lett 4:3815
91. Cachoux F, Isarno T, Wartmann M, Altmann K-H (2005) Angew Chem Int Ed 44:7469
92. Cachoux F, Schaal F, Teichert A, Wagner T, Altmann K-H (2004) Synlett, 2709
93. Nicolaou KC, Pratt BA, Arseniyadis S, Wartmann M, O'Brate A, Giannakakou P (2006) Chem Med Chem 1:41
94. Nicolaou KC, Scarpelli R, Bollbuck B, Werschkun B, Pereira MMA, Wartmann M, Altmann K-H, Zaharevitz D, Gussio R, Giannakakou P (2000) Chem Biol 7:593
95. Nicolaou KC, Hepworth D, King NP, Finlay MRV, Scarpelli R, Pereira MMA, Bollbuck B, Bigot A, Werschkun B, Winssinger N (2000) Chem Eur J 6:2783

96. Nicolaou KC, Ritzen A, Namoto K, Buey RM, Diaz JF, Andreu JM, Wartmann M, Altmann K-H, O'Brate A, Giannakakou P (2002) Tetrahedron 58:6413
97. Nicolaou KC, King NP, Finlay MRV, He Y, Roschangar F, Vourloumis D, Vallberg H, Sarabia F, Ninkovic S, Hepworth D (1999) Bioorg Med Chem 7:665
98. Höfle G, Glaser N, Kiffe M, Hecht HJ, Sasse F, Reichenbach H (1999) Angew Chem Int Ed 38:1971
99. Sefkow M, Höfle G (1998) Heterocycles 48:2485
100. Nicolaou KC, Finlay MRV, Ninkovic S, King NP, He Y, Li TH, Sarabia F, Vourloumis D (1998) Chem Biol 5:365
101. Kolman A (2004) Curr Opin Invest Drugs 5:1292
102. End N, Bold G, Caravatti G, Wartmann M, Altmann K-H (2000) Proceedings of ESOC-4: 4th International Electronic Conference on Synthetic Organic Chemistry
103. Nettles JH, Li HL, Cornett B, Krahn JM, Snyder JP, Downing KH (2004) Science 305:866
104. Sánchez-Pedregal VM, Kubicek K, Meiler J, Lyothier I, Paterson I, Carlomagno T (2006) Angew Chem Int Ed 45:7388
105. Charette AB, Juteau H, Lebel H, Molinaro C (1998) J Am Chem Soc 120:11943
106. Takai K, Kimura K, Kuroda T, Hiyama T, Nozaki H (1983) Tetrahedron Lett 24:5281
107. Jin H, Uenishi J, Christ WJ, Kishi Y (1986) J Am Chem Soc 108:5644
108. Wartmann M, Loretan J, Reuter R, Hattenberger M, Müller M, Vaxelaire J, Maira SM, Floersheimer A, O'Reilly T, Nicolaou KC, Altmann K-H (2004) Proc Am Assoc Cancer Res. p 45
109. Nicolaou KC, Sasmal PK, Rassias G, Reddy MV, Altmann K-H, Wartmann M, O'Brate A, Giannakakou P (2003) Angew Chem Int Ed 42:3515
110. Altmann K-H, Bold G, Caravatti G, Florsheimer A, Guagnano V, Wartmann M (2000) Bioorg Med Chem Lett 10:2765
111. Rudolph J, Reddy KL, Chiang JP, Sharpless KB (1997) J Am Chem Soc 119:6189
112. Klar U, Buchmann B, Schwede W, Skuballa W, Hoffinann J, Lichtner RB (2006) Angew Chem Int Ed 45:7942
113. Cachoux F, Isarno T, Wartmann M, Altmann K-H (2006) Synlett 1384
114. Cachoux F, Isarno T, Wartmann M, Altmann K-H (2006) ChemBioChem 7:54
115. Bold G, Wojeik S, Caravatti G, Lindauer R, Stierlin C, Gertsch J, Wartmann M, Altmann K-H (2006) Chem Med Chem 1:37
116. Hearn BR, Zhang D, Li Y, Myles DC (2006) Org Lett 8:3057
117. Alhamadsheh MM, Gupta S, Hudson RA, Perera L, Tillekeratne VLM (2008) Chem Eur J 14:570
118. Quinoà E, Kakou Y, Crews P (1988) J Org Chem 53:3642
119. Corley DG, Herb R, Moore RE, Scheuer PJ, Paul VJ (1988) J Org Chem 53:3644
120. Tanaka JI, Higa T, Bernardinelli G, Jefford CW (1996) Chem Lett 255
121. Cutignano A, Bruno I, Bifulco G, Casapullo A, Debitus C, Gomez-Paloma L, Riccio R (2001) Eur J Org Chem 775
122. Pryor DE, O'Brate A, Bilcer G, Diaz JF, Wang Yu, Wang Yo, Kabaki M, Jung MK, Andreu JM, Ghosh AK, Giannakakou P, Hamel E (2002) Biochemistry 41:9109
123. Gapud EJ, Bai R, Ghosh AK, Hamel E (2004) Mol Pharmacol 66:113
124. Buey RM, Barasoain I, Jackson E, Meyer A, Giannakakou P, Paterson I, Mooberry S, Andreu JM, Diaz JF (2005) Chem Biol 12:1269
125. Pineda O, Farras J, Maccari L, Manetti F, Botta M, Vilarrasa J (2004) Bioorg Med Chem Lett 14:4825
126. Clark EA, Hills PM, Davidson BS, Wender PA, Mooberry SL (2006) Mol Pharmacol 3:457
127. Lu H, Murtagh J, Schwartz EL (2006) Mol Pharmacol 69:1207
128. Jefford CW, Bernardinelli G, Tanaka J-I, Higa T (1996) Tetrahedron Lett 37:159
129. Mulzer J, Öhler E (2003) Chem Rev 103:3753
130. Ghosh AK, Mathivanan P, Cappiello J (1997) Tetrahedron Lett 38:2427
131. Ghosh AK, Wang Y (2000) Tetrahedron Lett 41:2319

132. Ghosh AK, Wang Y (2000) Tetrahedron Lett 41:4705
133. Shimizu A, Nishiyama S (1997) Tetrahedron Lett 38:6011
134. Shimizu A, Nishiyama S (1998) Synlett 1209
135. Mulzer J, Hanbauer M (2000) Tetrahedron Lett 41:33
136. Dorling EK, Öhler E, Mulzer J (2000) Tetrahedron Lett 41:6323
137. Dorling EK, Öhler E, Mantoulidis M, Mulzer J (2001) Synlett 105
138. Ahmed A, Öhler E, Mulzer J (2001) Synthesis 2007
139. Pitts M, Mulzer J (2002) Tetrahedron Lett 43:8471
140. Nadolski GT, Davidson BS (2001) Tetrahedron Lett 42:797
141. Messenger BT, Davidson BS (2001) Tetrahedron Lett 42:801
142. Sivaramakrishnan A, Nadolski GT, McAlexander IA, Davidson BS (2002) Tetrahedron Lett 43:213
143. Paterson I, De Savi C, Tudge M (2001) Org Lett 3:213
144. Lee HW, Jeong C-S, Yoon SH, Lee I-YC (2001) Bull Korean Chem Soc 22:791
145. Lee HW, Yoon SH, Lee I-YC, Chung BY (2001) Bull Korean Chem Soc 22:1179
146. Ghosh AK, Wang Y (2000) J Am Chem Soc 122:11027
147. Ghosh AK, Wang Y (2001) Tetrahedron Lett 42:3399
148. Ghosh AK, Wang Y, Kim JT (2001) J Org Chem 66:8973
149. Mulzer J, Öhler E (2001) Angew Chem Int Ed 40:3842
150. Enev VE, Köhlig H, Mulzer J (2001) J Am Chem Soc 123:10764
151. Mulzer J, Hanbauer M (2002) Tetrahedron Lett 43:3381
152. Ahmed A, Hoegenauer EK, Enev VE, Hanbauer M, Köhlig H, Öhler E, Mulzer J (2003) J Org Chem 68:3026
153. Paterson I, De Savi C, Tudge M (2001) Org Lett 3:3149
154. Wender PA, Hegde SG, Hubbard RD, Zhang L (2002) J Am Chem Soc 124:4956
155. Crimmins MT, Stanton MG, Allwein SP (2002) J Am Chem Soc 124:5958
156. Williams DR, Mi L, Mullins RJ, Stites RE (2002) Tetrahedron Lett 43:4841
157. Nelson SG, Cheung WS, Kassick AJ, Hilfiker MA (2002) J Am Chem Soc 124:13654
158. Jadhav PK, Bhat KS, Perumal T, Brown HC (1986) J Org Chem 51:432
159. Brown HC, Bhat KS, Randad RS (1989) J Org Chem 54:1570
160. Racherla US, Brown HC (1991) J Org Chem 56:401
161. Scott W, McMurry E (1988) Acc Chem Res 21:47
162. Comins DL, Dchghani A (1992) Tetrahedron Lett 33:6299
163. Kumada M (1972) J Am Chem Soc 94:4374
164. Kumada M (1980) Pure Appl Chem 52:669
165. Luche JL (1978) J Am Chem Soc 100:2226
166. Uenishi J, Ohmi M (2005) Angew Chem Int Ed 44:2756
167. Jin H, Uenishi J, Christ WJ, Kishi Y (1986) J Am Chem Soc 108:5644
168. Takai K, Tagashira M, Kuroda T, Oshima K, Utimoto K, Nozaki H (1986) J Am Chem Soc 108:6048
169. Saito S, Hara T, Takahashi N, Hirai M, Moriwake T (1992) Synlett 237
170. Wender PA, Hegde SG, Hubbard RD, Zhang L, Mooberry SL (2003) Org Lett 5:3507
171. Mooberry SL, Randall-Hlubek DA, Leal RM, Hegde SG, Hubbard RD, Zhang L, Wender PA (2004) Proc Natl Acad Sci USA 101:8803
172. Gallagher BM Jr, Fang FG, Johannes CW, Pesant M, Tremblay MR, Zhao H, Akasaka K, Li XY, Liu J, Littlefield BA (2004) Bioorg Med Chem Lett 14:5753
173. Paterson I, Bergmann H, Menche D, Berkessel A (2004) Org Lett 6:1293; erratum (2006) Org Lett 8:1511
174. Gallagher BM Jr, Zhao H, Pesant M, Fang FG (2005) Tetrahedron Lett 46:923
175. Paterson I, Menche D, Hakansson AE, Longstaff A, Wong D, Barasoain I, Bury RM, Diaz JF (2005) Bioorg Med Chem Lett 15:2243
176. Wender PA, Hilinski MK, Soldermann N, Mooberry SL (2006) Org Lett 8:1507
177. Johnson TA, Tenney K, Cichewicz RH, Morinaka BI, White KN, Amagata T, Subramanian B, Media J, Mooberry SL, Valeriote FA, Crews P (2007) J Med Chem 50:3795

178. Paterson I, Menche D, Britton R, Hakansson AE, Silva-Martinez MA (2005) Tetrahedron Lett 46:3677
179. Thepchatri P, Cicero DO, Monteagudo E, Ghosh AK, Cornett B, Weeks ER, Snyder JP (2005) J Am Chem Soc 127:12838
180. Pettit GR, Cichacz ZA, Gao F, Boyd MR, Schmidt JM (1994) Chem Commun 1111
181. Shin Y, Choy N, Turner TR, Balachandran R, Madiraju C, Day BW, Curran DP (2002) Org Lett 4:4443
182. Gunasekera SP, Gunasekera M, Longley RE, Schulte GK (1991) J Org Chem 56:1346
183. Madiraju C, Edler MC, Hamel E, Raccor BS, Brianne S, Van Balachandran R, Zhu G, Giuliano KA, Vogt A, Shin Y, Fournier JH, Fukui Y, Brückner AM, Curran DP, Day BW (2005) Biochemistry 44:15053
184. Paterson I, Britton R, Delgado O, Wright AE (2004) Chem Commun 632
185. Matsumori N, Kaneno D, Murata M, Nakamura H, Tachibana K (1999) J Org Chem 64:866
186. Paterson I, Britton R, Delgado O, Meyer A, Poullennec KG (2004) Angew Chem Int Ed 43:4629
187. Shin Y, Fournier J, Fukui Y, Brückner AM, Curran DP (2004) Angew Chem Int Ed 43:4634
188. O'Neil G, Phillips A (2006) J Am Chem Soc 128:5340
189. Ramachandran PV, Srivastava A, Hazra D (2007) Org Lett 9:157
190. Prusov E, Röhm H, Maier ME (2006) Org Lett 8:1025
191. Saibaba V, Sampath A, Mukkanti K, Iqbal J, Das P (2007) Synthesis 18:2797
192. Monti C, Sharon O, Gennari C (2007) Chem Commun (Cambridge, United Kingdom) 41:4271
193. Sharon O, Monti C, Gennari C (2007) Tetrahedron 63:5873
194. Jaegel J, Maier ME (2006) Synlett 693
195. Paterson I, Delgado O, Florence GJ, Lyothier I, Scott JP, Sereinig N (2003) Org Lett 5:35
196. Myers AG, Yang BH, Chen H, McKinstry L, Kopecky DJ, Gleason JL (1997) J Am Chem Soc 119:6496
197. Paterson I, Florence GJ, Gerlach K, Scott JP (2000) Angew Chem 112:385; (2000) Angew Chem Int Ed 39:377
198. Paterson I, Florence GJ, Gerlach K, Scott JP, Sereinig N (2001) J Am Chem Soc 123:9535
199. Devos A, Remion J, Frisque-Hesbain AM, Colens A, Ghosez L (1979) J Chem Soc Chem Commun 1180
200. Allred GD, Liebeskind LS (1996) J Am Chem Soc 118:2748
201. Kalesse M (2000) ChemBioChem 1:171
202. Smith III AB, Beauchamp TJ, LaMarche MJ, Kaufman MD, Qiu YP, Arimoto H, Jones DR, Kobayashi K (2000) J Am Chem Soc 122:8654
203. Paterson I, Florence GJ (2003) Eur J Org Chem, p 2193
204. Mickel SJ, Sedelmeier GH, Niederer D, Daeffler R, Osmani A, Schreiner K, Seeger-Weibel M, Berod B, Schaer K, Gamboni R (2004) Org Process Res Dev 8:92, and succeeding papers in that issue
205. Weinreb amide **247** was made in five steps from (2*S*)-3-hydroxy-2-methylpropionic acid methyl ester (Roche ester) in 39% yield
206. Marshall JA, Bourbeau MJ (2003) Org Lett 5:3197
207. Matsumura K, Hashiguchi S, Ikariya T, Noyori R (1997) J Am Chem Soc 119:8738
208. Still WC, Gennari C (1983) Tetrahedron Lett 24:4405
209. Brown HC, Bhat KS (1986) J Am Chem Soc 108:293
210. Williams DR, Kissel WS (1998) J Am Chem Soc 120:11198
211. Inanage J, Hirata K, Saeka H, Katsuki TJ, Yamaguchi M (1979) Bull Chem Soc Jpn 52:1989
212. Paterson I, Gardner NM (2007) Chem Commun 49
213. Gunasekera SP, Gunasekera M, Longley RE, Schulte GK (1990) J Org Chem 55:4912
214. Jung W, Harrison C, Shin Y, Fournier J, Balachandran R, Raccor BS, Sikorski RP, Vogt A, Curran DP (2007) J Med Chem 50:2951

215. Shin Y, Fournier J, Brückner A, Madiraju C, Balachandran R, Raccor BS, Edler MC, Hamel E, Sikorski RP, Vogt A, Day BW, Curran DP (2007) Tetrahedron 63:8537
216. Shin Y, Fournier J, Balachandran R, Madiraju C, Raccor BS, Zhu G, Edler MC, Hamel E, Day BW, Curran DP (2005) Org Lett 7:2873
217. Fukui Y, Brückner AM, Shin Y, Balachandran R, Day BW, Curran DP (2006) Org Lett 8:301
218. Paterson I, Gardner NM, Poullennec KG, Wright AE (2007) Bioorg Med Chem Lett 17:2443
219. Paterson I, Gardner NM, Poullennec KG, Wright AE (2008) J Nat Prod 71:364
220. West LM, Northcote PT, Battershill CN (2000) J Org Chem 65:445
221. Liao X, Wu Y, De Brabander JK (2003) Angew Chem Int Ed 42:1648
222. Gaitanos TN, Buey RM, Diaz JF, Northcote PT, Teesdale-Spittle P, Andreu JM, Miller JH (2004) Cancer Res 64:5063
223. Pineda O, Farràs J, Maccari L, Manetti F, Botta M, Vilarrasa J (2004) Bioorg Med Chem Lett 14:4825
224. Jimenez-Barbero J, Canales A, Northcote PT, Buey RM, Andreu JM, Diaz JF (2006) J Am Chem Soc 128:8757
225. Hamel E, Day BW, Miller JH, Jung MK, Northcote PT, Ghosh AK, Curran DP, Cushman M, Nicolaou KC, Paterson I, Sorensen EJ (2006) Mol Pharmacol 70:1555
226. Wilmes A, Bargh K, Kelly C, Northcote PT, Miller JH (2007) Mol Pharm 4:269
227. Paterson I, Di Francesco ME, Kühn T (2003) sOrg Lett 5:599
228. Taylor RE, Jin M (2003) Org Lett 5:4959
229. Ghosh AK, Kim JH (2003) Tetrahedron Lett 44:3967
230. Ghosh AK, Kim JH (2003) Tetrahedron Lett 44:7659
231. Liu B, Zhou WS (2004) Org Lett 6:71
232. Gurjar MK, Pedduri Y, Ramana CV, Puranik VG, Gonnade RG (2004) Tetrahedron Lett 45:387
233. Engers DW, Bassindale MJ, Pagenkopf BL (2004) Org Lett 6:663
234. Roulland E, Ermolenko MS (2005) Org Lett 7:2225
235. Owen RM, Roush WR (2005) Org Lett 7:3941
236. Chen Z-L, Zhou WS (2006) Tetrahedron Lett 47:5289
237. Jin M, Taylor RE (2005) Org Lett 7:1303
238. Xu Z, Johannes CW, Houri AF, La DS, Cogan DA, Hofilena GE, Hoveyda AH (1997) J Am Chem Soc 119:10302
239. Chatterjee AB, Morgan JP, Scholl M, Grubbs RH (2000) J Am Chem Soc 122:3783
240. Bhattacharjee A, Soltani O, De Brabander JK (2002) Org Lett 4:481
241. Smith AB, Minbiole KP, Verhoest PR, Schelhaas M (2001) J Am Chem Soc 123:10942
242. Evans DA, Dart MJ, Duffy JL, Yang MG (1996) J Am Chem Soc 118:4322
243. Ihara M, Katsumata A, Setsu F, Tokunaga Y, Fukumoto K (1996) J Org Chem 61:667
244. Bartlett PA, Meadows JD, Brown EG, Morimote A, Jernstedt KK (1982) J Org Chem 47:4013
245. Duan JJW, Smith AB (1993) J Org Chem 58:3703
246. Luche JL, Rodriguez-Hahn L, Crabbé P (1978) J Chem Soc Chem Comm 601
247. Harris CR, Kuduk SD, Balog A, Savin K, Glunz PW, Danishefsky SJ (1999) J Am Chem Soc 121:7050
248. Lee CB, Wu ZC, Zhang F, Chappell MD, Stachel SJ, Chou TC, Guan YB, Danishefsky SJ (2001) J Am Chem Soc 123:5249

Top Curr Chem (2009) 286: 73–119
DOI: 10.1007/128_2008_7

Published online: 06 November 2008

The Chemical Synthesis of Discodermolide

I. Paterson and G.J. Florence

Abstract The marine sponge-derived polyketide discodermolide is a potent antimitotic agent that represents a promising natural product lead structure in the treatment of cancer. Discodermolide shares the same microtubule-stabilising mechanism of action as Taxol®, inhibits the growth of solid tumours in animal models and shows synergy with Taxol. The pronounced cytotoxicity of discodermolide, which is maintained against cancer cell lines that display resistance to Taxol and other drugs, combined with its scarce availability from its natural source, has fuelled significant academic and industrial interest in devising a practical total synthesis as a means of ensuring a sustainable supply for drug development. This chapter surveys the various total syntheses of discodermolide that have been completed over the period 1993–2007, focusing on the strategies employed for introduction of the multiple stereocentres and achieving control over the alkene geometry, along with the various methods used for realising the pivotal fragment couplings to assemble progressively the full carbon skeleton. This dedicated synthetic effort has triumphed in removing the supply problem for discodermolide, providing sufficient material for extensive biological studies and enabling its early stage clinical development, as well as facilitating SAR studies for lead optimisation.

Keywords Anticancer, Natural products, Polyketides, Stereocontrol, Tubulin

Contents

I. Paterson (✉)
University Chemical Laboratory, Lensfield Road, Cambridge, CB2 1EW UK
e-mail: ip100@cam.ac.uk

G.J. Florence
School of Chemistry and Centre for Biomolecular Sciences, University of St Andrews, North Haugh, St Andrews, KY16 9ST UK

1 Introduction

The marine ecosystem provides an extensive source of structurally diverse natural products isolated from numerous organisms including algae, molluscs, corals, sponges, tunicates and phytoplankton, as well as associated microorganisms [1–4]. The biological activity of these compounds is often startling, demonstrating, for example, potent cytotoxic, immunosuppressive and antibiotic properties making them of interest to the pharmaceutical industry [5–8]. However, the low natural abundance of many of these lead structures means that realistic and practical synthetic routes are required to provide material to investigate and exploit further their biological activity [8, 9]. These factors, combined with the exquisite molecular architectures that many of these compounds possess, offer demanding challenges to the modern synthetic chemist. In particular, the marine polyketide discodermolide (**1**, Fig.1) has inspired intense synthetic activity, due to its biological profile and potential as a new generation anticancer agent given the onset of multidrug resistance in established cancer chemotherapies (see [10–13] for previous reviews on the synthesis of discodermolide; see [14] for a recent review on the synthesis of bioactive marine polyketides; see [15, 16] for an excellent recent review of microtubule-stabilising natural products.

1.1 Isolation and Structure of Discodermolide

Discodermolide (**1**) is a unique polyketide isolated by Gunasekera and co-workers at the Harbor Branch Oceanographic Institution in 1990 from the Caribbean deep-sea sponge *Discodermia Dissoluta* [17, 18]. This sponge was collected at a depth of 33m and several other new *Discodermia* species containing discodermolide were collected by manned submersibles at depths between 185 and 220m. These samples were exhaustively extracted and purified to provide discodermolide in an initial isolation yield of 0.002wt% from frozen sponge. Its gross structure was determined by extensive spectroscopic studies and the relative configuration was established by single crystal X-ray crystallography as shown in Fig.1. Structurally, discodermolide bears 13 stereogenic centres, a tetrasubstituted δ-lactone (C1–C5), one di- and one

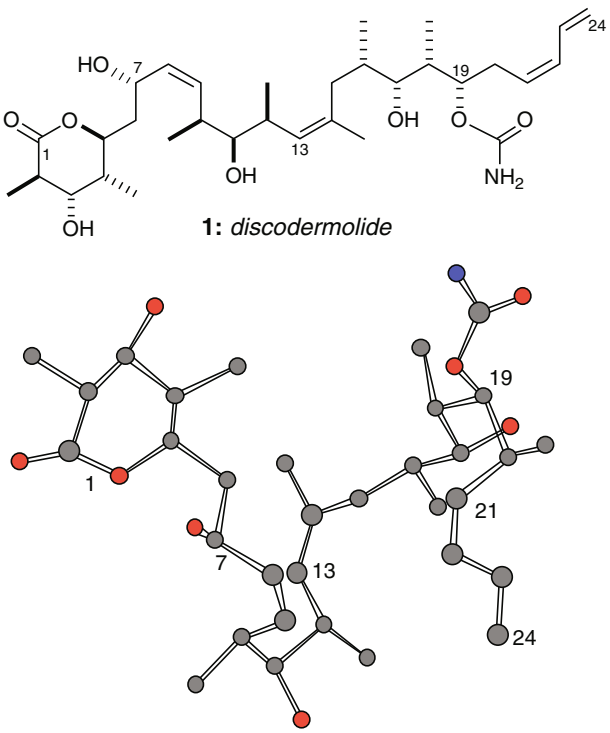

Fig.1 Structure of discodermolide

tri-substituted (*Z*)-double bond, a carbamate moiety (C19) and a terminal (*Z*)-diene (C21–C24). Discodermolide adopts a U-shaped conformation in the solid state, where the (*Z*)-olefins at C13–C14 and C8–C9 act as conformational locks by minimising A(1, 3) strain between their respective substituents. The δ-lactone adopts a boat-like conformation with H-bonding between the lactone moiety and the C7-OH group, which is retained in solution [19].

1.2 Biology of Discodermolide

Discodermolide was initially reported to be a potent immunosuppressive agent, both in vivo and in vitro, comparable with FK-506 and rapamycin, as well as displaying antifungal activity. It inhibited T-cell proliferation with an IC_{50} of 9nM in the mixed leukocyte reaction and graft vs host disease in transplanted mice [20, 21]. Further biological screening revealed pronounced cytotoxicity, causing cell cycle arrest at the G2/M phase in a variety of human and murine cell lines, with

IC_{50} values ranging from 3 to 80nM. In a similar fashion to Taxol, discodermolide functions by microtubule stabilisation, halting mitosis and causing cell death by apoptosis [22]. Discodermolide is an important member of a unique group of secondary metabolites (Fig.2) that act as microtubule-stabilising agents and mitotic spindle poisons, which currently include Taxol (paclitaxel) (**2**) [23], epothilones A (**3**) and B (**4**) [24], sarcodictyin A (**5**) [25], eleutherobin (**6**) [26], laulimalide (**7**) [27], FR182877 (cyclostreptin) (**8**) [28], peloruside A (**9**) [29], dictyostatin (**10**) [30–32] and the semi-synthetic Taxol analogue, Taxotere (**11**) [33]. Despite the lack of structural similarities, the cytotoxicity and microtubule stabilising properties of discodermolide are comparable to Taxol. Moreover, the growth of Taxol-resistant ovarian and colon carcinoma cells are inhibited by discodermolide (IC_{50}<2.5nM) [34]. Initial investigations into determining the discodermolide binding site through competition studies with radiolabelled Taxol suggested it occupied an identical or similar binding site on β-tubulin [35]. In comparative studies with the Taxol-dependent human lung carcinoma cell line A549-T12, discodermolide was unable to act as a substitute for Taxol, whereas the epothilones and eleutherobin were able to maintain the viability of the cell line [36]. Significantly, a synergistic potentiation of discodermolide's cytotoxicity was observed, when used in combination with Taxol, suggesting that discodermolide may bind to tubulin at a distinct site from Taxol. More recent in vivo studies on ovarian tumour xenograft bearing mice have also shown this synergy, inducing tumour regression without toxicity to the mouse [37]. Notably, these studies suggest that the synergistic combination of Taxol and discodermolide may offer a useful therapy, minimising the plethora of

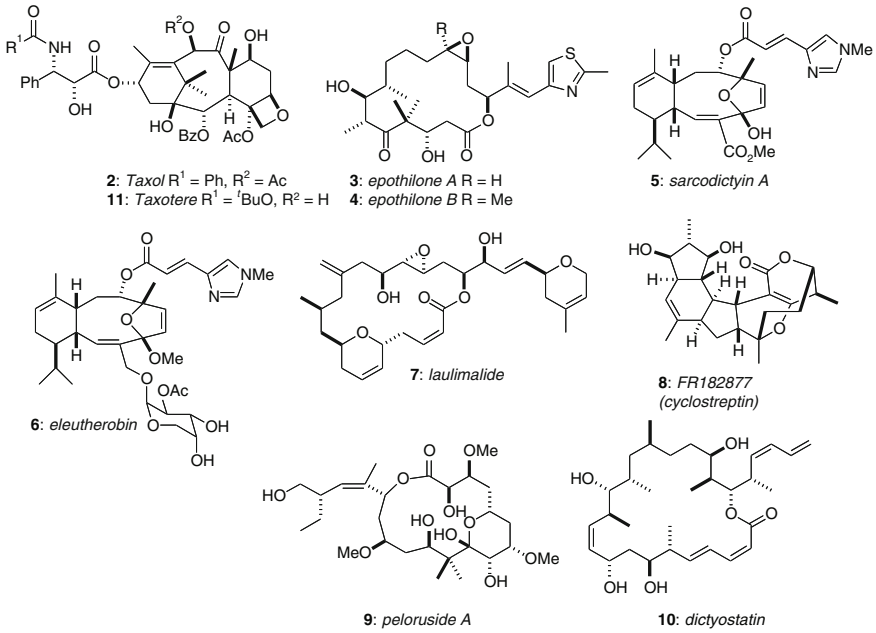

Fig. 2 Structures of other microtubule-stabilizing natural products

toxicity related side-effects that are observed in the clinic with high doses of Taxol. In 2006, the group of Carlomagno elucidated the bioactive conformation of discodermolide bound to soluble tubulin by using elegant NMR studies and proposed a common pharmacophore with the epothilones [38].

The highly encouraging biological profile of discodermolide led it to become a promising candidate for clinical development as a chemotherapeutic agent for breast cancer and other multi-drug-resistant cancers. This potential was recognised by Novartis Pharma AG, who licensed discodermolide from the Harbor Branch Oceanographic Institution and launched an impressive large-scale total synthesis campaign to supply material for clinical trials for the treatment of advanced solid malignancies. However, these trials have since been halted due to toxicity associated with the chemotherapy [39].

2 Total Synthesis

While the early clinical development of Taxol was severely hampered by the supply problem, this was eventually resolved by semi-synthesis from 10-deacetyl baccatin III, obtained from the needles of the common European yew tree. In comparison, the epothilones, which are currently in advanced clinical trials as anticancer agents, are obtained by fermentation [40]. Ixempra®, the lactam analogue of epothilone B which is obtained by semi-synthesis, has recently been approved by the FDA in the United States for the treatment of advanced breast cancer [41]. Unfortunately, a fermentation process is not as yet possible for discodermolide, even though as a polyketide it is presumably produced by a symbiotic microorganism associated with the sponge source (see [42] for a review on symbiotic bacteria as a source of marine natural products). Therefore, the supply problem for discodermolide could only be resolved via total synthesis. Consequently, there has been considerable synthetic effort directed towards discodermolide, culminating in 13 completed total syntheses reported by 8 groups [43–55] and numerous fragment syntheses [55–97]. This chapter highlights the total syntheses of discodermolide by ourselves and the groups of Schreiber, Smith, Myles, Marshall, Panek, Ardisson, and the Novartis process chemistry team in Basel led by Mickel. The key carbon-carbon bond disconnection strategies employed in all these approaches are highlighted in Fig.3. In particular, we focus on the strategies employed to configure the multiple stereogenic centres, the methods employed to introduce the synthetically challenging (*Z*)-olefins and the pivotal fragment coupling steps.

2.1 Schreiber Total Synthesis

Schreiber and co-workers reported the first total synthesis of (–)-discodermolide (*ent*-**1**) in 1993, confirming the relative stereochemistry and establishing the absolute configuration [43, 44]. In 1996, they reported the first synthesis of the natural

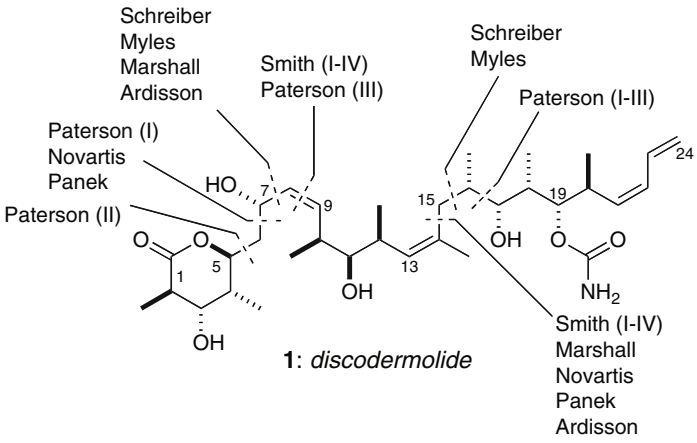

Fig. 3 Key disconnections employed in completed syntheses of discodermolide

antipode (+)-discodermolide (**1**), following an almost identical route performed in the correct enantiomeric series (Scheme 1), along with several analogues designed to study the mode of tubulin binding and microtubule stabilizing properties [44]. Their synthetic strategy towards (+)-discodermolide involved key fragment couplings via Nozaki-Kishi addition [98–101] at C7–C8 and enolate alkylation at C15–C16, requiring the three key subunits **12** (C1–C7), **13** (C8–C15) and **14** (C16–C24). In turn, the homoallylic alcohols **15** and **16** served as building blocks for the subunit synthesis, accessible via Roush crotylation reactions with the aldehyde **17** [102], derived from Roche ester **18** which serves as a starting point in all of the synthetic endeavours reported to date.

The C1–C7 aldehyde **12** was prepared in eight steps starting with the Roush crotylation of aldehyde **17** (Scheme 2) [102]. Ozonolysis and chain extension of **15** provided (*E*)-enoate **19**; the C5 stereocentre was then introduced via an Evans-Prunet hetero-Michael addition [103]. Transformation of **20** into aldehyde **12** was completed in six steps. The C16–C24 methyl ketone **14** was obtained in seven steps from homoallylic alcohol **15**. Protection, ozonolysis and Stork-Wittig olefination [104] of the intermediate aldehyde was followed by a palladium-catalysed Negishi coupling [105] of vinyl iodide **21** with vinyl zinc bromide to introduce the terminal (*Z*)-diene unit in **14**. The synthetically demanding C13–C14 trisubstituted (*Z*)-alkene found in **13** was introduced by Still-Gennari HWE olefination (*Z:E*≥20:1) [106], following silyl protection and ozonolysis of **16**. Protecting group manipulations with the resulting (*Z*)-enoate **22** and homologation to iodoacetylene **13** via oxidation, alkylation and iodination at C8 completed the final subunit.

Assembly of the subunits began with the Nozaki-Kishi coupling reaction of iodoacetylene **13** and aldehyde **12**, in the presence of $CrCl_2$/$NiCl_2$, to provide propargylic alcohol **23**, with 3:1 dr at C7 (Scheme 3). The four-step conversion to bromide **24** was followed by the enolate alkylation of methyl ketone **14**.

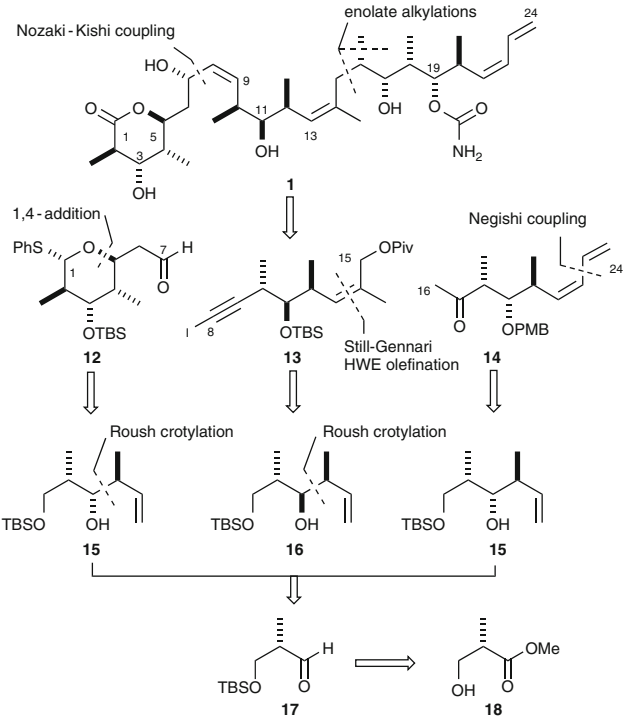

Scheme 1 Schreiber's synthetic strategy

Further alkylation of the lithium (*Z*)-enolate of **25** with methyl iodide gave **26**, introducing the C16 stereocentre (3:1 dr) and completing the carbon backbone. Oxidation at C1 and carbamate formation gave **27** which underwent a chelation-controlled reduction at C17 (30:1 dr). Finally, global deprotection completed the synthesis of discodermolide (**1**), with an overall yield of 4.3% achieved over 24 steps in the longest linear sequence.

The Schreiber synthesis is particularly noteworthy in that the absolute configuration of discodermolide was assigned unambiguously, and through the preparation of numerous analogues the first structure-activity relationship study was possible [35, 44]. Their synthesis of the unnatural antipode (*ent*-**1**) also led to the unexpected discovery that it causes cell cycle arrest in the S-phase [107].

2.2 Smith Total Syntheses

2.2.1 First Generation (1995)

Smith and co-workers reported their initial synthesis of (–)-discodermolide (*ent*-**1**) in 1995 [45]. They invoked key fragment unions at C8–C9 and C14–C15 via Wittig

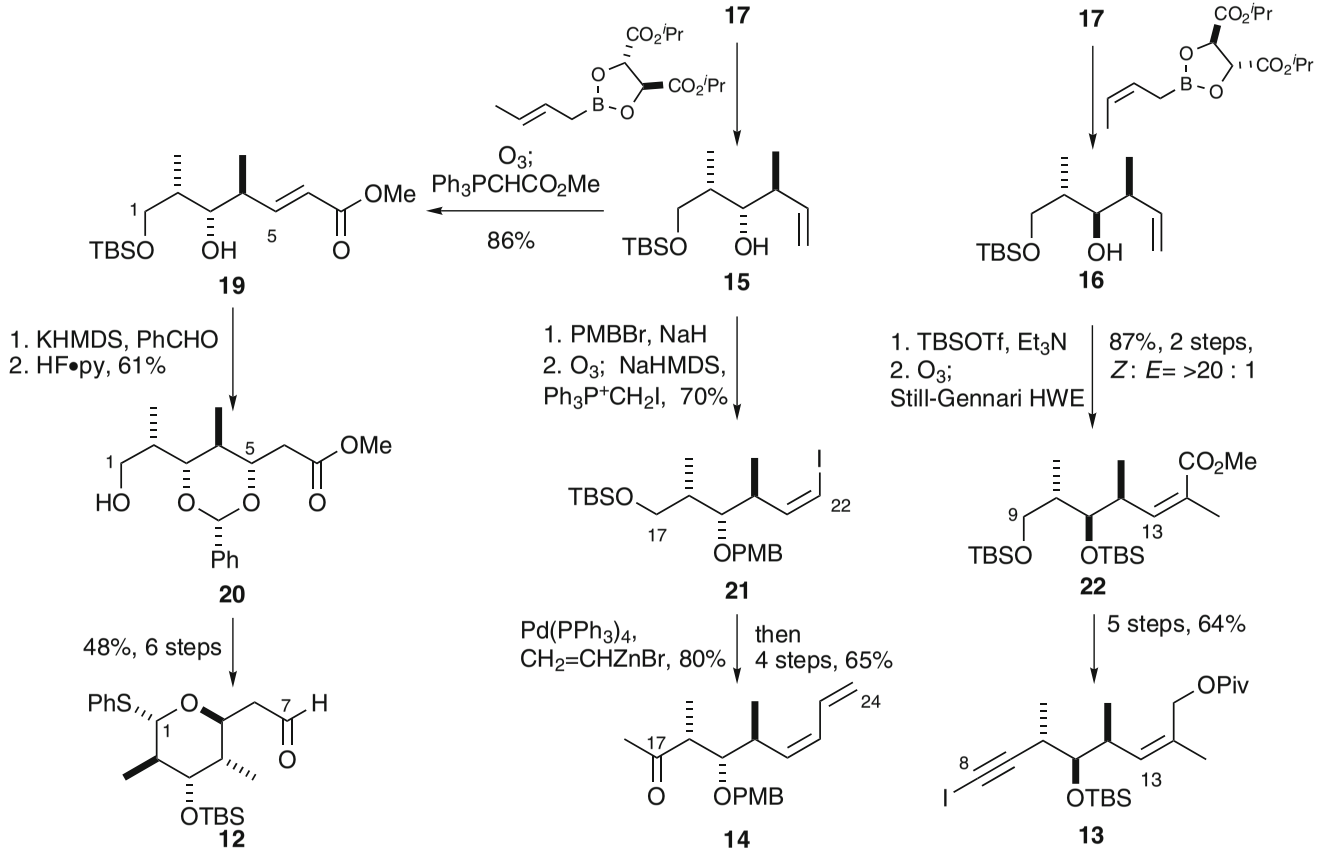

Scheme 2 Schreiber's synthesis of C1–C7, C8–C15 and C16–C24 subunits

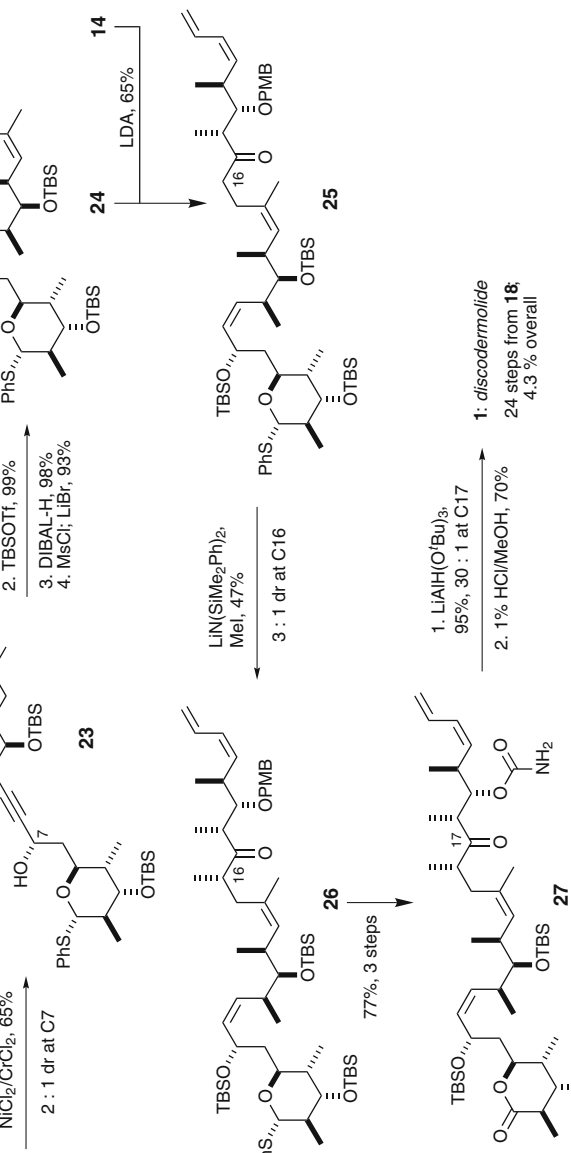

Scheme 3 Schreiber's subunit assembly and completion of discodermolide

olefination and Negishi cross-coupling [105], respectively (Scheme 4), dividing the carbon skeleton into three key subunits **28** (C1–C8), **29** (C9–C14) and **30** (C15–C21). Smith recognized the repeating stereotriad found in all three subunits and took advantage of a common precursor **31** for fragment synthesis. For clarity of presentation, the Smith first-generation synthesis is shown here in the correct enantiomeric series corresponding to natural (+)**-1**.

The common precursor **31** was configured using the Evans *syn* aldol reaction of propionimide **33** with the aldehyde **32**, available in three steps from Roche ester **18** (Scheme 5) [108–111]. The (*Z*)-alkenyl iodide at C14 was introduced by a Zhao-Wittig olefination on aldehyde **34** in moderate yield with variable selectivity (*Z:E* = 8–17:1) [112, 113]. The synthesis of the C15–C21 segment **30** utilized a second Evans aldol reaction to configure the C16–C17 *syn*-relationship to provide **35** which was transformed into iodide **30**. A palladium-catalysed Negishi cross-coupling of the corresponding zincate from the C14 vinyl iodide **29** with iodide **30** then gave the C9–C21 segment **36** [105]. The synthesis of the C1–C8 thioacetal aldehyde **28** began with the six-step elaboration of **31** to dithiane **37**, coupling with epoxide **38** was then followed by dithiane cleavage and Evans-Saksena 1,3-*anti* reduction of the intermediate β-hydroxy ketone to provide **39** [114], and installing the C7 stereocentre. A further 5 steps were then required to access the β-ethylthioacetal aldehyde **28**, giving a total of 14 steps from **31**.

As shown in Scheme 6, the elaboration of the C9–C21 fragment **36** to phosphonium salt **40** proved problematic, requiring the treatment of the intermediate iodide **41** with triphenylphosphine at ultrahigh pressure (12.8kbar) for six days. The (*Z*)-selective Wittig coupling of aldehyde **28** and phosphonium salt **40** then gave the C1–C21 intermediate **42**

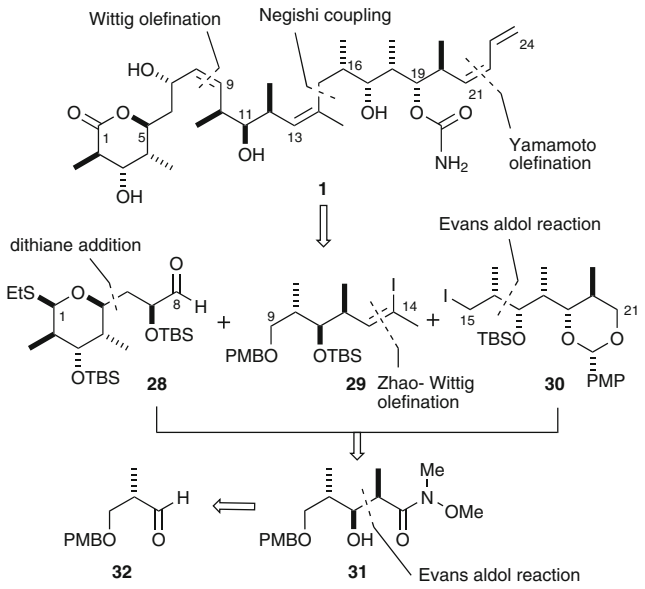

Scheme 4 Smith's first-generation strategy

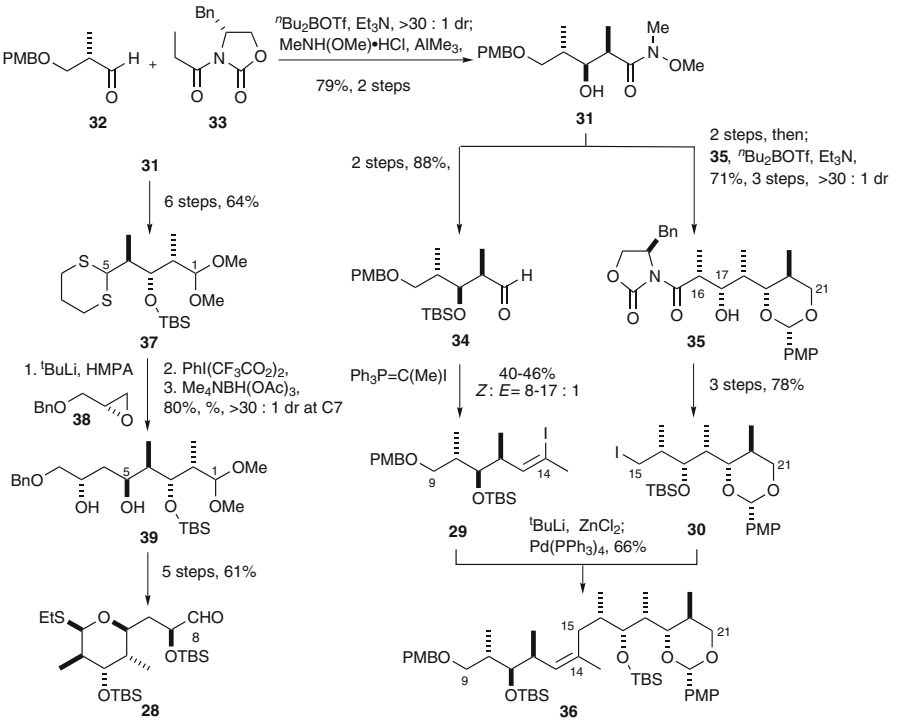

Scheme 5 Smith's synthesis of C1–C8, C9–C14 and C15–21 subunits, and assembly of C8–C21 intermediate

(*Z:E* = 49:1). At this stage, the (*Z*)-diene unit was introduced utilizing the Yamamoto olefination protocol to give **43** [115]. A further five steps were then required to complete Smith's first-generation synthesis of (–)-discodermolide (*ent*-**1**), in 2.2% overall yield over 28 steps in the longest linear sequence based on the C1–C8 aldehyde **28**.

2.2.2 Second Generation (1999)

Smith and co-workers reported their second-generation approach to discodermolide in 1999, which was now performed in the correct enantiomeric series [46–48]. By carefully redesigning the route, the overall number of steps was significantly reduced and, importantly, it enabled a gram-scale synthesis. As outlined in Scheme 7, the key bond constructions at C8–C9 and C14–C15 were retained, while strategic modifications involved the earlier introduction of the terminal (*Z*)-diene unit in **44** and a revised C1–C8 subunit **45**.

As shown in Scheme 8, the synthesis of aldehyde **45** was achieved in eight steps utilizing the common precursor **31** [46–48]. Remarkably, the Mukaiyama aldol addition of silyl enol ether **46** to aldehyde **47** proceeded with anti-Felkin selectivity, which was attributed to involvement of the Weinreb amide and aldehyde carbonyl

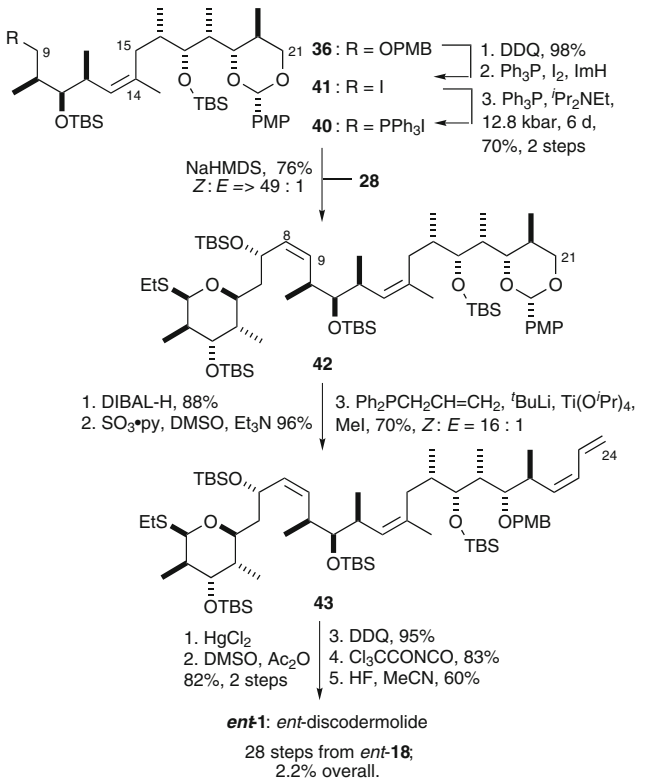

Scheme 6 Smith's first-generation assembly of discodermolide

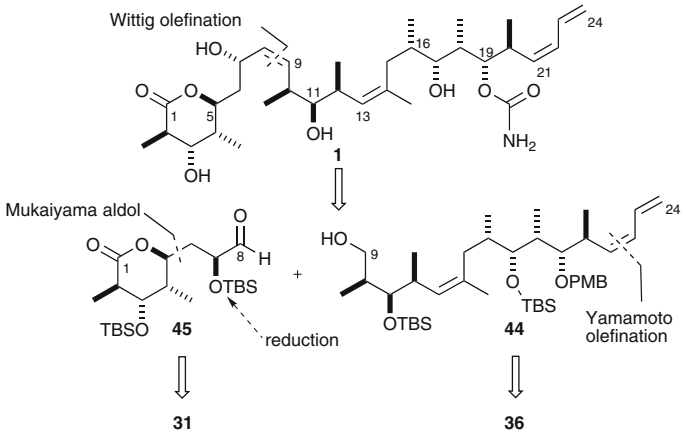

Scheme 7 Smith's second-generation strategy

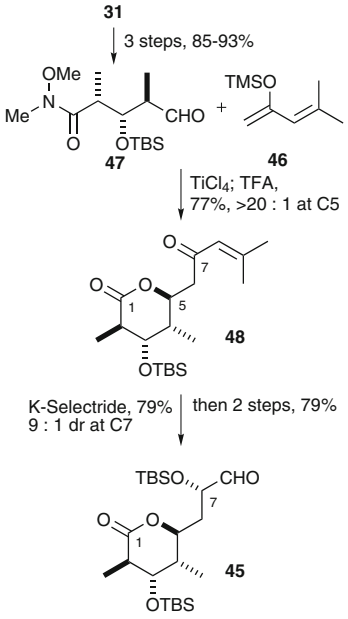

Scheme 8 Smith's synthesis of revised C1–C8 subunit

oxygens in forming an eight-membered chelate with the titanium Lewis acid, and after work-up and acid-catalysed δ-lactonisation with TFA this gave the ketone **48**. K-Selectride reduction at C7 (9:1dr), followed by TBS protection and ozonolysis provided **45**, in 13 steps and 21% overall yield from **18** [70–97].

Starting from the C9–C21 fragment **36**, the installation of the terminal *Z*-diene unit was achieved in a five-step sequence, in which the Yamatoto olefination gave a *Z:E* ratio of 8–14:1 (Scheme 9) [115]. The phosphonium salt **49** was prepared from **44** in two steps, again requiring ultrahigh pressure conditions. The Wittig coupling of phosphonium salt **49** and aldehyde **45** then gave **50** (*Z:E* = 15–24:1). A further three steps were required to complete Smith's second-generation synthesis of discodermolide, which proceeded in an improved 6% yield over 24 steps (longest linear sequence). The Smith second-generation synthesis is notable in that it provided an impressive 1.04 g of discodermolide, enabling extensive biological and preclinical evaluation. However, further scale up of this route would pose significant technical challenges due, in particular, to the limited availability of suitable ultrahigh pressure reactors for performing large-scale preparations of the pivotal phosphonium salt **49**. This limiting factor was then addressed in a third-generation approach [49].

2.2.3 Third Generation (2003)

Although the Smith second-generation synthesis offered several improvements over their initial route, the use of the ultrahigh pressure over extended time periods in the formation of the key Wittig salt **49** severely limited the possibility of further

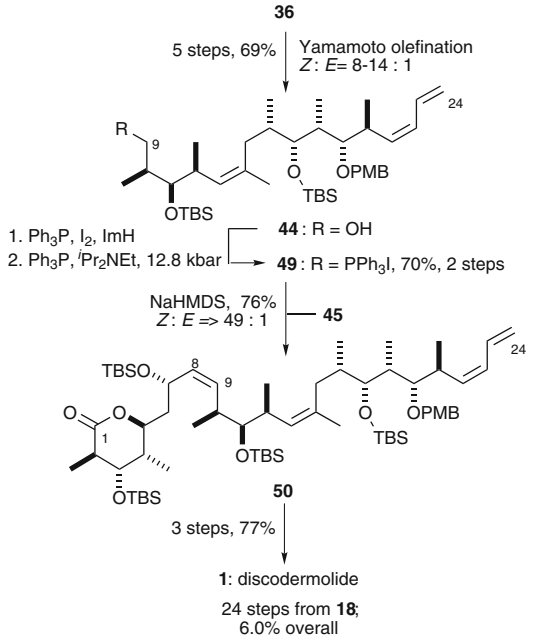

Scheme 9 Completion of Smith's second-generation synthesis

scale-up. Thus, the Smith group's third-generation synthesis addressed this limiting step [49], through the simple replacement of the sterically demanding TBS group at C11 with a MOM group in **51**, while retaining the successful C14–C15 and C8–C9 coupling strategy (Scheme10).

As detailed in Scheme11, a Negishi-type coupling of **30** and the revised C9–C14 subunit **52**, readily derived from **31**, followed by an established sequence gave alcohol **53** [46–48], in preparation for phosphonium salt formation. Conversion into the intermediate iodide and reaction with triphenylphosphine at ambient pressure proceeded smoothly to give **51** in 70% yield. However, Wittig olefination of aldehyde **45** with **51** using methyl lithium/lithium bromide for deprotonation generated the C8–C9 (*Z*)-olefin with substantially reduced selectivity (third generation = 4:1, *cf* second generation = 24:1). Conversion into discodermolide then required three steps, giving a 1.9% overall yield over 24 steps in the longest linear sequence.

This revised strategy demonstrates that a simple change in hydroxyl protecting groups can markedly influence reactivity and selectivity. While formation of the Wittig salt **51** could now be achieved at atmospheric pressure, its coupling with aldehyde **45** only proceeded in moderate yield and selectivity.

2.2.4 Fourth Generation (2005)

In 2005, Smith and co-workers reported their fourth-generation synthesis of discodermolide [50]. Using the Suzuki-coupling at C13–C14 developed by Marshall [53, 54,

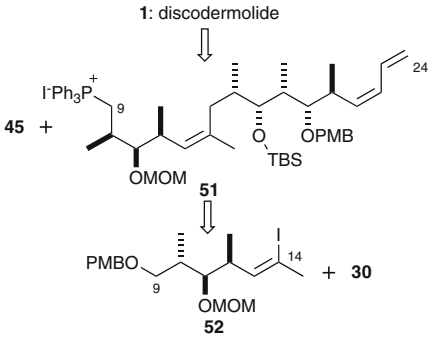

Scheme 10 Smith's third-generation strategy

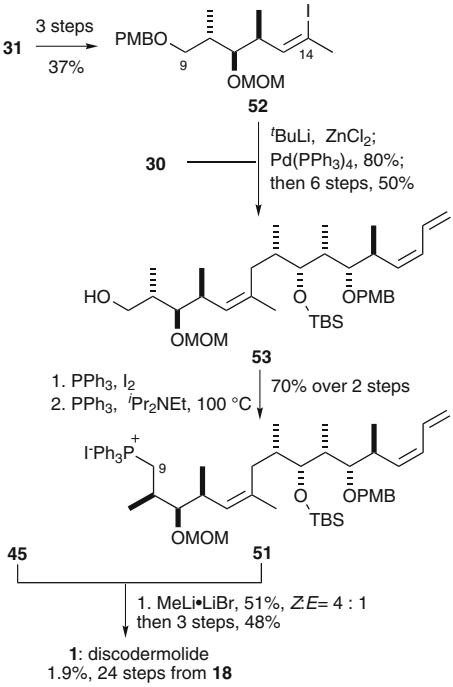

Scheme 11 Smith's third-generation synthesis

116], a revised strategy was devised based on reversing the order of the key fragment couplings. Thus, a Wittig olefination at C8–C9 between a modified C1–C8 aldehyde **54** and phosphonium salt **55** was followed by C14–C15 bond formation with the C15–C24 subunit **56**, as shown in Scheme12. These modifications were designed to further increase the overall efficiency and convergency of their approach.

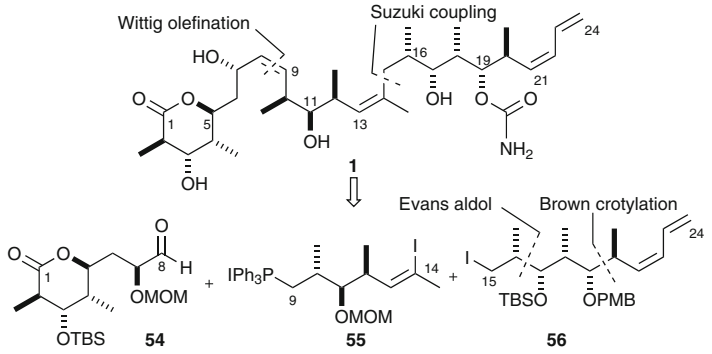

Scheme 12 Smith's fourth-generation strategy

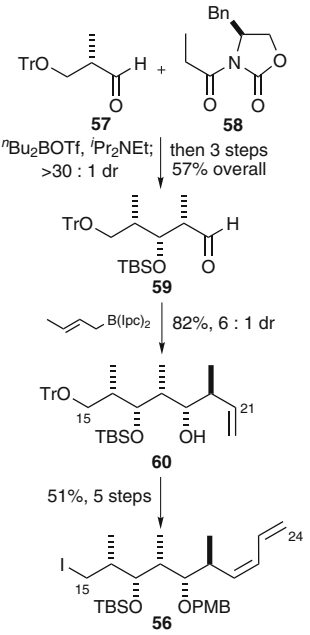

Scheme 13 Smith's synthesis of the C15–C24 subunit

As outlined in Scheme13, the synthesis of the C15–C24 subunit **56** started with an Evans aldol reaction between the aldehyde **57** and **58** [108–111]. Transformation into aldehyde **59** and a Brown crotylation then gave **60** [117], which was converted into **56** in five steps.

The C1–C8 aldehyde **54** and the C9–C14 Wittig salt **55** were accessed from previously reported intermediates **48** and **52** (Scheme14). A Wittig olefination of aldehyde **54** with **55** gave the C1–C14 intermediate **61**. In turn, a Suzuki coupling of the boronate derived from **56** with **61** provided **62** [116]. Following their established endgame, the synthesis of discodermolide was now achieved in 9.0% overall yield with 17 steps in the longest linear sequence.

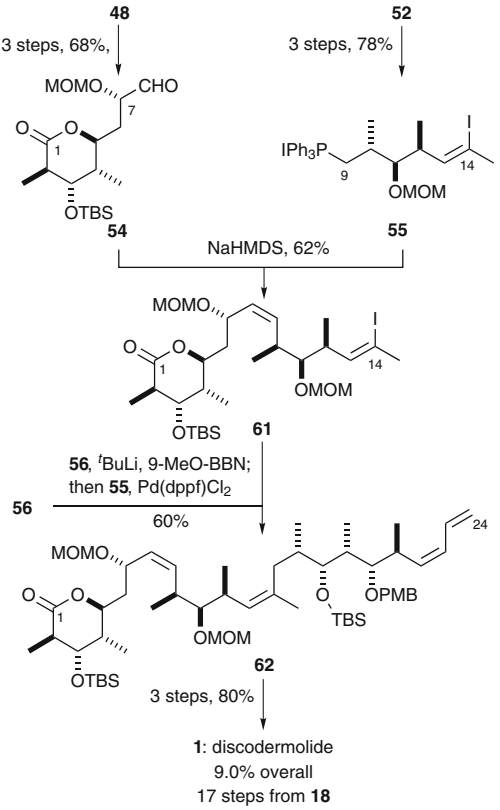

Scheme 14 Completion of Smith's fourth-generation synthesis

2.3 Myles Total Synthesis

Myles and co-workers reported the synthesis of (–)-discodermolide (*ent*-**1**) in 1997 [51]. This was followed by their synthesis of the natural antipode in 2003, exploiting an analogous coupling strategy with improved subunit syntheses, the details of which are presented here [52]. The Myles approach to discodermolide relied on key bond unions at C7–C8 (Nozaki-Kishi) and C15–C16 (enolate alkylation) giving rise to the subunits **63** (C1–C7), **64** (C9–C15), and **65** (C16–C21) (Scheme 15). The synthesis of these subunits utilized a combination of both substrate and reagent controlled reactions, including a novel solution to the installation of the C13–C14 (*Z*)-trisubstituted olefin using the cycloadduct **66** [118].

The synthesis of the C9–C15 subunit **64** commenced with the cyclocondensation of aldehyde **67** and diene **68** to provide dihydropyrone **66** (Scheme 16) [118]. A Luche reduction [119, 120] and acid-mediated Ferrier rearrangement gave lactol **69** [121], installing the C13–C14 (*Z*)-trisubstituted olefin. A further five steps

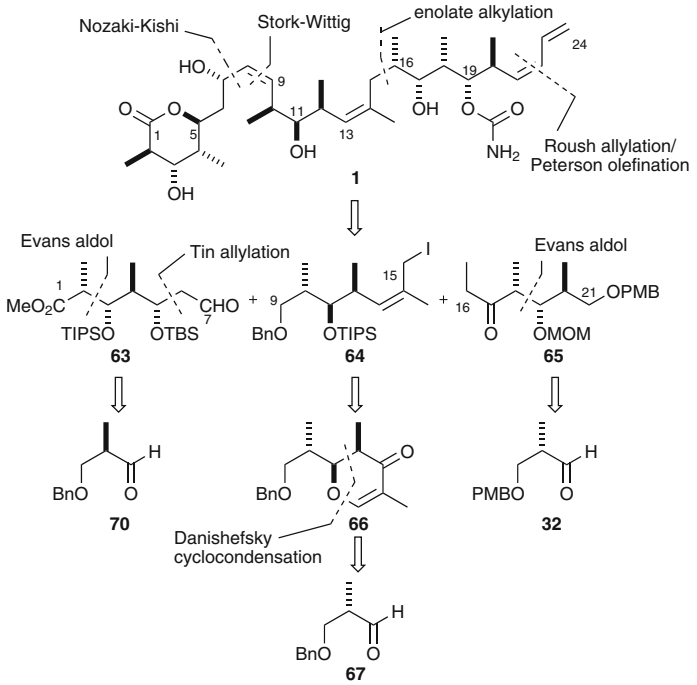

Scheme 15 Myles' synthetic strategy

were then required to access **64**, involving the reductive opening of **69** followed by a series of protecting and functional group manipulations. The C16–C21 subunit **65** was conveniently accessed from the Smith common precursor **33**. Myles' improved synthesis of the C1–C7 subunit **63** began with the tin-mediated allylation [122–124] of **70** under chelation control (>20:1dr), which after silyl protection and debenzylation provided **71**. The C2 and C3 stereocentres were configured via an Evans aldol reaction [108–111] and the resulting adduct was converted into **63** over four steps.

As shown in Scheme17, Myles' fragment assembly began with the demanding enolate alkylation of ketone **65** with iodide **64** to form the C15–C16 bond, a tactic previously explored by both Schreiber and Heathcock with little success [44, 71]. The combination of MOM protection at C19 in **65** and lithium amide base in a mixed hexanes/THF solvent system proved essential to the success of this alkylation (6:1dr at C16) [51, 52]. A chelation directed reduction of **72** afforded 8:1 selectivity at C17, which after a series of protecting group manipulations provided **73**. A Stork-Wittig olefination (*Z:E* = 20:1) [104] and elaboration into aldehyde **74** was followed by the introduction of the terminal (*Z*)-diene unit via addition of allylboronate **75** and Peterson-type elimination of the resulting 1,2-*anti* hydroxy-silane to give **76** (*Z:E* ≥ 20:1) [125, 126]. Following formation of carbamate **77**, the stage was set for

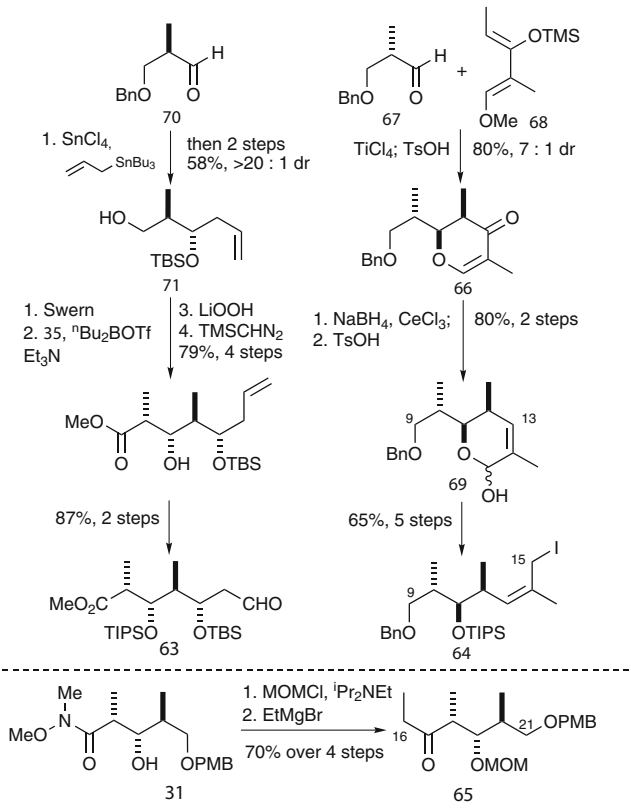

Scheme 16 Myles' synthesis of C1–C7, C9–C15 and C16–C21 subunits

the Nozaki-Kishi coupling with **63**. In Myles' initial synthesis of *ent*-**1** employing 1mol% $NiCl_2/CrCl_2$ in DMSO, this coupling gave low yields and selectivity at C7 (20–40%, 2.5:1dr). However, employing Kishi's chiral bispyridinyl ligand with 20mol% $NiCl_2/CrCl_2$ in THF provided adduct **78** in more reliable, albeit moderate, yields with slightly improved selectivity at C7 (3:1dr) [127]. Finally, global deprotection with concomitant δ-lactonization gave discodermolide in 1.1% overall yield over 22 steps in the longest linear sequence from **67**. The Myles synthesis, akin to the Schreiber approach, highlighted the limited utility of the Nozaki-Kishi bond disconnection at C7–C8 in terms of both yield and control over the C7 stereocentre.

2.4 Marshall Total Synthesis

In 1998, Marshall and co-workers demonstrated the utility of allenyl metal addition methodology for the synthesis of the polypropionate subunits contained in discodermolide [53, 54]. As outlined in Scheme 18, Marshall divided the carbon backbone

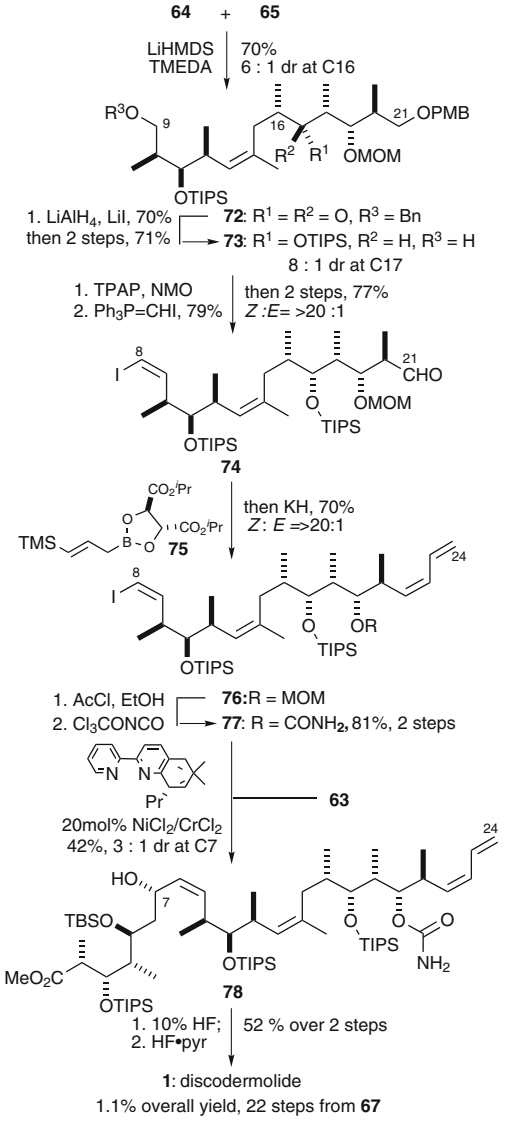

Scheme 17 Myles' subunit assembly and completion of discodermolide

of **1** into three segments **79** (C1–C7), **80** (C8–C13) and **81** (C15–C24), reliant on lithium acetylide addition to an aldehyde at C7–C8 and Suzuki cross-coupling at C14–C15 [116]. This latter bond construction appears to have significant advantages over Smith's Negishi-type coupling due to its greater robustness and scalability, and was subsequently adopted by Novartis in their process development scale-up effort (see Sect. 2.8) [65–69].

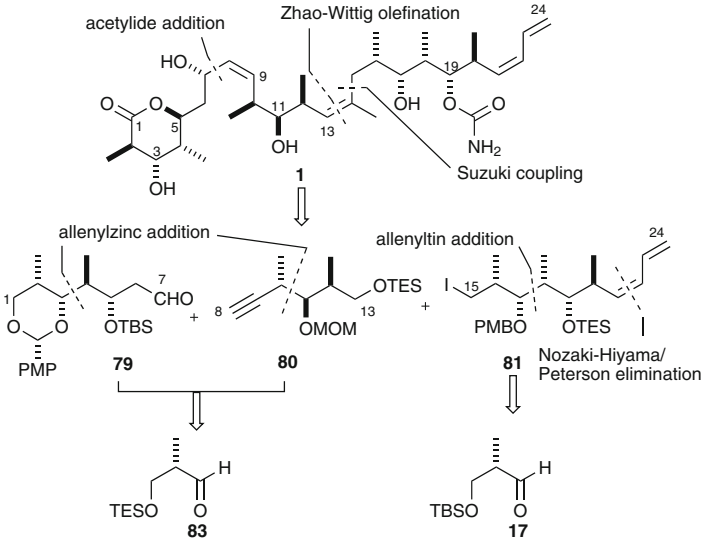

Scheme 18 Marshall's synthetic strategy

The synthesis of the C1–C7 and C8–C13 subunits **79** and **80** began with the addition of the chiral allenylzinc species, generated in situ from the treatment of propargylic mesylate **82** with Et_2Zn/catalytic Pd(0), to aldehyde **83** (Scheme19) [53, 54]. Completion of the C1–C7 subunit **79** required ten further steps in which **84** was converted into propargylic alcohol **85** and subsequently underwent alkyne reduction, Sharpless epoxidation and directed hydride opening of the resulting epoxide to introduce the C5-OH stereocentrem [54]. Stereoselective addition of the lithium anion of **80–79** (6:1dr at C7), followed by a Lindlar hydrogenation and protecting group adjustments gave **86**. Oxidation and a Zhao-Wittig olefination provided the C1–C14 intermediate **87** in moderate yields with variable *Z:E* ratios ranging from 1.3 to 9:1.

In the synthesis of the C15–C24 subunit **81**, Marshall utilized the Lewis-acid promoted addition of the allenylstannane **88** to aldehyde **17** to configure the *syn* stereotriad in **89** (Scheme 20) [128, 129]. A five-step sequence was then required to configure the C19–C20 stereocentres, involving hydroalumination, Sharpless epoxidation and epoxide opening with lithium dimethylcyanocuprate. Conversion of **90** into aldehyde **91** was followed by (*Z*)-diene installation using the Paterson and Schlapbach protocol [75], involving sequential Nozaki-Hiyama addition of allylbromosilane **92** and Peterson-type elimination. Following manipulation of the C15-terminus, iodide **81** was transformed into the intermediate C15–C24 boronate **93** for the Suzuki cross-coupling reaction with **87**, thus assembling the C1–C24 intermediate **94**. A further nine steps involving a series of protecting group manipu-

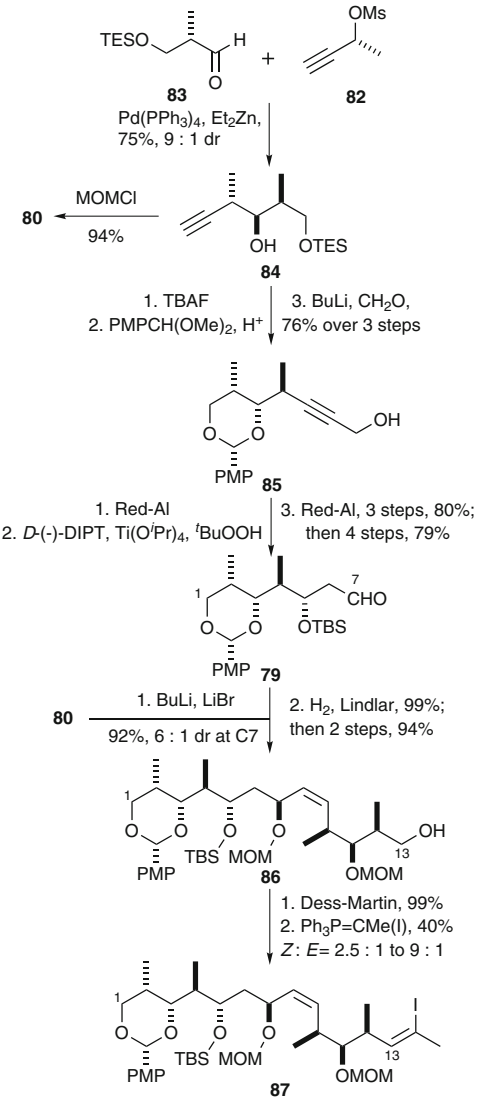

Scheme 19 Marshall's synthesis of the C1–C14 intermediate

lations and oxidation state adjustments then completed Marshall's synthesis of discodermolide in 2.2% overall yield over 29 steps (longest linear sequence).

The Marshall synthesis clearly demonstrated both the versatility of allenyl metal methodology for the preparation of polypropionate arrays and the utility of the Suzuki cross-coupling in complex fragment assembly.

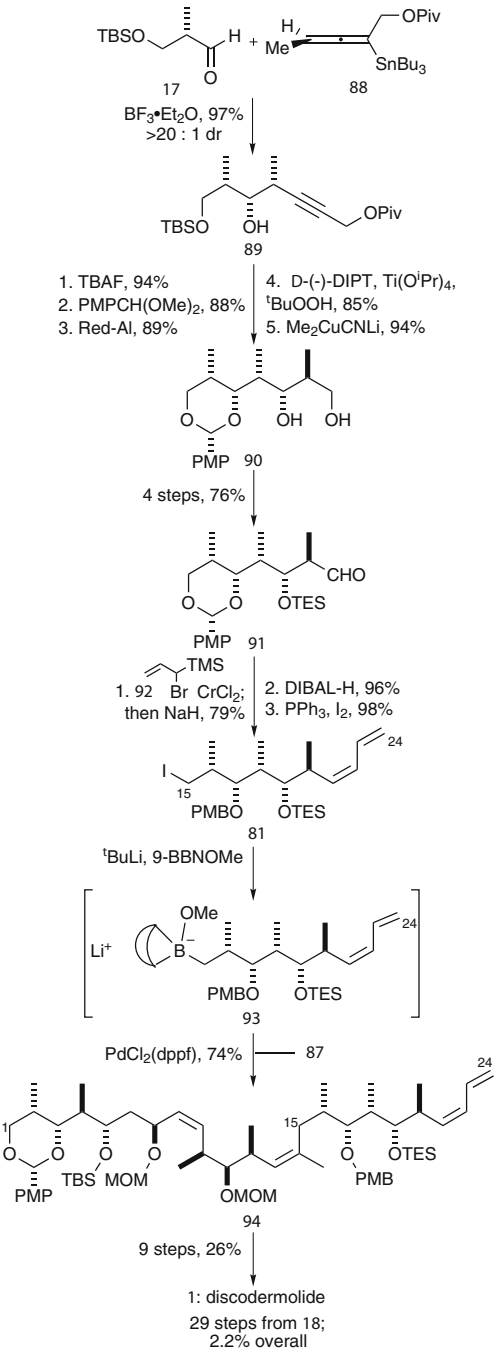

Scheme 20 Marshall's synthesis of the C15–C24 subunit and completion of discodermolide

2.5 *Paterson Total Synthesis*

2.5.1 First Generation (2000)

In 2000, Paterson and co-workers reported their first-generation synthesis of discodermolide [55–57]. As shown in Scheme 21, their novel construction of the carbon skeleton of discodermolide relied on an ambitious boron aldol coupling reaction at C6–C7 between methyl ketone **95** and the advanced (*Z*)-enal **96**, and an equally challenging lithium-mediated aldol reaction at C16–C17 between aryl ester **97** and aldehyde **98**, thus installing three new stereogenic centres in the fragment union steps. In turn, the *anti* aldol reactions of the respective chiral ethyl ketones **100–102** were used to configure the stereochemical motifs in the three subunits **95** (C1–C6) [130], **97** (C9–C16) [131] and **98** (C17–C24) [131–138] (see [139] for a review). In addressing the installation of the trisubstituted (*Z*)-alkene in **97**, the application of Holmes' Claisen rearrangement methodology provided a further novel solution [140–144], which also introduced the correct oxidation state for the planned C16–C17 aldol coupling.

As outlined in Scheme 22, the synthesis of the C1–C6 subunit **95** commenced with the *anti* aldol reaction of the ethyl ketone **100**, prepared in three steps from Roche ester **18**, and acetaldehyde, with in situ reduction to give diol **103** (>30:1dr) [130, 132–136, 145, 146]. Completion of **103** then required a series of protecting group manipulations

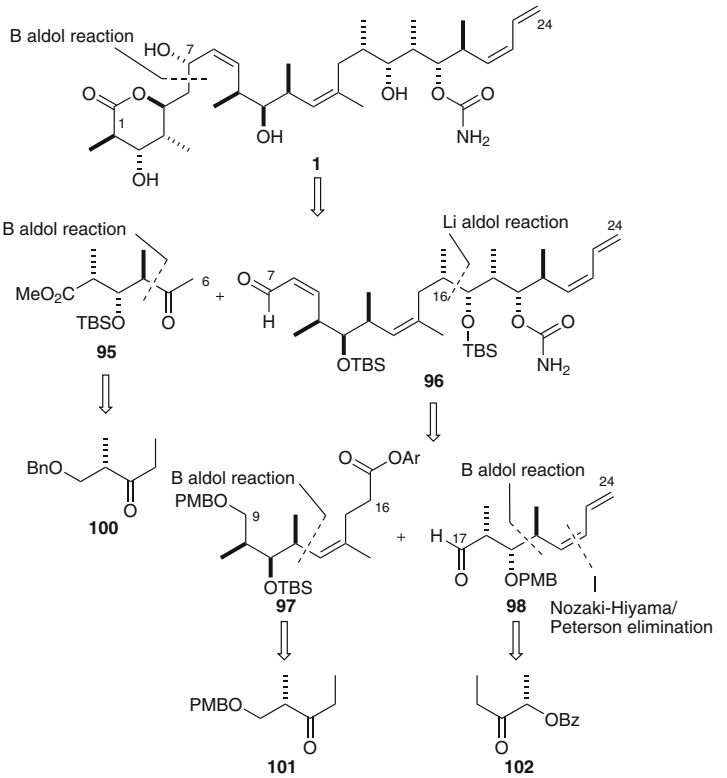

Scheme 21 Paterson's first-generation strategy

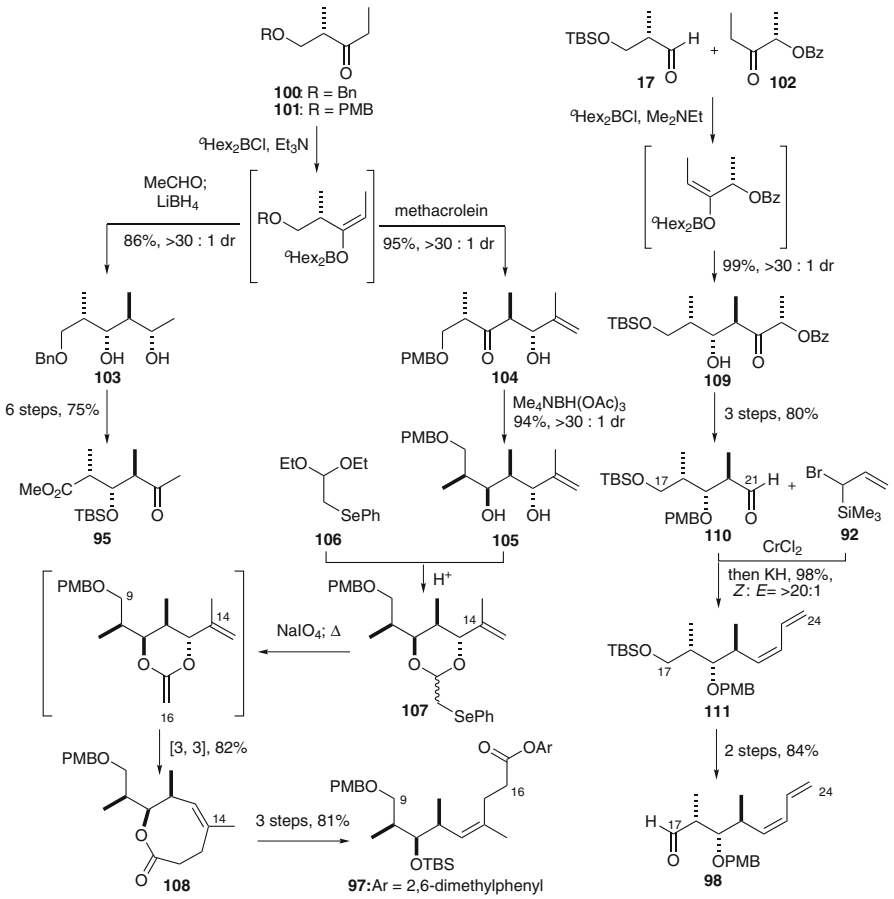

Scheme 22 Paterson's synthesis of the C1–C6, C9–C16 and C17–C24 subunits

and oxidation state adjustments. The synthesis of the C9–C16 aryl ester **97** began with the *anti* aldol reaction of ethyl ketone **101** and methacrolein to provide **104** (>30:1dr) [130, 132–136]. A 1,3-*anti* reduction provided diol **105** (>30:1dr) [114], which then underwent transacetalisation with **106**. Following the Holmes protocol [140–144], oxidation of **107** followed by thermal selenoxide elimination gave the transient ketene acetal which underwent Claisen [6, 6] rearrangement to afford the 8-membered lactone **108**, introducing the trisubstituted C13–C14 (*Z*)-alkene cleanly. Opening of **108**, esterification and TBS protection then completed **97**. The synthesis of the C17–C24 aldehyde **98** began with an *anti* aldol reaction between the lactate-derived ketone **102** and the aldehyde **17** to provide **109** (>30:1dr) [131, 137, 138]. Transformation to aldehyde **110** was followed by the Paterson and Schlapbach diene installation, involving sequential Nozaki-Hiyama allylation with bromide **92** and Peterson elimination [75]. Conversion of **111** into aldehyde **98** then paved the way for the first of the key fragment unions.

As shown in Scheme 23, the lithium-mediated *anti* aldol reaction of the aryl ester **97** and aldehyde **98** gave the expected Felkin-Anh adduct **112** (30:1dr) [147, 148].

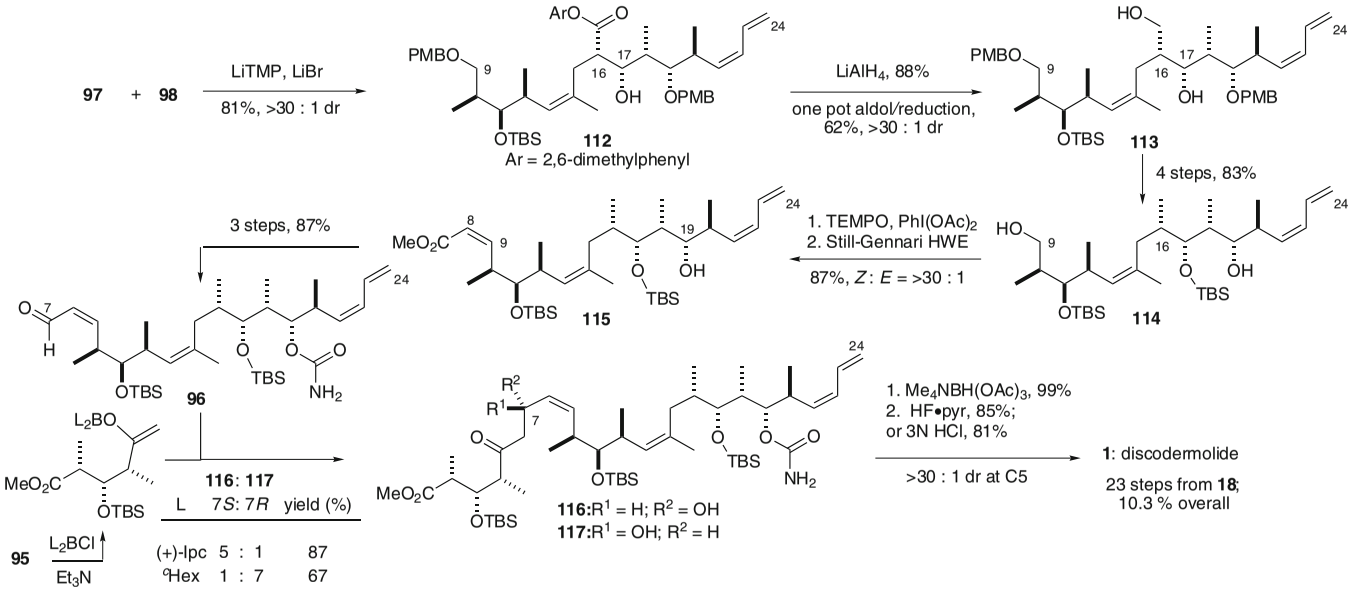

Scheme 23 Paterson's subunit assembly and completion of discodermolide

Following ester reduction, either in situ or upon isolation of **112**, the superfluous oxygen functionality at C16 in diol **113** was removed and converted into intermediate **114** in four steps. Selective primary oxidation with TEMPO [149], followed by a Still-Gennari HWE olefination [106] installed the C8–C9 (*Z*)-olefin in **115** (*Z:E* => 30:1). Transformation into enal **96** required three further steps, prior to the final C6–C7 aldol coupling. Considerable effort was required to secure the desired adduct **116** bearing the correct C7 configuration [56, 57]. Using the achiral boron reagent *c*Hex$_2$BCl for enolization of **95** gave the undesired (7*R*)-adduct **117** (7:1dr). This unprecedented selectivity arose from high levels of remote 1,4-stereoinduction imparted by the aldehyde component. In order to overturn the π-facial bias of aldehyde **96**, the chiral (+)-Ipc$_2$BCl reagent was employed and the desired (7*S*)-adduct **116** was now obtained with 5:1 dr (see [139] for a review) [150–152]. An Evans 1,3-*anti* reduction of **116** introduced the final stereogenic centre at C5 (>30:1dr) [114], which following acid-mediated desilylation and δ-lactonization gave discodermolide, completing the Paterson group's first-generation synthesis in 10.3% yield over 23 steps (longest linear sequence).

The Paterson first-generation synthesis of discodermolide provides a clear demonstration of the utility of complex boron aldol reactions in the context of polyketide natural product synthesis. Recently, Paton and Goodman reported theoretical DFT studies of related boron aldol transition states to rationalise the very high degrees of stereoselectivity obtained in these powerful reactions [153]. In contrast to previous syntheses, essentially complete control was now achieved over the double bond geometries and the only step proceeding with less than optimal stereocontrol was the final mismatched aldol coupling. However, it is notable that the Novartis process group chose to adopt the key C6–C7 aldol disconnection in their large-scale synthesis of discodermolide for clinical trials (see Sect. 2.8).

2.5.2 Second Generation (2003)

In 2003, Paterson and co-workers reported a second-generation strategy for the synthesis of discodermolide, which aimed to eliminate the use of all chiral reagents and auxiliaries, and reduce the total number of synthetic steps (Scheme 24) [58, 59]. These specific aims were achieved by employing an unprecedented aldol coupling at C5–C6 between C1–C5 aldehyde **118** and the advanced C6–C24 methyl ketone **119** and utilising diol **120** as a common precursor for the synthesis of the three subunits **118**, **121** (C9–C16) and **98** (C17–C24).

The common precursor **120** was prepared in two steps from ethyl ketone **101** on a multigram scale (Scheme 25), where the 1,3-*anti* methyl groups were configured by a boron aldol reaction with formaldehyde (20:1dr) [130, 132–136]. Aldol adduct **122** then underwent a hydroxyl-directed reduction to provide diol **120** (10:1dr). The C1–C5 subunit **118** was prepared in six steps from diol **120**, starting with the selective TEMPO oxidation of the C1-OH to give aldehyde **123**, and five further steps involving oxidation state adjustments and protecting group manipulations followed. Aldehyde **123** was also used in the five-step preparation of the C9–C16 subunit **121**.

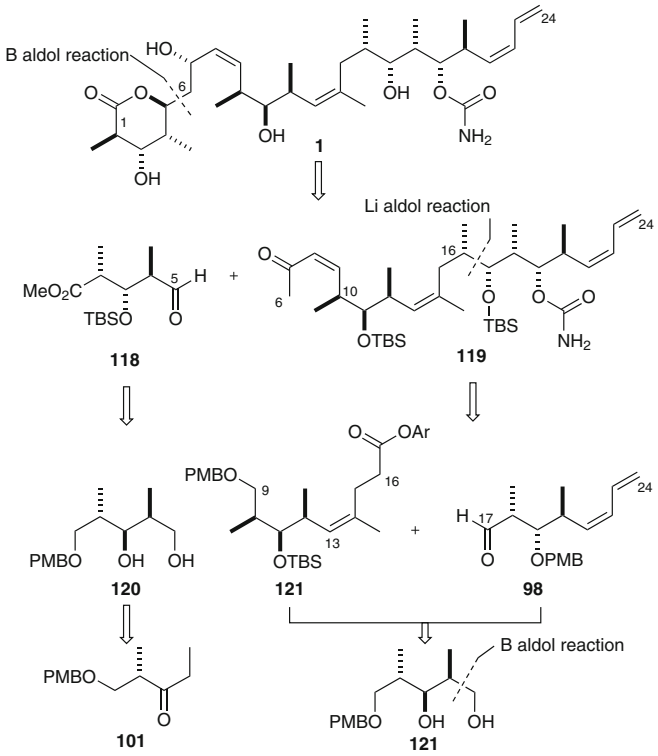

Scheme 24 Paterson's second-generation strategy

The trisubstituted (*Z*)-olefin was introduced by Still-Gennari HWE olefination, as precedented by Schreiber [43, 44, 106], and following silyl protection provided **124**. Conversion into the iodide **125** was followed by alkylation with the lithium enolate of aryl ester **126**, to complete the C9–C16 subunit **121**. The synthesis of the C17–C24 subunit **98** from **120** began with a four-step sequence involving protecting group manipulations and oxidation at C21 to provide aldehyde **127**, converging with the earlier route to **98** [55–57].

As outlined in Scheme **26**, assembly of the subunits began with the lithium-mediated aldol coupling of **121** and **98** to provide **129** (6:1dr) [147, 148]. which was converted into the diol **114**, following the first-generation route [55–57]. Primary oxidation of **114** and modified Still-Gennari olefination introduced the (*Z*)-enone moiety in **119** (*Z:E* = 12:1) [106, 154]. The boron aldol reaction of methyl ketone **119** and aldehyde **118** gave the desired (5*S*)-adduct **130** with 20:1dr, arising from long-range 1,6-asymmetric induction from the remote C10 γ-stereocentre in the ketone component. Acid-promoted δ-lactonisation of **130**, K-Selectride reduction of the C7 ketone (>30:1dr) [46–48] and global deprotection then completed the second-generation synthesis of discodermolide in 5.1% overall yield, with 24 steps in the longest linear sequence.

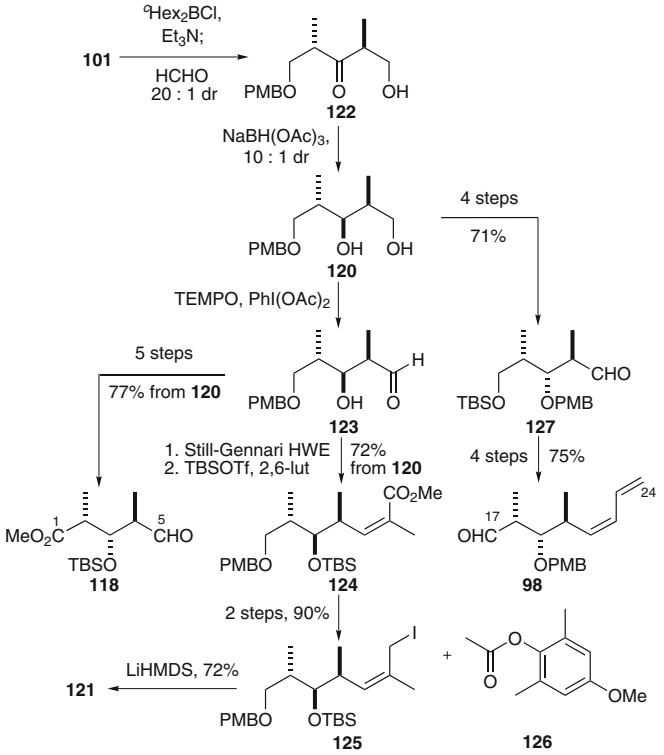

Scheme 25 Paterson's synthesis of C1–C5, C9–C16 and C17–C24 subunits from common precursor diol

The Paterson second-generation approach substantially reduced the total number of steps required to complete discodermolide. Notably, the use of chiral reagents and auxiliaries was completely eliminated, relying solely on substrate control to configure all the remaining stereocentres from the ubiquitous Roche ester (**18**), achieving a more cost-effective route.

2.5.3 Third Generation (2004)

In 2004, the Paterson group implemented a further revision to their strategy designed to overcome the perceived technical difficulties of performing late-stage boron aldol couplings on an industrial scale (Scheme 27) [60, 61]. Building on the experience already gained and their contemporary synthesis of dictyostatin (**2**), a third-generation approach to discodermolide involved the application of a Still-Gennari-type HWE olefination in the final fragment coupling step using the highly functionalized C1–C8 β-ketophosphonate **131** and the C9–C24 aldehyde **132**.

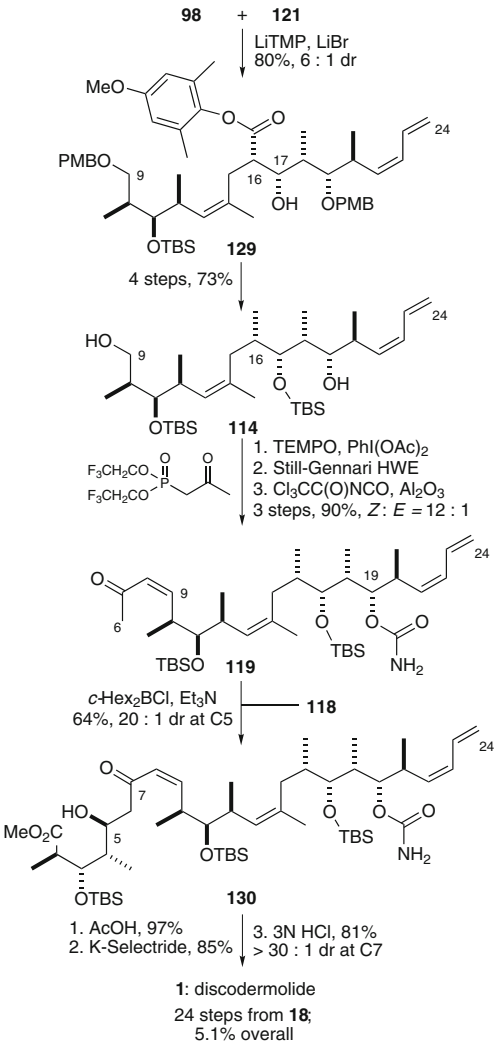

Scheme 26 Paterson's second generation subunit assembly and completion of discodermolide

As outlined in Scheme 28, the synthesis of the β-ketophosphonate **131** began with a one-pot *anti*-aldol/reduction step between ethyl ketone **101** and aldehyde **133**, giving the 1,3-syn diol **134** (>30:1dr) [130, 132–136, 145, 146]. The diol **134** was then converted into the carboxylic acid **135** in six steps. Completion of the subunit **131** required conversion into the acid chloride and reaction with the lithium anion of methyl-(di-1,1,1-trifluoroethyl)-phosphonate. The C9–C24 aldehyde **132** was prepared in two steps from **136**, an intermediate from previous routes [55–58]. The Still-Gennari-type coupling of **131** and **132** was readily achieved via treatment with

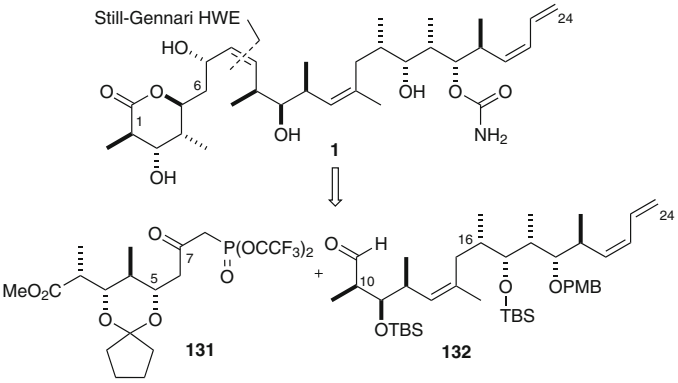

Scheme 27 Paterson's third-generation strategy

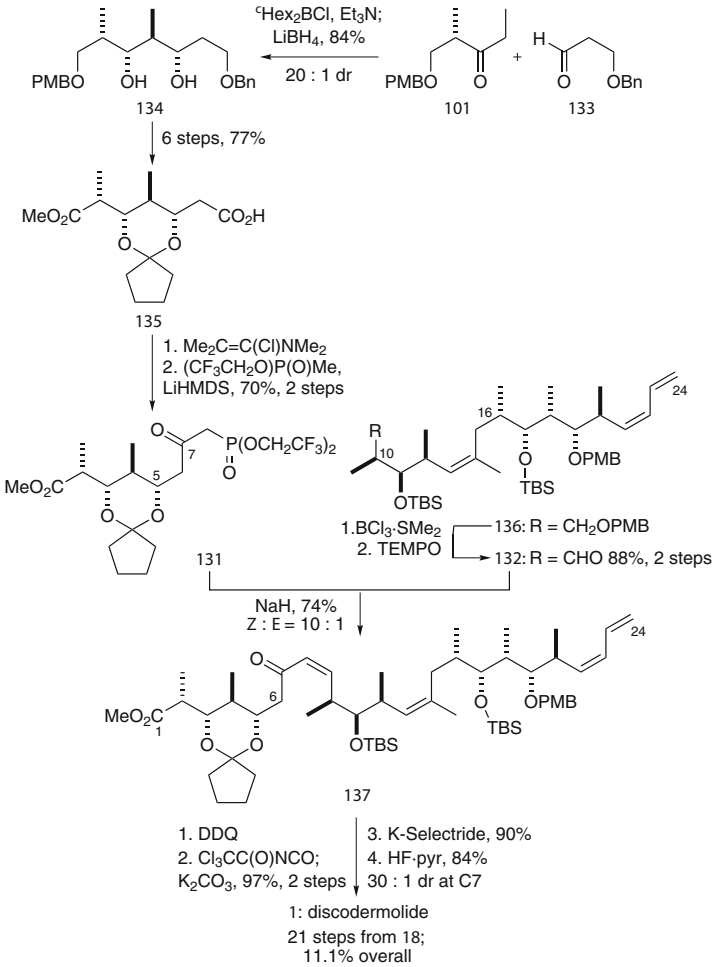

Scheme 28 Paterson's synthesis of C1–C8 phosphonate and completion of third-generation synthesis

NaH to give the advanced enone **137** (*Z:E* = 10:1). A further four steps were then required to complete the third-generation synthesis, beginning with C19 carbamate installation, followed by K-Selectride reduction to introduce the requisite (*7S*)-stereocentre. Finally, global deprotection with concomitant δ-lactonisation gave discodermolide (**1**) in 11.1% overall yield over 21 steps (longest linear sequence).

In summary, the Paterson group's third-generation synthesis demonstrated the versatility of the Still-Gennari HWE coupling of advanced polypropionate subunits. This revised endgame gave improved levels of efficiency and, importantly, the overall linear sequence was shortened with increased yields. The experimentally undemanding conditions of the Still-Gennari-type HWE coupling protocol offers distinct advantages over previous routes using boron aldol reactions, offering a viable alternative for industrial scale-up.

2.6 Panek Total Synthesis

Panek and co-workers reported their synthesis of discodermolide in 2005 [62, 63], relying on the application of their crotylsilane methodology for the synthesis of polypropionate motifs [155, 156] (see [157] for a review) [158, 159, 182]. Their strategy involved key bond disconnections at C6–C7 and C14–C15, based on an aldol coupling and the established Suzuki cross-coupling respectively, employing the key subunits **137** (C1–C6), **138** (C7–C14) and **81** (C15–C24) (Scheme 29).

As outlined in Scheme 30, the synthesis of the C1–C6 subunit **137** began with the crotylation of aldehyde **139** with the (*S*)-allylsilane **140**, which following silyl depro-

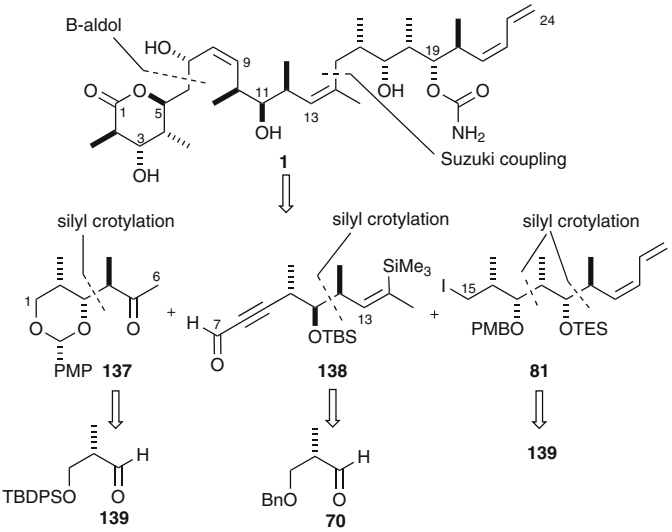

Scheme 29 Panek's synthetic strategy

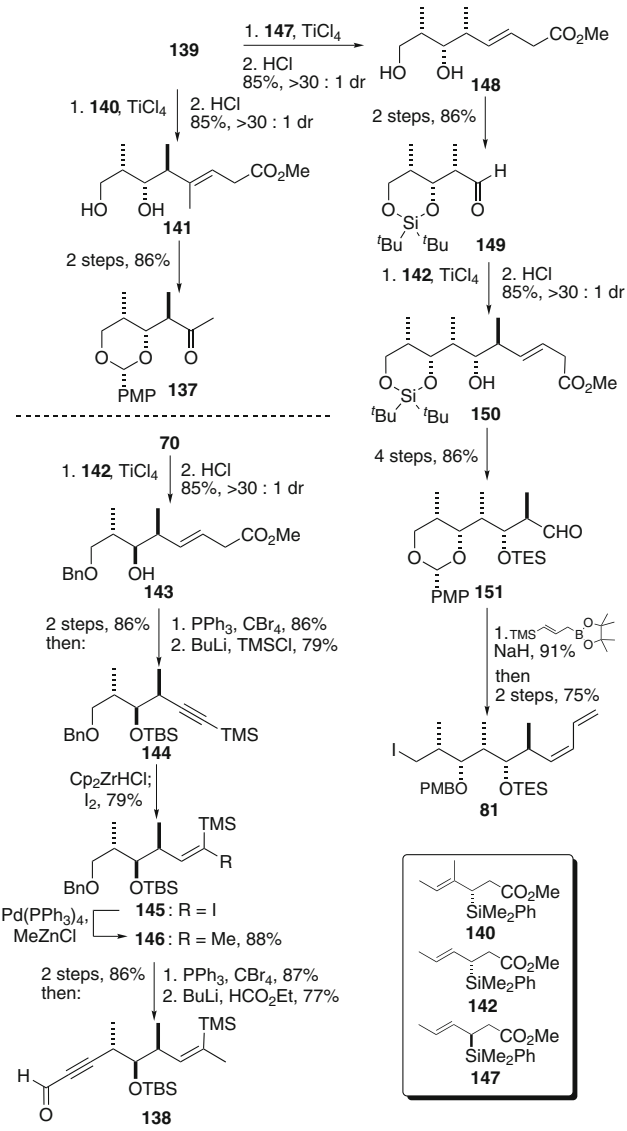

Scheme 30 Panek's synthesis of C1–C6, C7–C14 and C15–C24 subunits

tection gave diol **141** (dr > 30:1) [81, 168, 170, 171] (see [157] for a review). Subsequent anisylidene acetal formation and ozonolysis completed **137**. The (*S*)-crotylsilane **142** was used as the starting point for the synthesis of the C7–C14 subunit with its addition to aldehyde **70**. A four-step sequence on **143** was then used to access the silylacetylene **144**, which upon treatment with Schwartz's reagent [160, 161] and quenching with iodine gave (*Z*)-iodovinylsilane **145**. A palladium-mediated

coupling of **145** with methylzinc chloride gave the (*Z*)-vinylsilane **146** exclusively, providing a further solution for the installation of the C13–C14 trisubstituted olefin. The subunit **138** was then completed by the Corey-Fuchs olefination at C9, treatment of the intermediate vinyl dibromide with BuLi and quenching with ethyl formate. The synthesis of the C17–C24 subunit **81** started with the crotylation of aldehyde **139** with (*R*)-crotylsilane **147** to configure the all-*syn* stereotriad in **148**. Conversion into the aldehyde **149** was followed by a second crotylation, now with (*S*)-crotylsilane **142**, to configure the C19–C20 stereocentres in **150**, which was then transformed into the aldehyde **151** in four steps. Treatment of **151** with a Roush-type allylboronate reagent and subsequent Peterson elimination selectively introduced the terminal (*Z*)-diene [51, 52, 125], which was readily transformed into iodide **81**.

As outlined in Scheme 31, Panek's assembly of subunits began with the boron-mediated aldol reaction of ketone **137** and aldehyde **138**, which gave the expected 1,4-*syn*-1,5-*anti* aldol product **152** [162, 163]. An Evans-Tischenko reduction efficiently introduced the C5-stereocentre in **153** [164]. Methanolysis, acid-mediated migration of the PMP acetal and primary oxidation with Oshima's reagent [165] gave aldehyde **154**, which was converted into **155** in three steps. Lindlar reduction of the C8–C9 alkyne, and conversion of the C14-vinyl silane into the vinyl iodide **156**, then set the stage for the C14–C15 bond formation. The success of both Suzuki- and Negishi-type couplings required exchange of the protecting group at C13 from TBS in **156** to MOM in **157**, which then underwent cross-coupling with iodide **81** to provide **158** [53, 54, 105, 116]. The completion of discodermolide from **159** then required an additional four steps. Overall, Panek's synthesis proceeded in 2.1% yield based on 27 steps (longest linear sequence).

2.7 Ardisson Total Synthesis

In 2007, Betzer, Ardisson and co-workers reported their synthesis of discodermolide [64] following the Marshall disconnection strategy of C7–C8 acetylide addition and Suzuki cross-coupling at C14–C15 (Scheme 32) [53, 54]. The synthesis of the key subunits **160** (C1–C7), **161** (C8–C14) and **162** (C15–C24) demonstrated the versatility of the Hoppe crotyltitanation reaction [166–169] in the synthesis of polypropionate motifs, using the incorporated (*Z*)-*O*-enecarbamate to configure the requisite alkene substitution patterns [170, 171].

As shown in Scheme 33, the synthesis of the C1–C7 amide **160** began with a Hoppe crotyltitanation reaction between the aldehyde **17** and the (*R*)-crotyltitanium **163**, prepared in situ (crotyl diisopropylcarbamate with *s*BuLi/(−)-sparteine/$Ti(OiPr)_4$), to give *O*-enecarbamate **164** (>30:1dr) [166–169]. Ozonolysis and HWE chain extension was followed by an Evans-Prunet 1,4-addition to install the C5-stereocentre to complete **160** [103]. The synthesis of the C8–C14 subunit **161** started with an elegant installation of the C13–C14 (*Z*)-olefin. Deprotonation of the dihydrofuran **165**, available in three steps from bromo alcohol **166**, with *t*BuLi and transmetallation with $Me_2CuLi{\cdot}LiCN$, and subsequent 1, 2-cuprate transfer gave the

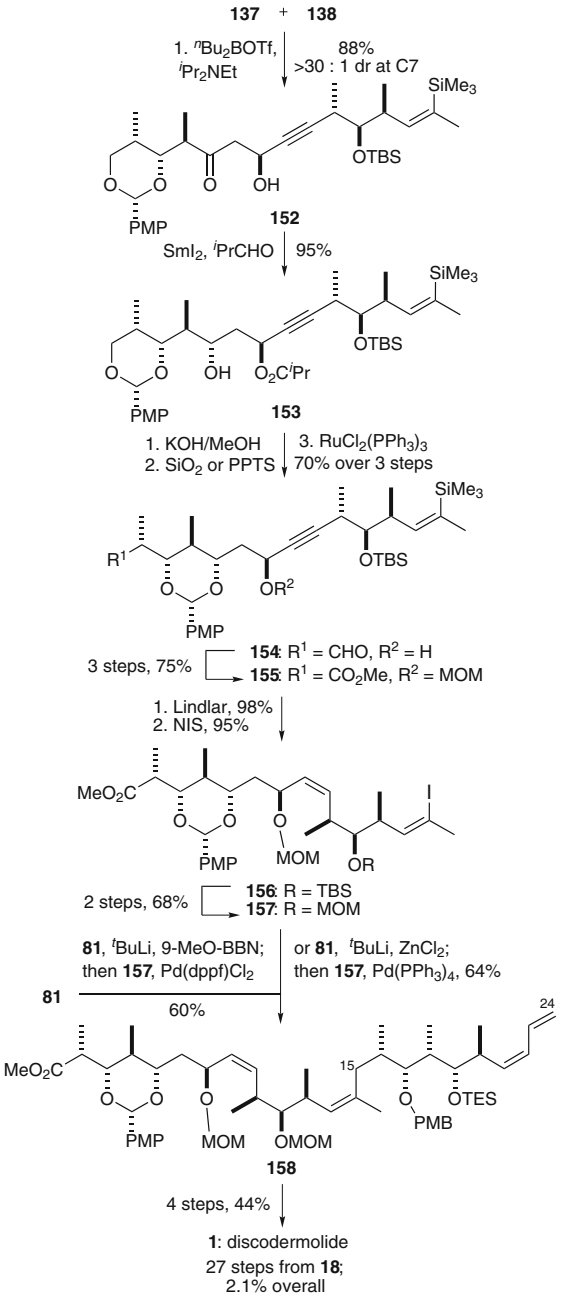

Scheme 31 Panek's subunit assembly and completion of discodermolide

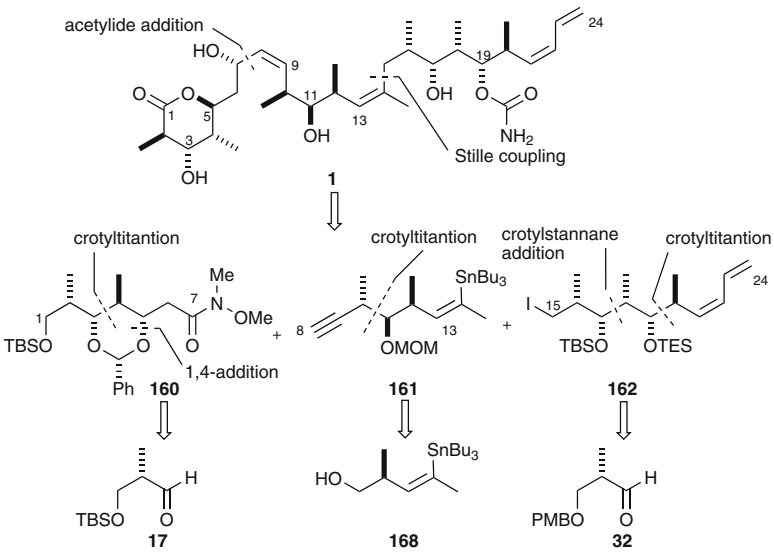

Scheme 32 Ardisson's synthetic strategy

intermediate **167**, which was trapped with tributyltin chloride to provide the (*Z*)-vinyl stannane **168** exclusively [172–175]. Oxidation of **168** was followed by a second Hoppe reaction with **163** to give the intermediate (*Z*)-*O*-enecarbamate, which underwent Fritsch-Buttenberg-Wiechell rearrangement to give, after MOM protection, alkyne **161** (see [176] for review) [177]. The synthesis of the C15–C24 subunit **162** commenced with the diastereoselective crotylation of aldehyde **32** with (*E*)-crotylstannane to give **169**. Conversion into aldehyde **170** was followed by a third crotylatitanation reaction with **163** (>30:1dr). A four-step sequence was then required to complete **162**, in which the terminal (*Z*)-diene was installed via a nickel-catalysed cross coupling of the C22-carbamate with vinylmagnesium bromide.

The assembly of the subunits began with the addition of the lithium anion of acetylene **161** to Weinreb amide **160**, followed by CBS reduction to give **171** installing the C7 stereocentre with > 20:1dr (Scheme 34) [178]. Following elaboration to vinyl iodide **157**, an intermediate shared with the Panek route [62, 63], Suzuki cross-coupling with the boronate derived from iodide **162** gave the advanced C1–C24 intermediate **172**, which following a three-step sequence provided discodermolide in 1.6% yield over 21 steps (longest linear sequence).

2.8 Novartis Process Chemistry Group Synthesis

Early preclinical development of discodermolide had shown its clear potential as a new generation anticancer agent for the treatment of a range of multidrug-resistant human cancers. This attracted the attention of Novartis Pharma AG, who with a

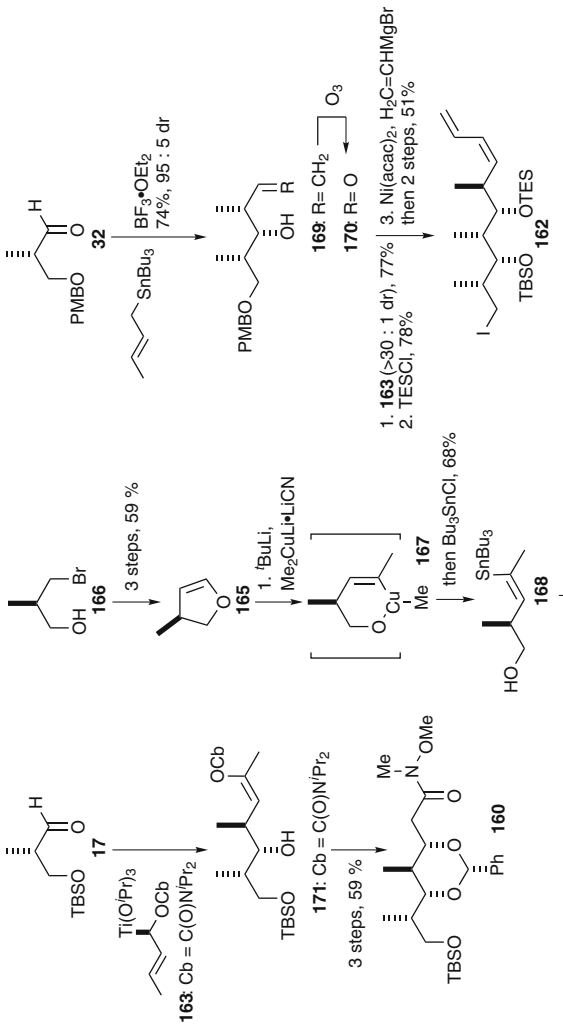

Scheme 33 Ardisson's synthesis of C1–C7, C8–C14 and C15–C24 subunits

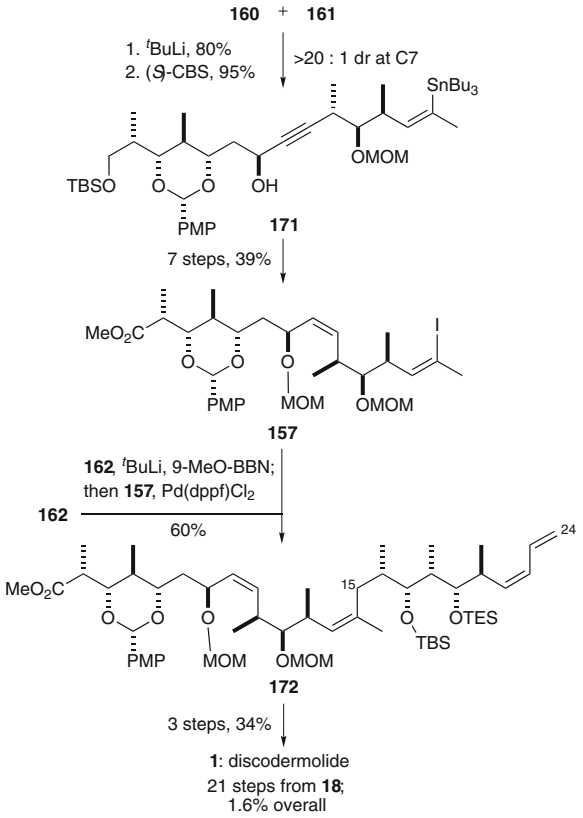

Scheme 34 Ardisson's subunit assembly and completion of discodermolide

license agreement from the Harbor Branch Oceanographic Institution, took on the task of progressing discodermolide into clinical trials. This required a practical synthetic solution [65–69, 90, 92, 95], as eco-harvesting the rare natural source was clearly not an option, either economically or ecologically. Rising to this challenge, the Novartis Process Chemistry group in Basel led by Mickel reported in 2004 the synthesis of 64 g of discodermolide.[65–69]. Following careful consideration of the successful approaches to discodermolide at the time, Mickel and co-workers adopted a hybrid synthesis incorporating features of the Smith [45, 46] and Paterson [55–57] routes (Sects. 2.2 and 2.5, respectively), providing valuable insights into the complexities of performing a multistep "academic" synthesis in an industrial setting. As outlined in Scheme 35, the Novartis strategy opted for Paterson's aldol disconnection at C6–C7 and the Smith/Marshall cross-coupling at C14–C15. In turn, the three key subunits **173** (C1–C6), **29** (C9–C14) and **30** (C15–C24) would be accessed on a kilogram-scale from Smith's common precursor **31** [46–48].

As shown in Scheme 36, the Novartis group's large-scale (20–25kg) preparation of Smith's common precursor **31** began with the established Evans aldol reaction between the Roche ester-derived aldehyde **32** and the propionimide **33** [65].

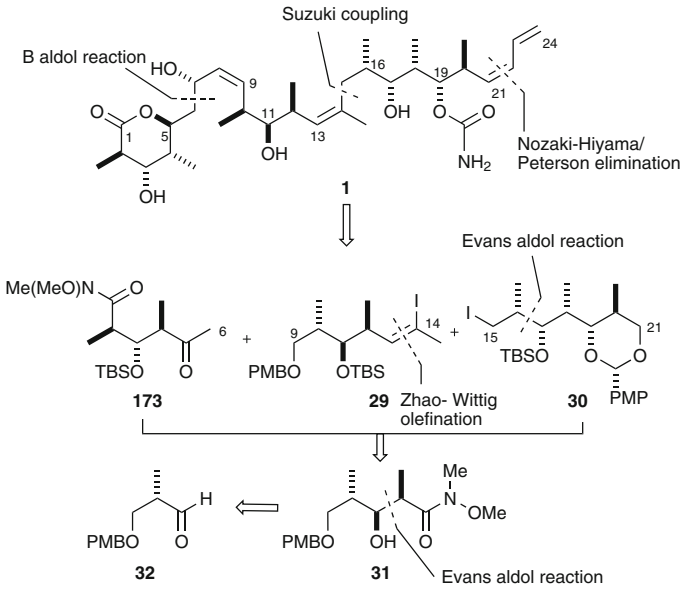

Scheme 35 Novartis synthetic strategy

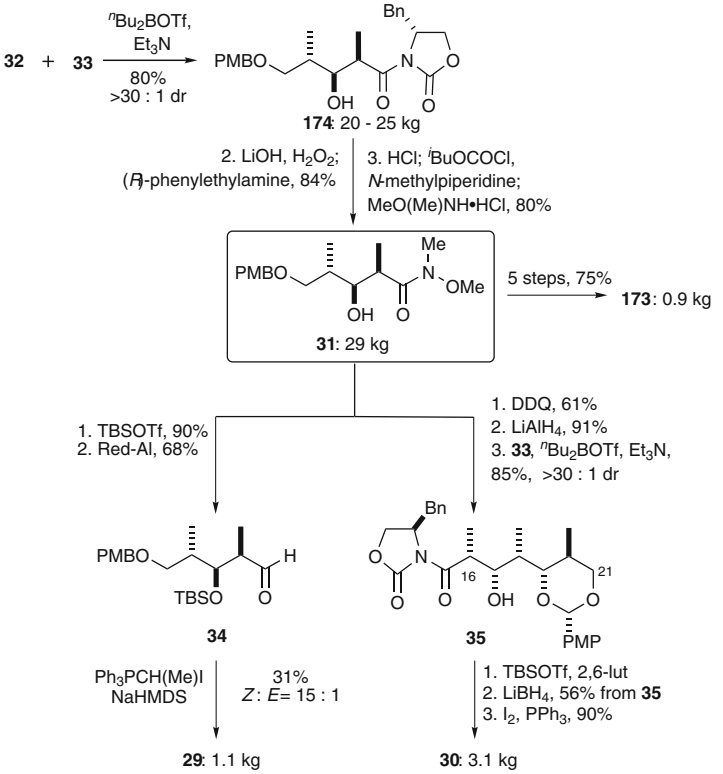

Scheme 36 Novartis large-scale synthesis of C1–C6, C9–C14 and C15–C21 subunits

Transformation of **174** into the common precursor **31** could not be achieved directly due to safety considerations regarding the use of Me_3Al on pilot plant scale. Thus, hydrolysis of **174** and isolation of the intermediate acid salt, was followed by the formation of a mixed anhydride and subsequent amide formation to provide 29kg of **31** [179, 180]. Having achieved access to the common precursor, the synthesis of the C1–C6 subunit **142** was completed in five steps in 66% yield on scales of several kilograms, only requiring chromatographic purification at the final stage [66]. The synthesis of the C9–C14 subunit **31** essentially followed an analogous route to Smith [46–48, 66]. Following TBS protection of **31**, Red-Al was used in preference to DIBAL-H for the reduction to aldehyde **34**. At this stage, introduction of the C13–C14 (*Z*)-vinyl iodide was required and, as expected from the work of Smith and Marshall, the Zhao-Wittig olefination gave only moderate yields of **29**, limiting the scale of the reaction to a maximum of 2.5 kg substrate. The synthesis of the C15–C21 subunit **30** followed the Smith route [46–48, 67], beginning with the conversion of **31** into the intermediate aldehyde for the Evans aldol reaction with **33**. In order to minimise the formation of by-products in this reaction, it was necessary to maintain the reaction below –10°C at all times and required a "rapid workup and isolation" to prevent epimerization at C16 which was readily observed at ambient temperatures [67]. The problems associated with epimerisation were negated by the subsequent silyl protection of **35**. However, the reductive removal of the auxiliary with $LiBH_4$ led to the formation of numerous by-products requiring careful chromatographic purification of ca. 1-kg batches of crude material, prior to the formation of iodide **30**.

As outlined in Scheme 37, the Novartis assembly of discodermolide began with the Marshall Suzuki-type cross-coupling of vinyl iodide **29** and iodide **30** to give **36** on a kilogram scale [68]. At this point, the crossover of routes required the introduction of the terminal (*Z*)-diene to give the Paterson intermediate **175** [55–57]. Following an analogous six-step sequence to that reported by the Paterson group, 810g of the C7–C24 (*Z*)-enal **96** was prepared from **175**. Notably, this only required two chromatographic purifications – after the Still-Gennari HWE reaction to introduce the (*Z*)-olefin at C8–C9 and following the final oxidation step. With substantial quantities of **96** available, the reagent-controlled boron aldol coupling with ketone **173** posed the largest challenge of the entire scale-up campaign [55–57, 69, 181]. In order to obtain reproducible yields of the desired aldol adduct **176**, a number of limiting factors were identified, namely reagent quality and handling, work-up and isolation procedures. It was found that a commercial solution of (+)-Ipc_2BCl in hexane proved to be more reliable in terms of quality than the highly hygroscopic solid form and also conveniently negated the issue of handling the solid reagent. It was found that an oxidative work-up procedure should be avoided in favour of the direct purification of the crude product mixture by reverse phase chromatography, leading to the formation of **176** in 50–55% yield. In contrast, the introduction of the C7-stereocentre by Evans-Saksena reduction and global deprotection proved uneventful. Finally, reverse phase chromatography and crystallisation provided a 64-g batch of pure discodermolide monohydrate [69].

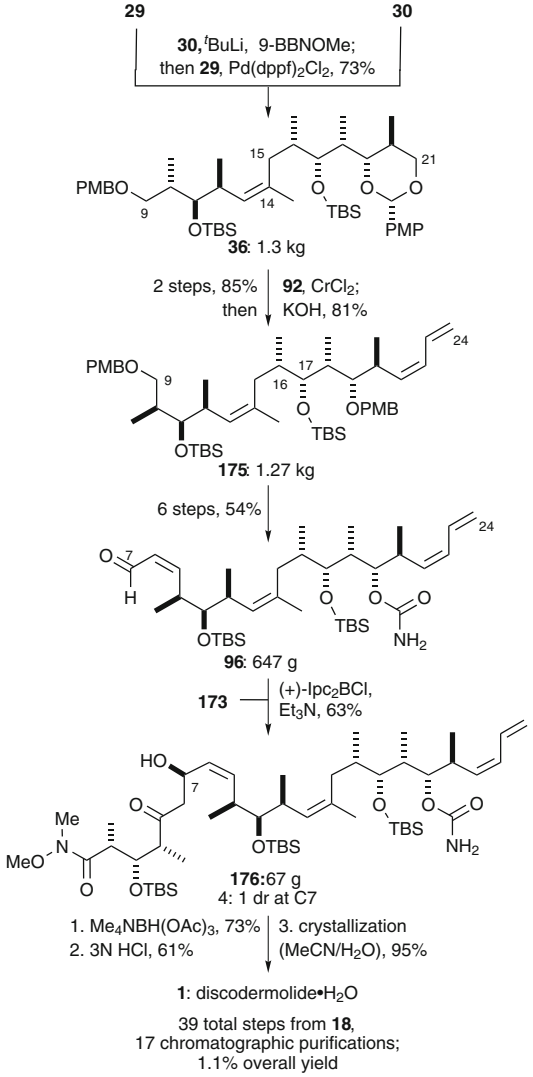

Scheme 37 Novartis fragment assembly and completion of discodermolide

The Novartis Process Chemistry group's preparation of discodermolide represents a landmark in the industrial synthesis of complex natural products and pharmaceutical development. Having taken the bold decision to pursue the clinical development of discodermolide under tight time constraints, they met the challenge of combining the approaches of Smith and Paterson and delivering sufficient quantities of active pharmaceutical ingredient to enable clinical trials.

Table1 Comparison of the completed syntheses of discodermolide (1993–2007)

Research group	Year	Linear sequence	Overall yield(%)	Substrate-controlled stereocentres[a]	Reagent-controlled stereocentres[b]	Chiral pool stereocentres[c]
Schreiber	1993	24	4.3	4	6	3
Smith I	1995	28	2.2	1	8	4
Myles[d]	1997	22	1.1	5	5	3
Marshall	1998	29	2.2	2	8	3
Smith II	1999	24	6.0	2	8	3
Paterson I	2000	23	10.3	7	3	3
Paterson II	2003	24	5.1	10	0	3
Smith III	2003	24	1.9	2	8	3
Novartis	2004	25	1.1	1	9	3
Paterson III	2004	21	11.1	10	0	3
Panek	2005	27	2.1	2	8	3
Smith IV	2005	17	9.0	2	8	3
Ardisson	2007	21	1.6	3	7	3

[a]Stereocentres configured by substrate-controlled reactions
[b]Stereocentres configured by reagent–auxiliary-controlled reactions
[c]Stereocentres accessed from chiral pool starting materials
[d]Data from Myles' full disclosure in 2003 [52]

3 Summary

The various synthetic approaches developed to date have served to eliminate the supply problem for discodermolide, enabling extensive biological evaluation and early stage clinical development of this remarkable microtubule-stabilising anticancer agent. Discodermolide has inspired many creative and elegant total syntheses based on the application of contemporary methods of substrate and reagent based stereocontrol; these approaches are summarized chronologically in Table1. Importantly, this shows that natural products with challenging molecular architectures can be accessed synthetically in an efficient and timely manner, and further underlines their resurgence as serious candidates for drug development [8]. Thanks to the power of modern organic synthesis, one can contemplate the practical synthesis of other such complex natural products where the natural supply is insufficient for detailed biological evaluation, let alone potential clinical application.

References

1. Blunt JW, Copp BR, Hu WP, Munro MHG, Northcote PT, Prinsep MR (2007) Nat Prod Rep 24:31
2. Blunt JW, Copp BR, Munro MHG, Northcote PT, Prinsep MR (2006) Nat Prod Rep 23:26
3. Blunt JW, Copp BR, Munro MHG, Northcote PT, Prinsep MR (2005) Nat Prod Rep 22:15
4. Blunt JW, Copp BR, Munro MHG, Northcote PT, Prinsep MR (2003) Nat Prod Rep 20:1
5. Koehn FE, Carter GT (2005) Nat Rev Drug Discov 4:206
6. Butler MS (2005) Nat Prod Rep 22:162

7. Newman DJ, Cragg GM (2007) J Nat Prod 70:461
8. Paterson I, Anderson EA (2005) Science 310:451
9. Hamann MT, Hill R, Roggo S (2007) Chimia 61:313
10. Paterson I, Florence GJ (2003) Eur J Org Chem 2193
11. Mickel SJ (2007) Pure Appl Chem 79:685
12. Kalesse M (2000) ChemBioChem 1:171
13. Smith AB, Freeze BP (2008) Tetrahedron 64:261
14. Paterson I, Yeung KS (2005) Chem Rev 105:4237
15. Altmann KH, Gertsch J (2007) Nat Prod Rep 24:327
16. Kuppens IELM (2006) Curr Clin Pharmacol 1:57
17. Gunasekera SP, Gunasekera M, Longley RE, Schulte GK (1990) J Org Chem 55:4912; correction (1991) J Org Chem 56:1346
18. Gunasekera SP, Paul GK, Longley RE, Isbrucker RA, Pomponi SA (2002) J Nat Prod 65:1643
19. Smith AB, LaMarche MJ, Falcone-Hindley M (2001) Org Lett 3:695
20. Longley RE, Caddigan D, Harmody D, Gunasekera M, Gunasekera SP (1991) Transplantation 52:650
21. Longley RE, Caddigan D, Harmody D, Gunasekera M, Gunasekera SP (1991) Transplantation 52:656
22. ter Haar E, Kowalski RJ, Hamel E, Lin CM, Longley RE, Gunasekera SP, Rosenkranz HS, Day BW (1996) Biochemistry 35:243
23. Horwitz SB, Cohen D, Rao S, Shen HJ, Yang CP (1993) J Natl Cancer Inst 15:55
24. Bollag DM, McQueney PA, Zhu J, Hensens O, Koupal L, Liesch J, Goetz M, Lazarides E, Woods CM (1995) Cancer Res 55:2325
25. D'Ambrosio M, Guerriero A, Pietra F (1987) Helv Chim Acta 70:2019
26. Lindel T, Jensen PR, Fencial W, Long BH, Casazza AM, Carboni J, Fairchild CR (1997) J Am Chem Soc 119:8744
27. Mooberry SL, Tien G, Hernez AH, Plubrukarn A, Davidson BS (1999) Cancer Res 59:653
28. Sato B, Nakajima H, Hori Y, Hashimoto S, Terano H (2000) J Antibiot 53:204
29. Hood KA, West LM, Rouwe B, Northcote PT, Berridge MV, Wakefield J, Miller JH (2002) Cancer Res 62:3356
30. Pettit GR, Chicacz ZA, Gao F, Boyd MR, Schmidt JM (1994) J Chem Soc Chem Commun 1111
31. Isbrucker RA, Cummins J, Pomponi SA, Longley RE, Wright AE (2006) Biochem Pharmacol 66:75
32. Paterson I, Britton R, Delgado O, Wright AE (2004) Chem Commun 632
33. Boven E, Venema-Gaberscek E, Erkelens CA, Bissery MC, Pinedo HM (1993) Ann Oncol 4:321
34. Kowalski RJ, Giannakakou P, Gunasekera SP, Longley RE, Day BW, Hamel E (1997) Mol Pharmacol 52:613
35. Schreiber SL, Chen J, Hung DT (1996) Chem Biol 3:287
36. Martello LA, McDaid HM, Regl DL, Yang CH, Meng D, Pettus TRR, Kaufman MD, Arimoto H, Danishefsky SJ, Smith AB, Horowitz SB (2000) Clin Cancer Res 6:1978
37. Huang GS, Lopez-Barcons L, Freeze BS, Smith AB, Goldberg GL, Horwitz SB, McDaid HM (2006) Clin Cancer Res 12:298
38. Sanchez-Pedregal VM, Kubicek K, Meiler J, Lyothier I, Paterson I, Carlomagno T (2006) Angew Chem Intl Ed 45:7388
39 Mita A, Lockhart C, Chen TL, Bocinski K, Curtright J, Cooper W, Hammond L, Rothenberg M, Rowinsky E, Sharma S (2004) ASCO Annual Meeting Proceedings (Post-Meeting Edition) J Clin Oncol 22(14S) (July 15 Suppl) Abstract 2025
40. Altaha R, Fojo T, Reed E, Abraham J (2002) Curr Pharm Design 8:1707
41 http://www.fda.gov/bbs/topics/NEWS/2007/NEW01732.html
42. Piel J (2004) Nat Prod Rep 21:519
43. Nerenberg JB, Hung DT, Somers PK, Schreiber SL (1993) J Am Chem Soc 115:12621

44. Hung DT, Nerenberg JB, Schreiber SL (1996) J Am Chem Soc 118:11054
45. Smith AB, Qiu YP, Jones DR, Kobayashi K (1995) J Am Chem Soc 117:12011
46. Smith AB, Beauchamp TJ, LaMarche MJ, Kaufman MD, Qiu YP, Arimoto H, Jones DR, Kobayashi K (2000) J Am Chem Soc 122:8654
47. Smith AB, Kaufman MD, Beauchamp TJ, LaMarche MJ, Arimoto H (1999) Org Lett 1:1823
48 Smith AB, Kaufman MD, Beauchamp TJ, LaMarche MJ, Arimoto H (2000) Org Lett 2:1983
49. Smith AB, Freeze BS, Brouard I, Hirose T (2003) Org Lett 5:4405
50. Smith AB, Freeze BS, Xian M, Hirose T (2005) Org Lett 7:1825
51. Harried SS, Yang G, Strawn MA, Myles DC (1997) J Org Chem 62:6098
52. Harried SS, Lee CP, Yang G, Lee TIH, Myles DC (2003) J Org Chem 68:6646
53. Marshall JA, Johns BA (1998) J Org Chem 63:7885
54. Marshall JA, Lu ZH, Johns BA (1998) J Org Chem 63:817
55. Paterson I, Florence GJ, Gerlach K, Scott JP (2000) Angew Chem Intl Ed 39:377
56. Paterson I, Florence GJ (2000) Tetrahedron Lett 41:6935
57. Paterson I, Florence GJ, Gerlach K, Scott JP, Sereinig N (2001) J Am Chem Soc 123:9535
58. Paterson I, Delgado O, Florence GJ, Lyothier I, Scott JP, Sereinig N (2003) Org Lett 5:35
59. Paterson I, Delgado O, Florence GJ, Lyothier I, O'Brien M, Scott JP, Sereinig N (2005) J Org Chem 70:150
60. Paterson I, Lyothier I (2004) Org Lett 6:4933
61. Paterson I, Lyothier I (2005) J Org Chem 70:5494
62. Arefolov A, Panek JS (2005) J Am Chem Soc 127:5596
63. Arefolov A, Panek JS (2002) Org Lett 4:2397
64. de Lemos E, Porée FH, Commerçon A, Betzer JF, Pancrazi A, Ardisson J (2007) Angew Chem Intl Ed 46:1917
65. Mickel SJ, Sedelmeier GH, Niederer D, Daeffler R, Osmani A, Schreiner K, Seeger-Weibel M, Bérod B, Schaer K, Gamboni R, Chen S, Chen W, Jagoe CT, Kinder FR, Loo M, Prasad K, Repic O, Shieh W-C, Wang R-M, Waykole L, Xu DD, Xue S (2004) Org Process Res Dev 8:92
66. Mickel SJ, Sedelmeier GH, Niederer D, Schuerch F, Grimler D, Koch G, Daeffler R, Osmani A, Hirni A, Schaer K, Gamboni R, Bach A, Chaudhary A, Chen S, Chen W, Hu B, Jagoe CT, Kim H-Y, Kinder FR, Liu Y, Lu Y, McKenna J, Prashad M, Ramsey T M, Repic O, Rogers L, Shieh W-C, Wang R-M, Waykole L (2004) Org Process Res Dev 8:101
67. Mickel SJ, Sedelmeier GH, Niederer D, Schuerch F, Koch G, Kuesters E, Daeffler R, Osmani A, Seeger-Weibel M, Schmid E, Hirni A, Schaer K, Gamboni R, Bach A, Chen S, Chen W, Geng P, Jagoe CT, Kinder FR, Lee GT, McKenna J, Ramsey TM, Repic O, Rogers L, Shieh W-C, Wang R-M, Waykole L (2004) Org Process Res Dev 8:107
68. Mickel SJ, Sedelmeier GH, Niederer D, Schuerch F, Seger M, Schreiner K, Daeffler R, Osmani A, Bixel D, Loiseleur O, Cercus J, Stettler H, Schaer K, Gamboni R, Bach A, Chen G-P, Chen W, Geng P, Lee GT, Loeser E, McKenna J, Kinder FR, Konigsberger K, Prasad K, Ramsey TM, Reel N, Repic O, Rogers L, Shieh W-C, Wang R-M, Waykole L, Xue S, Florence G, Paterson I (2004) Org Process Res Dev 8:113
69. Mickel SJ, Niederer D, Daeffler R, Osmani A, Kuesters E, Schmid E, Schaer K, Gamboni R, Chen W, Loeser E, Kinder FR, Konigsberger K, Prasad K, Ramsey TM, Repic O, Wang R-M, Florence G, Lyothier I, Paterson I (2004) Org Process Res Dev 8:122
70. Paterson I, Wren SP (1993) J Chem Soc Chem Commun 1790
71. Clark DL, Heathcock CH (1993) J Org Chem 58:5878
72. Golec JMC, Jones SD (1993) Tetrahedron Lett 34:8159
73. Evans PL, Golec JMC, Gillespie RJ (1993) Tetrahedron Lett 34:8163
74. Golec JMC, Gillespie RJ (1993) Tetrahedron Lett 34:8167
75. Paterson I, Schlapbach A (1995) Synlett 498
76. Miyazawa M, Oonuma S, Maruyama K, Miyashita M (1997) Chem Lett 1191
77. Miyazawa M, Oonuma S, Maruyama K, Miyashita M (1997) Chem Lett 1193
78. Misske AM, Hoffmann HMR (1999) Tetrahedron 55:4315
79. Evans DA, Halstead DP, Allison BD (1999) Tetrahedron Lett 40:4461

80. Filla SA, Song JJ, Chen LR, Masamune S (1999) Tetrahedron Lett 40:5449
81. Yadav JS, Abraham S, Reddy MM, Sabitha G, Sankar AR, Kunwar AC (2001) Tetrahedron Lett 42:4713. Correction (2002) Tetrahedron Lett 43:3453
82. Arjona O, Menchaca R, Plumet J (2001) Tetrahedron 57:6751
83. BouzBouz S, Cossy J (2001) Org Lett 3:3995
84. Chakraborty TK, Laxman P (2001) J Indian Chem Soc 78:543
85. Shahid KA, Li YN, Okazaki M, Shuto Y, Goto F, Kiyooka S (2002) Tetrahedron Lett 43:6373
86. Shahid KA, Mursheda J, Okazaki M, Shuto Y, Goto F, Kiyooka S (2002) Tetrahedron Lett 43:6377. Correction (2003) Tetrahedron Lett 44:1519
87. Day BW, Kangani CO, Avor KS (2002) Tetrahedron-Asymmetry 13:1161
88. Yakura T, Kitano T, Ikeda M, Uenishi J (2003) Heterocycles 59:347
89. Kiyooka S-I, Shahid KA, Goto F, Okazaki M, Shuto Y (2003) J Org Chem 68:7967
90. Francavilla C, Chen W, Kinder FR (2003) Org Lett 5:1233
91. Baz àn-Tejeda B, Georgy M, Campagne J-M (2004) Synlett 720
92. Loiseleur O, Koch G, Wagner T (2004) Org Process Res Dev 8:597
93. BouzBouz S, Cossy J (2004) Synlett 2034
94. Ramachandran PV, Prabhudas B, Chandra JS, Reddy MVR (2004) J Org Chem 69:6294
95. Loiseleur O, Koch G, Cercus J, Schürch F (2005) Org Process Res Dev 9:259
96. Parker KA, Cao H (2006) Org Lett 8:3541
97. Burlingame MA, Mendoza E, Ashley GW, Myles DC (2006) Tetrahedron Lett 47:1209
98. Aicher TD, Kishi Y (1987) Tetrahedron Lett 28:3463
99. Takai K, Kuroda T, Nakatsukasa S, Oshima K, Nozaki H (1985) Tetrahderon Lett 26:5585
100. Takai K, Tagashira M, Kuroda T, Oshima K, Utimoto K, Nozaki H (1986) J Am Chem Soc 108:6048
101. Jin H, Uenishi J, Christ WJ, Kishi Y (1986) J Am Chem Soc 108:5644
102. Roush WR, Palkowitz AD, Ando K (1990) J Am Chem Soc 112:6348
103. Evans DA, Gauchet-Prunet JA (1993) J Org Chem 58:2446
104. Stork G, Zhao K (1989) Tetrahedron Lett 30:2173
105. Negishi E, Valente LF, Kobayashi M (1980) J Am Chem Soc 102:3298
106. Still WC, Gennari C (1983) Tetrahedron Lett 24:4405
107. Hung DT, Nerenberg JB, Schreiber SL (1994) Chem Biol 1:67
108. Evans DA, Bartoli JA, Shih TL (1981) J Am Chem Soc 103:2127
109. Evans DA, Takacs JM, McGee LR, Ennis MD, Mathre DJ, Bartoli JA (1981) Pure Appl Chem 53:1109
110. Gage JR, Evans DA (1990) Org Syn 68:77
111. Gage JR, Evans DA (1990) Org Syn 68:83
112. Chen J, Wang T, Zhao K (1994) Tetrahedron Lett 35:2827
113. Arimoto H, Kaufman MD, Kobayashi K, Qiu YP, Smith AB (1998) Synlett 765
114. Evans DA, Chapman KT, Carreira EM (1998) J Am Chem Soc 110:3560
115. Ikeda Y, Ukai J, Ikeda N, Yamamoto H (1987) Tetrahedron 43:723
116. Miyaura N, Suzuki A (1995) Chem Rev 95:2457
117. Brown HC, Bhat KS (1986) J Am Chem Soc 108:293
118. Danishefsky SJ, Larson E, Askin D, Kato N (1985) J Am Chem Soc 107:1246
119. Luche JL, Gemal AL (1979) J Am Chem Soc 101:5848
120. Gemal AL, Luche JL (1981) J Am Chem Soc 103:5454
121. Ferrier RJ (1964) J Chem Soc 5443
122. Keck GE, Abbott DE (1984) Tetrahedron Lett 25:1883
123. Linderman RJ, Cusack KP, Jaber MR (1996) Tetrahedron Lett 37:6649
124. White JD, Nylund CS, Green NJ (1997) Tetrahedron Lett 38:7329
125. Roush WR, Grover PT (1992) Tetrahedron 48:1981
126. Tsai DJ-S, Matteson DS (1981) Tetrahedron Lett 22:2751
127. Chen CP, Tagami K, Kishi Y (1995) J Org Chem 60:5386

128. Marshall JA, Perkins JF, Wolf MA (1995) J Org Chem 60:5556
129. Marshall JA, Palovich MR (1997) J Org Chem 62:6001
130. Paterson I, Norcross RD, Ward RA, Romea P, Lister MA (1994) J Am Chem Soc 116:11287
131. Paterson I, Wallace DJ, Cowden CJ (1998) Synthesis 639
132. Paterson I, Lister MA (1988) Tetrahedron Lett 29:585
133. Paterson I, Channon J (1992) Tetrahedron Lett 33:797
134. Paterson I, Tillyer RD (1992) Tetrahedron Lett 33:4233
135. Paterson I, Goodman JM, Isaka M (1989) Tetrahedron Lett 30:7121
136. Paterson I, Arnott EA (1998) Tetrahedron Lett 39:7185
137. Paterson I, Wallace DJ, Velàzquez SM (1994) Tetrahedron Lett 35:9083
138. Paterson I, Wallace DJ (1994) Tetrahedron Lett 35:9087
139. Cowden CJ, Paterson I (1997) Org React 51:1
140. Carling RW, Holmes AB (1986) J Chem Soc Chem Commun 325
141. Curtis NR, Holmes AB, Looney MG (1991) Tetrahedron 47:7171
142. Holmes AB, Looney MG (1993) J Am Chem Soc 115:5815
143. Fuhry MAM, Holmes AB, Marshall DR (1993) J Chem Soc Perkin Trans 1:2743
144. Burton JW, Clark JS, Derrer S, Stork TC, Bendall JG, Holmes AB (1999) Synlett 972
145. Paterson I, Perkins MV (1996) Tetrahedron 52:1811
146. Paterson I, Perkins MV (1992) Tetrahedron Lett 33:801
147. Pirrung MC, Heathcock CH (1980) J Org Chem 45:1727
148. Paterson I (1983) Tetrahedron Lett 24:1311
149. De Mico A, Margarita R, Parlanti L, Vescovi A, Piancatelli G (1997) J Org Chem 62:6974
150. Paterson I, Goodman JM, Lister MA, Schumann RC, McClure CK, Norcross RD (1990) Tetrahedron 46:4663
151. Paterson I, Cumming JG, Smith JD, Ward RA (1994) Tetrahedron Lett 35:441
152. Paterson I, Oballa RM, Norcross RD (1996) Tetrahedron Lett 37:8581
153. Paton, RS, Goodman JM (2006) Org Lett 8:4299
154. Wensheng Y, Su M, Jin Z (1999) Tetrahedron Lett 40:6725
155. Jain NF, Takenaka N, Panek JS (1996) J Am Chem Soc 118:12475
156. Jain NF, Crillo PF, Pelletier R, Panek JS (1995) Tetrahedron Lett 36:8727
157. Masse CE, Panek JS (1995) Chem Rev 95:1293
158. Panek JS, Beresis RT (1993) J Org Chem 58:809
159. Panek JS, Crillo PF (1993) J Org Chem 58:294
160. Hart DW, Schwartz J (1974) J Am Chem Soc 96:8115
161. Buchwald SL, LaMaire SJ, Nielsen RB, Watson BT, King SM (1987) Tetrahedron Lett 28:3895
162. Paterson I, Gibson KR, Oballa, RM (1996) Tetrahedron Lett 47:8585
163. Evans DA, Coleman PJ, Côté B (1997) J Org Chem 62:788
164. Evans DA, Hoveyda AH (1990) J Am Chem Soc 112:6447
165. Tomioka H, Takai K, Oshima K, Nozaki H (1981) Tetrahedron Lett 22:1605
166. Hoppe D (1984) Angew Chem 96:930
167. Hoppe D, Hense T (1997) Angew Chem 109:2376
168. Hoppe D, Zchage O (1989) Angew Chem 101:67
169. Hoppe D, Zchage O (1992) Tetrahedron 48:8389
170. Fargeas V, Le Ménez P, Berque I, Ardisson J, Pancrazi A (1996) Tetrahedron 52:6613
171. Berque I, Le Ménez P, Razon P, Mahuteau J, Férézou J-P, Pancrazi A, Ardisson J, Brion J-D (1999) J Org Chem 64:373
172. Kocienski P, Wadman S, Cooper K (1989) J Am Chem Soc 111:2363
173. Kocienski P, Barber C (1990) Pure Appl Chem 62:1933
174. Le M Énez P, Fargeas V, Berque I, Poisson J, Ardisson J, Lallem JY, Pancrazi A (1995) J Org Chem 60:3592
175. Fargeas V, Le M énez P, Berque I, Ardisson J, Pancrazi A (1996) Tetrahedron 52:6613
176. Braun M (1998) Angew Chem Int Ed 37:430

177. Knorr R (2004) Chem Rev 104:3795
178. Corey EJ, Bakshi RK, Shibata S (1987) J Am Chem Soc 109:5551
179. Kaminski ZJ (1987) Synthesis 10:917
180. Kaminski ZJ, Paneth P, Rudzinski J (1998) J Org Chem 63:424
181. Mickel SJ, Daeffler R, Prikoszovich W (2005) Org Process Res Dev 9:113
182. Panek JS, Beresis RT, Xu F, Yang M (1991) J Org Chem 56:7391

Top Curr Chem (2009) 286: 121–149
DOI: 10.1007/128_2008_12

Published online: 06 November 2008

The Interaction of Microtubules with Stabilizers Characterized at Biochemical and Structural Levels

J.F. Díaz, J.M. Andreu, and J. Jiménez-Barbero

Abstract Since the discovery of paclitaxel and its peculiar mechanism of cytotoxicity, which has made it and its analogues widely used antitumour drugs, great effort has been made to understand the way they produce their effect in microtubules and to find other products that share this effect without the undesired side effects of low solubility and development of multidrug resistance by tumour cells. This chapter reviews the actual knowledge about the biochemical and structural mechanisms of microtubule stabilization by microtubule stabilizing agents, and illustrates the way paclitaxel and its biomimetics induce microtubule assembly, the thermodynamics of their binding, the way they reach their binding site and the conformation they have when bound.

Keywords Antitumour drugs, Bioconformer, Microtubule stabilizing agents, Paclitaxel

Contents

J.F. Díaz (✉), J.M. Andreu, and J. Jiménez-Barbero
Centro de Investigaciones Biológicas, Consejo Superior de Investigaciones Científicas, Ramiro de Maeztu 9, 28040 Madrid, Spain
e-mail: fer@cib.csic.es,

Abbreviations

MSA	Microtubule stabilizing agent
Cr	critical concentration
GMPCPP	Guanosine-5'-[(α,β)-methyleno]triphosphate
PEDTA	10mM phosphate, 1mM EDTA pH6.7 buffer
RMSD	Root mean square deviation, NOE, Nuclear Overhauser Enhancement
REDOR	Rotational Echo Double Resonance; tr-NOE, transferred Nuclear Overhauser Enhancement
NOESY/STD	Nuclear Overhauser Enhancement spectroscopy/saturation transfer difference

1 Biochemical Background on Microtubule Stabilizing Agents. What is a Microtubule Stabilizer?

1.1 Microtubules and Drugs

Small molecules modulating microtubule assembly have played major roles as tools in microtubule research, in a manner closely related to their chemotherapeutic interest [1]. Tubulin was first purified in the last century as the colchicine-binding protein proposed to be the subunit of cellular microtubules [2]. More recently, a colchicine derivative was employed to help crystallization and determine the structure of tubulin by X-ray diffraction [3]. The colchicine, vinblastine [4] and paclitaxel [5] sites are main drug binding sites of tubulin, to which many other substances bind. The discovery of microtubule stabilization by paclitaxel [6] prompted its clinical development [7] and a burst of research on new MSAs, as well as the generalized use of paclitaxel or docetaxel as convenient reagents to assemble (see Fig. 1), stabilize or detect microtubules in the laboratory. One example is the development

of the active fluorescent paclitaxel derivatives Flutax-1 and Flutax-2 [8] employed to study cellular microtubules [9] (see Fig. 2) and as probes of the paclitaxel binding site [10, 11]. The electron crystallography determination of the structure of tubulin was made on two-dimensional tubulin crystals assembled with zinc and paclitaxel, providing the first atomic view of tubulin and bound paclitaxel [5, 12]. In this structure, tubulin forms protofilaments which associate in a different fashion with respect to a microtubule.

1.2 Function and Evolution

It was speculated that the paclitaxel binding site of tubulin might bind an unknown endogenous regulator of microtubule assembly [6], but such a substance has not been convincingly documented so far. Therefore, we do not know

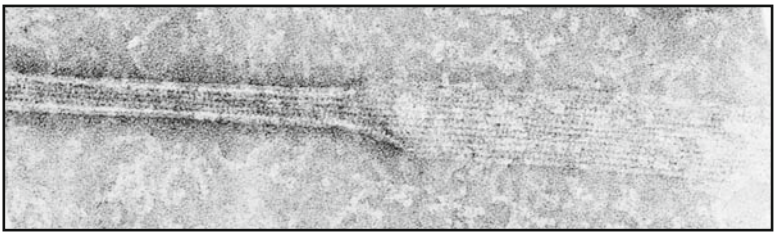

Fig. 1 Electron micrograph of a negatively stained microtubule assembled from purified tubulin and docetaxel. The *left side* shows the lateral projection of the protofilaments forming a microtubule cylinder ~24nm in diameter which has opened into a sheet on the *right side*. There are also tubulin oligomers in the image

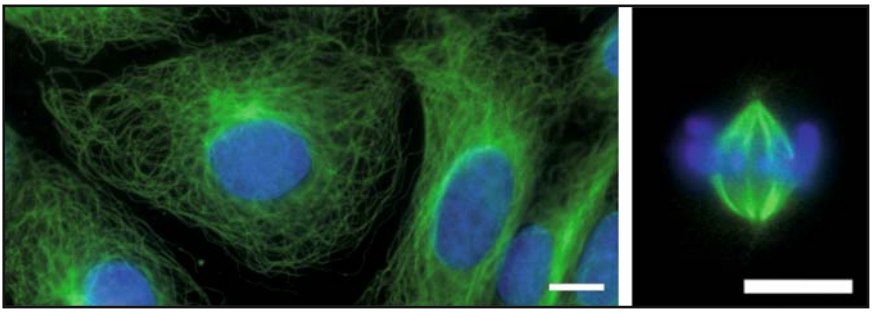

Fig. 2 *Left*: cytoplasmic microtubules in interphase kidney epithelial cells imaged with the fluorescent paclitaxel derivative Flutax-2 (*green*) and nuclear DNA stained with Hoescht 33342 (*blue*). *Right*: mitotic spindle from a dividing metaphase cell with similarly imaged microtubules and chromosomes. *Bars* indicate 10 μm (micrographs courtesy of Isabel Barasoain)

whether the paclitaxel binding cavity has any physiological functions. The zones of microtubule associated proteins and motor proteins do not, in most cases, overlap with the paclitaxel or other drug binding sites. Tubulin promiscuously binds a variety of exogenous small molecules, particularly from natural sources, some of which are plant poisons known since antiquity, which suggests that the production of microtubule poisons is an effective defensive mechanism against predators. Interestingly, a simpler relative of tubulin, bacterial cell division protein FtsZ [13], forms tubulin-like protofilaments which do not associate into microtubules [14] and does not bind most of these substances (JMA, unpublished), suggesting that the binding of antimitotic drugs by tubulin appeared with its ability to associate laterally into microtubules, or that plants and sponges have not developed a defensive mechanism targeting bacterial FtsZ.

1.3 What an MSA is and How it Works

A microtubule stabilizer or destabilizer molecule is, in a general thermodynamic definition, a molecule able to change the ratio between assembled and dimeric tubulin; to do so, it has to bind to microtubules differently from unassembled tubulin. A ligand which preferentially binds to the dimeric protein will inhibit polymer formation, whereas a ligand which binds more to the polymers than to the dimeric protein will stabilize the polymers, due to thermodynamic linkage [15]. This definition implies neither knowledge of the site of binding nor of the changes in the structural dynamics of ligand and protein upon binding. Since from a structural point of view a microtubule modulator may modify, either directly or allosterically, the polymerization interfaces of the tubulin molecule, one may obviously wish to know the mechanism by which such a ligand modifies microtubule assembly, which requires kinetic and structural investigation. Structural modifications may in principle range from local side-chain rearrangements to significant domain movements, but translate in a few kilojoules per mol tubulin of microtubule stabilization. GTP is a natural cofactor that binds at the axial association interfaces between tubulin subunits [5, 16]. Several microtubule inhibitors are in a broad sense interfacial ligands [17] which bind like wedges at or near association interfaces between tubulin molecules [4] and therefore perturb their polymerization geometry to different extents. MSAs subtly modify microtubule structure. Paclitaxel, by binding near the lateral association interface between protofilaments, reduces the average number of protofilaments in microtubules made of purified tubulin from 13 to 12 [18], whereas its side-chain analogue docetaxel does not [19], and the fluorescent analogues Flutax-1 and Flutax-2 carrying a bulky fluorescent moiety increase the average number of protofilaments from 13 to 14 [10]. Finally, any substance that stabilizes cellular microtubules may be considered an MSA irrespective of its molecular target or mechanism.

1.4 Chemical Diversity of MSAs in Short

MSAs with different chemical structures have been discovered in different natural sources. Taxanes come from plants, epothilones and cyclostreptin are of microbial origin, whereas discodermolide, dictyostatin, eleutherobin, laulimalide and peloruside were discovered in sea organisms (for a classification and MSA structures see [20]). We do not know of MSAs from a purely synthetic chemistry not related to natural products.

1.5 Three MSA Binding Sites in Microtubules

Many MSAs, including epothilones, discodermolide, dictyostatin, eleutherobin, sarcodictyin and a steroid derivative reversibly compete with taxanes to bind to the β-tubulin subunit in microtubules whereas cyclostreptin irreversibly inhibits taxane binding [20, 21]. Cyclostreptin binds covalently to a microtubule pore and to the lumenal taxoid binding site, indicating the entry pathway of taxanes into microtubules (Fig. 3) [21]. Binding to one site appears to exclude binding to the other, apparently because both sites use residues from the β-tubulin loop between helices H6 and H7 [22]. This opens the possibility that some MSAs may stop at the pore and not reach the lumenal site, as seems to be the case, at least partially, for fluorescent paclitaxel derivatives Flutax-2 and Hexaflutax [23]. On the other hand, laulimalide [24] and peloruside [25] share a binding site biochemically distinct from the paclitaxel site. Peloruside virtually docks into a zone of α-tubulin equivalent to that occupied by paclitaxel in β-tubulin [26, 27], yet its binding site has not been experimentally located. We still do not know whether any more binding sites for stabilizing ligands may exist in microtubules.

1.6 Mechanisms and Cellular Consequences of Microtubule Stabilization

Microtubule stabilizing agents at relatively high concentrations induce assembly of all tubulin available into microtubules, typically with accumulation of microtubule bundles in cells. The paclitaxel ligation of most tubulin molecules in a microtubule has interesting structural consequences, modifying microtubule flexural rigidity [28] and the curvature of dissociated protofilaments [29]. However, MSAs are active at lower concentrations at which they bind substoichiometrically to only a fraction of tubulin molecules in a microtubule. Under these substoichiometric conditions they suppress microtubule dynamic instability, a property in common with microtubule inhibitors, resulting in mitotic block or impairment, which eventually triggers tumour cell death [1] or senescence [30]. In addition, microtubule drugs can target tumour vasculature [1].

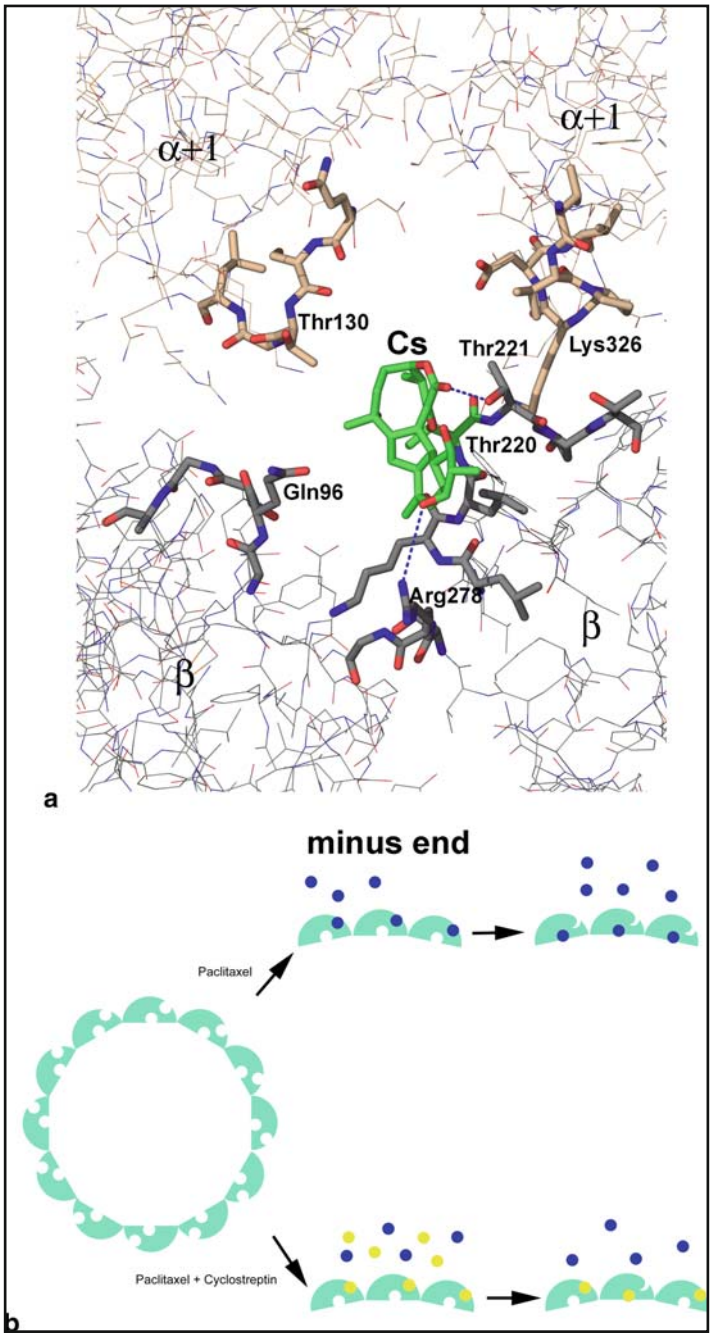

Fig. 3 **a** Model for the binding of cyclostreptin at the proposed initial MSA binding site at pore type I. Taken from [21]. **b** Scheme of the route of paclitaxel to its lumenal site in the microtubules. Paclitaxel binds to the external site at the pores of the microtubules, being later transported to its lumenal site while the external site gets blocked. In the presence of cyclostreptin the external site gets irreversibly blocked; thus, paclitaxel cannot reach the lumenal site

2 Thermodynamics and Kinetic Mechanisms of the Interaction of Stabilizing Agents with Microtubules. How do they Bind?

2.1 Thermodynamics of MSA Induced Microtubule Assembly. How do they Induce Assembly?

The main ability of microtubule stabilizing agents and the basis of their mechanism of action is their capacity to induce microtubule assembly. Although different models [31, 32], based on the structure of the paclitaxel binding site [5], have been proposed to explain the paclitaxel mechanism of action on the basis of a structural effect on the tubulin molecule, it is unlikely, given the wide structural diversity of paclitaxel binding site ligands and the fact that there are at least three different binding sites (the internal and external paclitaxel sites and laulimalide one) that all of them produce the same structural effect at the atomic level on the microtubules.

On the other hand, from a thermodynamical point of view, a common mechanism for assembly induction can be proposed. All microtubule stabilizing agents bind tightly to the assembled form, while they do not bind with a measurable affinity to the dimeric tubulin [33], indicating that the taxane binding pocket is either not formed or not-completely formed in non-microtubular tubulin.

Considering the difference in affinities for the assembled and dimeric tubulin, it is straightforward to deduce that the compounds should displace the assembly equilibrium towards the polymerized form, as they fill the binding sites in microtubules.

However, preferential binding does not explain how microtubule assembly starts. Highly active microtubule stabilizing agents induce tubulin assembly in solution conditions in which no microtubules exist, and thus in which there is no equilibrium to be displaced [20, 33], implying that microtubule stabilizing agents have to bind unassembled tubulin (in dimeric or oligomeric form) to make it assemble into microtubules.

Microtubule assembly in the absence of ligands follows a non-covalent nucleated condensation polymerization, characterized by cooperative behaviour and by the presence of a critical concentration Cr, below which no significant formation of large polymers takes place [33] (Fig. 4). It can be demonstrated [34] that the apparent equilibrium constant for the growth reaction, i.e. the addition of a protomer to the polymer, is in good approximation, equal to the reciprocal critical concentration $Kel_{app} = Cr^{-1}$, which renders the apparent standard free energy change of elongation amenable to simple measurement (as long as nucleotide hydrolysis is disregarded).

For ligand-induced assembly an apparent critical concentration, dependent on the ligand concentration, is observed [33]. Paclitaxel- and epothilone-induced assembly of GDP-tubulin have been extensively characterized. Under these conditions, in which tubulin is unable to assemble in the absence of ligand, assembly and binding are linked processes, there being no assembled unligated tubulin and showing an apparent critical concentration that saturates with ligand concentration (Fig. 5 of [35] and Fig. 2 of [36]), the latter not being compatible with a simple mechanism in which MSA stabilize microtubules binding to the empty sites in them.

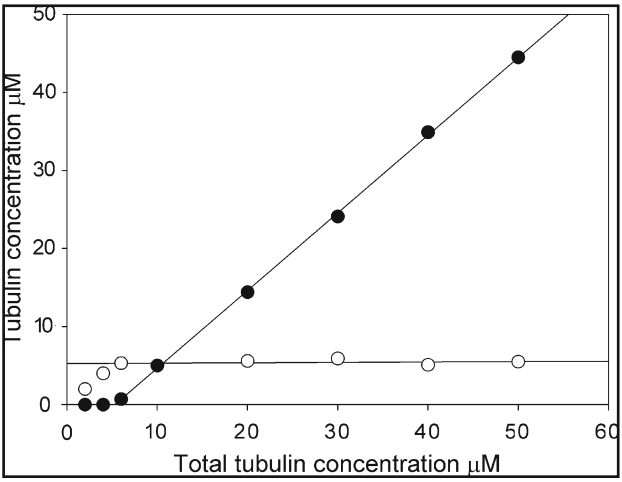

Fig. 4 Polymerization of GTP-tubulin in 3.4 M glycerol, 10mM sodium phosphate, 1mM EGTA, 1mM GTP, pH 6.7 buffer at 37°C measured by sedimentation. *Solid circles*, pelleted tubulin; hollow circles, tubulin in the supernatant. The critical concentration determined is 5.3 μM; under this total concentration no tubulin is pelleted while over this total concentration all tubulin in excess is pelleted

In principle, ligand induced tubulin assembly may proceed in two different ways [33] (Fig. 5), the most intuitive being the ligand-facilitated pathway (stabilization by binding to the empty sites, in which elongation precedes binding, Eq.1, Fig. 5a), i.e. the binding of a tubulin dimer creates a new high affinity binding site for the ligand, whose binding displaces the equilibrium towards the assembled form.

$$\mathrm{Tub} + \mathrm{Mtb} \xleftrightarrow{\mathrm{Kel}_1} \mathrm{Tub-Mtb} + \mathrm{Lig} \xleftrightarrow{\mathrm{Kbin}_1} \mathrm{Tub-Mtb-Lig} \qquad (1)$$

Although this mechanism cannot explain microtubule induced assembly in conditions in which tubulin is unable to assemble in absence of ligands, the ligand facilitated pathway is supported by the fact that paclitaxel does not bind tightly to unassembled tubulin (at least under non-assembly conditions) [33].

However, there is a strong argument against the ligand facilitated pathway: if the reaction proceeds via the ligand-facilitated pathway, the apparent elongation constant Kel_{app} (the equilibrium constant of addition of a dimer to the end of the microtubule), which reflects the power of assembly induction, should depend linearly on the free concentration of ligand and its binding constant to the empty site (Eq. 2).

$$\mathrm{Kel}_{app} = \frac{[\mathrm{Tub-Mtb-Lig}] + [\mathrm{Tub-Mtb}]}{[\mathrm{Tub}][\mathrm{Mtb}]} = \mathrm{Kel}_1 \left(1 + [\mathrm{Ligand}]\mathrm{Kb}_1\right) \qquad (2)$$

This means that given two different ligands, at the same concentration, their power of assembly induction should depend linearly on the binding constant of the ligand,

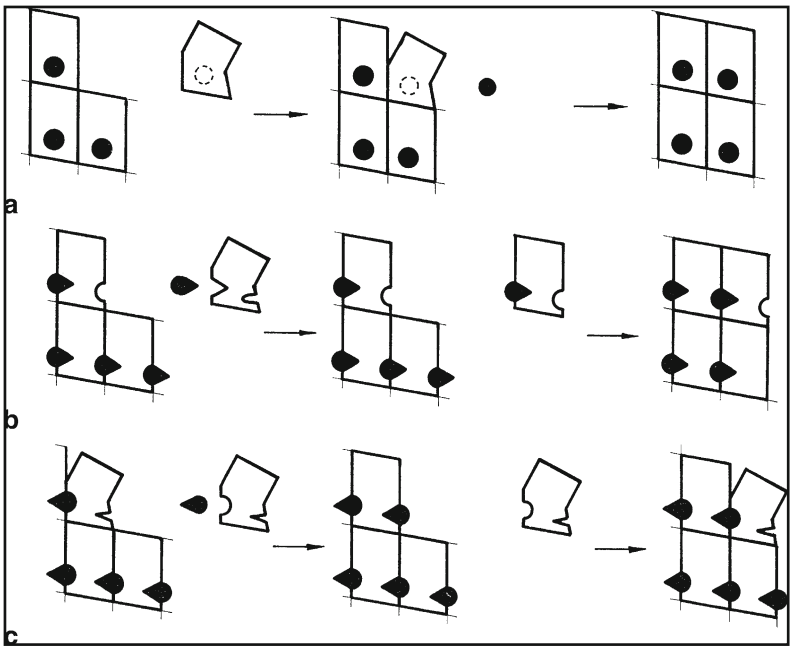

Fig. 5 Models of ligand induced tubulin assembly. The ligand induced addition of a tubulin molecule to the microtubule latice is represented. **a** Ligand facilitated pathway, a ligand molecule binds to an empty site at the end of a microtubule thus stabilizing the microtubule end. **b** Ligand mediated pathway 1. The ligand binds to unassembled tubulin and the ligated dimer has a higher affinity for the microtubules. **c** Ligand mediated pathway 2. The binding of a ligand to a non completed site at the end of the microtubule increases the affinity for the binding of the next dimer. Adapted from [33]

independently of the specific effect that the ligand causes on tubulin. Equation(2) predicts a continuous increase of Kel_{app} observed at overstoichiometric concentrations of microtubule stabilizing agents.

Apparently this is not the case. Although, in general, better binders are better assembly inductors, there are compounds that significantly deviate from the best regression line (see Fig. 4a of [36], and Fig. 4a [20]), while a saturating behaviour of critical concentration Cr (inverse of apparent elongation constant Kel_{app}) with ligand concentration is observed (Fig. 2 of [36] and Fig. 5 of [35]).

This saturating behaviour observed is explained with both possible ligand-mediated pathways (binding precedes elongation), which are thermodynamically equivalent: (1) the ligand binds to unassembled tubulin and the ligated dimer has a higher affinity for the microtubules, so decreasing the critical concentration (3a, Fig. 5b); (2) the binding of a ligand to a non completed site at the end of the microtubule increases the affinity for the binding of the next dimer (Eq. 3b, Fig. 5c).

$$\boxed{\mathrm{Tub} + \mathrm{Lig} \xleftrightarrow{\mathrm{Kbin}_2} \mathrm{Tub} - \mathrm{Lig} + \mathrm{Mtb} \xleftrightarrow{\mathrm{Kel}_2} \mathrm{Tub} - \mathrm{Mtb} - \mathrm{Lig}} \qquad (3a)$$

$$\boxed{\mathrm{Mtb} + \mathrm{Lig} \xleftrightarrow{\mathrm{Kbin}_2} \mathrm{Mtb} - \mathrm{Lig} + \mathrm{Tub} \xleftrightarrow{\mathrm{Kel}_2} \mathrm{Tub} - \mathrm{Mtb} - \mathrm{Lig}} \quad (3b)$$

Mass action law predicts that if the ligand-mediated pathway were the only one that worked, the apparent elongation constant should saturate with the ligand concentration (Eq. 4), notwithstanding which of the pathways the reaction followed (in case path 3b is followed the term ([Tub–Lig]+[Tub]) [Mtb] should be replaced by ([Mtb–Lig] + [Mtb]) [Tub]).

$$\boxed{\mathrm{Kel}_{\mathrm{app}} = \frac{[\mathrm{Tub} - \mathrm{Mtb} - \mathrm{Lig}]}{\left([\mathrm{Tub} - \mathrm{Lig}] + [\mathrm{Tub}]\right)[\mathrm{Mtb}]} = \frac{\mathrm{Kel}_2 \mathrm{Kbin}_2 [\mathrm{Ligand}]}{\left(1 + \mathrm{Kbin}_2 [\mathrm{Ligand}]\right)}} \quad (4)$$

So the elongation constant measured will depend on the elongation constant of the ligated dimer, which will depend on the specific effect that the ligand employed causes upon binding to a tubulin molecule.

However, since microtubule stabilizing agents will bind tightly to unoccupied sites, it is reasonable to assume that both mechanisms should work; however, in this case the apparent critical concentration will saturate following Eq. (5) (as in Eq. 4); in the case where path 3b is followed the term ([Tub–Lig]+[Tub])[Mtb] should be replaced by ([Mtb–Lig] + [Mtb]) [Tub]):

$$\boxed{\mathrm{Kel}_{\mathrm{app}} = \frac{[\mathrm{Mtb} - \mathrm{Tub}] + [\mathrm{Mtb} - \mathrm{Tub} - \mathrm{Lig}]}{\left([\mathrm{Tub}] + [\mathrm{Tub} - \mathrm{Lig}]\right)[\mathrm{Mtb}]} = \mathrm{Kel}_2 \mathrm{Kbin}_2 \frac{[\mathrm{Ligand}] + \frac{1}{\mathrm{Kbin}_1}}{\left(1 + \mathrm{Kbin}_2 [\mathrm{Ligand}]\right)}} \quad (5)$$

In practice, since at the paclitaxel or epothilone concentrations necessary to induce assembly, the concentrations of free ligand are of the order of 10^{-6} M, and $1/K_{bin_1}$ for the strong assembly inducers is of the order of 10^{-7} to 10^{-9} M, the term $1/K_{bin_1}$ can be neglected and so Eq. (5) becomes equivalent to Eq. (4).

Following Eqs. (4) or (5), it can be deduced that the measured Kel_{app} in saturation conditions (the experimental conditions) corresponds to the Kel of the ligated tubulin (or Kel of unligated tubulin to the ligated microtubule end), i.e. Kel_2.

Although the ligand mediated pathways easily explain both the experimental results of assembly induction in conditions in which tubulin cannot assemble in the absence of the ligands and the saturation behaviour of Kel_{app}, it seems contradictory with the absence of observed binding of ligands to dimeric tubulin. Nevertheless, evidence of ligand binding to dimeric tubulin and to an alternative binding site in microtubules was obtained, supporting the hypothesis that the ligand mediated pathway is involved in the assembly induction by the microtubule stabilizing agents. Cyclostreptin, a covalent binding microtubule stabilizing agent of the paclitaxel site [37], binds to the tubulin dimer [21] although with a slow kinetic rate in non-assembly conditions, and epothilone binding to tubulin to a mixed state of dimers and non-microtubule assemblies have been detected by NMR [38].

Thus, the most plausible hypothesis is that microtubule stabilizing agents induce microtubule assembly via a mechanism involving binding to dimeric tubulin. As described in Eq.(4), although microtubule stabilizing agents bind with high affinity to the

empty sites in the microtubules, the equilibrium of the assembly process (Kel_{app}) is determined by the change in the assembly properties of the dimer after binding to the microtubule stabilizing agent (Kel_2), and not by the binding affinity to the site itself ($Kbin_2$).

2.2 *Thermodynamics of MSA Binding to Microtubules. How to Make Them Sticky?*

Microtubule stabilizing agents work because they bind microtubules. Improving this property is important for their action, since the better they bind to tubulin, the better cytotoxic agents they are [20, 36, 39]. In addition to this, high affinity or covalent microtubule stabilizing agents get trapped inside the cell due to the chemical potential of their interaction with tubulin, thus escaping the detoxification mechanism by membrane pumps overexpression, used by multidrug resistant cells [21, 39].

Early studies of the interaction between microtubule stabilizing agents with their binding sites were greatly hampered by the thermodynamics of ligand induced assembly [6, 40]. Since microtubule stabilizing agents significantly perturb the assembly state of the protein, assembly and binding are linked processes and thus it is difficult to separate the contributions from both assembly and binding. It is thus, important to find conditions in which the assembly is not significantly perturbed due to the presence of the ligand.

Our first attempt to characterize the binding of paclitaxel and docetaxel to microtubules [35] was done at high concentrations of tubulin. Since in the conditions of the assay most of the tubulin gets assembled, the perturbation in the amount of assembled polymer is minimal, and a rigorous comparison between the binding affinity and the power of assembly induction of paclitaxel and docetaxel can be carried out. The study shows a single common binding site for paclitaxel and docetaxel for which docetaxel has double the affinity than paclitaxel (Fig. 6). However, it was not possible to measure directly the binding constant of paclitaxel and docetaxel. In order to do so, it would be necessary to have empty assembled binding sites. Although empty sites can be assembled in the absence of ligand at high concentrations of tubulin, the high affinity observed for paclitaxel and docetaxel made it impossible to find conditions in which the reaction is not completely displaced towards the bound state.

The problem was overcome with the use of mildly fixed microtubules [10] in which the paclitaxel binding site is unaltered, while protected from cold and dilution depolymerisation and a paclitaxel molecule bound to a fluorescent probe (either fluorescein or difluorofluorescein) [8]. The fluorescent derivatives of paclitaxel were then tested to check that they compete with taxoids for the same site, with the same 1:1 stoichiometry producing the same celular effects as paclitaxel and docetaxel, thus it can be assumed that they bind for the same site [9]. Using these stabilized microtubules, it is possible to determine precisely the binding constant of the fluorescent taxoid which was found to be of the order of 10^8 M^{-1} at 25°C.

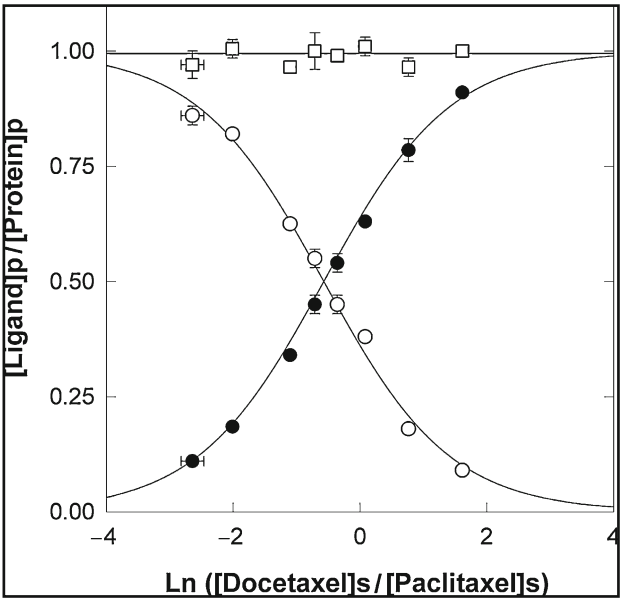

Fig. 6 Competition between ^{3}H-paclitaxel and ^{14}C-docetaxel for binding to microtubules. 11.3 μM tubulin was assembled at 37°C in PEDTA, 1mM GDP, 1mM GTP, 8mM $MgCl_2$, pH6.7 by the addition of paclitaxel and docetaxel at a total concentration of 20 μM, at different molar ratios of paclitaxel to docetaxel. The total concentration of microtubules was 11.0 ± 0.10 μM; the concentration of tubulin in supernatants (not polymerized tubulin) varied between ca. 0.4 (in paclitaxel excess) and 0.2 μM (in docetaxel excess). *Open circles*, ^{3}H-paclitaxel bound per polymerized tubulin dimer; *solid circles*, ^{14}C-docetaxel bound; *squares*, total ligand (paclitaxel plus docetaxel) bound per polymerized tubulin dimer. The *solid lines* are the best fit to the data, employing a simple competition model of the two ligands for the same site, taken from [35]

Having a fluorescent probe with a known binding site affinity, it was possible to design competition tests for the evaluation of the binding affinity of paclitaxel, docetaxel and baccatin III to microtubules [11, 22] that can be used for fast and precise evaluation of a large series of compounds thus allowing precise studies of structure-affinity relationship [36] and to classify the microtubule stabilizing agents according to their binding sites [20, 24, 25].

The test has been used to measure the binding affinity of a set of 19 epothilones [36]. The study showed that it is possible to optimize the binding affinity of complex molecules by studying the effect of single changes in the substituents of the core of the molecule and combining the most favourable substitutions to obtain a 500-fold increase in the binding affinity of the epothilone molecule from Epothilone A (compound 1) to *cis*-CP-*tmt*-Epo B (compound 19) (Fig. 7).

Moreover, the study demonstrates that the cytotoxicity of the compound on tumour cells is related to the binding affinity, being affinity of the compounds a variable to maximize in order to obtain more cytotoxic compounds.

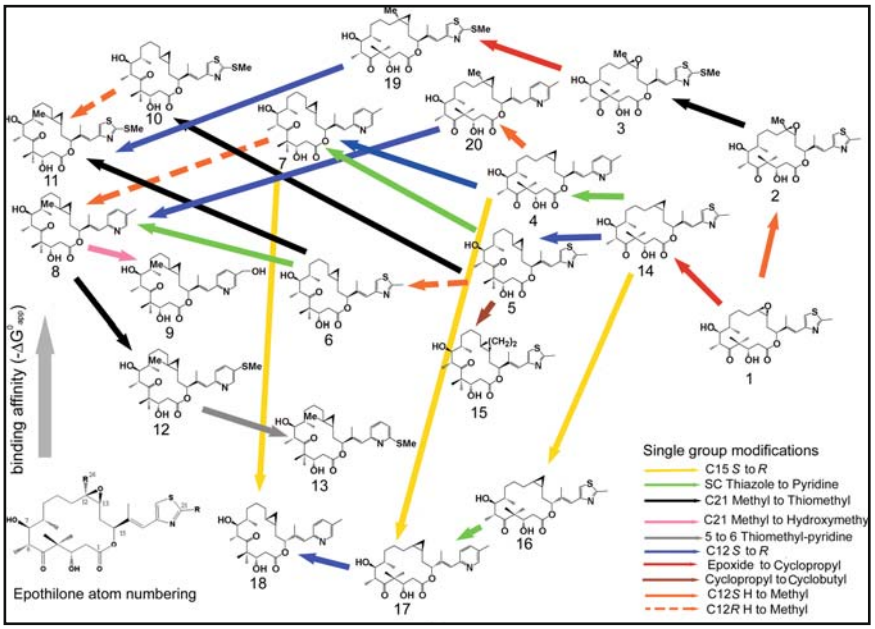

Fig. 7 Scheme of the structures of epothilone analogues studied in [36], the chemical differences between them, and the effect of these modifications in the free energy of binding to their site in microtubules at 35°C. Taken from [36]

The latter was generalized [20] for all paclitaxel binding site ligands known thus showing that the higher the affinity of the paclitaxel binding site the more cytotoxic the ligand.

From the equilibrium studies of microtubule stabilizing agents binding to the taxane site we learned the following: Microtubule stabilizing agents of the paclitaxel site bind microtubules with a well defined 1:1 stoichiometry. Binding affinity for a given fixed conformation of the molecule core can be modulated by selecting the side chain substituents with the highest contributions for the free energy of binding and combining them into a single molecule. The affinity of a compound is predictive of its cytotoxicity; thus it is possible to design more cytotoxic taxanes by studying the effect of each substitution on the binding affinity to select those which provide larger free energy changes to the binding.

2.3 Kinetics of MSA Binding to Microtubules. How Do They Reach Their Site in the Microtubules?

The kinetics of binding of ligands to a binding site provides information about the way the ligands reach the site. They may bind fast, indicating an easily accessible site, or they may bind slowly indicating an occluded site. They may bind in a single

step, indicating simple binding to a site or in successive steps, indicating a processing after early binding to a site.

One of the first effects of taxanes in microtubules observed was the fact that the structure of the paclitaxel-induced microtubules is different from that of the microtubules assembled in its absence [18]. Moreover, paclitaxel is able to change the structure of preformed docetaxel-induced assembled microtubules within a time range of the order of tens of seconds, indicating a fast exchange of taxanes in the site [41].

The modification of the microtubule structure should come from the perturbation of the interprotofilament contacts, which allows the accommodation of extra protofilaments in the microtubule lattice. The experimental fact that taxane binding modifies the interprotofilament contacts rapidly lead to the conclusion that the taxane binding site in microtubules was located in the interprotofilament space [18, 19].

The first structural location of the taxane binding site [42] placed it in the interprotofilament space, thus supporting the biochemical results. However, this changed when the first high resolution 3D structure of the paclitaxel-tubulin complex was solved by electron-crystallography of a two-dimensional zinc-induced tubulin polymer [5]. The fitting of this structure into a three-dimensional reconstruction of microtubules from cryoelectron microscopy allowed a pseudo atomic resolution model of microtubules [43] in which the paclitaxel binding site was placed inside the lumen of the microtubules hidden from the outer solvent.

The kinetics of taxane binding to microtubule were subsequently determined; taxanes and epothilones [10, 22, 23, 44] bind to microtubules extremely fast (Fig. 8, Table 1).

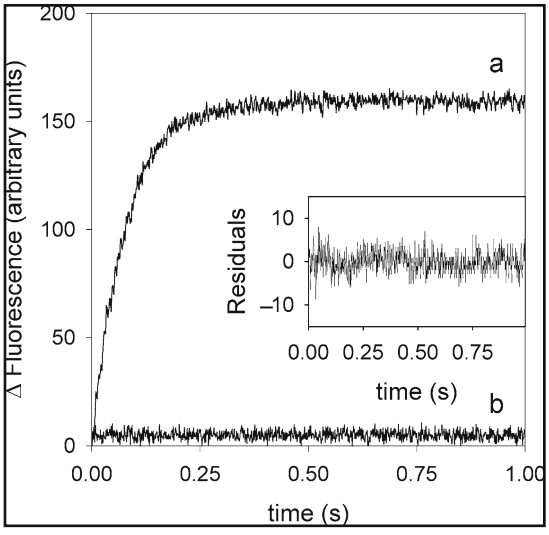

Fig. 8 Kinetics of binding of Flutax1 to microtubules at 35°C. In the stopped-flow device a 1 μM solution of Flutax1 was mixed with 25 μM pure tubulin assembled into microtubules (concentration of sites 20 μM) (final concentrations of 500 nM Flutax and 10 μM sites) in the absence (**a**) and presence (**b**) of 50 μM docetaxel. Curve **a** is fitted to an exponential decay. *Inset*: residues between the experimental and theoretical curves. Taken from [10]

Table 1 Kinetic rates of taxane site ligands binding to microtubules (37°C)

	$k_{+1}\times10^5M^{-1}s^{-1}$	$k_{-1}s^{-1}$	$k_{+2}s^{-1}$	$k_{-2}s^{-1}$
Flutax-1[a]	6.10 ± 0.22	0.99 ± 0.27	0.0243 ± 0.0007	0.026 ± 0.0012
Flutax-2[a]	13.83 ± 0.18	1.63 ± 0.18	2.7 ± 0.8	0.022 ± 0.0012
Paclitaxel[b]	3.63 ± 0.08	ND	ND	0.091 ± 0.0061
Epothilone A[c]	3.3 ± 0.03	ND	ND	0.138 ± 0.37 (slow)
				0.463 ± 0.32 (fast)

k_{+1} and k_{-1} – kinetic on and off rate constants of the first fast bimolecular step
k_{+2} and k_{-2} – kinetic on and off rate constants of the second slow monomolecular step
[a]Data from [10]
[b]Data from [22]
[c]Data from [44]

The binding of taxanes has been well characterized [10, 22] and shows a series of consecutive reactions involving a first fast bimolecular step (k_{+1} and k_{-1}), a second slow monomolecular step (k_{+2}, k_{-2}) and a third step which is the structural change involving the change in the number of microtubule protofilaments. It can be proved numerically that the first bimolecular fast step of binding is diffusion controlled, thus indicating that taxanes can not directly bind to the lumenal site [22].

Since the lumenal site of microtubules was well supported by the structural data and also by the fact that mutations in the lumenal site confer resistance to taxanes [45], an alternative mechanism with binding to an initial exposed binding site located in pore type I of the microtubule wall and later transportation of the ligand to the lumenal site was proposed in [22] (Fig. 9).

The existence of the external site was further confirmed with a fluorescein-tagged taxane, Hexaflutax, specially tailored with a spacer between the taxane moiety and the fluorescein tag, long enough to allow binding to an external site while keeping the fluorescent tag exposed to an antibody but short enough to avoid antibody binding if the taxane moiety is bound to the lumenal site. It was shown that monoclonal and polyclonal antibodies bind to Hexaflutax bound to microtubules at a kinetic rate consistent with a diffusion controlled bimolecular reaction between two objects of the size of a microtubule and an antibody, forming an stable ternary complex, thus indicating that at least a significant part of the taxane is bound to an external site [23].

The route of taxanes was finally unveiled with the use of a covalent ligand of the taxane binding site [21]. Cyclostreptin, a bacterial natural product [46, 47] with weak, but irreversible tubulin assembly activity and strong apparent binding affinity for the paclitaxel site, covalently labels both a residue placed in the lumenal site of paclitaxel Asn228 and a residue previously proposed to be in the external binding site Thr220 (Fig. 3a).

From these results a structural binding pathway consistent with that observed kinetically was proposed [21]. Paclitaxel binds fast to a site located in the surface of the microtubules, into the pore type I. Then it has to be transferred to the second luminal, final location. The transfer involves probably the switch of some of the elements of the first site, since only one molecule of paclitaxel can bind to each molecule of β-tubulin (Fig. 3b).

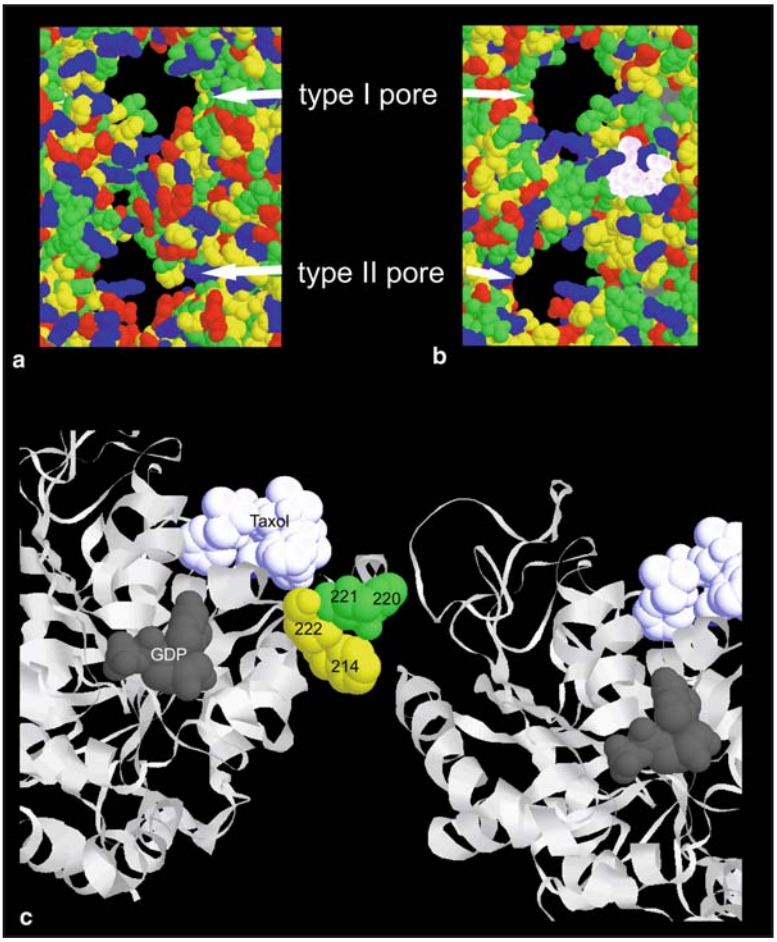

Fig. 9 Insight of the outer (**a**) and (**b**) inner surface of a high resolution microtubule model, showing two different types of pores, I and II (see text). *Green beads*, polar residues; *yellow beads*, hydrophobic residues; *red beads*, acid residues; *blue beads*, basic residues; *white beads*, paclitaxel bound at its site; *grey beads*, nucleotide. Detail of a pore type I viewed from above (**c**). Ribbon representation of two neighbour β-tubulin subunits as seen from the plus end of the microtubule, paclitaxel, GDP and the four residues forming a putative taxoid binding site are shown in Van der Waals representation. Taken from [22]

The kinetic information can be used as well to deduce if a compound is bound homogeneously or not. The kinetics of flutax and paclitaxel dissociation from β-tublin are monophasic, which indicates a single rate limiting step, consistent with most of the compound bound to the same site. However, dissociation of Epothilone A from the binding site shows biphasic behaviour, which would be consistent with the compound distributed between the external and the luminal site, with a temperature-dependant equilibrium (Table 2) which favours the outer site at higher temperatures.

Table 2 Kinetic rates of epothilone A dissociation[a]

	25°C	30°C	35°C	37°C	40°C
$k_{fast}s^{-1}$	ND	ND	0.445	0.463	0.635
A_{fast}	ND	ND	0.25	0.35	0.38
$k_{slow}s^{-1}$	0.020	0.052	0.126	0.138	0.199
A_{slow}	1	1	0.74	0.65	0.62

k_{fast} – apparent kinetic rate constant of the fast phase
A_{fast} – amplitude of the fast phase
K_{slow} – apparent kinetic rate constant of the slow phase
A_{slow} – amplitude of the slow phase
[a] Determined for this work as described in [44]

From the kinetics of ligand binding to microtubules we can obtain valuable information about the way paclitaxel microtubule stabilizing agents reach their binding site. They bind to an external binding site located in the pores of the microtubule wall from which they are totally or partially relocated to an inner luminal site.

3 The Bioactive Conformations of MSA. What Do They Look Like When Bound?

Many attempts have been made over the last years to deduce the actual pharmacophore/s for the recognition of MSA by microtubules. For newly designed MSA to serve as effective anticancer drugs, it seems reasonable that they should be able to achieve a conformation compatible with the binding pocket of the target protein. On this basis, many scientists have focused on determining the bioactive conformation of the different MSAs.

3.1 Paclitaxel and Related Molecules. The Single Conformer Hypothesis

The study of the tubulin-bound conformation of paclitaxel has resulted in a number of protein-ligand models, partially or fully based on the electron diffraction structure of αβ-tubulin in paclitaxel-stabilized Zn^{2+}-induced sheets [5, 12]. Obviously, the nature of the paclitaxel binding site and the paclitaxel conformation in the binding site have key implications for the design of new MSA. A deep knowledge of the bioactive conformation would also help to explain how compounds as structurally diverse as the epothilones [48], discodermolide [49], and eleutherobin [50] have very similar mechanisms of action.

After the first photoaffinity labelling studies, which were the first methods used to define the paclitaxel binding site on tubulin, and indeed allowed identification of different amino acids of β-tubulin as putative parts of the binding site [51], the initial efforts to correlate activity (or binding) with the solid state, solution or modelled conformations of MSA in their free states led to the first pharmacophore proposals

[52]. At first, the existence of only a very limited set of conformations for these molecules was assumed [53], while more recently, it was considered that most of these molecules are intrinsically flexible and may assume a variety of shapes [54].

Previous investigations on this topic up to the beginning of 2002 have already been reviewed [55] and further expanded more recently [56], gathering the knowledge of the conformation of these molecules under different conditions. Up to 2001, also corresponding to the availability of the αβ-tubulin coordinates from the electron crystallography structure [5, 12], the attempts to codify the bound conformation of MSA were derived from ligand conformations acquired in the free state by either X-ray crystallography or NMR studies. An assumed or modelled bioactive form was then employed as a template for superimposition by other ligands to try to deduce the pharmacophore [57].

After the availability of the 3.7Å resolution electron crystallographic structure of paclitaxel bound to αβ-tubulin [5], further refined at 3.5Å resolution [12], different research groups tried to probe the binding conformation of MSA at the key β-subunit. Nevertheless, although paclitaxel indeed stabilized the actual microtubule sheets examined by electron crystallography, the first coordinates of tubulin deposited (1TUB) contained the single crystal coordinates for docetaxel [58] instead of the actual ligand, due to problems to characterize fully either the binding mode or the conformation of bound paclitaxel. On this basis, only qualitative statements could first be made concerning the details of ligand binding. Nonetheless, the location of the drug was consistent with the former photoaffinity labelling results and showed that paclitaxel occupied a hydrophobic cleft on β-tubulin. Furthermore, the ligand density suggested that one of the phenyl rings at the C-3′ terminus was near the top of helix H1, while the C-2 benzoyl moiety was close to H5 and to the H5–H6 loop. In the refined structure (1JFF) [12], the taxane ring was better defined, but the densities for both the 2-phenyl side-chain and the *N*′-phenyl group still remained low, suggesting certain mobility of these groups. Nevertheless, according to the authors, the refined paclitaxel structure adopted a geometry very similar to that determined independently by energy-based refinement [59], except for the key torsional rotations of the side-chain phenyl rings. We will return to this point below.

Before these investigations, most of the models of the paclitaxel-tubulin interaction had been directly extrapolated from the conformations of paclitaxel found either in polar [60] or non-polar media [61] and from the single crystal X-ray structure of docetaxel (Fig. 10a) [58].

3.2 Paclitaxel and Related Molecules. Flexibility

Indeed, before 2000, single conformers had been basically considered, although it was possible that the multiple torsional degrees of freedom of these molecules would produce a complex multidimensional energy surface, and therefore a variety of putative 3D geometries capable of interacting with the tubulin binding site [62, 63]. Numerous research teams pursued different indirect approaches to the pharmacophore

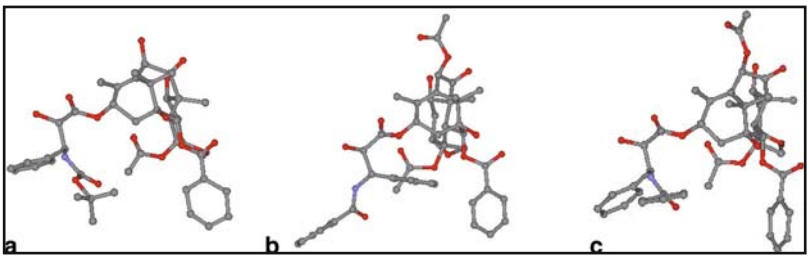

Fig. 10 **a** X-ray structure of docetaxel [58]. **b** Polar conformer of paclitaxel. **c** T-Taxol conformer

determination. The first and earliest attempts relied on studies of the structure–activity relationship of the taxane skeleton [52–54, 64] which included quantitative calculations [53]. These studies demonstrated that the presence and the spatial disposition of the three flexible side chains at C-4, C-2 and C-13 defined the conformations proposed or determined in both solution, in the solid state and at the β-tubulin binding site, since the baccatin core (A–D rings) was conformationally well-defined [65].

A more complete structure-based approach used (bio-)physical methods, in particular X-ray, NMR spectroscopy and/or molecular modelling, to study the structure and conformations of paclitaxel in its uncomplexed state, trying to extrapolate these findings to the bound form. Single crystal X-ray analysis in the solid state defined different conformers for different analogues [66], while NMR analysis in polar and non-polar media indeed identified others [67–73]. In all cases, these reports assumed a major single conformation, although later Snyder's group, through deconvolution of the NMR data obtained for paclitaxel in $CDCl_3$ [62] and D_2O/DMSO-d_6 [100] solutions, identified many (9–10) conformations in these solvents, none of them showing a population above 30%. Nevertheless, the structural details from NMR were interpreted in terms of the key features of the dominant conformations: the NOE data in polar solvents showed that, to some extent, the C-3′ phenyl group is hydrophobically collapsed with the C-2 benzoyl phenyl (the "polar" conformer, Fig. 10b), while in non-polar solvents the data evidenced an analogous phenyl–phenyl association between the C-3′ benzamido phenyl and the one at the terminus of the C-2 side chain (the "nonpolar" conformer) [52–54, 57, 74, 75]. As previously reviewed [55], both the polar and the nonpolar conformations were proposed as the bioactive forms. It was also speculated that an eclipsed conformer related to the polar form could be the one recognized by the tubulin binding site [75].

3.3 Synthetic Analogues. Quest for the Actual Bioactive Geometry

These interpretations prompted many organic chemists to prepare synthetic analogues, bridging different regions of the paclitaxel molecule, aimed at locking or at least favouring the putative bioactive conformation of paclitaxel on tubulin

(see below for further discussion) [56, 76]. Wide discussion and controversy among different groups has been established on the bioactive three-dimensional form of paclitaxel. In a first REDOR NMR study, F-^{13}C distances between the fluorine of a 2-(*p*-fluorobenzoyl) paclitaxel and both the C-3′ amide carbonyl and C-3′ methine carbons were estimated [77], permitting a serious attempt to determine key aspects of the ligand conformation at the β-tubulin binding site [78]. Complementary measurements of fluorescence-resonance energy transfer suggested a model for the paclitaxel binding mode. In a second study, a distance of 6.5Å was determined between the fluorine atoms of 2-(*p*-fluorobenzoyl)-3′-(*p*-fluorophenyl)-10-acetyldocetaxel [79]. Recent studies using a variety of fluorinated and deuterated analogues, also using REDOR [80] have led the authors of this investigation to conclude that the bound form is in agreement with the so-called T-Taxol geometry (see below) [59, 81], and not with other REDOR-based geometry proposed by another research group, dubbing New York (NY-Taxol) [78].

3.4 The T-Taxol Conformer

Computational studies have been of paramount importance in order to integrate the results of the experimental studies indicated above with the electron crystallographic data known. According to Snyder and co-workers, a satisfactory and experimentally verifiable model of the tubulin-binding site and of the conformation of paclitaxel has been obtained by computational methods on the first electron crystallographic model. In this context, a new paclitaxel conformer, T-Taxol (Fig. 10c), was proposed [59, 81, 82].

Further refinement of the electron crystallographic structure of tubulin-paclitaxel at 3.5Å resolution delivered a similar result. Nevertheless, the T-Taxol model has not been completely accepted as the actual bioactive conformation [78]. It is evident that the low 3.5–3.7Å resolution of the complex limits the precision of the resulting model. In addition, the Zn^{2+}-stabilized tubulin preparation employed in the electron crystallographic study involves antiparallel protofilaments organized in sheets, which strongly differ from genuine microtubules. Consequently, concern has been expressed that the sheets may not be representative of cellular microtubules and that sheet-bound paclitaxel geometry may differ from its bioactive form in microtubules.

In this context, using the different models as templates, different synthetic organic chemistry groups have prepared cyclic, conformationally-constrained analogues based on the T-Taxol structure, leading to molecules with potencies similar or even greater than the lead structure [56, 76, 78, 83]. Different research groups have introduced constraints into the paclitaxel molecule involving the C-4, C-2 and C-13 side chains. Interestingly, it has been reported that forming a tether between the C-4 acetate methyl and the *ortho*- center of the C-3′ phenyl, in agreement with the proposed T-Taxol conformation, permits the access to compounds with much better activities (3-, 30- or 50-fold) than the activity of paclitaxel, even when tested

against both paclitaxel- and epothilone-resistant cell lines. It has been proposed that the origin of the bioactivities is related to the degree of rigidification introduced by the C-4–C-3′ bridging moieties. While for paclitaxel, the T-form was estimated to be present in only 2–5% of the variety of conformations [59, 83], the key constrained compounds appeared with 76 and 86% contributions from T-Taxol-like geometries. Nevertheless, the authors have also warned that the significant activity increases measured for these substances could not be attributed completely to conformational biasing, although it seems to be a dominating factor. Indeed, they proposed that reinforcing the T-Taxol conformation is a necessary but not sufficient condition to elicit high levels of drug potency [83]. Especially, in addition to the appropriate molecular conformation, the ligand must also show a tubulin-compatible molecular volume.

3.5 Epothilones. Different Geometries are Found Under Different Experimental Conditions

As for all MSAs, the investigation of the complex of epothilones [57] with tubulin has also been attempted. The solid state (deduced by either X-ray or solid state NMR) structure of free epothilone B is known, as well as its conformations in organic solvents [84–86]. However, its actual bioactive conformation is also a matter of debate.

For the free state, the major conformation of the macrocycle in solution is similar to that found in the crystal, although there was no preferred conformation of the thiazole side chain, which showed a substantial freedom of the side chain around the C17–C18 bond.

In contrast, approach to the structure determination by solid-state NMR [86], has proposed a more defined geometry of both the macrocycle and the side chain. In fact, the 10 solid-state NMR structures derived were very well defined, while the average RMSD of the heavy atom to the X-ray structure was only 0.75Å. When comparing assignments of the solid-state NMR with the previously reported solution-state NMR data [84], a qualitative correlation was found between the chemical-shift variations observed and the possibility of intermolecular hydrogen-bonding [86].

The first study of the bioactive conformation of epothilones was conducted through solution-state NMR for epothilone A, which lacks the methyl group at C12, bound to non-microtubular αβ-tubulin [38, 87]. Almost immediately, the tubulin/epothilone A complex was studied through electron-crystallography for Zn^{2+}-stabilized αβ-tubulin layers [88]. The conformation of the tubulin-bound epothilone was strikingly different in the two studies, suggesting the need for further investigation. As this discrepancy may reflect the dependence of the epothilone binding mode on the tubulin polymerization state, further studies are still expected.

From the viewpoint of NMR, the existence of specific and transient binding of epothilone A to non-microtubular tubulin enabled the structural analysis of the active conformation [38, 87] of the epothilones by using trNOESY experiments, in

particular, using the interligand NOE for pharmacophore mapping (INPHARMA) methodology [89] and molecular modeling.

For the NMR structural investigation of the epothilone-tubulin complex in solution, microtubule assembly was prevented. Evident conformational differences were observed between the X-ray crystal structure and the tubulin-bound NMR conformation of epothilone A. However, the authors rationalized many structure-activity relationship data available on the tubulin-polymerization activity of several epothilone derivatives [90]. According to these authors, the electron crystallography-derived model [88] of the epothilone A-tubulin complex did not support some of the structure activity relationship data. Nevertheless, as also stated in [89], the high flexibility of the M loop, the S9–S10 loop, and the H6–H7 loop forming the binding pocket could be responsible for different binding modes of epothilone A to tubulin, depending on the polymerization state.

Although, according to the NMR analysis in non-polar solvents [84], the most populated conformer is indeed very similar to the X-ray conformer, evidences of other conformers are also clearly observed in the NMR data in solution for the free state. The comparison of the torsion angles of epothilone A in the tubulin-bound and in the free conformation revealed two major changes: the first occurred in the O1–C6 region, while the second affected the orientation of the thiazole ring respect to the C16–C17 double bond. Neither the C6–C7 dihedral angle, nor the C10–C15 region exhibited significant conformational changes upon binding to tubulin. The most significant difference between the free and tubulin-bound conformations of epothilone occurred in the side chain with the thiazole ring. In the geometry of the bound conformation, the nitrogen atom of the thiazole ring becomes more accessible for potential formation of hydrogen bonds with the protein, which may more than offset the deduced high-energy epothilone side-chain conformation. The design of epothilone analogues should now use the knowledge about the conformation of epothilone in its tubulin-bound state.

3.6 Discodermolide and Dictyostatin. The Free and Bound Conformers

An elegant recent work by Carlomagno et al. [91] has reported a non-microtubular-tubulin-bound conformation of discodermolide. Since the conditions in which the discodermolide conformation was determined tubulin is not assembled into microtubules, it might be possible that the tubulin-bound conformation observed therein [91] is not identical to the conformation bound to microtubules. Nevertheless, under these experimental conditions, the tubulin-bound conformation of discodermolide in solution from NMR tr-NOE data is a compact globular shape. With the help of both protein-mediated interligand NOE signals between discodermolide and Epothilone [91] and the SAR data available for the two drugs, a common pharmacophore model was proposed. Similarities and differences in the pharmacophore of the two drugs may provide a rationale for the analogous but not fully equivalent

biological activities of the two natural products. Also, the similarity between the tubulin-bound conformation of discodermolide and its X-ray structure [92] provides a rationale for the powerful biological activity of the marine natural product dictyostatin, a 22-membered macrocyclic lactone which is structurally and biogenetically related to discodermolide. Not surprisingly, the tubulin-bound conformation of discodermolide derived therein [91] was closely related to the solution structure of dictyostatin [93], which supports a common mechanism for the MT-stabilizing activity of the two compounds.

A variety of NMR data, including trNOESY/STD, line broadening analysis, and STD-based NMR competition experiments, assisted by molecular mechanics calculations, have also been recently employed to deduce the microtubule-bound conformation of the previously mentioned two MSA, discodermolide and dictyostatin [94] Since it is well known that tubulin in plain phosphate buffer does not assemble into microtubules, and it has been described that the microtubule taxoid binding site does not exist in dimeric tubulin, at least with an affinity higher than millimolar, we rather preferred to search for biochemical conditions in which stable microtubules were assembled from native tubulin with GMPCPP [27]. The NMR data obtained indicated that microtubules recognize discodermolide through a conformational selection process, in which the half-chair conformer (and not the predominant in water solution, skew boat form) of the lactone moiety is bound by the receptor. There are minor changes in the rest of the molecular skeleton between the major conformer in water solution and that bound to assembled microtubules. Indeed, despite the many torsional degrees of freedom of discodermolide, intramolecular interactions within the molecule and hydration strongly affect its conformational features, which indeed only shows conformational mobility around a fairly narrow part of the molecule. This evidence contrasts strongly with the observations on other solvents, in which discodermolide shows different degrees of flexibility. Therefore, while in acetonitrile [95] or dimethyl sulfoxide [96], the different torsional degrees of freedom of discodermolide show different flexibilities, the orientation of the C5–C24 chain is highly pre-organized in water solution [94] with respect to that bound by tubulin, probably to minimize entropic penalties. There are some slight changes in the deduced microtubules-bound conformation with respect to that described by Carlomagno et al. using non-assembled tubulin (Fig. 11). The structure provided by Carlomagno et al. [91] shows a chair for the six-membered ring and its orientation is different from the rest of the chain. In any case, the presentation of the molecule is remarkably similar, despite the change in the mode of preparation of tubulin in the two cases. In particular, van der Waals contacts and torsional constraints strongly bias its conformational behaviour. Yet this feature serves to modulate the presentation of polar and non-polar surfaces to interact with the binding site of tubulin. A model of the binding mode of discodermolide to tubulin has also been proposed, involving the β-tubulin monomer by using docking simulations [94]. This model involves the taxane binding site of tubulin and comprises both polar and non polar interactions between discodermolide and the receptor.

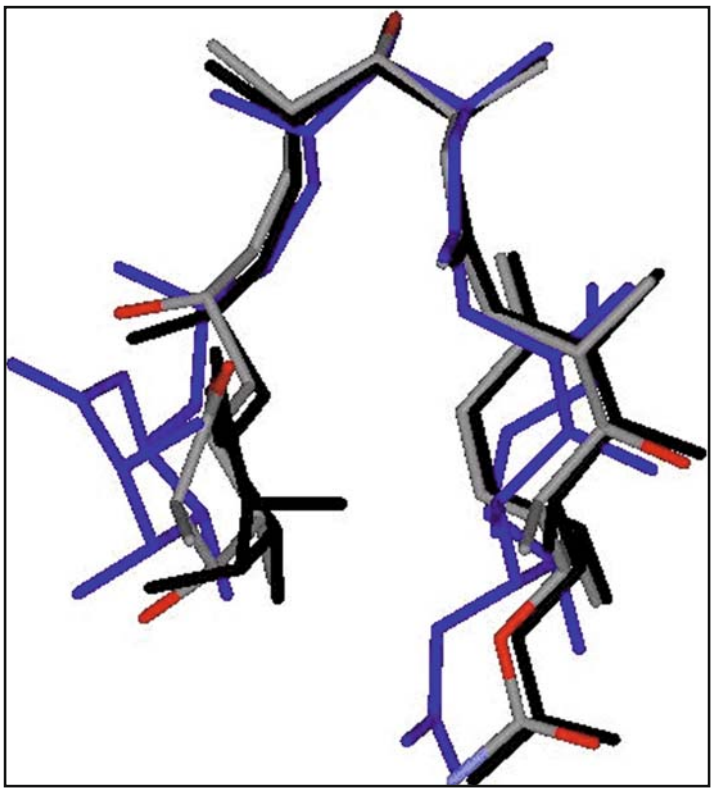

Fig. 11 Superimposition of the X-ray structure of discodermolide (*black*) [92], bound to non-assembled tubulin (*blue*) [91] and bound to microtubules [94]. Minor adjustments are observed

The microtubule-bound conformation of an analogous MSA, dictyostatin, has also been derived by using the same combined protocol of NMR spectroscopy and molecular docking [94]. The bound geometry deduced (Fig. 12) presents some key conformational differences against the major one existing in solution [97] around torsion angles at the C-7 region, and additionally displays mobility (even when bound) along the lateral C22–C26 chain. In any case, the bound conformer of dictyostatin resembles that of discodermolide and provides very similar contacts with the receptor. Competition experiments with a paclitaxel bindig site ligand (Baccatin III [11]) have indicated that both molecules compete with the taxane-binding site, providing further support to previously described biochemical data.

3.7 Peluroside A

Peluroside A bound to microtubules has also been investigated. Two low energy conformations of Peloruside A have been found in water solution [27], which

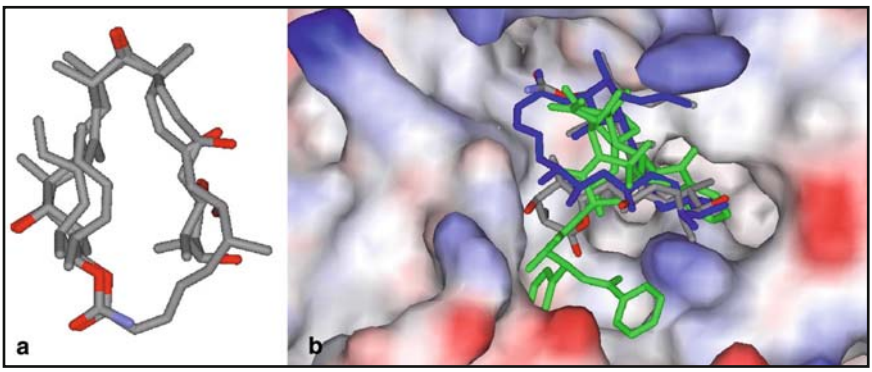

Fig. 12 **a** Superimposition of the bound conformers of discodermolide and dictyostatin bound to assembled microtubules [94]. **b** AUTODOCK solution of discodermolide and dictyostatin (*blue*) bound to tubulin (1JFF), also compared with bound paclitaxel (*green*)

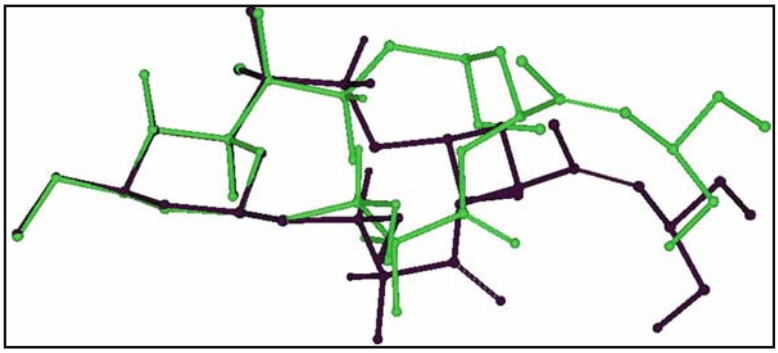

Fig. 13 Superimposition of the two major conformers of Peluroside A coexisting in water solution [27]

mainly differ in the relative orientation of the C10–C15 region (Fig. 13). One of these geometries (A) is in agreement with that postulated for Peloruside A in chloroform solution [98, 99]. From the viewpoint of energy, and using MM3*, the new conformer (B) is more stable than A. The major energy component that stabilizes B is solvation energy. Nevertheless, according to molecular dynamics simulations, both conformers are flexible along the backbone, with somehow higher variations for the lateral chain. Nevertheless, despite the large size of the macrocyclic ring, intramolecular interactions (van der Waals contacts and torsional constraints) within the Peloruside A ring strongly affect the conformational features of this molecule, which indeed only shows conformational mobility around a fairly narrow part of the molecule. Yet, this existing conformational freedom, in the presence of a given solvent, serves to modulate the presentation of polar and nonpolar surfaces to interact with the binding site.

Peluroside A was the first microtubule stabilizing agent whose conformation has been determined bound to microtubules (those of Paclitaxel and Epothilone were determined in non-microtubular tubulin [5, 12, 38, 91]). In the bound state, the NMR data, assisted by molecular mechanics calculations and docking experiments, indicated that only one (that present in water, B) of the two major conformations existing in water solution is bound to microtubules (α-tubulin). A model of the binding mode to tubulin has also been proposed [27], involving the α-tubulin monomer, in contrast with paclitaxel, which binds to the β-monomer.

It can be expected that the near future will provide tubulin-ligand structures with sufficient accuracy to define precisely the conformation and binding mode for these compounds and thereby validate or reject the current set of models. For the time being, the methodologies schematically reviewed here may provide additional data for understanding the action of MSAs and hopefully to design new potent analogues.

Note added in proof: Recently, taxane binding to microtubules has been optimized by affinity dissection and incremental construction o high affinity analogues of paclitaxel which are not affected by multidrug resistance in P-glycoprotein overexpressing cells [101]. The conformational preferences of epothilone A and C3-modified derivatives in aqueous solution have been found to include the previously proposed bioactive conformation bound to non-microtubular tubulin [102]. A different site of peloruside binding in beta-tubulin has been proposed from hydrogen-deuterium exchange and data-directed molecular docking [103]

References

1. Jordan MA, Wilson L (2004) Nat Rev Cancer 4:253
2. Weisenberg RC, Borisy GG, Taylor EW (1968) Biochemistry 7:4466
3. Ravelli RB, Gigant B, Curmi PA, Jourdain I, Lachkar S, Sobel A, Knossow M (2004) Nature 428:198
4. Gigant B, Wang C, Ravelli RB, Roussi F, Steinmetz MO, Curmi PA, Sobel A, Knossow M (2005) Nature 435:519
5. Nogales E, Wolf SG, Downing KH (1998) Nature 391:199
6. Schiff PB, Fant J, Horwitz SB (1979) Nature 277:665
7. Wall ME, Wani MC (1995) Cancer Res 55:753
8. Souto AA, Acuña AU, Andreu JM, Barasoain I, Abal M, Amat-Guerri F (1996) Angew Chem Int Ed Engl 34:2710
9. Evangelio JA, Abal M, Barasoain I, Souto AA, Lillo MP, Acuña AU, Amat-Guerri F, Andreu JM (1998) Cell Motil Cytoskeleton 39:73
10. Díaz JF, Strobe R, Engelborghs Y, Souto AA, Andreu JM (2000) J Biol Chem 275:26265
11. Andreu JM, Barasoain I (2001) Biochemistry 40:11975
12. Lowe J, Li H, Downing KH, Nogales E (2001) J Mol Biol 313:1045
13. Lowe J, Amos LA (1998) Nature 391:203
14. Huecas S, Llorca O, Boskovic J, Martín-Benito J, Valpuesta JM, Andreu JM (2008) Energetics and geometry of FtsZ polymers: nucleated self-assembly of single protofilaments. Biophys J 94, 1798
15. Wyman J, Gill SJ (1990) Binding and linkage. University Science Books, Mill Valley, CA

16. Menéndez M, Rivas G, Díaz JF, Andreu JM (1998) J Biol Chem 273:167
17. Pommier Y, Cherfils J (2005) Trends Pharmacol Sci 26:138
18. Andreu JM, Bordas J, Díaz JF, Garcia de Ancos J, Gil R, Medrano FJ, Nogales E, Pantos E, Towns-Andrews E (1992) J Mol Biol 226:169
19. Andreu JM, Díaz JF, Gil R, de Pereda JM, Garcia de Lacoba M, Peyrot V, Briand C, Towns-Andrews E, Bordas J (1994) J Biol Chem 269:31785
20. Buey RM, Barasoain I, Jackson E, Meyer A, Giannakakou P, Paterson I, Mooberry S, Andreu JM, Díaz JF (2005) Chem Biol 12:1269
21. Buey RM, Calvo E, Barasoain I, Pineda O, Edler MC, Matesanz R, Cerezo G, Vanderwal CD, Day BW, Sorensen EJ, Lopez JA, Andreu JM, Hamel E, Díaz JF (2007) Nat Chem Biol 3:117
22. Díaz JF, Barasoain I, Andreu JM (2003) J Biol Chem 278:8407
23. Díaz JF, Barasoain I, Souto AA, Amat-Guerri F, Andreu JM (2005) J Biol Chem 280:3928
24. Pryor DE, O'Brate A, Bilcer G, Diaz JF, Wang Y, Kabaki M, Jung MK, Andreu JM, Ghosh AK, Giannakakou P, Hamel E (2002) Biochemistry 41:9109
25. Gaitanos TN, Buey RM, Díaz JF, Northcote PT, Teesdale-Spittle P, Andreu JM, Miller JH (2004) Cancer Res 64:5063
26. Pineda O, Farras J, Maccari L, Manetti F, Botta M, Vilarrasa J (2004) Bioorg Med Chem Lett 14:4825
27. Jimenez-Barbero J, Canales A, Northcote PT, Buey RM, Andreu JM, Diaz JF (2006) J Am Chem Soc 128:8757
28. Dye RB, Fink SP, Williams RC (1993) J Biol Chem 268:6847
29. Elie-Caille C, Severin F, Helenius J, Howard J, Muller DJ, Hyman AA (2007) Current Biology 17:1765
30. Klein LE, Freeze BS, Smith AB, Horwitz SB (2005) Cell Cycle 4:501
31. Amos LA, Lowe J (1999) Chem Biol 6:R65
32. Li H, DeRosier DJ, Nicholson WV, Nogales E, Downing KH (2002) Structure (Camb) 10:1317
33. Díaz JF, Menéndez M, Andreu JM (1993) Biochemistry 32:10067
34. Oosawa F, Asakura S (1975) Thermodynamics of the polymerization of protein,. Academic, London
35. Díaz JF, Andreu JM (1993) Biochemistry 32:2747
36. Buey RM, Díaz JF, Andreu JM, O'Brate A, Giannakakou P, Nicolaou KC, Sasmal PK, Ritzen A, Namoto K (2004) Chem Biol 11:225
37. Edler MC, Buey RM, Gussio R, Marcus AI, Vanderwal CD, Sorensen EJ, Díaz JF, Giannakakou P, Hamel E (2005) Biochemistry 44:11525
38. Carlomagno T, Blommers MJ, Meiler J, Jahnke W, Schupp T, Petersen F, Schinzer D, Altmann KH, Griesinger C (2003) Angew Chem Int Ed Engl 42:2511
39. Yang C, Barasoain I, Li X, Matesanz R, Liu R, Sharom FJ, Díaz JF, Fang W (2007) Chem Med Chem 2:691
40. Schiff PB, Horwitz SB (1981) Biochemistry 20:3247
41. Díaz JF, Valpuesta JM, Chacón P, Diakun G, Andreu JM (1998) J Biol Chem 273:33803
42. Nogales E, Wolf SG, Khan IA, Luduena RF, Downing KH (1995) Nature 375:424
43. Nogales E, Whittaker M, Milligan RA, Downing KH (1999) Cell 96:79
44. Díaz JF, Buey RM (2007) In: Zhou J (ed) Methods in molecular medicine, vol 137. Humana, Totowa, NJ p 245
45. Giannakakou P, Sackett DL, Kang YK, Zhan Z, Buters JT, Fojo T, Poruchynsky MS (1997) J Biol Chem 272:17118
46. Sato B, Muramatsu H, Miyauchi M, Hori Y, Takase S, Hino M, Hashimoto S, Terano H (2000) J Antibiot (Tokyo) 53:123
47. Sato B, Nakajima H, Hori Y, Hino M, Hashimoto S, Terano H (2000) J Antibiot (Tokyo) 53:204
48. Nicolaou KC, Roschangar F, Vourloumis D (1998) Angew Chem Int Ed Engl 37:2015
49. Kalesse M (2000) Chembiochem 1:171
50. Lindel T, Jensen PR, Fenical W, Long BH, Casazza AM, Carboni J, Fairchild CR (1997) J Am Chem Soc 119:8744
51. Rao S, He LF, Chakravarty S, Ojima I, Orr GA, Horwitz SB (1999) J Biol Chem 274:37990
52. Czaplinski KHA, Grunewald GL (1994) Bioorg Med Chem Lett 4:2211

53. Morita H, Gonda A, Wei L, Takeya K, Itokawa H (1997) Bioorg Med Chem Lett 7:2387
54. Wang M, Xia X, Kim Y, Hwang D, Jansen JM, Botta M, Liotta DC, Snyder JP (1999) Org Lett 1:43
55. Jiménez-Barbero J, Amat-Guerri F, Snyder JP (2002) Curr Med Chem Anti-Canc Agents 2:91
56. Kingston DGI, Bane S, Snyder JP (2005) Cell Cycle 4:279
57. Giannakakou P, Gussio R, Nogales E, Downing KH, Zaharevitz D, Bollbuck B, Poy G, Sackett D, Nicolaou KC, Fojo T (2000) Proc Natl Acad Sci USA 97:2904
58. Gueritte-Voegelein F, Guenard D, Mangatal L, Potier P, Guilhem J, Cesario M, Pascard C (1990) Acta Cryst C 46:781
59. Snyder JP, Nettles JH, Cornett B, Downing KH, Nogales E (2001) Proc Natl Acad Sci USA 98:5312
60. Vandervelde DG, Georg GI, Grunewald GL, Gunn GW, Mitscher LA (1993) J Am Chem Soc 115:11650
61. Williams HJ, Scott AI, Dieden RA, Swindell CS, Chirlian LE, Francl MM, Heerding JM, Krauss NE (1994) Can J Chem 72:252
62. Snyder JP, Nevins N, Cicero DO, Jasen J (2000) J Am Chem Soc 122:724
63. Johnson SA, Alcaraz AA, Snyder JP (2005) Org Lett 7:5549
64. Zhu QQ, Guo ZR, Huang N, Wang MM, Chu FM (1997) J Med Chem 40:4319
65. Moyna G, Williams HJ, Scott AI, Ringel I, Gorodetsky R, Swindell CS (1997) J Med Chem 40:3305
66. Mastropaolo D, Camerman A, Luo YG, Brayer GD, Camerman N (1995) Proc Natl Acad Sci USA 92:6920
67. Gómez Paloma L, Guy RK, Wrasidlo W, Nicolaou KC (1994) Chem Biol 1:107
68. Dubois J, Guenard D, Gueritte-Voegelein F, Guedira N, Potier P, Gillet B, Beloeil JC (1993) Tetrahedron 49:6533
69. Cachau RE, Gussio R, Beutler JA, Chmurny GN, Hilton BD, Muschik GM, Erickson JW (1994) Int J Supercomput Appl High Perform Comput8:24
70. Boge TC, Himes RH, Vandervelde DG, Georg GI (1994) J Med Chem 37:3337
71. Ojima I, Kuduk SD, Chakravarty S, Ourevitch M, Begue JP (1997) J Am Chem Soc 119:5519
72. Georg GI, Harriman GCB, Hepperle M, Clowers JS, VanderVelde DG, Himes RH (1996) J Org Chem 61:2664
73. Jiménez-Barbero J, Souto AA, Abal M, Barasoain I, Evangelio JA, Acuña AU, Andreu JM, Amat-Guerri F (1998) Bioorg Med Chem 6:1857
74. Ojima I, Chakravarty S, Inoue T, Lin S, He L, Horwitz SB, Kuduk SD, Danishefsky SJ (1999) Proc Natl Acad Sci USA 96:4256
75. Magnani M, Ortuso F, Soro S, Alcaro S, Tramontano A, Botta M (2006) Febs J 273:3301
76. Shanker N, Kingston DGI, Ganesh T, Yang C, Alcaraz AA, Geballe MT, Banerjee A, McGee D, Snyder JP, Bane S (2007) Biochemistry 46:11514
77. Li YK, Poliks B, Cegelski L, Poliks M, Gryczynski Z, Piszczek G, Jagtap PG, Studelska DR, Kingston DGI, Schaefer J, Bane S (2000) Biochemistry 39:281
78. Geney R, Sun L, Pera P, Bernacki RJ, Xia SJ, Horwitz SB, Simmerling CL, Ojima I (2005) Chem Biol 12:339
79. Ojima I, Inoue T, Chakravarty S (1999) J Fluorine Chem 97:3
80. Paik Y, Yang C, Metaferia B, Tang SB, Bane S, Ravindra R, Shanker N, Alcaraz AA, Johnson SA, Schaefer J, O'Connor RD, Cegelski L, Snyder JP, Kingston DGI (2007) J Am Chem Soc 129:361
81. Alcaraz AA, Mehta AK, Johnson SA, Snyder JP (2006) J Med Chem 49:2478
82. Ganesh T, Guza RC, Bane S, Ravindra R, Shanker N, Lakdawala AS, Snyder JP, Kingston DGI (2004) Proc Natl Acad Sci USA 101:10006
83. Ganesh T, Yang C, Norris A, Glass T, Bane S, Ravindra R, Banerjee A, Metaferia B, Thomas SL, Giannakakou P, Alcaraz AA, Lakdawala AS, Snyder JP, Kingston DGI (2007) J Med Chem 50:713
84. Höfle G, Bedorf N, Steinmetz H, Schomburg D, Gerth K, Reichenbach H (1996) Angew Chem Int Ed Engl 35:1567

85. Taylor RE, Zajicek J (1999) J Org Chem 64:7224
86. Lange A, Schupp T, Petersen F, Carlomagno T, Baldus M (2007) Chemmedchem 2:522
87. Carlomagno T, Sanchez VM, Blommers MJ, Griesinger C (2003) Angew Chem Int Ed Engl 42:2515
88. Nettles JH, Li H, Cornett B, Krahn JM, Snyder JP, Downing KH (2004) Science 305:866
89. Reese M, Sanchez-Pedregal VM, Kubicek K, Meiler J, Blommers MJJ, Griesinger C, Carlomagno T (2007) Angew Chem Int Ed Engl 46:1864
90. Nicolaou KC, Scarpelli R, Bollbuck B, Werschkun B, Pereira MMA, Wartmann M, Altmann KH, Zaharevitz D, Gussio R, Giannakakou P (2000) Chem Biol 7:593
91. Sanchez-Pedregal VM, Kubicek K, Meiler J, Lyothier I, Paterson I, Carlomagno T (2006) Angew Chem Int Ed Engl 45:7388
92. Gunasekera SP, Gunasekera M, Longley RE, Schulte GK (1990) J Org Chem 55:4912
93. Paterson I, Britton R, Delgado O, Meyer A, Poullennec KG (2004) Angew Chem Int Ed Engl 43:4629
94. Canales A, Matesanz R, Gardner NM, Andreu JM, Paterson I, Díaz JF, Jiménez-Barbero J (2008) The bound conformation of microtubule-stabilizing agents (II): NMR insights on the bioactive 3D structure of discodermolide and dictyostatin. Chemistry (DOI: 10.1002/chem.200800039)
95. Smith AB III, LaMarche MJ, Falcone-Hindley M (2001) Org Lett 3:695
96. Monteagudo E, Cicero DO, Cornett B, Myles DC, Snyder JP (2001) J Am Chem Soc 123:6929
97. Paterson I, Britton R, Delgado O, Wright AE (2004) Chem Commun (Camb):632
98. West LM, Northcote PT, Battershill CN (2000) J Org Chem 65:445
99. Liao XB, Wu YS, De Brabander JK (2003) Angew Chem Int Ed Engl 42:1648
100. Snyder JP, Nevins N, Jímenez-Barbero J, Cicero D, Jansen JM. Unpublished
101. Matesanz R, Barasoain I, Yang CG, Wang L, Li X, de Inés C, Coderch C, Gago F, Barbero JJ, Andreu JM, Fang WS, Díaz JF. (2008) Chem Biol.15:573
102. Erdélyi M, Pfeiffer B, Hauenstein K, Fohrer J, Gertsch J, Altmann KH, Carlomagno T. (2008) J Med Chem. 51:1469
103. Huzil JT, Chik JK, Slysz GW, Freedman H, Tuszynski J, Taylor RE, Sackett DL, Schriemer DC. (2008) J Mol Biol. 378:1016

Top Curr Chem (2009) 286: 151–208
DOI: 10.1007/128_2008_22

Published online: 18 November 2008

The Tubulin Binding Mode of MT Stabilizing and Destabilizing Agents Studied by NMR

Víctor M. Sánchez-Pedregal and Christian Griesinger

Abstract Tubulin is a fascinating molecule that forms the cytoskeleton of the cells and plays an important role in cell division and trafficking of molecules. It polymerizes and depolymerizes in order to fulfill this biological function. This function can be modulated by small molecules that interfere with the polymerization or the depolymerization. In this article, the structural basis of this behavior is reviewed with special attention to the contribution of NMR spectroscopy. Complex structures of small molecules that bind to tubulin and microtubules will be discussed. Many of them have been determined using NMR spectroscopy, which proves to be an important method in tubulin research.

Keywords Bioactive conformation, Drug-target complex, NMR, Tubulin, Structure

Contents

V.M. Sánchez-Pedregal
Departamento de Química Orgánica, Facultad de Química, Universidad de Santiago de Compostela. Campus Universitario Sur, s/n, 15782 Santiago de Compostela, Spain

C. Griesinger (✉)
Abteilung für NMR-basierte Strukturbiologic, Max Planck Institute for Biophysical Chemistry. Am Faßberg 11, 37077 Göttingen, Germany
e-mail: cigr@nmr.mpibpc.mpg.de

Abbreviations

2D	two-dimensional
3D	three-dimensional
BSA	bovine serum albumin
C19-BPC-DDM	C19-[4-(4-^{3}H-benzoyl-phenyl)-carbamate]-discodermolide
CCR	cross-correlated relaxation
CSA	chemical shift anisotropy
DDM	discodermolide
DFT	density functional theory
DMAT	*N*-debenzoyl-*N*-[3-(dimethylamino) benzoyl]paclitaxel
DTX	docetaxel (taxotere)
EC	electron crystallography
Epo	epothilones
EpoA	epothilone A
EpoB	epothilone B
FRM	full relaxation matrix
GMPCPP	guanylyl-(α,β)-methylene-diphosphonate
HTI-286	taltobulin I (analogue of hemiasterlin)
INPHARMA	Interligand NOE for PHARmacophore MApping
MAS	magic angle spinning
MT	microtubule
NMR	nuclear magnetic resonance
NOE	nuclear Overhauser effect
NAMFIS	NMR Analysis of Molecular Flexibility in Solution
PTX	paclitaxel (taxol)
PTX-NY	PTX "New York," a proposed conformation of PTX
RB3-SLD	SLD of protein RB3
REDOR	Rotational Echo DOuble Resonance
rf	radio-frequency
SAR	structure-activity relationship
SLD	stathmine-like domain
STD	saturation transfer difference NMR spectroscopy
ss-NMR	solid-state NMR
T2R	complex of unpolymerized tubulin with RB3–SLD

tr-CCR	transferred CCR
tr-NOE	transferred NOE

1 Tubulin and Microtubules

1.1 Microtubules: A Drug Target for Cancer Therapy

Antimitotic drugs that target microtubules (MT) or its constituent protein tubulin are one of the most successful classes of anticancer agents discovered so far. MT are long, filamentous, tube-shaped protein polymers that are essential in all eukaryotic cells. Antimitotic agents are compounds that arrest cells in mitosis, which results in the slowing or blocking of mitosis and induction of apoptotic cell death.

MT-targeting antimitotic agents include a large number of small-molecule compounds from different sources and diverse chemical structures that have a common mechanism of action, that is to interfere with the polymerization equilibrium of tubulin into MT. Tubulin-targeting agents may be divided into two major categories according to their effects on the polymerization of tubulin: some of them inhibit the polymerization of tubulin to form microtubules, while others promote the polymerization of tubulin and stabilize the resultant microtubules. Many of these compounds are potent antitumor drugs and several have found wide use in the clinic, like the MT-destabilizing Vinca alkaloids or the MT-stabilizing taxanes (Fig. 1) Paclitaxel (PTX) and Docetaxel (DTX), while others, like the epothilones, are in the advanced stages of clinical trials [1–3].

A detailed knowledge of the atomic structure of protein/ligand complexes is desirable to understand the mechanism of action of the drugs and to help optimize their activity or to identify new leads. In this article we will review how nuclear magnetic resonance (NMR) has contributed to the understanding of the binding mode of some of the most important tubulin-targeting drugs. We will discuss the sources of structural information with special emphasis on NMR spectroscopy but not neglecting X-ray crystallography, electron crystallography, and molecular modeling. We will also

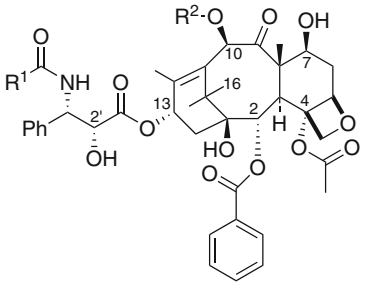

1 PTX: R^1 = Ph, R^2 = Ac
2 DTX: R^1 = t-Bu, R^2 = H

Fig. 1 Structures of the taxanes paclitaxel (PTX, taxol) and docetaxel (DTX, taxotere)

discuss difficulties encountered in obtaining high-resolution structural information and how the incomplete information derived from these different techniques is combined with other biochemical information available in order to understand the mode of action of these drugs.

1.2 Constitution of Tubulin and Microtubules

Tubulin is a 110-kDa heterodimeric protein composed of two subunits α- and β- (~450 amino acids each) and it is the basic subunit of MT. MT are hollow cylindrical protein fibers formed by the lateral association of protofilaments, where each protofilament is a linear polymer of tubulin heterodimers that are bound head to tail. The parallel arrangement of protofilament forms the cylindrical MT wall. Typically, MT contain 13 protofilaments in cross-section aligned with the same polarity. The two ends of a MT are not identical. The minus end is crowned by α-tubulin subunits and serves as the site of nucleation at the centrosome, while the plus end is crowned by β-tubulin subunits and faces outward from the nucleus to the plasma membrane. The repeating subunits are held together in the polymers by non-covalent interactions [4–6].

The self-assembly of α/β-tubulin heterodimers into protofilaments and MT is a highly regulated process. MT are highly dynamic polymers that can switch between growing and shrinking phases. This non-equilibrium behavior is essential for MT cellular functions and is tightly regulated. Although both ends of the MT can either grow or shorten, the plus end is kinetically more dynamic and experiences much larger changes in length than the minus end [5].

MT interact with a large number of other proteins that modulate the MT dynamic stability or that act as active motor proteins. Microtubule-associated proteins (MAPs) stabilize MT by binding to polymers and promoting interactions with other cellular components [7]. Other proteins, like those of the stathmin family, destabilize MT [8] either by preventing assembly or by promoting disassembly of MT.

1.3 Classification of Binding Sites and Agents

A large number of small-molecule ligands, both of natural and semi-synthetic origin, bind to soluble tubulin or to MT and inhibit cell proliferation. The MT-targeting drugs include compounds of diverse chemical structures that share the property of disrupting MT function by interfering with MT dynamics [9]. From the functional point of view, these antimitotic ligands can be grouped in two classes according to their effect on MT dynamics when administered at high concentrations. Some inhibit the polymerization of tubulin to form microtubules while others promote microtubule assembly and stabilization. Even though their effects at high concentration are opposed, both groups of drugs share a common effect at low concentration, that is to cause mitotic arrest by inhibiting normal MT dynamic instability without appreciably changing the mass of

MT in the cell [5, 10]. The interference with microtubule polymerization dynamics is regarded as the basis of drug activity rather than their effect on MT polymer mass.

As for the localization of their binding sites, most of them bind to one of three sites on different parts of the protein: the colchicine, vinblastine and taxol sites [11–13]. Most MT-stabilizing agents bind at the PTX-binding site on β-tubulin, including the taxanes, epothilones, eleutherobin and discodermolide. Known MT-destabilizing agents bind either to the colchicine or to the vinblastine binding sites. There are drugs representative of the three groups undergoing clinical trials, alone or in combination with others, for a number of therapeutic uses [1–3]. In addition, other binding sites have been proposed for novel classes of compounds, like those for the MT-stabilizers laulimalide and peloruside A [14–17], tryprostatin A [18] or estramustine [19, 20]. The localization and properties of these binding sites will be reviewed in the next section.

1.4 Structure of the Tubulin Dimer and Microtubules

The strong tendency of tubulin to polymerize into heterodisperse aggregates and its inherent instability in solution precluded for many years the preparation of suitable crystals and the determination of its high-resolution structure [21, 22]. Finally, two approaches succeeded in obtaining crystalline samples of tubulin suitable for diffraction studies. The near-atomic resolution structures of tubulin thus derived reflect two different environments: tubulin polymerized into protofilaments and unpolymerized tubulin. The first structure of the tubulin dimer to be obtained was solved by electron crystallography (EC) based on the electron density maps of two-dimensional sheets of polymerized tubulin in complex with the MT-stabilizing agent PTX [11]. More recently, the structure of unpolymerized tubulin stabilized with a stathmine-like peptide was solved by X-ray crystallography [21].

In addition, docking the EC-derived near-atomic resolution structures of tubulin into cryoelectron microscopy maps of MT, has provided more precise insights into the structure of MT, their polymerization dynamics and the way how normal MT behavior is disrupted by antimitotic drugs [23, 24].

The atomic coordinates from these structures are nowadays the basis of the new computational and NMR spectroscopic studies aimed at the derivation of binding models of other drugs. Therefore, we will describe the main features of tubulin structures in the next section.

1.4.1 Structures Derived by Electron Crystallography: Straight Tubulin

The first near-atomic resolution structure of the tubulin dimer was determined from a 3.7-Å electron density map obtained by EC from the two-dimensional, crystalline sheets of tubulin that form in the presence of Zn ions and PTX [11]. This polymerized form of tubulin consists of protofilaments arranged in an antiparallel way, while protofilaments are parallel in genuine MT. Despite this different orientation of adjacent protofilaments, 3D reconstruction of intact MT from cryoelectron microscopy images at 20 Å or 8 Å resolution demonstrate that the conformation of tubulin is

overall the same in the Zn-induced sheets and in MT [23, 24], and only the location of the mobile M loop involved in the lateral contacts between protofilaments is different in the two polymers.

The overall structure of the α and β tubulin subunits is very similar and consists of a core of β-sheet surrounded by helices, forming a compact globular protein composed of three sequential domains (Fig. 2) [11]. The *N*-terminal, nucleotide-binding

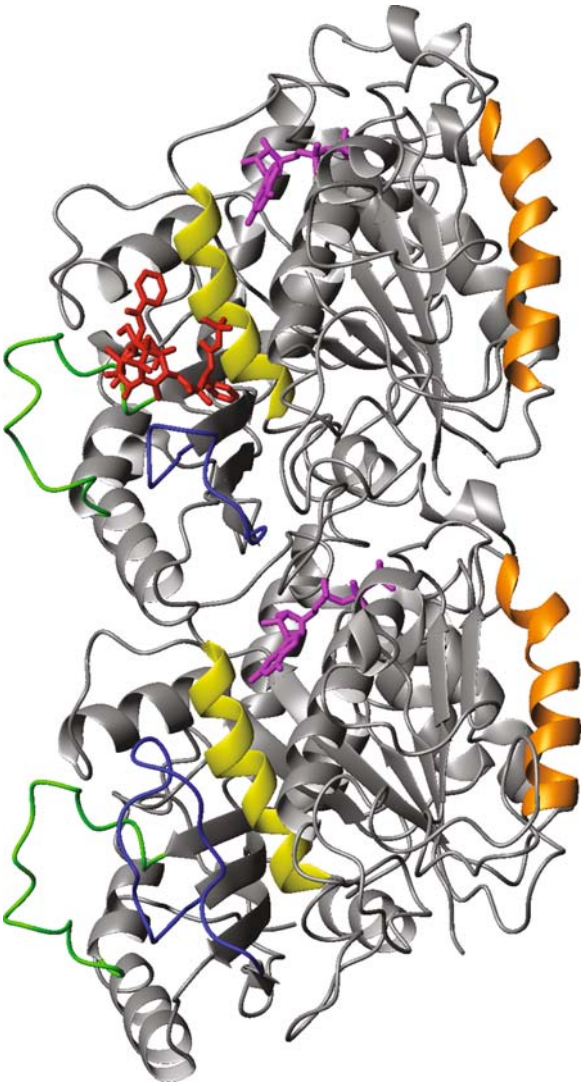

Fig. 2 Ribbon diagram of the structure of the α/β-tubulin dimer in 2D zinc-induced sheets (PDB entry 1TUB). The β monomer is *on top*. Some elements involved in PTX binding and lateral contacts are *colored*: M loop in *green*, S9–S10 loop in *blue*, helix H7 in *yellow*, and helix H3 in *orange*. Small-molecule ligands are represented as *sticks*: PTX in *red*, GDP and GTP in *magenta*. The α-tubulin S9–S10 loop occupies a position equivalent to that of PTX in β-tubulin

domain forms a classical Rossman fold. The intermediate domain is formed by three helices and a mixed beta sheet and contains the taxol-binding site. The small C-terminal region is formed by two antiparallel helices.

The high-resolution model of the MT derived by docking tubulin into the 8-Å reconstruction of the MT shows that the critical lateral contacts between protofilaments are established from the M loop of one side to loop H1–S2 and helix H3 of the other side (Fig. 3). While helix H3 is locked into its position, the M loop is flexible enough to accommodate different angles between protofilaments without compromising the interactions between subunits, thus allowing the formation of MT with different numbers of protofilaments [23, 24].

The most relevant structural difference between the α and β monomers is located in the loop S9–S10, which is 8 residues longer in α-tub than in β-tub owing to an insertion. In the α-subunit, the long S9–S10 loop stabilizes the M loop. In the β-subunit, the equivalent position is occupied by the PTX binding site. This suggests that PTX mimics the 8-residue insertion of the α-subunit loop. In fact, the atomic model shows that the PTX molecule acts as a linker between helix H7 and the M loop, possibly stabilizing an M loop conformation that favors the lateral interprotofilament interaction and contributes to MT stabilization [24, 25]. Both side chains and the baccatin core of PTX participate in these interactions [25].

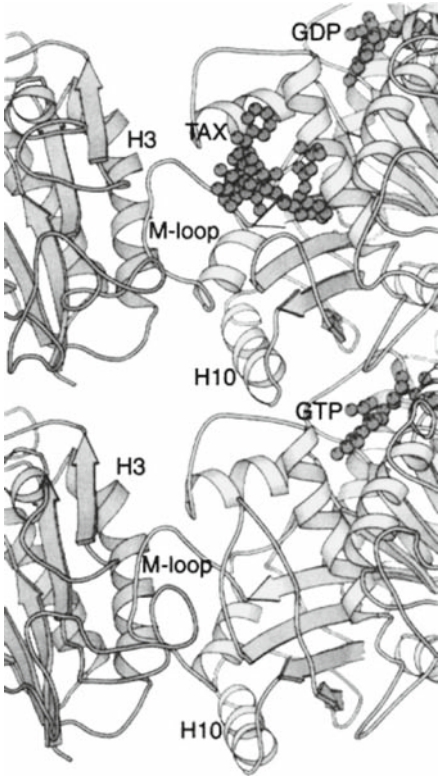

Fig. 3 Lateral interactions between protofilaments are shown in this ribbon diagram representing two dimers that have been docked into the three-dimensional reconstruction of a microtubule. The view is from the inside of the MT, with the β monomer *at the top*. The nucleotides (GDP and GTP) and Taxotere (TAX) are shown as *spheres*. The primary interactions across the interprotofilament interface involve the M loops from the dimer on the *right* with helix H3 on the *left*. (Reprinted with permission from [22]. Copyright 2000 Annual Reviews)

Given that the two-dimensional tubulin crystals are composed of protofilaments, the longitudinal interactions between monomers are observable in the model and result from a combination of hydrophobic and polar contacts. Interestingly, these longitudinal contacts between monomers are very similar in the inter-dimer and in the intra-dimer interfaces [4, 5, 23].

The structure of a similar complex with epothilone A (EpoA) was also determined by EC [26]. The resulting tubulin/EpoA model is quite similar to the tubulin/PTX model except for the position of M-loop residues and the orientation of His227 within the binding site [27]. Similarly to PTX, the molecule of EpoA bridges the M loop and helix H7. This will be discussed further on in the context of the NMR studies of EpoA.

1.4.2 Structures Derived by X-Ray Crystallography: Curved Tubulin

More recently, the crystal structure of a complex of tubulin and the stathmin-like domain (SLD) of protein RB3 was solved [21, 28]. The stathmin family of proteins destabilizes MT [8]. In vitro, stathmin sequesters two tubulin heterodimers to form a ternary complex [29, 30], offering a way to stabilize tubulin in solution for crystallization. Instead of stathmin itself, the 91-residue long RB3–SLD α-helix was used to prepare the crystals. The complex tubulin/RB3–SLD (T2R) is formed by two tubulin heterodimers assembled head to tail, and one RB3–SLD α-helix that extends between the two ends of the tubulin assembly with its *N*-terminal domain capping the last tubulin subunit, thereby preventing its incorporation into protofilaments (Fig. 4).

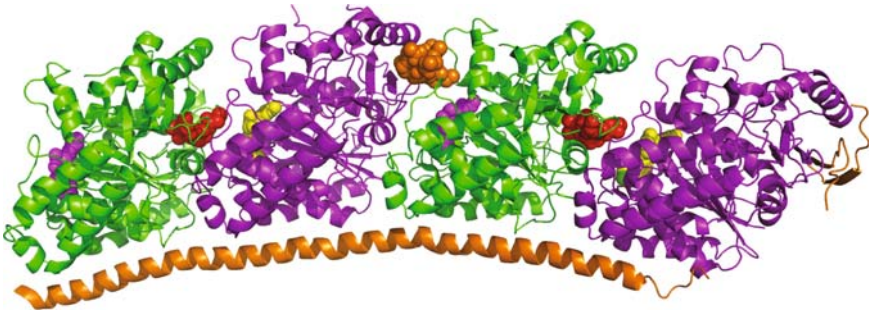

Fig. 4 Diagram of the crystal structure of the T2R complex showing the binding sites of MT-destabilizing drugs (PDB entry 1Z2B) [13]. Protein subunits are represented as *ribbons*. RB3–SLD is *colored orange*, α-tubulin is *purple*, and β-tubulin is *green*. Small-molecule ligands are represented as *spheres* (vinblastine *orange*, colchicine *red*, GTP *yellow*, and GDP *magenta*). Colchicine binds to the β-subunit at the intradimer interface. Vinblastine binds at the interdimer interface

By contrast with the straight arrangement of tubulin subunits in protofilaments both in Zn-induced sheets and in MT, the T2R complex is curved. Interestingly, the curvature of T2R is very similar to that of the depolymerization products of MT, suggesting that the structure of tubulin in T2R reflects the structures of GDP/tubulin in oligomers and in curved tubulin protofilaments. Therefore, comparison of the structures of curved and straight tubulins can help one to understand the mechanism of the MT assembly-disassembly process.

Comparison of the structure of tubulin heterodimers in curved T2R and in straight protofilaments shows important differences in the relative orientation of the domains within each tubulin monomer and in the relative orientation of the α and β monomers in the polymer. Besides, there are significant conformational changes in loops located at longitudinal interfaces in protofilaments as well as in the M and H1–S2 loops, which participate in lateral contacts. The conformational change at the intradimer α/β interface is noticeable, that affects elements of β-tubulin near the colchicine-binding site and some loops of the α subunit. At the interdimer interface, changes are even more extensive and concentrate in the β subunit, involving a different T5 loop conformation and a translation of helix H7 and loop H6–H7.

Complexes of T2R with drugs that target either the colchicine or the vinblastinte binding site have also been crystallized, allowing the definitive identification of their respective binding sites.

Colchicine Binding Site

The colchicine binding site was definitely identified by co-crystallizing the T2R complex with colchicine-site inhibitors, such as colchicine itself (Fig. 5), DAMA-colchicine, and podophyllotoxin [12]. The binding site lies at the interdimer interface, such that colchicine interacts with elements from both the α and the β tubulin subunits, displacing T7 loop and H8 helix to make space for the drug. This location explains how colchicine binding prevents curved tubulin from adopting a straight structure.

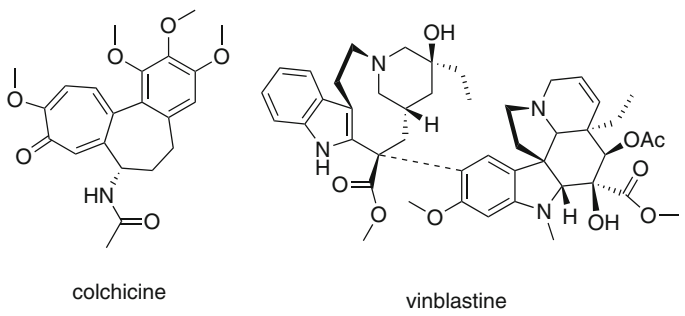

Fig. 5 Structures of the MT-destabilizing agents colchicine and vinblastine

It is noticeable that the observed colchicine site differs from previously proposed binding sites that had been derived by molecular modeling [31]. The reason of this discrepancy is that these computational models were based on the EC-derived structure of tubulin (i.e., protofilaments of straight tubulin) and failed to predict the tubulin curved conformation at the intradimer interface. Given that the straight tubulin conformation is not adopted in the T2R/colchicine complex (as it would lead to a steric clash of colchicine with the α subunit), the M loop is displaced by more than 9 Å compared to straight tubulin [12]. It was proposed that, due to this position of the M loop, the lateral contacts cannot be established, thus explaining why protofilaments cannot assemble into MT in the presence of colchicine.

Vinblastine Binding Site

The structure of the complex of T2R with vinblastine (Fig. 5) was also determined by X-ray crystallography, leading to the localization of its binding site, which is situated at the α/β interface between neighboring heterodimers and is therefore involved in longitudinal protofilament contacts [13]. Vinblastine interacts to the same extent with both flanking tubulin subunits. In comparison to T2R, local conformational changes take place in tubulin subunits in order to accommodate vinblastine into its binding site. The curvature of this structure explains how vinblastine induces tubulin self-association into spiral aggregates at the expense of MT growth [13].

These structures of T2R complexes demonstrate that vinblastine and colchicine, that are representative examples of the two classes of MT-destabilizing antimitotics, prevent the formation of straight protofilaments by disrupting longitudinal contacts at the α/β interfaces, hence inducing curvature into tubulin assemblies. They induce curvature by binding at different sites in the tubulin heterodimer, vinblastine at inter-dimer interfaces and colchicine at intra-dimer interfaces. In addition, conformational changes induced by the drugs inside each tubulin monomer prevent the formation of lateral contacts, especially due to their effect on the position of the highly mobile M loop. All these differences between straight and curved tubulins provide a rationale for the effect of MT-destabilizing drugs and for the mechanism of MT dynamic instability [12, 13].

1.5 Implications of the Flexibility and Dynamics of Tubulin for Its Structural Investigation

As we have seen, the flexible and dynamic behavior of tubulin has consequences at two levels. Tubulin α/β heterodimers are flexible molecules in nature and change conformation in response to a series of stimuli, such as the polymerization status or the binding of ligands. Besides, tubulin heterodimers can self-assemble into MT and a number of other polymer forms like protofilaments, rings or spirals [5]. The complexity of this dynamic behavior makes its structural studies both experimentally

and computationally difficult. Tubulin's intrinsic instability in solution and its tendency to polymerize prevented for a long time the formation of useful crystals for crystallographic studies. The crystals obtained are in most cases non-physiological crystals, such as the 2D Zn-sheets used in the EC structural studies. Computational prediction of binding sites and bioactive conformations suffer from the fact that binding of different drugs alter the conformation of tubulin heterodimers in different, often unpredictable ways and hence conclusions from these studies must be regarded with caution.

Even though near-atomic resolution structures are available only for a few tubulin binders, these structures are very valuable as their represent the basis for a number of studies aimed at discovering the binding modes of other MT-targeting drugs.

2 NMR Methods for the Investigation of Macromolecular Complexes

2.1 General Considerations

High resolution NMR in solution is a well established technique for the determination of the structure of proteins and their complexes [32] provided the rotational correlation time of such complexes remains sufficiently short. In practice, this means that the structure of protein complexes with a mass up to 20–30 kDa can be determined by applying classical heteronuclear isotope labeling and NMR methodology [33, 34]. Larger systems can be tackled using perdeuteration or selective isotope labeling (for a recent review, see for instance [35]) in conjunction with high field and relaxation optimized NMR techniques. In particular, selective amino acid labeling provides information in congested spectra with maximum precision that would otherwise be impossible to obtain [36].

Solid-state NMR does not have the size limit because it does not rely on the fast rotational tumbling of molecules. However, line widths are larger such that overlap becomes an issue limiting the number of amino acids that could be assigned to presently around 100. Still, partial information could be extracted from much larger systems approaching several tens of kD. Solid-state NMR relies on detection of heteronuclei, so that labeling of the protein is mandatory.

Despite the great progress experienced in these fields, the determination of the structure of tubulin is beyond the possibilities offered by solution NMR spectroscopy due to a number of factors, like the high molecular mass of the unpolymerized tubulin heterodimer (~110 kDa), its instability in solution, its strong tendency to polymerize into species of much larger molecular mass, and the impossibility presently to express it in bacterial systems, preventing for the moment the labeling with NMR active isotopes. Therefore, NMR activities that will be described in the following have mainly concentrated on the description of the ligand's conformation as well as its binding site and binding pose in tubulin.

2.2 Derivation of Bioactive Conformations of Ligands by NMR

2.2.1 Exchange-Transferred NMR Experiments

Fortunately, the possibilities offered by NMR spectroscopy to characterize ligand/protein complexes are not always limited to the direct observation of the protein receptor. If the soluble ligand binds to the macromolecule transiently instead of forming a tight complex, the receptor-bound conformation of the ligand can be characterized by observing the resonances of the ligand by means of exchange-transferred experiments such as transferred nuclear Overhauser effect (tr-NOE) [37], saturation transfer difference (STD) [38] or transferred cross-correlated relaxation (tr-CCR) [39, 40], among others. Exchange-transferred experiments take advantage of the large differences in the relaxation rates of the small molecule resonances in the free state compared to those in the protein-bound complex [37, 41–43], provided the binding equilibrium is in the fast exchange regime. This fast-exchange condition means that the dissociation rate (k_{off}) of the complex must be faster than the relaxation rates of the ligand in the complex. In practice, and assuming that the on-rate is controlled by diffusion (10^7–10^8 M^{-1} s^{-1}), this implies that the dissociation constant (K_d) value must lie in the low micromolar to millimolar range, which excludes very tight binders from observation but makes these experiments very suitable for ligands with intermediate to weak affinities [37, 41–43]. One advantage of monitoring the small molecule is that there is no need to isotopically enrich the target protein and that only small quantities of protein are required. Typical experimental conditions use small amounts of unlabeled target protein (1–50 μM in 0.5 ml of solution) and a high ligand:protein ratio (in the range 10:1–100:1). Under these conditions, measurement of exchange-transferred experiments observing the resonances of the free ligand that is present in stoichiometric excess reflects mainly its bioactive conformation, i.e., the conformation of the protein-bound ligand. Interestingly, for the application of transferred NMR methods it is advantageous that the weight of the macromolecule is larger than 35 kDa. There is no upper limit observed so far.

Among the existing exchange-transferred NMR methods, we will highlight in the following those that have been employed to determine the bioactive conformation of tubulin-bound drugs.

Transferred NOE

In a typical “free” NOESY experiment of a molecule in the absence of any interacting protein, cross-peak volumes are interpreted in terms of a set of interproton distances r_{ij} that can be used as distance restraints in structure determination procedures, like restrained simulated annealing protocols [44]. In a tr-NOESY, i.e. a NOESY measured under exchange-transferred conditions in the presence of a protein – i.e., an excess of soluble ligand is in fast exchange equilibrium with a smaller amount of protein-bound ligand – , these r_{ij} reflect the interproton distances of the ligand in the bound

complex and application of the same kind of structure calculation procedures provides the bioactive conformation of the ligand. This can be understood by considering the cross-relaxation rate of two protons with the distance r_{ij}^{free} in the free conformation and r_{ij}^{bound} in the bound conformation:

$$\sigma^{I} = \left(b_{\mathrm{ij}}^{\mathrm{free}}\right)^2 p^{\mathrm{free}} \left(\frac{3}{4} J^{\mathrm{free}}(\omega_1 + \omega_2) - \frac{1}{8} J^{\mathrm{free}}(\omega_1 - \omega_2)\right) + \left(b_{\mathrm{ij}}^{\mathrm{bound}}\right)^2 p^{\mathrm{bound}} \left(\frac{3}{4} J^{\mathrm{bound}}(\omega_1 + \omega_2) - \frac{1}{8} J^{\mathrm{bound}}(\omega_1 - \omega_2)\right) \quad (1)$$

with

$$J(\omega) = \frac{4}{5} \frac{\tau_c}{1 + \omega^2 \tau_c^2} \quad (2)$$

and

$$b_{ij} = -\mu_0 \frac{\gamma_i \gamma_j \mathrm{h}}{4\pi r_{ij}^3} \quad (3)$$

From (1), it follows that the bound conformation is predominant in the tr-NOESY if

$$\tau_{\mathrm{c}}^{\mathrm{bound}} p^{\mathrm{bound}} >> \tau_{\mathrm{c}}^{\mathrm{free}} p^{\mathrm{free}} \quad (4)$$

Structure calculations for the bound conformation of the ligand can be done in the absence of any knowledge on the actual structure of the receptor protein, as they involve only interproton distances of the ligand molecule. However, if the 3D structure of the protein is known, a model of the complex can be generated by using the tr-NOE distances as restraints to lock the otherwise flexible ligand in the bound conformation, which reduces the number of docking calculations considerably.

It is worth noting the remarkable differences in the NOESY spectra of a small-molecule ligand measured in exchange-transferred conditions compared to the "free" NOESY recorded in the absence of protein. The integral of the cross-peaks is much larger in the tr-NOE spectrum. Besides, the sign of the cross-peaks is opposite in the two spectra. These differences are due to the large difference in the correlation times of the free ligand and the complex, which translates into cross-relaxation rates of different magnitude and opposite sign.

Saturation Transfer Difference (STD) NMR

Saturation transfer difference NMR stands for a difference experiment in which the protein resonances are selectively saturated but not the resonances of the ligand [38]. In the second experiment, the proton resonances of neither the ligand nor the protein are saturated. If the ligand binds to the protein with a K_d between mM and

nM, in the first experiment saturation is transferred from the protein to the ligand via proximity of protein protons and ligand protons, reducing the intensity of the signals of the ligand. In the second experiment, the normal ligand spectrum is obtained. The difference for the ligand spectrum is then non-zero. A non-binding ligand is not affected by the selective irradiation of the protein and therefore does not give signal in the difference spectrum.

One might argue that the selective saturation of the protein may saturate only those protein protons that are not in contact with ligand protons. However, saturation is usually achieved by applying the saturation rf field for a relatively long time. This ensures that all protein protons are eventually saturated by spin diffusion, which is equivalent to flip-flop energy transitions. It is a feature of cross-relaxation between protons in increasingly bigger proteins that the overall magnetization of the protons relaxes increasingly slower while the cross-relaxation between protons becomes increasingly faster. Thus, magnetization from selectively saturated protein protons can be transferred through space to non-saturated nearby protons, which will be saturated as well. Since, as explained above, STD exploits the transfer of magnetization from the saturated protons of the protein to the protons of a ligand that transiently binds to the protein, a difference spectrum is obtained from spectra collected with and without selective pre-irradiation of resonances of the protein. The resulting subtracted spectrum contains only the signals of the protons of the ligand that interact with the protein. Protons of the ligand that are closer in space to those of the protein will receive a larger fraction of magnetization and hence experience a larger signal enhancement relative to the reference spectrum recorded without pre-irradiation. In consequence, analysis of the relative enhancement of the signal of each atom can be used to determine the binding epitope of the ligand [38], i.e. to identify the protons of the ligand that lie closer to the protein surface and contribute more strongly to the binding interaction. Of course, there will still be some unequal distribution of saturation in the protein that also has to be taken into account. Therefore, a quantitative analysis of STD effects requires a rather precise knowledge of the structure of the protein and the chemical shifts of the protein protons. Such investigations have been recently summarized [45].

Another experimental problem that may arise when trying to interpret STD data non-quantitatively stems from the fast relaxation of some ligand protons, which reduces the STD effect compared to other slower relaxing ligand protons [46]. Then, STD effects appear weaker for those faster relaxing protons and a binding epitope involving those faster relaxing protons may be missed. On the other hand, slowly relaxing protons may show larger STD enhancements. This behavior of STD is not unique, but it is common to all saturation NOE experiments. Under saturation conditions, the NOE enhancement does not strongly correlate with the distance between saturated and observed nucleus. The only way out is to use shorter irradiation times, so-called relaxation-compensated STD, very similar to truncated 1D NOE spectroscopy [46, 47]. Of course, short irradiation times will not lead to equal saturation of the protein protons, so that a balance has to be found if the ligand has very differently relaxing protons. Full relaxation matrix analysis takes care of both problems.

Transferred Cross-Correlated Relaxation (tr-CCR)

The cross correlation between two separate relaxation interactions such as two dipolar interactions between, e.g., two carbon proton pairs C_iH_i and C_jH_j can be used to determine the projection angle between these two vectors (Fig. 6). Such projection vectors can be translated in many cases into dihedral angles offering a good alternative to the measurement of ^3J couplings [48]. Since CCR rates linearly depend on the correlation time, they can be used in transferred experiments similarly to tr-NOEs to determine selected dihedral angles of the bioactive conformation of the ligand [39, 40]. Different kinds of CCR rates can be measured, depending on the structure of the molecule and the kind of nuclei involved in the interaction. For example, the above-mentioned CCR rate due to the dipolar coupling of two different C–H pairs (C_iH_i and C_jH_j) is given by

$$\Gamma_{C_iH_i,C_jH_j} = \frac{\gamma_H^2\gamma_C^2\mu_0^2\hbar^2}{40\pi^2 r_{C_iH_i}^3 r_{C_jH_j}^3} S_{ij}^2 \frac{3\cos^2\theta_{ij} - 1}{2}\tau_c \tag{5}$$

where γ_C and γ_H are the gyromagnetic ratios of carbon and proton respectively, $r_{Ci,Hi}$ and $r_{Cj,Hj}$ are the C–H interatomic distances, τ_C is the correlation time of the molecule, θ_{ij} is the projection angle between the two C–H vectors, and S_{ij}^2 is the order parameter, which takes into account the possible internal motion. Transferred cross-correlated relaxation has been used successfully for the characterization of small molecules bound to tubulin as will be discussed later in this article. It has also been applied to several other systems [49] such as nucleotides bound to enzymes [39, 50] and peptides bound to proteins [40].

Limitations of Transferred Relaxation NMR Experiments

One precaution to be taken when interpreting data from transferred experiments is to make sure that only the bioactive conformation of the ligand is contributing to the NMR signal. As transferred experiments are recorded with a high molar excess of ligand over the macromolecule, it may happen that the ligand binds nonspecifically to the protein, leading to complexes that also contribute to the averaged tr-NOE, tr-CCR or STD NMR signals. Interpretation of these signals as if they were derived from a unique conformer would lead to incorrect results. Therefore, appropriate control experiments need to be done to rule out nonspecific binding. The situation is similar to many assays in which fluorescence anisotropy decays are used as

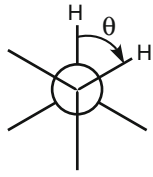

Fig. 6 CCR helps in determining the projection angle between two dipolar interaction vectors

a signal for the interaction of a ligand with a protein. Also there, the signal does not tell whether the ligand binds to the correct binding site.

2.2.2 Determination of Solution Conformations of the Uncomplexed Ligand

Despite the opportunities offered by NMR transferred methods to determine the bioactive conformation of ligands, their application to the study of tubulin complexes has been started only recently and the number of applications is still limited. While structural data could not be obtained experimentally from the macromolecular complexes, another NMR-based approach often used in the drug discovery context analyzes the conformational properties of the uncomplexed molecule in solution. The basic assumption is that the bioactive conformer is very likely one of those present in the solution conformational ensemble, even though it might not be the most populated conformer [51, 52]. This had been found to be the case in a number of examples such as the binding of geldanamycin and radicicol to Hsp90 [52] or the binding of a water soluble analogue of the flexible cyclic peptide cyclosporine A to cyclophilin [53, 54]. So, it came as no surprise that, in the case of taxol, one of the conformers found in free solution is the best candidate for binding to β-tubulin [25]. However, care has to be taken when using this approach because, if the bioactive conformation is a minor conformation in equilibrium with other major in solution, it may escape detection by the usual NMR methods.

NMR is the experimental tool of choice to explore conformational properties, especially of flexible small molecules in solution [55–57]. Interpretation of NMR-derived structural parameters in combination with molecular modeling usually offers a view of the accessible conformations to ligands. The most relevant structural parameters derived from NMR are interproton distances obtained from NOE or ROE experiments, dihedral angle restraints from ^{3}J scalar coupling measurements and, recently, residual dipolar couplings (RDCs) [58].

NAMFIS Deconvolution Analysis

Flexible molecules with rotatable single bonds usually do not exist as a single conformer in solution. Instead, they exist as an ensemble of different conformers interconverting in a fast exchange equilibrium at room temperature. NMR parameters such as NOEs or J couplings are the weighted average of the contributions of each conformation present in the sample [59]. Trying to fit the averaged NMR data to a single conformation would lead very likely to a virtual conformation [60]. If the number of restraints is large, however, there are very likely intrinsic inconsistencies that suggest multiple conformations [56].

Describing the ensemble of conformations would imply knowing the structure and the relative population of each conformer in solution. In many cases this problem is underdetermined, since the number of NMR-derived experimental restraints is smaller than the degrees of freedom of the system. In consequence,

computational methods are used to find possible solutions that are compatible with the experimental NMR data, as explained in the following. Still, with the larger number of independent restraints available nowadays (distance, dihedral and orientational), this problem has become less severe and the faithful description of conformational ensembles is possible for favorable cases in cyclic systems [61] and even in open chain systems [58].

One of these methods is NAMFIS (NMR Analysis of Molecular Flexibility in Solution) [62], which considers all candidate conformations that are theoretically accessible to the molecule and optimizes their mole fractions until their computed variables match the experimental NMR data (usually NOEs and J couplings, in the future potentially also residual dipolar couplings). NAMFIS has been used to analyze the solution structures of several tubulin-binding drugs, such as PTX [63], epothilones [26], discodermolide [60] or laulimalide [64].

One advantage of the NAMFIS approach is that it does not rely on the calculated energies of the conformers, which have proven to provide unreliable values at least with highly polar molecules like PTX [65]. Instead, NAMFIS uses all reasonable conformational minima proposals regardless of their energies and selects them on the basis of their fitting to the experimental NMR data.

Of course, one cannot expect from NAMFIS that it substitutes the analysis of the bound structure of a ligand. NAMFIS tries to extract from a set of averaged restraints the underlying multitude of structures [62, 64]. The problem of deconvoluting an averaged NMR spectrum is underdetermined (due to the large number of unknowns and the scarcity of experimental data), i.e., there is no unique solution. Among all feasible solutions, NAMFIS finds the one that best fits the available experimental data. The solution of NAMFIS deconvolution is given in the form of the mole fractions of a set of conformations that can be clustered in a few structural families. The existence of these families is supported by rigorous analysis of data, although the precise values for the population of each family have a certain degree of uncertainty. Also NAMFIS may not suggest the presence of exactly one of the conformations present in solution but it will suggest conformers very similar to the "missed" one [64].

2.2.3 Solid-State NMR (ss-NMR)

The opportunities offered by NMR for the study of biomacromolecules are not limited to solution techniques. Especially tight complexes between a ligand and a protein can be studied very well by solid-state NMR spectroscopy (for a recent review refer to [66]). In ss-NMR, the size limitation does not exist since the rotational tumbling is not required for line narrowing but rather fast spinning at the magic angle [67], cross polarization from ^{1}H to ^{13}C [68], and detection of ^{13}C instead of ^{1}H [69]. The line widths in the spectra are the limiting factor for the number of resonances that can be dealt with easily. If one concentrates on small systems interacting with large systems such as a small ligand with tubulin, ss-NMR can be ideally used provided the ligand can be labeled with ^{13}C. Indeed, structures

of complexes of peptides with membrane proteins could be successfully characterized by ss-NMR spectroscopy [70, 71].

The main source of conformational information for biopolymers are the easy-to-obtain chemical shifts that can be translated into dihedral restraints. In addition, for fully ^{13}C labeled compounds, proton-driven spin diffusion between carbons [72] can be used to measure quantitatively distances between carbons. The CHHC experiment is the equivalent of the NOESY in solution that measures distances between protons by detecting the resonances of the attached carbons. While both techniques, proton-driven spin diffusion and CHHC experiment [73], allow for some variation in the distance as determined from cross-peak integrals, REDOR [74] experiments in selective labeled compounds measure very accurate distances by direct observation of the oscillation of a signal by the dipolar coupling. While the latter technique provides very accurate distances, it provides only one piece of information per sample. Therefore, the more powerful techniques proton-driven spin diffusion and CHHC have taken over when it comes to structure determination by ss-NMR of fully labeled ligands.

2.3 Derivation of the Orientation of the Ligand in Its Binding Site (INPHARMA)

Knowing the bioactive conformation of the ligand does not solve the question of its orientation into the protein binding site. In some instances, e.g., when the 3D structure of the protein is unknown, the bioactive conformation can be used to deduce a common pharmacophore with other drugs that target the same site of the protein. In addition, when the 3D coordinates of the protein are available, the ligand bioactive conformation can be computationally docked into its binding site. However, it would be desirable to have additional direct experimental data on the orientation of the ligand and not only on its conformation or its binding epitope.

In structure-based drug design it often occurs that the coordinates of a complex of the protein target with a ligand A are known and we are interested in the binding pose of a second ligand B that targets the same binding site. In this case, the problem of the binding orientation of B can be reduced to determine the relative orientation of the two ligands A and B in the protein binding site. A new NMR-based method (INPHARMA) was developed to address this question and applied to the binding of EpoA and tubulin [75, 76].

INPHARMA is based on the observation of inter-ligand NOE peaks between two ligands that bind competitively (not simultaneously) to the same site on the target protein (Fig. 7). Similarly to tr-NOE, INPHARMA requires that binding of the two ligands occurs under the fast-exchange regime and that both are in excess with respect to the protein. For INPHARMA measurements, the two competing ligands are present simultaneously in the sample so that a fast equilibrium is established between the protein target T, the two free ligands A and B, and the complexes TA and TB.

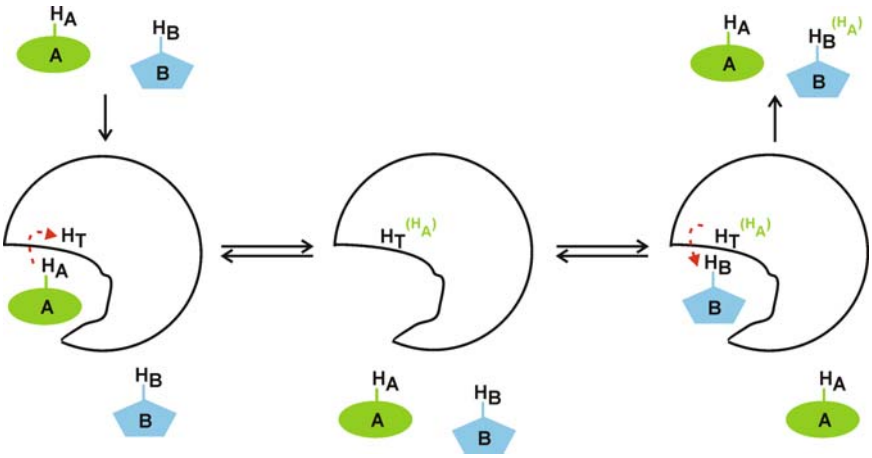

Fig. 7 Schematic representation of the principle ot the interligand NOEs observed between two competitive ligands A (*green*) and B (*blue*) that bind consecutively to the same target receptor T. (Reprinted with permission from [75]. Copyright 2005 Wiley-VCH Verlag GmbH & Co. KGaA, Weinheim)

An INPHARMA inter-ligand peak between a proton H_A of ligand A and a proton H_B of ligand B originates from spin diffusion mediated by protons H_T of the protein target. During the NOESY mixing time, magnetization is transferred from H_A to H_T in the complex TA. Then the complex TA dissociates and B binds to T. The magnetization from H_A, that had been transferred to H_T, is now transferred from H_T to H_B in the complex TB, resulting in an interligand cross-peak H_A–H_B in the NOESY spectrum. Due to the distance dependence of the NOE transfers, this peak can only exist if protons H_A and H_B are close to the same proton H_T in their respective complexes TA and TB. It has to be noted that protons H_A and H_B are never close in space. Instead, they bind consecutively in the proximity of the same proton H_T, which mediates the transfer of magnetization from H_A to H_B. The origin and information content of the INPHARMA interligand cross-peaks are different from those ILOE (Inter-Ligand Overhauser Effect) cross-peaks described by London [77] that occur between ligands binding simultaneously to the protein in adjacent or partially overlapping binding pockets.

Assuming that the coordinates of the complex TA are known, the orientation of ligand B in the binding pocket could be deduced from a set of such interligand H_A–H_B cross-peaks. In practice, these interligand NOEs should be interpreted with the help of theoretical full-relaxation-matrix (FRM) calculations in order to account properly for the effects of spin diffusion. The procedure consists of three steps: 1. generate by computer docking a set of TB binding poses differing in the binding orientation of ligand B; 2. compute the expected intermolecular NOEs for each binding pose of B in the TB complex; 3. rank each binding pose according to the agreement between computed and experimental intermolecular NOEs.

3 NMR-Derived Bioactive Conformation of Tubulin-Binding Agents

Since the discovery of the therapeutic potential of tubulin targeting drugs, there has been a demand for structural information at the molecular level about the binding pose of the small-molecule ligands, very much needed by the medicinal chemists for the rational design of novel derivatives. Even nowadays, near-atomic resolution structures are available only for a few tubulin binders, namely, the EC-derived structures of the MT-stabilizers PTX [11] and EpoA [26], and the X-ray structures of complexes of tubulin/RB3–SLD with the MT-destabilizers colchicine [12] and vinblastine [13].

Regarding the rest of the MT-targeting compounds, there is no complete 3D structure of protein/drug complexes available based on crystallography data. For some of these complexes, there is high resolution structural information available on the conformation of the ligand when bound to tubulin. Such conformations have been derived over the years from solution NMR, solid-state NMR and molecular modeling, often in combination with the atomic coordinates of the available structures of the free protein or the protein in complex with other ligands. Knowledge of the bioactive conformation of the drugs may give clues on the critical interactions that are responsible for their activity and may suggest modifications for the synthesis of analogues with improved properties.

There are three NMR-based approaches suitable to propose the bioactive conformation of ligands in the absence of the coordinates of the whole complex: 1. conformation analysis of free ligand in solution has a high chance to find with some population the bound conformation, although it may be solvent dependent (refer to Sect. 2.2.2); 2. determination of bound ligand conformation by means of transferred NMR methods if the dissociation constant is not smaller than approximately 50 μM (refer to Sects. 2.1 and 2.3); 3. solid-state NMR of the complex if the ligand can be obtained with ^{13}C labels (Sect. 2.2.3).

3.1 Microtubule-Stabilizing Agents

3.1.1 Taxol Binding Site

Paclitaxel (Taxol)

PTX (taxol, Scheme 1) was the first antimitotic compound known to act by stabilizing MT. Nowadays, PTX is one of the most important anticancer drugs and is used clinically for the treatment of ovarian, breast, and non-small cell lung cancer, as well as AIDS-related Kaposi's sarcoma [78]. After PTX, many other MT-stabilizing agents have been discovered and are at different stages of clinical development. Most MT-stabilizing agents bind to the taxol binding site.

There has been long controversy regarding the bioactive conformation of PTX due to the difficulties to obtain high-resolution structural data from PTX bound to MT. Before the EC structure of PTX-stabilized tubulin polymer sheets [11] was available, solution NMR spectroscopy was used to derive candidate conformations for the tubulin-bound state of PTX. Early solution NMR studies on PTX have been reviewed by Jiménez-Barbero et al. [51] and only the fundamental results are summarized here.

For solution NMR studies on the free PTX, organic solvents (such as $CDCl_3$, CD_2Cl_2, CD_3OD, DMSO) or DMSO/H_2O mixtures were used due to the low aqueous solubility of taxol. In these first solution studies, NMR data were interpreted on the assumption that a single conformation was dominant in solution. Among the many conformers proposed based on NMR and molecular dynamics, two conformations were regarded as candidates for the bioactive form of taxol that were named the polar and the nonpolar conformation (Fig. 8) [51]. Both conformations share the characteristic of being hydrophobically collapsed because in both cases the 2-benzoyloxy substituent is in close proximity to one of the two C13 side chain phenyl groups, making hydrophobic phenyl–phenyl contacts.

Further insight into the conformations of taxol in solution was gained by the use of fluorinated analogues of PTX. Variable temperature NMR measurements of ^{19}F chemical shifts and H2′–H3′ scalar couplings combined with molecular modeling indicated that there is a dynamic equilibrium between three conformers, especially in protic solvents [79]. Later, NAMFIS analysis of PTX [63] showed that the NMR data are consistent with a set of eight conformations in equilibrium that can be grouped into three structural families. Two of these families resemble the hydrophobically collapsed polar and apolar conformations previously described. The third subset includes "open" or extended conformers, (where the side-chain phenyl groups are unclustered) including the so-called "T-conformers" that had also been proposed in previous studies (Fig. 8) [80–82].

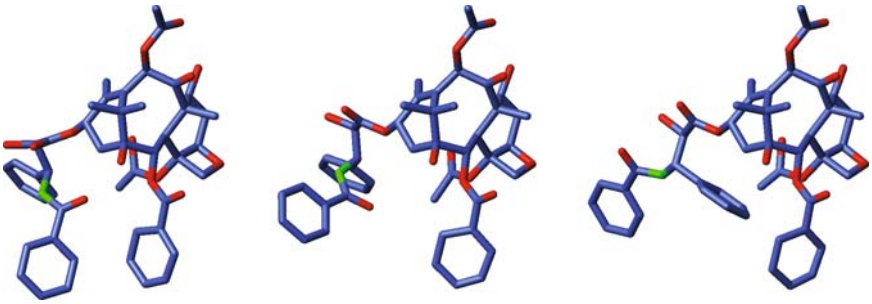

Fig. 8 Conformations of PTX in solution (C *blue*, O *red*, N *green*). *Left*: nonpolar conformation. *Middle*: T-taxol conformation. *Right*: polar conformation. The drawings are representative structures of each class and do not correspond exactly to any physically determined structure. Coordinates were generated by manual manipulation with Kryomol (http://galileo.usc.es/~armando/software) of the PTX coordinates in the PDB entry 1JFF

The publication of the 3D structure of PTX-stabilized Zn-induced tubulin sheets based on electron crystallography represents a hallmark in the field [11, 83]. The 1998 structure confirmed the location of the binding site of taxol that had already been inferred from photoaffinity labeling. However, it did not solve the question of the conformation and orientation of taxol in the binding site. The reason is that the typical 3–4 Å resolution provided by EC densities sufficed to define the protein fold but not the precise conformation of the ligands in the complex. Therefore, determination of ligand conformation from these EC data relied on building models that make sense chemically. In addition, further information such as SAR (structure activity relationship) data, results from photoaffinity labeling and internuclear distances obtained from NMR analysis were essential.

Simultaneously with the refinement of the EC structure, additional data on the conformation of taxol bound to MT came from ss-NMR REDOR measurements [84]. As introduced above, the REDOR experiment exploits the dipolar interaction between nuclear spins to determine distances between atoms closer than 12 Å. A PTX analogue with suitable spin labeling for REDOR was prepared and complexed to MT. Labeling of the amide carbonyl and C3′ methine with ^{13}C, and position *p*- of the 2–O–benzoyl with ^{19}F (Fig. 9, compound **3**), allowed the measurement of the two ^{19}F–^{13}C distances **I** and **II** (Fig. 9), that could serve, in principle, to discriminate among candidates for PTX conformation. The respective values of 9.8 Å ±0.5 Å and 10.3 Å ±0.5 Å were interpreted by the authors as supportive of the hydrophobically collapsed polar conformation for PTX [84].

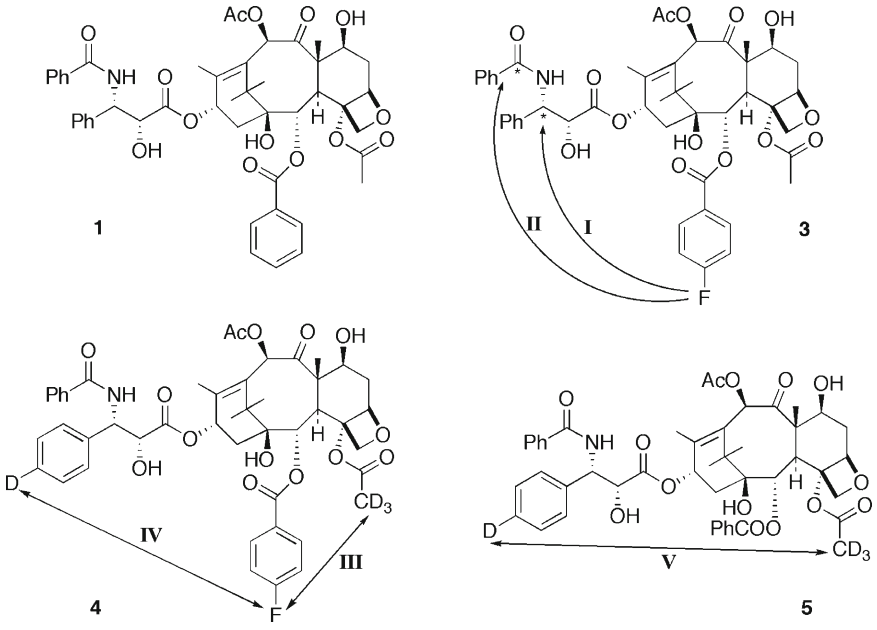

Fig. 9 Taxol and the derivatives used in REDOR NMR experiments. *Arrows* indicate the interatomic distances measured in each compound

Two independent studies based on the refinement of the EC structure of tubulin/taxol concluded that T-taxol is the conformation that best fits the EC density [25, 83], despite the fact that the two internuclear distances of T-taxol (9.1 Å and 9.9 Å, respectively) are in slight disagreement with those derived by REDOR NMR.

Another conformation different from T-taxol was proposed based on molecular dynamics simulations and computational docking restrained by the two REDOR distances [85]. The main difference between this conformer (named REDOR-taxol or PTX-NY) and T-taxol is the conformation of the C13 side chain, that places the 2′–OH in a different orientation. However, subsequent studies demonstrated that PTX–NY is not consistent with the EC density [86, 87].

The apparent contradiction between REDOR internuclear distances and the T-conformation compatible with the EC-density has been critically reviewed [86]. The discrepancy is solved by realizing the following three facts. First, as only two intermolecular distances were measured, there are many diverse PTX low-energy conformations compatible with them, including conformers of the T-taxol and polar conformation classes. Second, angle variations as small as 6–14° of the T-taxol conformer [25] suffice to satisfy the REDOR distances while still keeping the basic structural features of the T conformation. In fact, such small variations can be produced by molecular vibrations at room temperature. Third, detailed analysis of error boundaries of REDOR measurements give ±0.7 Å as a more realistic value instead of the previously reported value of ±0.5 Å. Moreover, molecular motion and other factors can easily explain even larger discrepancies.

If all these facts are taken into consideration, the T-taxol conformation can be regarded as consistent with the two ^{13}C-^{19}F REDOR distances. Other conformations apart from T-taxol that also conform with the REDOR distances, such as the polar PTX or PTX-NY, can be rejected on the basis of their poorer fitting to the EC density (Table 1).

Table 1 Summary of key internuclear distances for PTX conformations as compared to those determined experimentally from REDOR NMR experiments [87]

	Distance, Å					
Separation (Fig. 9)	Polar model[a]	Nonpolar model[b]	PTX-NY model[c,d]	1JFF[e]	T-taxol model[d,f]	REDOR distance
I	9.6	8.5	9.4	9.3	9.9	10.3[i]
II	10.4	6.2	10.0	8.1	9.1	9.8[i]
III[g]	7.4	8.0	7.3	6.5	7.9	7.8[h]
IV	4.5	12.5	13.1	11.6	12.2	>8[h]
V[g]	5.5	7.2	6.4	7.2	6.6	6.3[h]

[a][144]
[b][63, 80]
[c][85]
[d]The values of distances **I** and **II** were inadvertently switched in Fig. 1 of [86]
[e][25]
[f][81, 145, 146]
[g]Distances from the 4-OAc methyl group were taken as an average of the three hydrogen positions
[h][87], ±0.5 Å
[i][84]

More recently, additional $^{2}H\{^{19}F\}$ REDOR measurements on new PTX derivatives bound to MT provided three new interatomic distances that helped to define more precisely the bound conformation of PTX [87]. The two PTX analogues labeled with fluorine and deuterium were designed to determine the three key distances based on the measurement of $^{2}H–^{19}F$ distances, as indicated in Fig. 9 (compounds **4** and **5**). These interatomic distances rule out the polar and nonpolar conformers and further support the T-taxol conformation (Table1). The polar conformation is rejected on the basis of distance **IV**, as the 4.5 Å is much shorter than the > 8 Å determined by REDOR. The nonpolar conformation can be ruled out on the basis of distances **I** and **II**, that are too short in the nonpolar conformer compared to the experimental ones (1.8 and 3.6 Å short). Besides, bridged taxanes resembling the nonpolar conformation displayed no activity in the tubulin assembly assay [88]. PTX-NY closely matches the REDOR distances. Nevertheless, it is discarded as the bioactive form of PTX due to its poor fit to the EC density [87].

In summary, the T-taxol conformation is the only one that is compatible with the EC density and with the internuclear distances measured by REDOR ss-NMR. The conformation of T-taxol has been used as a template to design novel bridged taxanes. The fact that some of them possess improved bioactivity [89, 90] provides indirect additional evidence that T-taxol represents indeed the bioactive conformation.

Epothilones

Epothilones are macrolides of bacterial origin that stabilize MT in a similar way to taxol [91]. The first compounds of this class to be discovered were Epothilones A and B (Fig. 10) that were isolated from bacterial cultures [92]. Epothilones are competitive inhibitors of taxol binding to MT, indicating that they bind to the same or overlapping binding sites in tubulin. In comparison to taxol, epothilones are more water soluble and retain activity in taxol-resistant cell lines [93]. Hundreds of epothilone analogues have been synthesized in the search of more active compounds and six of them have entered clinical trials [3]. This high number of analogues represent an invaluable source of SAR data that has helped to design new active derivatives.

The X-ray (Fig. 11) and solution NMR structural studies of epothilones in the absence of tubulin have already been reviewed [51]. Most studies concluded that there are several conformers in a fast equilibrium exchange, as expected from the flexibility of the large macrocyclic ring [51, 94]. Analysis of 2D NOE and ROE

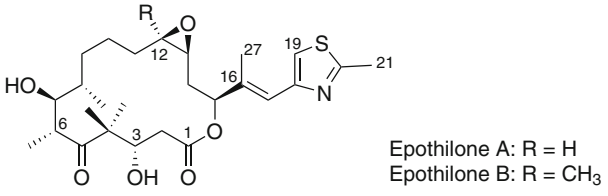

Fig. 10 Structure of Epothilones A and B

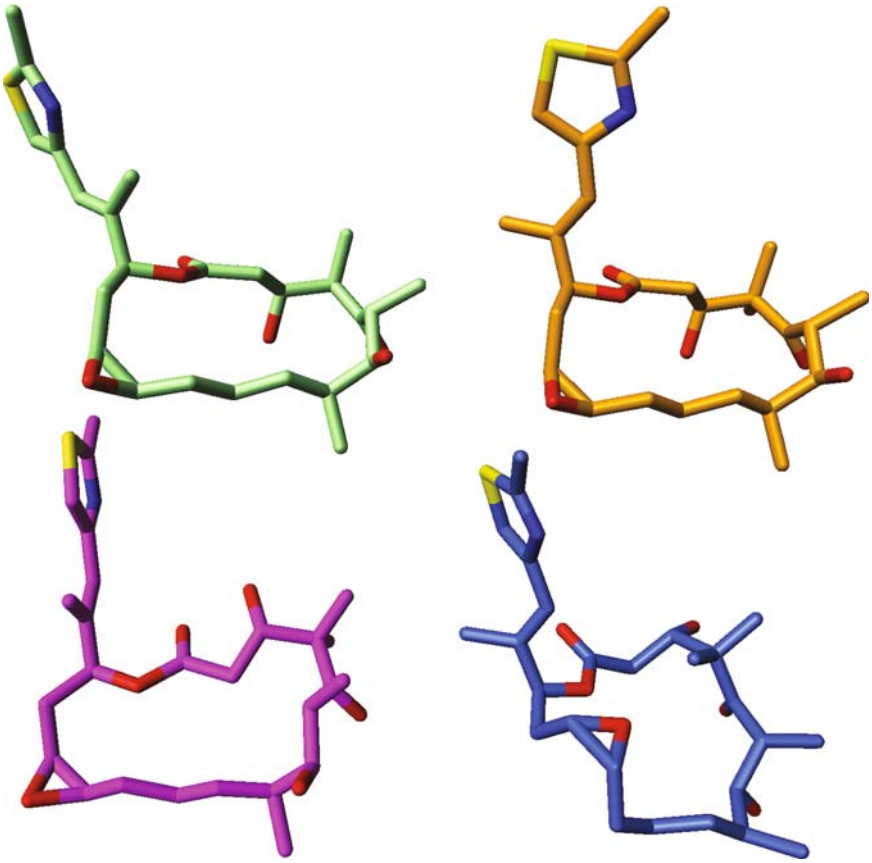

Fig. 11 Three-dimensional structures of epothilones determined in different environments (O *red*, S *yellow*, N *dark blue*). *Top*: structures of free EpoA determined by X-ray crystallography from dichloromethane/petroleum ether (*top left* [98](a)) and from methanol/water (*top right* [143](b)). *Bottom*: structures of EpoA bound to tubulin determined by solution NMR in aqueous medium (*bottom left* [96]) and by electron crystallography from zinc-stabilized tubulin sheets (*bottom right* [26]).(a) The crystal structure data have been available from the author to interested research groups since October 1995.(b) H.-J. Hecht, G. Höfle, unpublished results; CCDC 241333 and CCDC 241334 contain the crystallographic data of this structure. These data can be obtained free of charge via www.ccdc.cam.ac.uk/conts/retrieving.html (or from the Cambridge Crystallographic Data Centre, 12, Union Road, Cambridge CB2 1EZ, UK; fax: (+ 44) 1223-336-033; or deposit@ccdc.cam.ac.uk)

spectra of EpoA in dichloromethane or DMSO/D_2O in combination with computational conformational search was interpreted as consistent with two conformations in solution [94]. By contrast, based on NAMFIS analysis in those solvents, it was proposed that the NMR data is more consistent with an equilibrium of a set of 10–20 conformations with individual populations below 25% [51]. Recently, the

conformation of EpoA and two C3-modified analogues was also investigated in aqueous solution by means of NMR spectroscopy and NAMFIS calculations [95]; results will be discussed later in this section.

Two conformations of EpoA in complex with tubulin have been proposed on the basis of EC [26] and NMR [76, 96] data, respectively (Fig. 11). The tubulin-bound conformation of EpoA was determined by solution NMR spectroscopy [96] before the EC structure of EpoA bound to tubulin was available. The observation that, in a 100:1 mixture with tubulin, NOE cross-peaks of EpoA have negative sign, indicated that there is a fast exchange equilibrium in solution. This offered the opportunity to measure transferred NMR experiments, that report on the bound conformation of the ligand. A total of 46 interproton distances were derived from cross-peak volumes in tr-NOE spectra. However, these distance restraints did not suffice to define a unique conformation, as several distinct structures were consistent with them. Transferred cross-correlated relaxation (Sect. 2.2.1.3) provided the additional dihedral restraints that were crucial to define the bound conformation [96, 97]. One requirement to measure CH–CH dipolar and CH–CO dipolar-CSA CCR rates is that the carbon atoms involved in the interaction are labeled with ^{13}C. The availability of a ^{13}C-labeled sample of EpoA offered the opportunity to derive seven of these dihedral angle restraints from tr-CCR measurements (Fig. 12).

The NMR-derived tubulin-bound conformation of EpoA resembles the X-ray structure [98] of free EpoA except for two significant changes: the orientation of the thiazole ring and the torsions in the O1–C6 segment. The latter change affects mainly the position of the 3–OH that, upon binding, experiences a 3.8 Å shift movement from the inside of the macrocycle to an exposed position in its exterior. The authors proposed that this change makes the 3–OH more accessible for H-bonding to tubulin side chains [96], although more recent findings suggest that the 3–OH does not participate in direct contacts to tubulin but is rather exposed to the solvent (see next section) [76, 95]. The importance of the geometry of this segment

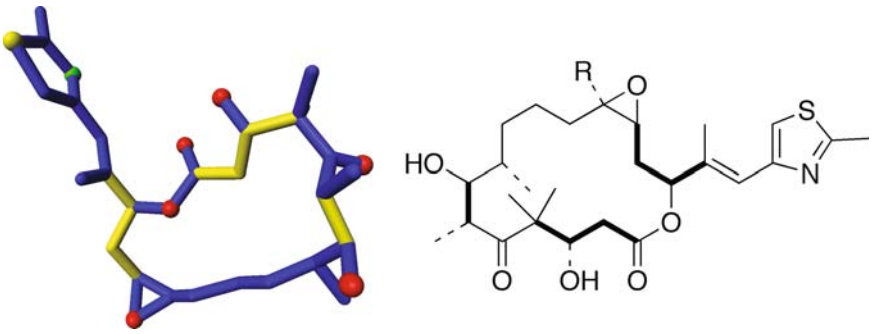

Fig. 12 Representation of the seven bonds for which torsion angles of EpoA were defined by tr-CCR NMR [96]. *Left*: stick model of the NMR-derived bioactive conformation. The torsions defined by the tr-CCR measurements are displayed as *yellow sticks*. Heteroatoms are displayed as *spheres*: O in *red*, S in *yellow*, and N in *green*. *Right*: the same torsions displayed as bold bonds

is underlined by the fact that inversion of the stereochemistry of C3 reduces its biological activity [99]. As for the orientation of the thiazole ring, the C17–C18 bond is rotated by 180° relative to the X-ray free conformation. This rotation places the thiazole nitrogen in a less hindered position compared to the X-ray conformation from dichloromethane/petroleum ether [98], where it is close to Me27, suggesting that the nitrogen may be involved in H-bonding interactions with tubulin. Such a hydrogen bonding pattern was indeed found in the EC structure of EpoA with Zn-sheets of tubulin [26]. No hydrogen bonding but stacking interactions were found, however, in the INPHARMA derived structure of tubulin and EpoA [76]. The hypothesis on the importance of the position of the nitrogen was supported by SAR of EpoB analogues where the thiazole ring had been replaced by several pyridyl heterocycles. The observation that the 2-pyridyl derivative retained its tubulin polymerization and cell growth inhibition potencies while the 3- and 4-pyridyl were less active, indicated that the position of the N atom in the ring has a significant influence on tubulin binding [100]. Methyl derivatives of the 2-pyridyl analogue provided additional SAR data [100]. When the methyl group is on positions 4 or 5, the derivatives are even more potent than the unsubstituted compound. Interestingly, the 3-methyl derivative is significantly less potent (IC50 39.4–50.5 nM) than the unsubstituted one (IC50 0.30 nM). The reported activities can be interpreted as supportive of the *syn* orientation of the thiazole N and H17 in the NMR-derived conformation. The reduced activity of the 3-methyl analogue can be due to the steric clash of the pyridyl 3-methyl with Me27, which prevents the Epo side chain from adopting the almost planar conformation that places the heterocycle N atom *syn* relative to H17. However it has to be mentioned that SAR of tubulin binding drugs need to be interpreted carefully. For instance, the analogue of EpoB with a phenyl ring replacing the 2-pyridyl (hence lacking the N atom) has a similar tubulin polymerization activity but is less potent in cell growth inhibition assays [101]. This piece of SAR data indicates that the H-bond between the thiazole ring and His227 is not necessary for the binding or EpoA to tubulin, but rather that the presence and position of the nitrogen of the thiazole ring may have a large effect on the transport of Epo inside the cells. Another study on a series of Epo derivatives with fused heteroaromatic side chains indicated that the position of the N atom has only a marginal influence on the polymerization activity of the compounds, which seems to contradict the observations with the said pyridine analogues [102]. This different SAR relative to the non-fused pyridine analogues may be the consequence of different binding modes to tubulin of the two classes of compounds, although this hypothesis has yet to be confirmed with structural or computational studies. Interestingly, the position of the N atom has a strong influence in the antiproliferation activity of the fused ring analogues, illustrating that tubulin-polymerization activity and antiproliferation activity do not always correlate [102].

Determination of EpoA Binding Orientation Based on INPHARMA

Although the NMR-derived bioactive conformation of EpoA is consistent with a large number of SAR data, it does not solve the question of the orientation of the ligand in the protein binding site. One approach to overcome the lack of the 3D

structure of the complex is the derivation of pharmacophore models and minireceptors. There have been many attempts to derive a common pharmacophore model for PTX and Epo that could provide their relative orientation in the tubulin binding pocket [103–107]. These models are usually derived from computational studies that use SAR data and molecular descriptors. They rely on the assumption that there is some equivalence between the pharmacophoric points of the two drugs and that they interact with the same subsites in the binding pocket. However, these models should be interpreted with caution, especially in cases when there is evidence of significant protein flexibility [108].

Due to this lack of information, we and others invented the INPHARMA method that has been described above [75, 76]. The prerequisites for INPHARMA are well fulfilled for EpoA and tubulin since the binding affinity is in the correct range, namely fast exchange. In addition, there is a 3D electron crystallography structure of the MT/taxol complex [11]. Thus, INPHARMA could rely on this structure and derive from the interligand NOEs the orientation of EpoA in the binding pocket of tubulin.

Due to PTX low solubility in aqueous medium, which makes it unsuitable for solution NMR experiments, a molecule of similar structure that could mimic its binding to tubulin was chosen instead as ligand A (Fig. 7). Although baccatin III (Fig. 13) has lower biological activity than PTX, it contains most of the structural elements of PTX, binds to the PTX binding site and is more water soluble [103, 109]. Baccatin delivers tr-NOE in the presence of tubulin, indicating that it is in a fast binding equilibrium with the protein. NOESY experiments recorded on a mixture of EpoA, baccatin and tubulin at several mixing times displayed up to 51 peaks of protein-mediated interligand NOEs, of which 19 peaks were already observed in the NOESY spectrum with 40 ms mixing time (Fig. 14). NOE buildup curves recorded with several mixing times indicated that those peaks were the consequence of spin diffusion.

For the structure calculation, 5000 binding poses of EpoA were generated by non-restraint docking of its NMR-derived conformation into the binding site of the EC-derived 3D structure of tubulin (complex TB). The docking protocol was designed to sample tubulin conformations that differed from the starting EC-derived

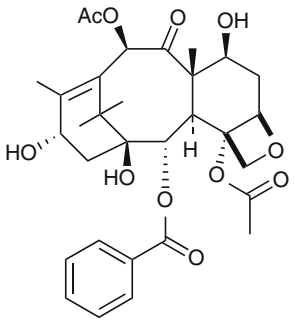

Fig. 13 Structure of Baccatin III

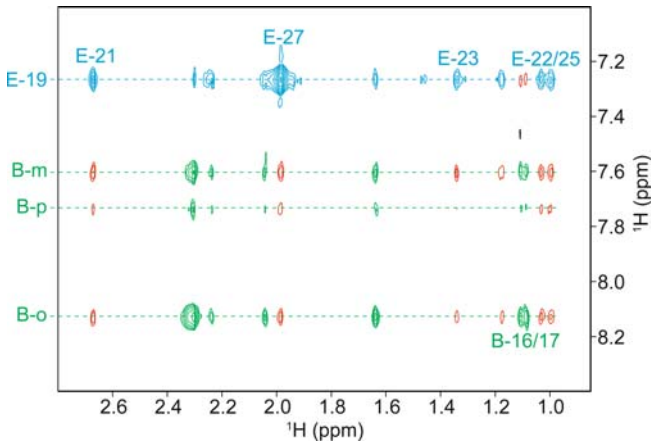

Fig. 14 Aliphatic/aromatic region of NOESY spectrum of a mixture of tubulin, EpoA, and baccatin III with concentrations of 12 μM, 0.6 mM, and 0.6 mM, respectively. The spectrum was acquired on a 900-MHz spectrometer equipped with a cryoprobe with a mixing time of 70 ms. The *blue* and *green peaks* are intramolecular transferred NOE peaks of EpoA and baccatin, respectively. The *red peaks* represent the interligand transferred NOEs mediated by the protein protons. The *numbering* of the atoms corresponds to that shown in the compound structures for EpoA (E) and baccatin (B). B-m, B-o, and B-p indicate the protons in the *meta*, *ortho*, and *para* positions of the benzene ring of baccatin, respectively. (Reprinted with permission from [75]. Copyright 2005 Wiley-VCH Verlag GmbH & Co. KGaA, Weinheim)

coordinates of Zn-induced tubulin sheets (PDB entries 1JFF and 1TVK). Other tubulin coordinates generated in other modeling studies were also used as starting coordinates. Thus, the protocol consisted of three stages that allowed increasing degrees of flexibility of the protein. The initial rigid docking was followed by a conformational search where the protein side chains and the M loop backbone were left flexible. Finally, a water refinement allowing full flexibility to the protein was done by covering the complex with a water layer of about 8 Å. Instead of assuming that baccatin binds to tubulin in the same orientation as PTX, 5000 binding poses of baccation were generated as well (complex TA). Pairwise combination of these poses gave 25 million relative orientations TA/TB (refer to Sect. 2.3). Quantitative analysis of these intermolecular NOEs by FRM calculations resulted in the NMR-derived binding mode of EpoA in solution.

In the NMR-derived binding mode of EpoA the macrolide ring partially overlaps the PTX baccatin core and the EpoA thiazole moiety lies close to the phenyl ring of PTX benzamido group (Fig. 15, right). The molecule of EpoA interacts simultaneously with both helix H7 and the M loop. This suggests that the MT-stabilizing effect of EpoA stems from its role as a linker that locks the relative positions of helix H7 and the M loop, thus favoring the straight form of protofilaments. This binding mode of EpoA partially resembles the EC-derived binding mode of PTX to polymerized tubulin (Fig. 15, left). The NMR-derived model explains quite well the available SAR data, like the effect of modifications of the thiazole ring, the importance

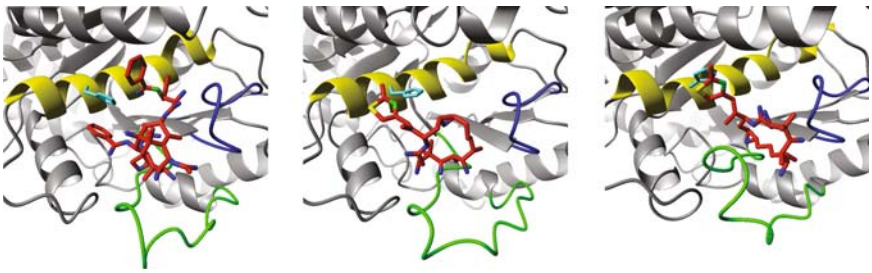

Fig. 15 Ribbon diagrams of tubulin in complex with MT-stabilizing drugs as determined by EC or NMR. *Left*: PTX/tubulin determined by EC (PDB entry 1JFF [83]). Center: EpoA/tubulin determined by EC (PDB entry 1TVK [26]). *Right*: EpoA/tubulin determined by solution NMR [76]. Drug molecules are represented as *stick models* (C *red*, O *blue*, N *green*, S *yellow*). Some secondary structure elements of tubulin are colored: helix H7 (*yellow*), M loop (*green*), S9–S10 loop (*blue*). The side chain of His227 is depicted as *cyan sticks*

of the stereochemistry of the 3–OH, or the higher activity of EpoB [76]. The thiazole ring of EpoA stacks with the imidazole of His227, with the two ring planes tilted about 30°. Contrary to what had been hypothesized based on the NMR-derived conformation of EpoA and SAR of pyridyl analogues, the thiazole nitrogen atom does not participate in direct H-bonds to the protein in the NMR-derived model, although it may be possible for the N to make a water bridge with the side chain of Asp24. The requirement of a nitrogen atom in the *ortho* position relative to the C16–C17 bond and *syn* to H17 had been interpreted as indicative of the N atom participating in an H-bond to tubulin [96, 100, 101]. However, lower tubulin polymerization activity is displayed by other derivatives also bearing a nitrogen atom in the *ortho* position of the side-chain heterocycle, such as pyrimidine (with a second N atom in the heterocycle) [101] or the aforementioned fused pyridine heterocycles [102]. If the effect of the heterocyclic N atom is not due to H-bonding, it can be conceived that it may be related to π-stacking, as proposed by the NMR-derived binding mode, or to factors other than direct binding to tubulin, such as transport inside the cells [102].

The fact that inversion of the stereochemistry of C3 reduces the potency of epothilone suggests that the 3–OH plays a role in the interaction of Epo and tubulin [99]. However, the NMR-derived model shows that the 3–OH does not directly contact tubulin (Fig. 15) but occupies a position close to the hydrophilic C1′-carbonyl and C2′–OH groups of taxol in the EC structure [76]. Moreover, dehydration of the C2–C3 bond to the (*E*)-alkene or replacement of the 3–OH by CN [99] or by H [95] yields analogues with similar tubulin polymerization activity. NAMFIS conformational analysis of EpoA and two 3-deoxy derivatives also showed that the 16-membered ring adopts a similar conformation even in the absence of the 3–OH group [95]. The NMR-derived structure is in agreement with these facts that indicate that the role of 3–OH may be other than directly contacting tubulin, e.g., just making a hydrophilic surface of the tubulin/epothilone complex to the solvent water. The

NMR-derived model also explains the higher activity of Epo analogues with small apolar substituents on C12, such as EpoB, which can occupy the hydrophobic cavity in the proximity of F270 and L369.

Significance of the NMR-Derived Bioactive Conformation of EpoA

For the following discussion it is important to mention the experimental conditions used for the NMR measurements. NMR samples contained a 100-fold excess of EpoA relative to tubulin (0.5 mM EpoA and 5 μM tubulin) in D_2O buffer. One critical requirement for the NMR experiments is to prevent tubulin polymerization and keep it in solution. This was achieved by using Ca^{2+} ions instead of Mg^{2+} in the buffer, as Ca^{2+} ions are known to inhibit tubulin polymerization [110].

It has been argued that the NMR-derived EpoA structure in the complex with tubulin may not represent its bioactive conformation because the conditions used for these NMR experiments do not reflect the true environment where EpoA acts as a drug and hence it is not sure that EpoA binds to the same site as in native MT [17]. One reason is that the dialysis and partial lyophilization of tubulin prior to the NMR experiments may cause its denaturation or inactivation. Besides, it has been proposed that PTX binding site only exists in MT and not in dimeric tubulin, at least with an affinity higher than millimolar [111]. In fact, in the NMR conditions tubulin is unable to form MT even in the presence of a 100-fold excess of EpoA. Therefore, it may happen that the interaction of EpoA with tubulin detected by NMR is not due to specific binding to the PTX binding site. Even if the interaction is specific, it may not be the bioactive conformation, i.e., the conformation that is active in vivo [17].

On the other hand, there is also evidence supporting the biological significance of the NMR-derived structure. Electron microscopy shows that tubulin dissolved in the NMR conditions forms ordered polymers upon addition of MT-stabilizing agents such as EpoA [76] or DDM [112]. These polymers are not MT but "microtubule sheets" or "open microtubules", that had been previously observed in MT preparations stabilized by EpoA or PTX [111] and by GMPCPP [113]. The induction of ordered polymers by MT-stabilizing agents confirms that tubulin is still active in the NMR solution and that it contains a binding site for PTX-site ligands. The fact that EpoA delivers tr-NOE indicates that it binds to soluble tubulin with a K_d value in the millimolar to low-micromolar range. This dissociation constant of EpoA for nonpolymerized tubulin is significantly larger than that for MT (K_d 34 ± 4 nM at 37°C [114]). Binding of MT-stabilizing agents to nonpolymerized tubulin had been suggested in a previous study with the fluorescent PTX analogue DMAT [115]. DMAT competes with PTX for binding to MT and is almost as effective as PTX in the MT-assembly assay. When binding to dimeric tubulin under non-assembly conditions, DMAT displays much lower affinity than for MT (K_d 49 ± 8 μM at 25°C) [115], that is of the same order as that proposed for EpoA in the NMR study. Weak binding of EpoA to soluble tubulin has also been postulated as the first step of one of the possible mechanisms of EpoA-induced MT assembly [114]. The lower affinity of EpoA and DMAT for unpolymerized tubulin

is not well understood. One explanation could be differences in the structure of the PTX-binding site of the two tubulin forms, allosteric effects or selection of conformations of tubulin that are more polymerization prone. However, the observation that EpoA induces tubulin assembly in conditions that disfavor polymerization [76] indicates that these structural differences cannot be too extensive.

Specificity of binding is supported by the observation of protein-mediated interligand NOEs [75, 76, 112] between pairs of ligands known to compete for the PTX-binding site (epothilones, taxanes, discodermolide, and baccatins) but not between ligands known to bind to different sites in MT, such as EpoA/vinblastine [76].

It has to be noted that EpoA molecules bound to tubulin polymers do not contribute to the NMR signal because only ligands in the fast-exchange regime are observable in these NMR experiments. Besides, tubulin polymers precipitate out of solution in a few hours. Therefore, the structure derived by NMR reflects the complex of EpoA binding transiently to the fraction of tubulin that remains soluble, that is very likely the first species formed during the drug-induced polymer assembly process.

Comparison of the NMR-Derived Binding Mode of EpoA with the EC Structure

The structure of the tubulin/EpoA complex was also determined by EC of 2D tubulin crystals induced by zinc and EpoA [26, 27]. Resolution was 2.9 Å in the plane parallel to the crystal and 4.2 Å in the perpendicular plane. As with the tubulin/PTX complex, this resolution is insufficient to define either the ligand conformation or its binding mode. Therefore, the EpoA structure was derived following the same procedure as with the tubulin/taxol structure [11, 83]. Namely, a large ensemble of EpoA binding poses was generated by molecular modeling starting from a set of X-ray and NMR-derived conformations. After checking their consistency with SAR data and further optimization, the model that best matched the EC density was selected as the EC-derived EpoA conformation (Fig. 15).

The conformation of EpoA differs significantly from that derived by NMR, regarding both the macrolide ring and the side chain. The macrolide ring of EpoA overlaps with the baccatin core of PTX but in a quite different orientation compared to the NMR structure. The main coincidence between the EC- and the NMR-derived structures resides in the role of the thiazole side chain. In both cases, the thiazole ring interacts with His227 and the nitrogen atom is moved away from Me27 due to a rotation about the C17–C18 bond that places H19 *syn* with respect to Me27 (Figs. 11 and 15). However, the two structures differ in the position of the thiazole ring in the binding site and in the nature of its interaction with His227. In the EC structure, the thiazole is in a position not occupied by PTX and forms an H-bond to the His227 side chain. The thiazole of the NMR structure is very close to the position of the PTX benzamido group and stacks with His227 instead of forming and H-bond with it.

When analyzed in detail, the rest of contacts EpoA/tubulin in the EC structure are quite different from those in the NMR structure. Excluding the anchoring point of the thiazole ring in the proximity of His227, the positions in the binding pocket of segments C1–C8, C9–C11 and the epoxide ring are different. Despite this fact,

the proposed overall effect of EpoA binding to tubulin is essentially the same in both structures, i.e., to lock the relative positions of helix H7 and the M loop in such a way that straight protofilaments are stabilized.

One remarkable aspect of the EC structure is that, although both EpoA and PTX ligands occupy the same binding cavity, each one interacts with the amino acid side chains of the binding site in an unrelated and unique way. This fact rules out the hypothesis of a common pharmacophore for Epo and PTX. It may turn out to be a property of rather flexible binding pockets to accommodate different small molecules in detail differently.

On the assumption that the protein-bound conformation of the ligand is one of those present in the free-ligand solution ensemble (refer to Sect. 2.2.2), NAMFIS analysis of the NOE and J data of uncomplexed EpoA in water was done to assess whether the EC- and NMR-derived tubulin-bound structures are among the feasible conformations in solution [95]. All the dihedral angles of the NMR-derived bioactive conformation are within the range values found by NAMFIS, meaning that this conformation is very likely present in solution. By contrast, the EC-derived conformation is not significantly populated in the solution ensemble and has four dihedral angles that deviate from the feasible values identified by NAMFIS.

The two structures of the tubulin/EpoA complex derived from EC and NMR data are significantly different, although both are able to explain many available SAR data. It is worth noting that both structures were derived from samples that were not microtubules. The EC data were obtained from 2D sheets of antiparallel protofilaments, while MT are formed of parallel protofilaments arranged into cylinders. In fact, the position of the M loop differs in the two tubulin forms, as shown by docking of the EC-derived structure of PTX/MT into the 8 Å cryoelectron microscopy images of MT [24].

The structure based on solution NMR data reflects the influence of epothilone on the early steps of the tubulin assembly process, when the tubulin/EpoA complex is still in its soluble unpolymerized form and binding of EpoA is not as tight as with polymerized tubulin. The binding site of unpolymerized tubulin is expected to differ to a certain extent from that in polymerized MT. Still, similar to PTX, epothilones interact with the M loop and it is highly conceivable that the M loop is locked in a conformation already in the tubulin-dimer/epothilone complex that enhances lateral M loop contacts required for MT formation.

The structures of complexes of drugs with tubulin dimers, microtubules and, to some extent, with zinc-sheets of tubulin need to be further explored to reveal the structural basis of polymerization and depolymerization of tubulin. Still, there is another level of insight, namely which one of these structures (or further ones yet to be discovered) represents optimally the conformation responsible for the clinical effects of the drug [78].

Solid-State NMR Structure of EpoB

Given the uncertainties that still exist regarding the structure of tubulin/Epo and the significance of the artificial systems used to study it, it would be desirable to have experimental data measured directly from Epo bound to MT. One such technique is

ss-NMR, which has already provided direct structural data on PTX bound to MT. One of the great advantages of ss-NMR is that it can be applied directly to samples of genuine MT.

Recently, it was shown that ss-NMR spectroscopy can be used to determine the conformation of EpoB in the solid state [116]. The method relies on the measurement of intramolecular short H–H distances (in the range 1.8–3.0 Å) from 2D CHHC correlations under MAS [117]. Regarding the sample preparation, a small amount of ^{13}C labeled compound was diluted with EpoB with natural abundance of carbon isotopes. This reduces the signal to noise but, on the other hand, it excludes contributions from intermolecular H–H polarization transfer. Under these conditions, all CHHC cross-peaks result from intramolecular polarization transfer and reflect intramolecular interproton distances.

As a proof of concept, this methodology was applied to a sample of EpoB in the polycrystalline state. The 30 H–H distance constraints derived from two 2D CHHC experiments sufficed to determine the high-resolution structure of EpoB, that happened to be identical to that determined by X-ray crystallography [98]. The authors proposed that the same strategy could be applied to elucidate the microtubule-bound structure of the drug by using labeled EpoB in complex with non-labeled MT. The completion of this study is awaited. One advantage of the CHHC ss-NMR experiment is that it uses a sample of the genuine drug (EpoB) with no chemical modification. By contrast, the REDOR experiments used for the study of PTX conformation were not applied to PTX itself but to fluorinated analogues, whose tubulin polymerization activity is different from that of PTX [84, 87].

Discodermolide

Discodermolide (DDM, Fig. 16) is a marine natural product that promotes MT assembly more potently than PTX and is active against some PTX-resistant cell lines [118–120]. The photoaffinity analogue C19–BPC-DDM labels β-tubulin in close proximity to the taxol binding site [121] and DDM itself is a competitive inhibitor of PTX binding to MT [120], suggesting that DDM also binds to the PTX binding site on β-tubulin.

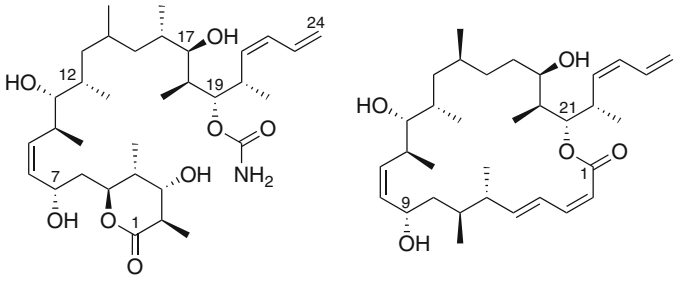

Fig. 16 Structures of the MT-stabilizing agents Discodermolide (*left*) and Dictyostatin (*right*)

The conformation of free DDM was first determined by X-ray crystallography [122]. The main carbon chain folds in a helical twist, leading to a compact conformation consisting of a hydrophobic core and a side-chain tail (Fig. 17a). Its bioactive conformation was addressed by NMR methods both with uncomplexed DDM in organic solvents and by tr-NOE in the presence of tubulin in aqueous medium.

The solution structure in acetonitrile was determined by analyzing NMR data in combination with a Monte Carlo conformational search [123]. The polar solvent acetonitrile was considered a good mimic of the water solution based on the similarity of the ^{1}H-NMR spectra of DDM in both solvents. The proposed conformation is very similar to that in the crystal and seems to result from minimization of the $A^{1,3}$ strain and *syn*-pentane interactions. Instead of assuming a single conformation in solution, Monteagudo et al. analyzed the spectra of DDM from DMSO solution following the NAMFIS methodology [60]. Data were consistent with a set of 14 conformations, that can be grouped into three families (Fig. 17b–d). It is remarkable that the crystal structure as a single conformer is not consistent with the NMR data. In fact, it contributes less than 1% to the conformational average, according to NAMFIS. None of these three conformational families is as compact as the crystal structure.

The tubulin-bound conformation of DDM in solution has been determined from tr-NOE data [112]. Sample conditions were similar to those used previously to determine the bioactive conformation of EpoA. Distance restraints were obtained from a series of tr-NOE spectra recorded at several mixing times and were used in the structure calculation based on the complete relaxation matrix methodology [37]. The NMR-derived bioactive conformation is quite similar to the crystal structure except for the conformation of the δ lactone ring, that is close to a flattened chair in solution but a twisted boat in the crystal (Fig. 18).

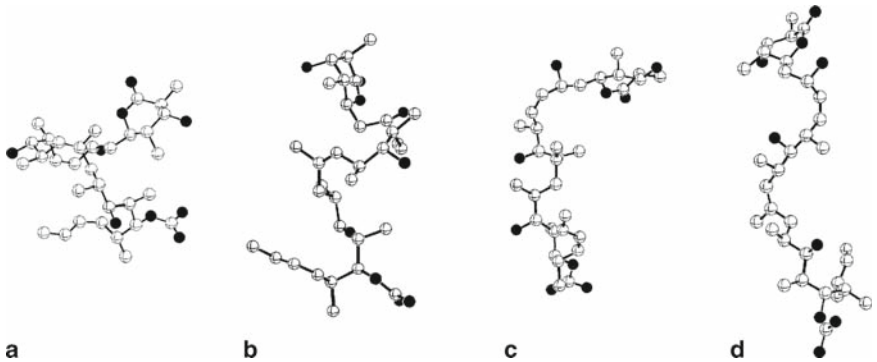

Fig. 17 The X-ray structure and three conformational classes of discodermolide identified by NAMFIS analysis of the NMR spectra in DMSO-d_6. **a** The X-ray conformation. **b** The corkscrew form. **c** The sickle motif. **d** An extended or awl form. (Reprinted with permission from [60]. Copyright 2001 American Chemical Society)

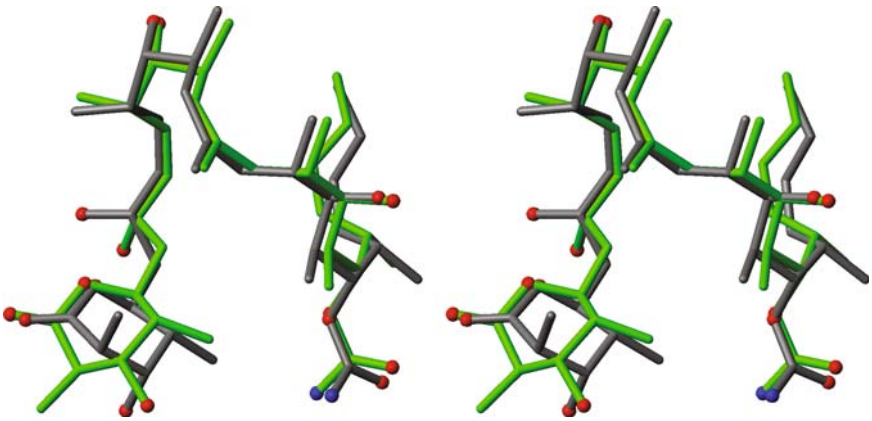

Fig. 18 Stereoview of the overlaid tubulin-bound (NMR-derived, in *gray* [112]) and free (X-ray derived, in *green* [122]) conformations of discodermolide. Heteroatoms are displayed as *spheres*: O in *red* and N in *blue*. The two conformations are quite similar except for the lactone moiety. (Reprinted with permission from [112]. Copyright 2006 Wiley-VCH Verlag GmbH & Co. KGaA, Weinheim)

It has been noted that the global shape of other taxoid site ligands, such as PTX, DTX or epothilones, can be described as consisting of a cyclic core and a side-chain tail [124]. Although DDM structure is not cyclic and hence its conformation is less restricted, it seems that DDM folds in such a way to resemble the shape of the other drugs.

The similarity of its bioactive and X-ray conformations had been anticipated on the basis of SAR data and of its structural homology to dictyostatin [125]. Dictyostatin (Fig. 16) is another MT-stabilizing agent that competes with PTX and has a similar effect on MT dynamics [125]. The preferred solution structure of the conformationally constrained dictyostatin overlays quite closely the tubulin-bound conformation of DDM, suggesting that they interact in a similar way with MT (Fig. 19). This hypothesis was further supported by the synthesis of a macrocyclic DDM/dictyostatin hybrid, that displays considerable antiproliferative activity [126].

Regarding the orientation of DDM in the β-tubulin binding site, the INPHARMA methodology was applied to a mixture of tubulin, EpoA and DDM [112]. NOESY spectra of the mixture showed a number of interligand cross-peaks. Given that DDM and EpoA compete with PTX for tubulin binding [127], simultaneous binding to tubulin can be ruled out and these NOE peaks can be regarded as protein-mediated peaks. Therefore, according to the principle of INPHARMA, these NOE peaks confirm that DDM and EpoA bind to the same binding site on tubulin and they can be used to determine the relative orientation of the two ligands in the binding site. Due to the weak intensity of these peaks, quantitative interpretation with full-relaxation-matrix (FRM) calculations was not possible. Instead, a pharmacophore model was proposed on the basis of the interligand NOEs and SAR data (Fig. 20).

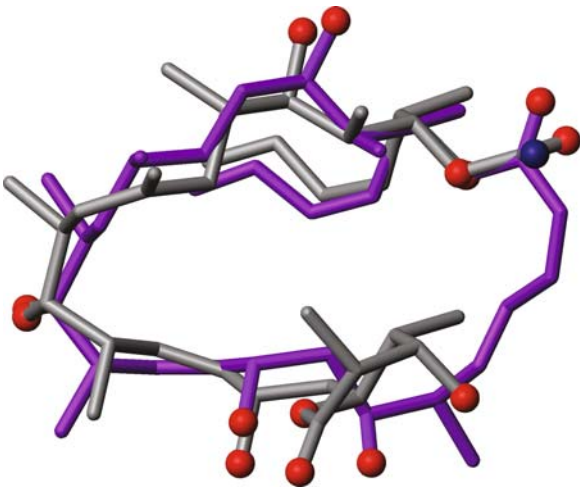

Fig. 19 Overlay of the NMR-derived bioactive conformation of DDM (*gray*) and the solution conformation of free Dictyostatin (*magenta*) [125]. (Reprinted with permission from [112]. Copyright 2006 Wiley-VCH Verlag GmbH & Co. KGaA, Weinheim)

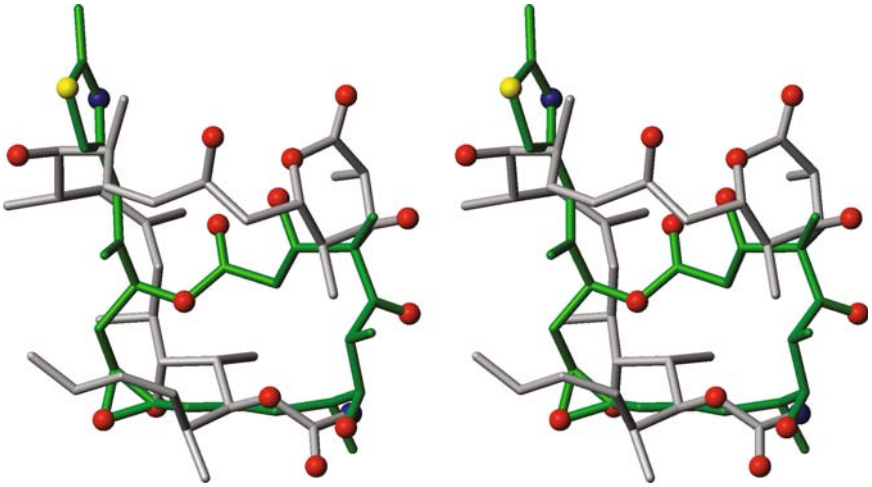

Fig. 20 Stereoview of the common pharmacophore model for EpoA (*green*) and discodermolide (*gray*) derived from INPHARMA NMR and literature SAR data. Heteroatoms are displayed as *spheres*: O *red*, S *yellow*, and N *blue*. In this model, the C20–C24 tail of DDM is on the same side as the section C10–C13 of EpoA, the carbamate group and the lactone ring occupy similar positions as the 7–OH group and C3–C4 unit of EpoA, respectively, while the C8–C15 segment of DDM corresponds to the C15–C18 region of the side chain of EpoA. (Reprinted with permission from [112]. Copyright 2006 Wiley-VCH Verlag GmbH & Co. KGaA, Weinheim)

According to this model, the side chain of EpoA overlaps with the C8–C15 segment of DDM, both segments containing unsaturated bonds. The proximity in space of EpoA 7–OH and the DDM C19-carbamate group suggests a site for H-bonding interaction with the protein. There is also a partial overlap between the hydrophobic moieties C10–C13 of EpoA and C20–C24 tail of DDM. In a previous study, a common pharmacophore had been derived by molecular modeling [106], that proposed that the C20–C24 tail of DDM corresponds to the side chain of EpoA. However, this model is not compatible with the observed interligand NOEs between the side chain of EpoA and the methyl groups of the C1–C11 stretch of DDM.

Finally, based on the fact that DDM conserves its activity in cell lines with mutations F270V and A364T, it was proposed that the C20–C24 tail of DDM occupies the same hydrophobic pocket that interacts with the C2 benzoyl side chain of PTX (Fig. 15). This pocket is formed by residues from helices H6 and H7 and is not occupied by EpoA neither in the EC- [26] nor in the NMR-derived [76] structures of the tubulin/EpoA complex. Studies of DDM bound to MTs are covered in the review by Diaz, Andreu and Jimenez-Barbero in this book [128].

3.1.2 Laulimalide Binding Site

Laulimalide [129, 130] and peloruside A [131] are compounds of marine origin that enhance MT assembly and retain activity in multidrug-resistant cell lines (Fig. 21) [14, 15, 132]. Previous work showed that laulimalide and peloruside A compete for the same or overlapping binding sites [15] but none of them inhibits the binding of taxoids to MT [14, 15]. Moreover, both laulimalide and peloruside A act synergistically with taxoid site drugs, like PTX, EpoA, EpoB, DDM and others such as dictyostatin, eleutherobin and cyclostreptin, while taxoid site drugs do not synergize with each other [133]. These observations suggest that laulimalide and peloruside A share a common binding site on tubulin that is distinct from the taxoid binding site. Although the location of this binding site has not yet been definitely identified,

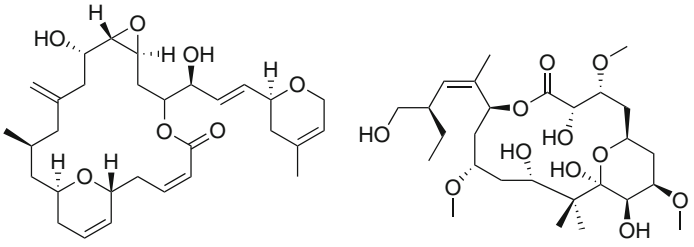

6 Laulimalide **7** Peloruside A

Fig. 21 Structures of the MT-stabilizing agents Laulimalide and Peloruside A

one study based on computational simulations proposed that the preferred laulimalide binding site occupies the position of the S9–S10 loop extension of the α subunit of tubulin, i.e., a position equivalent to the taxoid site of β-tubulin [16]. The same computational study also found that interaction of laulimalide and peloruside A with the taxoid site on β-tubulin is also energetically favorable, regarding it as a potential secondary binding site.

Laulimalide

The conformation of laulimalide in the free state has been studied by X-ray crystallography [129, 130] and solution NMR spectroscopy [64, 134].

In the work by Paterson [134], NMR spectra were recorded in CD_3OD that was selected as a close mimic of the biologically relevant aqueous media. Molecular dynamics simulations constrained with the experimental $^3J_{HH}$ and NOE NMR data converged to a family of closely related conformations (within kcal mol-1), that closely resemble the X-ray conformation. Overall, the molecule adopts a flattened conformation, with the macrolide and the side chain lying in the same plane (Figs. 22 and 23). It seems from this analysis that the C14–C20 and C1–C3 regions are relatively rigid and in agreement with SAR data, showing loss of antimitotic potency upon modification of these segments. In contrast, the C9–C12 segment and the side chain are more flexible.

A series of 11-demethyl analogues (Fig. 24) with modification or truncation of the side chain displayed reduced antimitotic potency [134]. The same kind of conformational analysis was applied to these derivatives based on molecular modeling restrained by NMR J and NOE data. Interestingly, the conformation of the macrocycle was not perturbed by these chemical modifications on the side chain, highlighting the essential role of the side chain for activity (Fig. 25).

In contrast, NAMFIS deconvolution of the NMR data in DMSO-d_6 followed by post-NAMFIS energy evaluation (see below) identified 15 laulimalide conformations belonging to five classes with populations in the range 7–27% [64]. NMR

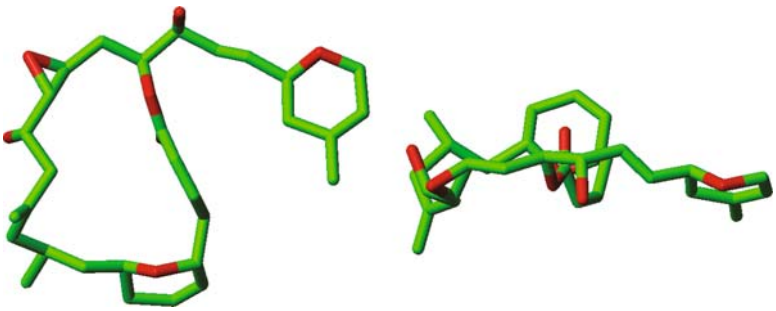

Fig. 22 Top and side views of laulimalide X-ray structure [129]. The molecule adopts a flattened conformation

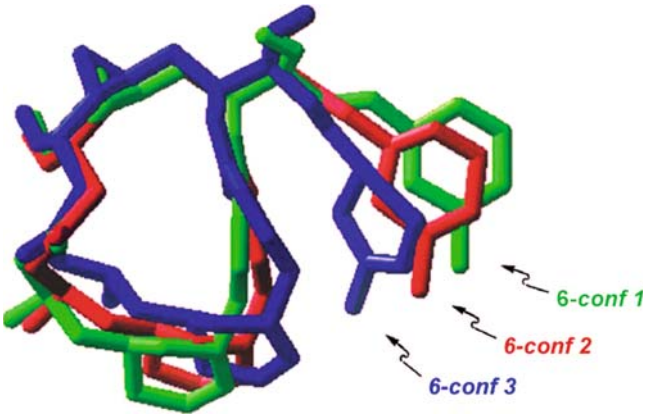

Fig. 23 Overlay of selected conformers of laulimalide within 2 kcal mol^{-1} of the global minimum determined from molecular modeling and NMR data in CD_3OD solution. These low-energy conformations closely resemble the X-ray conformation. (Reprinted with permission from [134]. Copyright 2005 Elsevier)

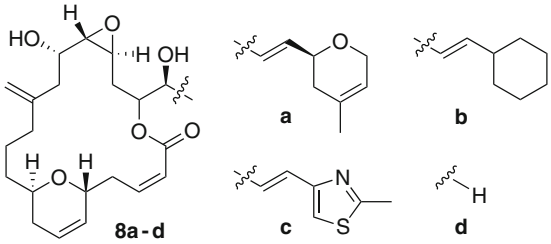

Fig. 24 Laulimalide 11-demethyl analogues with modified side chains [134]

experimental data consisted of 8 $^3J_{HH}$ couplings and 79 interproton distances derived from ROESY experiments recorded at several mixing times. The data deconvolution was complemented with a post-NAMFIS energy evaluation to discard those 7 out of 22 conformers that were neither energetically nor chemically reasonable. This energy check was required because relatively high energy deviations from the global minimum (6.2 kcal mol^{-1}) were allowed during the initial conformational search. The high energy deviation was allowed in order to not miss chemically reasonable structures.

The Supine motif (Fig. 26) is the most populated family (34%) and comprises six conformers. This motif is relatively flat and resembles the X-ray structure, although none of its family members matches it exactly. The Convex (Fig. 26) is the second most populated motif (30%). It is fairly similar to the Supine class but its macrocyclic ring is more curled than in the Supine motif.

The Cobra motif (Fig. 27) is characterized by the bending of the side chain such that its dihydropyran ring lies over the center of the face of the macrolide ring. All but one of the conformers of this class possess unreasonably high energies according to

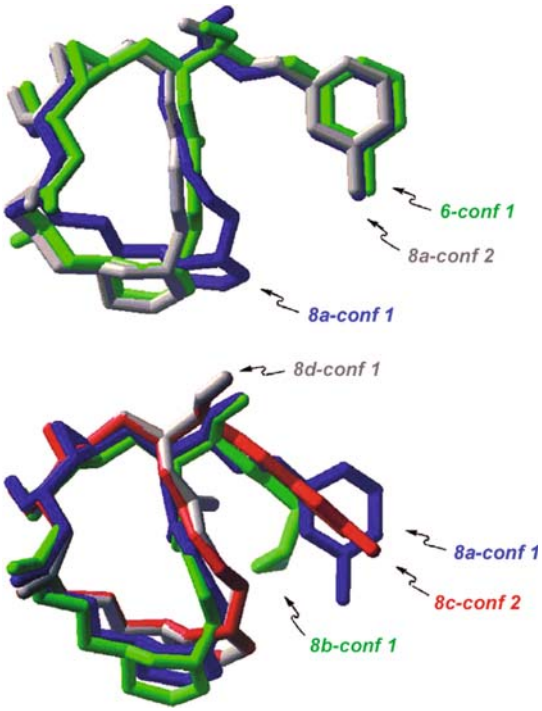

Fig. 25 Solution conformation of 11-demethyl-laulimalide **8a** in comparison to laulimalide **6** (*top*) and to its side-chain analogues **8b–d** (*bottom*). The conformation of the macrolide ring is nearly unperturbed by these chemical modifications. (Reprinted with permission from [134]. Copyright 2005 Elsevier)

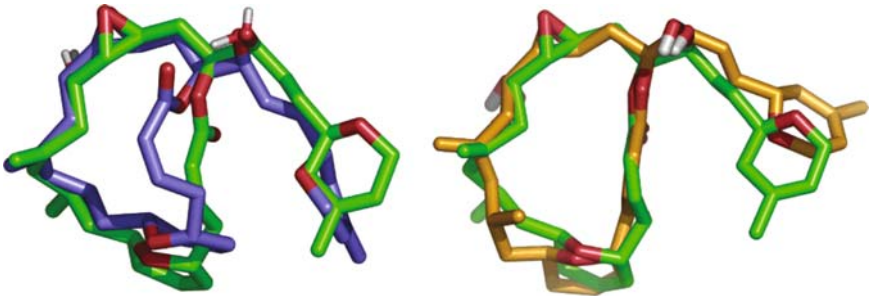

Fig. 26 Laulimalide crystal structure (*green*) overlapped with the most populated members of the Convex (left side, *blue*) and Supine (right side, *orange*) families. (Reprinted with permission from [64]. Copyright 2005 American Chemical Society)

post-NAMFIS DFT calculations and are ruled out on this basis. The other two classes (Concave and Stretch – Fig. 28) differ from the X-ray conformation, although not as much as the Cobra motif. By contrast with Paterson's proposal [134], inspection of the NAMFIS solution ensemble suggests that the segment C12–C20 is the most flexible part of the macrocycle.

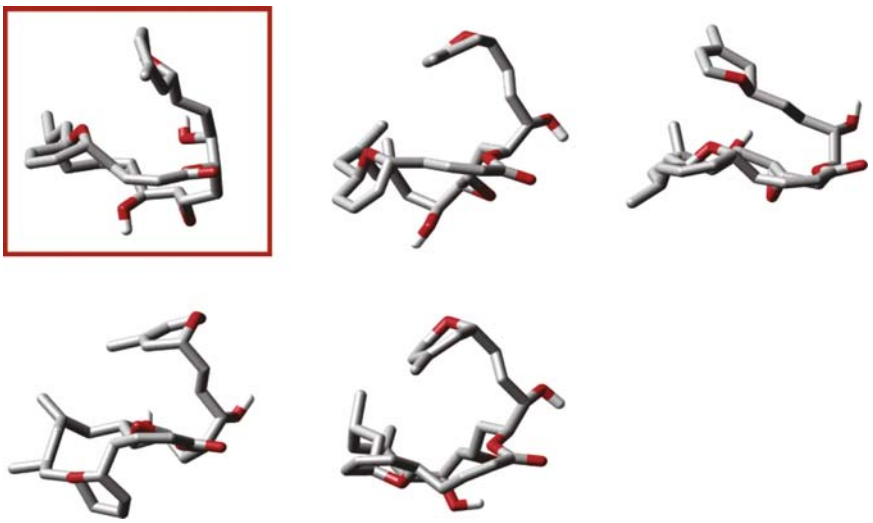

Fig. 27 Members of the Cobra class identified by NAMFIS. Only the top-left structure was found to be energetically reasonable by post-NAMFIS DFT calculations. (Reprinted with permission from [64]. Copyright 2005 American Chemical Society)

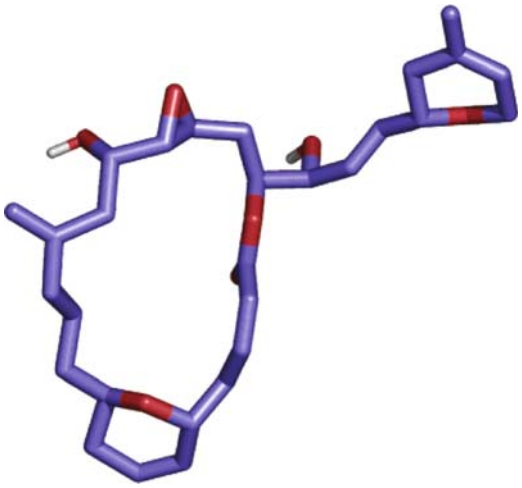

Fig. 28 The laulimalide Stretch motif differs from the Supine motif in that its side chain stretches away from the lactone ring. (Reprinted with permission from [64]. Copyright 2005 American Chemical Society)

As has been described under the subheading NAMFIS Deconvolution Analysis above, NAMFIS analysis cannot guarantee that a particular single conformation is present in the solution ensemble. Still, the method ensures that very similar conformers representative of the same family exit in the ensemble. In the case of laulimalide, it can be argued whether the low populated Concave and Cobra motifs may

not exist in DMSO based on the uncertainty values obtained initially for the conformer populations. However, a detailed analysis of the standard deviations provided narrower error limits and finally confirmed that the five families are present in the ensemble [64].

Peloruside A

The conformation of peloruside A (Fig 21) has been determined both in the absence and in the presence of tubulin in water solution [17]. Previously, its conformation had been studied in $CDCl_3$ [131, 135]. The large values of J couplings in water solution suggest that peloruside A conformation is well defined. Conformers present in water solution were identified by combining NMR data and molecular modeling. A computer conformational search provided a number of candidate conformations. Analysis of their match to the experimental ROESY-derived interproton distances indicated that only two conformational families exist in solution (Fig. 29). Conformers A and B differ mainly in the C10–C15 region. Molecular dynamics simulations indicate that both conformers are moderately flexible along the backbone, in agreement with the observed H2/H3, H3/H4 and H13/H14 coupling constants, that display values typical for conformational averaging. Ensemble average calculations using ROESY data and a set of 300 conformers of the A and B families led to the conclusion that both conformations are in equilibrium in water solution, with B somehow more populated than A [17].

As part of the same study, the bioactive conformation of peloruside A bound to MT was determined by means of tr-NOE experiments. It must be noted that the tubulin form used for these experiments is significantly different from that reported in the studies of EpoA [76] and DDM [112]. The tr-NOE experiments with peloruside A were done in the presence of tubulin assembled into MT and stabilized with

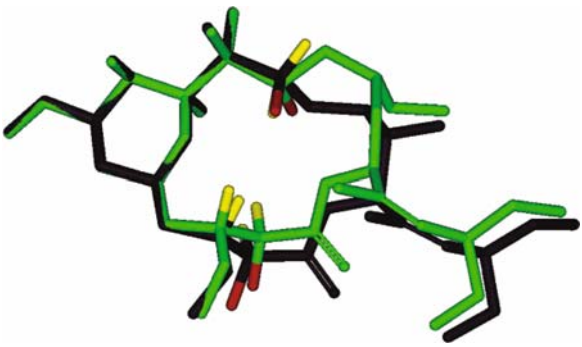

Fig. 29 Superposition of the two low-energy conformations of peloruside A in water solution. In *green*, conformer A. In *black*, conformer B. Key, H2, H3, and H11 hydrogens are shown in *yellow*, while O2 and O11 are in *red*. (Reprinted with permission from [17]. Copyright 2006 American Chemical Society)

GMPCPP. While the EpoA and DDM experiments report on the early events of ligand binding to nonpolymerized tubulin, the peloruside A experiments report on its association to polymerized MT. Transferred NOESY data were analyzed quantitatively following the FRM approach and were consistent with the B conformation. The binding epitope of peloruside A was deduced from STD experiments, that with short saturation times (<500 ms) displayed signal enhancements of protons H2, H8, H17, H19–H24, and the three methoxy rings.

Finally, the NMR-derived bioactive conformation was docked onto the EC-derived coordinates of tubulin in an attempt to find the laulimalide/peloruside binding site. The EC-derived coordinates of tubulin (PDB entry 1TUB) were used for the docking. The preferred binding region was found in the α subunit, in a site close to that found previously in the computational study by Pineda et al. [16]. This binding site is formed by helix H7, and loops S9–S10 and H1–S2 (Fig. 30). It is remarkable

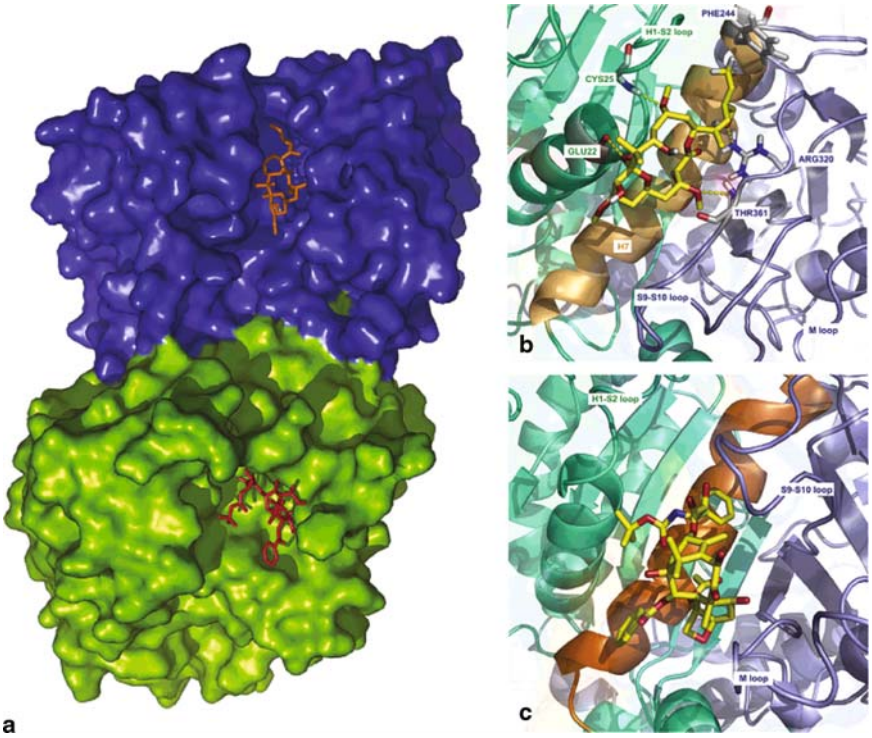

Fig. 30 Taxoid site on β-tubulin and predicted peloruside site on α-tubulin. **a** Surface representation (view from the inner side of the microtubule) of a tubulin dimer with PTX (*red*) bound to β-tubulin (*green*) and peloruside A (*orange*) bound to the predicted site in α-tubulin (*blue*). **b** View of the peloruside binding site. Hydrogen bonds are represented as *yellow* dashed lines, and the residues involved in these bonds are labeled. Some secondary structure elements are also labeled. **c** View of the taxol binding site. Some secondary structure elements are labeled. In panels **b** and **c**, H7 is colored in *orange*, and the N-terminal and intermediate domains are colored in *green* and *blue*, respectively. (Reprinted with permission from [17]. Copyright 2006 American Chemical Society)

that this model does not propose any contact between peloruside A and the α-tubulin loop equivalent to the β-tubulin M loop. The MT stabilizing effect of PTX and EpoA had been attributed to contacts of the ligand to the M loop, that lock its position thus enhancing the establishment of lateral contacts [11, 26, 76]. The peloruside model suggests that the MT stabilizing effect of laulimalide-site ligands may be caused by locking tubulin in its straight conformation rather than by directly contacting structural elements involved in lateral contacts.

3.2 Microtubule-Destabilizing Agents

3.2.1 Vinca Domain

Taltobulin I (HTI-286)

Taltobulin I (HTI-286, Fig. 31) is a synthetic analogue of the marine natural product hemiasterlin [136]. HTI-286 is a potent inhibitor of MT formation [137] and is undergoing clinical trials for the treatment of cancer [1].

HTI-286 binds to the tubulin heterodimer and induces formation of 13-membered tubulin rings [138]. Photoaffinity labeling with analogues of HTI-286 mapped to residues of α-tubulin close to the interdimer interface [139]. Competitive binding assays with dolastatin-10, cryptophycin A, vinblastine, PTX and colchicines, indicate that the hemiasterlins bind in a subsite of the Vinca domain, which is located at the interdimer interface [28].

The bioactive structure of HTI-286 was investigated by NMR in solution using a 200:1 ligand:tubulin ratio [47]. NMR relaxation-compensated STD enhancements were indicative of strong protein contacts with the aromatic protons and weak interaction with the *tert*-butyl group, in agreement with SAR data. Additional STD experiments with two analogues of HTI-286 support these results and suggest that the *tert*-butyl group occupies a spacious cavity in the binding site and hence does not make close contacts to the protein.

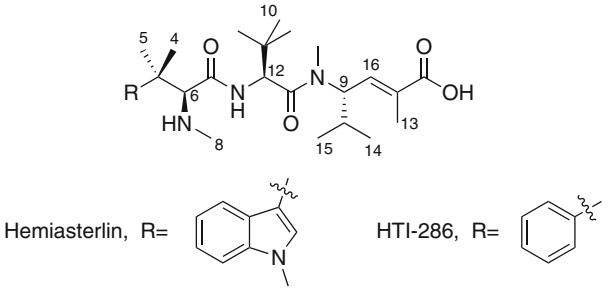

Fig. 31 Structures of the MT-destabilizing agents Hemiasterlin and its analogue Taltobulin I (HTI-286)

Some discrepancies between the initial STD enhancements and SAR data of HTI-286 initiated the authors to use a relaxation-compensated modification of the STD experiment. Initially, when a typical saturation time of 1s (relatively long saturation time) was used, weak STD was observed for all *tert*-butyl (H10) and *gem*-dimethyl groups (H4/5 and H14/15). However, this was inconsistent with SAR that indicated that the H14/15 and H4/5 *gem*-dimethyl are required for activity. Besides, the stronger STD of H13 and H16 suggested a closer interaction than with H4/5, while SAR indicate that the olefin does not establish close contacts with the protein. As explained under the subheading Saturation Transfer Difference (STD) NMR above, there may be different T1 relaxation times in the ligand that distort the STD effect. Following the suggestion of Yan et al. [46] this problem can be alleviated by measuring STD spectra with reduced saturation times. Full STD build-up curves were therefore measured with increasing saturation times. In the end, the 350 ms STD indicated close contacts for both *gem*-dimethyls H4/5 and H14/15, while H10 remained displaying weak STD (i.e., not close contact). Thus, the initial discrepancy between STD and SAR could be resolved by the STD experiment with shorter saturation times.

The bound conformation (Fig. 32) was determined from tr-NOESY data and restrained simulated annealing calculations. The NMR-derived bioactive conformation resembles the crystal structure of free hemiasterlin methyl ester [140]. The main difference is the displacement of the aromatic ring due to a rotation of 60° of its bonding axis. Besides, the NMR conformation is more compact than the X-ray structure.

A binding pose of HTI-286 was derived from iterative docking guided by experimental data from SAR and competitive inhibition, photoaffinity labeling, STD, and tr-NOE experiments (Fig. 33) [138]. Initially, a number of binding poses was generated by following computational procedures guided by all available experimental data, with the exception of NMR data. As a final step, the best scoring poses were compared to the experimental NMR STD and tr-NOE data, that had not been used to drive the prediction.

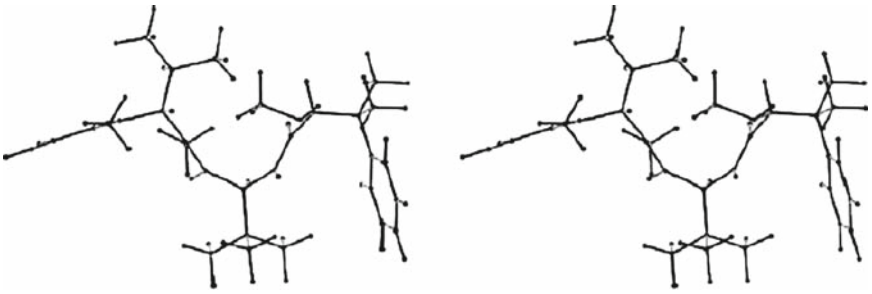

Fig. 32 Stereoview of the NMR-derived tubulin-bound conformation of HTI-286. (Reprinted with permission from [47]. Copyright 2006 Elsevier)

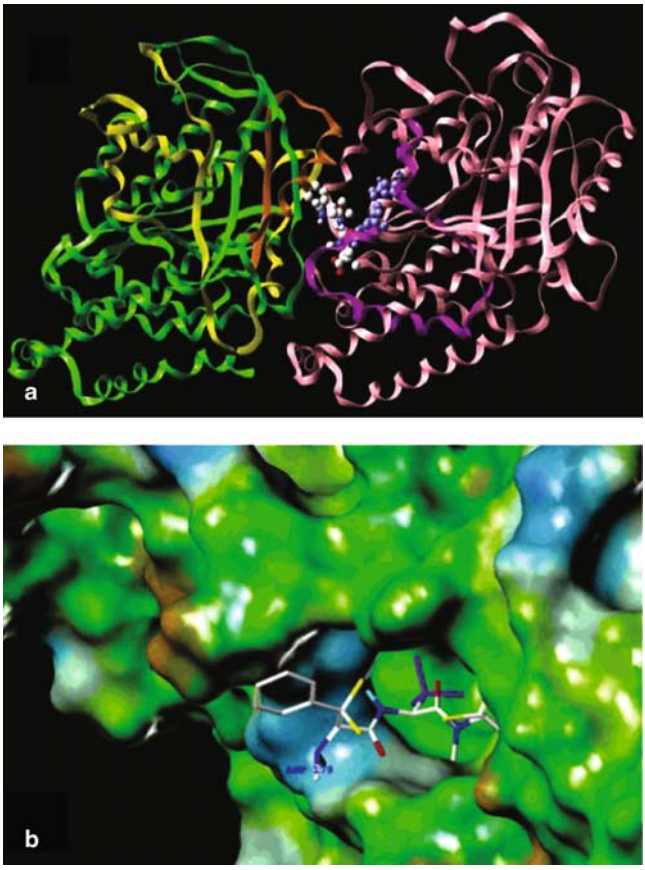

Fig. 33 Best HTI-286 binding pose and its interactions with tubulin. **a** Overview of the α/β-tubulin complex used in the docking studies and the best binding pose for HTI-286. The Vinca-binding region (175–213) of the β subunit is colored *purple*, and the remaining region of β-tubulin is colored *pink*. The photoaffinity cross-linking regions of probes 1 and 2 are colored *orange* and *yellow*, respectively, and the remaining region of α-tubulin is colored *green*. HTI-286 and GDP are shown in CPK representation, where GDP is colored *blue*, while HTI-286 is colored by atom type. **b** Surface view of HTI-286 docked to the β-tubulin portion of the interdimer interface, emphasizing the binding pocket. The *yellow*-colored carbon atoms are poised for intramolecular interactions, and the *tert*-butyl carbons are colored *purple*. (Reprinted with permission from [138]. Copyright 2005 American Chemical Society)

The selected binding pose scores well for HTI-286 and its analogues, agrees with photoaffinity labeling, competition experiments and SAR data, and it is consistent with the NMR-derived conformation. The model suggests that binding is driven by Van der Waals interactions and the hydrophobic effect. As predicted from the STD experiments, the *tert*-butyl group does not establish close contacts to the protein because it occupies a spacious cavity in β-tubulin, in the proximity of the nucleotide

binding site. The large STD enhancement of the aromatic protons is consistent with its π-stacking interaction with Phe351 of α-tubulin.

A different binding model had been proposed based on molecular modeling of hemiasterlin [141]. The ligand conformation and the binding region are similar in both models. However, the binding orientation in the model presented by Mitra et al. is different and it is not compatible with labeling of residues α:203–280 by the photoaffinity probe [139].

The NMR-based HTI-286 binding mode shows ligand-induced changes in the longitudinal contacts at the interdimer interface. Interaction of the HTI-286 aromatic ring with α:Phe351 perturbs contacts between several Phe and Tyr residues of the H9, S8, and S9 regions of α-tubulin. Also, distances between key residues of helix H8 and strand S9 change. Upon ligand binding, the relative position of some secondary elements (such as helices α:H8, α:H10, and β:H6), change, thus inducing curvature in the complex, similarly to the reported X-ray structure of the T2R complex [21]. Comparison of the tubulin-bound conformation of HTI-286 to a minimized uncomplexed conformation suggests that the phenyl and *gem*-dimethyl at C11 reorient upon binding (Fig. 34).

Interestingly, the initial tubulin coordinates used in the study of HTI-286 are those of straight tubulin in 2D sheets (PDB entry 1JFF) [83]. The X-ray structure of the T2R complex with vinblastine showed that the unpolymerized tubulin heterodimer is bent and that there are local conformational changes at the interdimer interface in comparison with straight tubulin [13]. The discrepancy between the experimental [12] and computationally predicted [31] binding modes of colchicine has been attributed to the fact that the computational model was derived from

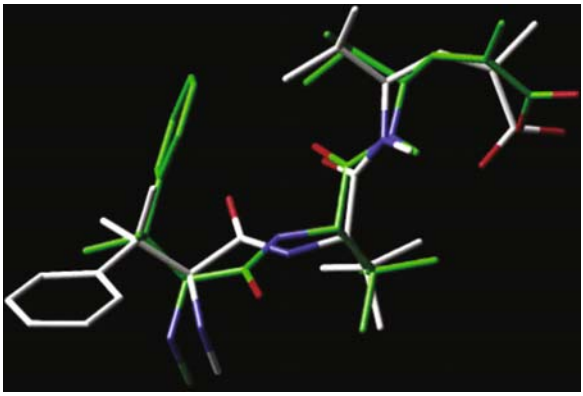

Fig. 34 Overlay of two HTI-286 conformations. The carbon atoms of the protein-bound conformation and a low-energy conformation are colored *white* and *green*, respectively. (Reprinted with permission from [138]. Copyright 2005 American Chemical Society)

the coordinates of straight tubulin determined by EC [11] and was unable to predict the bending of tubulin. Even though the HTI-286 binding pose of Ravi et al. is able to predict the curvature of tubulin, for future studies of Vinca domain ligands, it would be interesting to start the docking from the coordinates of the T2R/vinblastine complex, that is already bent and has a ligand bound into the Vinca domain [13].

N-Terminal Stathmin-Like Peptide I19L

The stathmin family of proteins destabilize MT [8]. The X-ray structures of complexes of tubulin with the 91-residue long stathmin-like domain of RB3 reveal that the RB3–SLD caps two tubulin heterodimers, thereby preventing the incorporation of tubulin into MT [12, 13, 21]. Apparently, the longitudinal interactions are impeded by the union of the SLD N-terminal cap domain to the α-subunit.

A series of small peptides were prepared in order to identify the minimal unit that could mimic the effect of the N-terminal cap domain. The structure of the most efficient (I19L, Fig. 35) was studied by NMR and molecular modeling [142]. The concentration dependence of inhibition of tubulin polymerization suggested that the peptides bind stoichiometrically to unpolymerized tubulin rather than to assembled MT. It is well known that the stability of the tubulin/stathmin complex decreases upon phosphorylation of stathmin [8]. In agreement with this, phosphorylated I19L was found to be fourfold less efficient than its unphosphorylated form.

The structure of I19L was determined in aqueous solution at pH 6.8 by NMR [142]. Chemical shift values and the scarcity of cross-peaks in NOESY and ROESY spectra indicated that the peptide is mostly disordered in solution, although it has a helical propensity at residues 10–14 (Fig. 36). The bound conformation was investigated by means of tr-NOESY and STD experiments using a 30:1 excess of peptide relative to tubulin. The presence of intense, negative cross-peaks in the tr-NOESY spectrum proved that there is a fast binding equilibrium (Fig. 36). Unspecific binding was ruled out based on the absence of tr-NOE peaks in a control experiment where the protein was BSA instead of tubulin. The existence

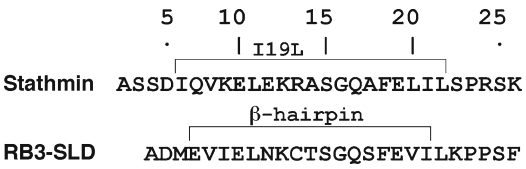

Fig. 35 Sequence of peptides from the N-terminal regions of human SLD and RB3–SLD. The sequences of peptide I19L (*top*) and the N-terminal β-hairpin of the T2R/colchicine complex (*down*) are shown

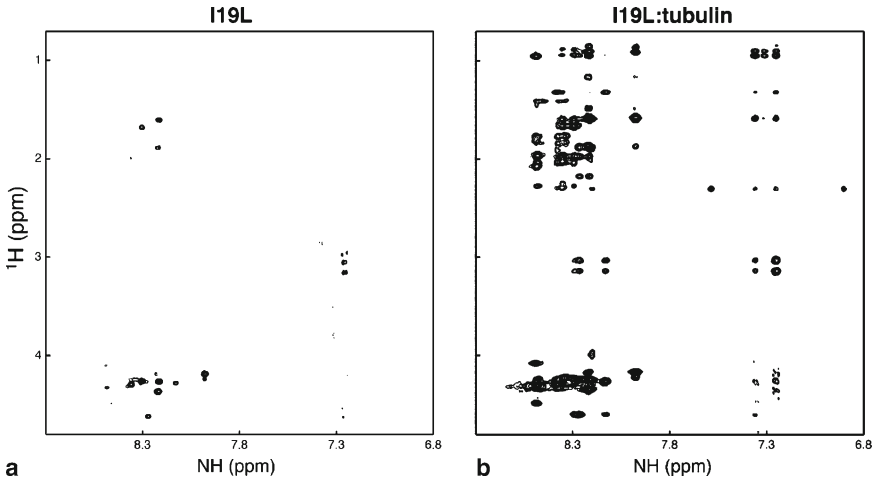

Fig. 36 Aliphatic/aromatic region of the NOESY spectra of I19L free and complexed with tubulin at pH 6.8. **a** Peptide I19L (0.6 mM) in the absence of tubulin. **b** Same region of the tr-NOESY spectrum of I19L in the presence of tubulin (30:1 ratio; 0.6 mM peptide and 20 μM tubulin). Spectra were recorded at 600 MHz with a mixing time of 200 ms. (Reprinted with permission from [142]. Copyright 2005 American Chemical Society)

of many medium- and long-range NOEs indicated that I19L adopts a well-defined fold when bound to tubulin. Structure calculations using the 176 NOE constraints provided the bound conformation of I19L (Fig. 37). The peptide adopts a beta-hairpin fold that resembles that observed in the X-ray structure of the T2R/colchicine complex [12]. However, there are some differences due to the mobility of the C- and N-termini of the short peptide and around its bulge. The latter difference is probably due to the better resolution of the NMR structure compared to the crystal. Additional NMR STD experiments mapped the close contacts to tubulin onto the methyl group of Ala19, the aromatic protons of Phe20, and the side chains of Leu22 and Leu24 (Fig. 38).

Finally, the bound conformation of I19L was docked into the α-tubulin structure determined from the T2R/colchicine crystal (Fig. 39). The peptide binds in a pocket between helix H10 and β-strand S9 on α-tubulin. The residues identified by STD interact with a number of tubulin hydrophobic side chains of H10 and S9. In addition, there is an ionic interaction between Arg14 and Asp-α245, and three intermolecular H-bonds. One interesting aspect of this model is that it explains the loss of efficiency upon phosphorylation of I19L. The docking model places the Ser16 side chain pointing towards tubulin in such a way that phosphorylation of Ser16 would hinder its association to tubulin.

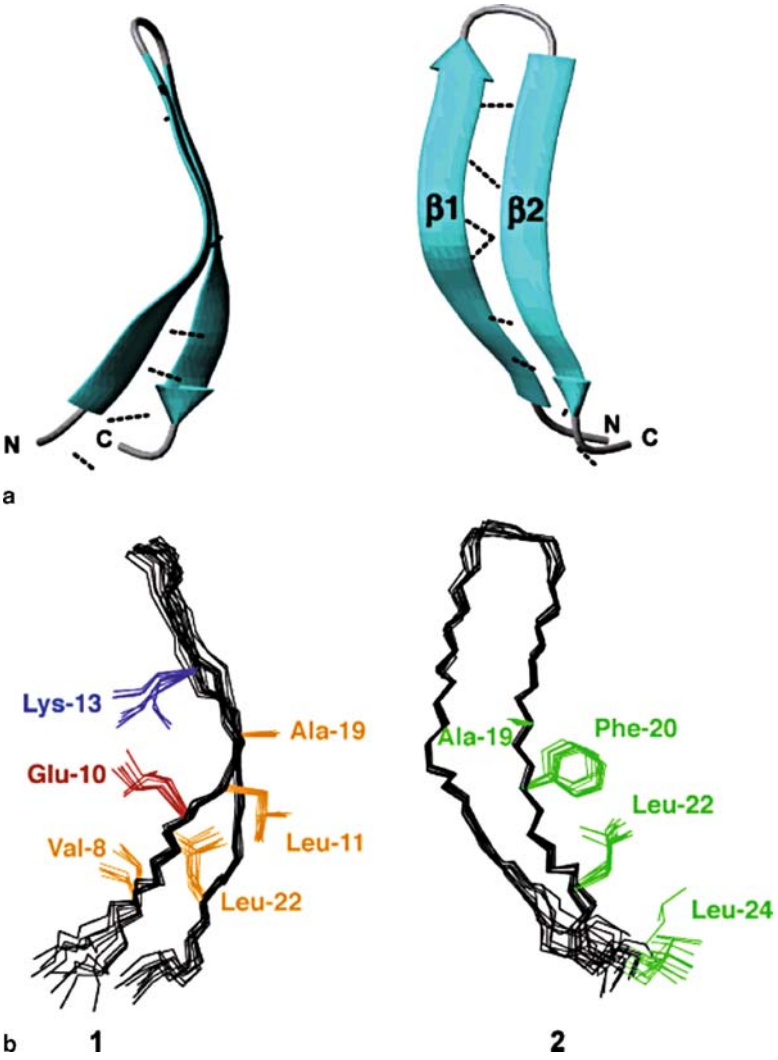

Fig. 37 NMR structure of I19L in interaction with tubulin. **a** Ribbon diagrams of the average structure of I19L showing the eight H-bonds between backbone atoms as *dotted lines*. The *left* and *right* figures are two views of the hairpin differing by a 90° rotation. **b** Superposition of backbone atoms of the ten best NMR structures of I19L. (1) Side chains of residues that stabilize the I19L folding are *highlighted*. (2) Side chains of I19L in contact with tubulin derived from STD experiments are displayed in *green*. (Reprinted with permission from [142]. Copyright 2005 American Chemical Society)

This example illustrates that the power of solution NMR is not limited to small-molecule ligands but can be applied also to medium-sized molecules provided the fast exchange condition is fulfilled.

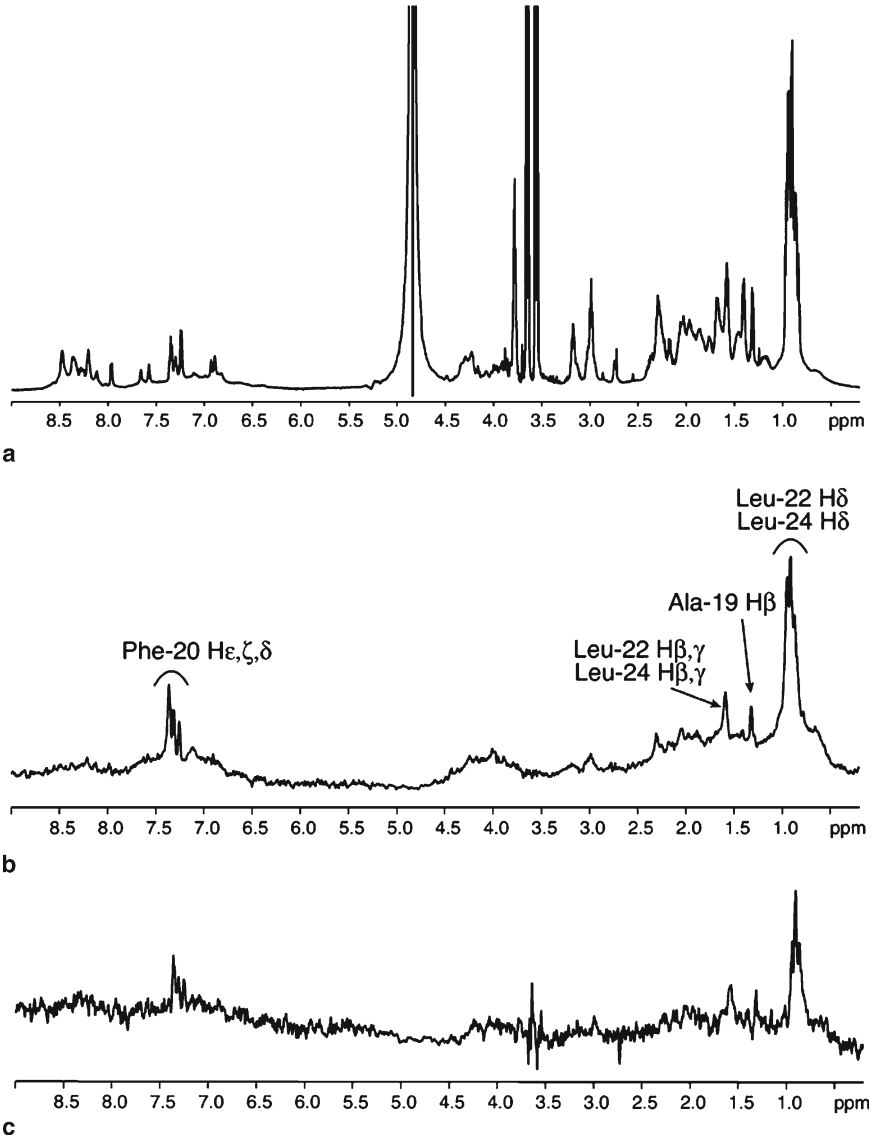

Fig. 38 STD NMR spectra map the close contacts of I19L with tubulin. **a** One-dimensional ^{1}H NMR spectrum of I19L in the presence of tubulin. **b**,**c** One-dimensional STD-NMR spectra of I19L in the presence of tubulin with selective saturation of protein resonances at 0 and 10 ppm, respectively. Protons of I19L affected by the selective saturation of tubulin are labeled. (Reprinted with permission from [142]. Copyright 2005 American Chemical Society)

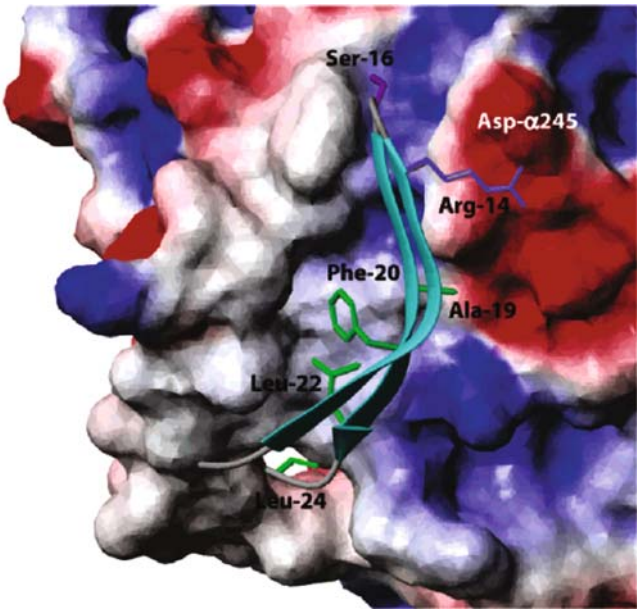

Fig. 39 I19L docked over the electrostatic surface representation of tubulin from the X-ray crystal data of Ravelli et al. [12]. Side chains of I19L residues in contact with tubulin (<5 Å) according to STD-NMR spectra are shown in *green*. The side chain of Arg14 might engage in the ionic interaction with residue Asp-α245. The side chain of Ser16 (phosphorylatable) points toward tubulin. Negative charge is shown in *red*, positive in *blue*, and neutral in *gray*. (Reprinted with permission from [142]. Copyright 2005 American Chemical Society)

4 Concluding Remarks

This review summarized – on the example of tubulin and its ligands – the relative merits of the different techniques to establish structures of complexes. Tubulin is a challenge since it exists as monomer and oligomers with different architecture among which the microtubules are the best known. For the latter, there is no high resolution structure available neither in the free form or complexed with ligands. Therefore, how drugs influence the monomer/oligomer ratios and change the structure of the oligomers is unclear, despite the fact that structures of tubulin/ligand complexes are emerging and structures of non-microtubule oligomers of tubulin with ligands have been determined. We focused in particular on the possibility of deriving ligand/tubulin complex structures from NMR in conjunction with computational chemistry provided the structure of the receptor in free form or in complex with another ligand is available. Rather than historical, our review puts the contribution of NMR in perspective to other techniques. We also

described techniques that will provide in the future structures of ligands bound to microtubules and that are therefore promising to address the above mentioned questions.

Acknowledgements V.M.S.-P. thanks the EU for a Marie Curie fellowship and the Spanish MEC for a "Ramón y Cajal" contract and for Grant Number CTQ2007-65310. C.G. thanks the Max Planck Society and the Fonds der Chemischen Industrie for support.

References

1. Sengupta S, Thomas SA (2006) Exp Rev Anticancer Ther 6:1433
2. Hait WN, Rubin E, Alli E, Goodin S (2007) Update Cancer Ther 2:1
3. Feyen F, Cachoux F, Gertsch J, Wartmann M, Altmann KH (2008) Acc Chem Res 41:21
4. Downing KH, Nogales E (1998) Curr Opin Struct Biol 8:785
5. Nogales E (2001) Annu Rev Biophys Biomol Struct 30:397
6. Amos LA (2004) Org Biomol Chem 2:2153
7. Olmsted JB (1986) Annu Rev Cell Biol 2:421
8. Lawler S (1998) Curr Biol 8:R212
9. Jordan MA, Wilson L (2004) Nat Rev Cancer 4:253
10. Jordan MA (2002) Curr Med Chem Anti-Cancer Agents 2:1
11. Nogales E, Wolf SG, Downing KH (1998) Nature 391:199
12. Ravelli RBG, Gigant B, Curmi PA, Jourdain I, Lachkar S, Sobel A, Knossow M (2004) Nature 428:198
13. Gigant B, Wang CG, Ravelli RBG, Roussi F, Steinmetz MO, Curmi PA, Sobel A, Knossow M (2005) Nature 435:519
14. Pryor DE, O'Brate A, Bilcer G, Diaz JF, Wang YF, Wang Y, Kabaki M, Jung MK, Andreu JM, Ghosh AK, Giannakakou P, Hamel E (2002) Biochemistry 41:9109
15. Gaitanos TN, Buey RM, Diaz JF, Northcote PT, Teesdale-Spittle P, Andreu JM, Miller JH (2004) Cancer Res 64:5063
16. Pineda O, Farras J, Maccari L, Manetti F, Botta M, Vilarrasa J (2004) Bioorg Med Chem Lett 14:4825
17. Jimenez-Barbero J, Canales A, Northcote PT, Buey RM, Andreu JM, Diaz JF (2006) J Am Chem Soc 128:8757
18. Usui T, Kondoh M, Cui CB, Mayumi T, Osada H (1998) Biochem J 333:543
19. Laing N, Dahllof B, HartleyAsp B, Ranganathan S, Tew KD (1997) Biochemistry 36:871
20. Panda D, Miller HP, Islam K, Wilson L (1997) Proc Natl Acad Sci U S A 94:10560
21. Gigant B, Curmi PA, Martin-Barbey C, Charbaut E, Lachkar S, Lebeau L, Siavoshian S, Sobel A, Knossow M (2000) Cell 102:809
22. Downing KH (2000) Annu Rev Cell Dev Biol 16:89
23. Nogales E, Whittaker M, Milligan RA, Downing KH (1999) Cell 96:79
24. Li HL, DeRosier DJ, Nicholson WV, Nogales E, Downing KH (2002) Structure 10:1317
25. Snyder JP, Nettles JH, Cornett B, Downing KH, Nogales E (2001) Proc Natl Acad Sci U S A 98:5312
26. Nettles JH, Li HL, Cornett B, Krahn JM, Snyder JP, Downing KH (2004) Science 305:866
27. Nettles JH, Downing KH (2009) The tubulin binding mode of microtubule stabilizing agents studied by electron crystallography. In: Carlomagno T (ed) Microtubule stabilizing and destabilizing agents: synthetic, structural and mechanistic insights (Topics in Current Chemistry, vol 286). Springer, Berlin Heidelberg New York
28. Gigant B, Cormier A, Dorleans A, Ravelli RBG, Knossow M (2009) Microtubule-destabilizing agents: structural and mechanistic insights from the interaction of colchicines and vinblastine with tubulin. In: Carlomagno T (ed) Microtubule stabilizing and destabilizing agents: synthetic,

structural and mechanistic insights (Topics in Current Chemistry, vol 286). Springer, Berlin Heidelberg New York
29. Curmi PA, Andersen SSL, Lachkar S, Gavet O, Karsenti E, Knossow M, Sobel A (1997) J Biol Chem 272:25029
30. Jourdain L, Curmi P, Sobel A, Pantaloni D, Carlier MF (1997) Biochemistry 36:10817
31. Bai RL, Covell DG, Pei XF, Ewell JB, Nguyen NY, Brossi A, Hamel E (2000) J Biol Chem 275:40443
32. Wüthrich K (1986) NMR of proteins and nucleic acids. Wiley-Interscience, New York
33. Cavanagh J, Fairbrother WJ, Palmer III AG, Skelton NJ, Rance M (2007) Protein NMR spectroscopy: principles and practice. Academic Press, Amsterdam, Boston
34. Sattler M, Schleucher J, Griesinger C (1999) Progr NMR Spectrosc 34:93
35. Foster P, McElroy A, Amero CD (2007) Biochemistry 46:331
36. Honndorf VS, Coudevylle N, Laufer S, Becker S, Griesinger C (2008) Angew Chem Int Ed: (in press)
37. Ni F (1994) Progr NMR Spectrosc 26:517
38. Mayer M, Meyer B (1999) Angew Chem Int Ed 38:1784
39. Carlomagno T, Felli IC, Czech M, Fischer R, Sprinzl M, Griesinger C (1999) J Am Chem Soc 121:1945
40. Blommers MJJ, Stark W, Jones CE, Head D, Owen CE, Jahnke W (1999) J Am Chem Soc 121:1949
41. Lian LY, Barsukov IL, Sutcliffe MJ, Sze KH, Roberts GCK (1994) Methods Enzymol 239:657
42. Clore GM, Gronenborn AM (1982) J Magn Reson 48:402
43. Clore GM, Gronenborn AM (1983) J Magn Reson 53:423
44. Nilges M, Clore GM, Gronenborn AM (1988) FEBS Lett 229:317
45. Krishna NR, Jayalakshmi V (2006) Progr NMR Spectrosc 49:1
46. Yan JL, Kline AD, Mo HP, Shapiro MJ, Zartler ER (2003) J Magn Reson 163:270
47. Milton MJ, Williamson RT, Koehn FE (2006) Bioorg Med Chem Lett 16:4279
48. Reif B, Hennig M, Griesinger C (1997) Science 276:1230
49. Peng JW (2003) J Am Chem Soc 125:11116
50. Maltseva T, Usova E, Eriksson S, Milecki J, Foldesi A, Chattopadhayaya J (2001) Nucleos Nucleot Nucl 20:1225
51. Jimenez-Barbero J, Amat-Guerri F, Snyder JP (2002) Curr Med Chem Anti-Cancer Agents 2:91
52. Thepchatri P, Eliseo T, Cicero DO, Myles D, Snyder JP (2007) J Am Chem Soc 129:3127
53. Wenger RM, France J, Bovermann G, Walliser L, Widmer A, Widmer H (1994) FEBS Lett 340:255
54. Theriault Y, Logan TM, Meadows R, Yu LP, Olejniczak ET, Holzman TF, Simmer RL, Fesik SW (1993) Nature 361:88
55. Abraham RJ, Cavalli L, Pachler KGR (1966) Mol Phys 11:471
56. Kessler H, Griesinger C, Lautz J, Muller A, Vangunsteren WF, Berendsen HJC (1988) J Am Chem Soc 110:3393
57. Sharman GJ (2007) Magn Reson Chem 45:317
58. Schuetz A, Junker J, Leonov A, Lange OF, Molinski TF, Griesinger C (2007) J Am Chem Soc 129:15114
59. Pachler KGR, Underwoo Wg (1967) Tetrahedron 23:1817
60. Monteagudo E, Cicero DO, Cornett B, Myles DC, Snyder JP (2001) J Am Chem Soc 123:6929
61. Thiele CM, Marx A, Berger R, Fischer J, Biel M, Giannis A (2006) Angew Chem Int Ed 45:4455
62. Cicero DO, Barbato G, Bazzo R (1995) J Am Chem Soc 117:1027
63. Snyder JP, Nevins N, Cicero DO, Jasen J (2000) J Am Chem Soc 122:724
64. Thepchatri P, Cicero DO, Monteagudo E, Ghosh AK, Cornett B, Weeks ER, Snyder JP (2005) J Am Chem Soc 127:12838

65. Lakdawala A, Wang M, Nevins N, Liotta DC, Rusinska-Roszak D, Lozynski M, Snyder JP (2001) BMC Chem Biol 1:2. http://www.biomedcentral.com/1472
66. Baldus M (2006) Curr Opin Struct Biol 16:618
67. Andrew ER (1971) Progr NMR Spectrosc 8:1
68. Pines A, Gibby G, Waugh JS (1973) J Chem Phys 58:569
69. Schaefer J, Stejskal EO (1976) J Am Chem Soc 98:1031
70. Lange A, Giller K, Hornig S, Martin-Eauclaire MF, Pongs O, Becker S, Baldus M (2006) Nature 440:959
71. Luca S, White JF, Sohal AK, Filippov DV, van Boom JH, Grisshammer R, Baldus M (2003) Proc Natl Acad Sci U S A 100:10706
72. Robyr P, Tomaselli M, Straka J, Grobpisano C, Suter UW, Meier BH, Ernst RR (1995) Mol Phys 84:995
73. Lange A, Luca S, Baldus M (2002) J Am Chem Soc 124:9704
74. Gullion T, Schaefer J (1989) J Magn Reson 81:196
75. Sanchez-Pedregal VM, Reese M, Meiler J, Blommers MJJ, Griesinger C, Carlomagno T (2005) Angew Chem Int Ed 44:4172
76. Reese M, Sanchez-Pedregal VM, Kubicek K, Meiler J, Blommers MJJ, Griesinger C, Carlomagno T (2007) Angew Chem Int Ed 46:1864
77. London RE (1999) J Magn Reson 141:301
78. Altmann KH, Gertsch J (2007) Nat Prod Rep 24:327
79. Ojima I, Kuduk SD, Chakravarty S, Ourevitch M, Begue JP (1997) J Am Chem Soc 119:5519
80. Williams HJ, Scott AI, Dieden RA, Swindell CS, Chirlian LE, Francl MM, Heerding JM, Krauss NE (1993) Tetrahedron 49:6545
81. Cachau RE, Gussio R, Beutler JA, Chmurny GN, Hilton BD, Muschik GM, Erickson JW (1994) Supercomput Appl High Perform Comput 8:24
82. Balasubramanian SV, Alderfer JL, Straubinger RM (1994) J Pharm Sci 83:1470
83. Lowe J, Li H, Downing KH, Nogales E (2001) J Mol Biol 313:1045
84. Li YK, Poliks B, Cegelski L, Poliks M, Gryczynski Z, Piszczek G, Jagtap PG, Studelska DR, Kingston DGI, Schaefer J, Bane S (2000) Biochemistry 39:281
85. Geney R, Sun L, Pera P, Bernacki RJ, Xia SJ, Horwitz SB, Simmerling CL, Ojima I (2005) Chem Biol 12:339
86. Alcaraz AA, Mehta AK, Johnson SA, Snyder JP (2006) J Med Chem 49:2478
87. Paik Y, Yang C, Metaferia B, Tang SB, Bane S, Ravindra R, Shanker N, Alcaraz AA, Johnson SA, Schaefer J, O'Connor RD, Cegelski L, Snyder JP, Kingston DGI (2007) J Am Chem Soc 129:361
88. Boge TC, Wu ZJ, Himes RH, Vander Velde DG, Georg GI (1999) Bioorg Med Chem Lett 9:3047
89. Ganesh T, Guza RC, Bane S, Ravindra R, Shanker N, Lakdawala AS, Snyder JP, Kingston DGI (2004) Proc Natl Acad Sci U S A 101:10006
90. Kingston DGI, Bane S, Snyder JP (2005) Cell Cycle 4:279
91. Bollag DM, McQueney PA, Zhu J, Hensens O, Koupal L, Liesch J, Goetz M, Lazarides E, Woods CM (1995) Cancer Res 55:2325
92. Hofle G, Bedorf N, Gerth K, Reichenbach H (1993)
93. Giannakakou P, Sackett DL, Kang YK, Zhan ZR, Buters JTM, Fojo T, Poruchynsky MS (1997) J Biol Chem 272:17118
94. Taylor RE, Zajicek J (1999) J Org Chem 64:7224
95. Erdelyi M, Pfeiffer B, Hauenstein K, Fohrer J, Gertsch J, Altmann KH, Carlomagno T (2008) J Med Chem 51:1469
96. Carlomagno T, Blommers MJJ, Meiler J, Jahnke W, Schupp T, Petersen F, Schinzer D, Altmann KH, Griesinger C (2003) Angew Chem Int Ed 42:2511
97. Carlomagno T, Sanchez VM, Blommers MJJ, Griesinger C (2003) Angew Chem Int Ed 42:2515
98. Hofle GH, Bedorf N, Steinmetz H, Schomburg D, Gerth K, Reichenbach H (1996) Angew Chem Int Ed Engl 35:1567

99. Regueiro-Ren A, Leavitt K, Kim SH, Hofle G, Kiffe M, Gougoutas JZ, DiMarco JD, Lee FYF,w Fairchild CR, Long BH, Vite GD (2002) Org Lett 4:3815
100. Nicolaou KC, Scarpelli R, Bollbuck B, Werschkun B, Pereira MMA, Wartmann M, Altmann KH, Zaharevitz D, Gussio R, Giannakakou P (2000) Chem Biol 7:593
101. Altmann KH, Blommers MJJ, Caravatti G, Florsheimer A, Nicolaou KC, O'Reilly T, Schmidt A, Schinzer D, Wartmann M (2009) Synthetic and semi-synthetic analogs of epothilones – chemistry and biological activity. In: Carlomagno T (ed) Microtubule stabilizing and destabilizing agents: synthetic, structural and mechanistic insights (Topics in Current Chemistry, vol 286). Springer, Berlin Heidelberg New York
102. Bold G, Wojeik S, Caravatti G, Lindauer R, Stierlin C, Gertsch J, Wartmann M, Altmann KH (2006) ChemMedChem 1:37
103. He LF, Jagtap PGF, Kingston DGI, Shen HJ, Orr GA, Horwitz SB (2000) Biochemistry 39:3972
104. Giannakakou P, Gussio R, Nogales E, Downing KH, Zaharevitz D, Bollbuck B, Poy G, Sackett D, Nicolaou KC, Fojo T (2000) Proc Natl Acad Sci U S A 97:2904
105. Wang MM, Xia XY, Kim Y, Hwang D, Jansen JM, Botta M, Liotta DC, Snyder JP (1999) Org Lett 1:43
106. Ojima I, Chakravarty S, Inoue T, Lin SN, He LF, Horwitz SB, Kuduk SD, Danishefsky SJ (1999) Proc Natl Acad Sci U S A 96:4256
107. Manetti F, Maccari L, Corelli F, Botta M (2004) Curr Top Med Chem 4:203
108. Nettles JH, Jenkins JL, Williams C, Clark AM, Bender A, Deng Z, Davies JW, Glick M (2007) J Mol Graphics Model 26:622
109. Andreu JM, Barasoain I (2001) Biochemistry 40:11975
110. Solomon F (1977) Biochemistry 16:358
111. Diaz JF, Andreu JM (1993) Biochemistry 32:2747
112. Sanchez-Pedregal VM, Kubicek K, Meiler J, Lyothier I, Paterson I, Carlomagno T (2006) Angew Chem Int Ed 45:7388
113. Wang H-W, Nogales E (2005) Nature 435:911
114. Buey RM, Diaz JF, Andreu JM, O'Brate A, Giannakakou P, Nicolaou KC, Sasmal PK, Ritzen A, Namoto K (2004) Chem Biol 11:225
115. Sengupta S, Boge TC, Georg GI, Himes RH (1995) Biochemistry 34:11889
116. Lange A, Schupp T, Petersen F, Carlomagno T, Baldus M (2007) ChemMedChem 2:522
117. Lange A, Seidel K, Verdier L, Luca S, Baldus M (2003) J Am Chem Soc 125:12640
118. Hung DT, Chen J, Schreiber SL (1996) Chem Biol 3:287
119. terHaar E, Kowalski RJ, Hamel E, Lin CM, Longley RE, Gunasekera SP, Rosenkranz HS, Day BW (1996) Biochemistry 35:243
120. Kowalski RJ, Giannakakou P, Gunasekera SP, Longley RE, Day BW, Hamel E (1997) Mol Pharm 52:613
121. Xia SJ, Kenesky CS, Rucker PV, Smith AB, Orr GA, Horwitz SB (2006) Biochemistry 45:11762
122. Gunasekera SP, Gunasekera M, Longley RE, Schulte GK (1990) J Org Chem 55:4912
123. Smith AB, LaMarche MJ, Falcone-Hindley M (2001) Org Lett 3:695
124. Ballone P, Marchi M (1999) J Phys Chem A 103:3097
125. Paterson I, Britton R, Delgado O, Meyer A, Poullennec KG (2004) Angew Chem Int Ed 43:4629
126. Paterson I, Gardner NM (2007) Chem Commun 49
127. Buey RM, Barasoain I, Jackson E, Meyer A, Giannakakou P, Paterson I, Mooberry S, Andreu JM, Diaz JF (2005) Chem Biol 12:1269
128. Diaz JF, Andreu JM, Jimenez-Barbero J (2009) The interaction of microtubules with stabilizers characterized at a biochemical and structural level. In: Carlomagno T (ed) Microtubule stabilizing and destabilizing agents: synthetic, structural and mechanistic insights (Topics in Current Chemistry, vol 286). Springer, Berlin Heidelberg New York
129. Jefford CW, Bernardinelli G, Tanaka J, Higa T (1996) Tetrahedron Lett 37:159
130. Tanaka J, Higa T, Bernardinelli G, Jefford CW .(1996) Chem Lett: 255
131. West LM, Northcote PT, Battershill CN (2000) J Org Chem 65:445

132. Mooberry SL, Tien G, Hernandez AH, Plubrukarn A, Davidson BS (1999) Cancer Res 59:653
133. Hamel E, Day BW, Miller JH, Jung MK, Northcote PT, Ghosh AK, Curran DP, Cushman M, Nicolaou KC, Paterson I, Sorensen EJ (2006) Mol Pharm 70:1555
134. Paterson I, Menche D, Britton R, Hakansson AE, Silva-Martinez MA (2005) Tetrahedron Lett 46:3677
135. Liao XB, Wu YS, De Brabander JK (2003) Angew Chem Int Ed 42:1648
136. Talpir R, Benayahu Y, Kashman Y, Pannell L, Schleyer M (1994) Tetrahedron Lett 35:4453
137. Anderson HJ, Coleman JE, Andersen RJ, Roberge M (1997) Cancer Chemother Pharmacol 39:223
138. Ravi M, Zask A, Rush TS (2005) Biochemistry 44:15871
139. Nunes M, Kaplan J, Wooters J, Hari M, Minnick AA, May MK, Shi C, Musto S, Beyer C, Krishnamurthy G, Qiu YC, Loganzo F, Ayral-Kaloustian S, Zask A, Greenberger LM (2005) Biochemistry 44:6844
140. Coleman JE, Patrick BO, Andersen RJ, Rettig SJ (1996) Acta Crystallogr Sect C 52:1525
141. Mitra A, Sept D (2004) Biochemistry 43:13955
142. Clement MJ, Jourdain I, Lachkar S, Savarin P, Gigant B, Knossow M, Toma F, Sobel A, Curmi PA (2005) Biochemistry 44:14616
143. Heinz DW, Schubert WD, Hofle G (2005) Angew Chem Int Ed 44:1298
144. Mastropaolo D, Camerman A, Luo YG, Brayer GD, Camerman N (1995) Proc Natl Acad Sci U S A 92:6920
145. Dubois J, Guenard D, Guerittevoegelein F, Guedira N, Potier P, Gillet B, Beloeil JC (1993) Tetrahedron 49:6533
146. Williams HJ, Scott AI, Dieden RA, Swindell CS, Chirlian LE, Francl MM, Heerding JM, Krauss NE (1994) Can J Chem 72:252

Top Curr Chem (2009) 286: 209–257
DOI: 10.1007/128_2008_24

Published online: 31 October 2008

The Tubulin Binding Mode of Microtubule Stabilizing Agents Studied by Electron Crystallography

James H. Nettles and Kenneth H. Downing

Abstract Since tubulin was discovered in 1967, drug probes have been used to manipulate mechanisms of microtubule polymerization and disassembly. In parallel, advances in optical imagery, electron microscopy, along with both electron and X-ray diffraction have provided ability to "see" the molecular underpinning of these machines. Nanoscale mapping of different tubulin polymers formed in the presence of different drugs and cofactors provide a context for examining the dynamic features relevant to their biological activity. Models built from EM maps have been used to understand the binding of stabilizing drugs such as taxanes and epothilones, to predict more effective molecules, and to explain mutation based resistance. Here, we discuss drug binding in the context of different polymeric forms and propose a trigger mechanism associated with microtubules' dynamic instability.

Keywords Diffraction, Dynamics, Electron crystallography, Epothilone, Laulimalide, Microtubules, Modeling, Paclitaxel, SAR, Taxol, Tubulin

Contents

J.H. Nettles (✉)
Department of Pediatrics, Emory University School of Medicine, Laboratory of Biochemical Pharmacology (LOBP) VA Medical Center – Medical Research, 151H/5A-146 1670 Clairmont Road, Decatur, GA 30033 USA
e-mail: jnettle@emory.edu

K.H. Downing
Life Sciences Division Lawrence Berkeley National Laboratory, 112 Donner Lab, Berkeley, CA 94720 USA

Abbreviations

DTX	docetaxel
EC	electron crystallography
EM	electron microscopy
epoA	epothilone-A
MAID	manually adjusted interval dynamics
MR	molecular replacement
MT	microtubules
pf	protofilament
PTX	paclitaxel
SAR	structure activity relationship
SNR	signal-to-noise ratio

1 Introduction

The nature of tubulin polymerization provides exquisite opportunities for study of dynamic protein behavior. Depending upon the presence of different environmental cofactors and binding partners, tubulin can spontaneously interconvert between dimeric subunits and 3D nanotubes of varying diameter, sheets of 1 molecule thickness, rings, spirals, and aggregates of less well defined geometries. Versatility is clearly a necessity for this protein to perform the diverse set of functions that it carries out throughout all eukaryotic organisms. However, these same dynamic properties present an extensive challenge to atomic structure determination. A discussion of the binding mode of any molecule to tubulin has to be carried out with respect to the polymeric state of the protein. As we will show here, the binding

mode relevant to one particular structural complex may or may not apply to another. We will illustrate how we have used data gleaned from electron diffraction experiments using both 2D sheets and microtubules (MTs) combined with biochemical, pharmacological, and imaging data to build models that provide testable atomic hypotheses about drug binding and mechanisms.

The framework for this discussion will be formed around three important classes of MT stabilizers shown in Scheme 1. Given the chemical similarity between epothilones and laulimalide, it is particularly surprising that, while taxanes and epothilones compete for the same binding site, laulimalide has been shown to be non-competitive with either. In fact, laulimalide may bind simultaneously with taxanes and produce a synergistic effect. This chapter provides details of experiments and analyses we have done to formulate and test hypotheses about these binding mechanisms.

Electron microscopy (EM) has played a central role in many aspects of research on microtubules and their main protein component, tubulin. MTs were first identified in electron micrographs of plant material [1]. Characteristics of the basic structural aspects of MTs were also determined by EM, revealing that MTs are hollow tubes composed of protofilaments (pf). There are most often 13 pfs, but this number can vary at least from 9 to 16. Subsequent work showed that the pfs are composed of αβ-tubulin dimers arranged head-to-tail.

The structure of tubulin was eventually solved by electron crystallography (EC) after many valiant attempts to produce crystals suitable for X-ray crystallography had come up empty. One of the great advantages of electron crystallography is that both amplitudes and phases for structure factors are determined directly, so that density maps can be used for atomic model building without extensive structure refinement. The tubulin structure was initially determined at nominal resolution of 3.7 Å directly from the experimental map. This structure was basically correct and provided a wealth of insight on functional aspects of tubulin, although there were significant deviations from conventional protein geometry and several errors in amino acid locations. The original crystal samples included the stabilizing agent paclitaxel (Taxol-Bristol Meyers Squib) PTX, and while the initial structural model

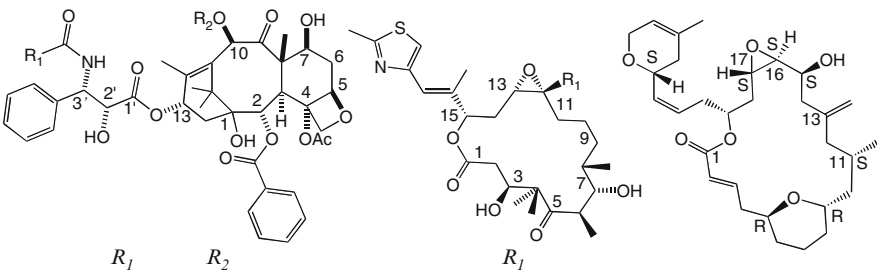

	R_1	R_2		R_1	
paclitaxel	Ph	AC	*epothilone A*	H	*laulimalide*
ocetaxel	t-BuO	H	*epothilone B*	Me	

Scheme 1

was built with the closely related compound docetaxel it revealed the PTX binding site and gave some idea of its mode of interaction. The structure served as a starting point for development of a detailed model for the interaction of PTX with tubulin [2]. Several errors were corrected when the structure was refined to a resolution of 3.5 Å using an expanded data set. A subsequent electron crystallographic structure has provided a model for the epothilone-A (EpoA)-tubulin complex, and several other structures appear to be forthcoming [3].

We start this chapter with a discussion of the technology of electron crystallography and various factors that affect the results of its application.

2 Evolution of EM Diffraction Methods

2.1 Electron vs X-Ray Diffraction

Among the factors that distinguish electron and X-ray crystallography is the fact that scattering factors for electrons are on the order of 10^5 times stronger than those for X-rays, owing to the strong Coulomb interactions that produce electron scattering. Scattering is sufficiently strong that well defined electron diffraction patterns can be obtained from crystals that contain as few as 10^4 molecules, for example monolayer crystals that are a single molecule thick and on the order of 1 μm on edge. This ability opens the way to study molecules that do not crystallize in three dimensions. The most frequent application of electron crystallography is with membrane proteins, which naturally occur – and occasionally crystallize – within the planar confines of a membrane. Tubulin is a rare case of a soluble protein that forms monolayer crystals. In the course of exploring the effects of divalent ions on microtubules it was discovered that the presence of Zn^{++} under polymerizing conditions led to the formation of crystalline sheets [4]. The sheets are formed with the same tubulin protofilament (pf) structures that are present in MTs, but whereas the pfs in MTs are parallel, in the sheets they are antiparallel. These early discoveries slightly predated the development of cryo-electron microscopy and the low-dose techniques that led to the first atomic models derived by electron microscopy. Once these newly developed techniques were applied to the tubulin sheets, promising electron diffraction patterns could be obtained (Fig. 1) [5], and continuing developments in specimen preparation and data recording and processing eventually led to determination of tubulin's structure [6].

As in X-ray crystallography, a full data set consists of both amplitudes and phases for a 3D array of structure factors. Amplitudes can be obtained most easily from electron diffraction patterns, and also from the computed Fourier transforms or power spectra of high-resolution images. The amplitudes measured from images are subject to a number of factors that degrade their accuracy and make them less accurate than amplitudes determined by electron diffraction. First, the area included in a micrograph is generally smaller than the entire crystal, so the statistical defini-

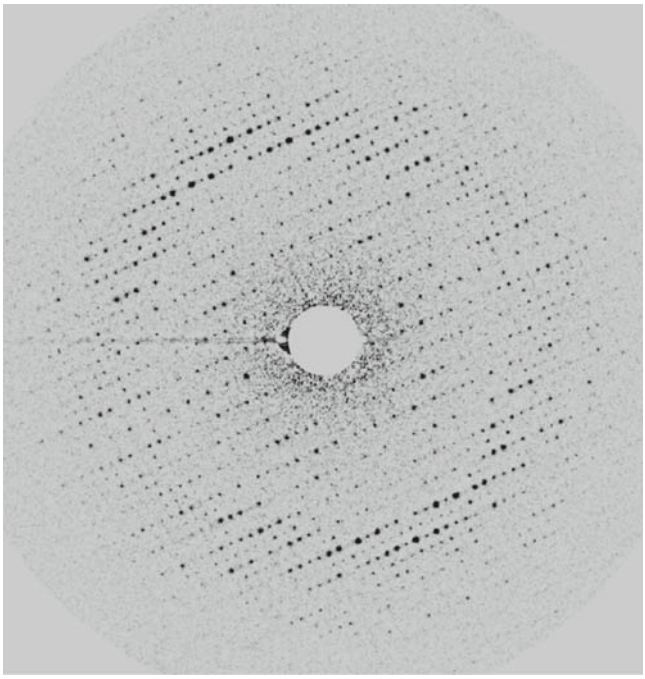

Fig. 1 Electron diffraction pattern of Zn-sheet stabilized with epothilone A. Reflections extend to the edge of the image at 2.5 Å resolution

tion is not as high. In addition, various effects of the contrast transfer function that depends on defocus, electron beam quality, specimen drift, etc. influence the amplitude in a way that can be well described in the Fourier transform of the image. Many of these can be corrected or compensated, but amplitudes are generally more accurate when derived directly from electron diffraction patterns. The (complex) Fourier transform of the image also yields crystallographic phases, as well as amplitudes. The phases from the images are generally highly accurate, particularly in the low-resolution range that is inaccessible to X-ray diffraction. One of the great benefits of this high accuracy is that density maps derived by electron crystallography can be interpreted directly as representations of mass density within the protein. Even at moderate resolution that is not sufficient to build an atomic model of the structure, much can be learned from maps that show elements of secondary structure or arrangements of subunits within a protein complex.

The one downside of the strong scattering of electrons is that specimens are highly sensitive to radiation damage by the electron beam. Elastic scattering, which produces the high-resolution image information and electron diffraction patterns, occurs with approximately the same frequency as inelastic scattering, which produces damage. The high sensitivity of the specimens requires that low exposures – on the order of ten electrons per square Angstrom – be used. At this level of exposure, fine details of the protein structure are masked by shot noise, or the

statistical variations in the number of electrons incident on any given area of the specimen. The way to get round this problem is to average many images of equivalent molecules. Crystallography gives the most straightforward approach to this averaging, since each micrograph contains images of many molecules, all in the same orientation. All the information in the protein is contained in the diffraction spots in the Fourier transform of the image, where the signal-to-noise ratio (SNR) is much higher than in the image itself. Thus, even though there is almost no detail visible in single images of protein crystals, image processing can yield averaged images that contain a wealth of detail.

The accuracy of the structure factor amplitudes can have a strong effect on the results, and an estimate of the number of electrons contributing to each diffraction spot helps to understand some of the limitations in this approach. A crystal 1 μm^2 in area can be exposed to about 10^9 electrons. Scattering factors for the tubulin crystals are in the range 10^{-6} to less than 10^{-7}, so there will be on the order of fewer than 100–1000 electrons contributing to each diffraction spot. Given the nature of the Poisson statistics that govern such processes, the signal to noise ratio for intensities would then be in the range of less than 10–30, assuming that all electrons are actually detected, leading to an accuracy in the range of 10–3%. Working with larger crystals, of course, can greatly increase the SNR. The overall accuracy of the measurements is increased by averaging many diffraction patterns.

In principle the accuracy of phases determined from images should be very high. It has been shown that, if a single scattered electron contributes to a diffraction spot in an image Fourier transform, the error in the phase should be about 45°. This compares quite well with phases determined by many of the methods used in X-ray crystallography. Unfortunately a number of factors conspire to reduce this accuracy. Basically, the efficiency of recording the high-resolution data is reduced by factors that include specimen motion due to beam damage and charging, limited beam coherence, and imperfect detectors. In general, we frequently capture only about 10% of theoretical signal at high resolution, and thus need about 100 times as much data to recover the loss in SNR.

Note that in the tubulin diffraction pattern shown in Fig. 1 alternate rows of diffraction spots are significantly weaker. The strong spots, on even-numbered rows, arise from the monomer–monomer spacing of about 40 Å. The weaker spots on odd-numbered rows arise from the dimer spacing, and thus reflect differences between the monomers. These differences are rather small at the low resolution range that corresponds to the secondary structure, so these spots are weak. At higher resolution where differences between side chains in the two monomers become significant the odd and even rows show more similar intensities.

2.2 Processing of EC Diffraction to Experimental Maps

Generation of a three-dimensional (3D) density map requires collection of a 3D set of structure factors. The 3D data set is built up with data collected from a large number of crystals tilted at various angles. In general, only one image or diffraction

pattern is recorded from each crystal. An estimate of the number of different tilt angles required to completely sample the 3D space is given by $n = \pi D/d$, where D is the size of the protein molecule and d is the target resolution. For tubulin, with a thickness of about 50 Å, at least 45 tilts would be required to ensure a resolution of 3.5 Å, considered a requirement for building an atomic model of a protein. In practice, the number used is several times this in order to provide an adequate amount of redundancy and averaging and to ensure that the angles are well sampled.

The relation of an individual image or diffraction pattern to the 3D structure factor set is important to understand. The 3D data for a single-layer crystal falls on a set of "reciprocal lattice lines," where one line passes through each of the diffraction spots in the pattern for an untilted crystal such as shown in Fig. 2. The data from a single crystal falls on a central section of the 3D data, that is a plane which passes through the origin and whose orientation corresponds to the orientation of the crystal. Thus, a crystal tilted to any orientation contributes one data point to each lattice line within the resolution limit for that particular orientation.

Several mathematical assumptions are involved in the way that the data is treated, for example that the specimen is a vanishingly thin, weakly scattering phase object and that the electron wavelength is vanishingly small. These assumptions depend on the energy of the electrons, and while they are quite good with a conventional 100 kV microscope, they all improve as the microscope accelerating voltage increases. All of the data for tubulin in our work has been collected at 400 kV.

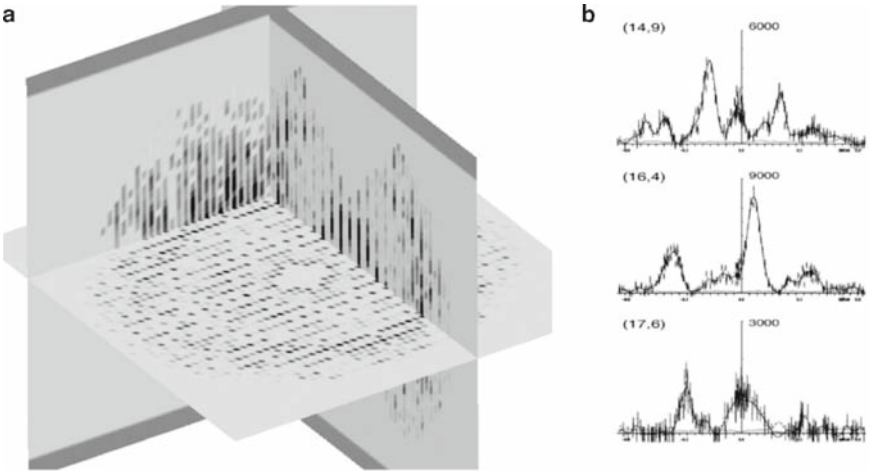

Fig. 2 **a** Representation of the 3D diffraction data from the monolayer tubulin crystals. Amplitudes (shown here) and phases vary continuously along "reciprocal lattice lines" that pass through each of the diffraction spots in the diffraction pattern of an untilted crystal, shown in the horizontal plane. The *two planes perpendicular to this plane* show amplitudes along some of the lattice lines. **b** Three lattice line curves. The *vertical axis* represents intensity in an arbitrary unit, while the *horizontal axis* is z*, the height along the lattice line in reciprocal space. Note the *odd numbered curve* (17,6); although the intensities are weak, the peaks are well defined because of the large number of measurements

2.3 Sample Preparation and Data Collection

As with most aspects of electron microscopy, specimen preparation is a critical factor in obtaining high quality data. A primary concern is that dehydration must be avoided in the high vacuum of the microscope. Specimens suspended in a thin layer of water can be frozen so rapidly that the water vitrifies rather than crystallizing, thus preserving the native, hydrated state of the protein. The use of a cryo-stage that holds the specimen at a temperature below about −160 °C in the microscope retains this frozen state. It is often simpler to replace the water with a substance, such as glucose, that provides essentially the same hydrogen bonding functions as water, and it has been found that this approach also retains the native protein structure, as evidenced by diffraction to high resolution. All of our tubulin crystals have been prepared in a mixture of glucose and tannin, while all of the studies with intact microtubules have been done with frozen-hydrated specimens.

We have found that nearly all of the compounds that stabilize MTs also stabilize the 2-D crystals. Compounds that have been used include paclitaxel, epothilone-A and B, discodermolide and eleutherobin. Laulimalide, however, disrupts the sheets and causes them to reform into MTs. Microtubule destabilizing compounds have also been found to disrupt the crystals.

Microtubule polymers form spontaneously from isolated tubulin in buffer solution with GTP and Mg^{++} at a temperature of 30–37 °C. Sheet polymers form spontaneously from tubulin in buffer with GTP, Mg^{++} and Zn^{++} [7]. The crystals must be exquisitely flat in order to yield good diffraction when tilted to high angles. This can be a limiting problem, since they are so thin and flexible. Careful attention to all of the preparation parameters and properties of the supporting film, though, produces specimens that can diffract remarkably well.

2.4 Zinc Sheets vs Microtubule Structure

Once a full set of 3D structure factors has been obtained, a density map is calculated by an inverse Fourier transform, just as in X-ray crystallography. Figure 3 shows parts of the 3D density maps and atomic models produced with the electron diffraction and image data. The density in Fig. 3a is from the original map computed directly from the experimental data to a resolution of 3.7 Å. The data set for this map included 130 images and 94 diffraction patterns. This is the density in which the original model was built, and it is easily seen that the protein backbone could be readily identified and that most of the side chains are in well-defined density. The data set was subsequently extended with an additional 100 diffraction patterns, providing significantly improved precision in the structure factor amplitudes. The structure was then refined using common X-ray crystallographic techniques to a resolution of 3.5 Å, and the same region of the structure is shown in Fig. 3b The refinement also improved the geometry of the protein

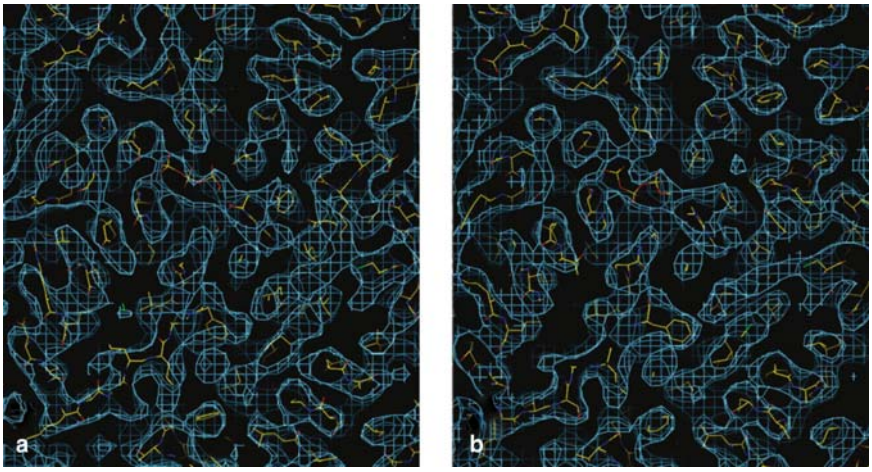

Fig. 3 EC derived maps of tubulin. **a** Pure experimental map F_o from diffraction amplitudes and image derived phases at 3.7 Å resolution [6] **b** Map after crystallographic refinement to 3.5 Å using diffraction amplitudes and both image and model derived phases [8]

model and corrected a number of small errors in regions where the original density was poorly defined [8].

2.4.1 Anti-Parallel vs Parallel

Because the protofilaments in the crystals are antiparallel, as opposed to the parallel arrangement in microtubules, it was necessary to determine both the polarity of the pfs and the pf–pf interactions. A first pseudo-atomic model of the microtubule was obtained by docking the EC derived structure of the dimer into a microtubule map determined by cryo-electron microscopy at a resolution of about 20 Å [9]. This model confirmed that β-tubulin caps the plus end of the MT, exposing the nucleotide binding site at the end where it is buried upon addition of another dimer. It also helped to define a single protein loop, the M-loop, as one of the main elements involved in the inter-protofilament contacts. In subsequent work, the resolution of the microtubule map was extended to 8 Å [10], revealing the secondary structure elements of the dimer and providing very strong constraints for the docking. At this resolution we also get some hints of differences between the dimer structure in the crystals and MTs, which are mainly restricted to the protofilament interface region which comprises the M-loop and longer loops on the adjacent pf.

Figure 4 illustrates sections from microtubules and sheets. Both polymeric forms are built from αβ-tubulin dimers that associate “head to tail” forming linear protofilaments. The protofilaments align laterally, abutting similar subunits, to form

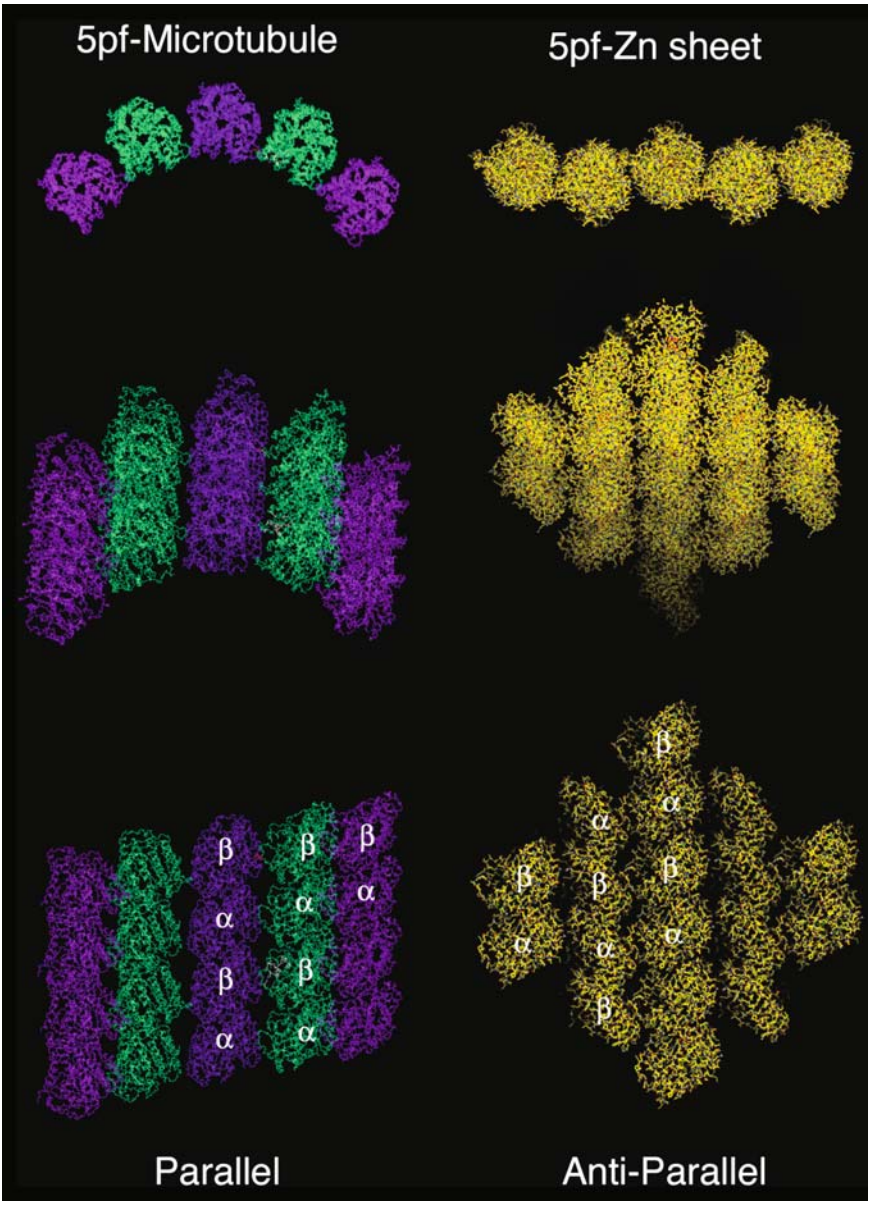

Fig. 4 Tubulin microtubules and Zn-sheets. The paired series of images show these polymeric forms of tubulin from different views. *Top* – parallel (in line) with the protofilament axis. *Middle* – 45° to the pf axis. *Bottom* – perpendicular to the pf axis (for the microtubule, this is the luminal view)

either microtubles or Zn-sheets. The difference is that protofilaments of the sheets are aligned "anti-parallel." The topographical difference is shown in Fig. 4. If one looks carefully at the "parallel" aligned microtube, one will see that the interface between adjacent protofilaments involves a single loop, the M-loop. Each α and β monomer has an M-loop that couples with its lateral neighbor. The specific angles of the M-loops at the interfaces affect the curvature of the microtubule, resulting in tubes of more or fewer pfs than the normal. The 5-pf microtubule section of Fig. 4 illustrates that the microtubule wall contains a significant amount of open space through which solvent and small molecules can pass. This model was built within the experimental 8 Å EM map of an actual 13-pf microtubule [10].

2.5 Location and Analysis of Binding Site

One surprise in analyzing the MT model was that the PTX binding site was located on the inside, luminal surface, of the MT. The binding site involves several residues of the M-loop, leading to the hypothesis that the stabilizing effect of these ligands arises from stabilization of an M-loop conformation that favors the inter-pf interactions. It has also become clear that the nucleotide-binding domains and intermediate domains of tubulin can rotate against each other [11], producing the curved protofilaments seen in rapidly depolymerizing MTs and GDP-containing tubulin [12]. The binding site is also at the interface between these domains, and it may be that PTX and other compounds bind in a way that inhibits this rotation, thus increasing MT stability by reducing the tendency for the pfs to peel away from each other.

Studies of other microtubule-stabilizing compounds have also been carried out using the electron crystallographic approach, collecting just diffraction amplitudes in an attempt to speed the process. Difference maps have been widely used in X-ray crystallography to study small conformational changes or ligand binding. The principle is that small structural changes will change both the amplitudes and phases of the structure factors, but that to a fair approximation one can ignore the changes in phase and still obtain an interpretable density map. One starts with a structure that has been well determined, so that both amplitudes and phases are known. Diffraction amplitudes are collected for a second crystal form in which the only differences are assumed to be in a small region of the structure. A difference map is then computed using the difference in amplitudes, combined with the phase of the known structure. In favorable circumstances, the difference image can be directly interpreted to show where material has been added or lost within the structure. Since collection of electron diffraction data is far faster than collection of images for determining phases, we have used the difference map approach to derive initial structural models and constraints for tubulin in complex with epothilone-A, discodermolide and eleutherobin. Because of the limited extent and SNR of the data, as well as the high degree of flexibility on each of these compounds, we then used computational methods to refine the structure.

3 Experimental Observations and Biological Relevance

The initial observation that paclitaxel (PTX) stabilized the zinc sheet form of tubulin at nanomolar concentrations suggested that there was a high affinity binding site in these polymers like that found on microtubules. However, it was not a priori certain that the binding site on sheets would have the same geometry even if it were in the same location. The derivation of high resolution models of both polymers that show the same dimer structure supports the conclusion that, indeed, they share the same binding site.

The original model of tubulin was built by hand into an experimental map that was limited at 3.7 Å resolution by the image derived phases [6]. At this resolution, densities were clearly resolved that corresponded to stable elements of secondary structure with occasional gaps due to more flexible loops. The detached volumes had to be threaded together in such a way that simultaneously matched the diffraction results with decades of biochemical data regarding protein structure and function. While this information was not used in the process of building the first atomic model of tubulin, much of the knowledge gleaned from studies of previous work in photolabeling, crosslinking, mutation analysis and electron microscopy was readily rationalized by the initial interpretations of the structure.

A significant portion of detached density was ultimately assigned to the bound ligand, PTX. The original model used for the bound PTX was an independent small molecule X-ray crystal structure of the analog docetaxel (Taxotere-Sanofi-Aventis) DTX (Scheme 1) obtained from the Cambridge Crystallographic Database [13] that was manually fit to the available density. It was noted that that the structure of DTX, added to the tubulin model as a placeholder, was in a slightly different conformation than those of PTX, derived from X-ray or NMR, proposed as the bioactive conformation [14–18]. This detail prompted collaborations using small molecule modeling methods to improve interpretation of the EC maps and models described in the next sections. Our goal was to examine the SAR of taxanes and other stabilizers in an effort to assess biological relevance of the binding site within 2D polymers.

4 Taxanes

4.1 The Minimized Structure of Tubulin and Binding of Taxanes

Computational modeling was used to refine the tubulin structure in order to understand better the nature of ligand binding. As the original tubulin/PTX (DTX) coordinates deposited at the PDB (1tub) had been built by hand without the aid of refinement software, they contained geometric anomalies not normally found in high-resolution structures. We set ourselves the task of simultaneously optimizing the best drug model into the protein model using a high quality chemical force field while maintaining a structure consistent with the experimental density map. The 1tub model was the input structure for ligand binding analysis, using force field

methods described elsewhere in greater detail [2]. Traditional gradient minimizers failed, due to the high force field energy from close atomic contacts in the unrefined model causing significant deviation from experimental data. The strained geometry made the unrefined tubulin solution a poor model for force field based analysis of drug receptor interactions without further optimization. It is important to note that the tubulin/PTX (DTX) structures 1tub, and 1jff use a numbering scheme based on structure alignment between αβ-subunits [6]. This differs from sequence based numbering which is used in this report.

4.1.1 Molecules MAID to Order

To produce a model receptor suitable for structure-based comparisons of different ligands, we utilized a slight modification of standard molecular dynamics protocols that we call Manually Adjusted Interval Dynamics (MAID). MAID is a powerful technique for qualitatively analyzing and optimizing low resolution and modeled systems (such as generated by electron diffraction or homology modeling). It is an empirically correlated implementation of traditional molecular dynamics (MD) simulation allowing fast evaluation of a biological model's structural usefulness. MD is a technique that uses force field-based atomic energies coupled with Newtonian dynamic motions to produce atomic trajectories exploring limited conformational space. It is important to realize that *the path of a given atomic trajectory is predetermined by its initial atomic vectors*. To overcome this systemic bias, other methods, such as Monte Carlo dynamics, introduce random number generated starts to explore an overall larger conformational window [19]. In a MAID session the trajectories are run for short intervals, then are manually analyzed and adjusted to fit empirical data. The user, hopefully having better than random knowledge, directs trajectories into biologically relevant conformation space and restarts the simulation. This process is repeated until the dynamic motion becomes harmonic and fits empirical data without manual intervention. This MAID method used in this work is similar to that integrated into Harvey's CONTRA MD [20], but affords greater flexibility in the case of strained starting structures. The use of low temperature in the setup of such calculations provides a mechanism to amplify and identify local atomic strain within a large biomolecular array. The greatest accelerations in any system occur in the regions of highest potential energy, or strain. If one evaluates the initial 500–1000 fs (femtoseconds) of a simulation run at low temperature, close to absolute zero, the outstanding displacement vectors will originate from loci of very high internal strain. Evaluation of these specific loci reveals the source of strain, usually Van der Wall's forces or bond irregularities, and provide the user the opportunity to adjust local coordinates, sometimes through torsions, as needed to reduce strain and correlate empirical markers. The empirical constraint used here is the EC map. It is important for the loci of high energy to be resolved before full optimization, as such anomalies cause distortions that would be dissipated into the bulk structure during direct real space minimization. The resultant MAID model has low force field energy, improved atomic geometries, and is an excellent starting structure for further study, such as docking or more extensive dynamic studies.

4.1.2 Geometry and Refinement

MAID-based optimization was applied in a stepwise fashion to increasingly larger portions of the unrefined tubulin complex (1tub) while holding the remainder as a fixed aggregate. This approach allowed a drop in force field energy from a very large positive number (>10^6) to a negative number. The drop in energy was accompanied by a large improvement in protein geometries, but with little overall deviation among the 1708 backbone atoms (RMSD 1.1 Å) (Fig. 5). The position of PTX,

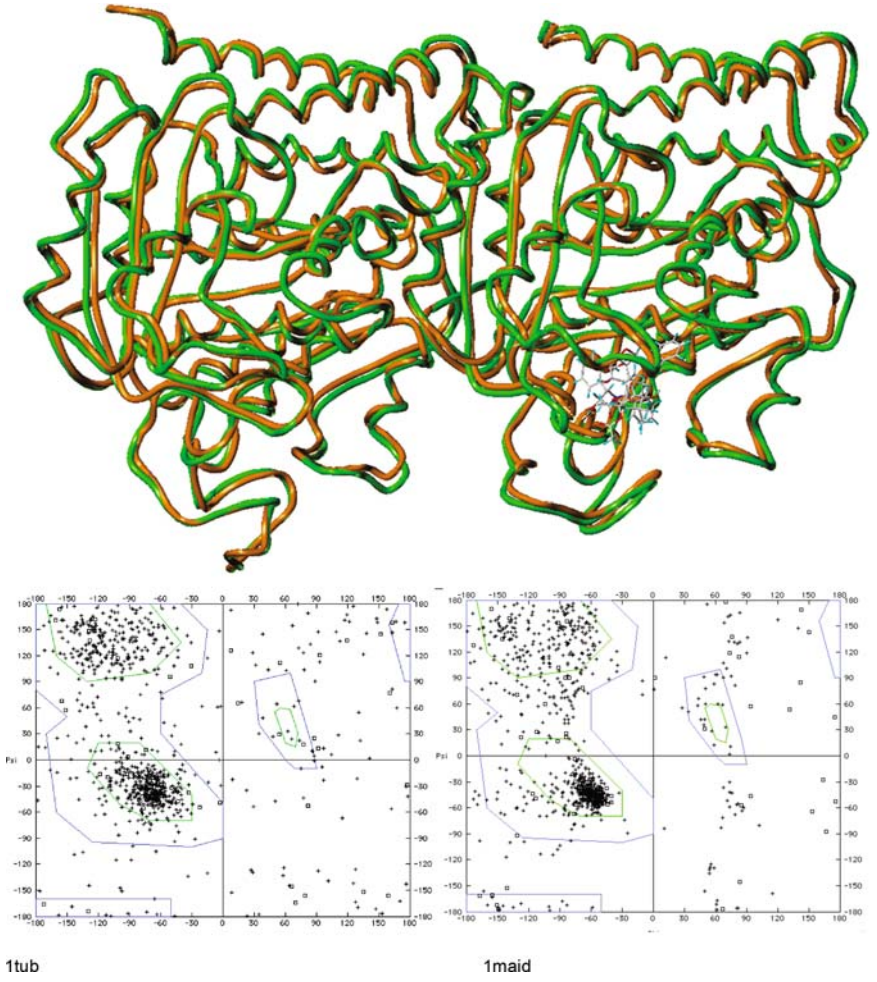

Fig. 5 Superposition of backbone atoms of MAID-optimized structure, *green*, and the high energy starting structure, 1tub, *orange*. Ramachandran plots of the two structures show a dramatic shift of phi/psi angles into the favored regions. The *blue* enclosed regions are associated with energetically favored geometries while the *green* enclosed regions represent the most favored peptide geometries as would be seen in the low energy packing geometries of protein secondary structures such as α-helices and β-sheets

used in the optimization, moved slightly within its tubulin binding site of the MAID model (maid1) relative to the DTX/tubulin model (1tub) (Fig. 6), but still fit the experimental map. It is important to note that attempts to optimize the system using conventional dynamic equilibration protocols resulted in structures with RMSD >2.0 Å for the backbone that did not fit the experimental maps. The PTX ligand in maid1 enjoys complementary packing of its C–3′ phenyl on the Van de Waal's surface of residue Phe270 at the binding site's hydrophobic floor as well as side chain in the hydrophobic depression between His227 on helix 7 and Leu215. The optimized model also gains hydrogen bond interactions between the ligand and adjacent site residues as well as within the protein's secondary structure leading to an overall improved internal geometry as seen in the comparative Ramachandran plots (Fig. 5).

The MAID-optimized PTX/tubulin was used as an input model for crystallographic refinement against the experimental diffraction data. The refinement, using an expanded diffraction data set that included amplitudes to 3.5 Å, corrected some threading errors of the original sequence and continued to improve the protein's geometry [21]. The general characteristics of the protein and PTX ligand positioned within its binding site changed little upon refinement.

The refined electron crystallography structure (1jff – 3.5 Å) [21] lacks numerous high-energy features found in the unrefined coordinates (1tub – 3.7 Å) [6], but the process of refinement against low resolution data inherently produced a model with some internal strain as shown by the increased scatter within the most favored region

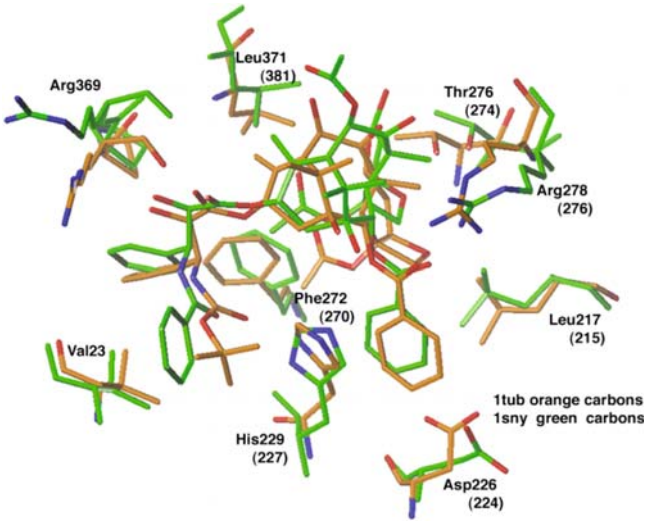

Fig. 6 Details of active site alignment with unrefined DTX/1tub model with orange carbons and PTX/maid1 with *green* carbons. Structure based site residue numbering from 1tub (Nogales 1999), parenthetical numbering is based upon sequence and used in the text

of the Ramachandran plot (Fig. 7). This may in part be due to ignoring explicit hydrogen or electrostatic contributions during refinement in weak data. Accordingly, we desired to produce a relatively strain-free model of the protein ligand complex including hydrogens and electrostatics for further force field analysis. The stepwise optimization producing the final model shown in Figs. 7 and 8 is detailed elsewhere [2].

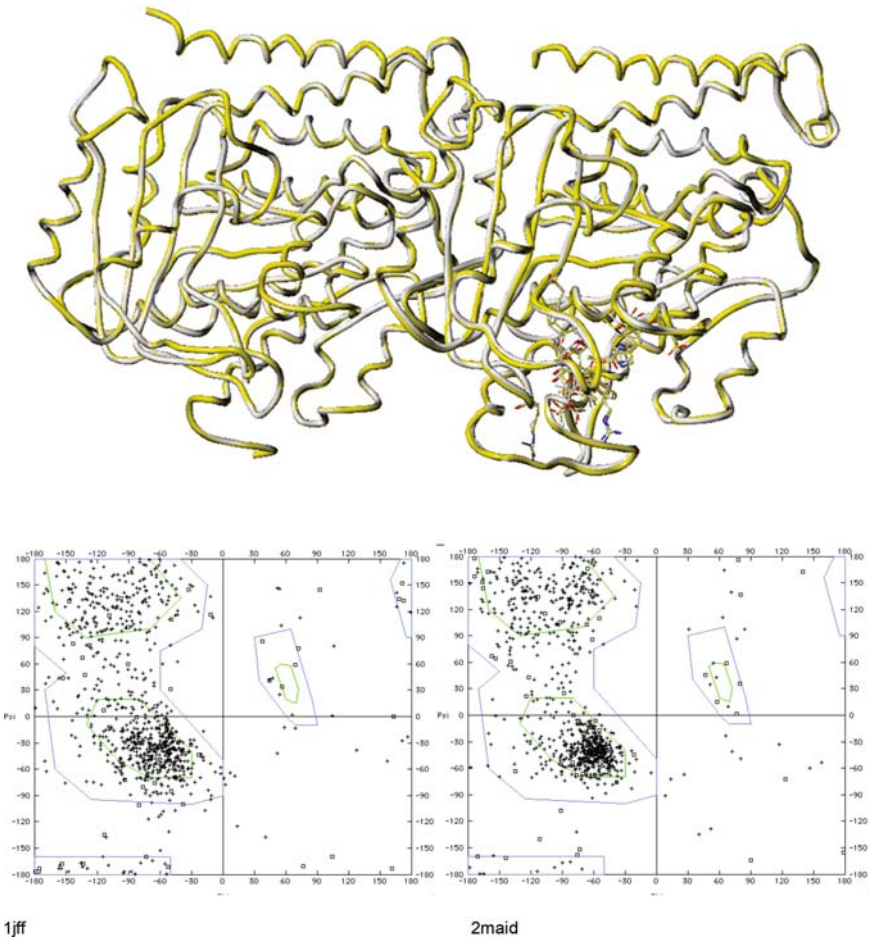

Fig. 7 MAID optimized protein model, 2maid – *yellow*, based upon the crystallographically refined tubulin model 1jff – *white*. C-α atoms show no difference, but Ramachandran plots show significant improvement of internal protein geometry after MAID (*right*) with most residues clustering within the green "most favored" region indicative of internally stabilized (hydrogen boded) secondary structures. This is further indication of the importance of hydrogen bonding and electrostatic contribution in finalizing protein structures

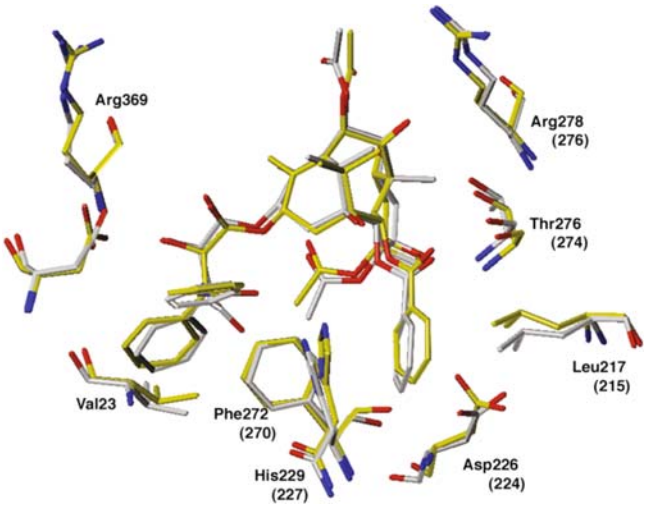

Fig. 8 "T"-Taxol within the MAID-optimized complex, *yellow*. Crystallographically refined tubulin model 1jff in *white*. Primary optimization occurred with the internal geometry of the C-3′ benzamido side chain

4.1.3 Conformation and Controversy

The energy-optimized EC solution of PTX supported the initial observation that the protein-bound conformation of the drug differed from those seen in solution by NMR. Although PTX has a rigid "baccatin" core of four rings, the C13 side-chain can rotate freely. Scheme 2 illustrates the extremes observed by NMR in polar or

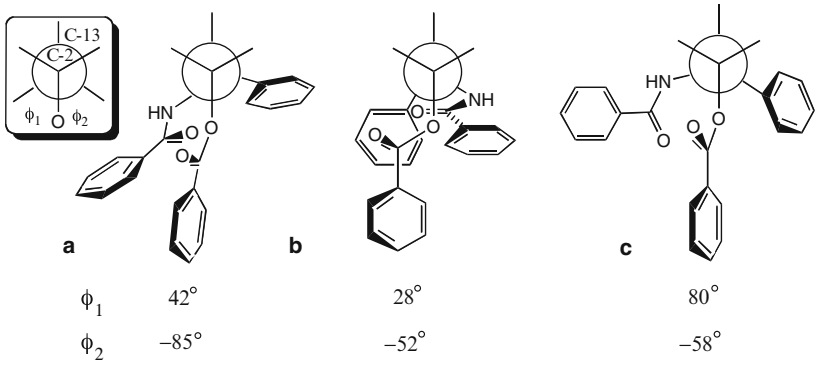

Scheme 2 Newman projections for PTX conformations in terms of the improper torsion angles O–C2–C3′–N(Bz) and O–C2–C3′–C(Ph) (ϕ1, ϕ2). The front atom is C–2, the unseen back atom, C–3′. **a** The "nonpolar" conformation as derived by NMR in CDCl3. **b** The "polar" conformation as observed in the solid state. **c** T-Taxol conformation bound to β tubulin from EC

non-polar solution compared to the EC structure. We observed that, upon binding, PTX's critical C2 side chain inserts into a deep hydrophobic pocket at the interface of helices 6 and 7 on beta tubulin with the baccatin core adjacent to the M-loop. The binding position seen in the zinc sheets requires the C13 side chain to be oriented in an intermediate conformation. This intermediate conformation, called "T" taxol, allows the C3′ phenyl to rest in contact with Val23 and Phe272(270) while the benzamido group enjoys favorable pi stacking with His229(227) above H7 at the luminal access to the pocket Fig. 9.

Although the ligand position within this pocket model makes chemical sense, one can still question how relevant the binding site determined from the 2D crystals is to that in a microtubule and, more importantly, to the drug-like properties of the compound. Two courses of validation were explored simultaneously. The direct method was to collect higher resolution 3D data of actual microtubules for model/map comparison, which has been discussed above. The conservation of the dimer and protofilament structures indicates that there is no need to posit a different binding site in the MT. The indirect method has used comparative modeling of empirical biological observations. Accordingly, we examined SAR associated with drug analogs' ability to stabilize microtubles, positioning of mutations associated with drug resistance and species selectivity between mammalian and yeast tubulin. Those studies found the EC based binding solution to be consistent with the majority of data available [2]. Subsequent studies have used the EC interaction model to engineer a yeast tubulin with PTX sensitivity [22], and to explain newly emerged resistance phenotypes [23].

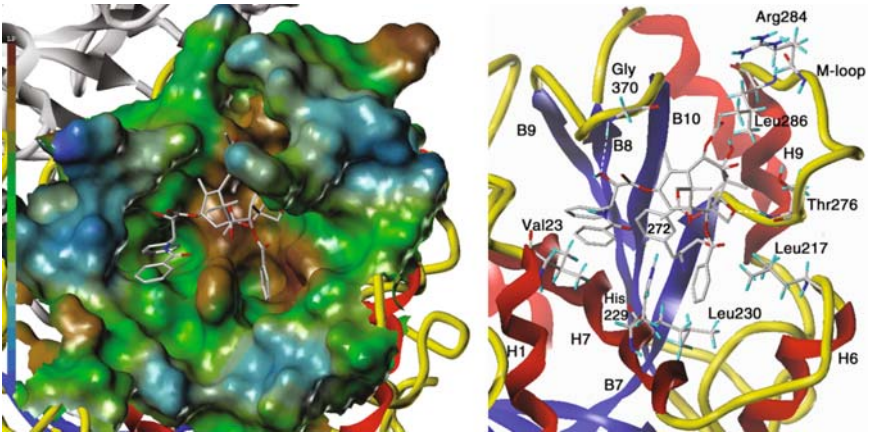

Fig. 9 The hydrophobic binding pocket for "T"-Taxol on beta tubulin. *Color* on the surface model ranges from most lipophilic (*brown*) to most hydrophilic (*blue*). The ribbon view of beta tubulin is *colored* by secondary structure with *red* – alpha helices and *blue* – beta sheets

However, the most significant development has been the development of PTX analogs that are constrained in the "T" geometry and the demonstration that these analogs have greater activity than the unconstrained parent compound [24]. By rigidifying the conformation of PTX to that found in the EC binding site, activity is seen to increase 100-fold against the parental 1A9 cell lines and over 1000-fold against cell line with resistance that was acquired though a Phe270Val mutation in the beta tubulin site (Fig. 10) [25].

Even while performing our validation analysis, we became aware of the potential for controversy. Data obtained by combining NMR and FRET technology suggested a different solution [26]. The work of Li and colleagues used a combination of two experimental techniques in an attempt to ascertain the bioactive conformation of PTX. The solid state NMR technique, REDOR, was used to determine interatomic distances in an isotopically labeled PTX analog. The technique has very high spatial resolution, but was performed on lyophilized microtubules. This procedure was used to measure intramolecular distances between the fluorine *para* at the 2-benzoyl position with the ^{13}C labeled C3′ carbon and the ^{13}C labeled carbonyl carbon of its adjacent amide. Fluorescence resonance energy transfer (FRET) is a lower resolution technique that was used to measure intermolecular distances between two PTX FRET donors, and pre-bound colchicine/tubulin (COL-TB) as the resonance acceptor system. The resultant PTX model was found to bind in the same tubulin site as our "T" Taxol, but with an orientation 180° opposite ours. Thus, both the binding conformation and orientation differ from the EC based solution.

A recent publication has detailed possible causes for some of the seemingly incongruent findings [27]. Those authors discuss static and dynamic properties of the PTX-tubulin complex that may resolve the discrepancy with the REDOR conformation. However, we believe the reversed orientation can best be explained

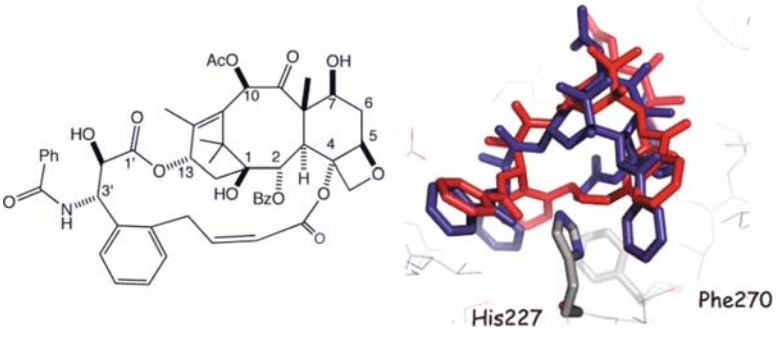

Fig. 10 Bridged analog (*red*) is designed to lock in EC derived "T" conformation like PTX (*blue*). It has been shown slightly more active than the parent Taxol for tubulin polymerization and significantly more active in both wild type and PTX resistant cell lines as discussed in text

by "non-microtubule" polymers present in the FRET study. More recent work examining cyclostreptin binding suggests that different binding sites for tubulin stabilizing compounds exist in the microtubule state vs solution or non-microtubule polymers [28]. The EC and FRET studies are likely detecting drugs in different binding environments. How the EC solution of PTX binding may or may not be extended to other microtubule stabilizers is discussed in the next sections.

5 Epothilones: An EC Derived Template for New Drug Design

Epothilones are an exciting class of chemotherapeutic currently in clinical trial that have shown promise in overcoming some of the taxane's primary limitations such as poor administration, and loss of efficacy in MDR resistant tumors. The EC solution of PTX's bound conformation prompted efforts to extend the collaboration to other known microtubule stabilizers. The original PTX/tubulin work generated an experimental map using diffraction data and phases that were derived from the electron microscopy (EM). Although a tremendous amount of effort was involved in optimizing crystallization conditions to improve the resolution of diffractions obtained [7, 29–31], the most time consuming activity was the collection and processing of images for phasing. Since crystallization procedures had been optimized, the next hurdle toward use of EC for rapid analysis of different ligands binding to tubulin was the phase problem.

A way to get round collecting and processing image sets for each new ligand tested was to use the phases from the original PTX experiment to process the diffraction amplitudes recorded for new drugs in the Zn sheets. As discussed above, this is not a new concept. The techniques "molecular replacement" (MR) and "phase switching" are often employed in X-ray crystal structure determination when actual phases aren't known [32]. The application and results of these experiments are described herein.

5.1 Model Preparation and Phasing

Two issues hamper MR and phase switching in the EC process: relatively low resolution and incomplete data. Diffraction resolution is an inherent property of a given crystal. Although we could conceivably improve the crystal preparation to get better resolution, completeness greater than 70% at the highest resolution is not likely for EC due to the problem that diffraction quality often decreases rapidly at high tilt angles, above about 60°. This presents a challenge during data processing because the maps resulting from the Fourier transform of experimental amplitudes are heavily dominated by phases at resolutions worse than 2.0 Å. To address this issue of phase bias, "difference Fouriers" were used to tease out what part of the new diffraction signal comes from the new drug [33].

Diffraction amplitudes for the epothilone A (epoA) stabilized crystals were better than those obtained with PTX and had useful data down to 2.88 Å. Although the accuracy and completeness of the data decreased at the highest resolution, incorporating the high resolution data contributes significantly to the quality of the maps. Figure 11 illustrates the effect of including the higher resolution reflections upon the "omit" density volume in the active site. Annealing of the model was initially performed in CNS using data between 3.5 and 20 Å resolution as had been done for 1jff. To remove previous ligand bias from the models used for phasing, PTX was removed from the 1jff coordinates, temperature factors were flattened, and a small random number was added to "shake" the coordinates before simulated annealing. However, as shown in panel 11d, maps produced with a 3.5-Å cutoff had little resemblance to our ligand. The two F_{obs}–F_{calc} maps shown were phased with the identical set of tubulin coordinates, but used different resolution cutoffs of the diffraction amplitudes. This set of experiments suggested to us that there may be real signal for a portion of the ligand extending above His227 that can be seen in the omit density at 2.88 Å in panel 11a. Panel 11f illustrates the positioning and mapping of our final ligand model using these same coordinates and the full set of diffraction amplitudes for comparison.

5.2 Fitting of the Ligand Density

Compared to PTX, epoA is a highly flexible molecule. A similar method was employed to generate conformations and reduce the test set using constraints from NMR derived NOE and coupling constants [3, 34]. However, without a reference of something like PTX's baccatin core, it was apparent that an automated solution was needed to fit all possible orientations of the epoA test set conformations to the density volume. The discontinuous ligand density illustrated in Fig. 11, obtained by annealing with amplitude data to 3.5 Å, did not readily lend itself to such a process. But running the annealing refinement again using all of the data to 2.88 Å resulted in the map shown in Fig. 12.

Automated ligand fitting to the EC density was performed using the X-ligand [35] module in QUANTA 2000 [36]. The largest unoccupied density took shape and volume compatible with both the macrocyclic ring and the side chain of epoA (Figs. 12 and Fig. 13a). Since the X-ligand algorithm does not explore alternative ring geometries, a database representing a diversity of low energy epoA conformations was constructed. Details of the database preparation are available in the supplemental material of the original work [3]. From thousands of automated fits, only two binding modes of epoA were found that were reasonably consistent with the experimental omit maps. These corresponded to orientations with the side chain directed toward either the M-loop or His227 (Fig. 12). Representative samples of conformation and orientation space were selected for further Fourier difference analysis. The set contained both native

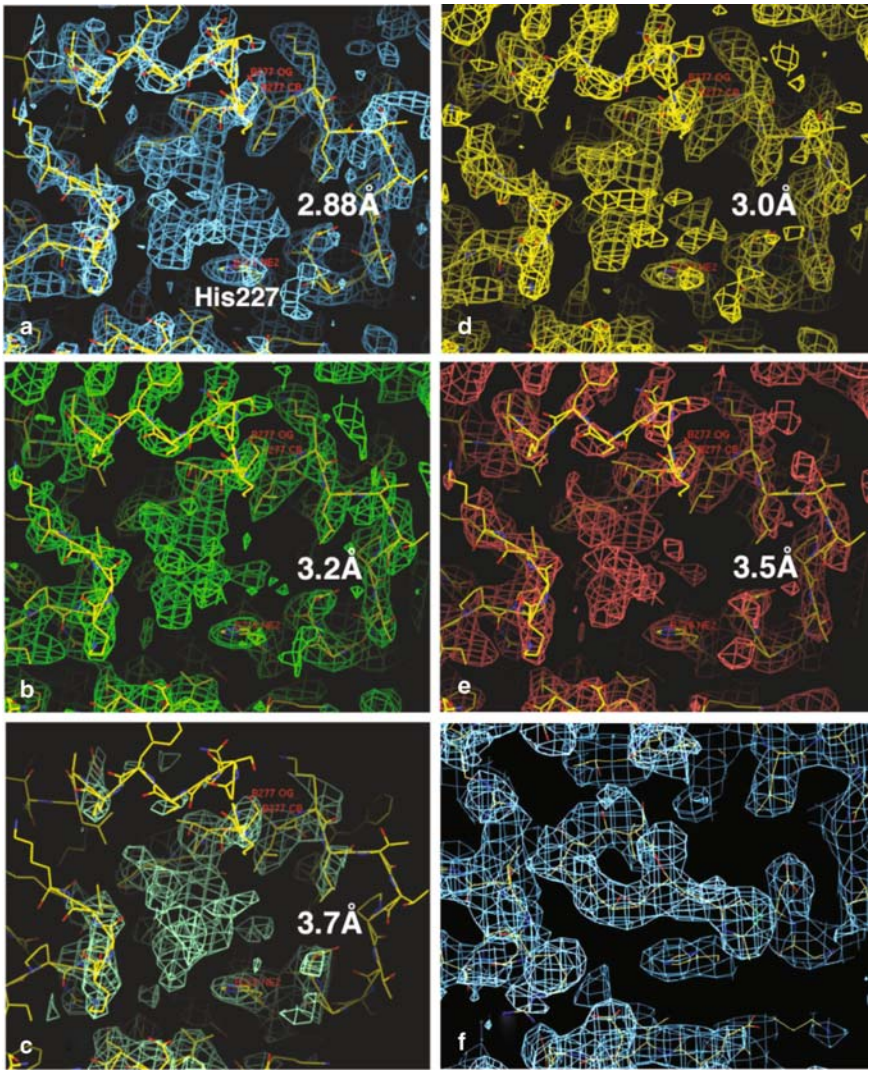

Fig. 11 The effect of diffraction resolution upon omit map projections. Frames (**a**–**e**) illustrate the differing results obtained as less diffraction data is included in calculation of $2F_{obs}–F_{calc}$ omit maps from CNS. The model of protein without ligand was obtained through high temperature simulated annealing cut off at 3.5 Å as described in text. Each map (**a**–**e**) was phased by the same model with the only change being the number of reflections used. The tubulin coordinates used for molecular replacement were obtained from the deposited structure, 1jff, with PTX ligand removed and B-factors uniformly set to 30 before annealing. **a** Ligand omit map using all data down to 2.88 Å. Unoccupied volumes of density above His227 approximate the shape and total spatial volume of epoA. Although appearing visually connected, unoccupied peaks are discontinuous at 1 sigma and become indistinguishable from noise at lower sigma levels. The discontinuous nature of this map makes it unsuitable for automated fitting. **b** Omit map calculated as in **a**, but with a high resolution cutoff of 3.00 Å. Considerable loss of peak density above His227 is evident, changing the overall character of the omit pattern. (**c**–**e**) Omit maps calculated with 3.2, 3.5, and 3.7 Å cutoffs, respectively, show a systematic degradation of ligand omit signal as less high resolution data is included in the analysis. **f** A $2F_{obs}–F_{calc}$ map calculated at 2.88 Å after manual fitting of the ligand and rigid refinement in Refmac (CCP4) supports the view that epoA volume with side chain placed above His 227 is consistent with the discontinuous peaks seen in **a**

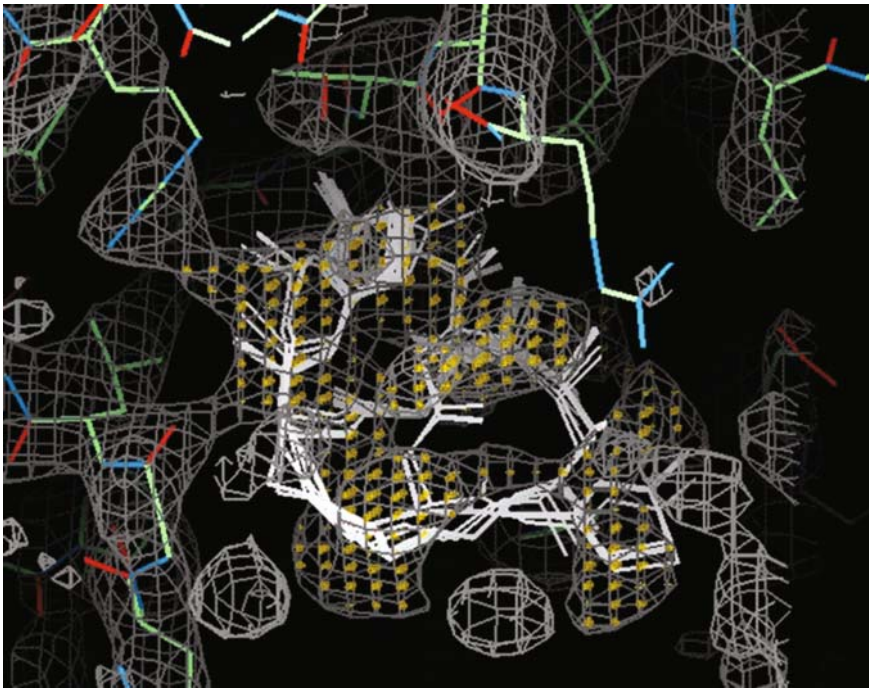

Fig. 12 The $2F_{obs}–F_{calc}$ "omit" map used in the automated query. The $2F_{obs}–F_{calc}$ omit map calculated with all reflections to 2.88 Å using CNS, map was phased from five "shaken" high temperature annealed protein models also run at 2.88 Å. This omit map exhibits a similar spatial distribution and total volume by comparison with the map in Fig. 11a, but it possesses a single contiguous volume suitable for automated fitting of conformational databases as described in the text. X-ligand was used to locate maximum unoccupied volume of density (*highlighted in gold*) and to flexibly fit epothilone rotamers from the conformational database. Only two orientations of ligand, as depicted above, were found to satisfy the density shape

and modified structures from X-ray, TNOE NMR, and NAMFIS analysis [34, 37, 38]. Each ligand/tubulin model was refined as a rigid body in Refmac5 [39] and analyzed by difference mapping as illustrated in Fig. 13. The corresponding Fo–Fc difference maps, which were generated in CCP4, favored models with side chains oriented toward His227 and main ring groups in contact with M-loop (see Fig. 13c compared to 13d). The modified NAMFIS conformation provided the superior match of all combinations tested as determined by difference mapping. To assure ourselves that the two binding modes sampled by X-ligand did not involve an incomplete search, we tested five other plausible binding orientations of epoA that had been suggested in the literature as a negative controls and are discussed in Sect. 6. All other model systems tested produced maps with similar or greater difference density than depicted in Fig. 13c or d.

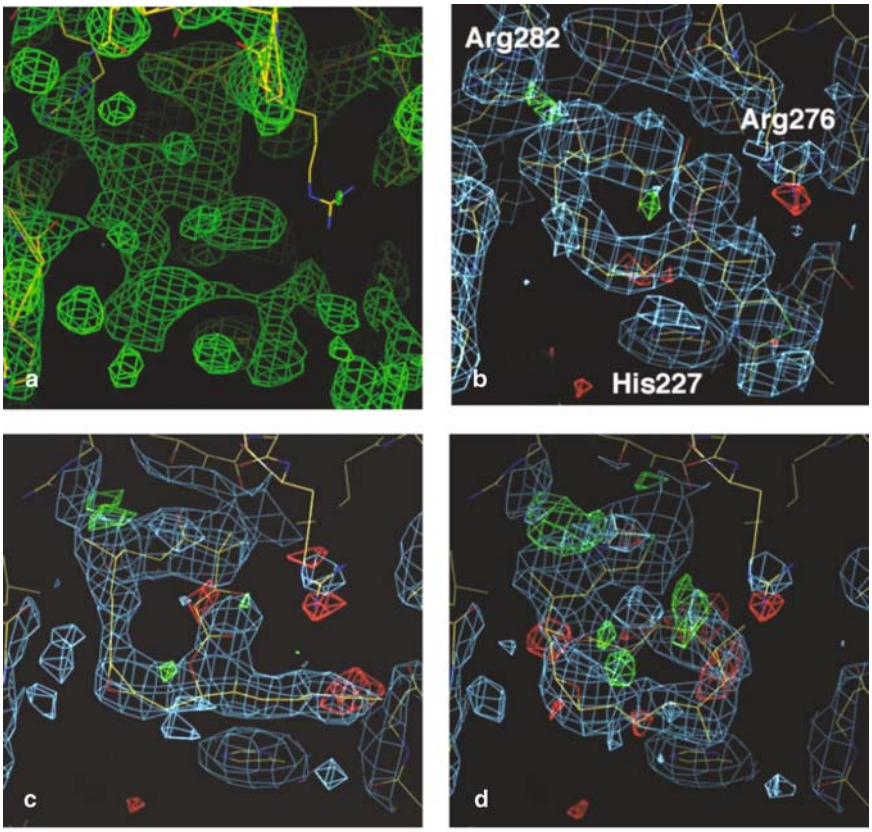

Fig. 13 The effect of varied ligand orientations and conformational models upon $2F_{obs}–F_{calc}$ and $F_{obs}–F_{calc}$ projections of the 2.88 Å diffraction data. **a** The same $2F_{obs}–F_{calc}$ omit map shown in Fig. 12 calculated in CNS with all reflections to 2.88 Å and phases from "shaken" high temperature annealed protein models. This omit map exhibits a similar spatial distribution and total volume by comparison to the map in Fig. 11a, but possesses a single contiguous volume suitable for automated fitting of conformational data bases as described in text. **b—d** $2F_{obs}–F_{calc}$ (*sky-blue*) and $F_{obs}–F_{calc}$ (*green* +3σ, *red* –3σ) maps calculated at 2.88 Å in CCP4 using model derived phases from identical protein models, but different ligand models. In all cases, *green* signifies diffraction data that is not being fit by the model and red represents atomic model positions that are not supported by the diffraction data. **b** "Induced fit" variant of a NAMFIS derived, solution NMR conformation of epothilone A, automatically positioned and real space refined using X-ligand and the omit map from **a**. The maximum negative difference (*red*) in this fit is associated with a poor positioning of Arg276 away from ligand and can also be seen in **c** and **d**. A small negative difference peak is located under the ligand, but is >1.5 Å from any model atoms. The positive difference (*green*), diminished upon local refinement, can also be seen near Arg282 in all maps. Atoms of residues within an 8-Å sphere of the ligand were refined by maximum likelihood in reciprocal space to the final solution. **c** The TNOE NMR derived conformation of epothilone A bound to tubulin, positioned and real space refined as in **b**. A negative difference is associated with this epothilone model's positioning of C2, C3, and thiazole. Upon reciprocal space refinement, this ligand model shifts the side chain toward the position seen in **b**, but the electron density quality deteriorates. **d** Same TNOE NMR starting conformation as **c**, but positioned and refined by X-ligand in an "opposite" orientation that clearly puts additional negative (*red*) difference densities below and positive (*green*) density volumes within the plane of the macrocycle models used in **b** and **c**

5.3 Structure Activity Relations and the EC Binding Model of Epothilone A

The conformation and orientation of epoA and tubulin side chains derived from the above fitting were refined in reciprocal space for the binding site region only and deposited in the PDB as 1tvk.pdb with no force field optimization. Like the refined PTX-tubulin structure described previously (Fig. 5), these coordinates contained strain from refinement in weak diffraction data. A cautionary note is that force field optimization without crystallographic based constraints can cause protein rearrangements that deviate significantly from those used here. Due to uncertainty about some regions of the protein beyond the binding site we did not proceed with full crystallographic refinement. Using a MAID protocol similar to that employed for PTX-tubulin optimization and analog development, we compared and evaluated a large volume of available epothilone analog SAR and resistance data [40]. Much of that analysis is discussed in the original publication, so this section will primarily bring forward analysis that was not explicitly described before [3].

The evidence associated with the PTX solution made us relatively confident that the EC binding site could provide a template for understanding the biological underpinnings of epothilone analog activity. Further, we expected that comparison of epothilone and taxane binding should give us insight regarding pharmacophoric principles that are common for the site. However, we spent more than a year retesting and analyzing models before publishing our structure. Excellent work had already been published describing a solution NMR based model for epoA's bioactive conformation reviewed in the previous chapter [37]. We tried to align those results with our data, but never achieved a better correlation than that pictured in Fig. 13c. This may not be surprising given the very different environments of the two experiments. While epo is held by anti-parallel protofilaments in EC, it interacts with free tubulin and polymeric spirals in the NMR experiment. We were, and still are, open to the possibility that neither of these experiments may accurately represent the precise interactions of epothilone interacting with a microtubule which are responsible for biological effect.

Fortunately, the medicinal chemical efforts applied to understand and improve the biological activity of epothilones have been enormous. Epothilones, unlike PTX with its baccatin core, can be produced through several synthetic approaches discussed in this volume. Accordingly, the structural variety of analogs tested has been vast. Three excellent reviews have highlighted developments over the past decade [40–42]. Many hundreds of analogs have been produced and tested, but very few have significantly better potency than the natural products.

To simplify discussion of epothilone SAR, we will divide the molecule into quadrants and explore only a few analog series representative of each region illustrated by Scheme 3 in the context of our EC solution. It can be seen that Quadrant 1 contains the namesake epoxide with a very important methyl stereoselectively positioned on carbon 12. Quadrant 2, with a single hydroxyl flanked

Scheme 3 Four sections of epothilone B used to evaluate structure activity relationships of analogs

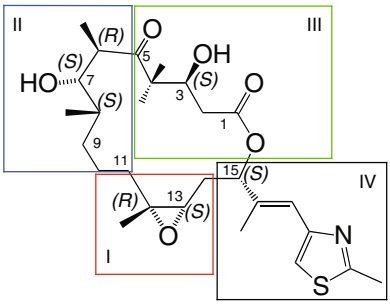

by aliphatic stereo centers, is primarily hydrophobic. This is contrasted by the highly polar Quadrant 3 containing lactone, hydroxyl and ketone moieties. The fourth quadrant contains the thiazole side-chain, which is projected from the (*S*) position on C15.

A significant complexity arose with the modeling of the EC epothilone interaction model compared to PTX. While docking could be used to fit PTX and analogs to the tubulin site, epoA was a challenge. Docking and scoring functions favor placing molecules into, rather than across the top of, binding sites. Many models had been proposed in the literature prior to ours that give results with a better theoretical energy score. We tested them all and came up with hundreds of our own over a period of several years [43]. Unfortunately, they didn't fit our data as we show in Sect. 2.6 on the uncommon pharmacophore. After several years of trying to fit the EC data onto proposed pharmacophore models (docking relates to underlying pharmacophoric functions), we chose to fit a model into our data and see if might teach us something new.

What follows is a most basic evaluation of the proposed EC binding mode as a template for potentially understanding activity of an analog series. It is important to recognize that our EC data tell us nothing about explicit conformations of the ligand or protein. Therefore, comparison of internal torsions between conformational families is not addressed in this work. For these analyses, the MAID optimized ligand from the tubulin complex was manually modified in the specific region dictated by the analog and subjected to three step minimization. The first two steps were performed with the ligand in vacuum to attain a local minima for the given analog. The first step minimization of the analog's local modification was performed while holding the overall molecular orientation in space with a single non-macrocycle atom fixed as an aggregate in each of the three remaining quadrants of the molecule. The second step allowed the full molecule to minimize to convergence with no constraints. The third step was performed by merging the minimized ligand back into the receptor, and simultaneously minimizing the complex including protein residues within 5 Å of the ligand. If either protein or ligand atoms moved >2.0 Å from the starting structure, this was scored as a conflict. For all cases, except as described in Fig. 20, Powell gradient minimization was performed in Sybyl using the Tripos force

field with Pullman charges on the ligand [45]. However, due to the large, system dependent effect charge plays upon computation of interaction energies, we ignored electrostatic contributions to the energy during optimization of these structures [46]. These models first address the question "can a local minimized version of this analog fit similarly to the EC derived binding mode?." In these tests, a bound active analog may have significantly different internal torsions than those of a parent while still allowing similar interaction with the receptor. The second question asked is if alignment of polar groups is consistent with observed activity patterns. Therefore, we are primarily looking at a possible binding mode related to the orientation suggested by the EC maps and not specific details of a single conformation or path between conformations here.

5.3.1 Quadrant I (Q1) C12–C14

The significant role of Q1 is underscored by dramatic activity differences due to substitutions shown in Scheme 4. Addition of a single methyl at the C12 position significantly increases the polymerization potency and cytotoxicity of epothilones B or D relative to epothilones A or C [40]. Conversely, single methyl substitution at C13, Scheme 4(5a), nearly destroys all activity [48].

The EC interaction model shown in Fig. 14 suggests that these results are due to favorable hydrophobic packing against His227 for the C12 analog (Fig. 14b) while causing steric clash for the C13 methyl (Fig. 14c). The positive impact of the C12 Van der Waals interaction with His227 is extended by its position adjacent

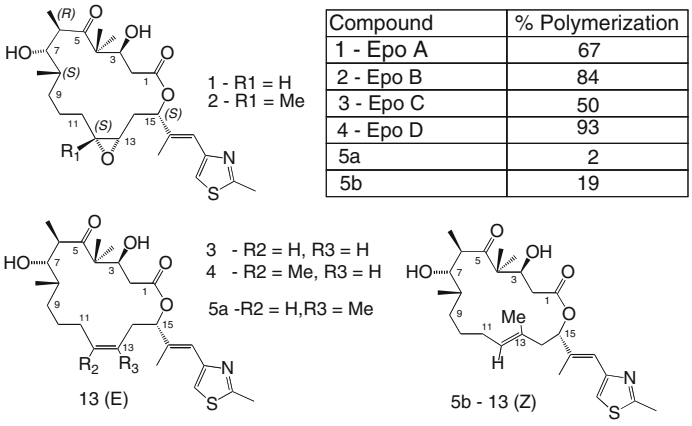

Compound	% Polymerization
1 - Epo A	67
2 - Epo B	84
3 - Epo C	50
4 - Epo D	93
5a	2
5b	19

Scheme 4 Modifications to Quadrant I atoms

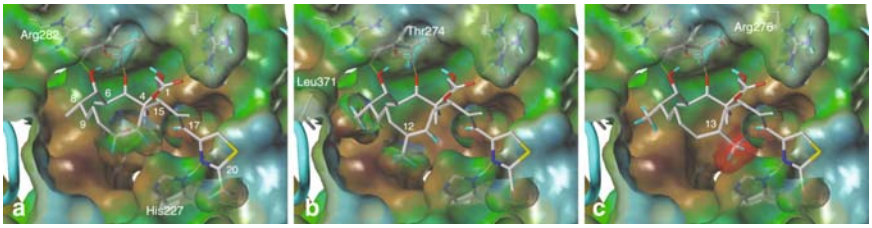

Fig. 14 A Connolly solvent accessible surface was projected from the tubulin receptor model using a 1.2-Å probe and lypophilic/hydrophilic potential was mapped as a color gradient *brown/blue*. **a** Epothilone A (Scheme 4(1)) can be seen spanning above, but not into, the deep hydrophobic pocket. Van der Waals (VDW) surfaces were projected from C–12–13, C–17, C–21 and associated hydrogens of the ligand illustrating near perfect packing around the hydrogen bond donor/acceptor pair between His227 N–H and thiazole (H-bonds are shown as *yellow dashes*). **b** The addition of a methyl to C–12 for epothilones B or D, as shown, produces a significant increase of polymerization activity as presented in the table of Scheme 4. VDW surfaces projected from the C–12 and C–8 methyls illustrate the favorable steric bridge formed by the ligand between residue Leu371 on loop B9–B10 and His227 on H7. **c** The *red* VDW surface around the C–13 methyl of Scheme 4 analog 5a, illustrates steric collision in the model that may account for its lack of activity

to the C8(S) methyl in contact with hydrophobic residue Leu371 on the B9–B10 loop (Fig. 14b). This hydrophobic packing is thought to provide solvent shielding which inherently strengthens the interaction of the Quadrant IV side chain with His227. It is interesting to note that, while the 13-Me (E) substituted analog, Scheme 4(5a) pictured in Fig. 14c, is forced into direct steric clash with His227, changing the stereochemistry to give the 13(Z) *trans* configuration, represented in Scheme 4(5b), frees macrocycle strain, places the methyl away from His227 and recovers some activity [48]. The EC model also suggests that analogs made *trans* across the C12 position would place the C11 methylene in a role similar to the C12 substitution of epothilone B and be active. This is particularly borne out in the cylcopropyl substituted analogs of Nicoloau which are discussed as part of Quadrant II (Fig. 15a) [49–51].

Other aliphatic chains may be accommodated in the hydrophobic space beneath C12, yet polar substitutions are destabilizing [42]. The SAR makes it clear that the epoxide's role is for conformational rigidity rather than hydrogen bonding. In analogs from BMS that replace the epoxide with substituted aziridines, polar extensions which can interact with His227 from within the pocket have lower activity that may be attributed to weakening the side chain interaction [52]. Analogs that add hydrophobic bulk beneath the ligand can enhance potency, also in compliance with the model [3]. Across the entire aziridine series, the EC model explains activity and inactivity analogs through direct steric or electronic interaction with the receptor.

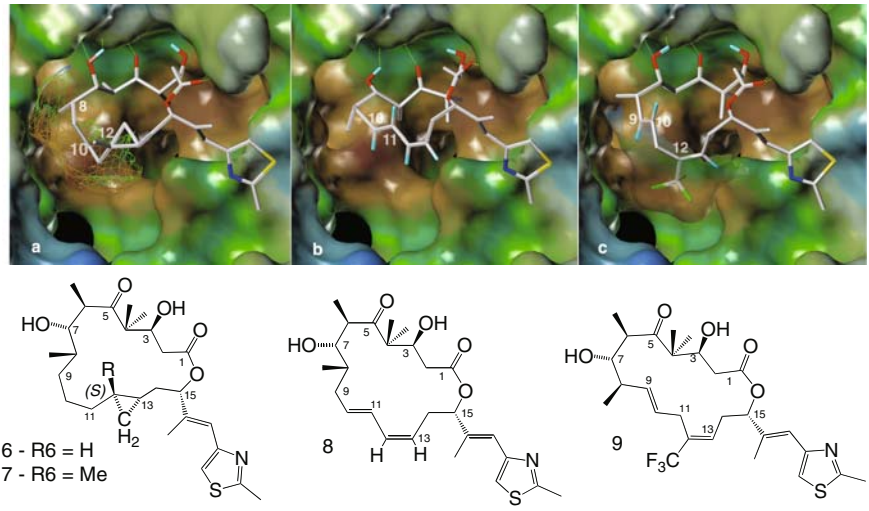

Fig. 15 Favorable modifications of Quadrant II atoms. **a** *trans* cyclopropyl analog (7) is shown with mesh Connally surface over the 8–11 section. The C12 methyl directed toward solvent explains why such substitutions have little effect on this framework's binding. **b** The rigidified 10–11 of (8) is associated with good potency. **c** Compound (9), Fludelone, is one of the most active epothilones tested. The trifloromethane at C12 has excellent complementarity shown as a translucent surface. The *trans* double bond at 9–10 rigidifies the contact relationships with the protein at C12–C13 and C8

5.3.2 Quadrant II (Q2) C6–C11

The hydrophobic pocket adjacent to Q2 atoms in the EC model accommodates the significant geometric variation and favorable positioning of C9–C11 in the highly active *trans* cyclopropyl analog shown in Fig. 15a. Additionally, the solvent-exposed orientation of the C12 methyl explains the reduced activity of this *trans*EpoB analog relative to *trans*EpoA analog not shown [51, 53]. The positioning of the critical C8(S) methyl [54], at the hydrophobic interface of loop B9–B10 and the M-loop in the EC model, suggests that chemical stabilization of this aliphatic section would be favorable. Indeed, analogs that incorporate a *trans* double bond at either C10–C11 (Fig. 15b) [55] or C9–C10 (Fig. 15c) [56] are highly active – consistent with the EC template.

It is important to acknowledge that the epothilone conformation in the published EC structure 1tvk differs significantly from both the solid phase X-ray and solution phase NMR structures in this region [41, 57, 58]. Directly relating conformation to activity of epothilones is not so straightforward as is described on other sections. Therefore it is intriguing that the most active analogs, when modeled using this EC mode, need to attain at least some of the internal torsions seen by NMR in this region. Along these lines, brilliant synthetic work produced compounds which constrained the anti-periplanar alignment of C8/C9, C9/C10, C10/C11 seen by both X-ray and NMR. Although these compounds lack measurable tubulin polymerization

activity, the authors point out that observation may be more due to poor steric fit of the bulky analogs within the receptor rather than the conformation [59]. Another hypothesis is that a molecule, presenting a particular conformation seen in solution, may bind to a somewhat open form of the site and be pushed over an internal energy barrier by the kinetic momentum of the undulating receptor. The small molecule then may flip like a latch into its active form to reduce further movement. Perhaps a shift in one of these torsions is a needed change.

Figure 15c shows the highly potent "Fludelone" analog from the Danishefsky lab [56, 60]. The bound conformation pictured is a local minimum, modeled from the EC template as described above. Coincidently, this model has a heavy atom RMSD for the macrocycle that is less than 1.1 Å from the global energy minimum found through stochastic searching using the MMFF94 force field with continuum solvent in MOE 2007 [44]. We have already mentioned that energy calculations of conformers are highly force field dependent for polar molecules [46], yet this model suggest the intuitively satisfying idea that a highly active molecule presents a low energy conformation in the binding site, and can still bridge interactions needed for stabilization of the receptor geometry. It would be particularly useful to see if small molecule X-ray or NMR structures of this analog family are consistent with this theory.

Most other modifications to Q2 geometry significantly reduce activity. An exception, pointed out by Wartman et al. [40], is found in patent applications filed by the Schering group. They indicate that alkene substitutions for the C6 methyl can be well tolerated. Figure 16 shows a cavity consistent with that data in the EC binding site. Although they are not as productive as the C6 (*R*) stereochemistry, hydrophobic (*S*) substitutions may also be tolerated in accord with an orientation pointing within the deep hydrophobic pocket.

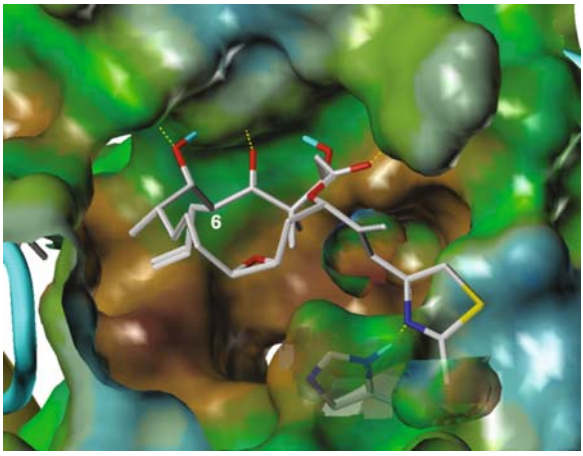

Fig. 16 Ethylene substitution at C6 (R) is positioned in a hydrophobic pocket

A most recent publication of modification in this region describes a C6–C8 bridged analog that was designed to constrain the EC conformation [61]. Unfortunately, the molecule's lack of activity in cells presents the inverse ambiguity we described for C10–C12 phenylene analog constrained to NMR data above [59]. Unlike the receptor interaction of the phenylene, the EC model provides ample room to accommodate the new methylene, however, we don't know if the molecule can attain the desired conformation. Likewise, lack of cellular activity may be caused by reduced transport or factors other than polymerization activity.

5.3.3 Quadrant III (Q3) C1–C5

Like the epoxide of Q1 and thiazole of Quadrant IV, the ketone and lactone of Q3 are signature peaks in IR spectra of the epothilone class. In the EC complex, this polar region of epoA, along with the C7 hydroxyl of Q2, is aligned with charged sidechains of the M-loop between residues Arg282 and Thr274. The ligand appears to have adopted a conformation that presents distinct spatial separation of hydrophilic and hydrophobic regions. The hydrogen bonding network of epoA, with key residues of the binding site, is discussed elsewhere [3]. Here, we focus on surprisingly large modifications that can be made to the ligand while still maintaining those productive interactions with the receptor.

The EC EpoA/tubulin model suggests that critical hydrogen bonding may occur between the C5 ketone and the side chain of Thr274, which is known to be involved in epothilone resistance [3, 62]; however, importance of the hydrogen bond from the C3 hydroxyl to the protein backbone is not so clear. We have previously illustrated that analogs with a cyano substitution in place of the alcohol can be equipotent with the parent [3]. More interesting is that compounds with complete removal of the C3 polar group, that cannot hydrogen bond, are essentially equal in potency to the parent. However, inversion of stereochemistry seems to cause significant loss of activity [42, 63, 64]. Furthermore, formation of a *trans* 2,3 unsaturated center is biologically equivalent [64]. Figure 17 shows the unsaturated analog with the three carbon is positioned over a hydrophobic pocket. Accordingly, the natural (*S*) groups point into polar space, while an (*R*) group would be buried into the hydrophobic interior. The *trans* 2,3 olefin perfectly positions the important C4 gem dimethyl within the hydrophobic pocket adjacent to Leu217 while presenting the C1 lactone carbonyl to Arg276 and the lumen of the microtubule. Such rigidification brings the C2–C3 torsion angle to 180° as suggested by NMR studies [37]. Upon further analysis, this rigid ligand geometry seems to have less internal strain than the C3–OH hydrogen bonded version seen in the published EC structure [3]. Here, like described in QII, it suggests that stabilizing specific vectors in receptor space are more important for analog activity than picking up binding energy. Also it suggests that there may be a, yet undiscovered, dynamic conformational solution which links the NMR and EC datasets. Toward that end, it would be interesting to test a 2,3 stabilized epothilone in cell lines with resistance due to hydrophobic tubulin mutations at position Thr274 [40, 62]. The EC model predicts that this rigidified epothilone may show

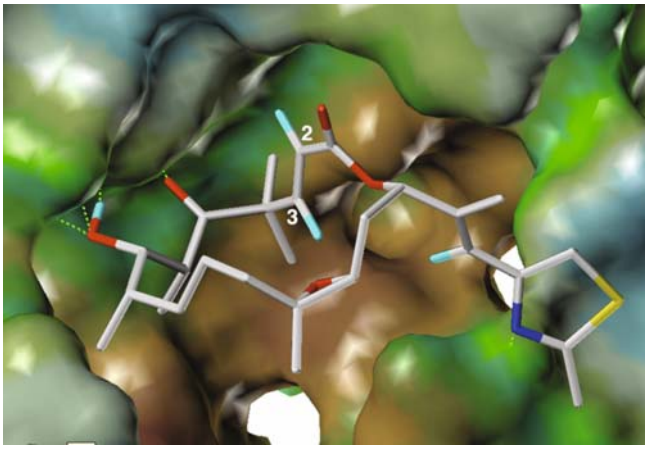

Fig. 17 Epothilone *trans* 2,3 unsaturated analog packs carbon 3 within the receptor's hydrophobic interior and projects the C1 lactone toward the polar exterior

reduced resistance relative to the parent compound like the rigidified PTX analog has for the Phe270 mutation. Such an experiment could be a test of this binding vector hypothesis with a known active compound. The linearization of Q3 described above also explains the activity of BMS analogs which replace the lactone with a lactam [65].

5.3.4 Quadrant IV (Q4) C15 Side Chain

Perhaps the most interesting and widely explored region of epothilone structure is the thiazole side chain. It is known that removal, or changing side chain stereochemistry, ablates polymerization potential [42]. The active (*S*) isomer projects the chain equatorial to the macrocycle. The question of side chain position was of primary concern to us in building our model into the EC map shown in Figs. 12 and Figs. 13a. Our expectation was that the epoA side chain would be buried within a pocket occupied by one of PTX's three side chains as suggested by the pharmacophore modeling. However, as we will show in the next section, none of our attempts to use a common pharmacophore model was consistent with the diffraction data. Only when we began to consider that the side chain was pointing out of the binding pocket toward the microtubule lumen could we make sense of the diffraction data and the wealth of epothilone SAR we have described thus far.

A key set of data that supported to placing the side chain in our original work is shown in Scheme 5. The Nicolaou lab had found that a pyridine could replace the thiazole with nearly the same potency as the parent epothilone. The key, it seemed, was placement of the nitrogen. It had already been shown that a phenyl could replace the thiazole with a loss of activity in cells [42], but three of the

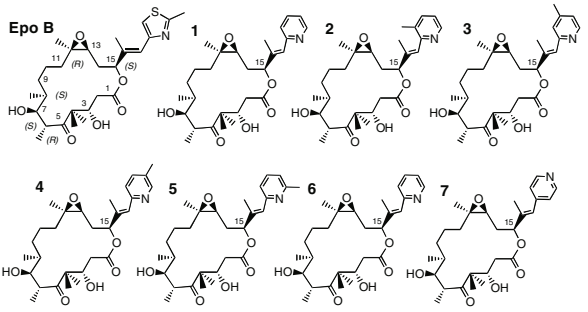

Compound	% Polymerization
Epo B	98
1	79.5
2	0
3	90.3
4	92
5	45
6	41.7
7	34.5

Scheme 5 Activity of pyridine analogs reproduced from Nicolaou et al. [47]

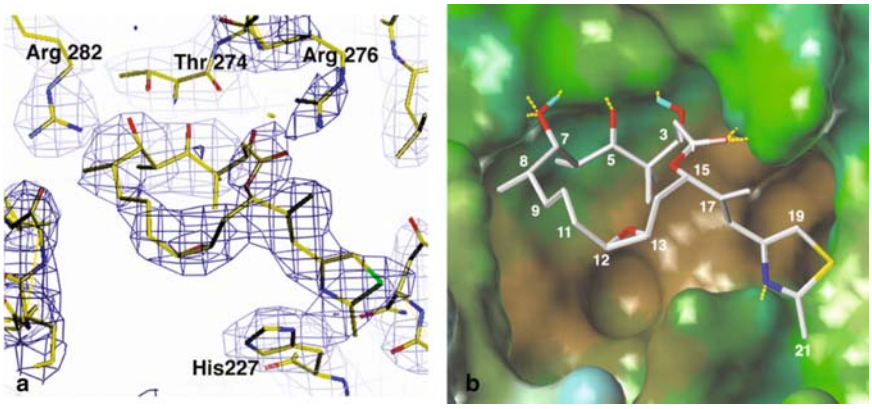

Fig. 18 The solution of epothilone bound to tubulin by electron crystallography. **a** 2Fo–Fc map and model of epothilone A bound to tubulin at 1σ (1tvk) [3]. **b** Energy optimized model derived from 1tvk through MAID protocol used as template for analysis of SAR and design of new analogs

analogs in this set, with a nitrogen at an ortho position (Scheme 5(1, 3, 4)), had both cellular and tubulin polymerization activity that was near the parent epothilone B. Interestingly, movement of the nitrogen to any other position dropped activity to that of a phenyl. Even more striking was that the nitrogen's effect could be enhanced (3,4), eliminated (5), or reduced (2) by the placement of a methyl. It has been shown that pyridine's role as a hydrogen bond acceptor may be enhanced dependent upon a methyl substitution pattern [66]. As we looked at the best-fit model coming out of the diffraction data shown in Fig. 13b, a structural rationale began to come together. Figure 18 illustrates the final EC model refined in the tubulin site.

Figure 19a shows pyridine analog (1) of Scheme 5 with the ortho nitrogen positioned to be a hydrogen bond acceptor like the thiazole nitrogen of the natural epothilone. Without the activating and shielding effect of the C21 methyl of the thiazole (Fig. 19b), pyridine (1) shows less activity. However, placement of

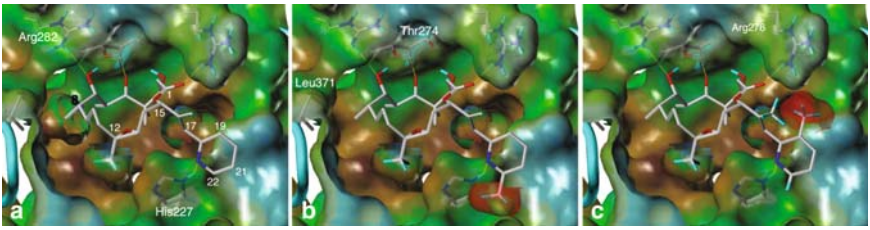

Fig. 19 EC modeling of pyridine analogs. Select pyridine analogs, with activities listed in Scheme 5, are shown in the context of the tubulin binding site. **a** Pyridine (1) with nitrogen ortho is able to make hydrogen bonding contact with His227 (*yellow dashes*). Contact surfaces projected from the C12 methyl of the epoxide and C16–C17 olefin of the side chain illustrate the complimentary packing that partially shields the H-bond from solvent and increases its strength. **b** Methyl substitution further activates pyridine, however steric conflict due to meta location drops analog (5) activity to that of a non-H bonding pyridine (6). **c** Analog (2) with methyl substitution at ortho position of pyridine conflicts with 17 methyl of side chain and induces a conformational change incompatible with His227 packing

the methyl adjacent to the acceptor nitrogen in the six membered ring (5) clashes with the donor and negates the nitrogen positional effect (Fig. 19b). Analog (2) Scheme 5, with ortho methyl substitution, has steric conflict with the C17 methyl of side chain (Fig. 19c) which may force some repositioning of the side chain, but we would not expect it to fully prevent binding. However, if this binding mode is correct, the complete loss of polymerization activity in this analog may point to specific structural requirement needed for microtubule stabilization separate from binding discussed in Sect. 6.4. Analogs (3) and (4) benefit from activation of H-bonding through the methyl without steric conflict. Nitrogen positions meta (6) or para (7) are unable to H-bond, but do not prevent the side chain from having Van der Waals contact with His227 which stabilizes overall binding.

When we initially prepared our EC model, we did not have access to polymerization data for a phenyl analog to compare with the pyridines, but cellular activity was considerably lower for the phenyl [67]. However, thorough work by Altman and coworkers convincingly demonstrates that hydrogen bonding is not required for polymerization activity [68]. While having substantially lower cellular activity, the phenyl analog retains tubulin polymerization activity that is essentially equal to the unsubstituted ortho pyridine (74.4 vs 79.5%). Clearly, an effect other than hydrogen bonding is enhancing the side chain affinity of those analogs. What we consider to be key from this analysis is that effective packing with His227 is apparently required for MT stabilization. Although the role of the nitrogen in pyridines is intriguing, a model of Van der Waal packing for the QIV side chain seems more general across epothilones and is congruent with the PTX mechanism of stabilization as discussed further in Sects. 6.4 and 8.

The explicit role of the nitrogen is further called into question by recent work of Bold et al. who used bicyclic side-chain analogs to test the role of nitrogen positions [69].

Their results, shown in Scheme 6, demonstrate that swapping positions of hetero atoms in a fused side chain has little effect on tubulin polymerization. This is true for both the 6,5 and 6,6 bicyclic scaffolds used in the original study. These results were modeled directly onto the EC template. The fused system is readily constructed by making a bond between the C16 methyl and C19 carbon. However, the most probable histidine tautomer in the protein changes depending upon heteroatom placement in the side-chain (tautomer potential calculated using "Protonate 3D" in MOE 2007 [44]). Figure 20 illustrates that both of the 6,6 Bold analogs fit the EC model well and would be predicted as active. The ring fusion stabilizes the outer ring in a conformation close to that held by the hydrogen bond and disturbed by the meta methyl in the pyridine series. Yet, it is thought to be the complimentary Van der Waals packing of that conformation with the receptor that is responsible for most of the microtubule stabilization. The hydrogen bond, then, is not generally required for efficacy.

Initially a concern, the orientation of the Q4 side-chain toward the microtubule lumen seems to explain most of the SAR associated with this region. A final example

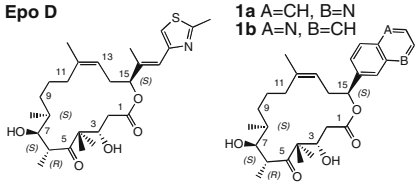

Compound	% Polymerization
Epo D	81
1a	94
1b	81

Scheme 6 Structure and activity of substituted side chains [69]

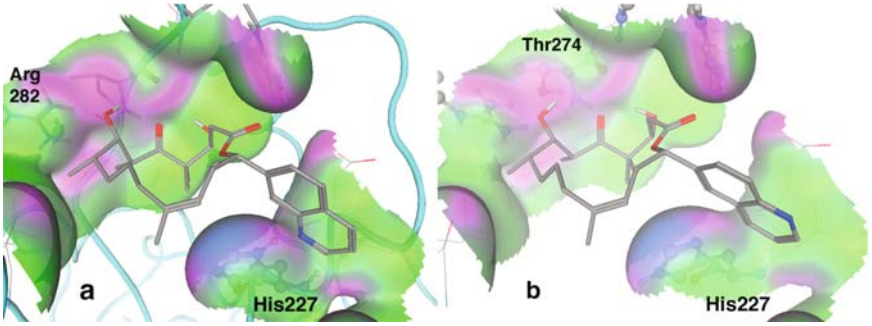

Fig. 20 Bicyclic sidechain analogs test role of nitrogen. Analogs described in Scheme 6 were built onto EC template and optimized in MOE 2007 [44]. Calculation of 3D protonation potential predicts different protonation states for His227 upon binding of the different analogs. **a** Compound 1a shown H-bonding to His227. **b** Compound 1b packs firmly against surface of opposite tautomer of His227

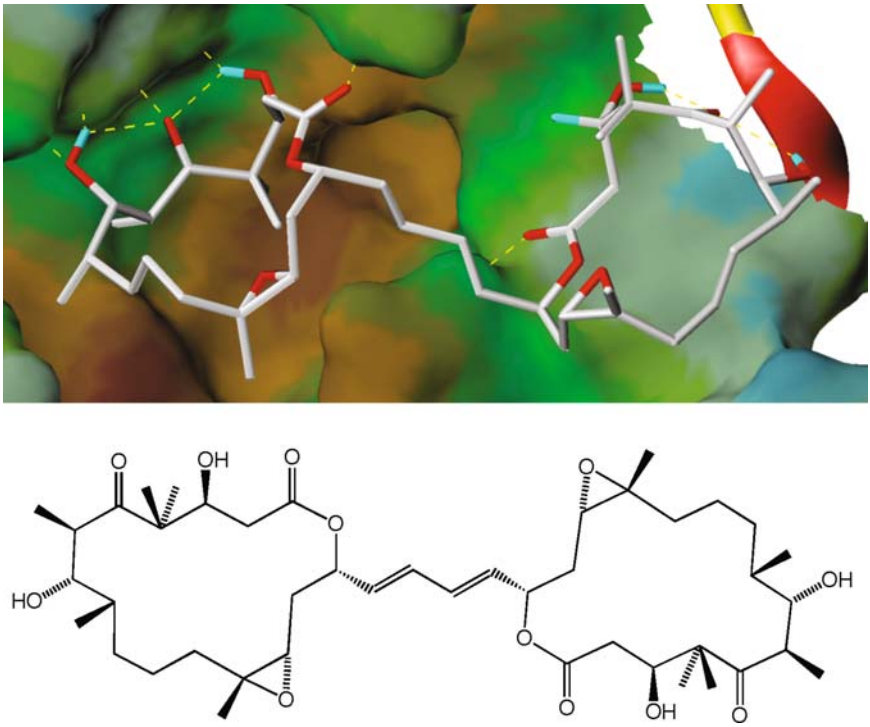

Fig. 21 Epothilone dimmer. This "dimeric" compound by Nicolaou et al. was first detected as a side product in the synthesis of other analogs. It exhibits very potent biological activity (no specific data are available) [40]

is a compound that was a side product of total synthesis. The dimer epothilone shown in Fig. 21 is reported to have high activity stabilizing microtubules. Surprisingly, it too makes sense within the context of the EC solution. Like the rigidified bicyclic compounds of Fig. 21, the conjugated linker of this dimer allows one half to bind as described in Q1–Q3 while projecting the remainder over His227. The lactone of the second macrocycle could then engage in H-bonds to His227 while packing against a complimentary surface along helix 7.

The luminal orientation of the epothilone sidechain provides a platform for understanding broad substitutions in the region that retain or enhance activity and suggests an uncommon pharmacophore described in the next section.

5.3.5 Epothilone SAR Summary

It may be possible to find a subset of SAR data that supports any model. In our approach to evaluation of SAR here, we have been specifically looking for data that can't be explained by the EC interaction. Accordingly, we have tried to show some of the more unusual, non-obvious cases here. The binding mode to which our EC analysis

has converged seems consistent with most SAR for all sections of the epothilone molecule relative to polymerization activity. However, to explain that activity, we need to allow that different analogs may span the site through different internal conformations. As will be discussed in a later section, we believe that the pharmacophore of binding may be separated from microtubule stabilization. We suggest that a conformational transition from initial ligand binding to a "latched" interaction may be needed for lateral stabilization in some cases. Importantly, one has to be careful drawing structural conclusions from cell-based assays of toxicity. Although there is a general correlation between MT stabilization and cytotoxicity, specific cases may be problematic, due to factors other than tubulin binding and stabilization.

6 An "Uncommon" Pharmacophore

6.1 Background

The concept of a "pharmacophore," a description of a drug molecule's chemical groups essential for imparting biological activity, has been an important driving force of medicinal chemistry since Paul Ehrlich's foundational works at the beginning of the twentieth century[1]. More recently, the advance of computational technology and computer graphics has provided tools for alignment of chemical features in three-dimensional coordinate space assisting qualitative and quantitative assessment of their relationships to biological function.

The pharmacophore definition given above inherently requires two separate, but related, geometric considerations. The first consideration is the conformation of a drug associated with its biological activity. Describing all possible conformations presents a significant challenge for the highly flexible epothilone, but is also complicated by the freely rotating C–13 sidechain of the taxanes. To define a "common" pharmacophore one often decides a priori the conformation of the reference molecule that is responsible for activity, and then fits conformations of the second molecule accordingly. The "fitting" is the second consideration and involves varying the orientation of a given conformation of the test molecule to define the "best" overlap of chemical functionality with the previously defined conformation of the reference. An alternative strategy could explore conformational flexibility of two or more molecules while attempting to simultaneously overlap chemical features known to be important for the activity of the molecules. The combinatorial interplay of these two considerations is responsible for the very different solutions obtained for the common pharmacopores described in this work.

[1]In 1908, Paul Ehrlich won the Nobel Prize for Chemistry and communicated his insights regarding the action of therapeutic substances and the *recognition de sedibus et causis pharmacorum* which we now loosely call a pharmacophore.

6.2 Paclitaxel/Epothilone "Common Pharmacopores"

The earliest discussion of a common pharmacophore in the tubulin literature was presented by Winkler and Axelsen [70], who employed the second strategy of simultaneous alignment while fitting only three points of SAR. Without a published 3D reference, we were not able to test their hypothesis. However, as pointed out by others [71], the predictions made based upon this earliest model were not supported by subsequent SAR studies.

The first presentation of a testable 3D pharmacophore was by Ojima et al. [71]. The reference conformation chosen for their alignment was that of the analog nonataxel as determined by 2D NMR performed in D_2O/DMSO, a conformation very similar to the X-ray structure of paclitaxel [72]. They sampled epothilone conformations through high temperature molecular dynamics and aligned them to the taxane template using a forced fitting protocol designed to qualitatively satisfy key elements of the two compounds' SAR. The bioactive conformation of epothilone defined in this study was nearly identical to that determined by X-ray crystallography.

A second study, by Wang et al., appeared soon after [73], choosing the 2D NMR conformation of paclitaxel recorded in $CDCl_3$ as its reference [74]. The effect of polar or hydrophobic environment makes a dramatic difference to the taxane, resulting in C–3 sidechains with groups reversed by nearly 180°. The hydrophobic $CDCl_3$ conformation of paclitaxel is similar to the X-ray crystal structure of taxotere [13]. In the absence of a structural model of tubulin, Wang and colleagues constructed a minireceptor that was optimized to correlate computed binding affinities with experimentally measured biological activities of taxanes and epothilones. A total of 568 unique epothilone conformations were obtained by Monte Carlo conformational searching and were fit for maximal steric and electrostatic overlap with the reference taxane [75]. The conformation of epothilone that was judged responsible for the observed activity differed significantly from conformation found by Ojima and coworkers, yet this novel orientation also provided rationale for the set of SAR considered.

The final two pharmacophore studies benefited from the publication of the atomic model of αβ-tubulin solved by electron crystallography at 3.7 Å resolution. The common pharmacophore proposed by Giannakakou and coworkers was invoked to explain the affect of two amino acids changes that were discovered by genomic sequencing of cells with drug resistance acquired through single step exposure to lethal doses (IC_{99}) of either epothilone A or B [62]. Using the EC interaction model 1tub as a reference, they showed that each of the mutated residues was located near the paclitaxel binding site, but affected taxane activity less than epothilone. Possible conformations of epothilone were generated by high temperature molecular dynamics (MD) and fit to the taxane in a force field minimized version of 1tub described above. The alignment utilized a template forcing protocol similar to that done for the Ojima work, but the pharmacophore points selected for fitting were based upon distance analysis performed for the epothilone conformer pool. When distances from the rigid C–12, C–13, epoxide oxygen to

other features of the epothilone molecule were measured, it was found that the mean location of 3–OH, 7–OH, and 4-gem dimethyl was very close to distances measured between the oxetane oxygen of PTX and its 1–OH, 9-carbonyl, and 15-gem dimethyl. The two conformers that provided the best alignment of these four key points were selected as the most probable common overlap. These two were qualitatively evaluated in the context of available SAR, and presented as possible solutions for epothilone binding.

The pharmacophore model devised by He and coworkers had its basis in the activity of a very interesting paclitaxel analog, 2-*m*-azido baccatin III [76]. This active analog lacks the C–13 sidechain, but has measurable potency in microtubule polymerization, and cytotoxicity assays – though less than PTX. This novel compound with only one aromatic sidechain projecting from the C–2 position of its baccatin core more closely resembles epothilone with its single side chain projecting from its macrocyclic core. By choosing the X-ray conformation of epothilone B and manually aligning it with a model of 2-*m*-azido baccatin III fit to the 1tub tubulin complex, the authors rationalized the importance of the epothilone thiazole sidechain in a way consistent with observed SAR.

6.3 Fourier Difference Testing of Comparative Models

The crystallographic model of epothilone A binding does not conform to any of the common pharmacophore alignments [3]. Rather than overlapping specific groups common between the two drug classes, it presents them to slightly different regions of the receptor pocket. Even more surprising, instead of interacting within the deep hydrophobic pocket as thought to be important for taxane activity, the epothilone is suspended across the pocket by hydrogen bonding interactions. This discrepancy from the expected binding mode prompted us to test explicitly alternative models as possible solutions to the diffraction data. Fourier difference mapping, as described in methods, was employed to test many possible solutions including the five common pharmacophore models described above.

Figure 22 illustrates the results of those five compared to the crystallographic solution. The red density (at -3σ) is associated with atomic placements of the model that are inconsistent with the diffraction data. Green density ($+3\sigma$) represents signal from the diffraction data that is not met in the model. The crystallographic solution (f) is the only one satisfying the diffraction data as evidenced by the relative lack of difference density. The speck of green above (f) may represent water interacting with polar, solvent exposed, face of the epothilone that is not included in the model. The location of positive (green) regions associated with models a–e is consistent with atomic placements fulfilled by f that are lacking in the other models or possible locations of water. The negative (red) regions in a–e show that each of the “common” alignments of epothilone and taxane functionality differ greatly from the signal obtained experimentally.

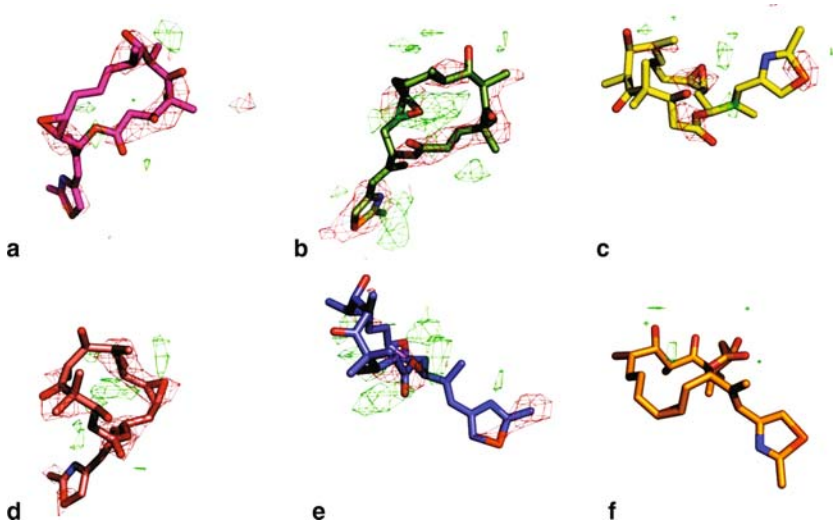

Fig. 22 Fourier difference (F_{obs}–F_{calc}) analysis of six epothilone models. Projections of structure factor amplitudes using model derived phases at +3σ (*green*) and −3σ (*red*). A perfect match of model to diffraction data would produce no difference density. *Red density* is associated with a placement of model atoms not supported by the experimental reflections. *Green density* represents locations of diffracting atoms in the experimental complex that are not in the model. The five common pharmacophore (**a**–**e**) and one crystallographic (**f**) models of epothilone binding are tested against data collected from an epothilone/tubulin complex using identical protocols. F_{obs}–F_{calc} residual density is shown within 3 Å of the ligand model used in the test. Comparison of models presented by: **a** Ojima; **b** Wang; **c** Giannakakou/Gussio1; **d** Giannakakou/Gussio2; **e** He, all show significant negative difference in *red*, indicating an incorrect solution, and positive difference, *green*, suggesting a pattern for repositioning of the fit. The model of **f** Nettles displays no negative difference in these tests, and *green* is likely due to water present in the crystal that is not included in the final model. Graphics were generated using MacPymol [77], and all molecular alignments in this figure were shot from the same camera angle

6.4 Bridging Biological Space – An "Effector Vector"

Although the tubulin bound positions of taxanes and epothilones determined by EC appear to have little overlap in chemical space, we know that they do have similar function in biological space. Figure 23 illustrates the overlap of the two models within the binding site. Given the additional information derived from our previous discussion of SAR, we can see a relationship emerge. Clearly His227 is an important anchor residue for each class. For the taxanes, the aromatic imidizole packs between hydrophobic groups of the ligand. For the epothilone B shown, His227 is likewise bracketed by hydrophobic residues. Given its location directly

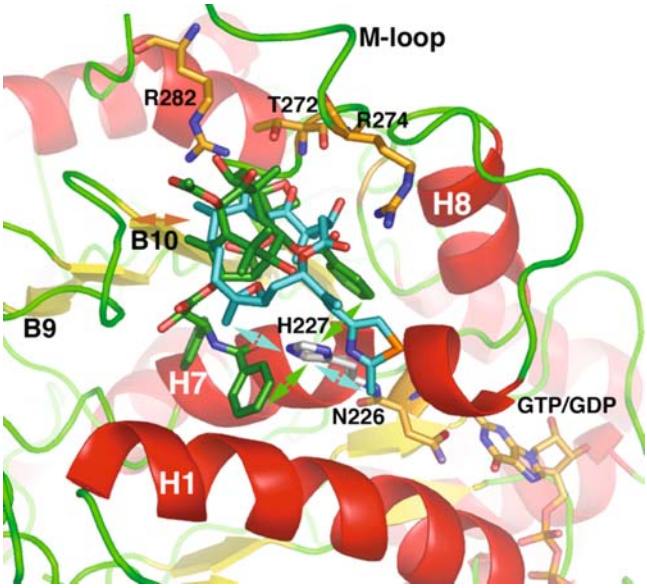

Fig. 23 Bridging biological space. The overlap of epothilone B (*cyan carbons*) and PTX (*green carbons*) models derived from EC reveal shared anchors between the exchangeable nucleotide site through H227 and the truncated B9–B10 loop of the beta tubulin site. Perhaps rigidifying this vector across the site is of greater importance to the MT stabilizing effect than picking up interactions within the deep hydrophobic pocket

opposite the exchangeable GTP/GDP site, stabilization of Helix 7 through this residue is likely important for each drugs effect on microtubules. However, the effect of these drugs binding is not just with the catalytic domain. It can be seen that the important C–8 methyl of epothilones and C–12 methyl of the taxanes overlap in the same region of the B9–B10 loop. The missing eight residues of B9–B10 in beta tubulin relative to alpha are thought to be key factors in microtubule's dynamic instability [78–80]. The M-loop forms the third critical domain which contacts the stabilizing ligands. So the common pharmacophore responsible for microtubule stabilization may not simply be due to binding. Indeed, the epothilone binding mode, which spans rather than fills the pocket, suggests that a directional vector of stabilization is more important for activity than picking up additional affinity. Likewise, the highly active constrained taxane analogs stabilize the otherwise mobile C–13 side chain to parallel the same "effector vector" that we propose for the epothilones. A very different proposal for epothilone binding has been suggested based upon NMR and modeling [58]. It will be interesting to test this new model within the diffraction data and evaluate SAR of compounds designed with these principles in mind.

7 Laulimalide: A New Class of Stabilizers

With the success of EC based modeling as a method to explore atomic interactions of PTX and epoA, we began looking at other classes of compounds such as discodermolide (DIS), eleutherobin (ELE), and laulimalide (LAUL). Although soaking solutions of DIS, and ELE into Zn-sheets of tubulin produced stable crystals that diffract as well or better than epoA (Fig. 1), LAUL was an anomaly.

Laulimalide (Scheme 1), was first isolated from sponges gathered in Okinawa and its absolute configuration was established by X-ray crystallography [81]. LAUL is highly flexible, incorporating a minimum of 15 rotatable bonds. LAUL was found to be a nanomolar inhibitor of cellular proliferation and a potent microtubule stabilizer [82]. Given the topological similarity of epoA and LAUL and a body of structural and biochemical data indicating that epoA, DIS, ELE, and other potent microtubule stabilizers [83] exert their action from the PTX site, we initially assumed that laulimalide binds to the taxoid site as well. Further experimental work revealed otherwise.

7.1 Disturbing Results

Figure 24 illustrates the effect of adding LAUL to 2D tubulin sheets. Rather than stabilizing the 2D tubulin sheets for diffraction, the addition of LAUL causes breakdown of the sheets and formation of microtubules. These surprising findings are made more intriguing by work showing that LAUL does not compete with paclitaxel at the taxoid site on β-tubulin, but binds to a separate site that can be occupied simultaneously with paclitaxel's residency in the taxoid pocket [84]. Perhaps a second binding site for LAUL, near the 2D crystal interface, could explain the phenomenon.

7.2 Speculation

Although disturbance of the crystals impedes direct examination, the potent breakdown of the 2D sheets gives us clues regarding the location of laulimalide's high affinity binding site. Modeling work has shown that LAUL presents a much more uniform hydrophobic surface than either epoA or PTX [43]. Accordingly, we used surface mapping of the αβ tubulin dimer to search for sites that might accommodate the drug's chemical potential and shape. A hydrophobic site is located between helices 9 and 10 on the apical surface of microtubules that seems most consistent with the data (Fig. 25). The site is thought to accommodate binding of the small hydrophobic LAUL through induced movement of H9,

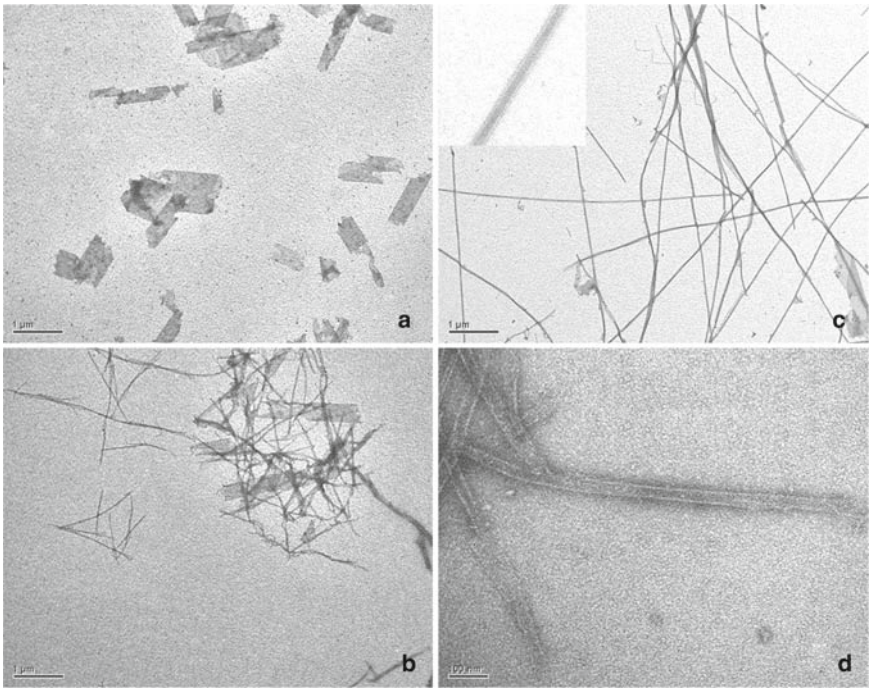

Fig. 24 Laulimalide stabilizes microtubules, but destabilizes zinc sheets. This multipart figure illustrates the effect of addition of laulimalide upon the polymerization of tubulin. Tubulin polymers, as sheets or microtubules, are inherently unstable and disassemble rapidly at low temperatures. Addition of paclitaxel (or epothilone, not shown) protect sheets from disassembly. **a** Control zinc sheets stabilized with PTX after 20 minutes in a bath of ice and water. **b** The effect of laulimalide under the same ice bath conditions as **a**. After 20 minutes, sheets exposed to laulimalide have significantly disassembled and reformed into microtubules. **c** Microtubules formed at room temperature from addition of laulimalide to zinc-stabilized sheets and incubated overnight. Almost all sheets have converted to microtubules (enlarged microtubules shown inset). By comparison, paclitaxel and epothilone-stabilized sheets remain intact under the same conditions. **d** Magnified microtubules seen in **b**. Figure provided by Huilin Li

which in turn positions the M-loop for productive lateral interactions in MT. The site also provides interaction with the B9–B10 loop. Importantly, that same movement causes a clash at the packing interface of the Zn sheets. Unfortunately, this does not offer specific binding mode. It does, though, suggest a specific tubulin region that may explain the activity of this class. Further investigation through methods such as designed or acquired mutational analysis will be needed for testing or validation.

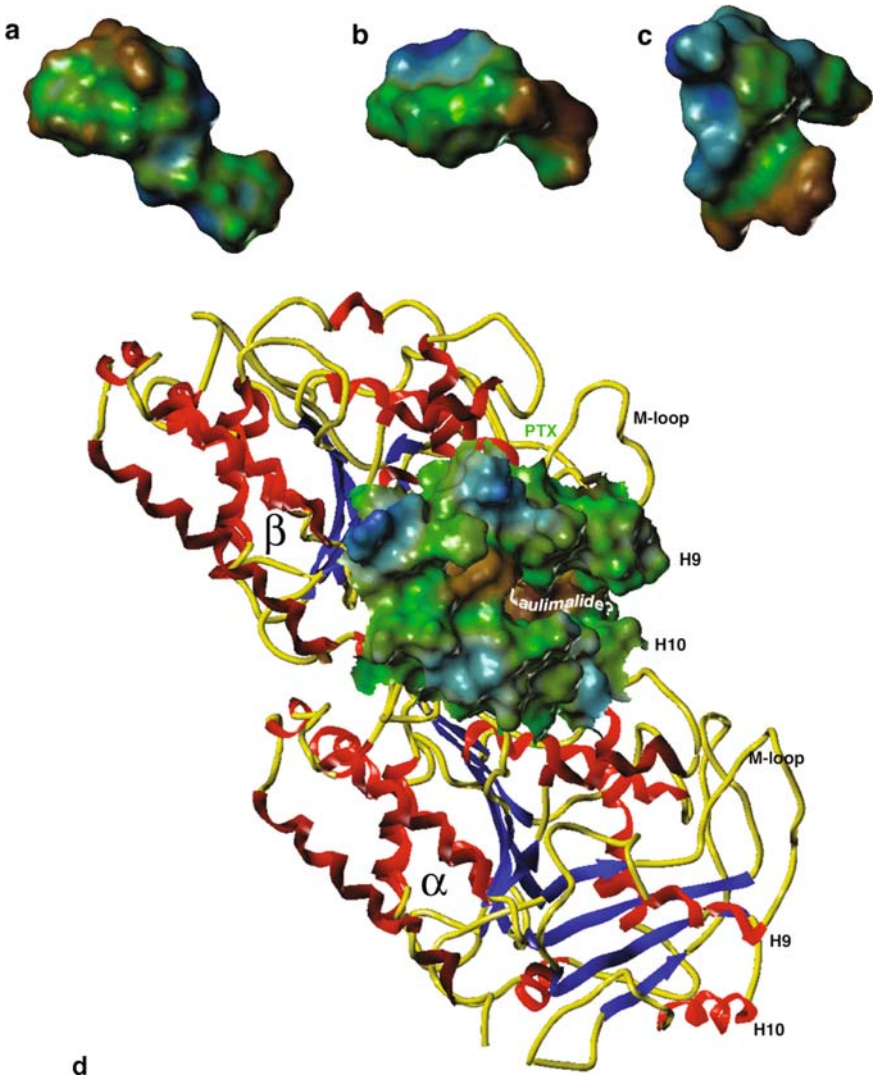

Fig. 25 Comparison of the predicted hydrophobicity of: **a** laulimalide; **b** epothilone B; **c** paclitaxel. Structures **a** and **b** correspond to a common solution conformation for the two macrolides. Solvent accessible surfaces are colored according to the degree of hydrophobicity: *brown* hydrophobic, *green* neutral, *blue* hydrophilic. **d** Laulimalide binding site on β-tubulin– after β–H9 movement described in text. The view is from the outside of the microtubule. The paclitaxel (PTX) site is labeled too, but it is accessed from the lumen

8 The Big Picture

Electron crystallography has proven to be a valuable tool for analysis of tubulin structure and drug interactions. Likewise, tubulin and its ability to form stable 2D crystals have driven development of EC methods that are now being used to study

other systems. However, any experimental technique in isolation is limited. Different experimental methods produce different readouts on related systems. Although adding to the complexity of the analysis, a combination of these different readouts is more likely to provide greater "truth" than one alone. While diffraction methods provide fuzzy maps of molecular interactions, NMR provides clues regarding environments of specific atoms. Pharmacology and biochemistry can teach us about larger system changes over greater time and probe the specific role of drugs. By comparing data collected under varied experimental conditions with multiple classes of drugs, we can build models of the different polymeric states and infer ideas about the dynamic intermediates. A graphical story that has emerged from our analysis of compounds that affect tubulin dynamics is summarized in Fig. 26. Molecules that bind to the PTX site represented by the green molecule span between β-tubulin domains to connect M-loop, B9–B10 loop, and Helix 7 via a high affinity site formed at the lumen of microtubules or at the interface of zinc stabilized 2D sheets. LAUL shown in purple is thought to bind at site on β-tubulin between helices H9 and H10. Microtubule stabilization through this site may occur due to a rigidifying effect on M-loop and B9–B10 loop, but destabilizes Zn sheets.

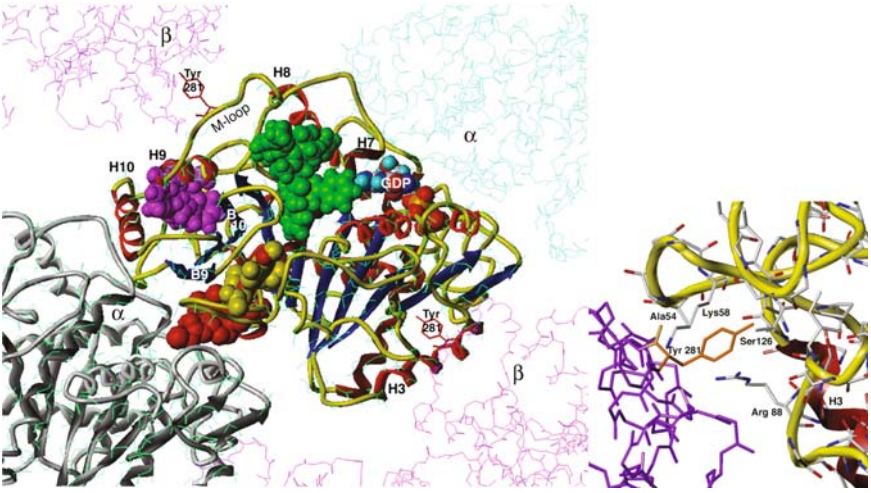

Fig. 26 Multiple drug sites that affect tubulin dynamics. This view of beta tubulin (*colored* by secondary structure) from a perspective within the lumen of a microtubule illustrates the relative location of various drug binding sites which affect its stability. Binding of MT stabilizers PTX (*green*) and LAUL (*purple*) are shown as well as the GDP/GTP exchangeable site (*colored* by atom type) and overlapped with models of colchicine binding from X-ray (*red*) and modeling of covalent labeling experiments (*yellow*). *Note*: The sites are not suggested to be occupied at the same time with this polymer conformation. Destabilizer binding is known to be associated with different polymer states. *Right/inset*: a detail is shown of M-loop residue Tyr 281 within lateral interaction site of adjacent protofilament as seen in the EC model of a microtubule

This is contrasted by placement of colchicine (COL) (yellow, red) in sites that can explain different parts of its destabilizing effects on both microtubules and Zn sheets. The yellow model is a theoretical representation of what may be the first site involved in COL's two-phase binding based upon covalent labeling of specific cysteine residues [43, 85, 86]. The red model, discovered through X-ray crystallography of stathmin stabilized polymers of tubulin [11], is discussed by Knossow et al. in Chapt. 3 and is associated with bent, depolymerizing structure. It seems that COL's binding involves B9–B10 loop movement and can release an internal trigger that shifts H7 upward, simultaneously destabilizing productive lateral interaction with the M-loop. An inset detail of M-loop residue Tyr281 interacting with its lateral site from our microtubule model is also provided. It is important to emphasize that destabilization of microtubules through colchine, stathmin binding, Ca or GDP substitution at the exchangeable site, and other methods, puts the Tyr 281/M-loop, H7 in a conformation/trajectory that is different than suggested here and is expected to have greater freedom of motion.

Electron crystallography, like all experimental methods, has its strengths and its limitations. Accordingly, this work has attempted to present both sides from a technical and practical perspective. Given the resolution limits of the experimental technique, we have used difference modeling to test possible solutions against our experimental results and correlate those findings with data obtained via other methods. It is our belief that thoughtful examination of models derived from diverse methods can direct us towards a fuller understanding of the atomic underpinnings of tubulin dynamics and the small molecules that affect them.

Acknowledgments JN and KD would particularly like to thank Drs. Eva Nogales and Huilin Li whose work is the platform for our understanding of tubulin and microtubule structure and the works of James Snyder, Joe Krahn, and Ben Cornet were pivotal in developing our EC models of small molecules interacting with tubulin. We also thank Dr. Rick Gussio for providing epothilone coordinates used for pharmacophore testing. JN thanks Dr. Harish Joshi for generously sharing his insight regarding tubulin dynamics and Drs. Dennis Liotta and Raymond Schinazi for scientific support.

References

1. Ledbetter MC, Porter KR (1963) J Cell Biol 19:239
2. Snyder JP, Nettles JH, Cornett B, Downing KH, Nogales E (2001) Proc Natl Acad Sci U S A 98:5312
3. Nettles JH, Li H, Cornett B, Krahn JM, Snyder JP, Downing KH (2004) Science 305:866
4. Larsson H, Wallin M, Edstrom A (1976) Exp Cell Res 100:104
5. Downing KH, Jontes J (1992) J Struct Biol 109:152
6. Nogales E, Wolf SG, Downing KH (1998) Nature 391:199
7. Wolf SG, Mosser G, Downing KH (1993) J Struct Biol 111:190
8. Lowe J, Li H, Downing KH, Nogales E (2001) J Mol Biol 313:1045
9. Nogales E, Whittaker M, Milligan RA, Downing KH (1999) Cell 96:79
10. Li H, DeRosier DJ, Nicholson WV, Nogales E, Downing KH (2002) Structure 10:1317
11. Ravelli RB, Gigant B, Curmi PA, Jourdain I, Lachkar S, Sobel A, Knossow M (2004) Nature 428:198
12. Nogales E, Wang HW, Niederstrasser H (2003) Curr Opin Struct Biol 13:256

13. Gueritte-Voegelein F, Guenard D, Mangatal L, Potier P, Guilhem J, Cesario M, Pascard C (1990) Acta Cryst C46:781
14. Boge TC, Himes RH, Vander Velde DG, Georg GI (1994) J Med Chem 37:3337
15. Dubois J, Guénard D, Guéritte-Voegelein F, Guedira N, Potier P, Gillet B, Beloeil J (1993) Tetrahedron 49:6533
16. Gao Q, Wei JM, Chen SH (1995) Pharm Res 12:337
17. Ojima I, Duclos O, Zucco M, Bissery MC, Combeau C, Vrignaud P, Riou JF, Lavelle F (1994) J Med Chem 37:2602
18. Vander Velde DG, Georg GI, Grunewald GL, Gunn CW, Mitscher LA (1993) J Am Chem Soc 115:11650
19. Brass A, Pendleton BJ, Chen Y, Robson B (1993) Biopolymers 33:1307
20. Harvey SC, Gabb HA (1993) Biopolymers 33:1167
21. Lowe J, Li H, Downing KH, Nogales E (2001) J Mol Biol 313:1045
22. Gupta ML Jr, Bode CJ, Georg GI, Himes RH (2003) Proc Natl Acad Sci U S A 100:6394
23. Hari M, Loganzo F, Annable T, Tan X, Musto S, Morilla DB, Nettles JH, Snyder JP, Greenberger LM (2006) Mol Cancer Ther 5:270
24. Ganesh T, Guza RC, Bane S, Ravindra R, Shanker N, Lakdawala AS, Snyder JP, Kingston DG (2004) Proc Natl Acad Sci U S A 101:10006
25. Ganesh T, Yang C, Norris A, Glass T, Bane S, Ravindra R, Banerjee A, Metaferia B, Thomas SL, Giannakakou P, Alcaraz AA, Lakdawala AS, Snyder JP, Kingston DGI (2007) J Med Chem 50:713
26. Li Y, Poliks B, Cegelski L, Poliks M, Gryczynski Z, Piszczek G, Jagtap PG, Studelska DR, Kingston DG, Schaefer J, Bane S (2000) Biochemistry 39:281
27. Alcaraz AA, Mehta AK, Johnson SA, Snyder JP (2006) J Med Chem 49:2478
28. Buey RM, Calvo E, Barasoain I, Pineda O, Edler MC, Matesanz R, Cerezo G, Vanderwal CD, Day BW, Sorensen EJ, Lopez JA, Andreu JM, Hamel E, Diaz JF (2007) Nat Chem Biol 3:117
29. Nogales E, Wolf SG, Downing KH (1997) J Struct Biol 118:119
30. Nogales E, Wolf SG, Khan IA, Ludueña RF, Downing KH (1995) Nature 375:424
31. Nogales E, Wolf SG, Zhang SX, Downing KH (1995) J Struct Biol 115:199
32. Perrakis A, Harkiolaki M, Wilson KS, Lamzin VS (2001) Acta Crystallogr 57:1445
33. Downing KH, Li H (2001) Microsc Microanal 7:407
34. Cornett B (2002) Solution conformational studies of microtubule-stabilizing agents. Dissertation, Emory University
35. Oldfield TJ (2001) Acta Crystallogr D Biol Crystallogr 57:696
36 Accelrys (2001). http://www.accelrys.com/
37. Carlomagno T, Blommers MJ, Meiler J, Jahnke W, Schupp T, Petersen F, Schinzer D, Altmann KH, Griesinger C (2003) Angew Chem Int Ed Engl 42:2511
38. Hofle G, Bedorf N, Steinmetz H, Schomburg D, Gerth K, Reichenbach H (1996) Angew Chem Int Ed Engl 35:1567
39. Collaborative Computational Project IV (1994) Acta Cryst D50:760
40. Wartmann M, Altmann KH (2002) Curr Med Chem Anti-Cancer Agents 2:123
41. Altmann KH, Pfeiffer B, Arseniyadis S, Pratt BA, Nicolaou KC (2007) ChemMedChem 2:396
42. Nicolaou KC, Roschangar F, Vourloumis D (1998) Angew Chem Int Ed Engl 37:2014
43 Nettles JH (2005) The molecular pharmacology of compounds that affect tubulin dynamics. Dissertation, Emory University
44 ChemicalComputingGroup (2007) Chemical Computing Group, Montreal, Quebec
45 Tripos (2004). Tripos, 1699 South Hanley Rd., St. Louis, MO 63144, USA
46. Lakdawala A, Wang M, Nevins N, Liotta DC, Rusinska-Roszak D, Lozynski M, Snyder JP (2001) BMC Chem Biol 1:2
47. Nicolaou KC, Scarpelli R, Bollbuck B, Werschkun B, Pereira MMA, Wartmann M, Altmann KH, Zaharevitz D, Gussio R, Giannakakou P (2000) Chem Biol 7:593
48. Sinha SC, Sun J, Wartmann M, Lerner RA (2001) ChemBioChem 2:656

49. Nicolaou KC, Namoto K, Li J, Ritzen A, Ulven T, Shoji M, Zaharevitz D, Gussio R, Sackett DL, Ward RD, Hensler A, Fojo T, Giannakakou P (2001) ChemBioChem 2:69
50. Nicolaou KC, Namoto K, Ritzen A, Ulven T, Shoji M, Li J, D'Amico G, Liotta D, French CT, Wartmann M, Altmann K-H, Giannakakou P (2001) J Am Chem Soc 123:9313
51. Nicolaou KC, Ritzen A, Namoto K, Buey RM, Diaz JF, Andreu JM, Wartmann M, Altmann K-H, O'Brate A, Giannakakou P (2002) Tetrahedron 58:6413
52. Regueiro-Ren A, Borzilleri RM, Zheng X, Kim S-H, Johnson JA, Fairchild CR, Lee FYF, Long BH, Vite GD (2001) Org Lett 3:2693
53. Buey RM, Diaz JF, Andreu JM, O'Brate A, Giannakakou P, Nicolaou KC, Sasmal PK, Ritzen A, Namoto K (2004) Chem Biol 11:225
54. Balog A, Bertinato P, Su D-S, Meng D, Sorensen E, Danishefsky SJ, Zheng Y-H, Chou T-C, He L, Horwitz SB (1997) Tetrahedron Lett 38:4529
55. Rivkin A, Njardarson JT, Biswas K, Chou TC, Danishefsky SJ (2002) J Org Chem 67:7737
56. Rivkin A, Yoshimura F, Gabarda AE, Cho YS, Chou TC, Dong H, Danishefsky SJ (2004) *J* Am Chem Soc 126:10913
57. Altmann KH, Gertsch J (2007) Nat Prod Rep 24:327
58. Reese M, Sanchez-Pedregal VM, Kubicek K, Meiler J, Blommers MJJ, Griesinger C, Carlomagno T (2007) Angew Chem Int Ed Engl 46:1864
59. End N, Furet P, van Campenhout N, Wartmann M, Altmann KH (2004) Chem Biodivers 1:1771
60. Rivkin A, Chou TC, Danishefsky SJ (2005) Angew Chem Int Ed Engl 44:2838
61. Zhan W, Jiang Y, Brodie PJ, Kingston DG, Liotta DC, Snyder JP (2008) Org Lett 10:1565
62. Giannakakou P, Gussio R, Nogales E, Downing KH, Zaharevitz D, Bollbuck B, Poy G, Sackett D, Nicolaou KC, Fojo T (2000) Proc Natl Acad Sci U S A 97:2904
63. Cachoux F, Isarno T, Wartmann M, Altmann K-H (2005) Angew Chem Int Ed Engl 44:7469
64. Regueiro-Ren A, Leavitt K, Kim SH, Hofle G, Kiffe M, Gougoutas JZ, DiMarco JD, Lee FY, Fairchild CR, Long BH, Vite GD (2002) Org Lett 4:3815
65. Borzilleri RM, Zheng X, Schmidt RJ, Johnson JA, Kim SH, DiMarco JD, Fairchild CR, Gougoutas JZ, Lee FYF, Long BH, Vite GD (2000) J Am Chem Soc 122:8890
66. Choi K-H, Lee H-J, Karpfen A, Yoon C-J, Park J, Choi Y-S (2001) Chem Phys Lett 345:338
67. Su DS, Balog A, Meng DF, Bertinato P, Danishefsky SJ, Zheng YH, Chou TC, He LF, Horwitz SB (1997) Angew Chem Int Ed 36:2093
68. Altmann K-H, Blommers MJJ, Caravatti G, Flörsheimer A, Nicolaou KC, O'Reilly T, Schmidt A, Schinzer D, Wartmann M (2001) In: Ojima I, Vite GD, Altmann K-H (eds) Anticancer agents – frontiers in cancer chemotherapy. ACS Symposium Series 796. American Chemical Society, Washington DC, p 112
69. Bold G, Wojeik S, Caravatti G, Lindauer R, Stierlin C, Gertsch J, Wartmann M, Altmann KH (2006) ChemMedChem 1:37
70. Winkler JD, Axelsen PH (1996) Bioorg Med Chem Lett 6:2963
71. Ojima I, Chakravarty S, Inoue T, Lin S, He L, Horwitz SB, Kuduk SD, Danishefsky SJ (1999) Proc Natl Acad Sci U S A 96:4256
72. Mastropaolo D, Camerman A, Luo Y, Brayer GD, Camerman N (1995) Proc Natl Acad Sci U S A 92:6920
73. Wang M, Xia X, Kim Y, Hwang D, Jansen JM, Botta M, Liotta DC, Snyder JP (1999) Org Lett 1:43
74. Williams HJ, Scott AI, Dieden RA (1993) Tetrahedron 49:6545
75. Kearsley SK, Smith GM (1990) Tetrahedron Comput Methodol 3:615
76. He L, Jagtap PG, Kingston DGI, Shen H-J, Orr GA, Horwitz SB (2000) Biochemistry 39:3972
77 Pymol (2008) DeLano Scientific LLC, Palo Alto
78. Downing KH, Nogales E (1998) Eur Biophys J 27:431
79. Downing KH, Nogales E (1998) Curr Opin Struct Biol 8:785
80. Downing KH, Nogales E (1999) Cell Struct Funct 24:269
81. Jefford CW, Bernardinelli G, Tanaka J, Higa T (1996) Tetrahedron Lett 37:159

82. Mooberry SL, Tien G, Hernandez AH, Plubrukarn A, Davidson BS (1999) Cancer Res 59:653
83. Jimenez-Barbero J, Amat-Guerri F, Snyder JP (2002) Curr Med Chem Anticancer Agents 2:91
84. Pryor DE, O'Brate A, Bilcer G, Diaz JF, Wang Y, Kabaki M, Jung MK, Andreu JM, Ghosh AK, Giannakakou P, Hamel E (2002) Biochemistry 41:9109
85. Bai R, Covell DG, Pei X-F, Ewell JB, Nguyen NY, Brossi A, Hamel E (2000) J Biol Chem 275:40443
86. Bai R, Pei X-F, Boye O, Getahun Z, Grover S, Bekisz J, Nguyen NY, Brossi A, Hamel E (1996) J Biol Chem 271:12639

Top Curr Chem (2009) 286: 259–278
DOI: 10.1007/128_2008_11

Published online: 16 October 2008

Microtubule-Destabilizing Agents: Structural and Mechanistic Insights from the Interaction of Colchicine and Vinblastine with Tubulin

B. Gigant, A. Cormier, A. Dorléans, R.B.G. Ravelli, and M. Knossow

Abstract Microtubules (MTs) are dynamic structures of the eukaryotic cytoskeleton that, during cell division, form the mitotic spindle. Perturbing them leads to mitotic arrest and ultimately to cell death. Consistently, MTs and their building block, αβ tubulin, are one of the best characterized targets in anti-cancer chemotherapy. Drugs that interfere with MTs either stabilize or destabilize them. The latter class is the subject of this review. These ligands bind to the colchicine site or to the vinca domain, two distinct sites located at a distance from each other on tubulin. Nevertheless the effects of both classes of ligands share a common theme, they prevent the formation of MT specific contacts, therefore triggering their disassembly.

Keywords Cytoskeleton, Microtubule dynamics, Mitosis, Structure Vinca domain

B. Gigant (✉), A. Cormier, A. Dorléans, and M. Knossow (✉)
Laboratoire d'Enzymologie et Biochimie Structurales (LEBS), CNRS, Bat. 34, 1 avenue de la Terrasse, 91198 Gif-sur-Yvette, France
e-mail: gigant@lebs.cnrs-gif.fr, knossow@lebs.cnrs-gif.fr

R.B.G. Ravelli
European Molecular Biology Laboratory (EMBL), Grenoble Outstation, 6 rue Jules Horowitz, BP 181, 38042, Grenoble, France

Present address: Leiden University Medical Center (LUMC) 2333 ZC Einthovenweg 20, Leiden, The Netherlands

A. Dorléans
Present Address: Laboratoire d'Enzymologie et Biochimie Structurales (LEBS), CNRS, Bat. 34, 1 avenue de la Terrasse, 91198 Gif-sur-Yvette, France
Institut de Biologie Physico-Chimique (IBPC), CNRS, 13, rue Pierre et Marie Curie - 75005 Paris, France

Contents

Abbreviations:

GAP	GTPase activating protein
GEF	guanosine-exchange factor
MT	microtubule
NOE	Nuclear Overhauser effect
SLD	stathmin-like domain
Tc	tubulin-colchicine complex
T_2R	complex of tubulin with the stathmin-like domain of the RB3 protein
$(Tc)_2R$	complex of tubulin with colchicine and with the stathmin-like domain of the RB3 protein
T_2SLD	tubulin-stathmin-like domain complex.

1 Introduction

Together with the actin network (microfilaments) and the intermediate filaments, MTs constitute the cytoskeleton of all eukaryotic cells. Among others, MTs are the "highways" along which kinesin and dynein molecular motors move to deliver their cargoes. As the cell starts division, they form the mitotic spindle, a structure required for the correct partitioning of chromosomes between the two daughter cells. To fulfil their wide range of functions, MTs alternate phases of growth and shrinkage in a process known as dynamic instability. In the cell, MT dynamics is highly regulated by endogenous proteins. MTs are also affected by small molecules having antimitotic properties: perturbing MT dynamics interferes with cell division and leads to cell death.

Colchicine is one of these small inhibitors that has long been used to block mitosis in metaphase (reviewed in [1]). The identification, in the 1960s, of the cellular target of colchicine, a protein called tubulin, also identified this protein as the MT building block ([2] and references therein). Tubulin is constituted of two 50-kDa monomers: an α-subunit and a related β-subunit, with ca. 40% sequence identity between them. During polymerization, αβ tubulin heterodimers arrange head-to-tail to form straight protofilaments, which are therefore polar structures. Protofilaments interact laterally to constitute the wall of the MT: MTs are hollow cylinders made of ~12–15 parallel protofilaments, with a marked preference for 13 protofilaments in vivo. The polar nature of protofilaments dictates in turn polarity to MTs, with a fast growing (+) end exposing β subunits and a slower growing (−) end exposing α subunits (Fig. 1).

In this review we will focus on small molecule compounds that destabilize MTs. In the first two parts, we will give an overview of (1) MT dynamics and its regulation, with an emphasis on our current knowledge of the structural variations of tubulin along the MT assembly/disassembly cycle, as well as of (2) drugs targeting tubulin. We will focus on the approaches that have been developed to map the tubulin–inhibitor interactions. In a third part, the molecular mechanism of the MT-destabilizing agents will be discussed in light of the recent structural definition of the binding sites of some of them and in relation with biochemical data. We will show that despite binding to two distant sites, these compounds inhibit tubulin polymerization by preventing MT-specific intermolecular tubulin–tubulin interactions from being established.

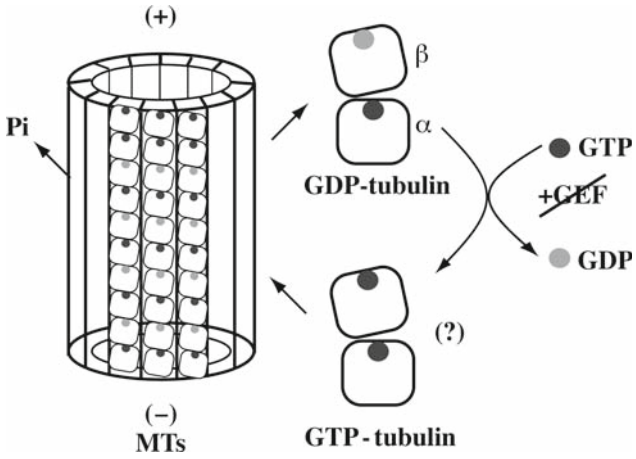

Fig. 1 The MT assembly/disassembly cycle. GDP-tubulin, which is curved, should be loaded with GTP to be competent for MT polymerization. The nucleotide exchange doesn't require a GEF to occur. GTP-tubulin, whose unassembled conformation is still unknown, hydrolyses its β GTP during polymerization. MTs are therefore mainly constituted of GDP-tubulin, which is released upon disassembly

2 The Microtubule Cycle and its Regulation

2.1 The Assembly-Disassembly of Tubulin into MT is Accompanied by a Nucleotide Cycle

Both tubulin monomers bind a GTP molecule. The α-tubulin GTP is non-exchangeable and non-hydrolysable whereas the β-tubulin-bound nucleotide is hydrolyzed into GDP during MT assembly [3]. The core of the microtubule is therefore mainly composed of GDP-tubulin (i.e. with GDP bound to the β subunit), which by itself does not polymerize into MT. This paradox is resolved as growing MTs are protected from disassembly by a GTP-tubulin stabilizing cap at their ends [4, 5]. Following the loss of the cap, MTs disassemble releasing GDP-tubulin. After exchange of the β subunit nucleotide into GTP, tubulin will be available again for another MT assembly/disassembly cycle.

Tubulin shares some features with classical G proteins. It alternates between a GDP inactive form and a GTP active state, as only GTP-tubulin is competent for MT polymerization under physiological conditions. Moreover, GTP hydrolysis is needed for the depolymerization step and so to complete the MT cycle: in the presence of non-hydrolysable analogs of GTP, MTs are stable and hardly depolymerize [6]. However, tubulin differs from these GTPases in several respects [7]. Indeed, the β subunit nucleotide of unassembled tubulin exchanges freely: tubulin doesn't need guanosine-exchange factors (GEFs) to load its GTP. In addition the nucleotide cycle is complete without the need of GTPase activating proteins (GAP) other than tubulin itself. Accordingly, the MT cycle can be reproduced in vitro with tubulin solely (Fig. 1).

2.2 Structural Variations of Tubulin along the MT Cycle

The structural cycle of tubulin coupled to MT assembly and disassembly has long been studied by electron microscopy and, more recently, by crystallography. At the tubulin level, the most striking difference highlighted by these studies is that tubulin changes from a straight to a curved conformation as it disassembles from MTs (Fig. 2). In the core of MTs, tubulin is straight: the α and β subunits are related by a translation along the protofilament axis [12]. By contrast, curved tubulin assemblies have been visualized at the ends of depolymerizing MTs [13]. Tubulin also forms curved oligomers, either spirals or closed rings, with variable curvatures [14]. In one case, in complexes of tubulin with stathmin-like domain (SLD) proteins, the tubulin curvature has been described at 3.5-Å resolution [15]. In this assembly of two tubulins and one SLD (T_2SLD) [16], the αβ heterodimers are arranged head-to-tail in a protofilament-like manner and make an angle of ca. 12° at the inter-tubulin interface. A similar angle is witnessed in-between the two subunits of each tubulin [17, 18]. The cumulated rotation over the four tubulin monomers in T_2SLD is therefore ~35°, compared to ~0° in the case of straight protofilaments (Fig. 2). Based on a comparison of the amplitude and the direction of the T_2SLD curvature to those of protofilaments

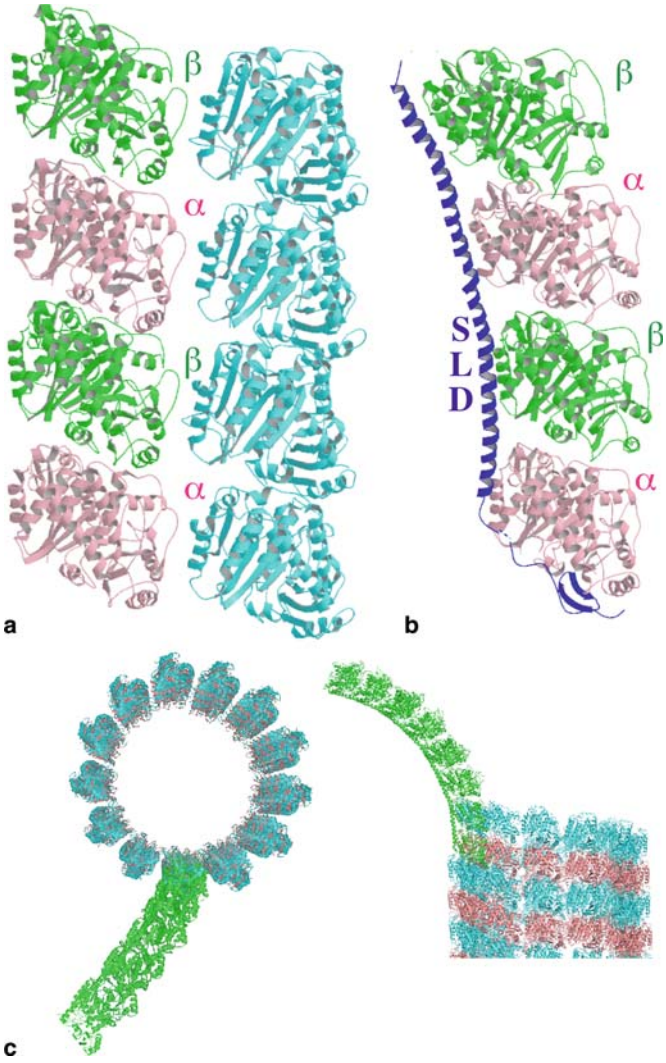

Fig. 2 The conformational switch of GDP-tubulin. **a** The straight conformation of tubulin when embedded in the MT (two tubulin segments of two adjacent protofilaments are drawn). **b** The curved structure of non-microtubular GDP-tubulin, as visualized here in a T_2SLD complex. The "first" α subunit (*at the bottom*) is in the same orientation as the one *at the bottom left* of **a. c** Model of a 13 protofilaments MT [8]: top view (*left*) and lateral view (*right*). One protofilament has been extended by a modeled tubulin assembly having the same curvature as in T_2SLD (*green*). Figures 2, 3, 6 and 7 were generated with MOLSCRIPT [9], RASTER 3D [10] and PYMOL [11]

at the ends of depolymerizing MTs [13], the T_2SLD complex is a good model of tubulin disassembling from MTs (Fig. 2c).

The tubulin shift from straight [19] to curved [15] is accompanied by conformational changes within the subunits (Fig. 3). Each monomer can be sub-divided into three domains [7]. The N-terminal domain accommodates the nucleotide.

An intermediate domain of ca 120 residues is connected to the first one by the central H7 helix. The last domain consists of a two helix hairpin which is terminated by an acidic and flexible C-terminus. Let us describe the conformational changes while taking the N-terminal domain as a reference. The C-terminal helices and the nucleotide-binding domain form a rigid block. On going from straight to curved, the H7 helix translates by 1.5–2.5 Å with respect to that rigid block. This translation is accompanied by an 8°–11° rotation of the intermediate domain, both movements being of larger amplitude in the β-subunit. In addition, there are some local changes in order to accommodate these movements. These concern the H6–H7 loop and the H6 helix which are adjacent to the H7 helix N-terminal and protrude at the longitudinal interface between tubulin subunits when they are in a curved conformation.

From a structural point of view, the current model of the MT cycle suggests that the relaxed conformation of GDP-tubulin is at the image of the one it has in the T_2SLD

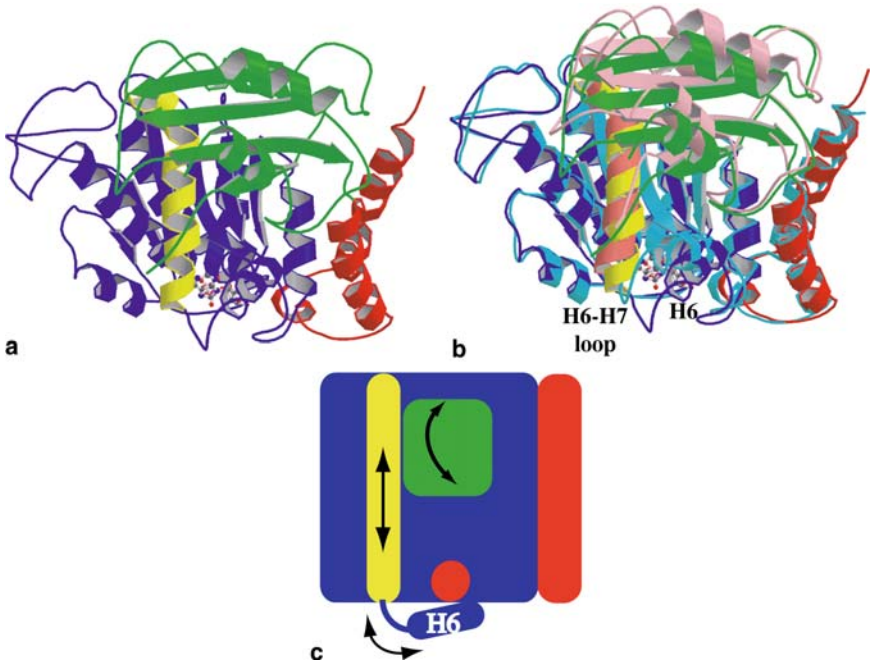

Fig. 3 Structural changes of tubulin subunits upon MT disassembly. **a** Structure of a β subunit of the T_2R complex (pdb id 1SA0 [15]). The monomer is sub-divided in an N-terminal domain (blue) with bound GDP (ball-and-stick drawing, *grey*), the central helix H7 (*yellow*), an intermediate domain (*green*), and the C-terminal helices (*red*). **b** Comparison of the β subunit conformation in the T_2R complex (same color code as in **a**) and in a straight protofilament (nucleotide binding domain and C-terminal helix hairpin in cyan, H7 helix in salmon, intermediate domain in pink, pdb id 1JFF [70]) after superposition of the secondary structural elements of their N-terminal domain. **c** Schematic representation recapitulating the movements between straight and curved tubulin monomers (domains are color-coded as in **a**; the nucleotide is depicted as a red sphere)

complex. When embedded in a MT, GDP-tubulin is straightened by MT-specific interactions that are lateral (between protofilaments) and longitudinal (between subunits within a protofilament). As soon as a tubulin heterodimer is not stabilized efficiently, it relaxes to its curved conformation. This leads in turn to the destabilization of its neighbors as lateral and longitudinal contacts are lost, providing a structural explanation for the fast, "autocatalytic" depolymerization of the MT. When released in solution GDP-tubulin cannot be incorporated in the core of the MT, as the conformation it adopts disables the establishment of MT longitudinal and lateral interactions.

In this model, the main unanswered question is why GTP-tubulin forms the only species competent for MT assembly. Since structural data at high resolution on unpolymerized GTP-tubulin are still missing, two hypotheses have been put forth. Tubulin might adopt a straight conformation as it loads GTP or, alternatively, the nucleotide GDP $\rightarrow$ GTP exchange step mostly lowers the energy barrier to go from a curved to a straight conformation and triggers only minor changes. According to this second hypothesis, the structural switch takes place later on, as MTs assemble [20, 21].

2.3 MT Dynamics is Tightly Regulated in the Cell

Whereas MT dynamics is an intrinsic property of tubulin, it is regulated in vivo by different classes of endogenous proteins. The classical microtubule-associated proteins (MAPs) bind to MTs and stabilize them. They also favor MT polymerization (reviewed in [22]). Another class is the + Tip proteins, so-called because they are targeted specifically to the (+) end of growing MTs [23], even though one of them has been very recently shown to mark both MT ends [24]. These proteins were originally assigned a role in the link of MTs (+) ends to specialized cellular structures. More recently, some of these proteins have been shown to promote MT polymerization [25, 26]. By contrast, some cellular factors induces MT disassembly either by sequestering free, unpolymerized, tubulin (e.g. stathmin [16]), or by direct interaction with the MT polymer (e.g. class 13 kinesins [27]). Tubulin and MTs undergo also posttranslational modifications. Although the roles of these modifications are still not well understood, they might regulate MT behavior either directly or by altering the interactions with tubulin of other MT regulating proteins (see [28] for a recent review).

3 Tubulin is the Target of Antimitotic Molecules

3.1 Tubulin has Three Main Binding Sites for Exogenous MT Inhibitors

We have seen in the previous section that MT dynamics is tightly regulated in cells, as one might have anticipated considering the important functions the MT network fulfils. MTs are also the target of exogenous small molecules, which "mimic" the

function of endogenous regulatory proteins: these compounds either stabilize or destabilize MTs. Most of them bind to one of the three characterized tubulin sites for exogenous ligands named after three extensively studied plant products. Paclitaxel (Taxol®) extracted from the common yew (*Taxus baccata*) was the first small inhibitor identified as a MT stabilizing agent [29]. It is being used in anti-cancer therapy since 1993. Its binding site and molecular mechanism were defined based on electron microscopy data on MTs [12] and on a related assembly in which straight protofilaments arrange in an anti-parallel way to form a sheet [19]. Taxol and molecules that bind to the same site enhance and reinforce lateral contacts between adjacent protofilaments, leading to stabilized MTs that are less prone to disassembly. Interestingly, taxol is also able to trigger the assembly into MT of the otherwise inefficient GDP-tubulin [30].

The two other locations are targeted by compounds that destabilize MTs. Colchicine, mentioned above, is the founding member of a large group of colchicine-binding site ligands. It is extracted from meadow saffron (*Colchicum autumnale*) which was identified as a medicinal plant as long as 2,500 years ago, with reported therapeutic usefulness for at least two centuries in particular in the treatment of acute gout [1]. The third tubulin-binding site for exogenous ligands is known as the tubulin vinca domain and is the target of vinblastine, first isolated from Madagascar periwinkles (*Catharanthus roseus*, also called *Vinca rosea*). The extracts of this plant, also long used in traditional medicine, were lent antidiabetic virtues before their anti-cancer properties were recognized [31]. Vinblastine and the related compound vincristine have effectively being used as anti-cancer drugs targeting tubulin since the early 1960s.

3.2 Most MT-Destabilizing Agents Bind to the Colchicine Site or to the Vinca Domain of Tubulin

Amongst the growing number of molecules that are referred as MT-destabilizing agents, most interfere either with colchicine or with vinblastine for tubulin binding (for a counter example see [32]). How the corresponding binding sites accommodate numerous and different molecules remains to be elucidated. For example, the formulae of a number of colchicine site ligands are presented in Fig. 4: whereas the chemical structure of some of them is obviously related to that of colchicine, others look quite different. Before getting into the definition of the binding sites of these two classes of drugs, we will describe some of the changes of tubulin biochemical properties when these drugs bind to it.

In addition to competing with colchicine for tubulin binding, the compounds chemically related to colchicine induce a polymerization-independent GTPase activity of tubulin [33]. Albeit being several orders of magnitude lower than the rate of GTP hydrolysis during MT assembly [34, 35], this activity is significant. This property shared by few molecules unrelated to colchicine (e.g. by nocodazole [36]) has probably no other main function than

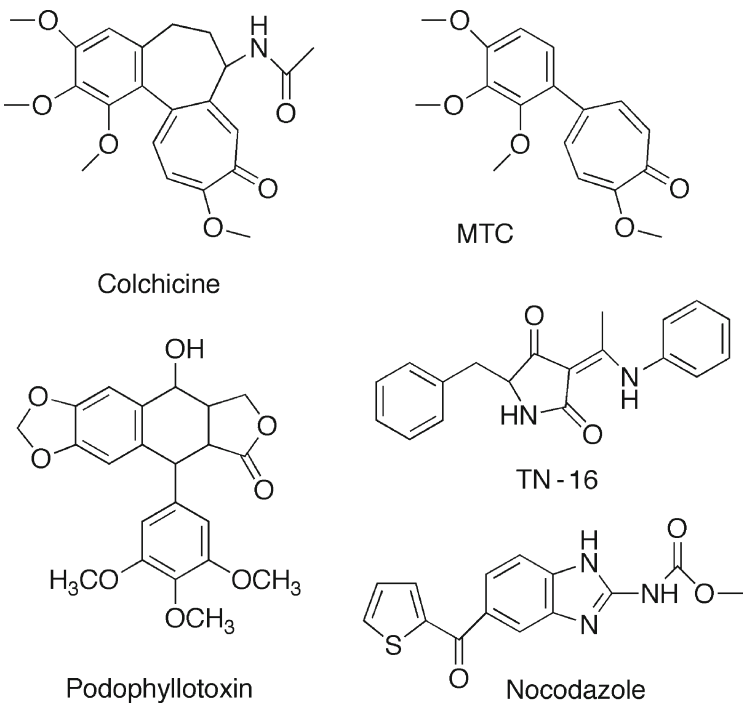

Fig. 4 Molecules that bind to the colchicine site of tubulin

to arouse the curiosity of biochemists. Nevertheless it is a simplified model allowing insight to be gained into the physiological GTP hydrolysis linked to MT assembly [37].

By contrast, colchicine stands apart from most of its competitors with respect to their tubulin binding kinetics. Its association is biphasic, a fast first step being followed by a slow isomerization of the tubulin-colchicine complex (Tc). Dissociation is also very slow, close to the lifetime of tubulin (reviewed in [38]). As series of simpler molecules are considered, e.g. going from colchicine to the bicyclic analog MTC (Fig. 4), this binding scheme is gradually lost to become a one step process [39]. Because of the slow binding of colchicine to tubulin, the preformed Tc complex is used for most of the biochemical experiments aiming at studying the effect of colchicine on the tubulin properties, instead of adding the ligand at the beginning of the experiment as most usually done.

As for colchicine [40, 41], numerous compounds have been reported to inhibit the binding of vinblastine to tubulin. But whereas the colchicine site ligands share the property of being relatively simple molecules easily amenable to chemical diversification, those targeting the tubulin vinca site are far more complex [41, 42].

They can be classified in two main classes: (poly)macrocyclic molecules (e.g. vinblastine) and (mostly linear) pseudopeptides (e.g. dolastatin 10). Some ligands (e.g. phomopsin) have characteristics of both classes (Fig. 5). Whether the tubulin binding sites of these widely diverse molecules overlap or not remains to be established. Whatever the case, taken together these sites define the tubulin vinca domain [43].

In addition to the inhibition of MT polymerization, more properties are shared by vinca domain compounds. As a hallmark, they inhibit the tubulin GTPase activity linked to MT assembly [42] as well as that induced by colchicine (see [33] and

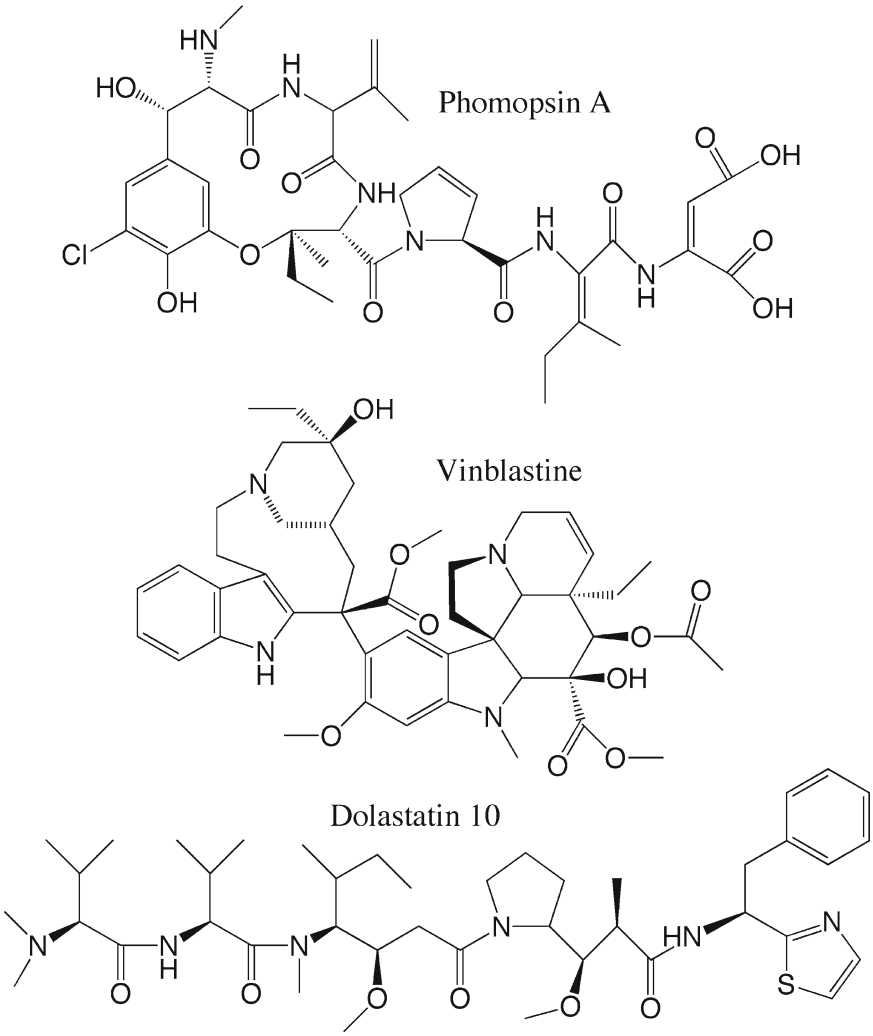

Fig. 5 Molecules targeting the tubulin vinca domain

unpublished observations). Most of them also induce non-microtubular polymers, either helices or rings, that may further interact together. In some conditions these big structures form paracrystals, both in vitro and in cells [44]. Finally the nucleotide exchange rate on the β subunit is slowed down by most of these compounds, suggesting that they bind close to the β subunit GTP site (reviewed in [42]).

3.3 Recent Advances Allow the Binding Sites of Tubulin Ligands to be Defined

Determining the molecular mechanism of a biological process would ideally require structural data at high resolution, as can be provided by X-ray crystallography. In the case of tubulin, crystals have been reported for more than three decades [45, 46] but useful crystals have only been obtained recently. Tubulin is a quite unstable protein, it aggregates readily in solution when it is not embedded in MTs and it has a high propensity to self-associate. For many of its ligands the situation is even worse as they induce further heterogeneous assemblies of tubulin; this is in particular the case for vinblastine [44] and colchicine [47]. All of these characteristics render tubulin a difficult case for high-resolution structural studies.

Other approaches have therefore been pursued to map the tubulin binding site of exogenous ligands. Some of them are based on genetic data, with the aim to identify tubulin mutants that behave differently in presence of the ligand of interest [48]. Mutations that confer resistance to that molecule may be part of its binding site. Indirect (e.g. see [49] and Sect. 4 below) or long-distance effects may also concur, rendering conclusions not straightforward. Another approach is based on the use of molecules that bind covalently with the protein target. After reaction, the modified residue(s), and so potentially part of the active site, are identified. Labeling experiments complemented by structural data at high resolution might serve as guides for modeling studies. These experiments have obvious limits. Indeed most molecules do not bear reactive groups. To be useful for labeling they need to be modified, with the assumption that the derivative behaves as the parent molecule. Other limits include poor labeling yield and unspecific binding. As crosslinking often involves a free cysteine on the protein side, the specificity of the reaction is a critical issue as tubulin comprises 20 cysteines with varying reactivities [50]. One can however make good use of this apparent limitation as exemplified in an elegant study by Kim and colleagues [51]. These authors quantified the cysteine reactivity changes in proteins following ligand binding, taking tubulin as an example. This method is theoretically applicable to all ligands and not only to those that make covalent bonds with the protein target. Its use led to evidence for structural changes induced at a distance, as mentioned for the genetic approach, in the case of tubulyzine: following its binding to tubulin, the reactivities of two β subunit cysteines located 25 Å apart are modified [52]. To summarize, although these experiments have been useful, indirect or long-distance effects are a severe limitation which applies in particular for tubulin studies.

In the last 10 years, 3 systems have been developed by structural biologists to visualize directly the binding mode of small molecules to tubulin. First, the structure of tubulin assembled in sheets of straight antiparallel protofilaments was determined by electron crystallography. This structure has permitted the identification of the taxol site [19]. This two-dimensional crystal system is of interest for the study of MT-stabilizing agents beyond taxol, as shown for epothilone A [53], provided they bind to that polymerized form of tubulin. Second, in our laboratory we have developed another crystallization protocol for tubulin, taking advantage of its interaction with the SLD of the RB3 protein [54]. In presence of RB3-SLD, tubulin forms tight and monodisperse complexes (called T_2R) whose size and stability are compatible with crystallization experiments. In that complex, tubulin has a curved conformation most probably alike that of unpolymerized GDP-tubulin [17]. Moreover, it was noticed that stathmin continues to interact with tubulin when this protein is in complex with colchicine [16]. And we have shown that vinblastine binds to T_2R [55]. Most importantly, upon binding to T_2R, neither colchicine nor vinblastine induces higher order assemblies as they do with tubulin. The T_2R complex is therefore a valuable tool for structural analysis of the interaction between tubulin and MT-depolymerizing small molecule inhibitors, as we will see in Sect. 4.

Third, as an alternative to crystallization, an NMR method has been developed by Carlomagno and colleagues ([56] and references therein). It is based on the use of interligand nuclear Overhauser effects (NOEs) between small molecules competing for the same site. This method has been called INPHARMA (for Interligand NOEs Pharmacophore Mapping). Provided that the site of one molecule is known, the binding mode of compounds displaying interligand NOEs with that molecule may be derived. This approach is complementary to crystallographic methods, as it indicates that Epothilone A binds to soluble tubulin [56] and to assembled tubulin in protofilament sheets [53] in significantly different ways. This case is not unique: using fluorescent molecules and classical biochemical techniques, such variations have also been proposed for taxol [57]. Overall, these results remind us that, in order to understand better the molecular mechanisms at work in ligand-driven tubulin assembly, structural data all along this pathway are needed.

4 MT-Destabilizing Agents: Insight into MT Inhibition from their Tubulin Binding Mode

4.1 Vinblastine Favors Curved Tubulin Assemblies

The X-ray crystallographic analysis of T_2R crystals soaked with vinblastine has revealed its binding site between the two tubulins of this short protofilament-like curved assembly (Fig. 6) [55]. It is equally contributed by the α-subunit of one tubulin and the β-subunit of the other. Vinblastine therefore belongs to the growing class of small molecules ligands known as interfacial inhibitors [58]: these

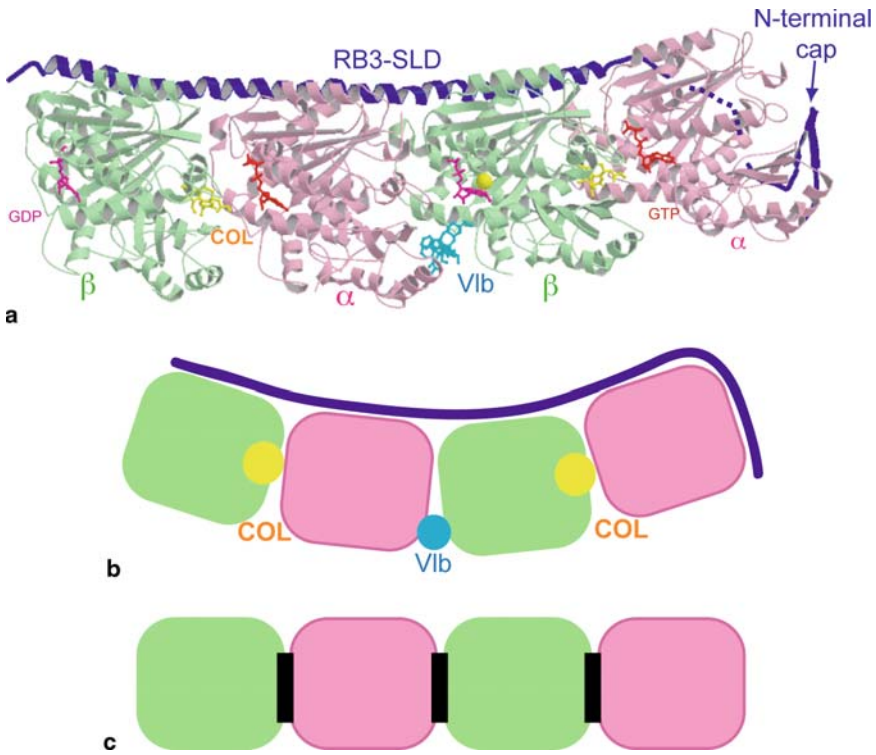

Fig. 6 The colchicine and vinblastine sites. **a** Ribbon representation of RB3-SLD and of the two tubulin αβ heterodimers. The nucleotides (GTP on α, GDP on β), colchicine (Col, *yellow*) and vinblastine (Vlb, *cyan*) are shown as ball-and-stick models. The *dashed line* shows the location of the RB3-SLD linker between the N-terminal cap and the C-terminal helix, which is the least ordered part of RB3-SLD. The sulfur atom of Cys 12 of the β subunit contacting vinblastine is highlighted as a *yellow sphere*. **b,c** Illustration of the interfacial interference of destabilizing molecules with MT assembly: schematic representation of the $(Tc)_2$R-vinblastine complex (**b**) and of a straight protofilament (**c**). Longitudinal MT-specific contacts (*black rectangles* in **c**) cannot be established between vinblastine- or colchicine-bound monomers

compounds target the interface between two (or more) macromolecular molecules and block their assembly in an inactive arrangement. In the case of vinblastine, tubulin can no longer assemble in MTs because of the direct interference of the ligand with the longitudinal interactions established in straight protofilaments and of the ensuing effect on microtubular lateral contacts [55]. Vinblastine inhibits the colchicine-induced GTPase activity of tubulin by a similar mechanism [37]. Albeit being lower, this activity shares features with that occurring during MT polymerization: in a transient protofilament-like assembly. catalytic α subunit residues of one tubulin acting as a GAP enhance hydrolysis of the β subunit-bound GTP of the neighboring heterodimer. The way it binds, vinblastine is a wedge that prevents establishment of the αβ interface needed both for polymerization into MTs and for positioning of the active site residues leading to GTP hydrolysis.

The vinblastine-$(Tc)_2R$ complex is amenable to crystallographic studies because, as opposed to tubulin, T_2R is not prone to polymerization by vinca domain ligands. Structural data shed light on this property. In the complex, the two tubulins stabilized by a vinblastine molecule are arranged in a curved assembly that most probably represents the building block of the tubulin spirals induced by this drug. In T_2R, the α subunit at one end of the complex is capped by the RB3-SLD N-terminal part (Fig. 6). This α subunit cannot interact with the β subunit of another tubulin heterodimer in the way the second α monomer of T_2R does, and therefore no oligomeric state larger than T_2R is formed. The model predicts that an SLD lacking its N terminal peptide would no longer protect tubulin from vinblastine aggregation. This is what we observed: upon incubation with vinblastine, very similar spirals are induced with tubulin alone or in complex with an SLD construct limited to its long C-terminal helix [55]. These results strongly suggest that the way the ligand interacts with tubulin in T_2R reflects the interaction of vinblastine with free tubulin.

Whereas the vinblastine interaction with T_2R has been mapped, the tubulin-binding site of other vinca domain molecules, including molecules as different from vinblastine as pseudopeptides, is still uncertain. To what extent do their sites overlap with the vinblastine one? To answer this question, modeling and different biochemical approaches have been pursued. The data does not always give clear results as to even establish the nature of the inhibition (competitive or noncompetitive) of vinblastine binding by other vinca domain ligands, as pointed out [43]. It should be noted that competition experiments are not straightforward in a system where binding induces assembly into either spirals or rings: analyses are complicated as ligands when embedded in such polymers will become less exchangeable. While modeling studies [59] suggest that the pseudopeptide sites overlap with that of vinblastine [55], labeling methods have identified cysteine 12 of the β subunit as part of the binding site of tubulyzine [52] and of dolastatin10 [60]. This residue is 10 Å away from vinblastine (Figs. 6 and 7). Another issue is the effect of these ligands on the β subunit nucleotide exchange rate. Albeit it binds close to GDP (Figs. 6 and 7), vinblastine interferes only weakly with nucleotide exchange. Other ligands (e.g. phomopsin A and dolastatin 10) are far better inhibitors (reviewed in [43]). They may bind to tubulin in a way that directly blocks this process. However, they could also act at a distance, one possibility being that they induce tubulin polymers in which the nucleotide is efficiently trapped between tubulin subunits and not exchangeable anymore, as in MTs. Mapping of the vinca domain beyond the vinblastine–tubulin interactions clearly remains an open issue that will require more direct indications than the biochemical or modeling results available so far. (see the note added in proof).

4.2 Colchicine Stabilizes a Curved Tubulin Conformation

The colchicine binding site in tubulin was initially identified using a colchicine derivative bearing a sulfhydryl group, permitting unambiguous orientation of the ligand in the electron density map [15]. We have also determined the structure of

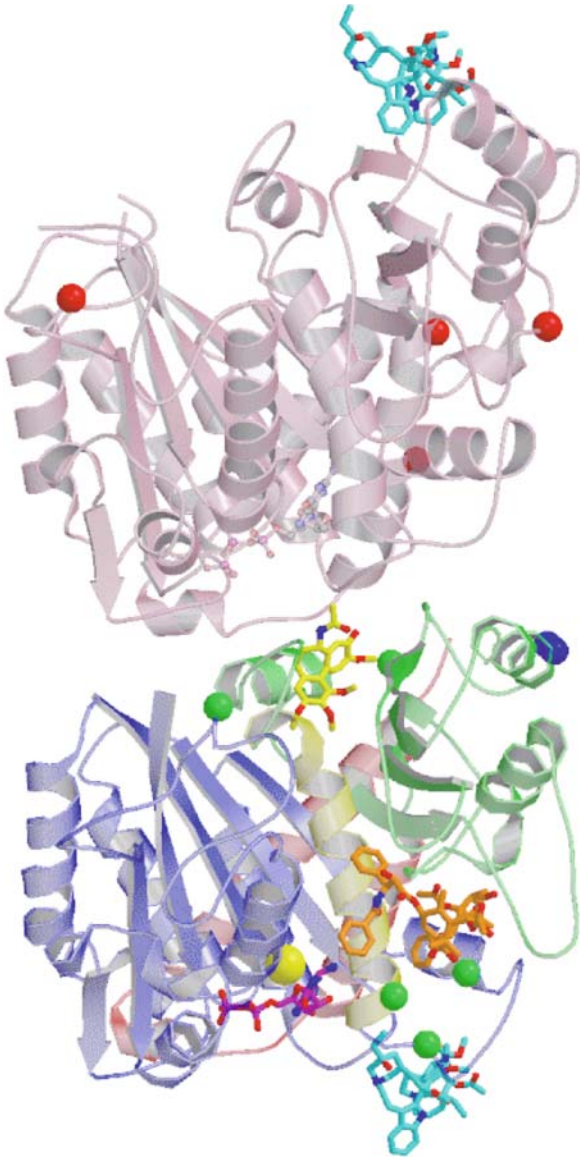

Fig. 7 The location on tubulin of residues that modulate the sensitivity to MT-destabilizing agents and the location of exogenous inhibitor and nucleotide sites on β tubulin. The α subunit is in semi-transparent pink together with a "composite" β-subunit color-coded as in Fig. 3a with ball-and-stick models of bound taxol (*orange*), colchicine (*yellow*) and GDP (*magenta*). Ball-and-stick models of vinblastine (*cyan*) are drawn on the two partial vinca sites on α and on β tubulin. The sulfur atom of Cys β12 is highlighted as a *yellow sphere*. The sites of nine amino acid substitutions [49] that both confer resistance to vinblastine and colchicine and stabilize MTs are depicted as *red* (on α tubulin) or *green* (on β tubulin) spheres. Two residues of the β H10 helix whose mutations enhance the sensitivity to colchicine site ligands and destabilize MTs [71] are also shown as *blue spheres*

the T_2R-colchicine complex ($(Tc)_2R$); it looks identical apart from the sulfhydryl group [15]. Colchicine binds to the β subunit at the interface with the α monomer of the same tubulin molecule, with little direct interaction with that subunit (Fig. 6). Nevertheless, because of ensuing steric hindrance, one cannot position an α subunit near a colchicine-bound β subunit as across an intradimer longitudinal contact in a straight protofilament [15]. Conversely, there is no more space available for colchicine when β tubulin is in a straight conformation. To help decipher whether colchicine-induced tubulin inhibition is due to the few direct interactions of colchicine with the α subunit or to indirectly induced steric hindrance, the structural characterization of a set of colchicine site binders complexed to tubulin is under way in our laboratory.

Colchicine site ligands are structurally simpler than taxol or vinblastine site compounds; the extent of the colchicine site is also smaller. This is confirmed with the observation that podophyllotoxin interacts with the same β tubulin residues as colchicine [15]. Modeling studies also suggest a pocket of restricted size for other colchicine site ligands [40] while some extensions of the site have been postulated in an approach combining modeling and virtual screening [61]. Biochemical evaluations have confirmed some of the hits as new tubulin inhibitors but no structural data are available yet that confirm whether they actually make use of an additional cavity near the colchicine site.

Whereas the sites for colchicine and podophyllotoxin largely overlap, the binding kinetics of podophyllotoxin does not present any peculiarity. Moreover, unlike colchicine, this molecule does not enhance the GTPase activity of soluble tubulin [37, 62]. Structural data do not give clear clues that can explain the different tubulin binding kinetics of these compounds or their effect on GTP hydrolysis. Apart from the ligand, the only significant structural variation between colchicine- and podophyllotoxin-bound T_2R is the conformation of the α subunit T5 loop, which is near the colchicine site [37]. Interestingly, in the structure of T_2R in complex with nocodazole this loop adopts the same conformation as in $(Tc)_2R$ (unpublished observation), and both ligands have been shown to enhance GTP hydrolysis by soluble tubulin. It should nevertheless be noticed that the colchicine site and the T5 loop are located at least 20 Å away from the β subunit nucleotide. Therefore more experiments, including high resolution data on the more relevant GTP-tubulin, will be required to identify the structural mechanism linking the GTPase activity to the binding of some colchicine site ligands.

Interestingly, the binding sites of the small molecule effectors of tubulin for which structural data are available all involve the β monomer (Fig. 7). In addition to colchicine, taxol targets the β subunit where it interferes with the MT lateral contact [12]. The β tubulin also contributes to the vinblastine site, although this is equally shared with α. During MT assembly the β tubulin-bound GTP is hydrolyzed, which is essential for MT dynamics, whereas the α subunit nucleotide never gets hydrolyzed. Therefore the β tubulin behaves as a regulatory subunit, which binds small effectors and inhibitors and whose conformation changes most along the MT assembly/disassembly cycle, compared to a more structural α subunit.

4.3 MT-Destabilizing Agents and MT Dynamics

MT-perturbing molecules induce different MT behaviors depending on their concentration. The classification as destabilizing or stabilizing agents relies on the effect on MTs at high inhibitor concentrations, i.e. in conditions where colchicine and vinblastine induce depolymerization. At low (substoichiometric) concentrations of MT-perturbing agents, the MT polymer mass does not vary significantly. Instead, MT dynamics is inhibited; MTs remain in a "pause" state (no recordable growth or shrinkage at the resolution of video microscopy) (reviewed in [63, 64]). Interestingly, this is observed at low concentration of both MT-destabilizing agents and MT-stabilizing drugs.

Structural data on MT-destabilizing compounds shed light on the way they trigger MT disassembly. The MT polymer is stabilized by specific longitudinal contacts between tubulin monomers within straight protofilaments and by lateral interactions between protofilaments. As MT-destabilizing agents maintain tubulin molecules in a curved conformation or in a curved assembly, these heterodimers are no longer available for MT growth as they cannot establish the required MT longitudinal contacts within the heterodimer (in the case of colchicine) or between tubulins (for vinblastine). Consequently, lateral interactions are prevented as the partners remain too distant for the corresponding contacts to occur. If the pool of uncomplexed tubulin is significantly lowered, MT growth is prevented or cannot be sustained, which leads to disassembly. Although they target different regions of tubulin, exogenous MT-destabilizing molecules truly mimic endogenous regulators like SLD proteins (Fig. 2): they all stabilize tubulin(s) in a curved conformation that prevents straight assembly.

The mechanisms by which low concentrations of MT-perturbing agents inhibit MT dynamics are presently not fully understood. In the case of MT-destabilizing drugs, it has been shown that the tubulin-colchicine complex [65] and vinblastine [66] bind to the ends of MTs. As little as one or two such molecules per MT end are enough to reduce significantly the dynamicity of the polymer (reviewed in [63]). This suggests that MT dynamics requires the integrity of inter-subunits contacts within and between protofilaments to occur. The underlying molecular mechanism might be different for taxol type ligands, as suggested by the identification of tubulin mutants that respond in opposite ways to different drugs. For example, the mutation of a proline located in the H6–H7 loop of the β subunit to a hydrophobic residue (Leu or Val) confers resistance to taxol and an enhanced sensitivity to the MT-destabilizing drugs vinblastine and colcemid [67]. The mutation of the same residue to a polar residue (Cys, Ser or Thr) leads to the reverse phenotype. Interestingly, in this work and in other studies (e.g. [49]), most of the mutated residues are away from the ligand sites (Fig. 7), the mutated tubulin displaying modified MT-polymerization properties that counteract the effect of the drug.

In the last 10 years the structural studies of tubulin and of its interactions with MT-perturbing agents have been very fruitful. This has been possible as new crystal forms have been obtained and analyzed by state-of-the-art electron microscopy and

X-ray crystallography, using in this case third generation synchrotron radiation facilities and recently developed crystallographic softwares. Despite these advances, more benefits for structure-based drug design programs remain to be gained from progress of structural data quality. Pushing the diffraction limit of αβ tubulin crystals to atomic resolution remains an as yet unmatched challenge. The effect on MTs of drugs at substoichiometric (therapeutic) doses is another unresolved issue. Very recently, the use of optical tweezers has been adapted to the study of MT dynamics [68, 69]. With a resolution that is a hundred times better than classical video-microscopy, it has now become possible to see what happens at the very tip of MTs, where dynamic instability takes place. This may well give new clues to the mechanism by which tubulin targeting drugs inhibit MT dynamics. These two examples are only two pending issues that will fuel the work of the laboratories interested in MT and in their inhibition by small molecules agents. Forty years after the discovery of tubulin [2], the study of MT remains an open field for scientists; a field in which progress will impact human healthcare, in particular anti-cancer chemotherapy.

Note added in proof: The structure of tubulin in complex with two other vinca domain ligands, namely with soblidotin, a dolastatin 10 analog, and with phomopsin A, has now been determined. These new results show that the site of these molecules overlaps only in part with the one of vinblastine. They put a structural explanation for the different properties of these compounds (e.g. an higher efficiency to inhibit the nucleotide exchange on tubulin) as compared to vinblastine [72].

Acknowledgments Financial support from ANR (grants N° ANR-05-BLAN-0292 and N° ANR-05-BLAN-0320), CNRS, and la Ligue contre le Cancer (équipe labellisée 2006) is gratefully acknowledged.

References

1. Peterson JR, Mitchison TJ (2002) Chem Biol 9:1275
2. Mohri H (1999) Cell Struct Funct 24:265
3. Vandecandelaere A, Brune M, Webb MR, Martin SR, Bayley PM (1999) Biochemistry 38:8179
4. Carlier MF (1982) Mol Cell Biochem 47:97
5. Chretien D, Jainosi I, Taveau JC, Flyvbjerg H (1999) Cell Struct Funct 24:299
6. Hyman AA, Salser S, Drechsel DN, Unwin N, Mitchison TJ (1992) Mol Biol Cell 3:1155
7. Nogales E, Downing KH, Amos LA, Lowe J (1998) Nat Struct Biol 5:451
8. Li H, DeRosier DJ, Nicholson WV, Nogales E, Downing KH (2002) Structure 10:1317
9. Kraulis P (1991) J Appl Crystallogr 24:946
10. Meritt EA, Bacon DJ (1997) Methods Enzymol 276:505
11. DeLano WL (2002) [CE1]DeLano Scientific, Palo Alto, CA, USA
12. Nogales E, Whittaker M, Milligan RA, Downing KH (1999) Cell 96:79http://pymol.sourceforge.net/
13. Mandelkow EM, Mandelkow E, Milligan RA (1991) J Cell Biol 114:977
14. Nogales E, Wang HW, Niederstrasser H (2003) Curr Opin Struct Biol 13:256
15. Ravelli RB, Gigant B, Curmi PA, Jourdain I, Lachkar S, Sobel A, Knossow M (2004) Nature 428:198
16. Jourdain L, Curmi P, Sobel A, Pantaloni D, Carlier MF (1997) Biochemistry 36:10817

17. Gigant B, Curmi PA, Martin-Barbey C, Charbaut E, Lachkar S, Lebeau L, Siavoshian S, Sobel A, Knossow M (2000) Cell 102:809
18. Steinmetz MO, Kammerer RA, Jahnke W, Goldie KN, Lustig A, van Oostrum J (2000) Embo J 19:572
19. Nogales E, Wolf SG, Downing KH (1998) Nature 391:199
20. Buey RM, Diaz JF, Andreu JM (2006) Biochemistry 45:5933
21. Wang HW, Nogales E (2005) Nature 435:911
22. Desai A, Mitchison TJ (1997) Annu Rev Cell Dev Biol 13:83
23. Akhmanova A, Hoogenraad CC (2005) Curr Opin Cell Biol 17:47
24. Bieling P, Laan L, Schek H, Munteanu EL, Sandblad L, Dogterom M, Brunner D, Surrey T (2007) Nature 450:1100
25. Arnal I, Heichette C, Diamantopoulos GS, Chretien D (2004) Curr Biol 14:2086
26. Slep KC, Vale RD (2007) Mol Cell 27:976
27. Howard J, Hyman AA (2007) Curr Opin Cell Biol 19:31
28. Verhey KJ, Gaertig J (2007) Cell Cycle 6:2152
29. Schiff PB, Fant J, Horwitz SB (1979) Nature 277:665
30. Diaz JF, Andreu JM (1993) Biochemistry 32:2747
31. Noble RL (1990) Biochem Cell Biol 68:1344
32. Medrano FJ, Andreu JM (1986) Eur J Biochem 158:63
33. David-Pfeuty T, Simon C, Pantaloni D (1979) J Biol Chem 254:11696
34. David-Pfeuty T, Erickson HP, Pantaloni D (1977) Proc Natl Acad Sci USA 74:5372
35. Melki R, Fievez S, Carlier MF (1996) Biochemistry 35:12038
36. Larsson N, Segerman B, Howell B, Fridell K, Cassimeris L, Gullberg M (1999) J Cell Biol 146:1289
37. Wang C, Cormier A, Gigant B, Knossow M (2007) Biochemistry 46:10595
38. Engelborghs Y (1998) Eur Biophys J 27:437
39. Chakrabarti G, Sengupta S, Bhattacharyya B (1996) J Biol Chem 271:2897
40. Nguyen TL, McGrath C, Hermone AR, Burnett JC, Zaharevitz DW, Day BW, Wipf P, Hamel E, Gussio R (2005) J Med Chem 48:6107
41. Kiselyov A, Balakin KV, Tkachenko SE, Savchuk N, Ivachtchenko AV (2007) Anticancer Agents Med Chem 7:189
42. Hamel E, Covell DG (2002) Curr Med Chem Anticancer Agents 2:19
43. Hamel E (1992) Pharmacol Ther 55:31
44. Haskins KM, Donoso JA, Himes RH (1981) J Cell Sci 47:237
45. Strahs KR, Sato H (1973) Exp Cell Res 80:10
46. Amos LA, Jubb JS, Henderson R, Vigers G (1984) J Mol Biol 178:711
47. Saltarelli D, Pantaloni D (1982) Biochemistry 21:2996
48. Richards KL, Anders KR, Nogales E, Schwartz K, Downing KH, Botstein D (2000) Mol Biol Cell 11:1887
49. Hari M, Wang Y, Veeraraghavan S, Cabral F (2003) Mol Cancer Ther 2:597
50. Britto PJ, Knipling L, Wolff J (2002) J Biol Chem 277:29018
51. Kim YJ, Pannell LK, Sackett DL (2004) Anal Biochem 332:376
52. Kim YJ, Sackett DL, Schapira M, Walsh DP, Min J, Pannell LK, Chang YT (2006) Bioorg Med Chem 14:1169
53. Nettles JH, Li H, Cornett B, Krahn JM, Snyder JP, Downing KH (2004) Science 305:866
54. Dorleans A, Knossow M, Gigant B (2007) In: Zhou J (ed) Microtubule protocols (methods in molecular medicine). Humana, Totowa, NJ, p 235
55. Gigant B, Wang C, Ravelli RB, Roussi F, Steinmetz MO, Curmi PA, Sobel A, Knossow M (2005) Nature 435:519
56. Reese M, Sanchez-Pedregal VM, Kubicek K, Meiler J, Blommers MJ, Griesinger C, Carlomagno T (2007) Angew Chem Int Ed Engl 46:1864
57. Diaz JF, Barasoain I, Souto AA, Amat-Guerri F, Andreu JM (2005) J Biol Chem 280:3928
58. Pommier Y, Cherfils J (2005) Trends Pharmacol Sci 26:138
59. Mitra A, Sept D (2004) Biochemistry 43:13955

60. Bai R, Covell DG, Taylor GF, Kepler JA, Copeland TD, Nguyen NY, Pettit GR, Hamel E (2004) J Biol Chem 279:30731
61. Kim do Y, Kim KH, Kim ND, Lee KY, Han CK, Yoon JH, Moon SK, Lee SS, Seong BL (2006) J Med Chem 49:5664
62. Heusele C, Carlier MF (1981) Biochem Biophys Res Commun 103:332
63. Wilson L, Panda D, Jordan MA (1999) Cell Struct Funct 24:329
64. Jordan MA (2002) Curr Med Chem Anticancer Agents 2:1
65. Skoufias DA, Wilson L (1992) Biochemistry 31:738
66. Wilson L, Jordan MA, Morse A, Margolis RL (1982) J Mol Biol 159:125
67. Yin S, Cabral F, Veeraraghavan S (2007) Mol Cancer Ther 6:2798
68. Kerssemakers JW, Munteanu EL, Laan L, Noetzel TL, Janson ME, Dogterom M (2006) Nature 442:709
69. Schek HT III, Gardner MK, Cheng J, Odde DJ, Hunt AJ (2007) Curr Biol 17:1445
70. Lowe J, Li H, Downing KH, Nogales E (2001) J Mol Biol 313:1045
71. Yang H, Cabral F (2007) J Biol Chem 282:27058
72. Cormier A, Marchand M, Ravelli RB, Knossow M, Gigant B (2008) Embo Rep in press

Top Curr Chem (2009) 286: 279–328
DOI: 10.1007/128_2008_20

Published online: 29 October 2008

Molecular Modeling Approaches to Study the Binding Mode on Tubulin of Microtubule Destabilizing and Stabilizing Agents

Maurizio Botta, Stefano Forli, Matteo Magnani, and Fabrizio Manetti

Abstract Tubulin targeting agents constitute an important class of anticancer drugs. By acting either as microtubule stabilizers or destabilizers, they disrupt microtubule dynamics, thus inducing mitotic arrest and, ultimately, cell death by apoptosis. Three different binding sites, whose exact location on tubulin has been experimentally detected, have been identified so far for antimitotic compounds targeting microtubules, namely the taxoid, the colchicine and the vinka alkaloid binding site. A number of ligand- and structure-based molecular modeling studies in this field has been reported over the years, aimed at elucidating the binding modes of both stabilizing and destabilizing agent, as well as the molecular features responsible for their efficacious interaction with tubulin. Such studies are described in this review, focusing on information provided by different modeling approaches on the structural determinants of antitubulin agents and the interactions with the binding pockets on tubulin emerged as fundamental for antitumor activity.

To describe molecular modeling approaches applied to date to molecules known to bind microtubules, this paper has been divided into two main parts: microtubule destabilizing (Part 1) and stabilizing (Part 2) agents. The first part includes structure-based and ligand-based approaches to study molecules targeting colchicine (1.1) and vinca alkaloid (1.2) binding sites, respectively. In the second part, the studies performed on microtubule stabilizing antimitotic agents (MSAA) are described. Starting from the first representative compound of this class, paclitaxel, molecular modeling studies (quantitative structure-activity relationships – QSAR – and structure-based approaches), performed on natural compounds acting with the same mechanism of action and temptative common pharmacophoric hypotheses for all of these compounds, are reported.

M. Botta (✉) and F. Manetti
Dipartimento Farmaco Chimico Tecnologico, Università degli Studi di Siena,
Via Alcide de Gasperi, 2, I-53100 Siena, Italy
e-mail: botta@unisi.it

S. Forli
Department of Molecular Biology, The Scripps Research Institute, La Jolla, CA 92037, USA

M. Magnani
Siena Biotech S.p.A., Therapeutic Research, Via Fiorentina 1, I-53100 Siena, Italy

Keywords Microtubule targeting agents, Molecular docking, Molecular modeling, Pharmacophore, Quantitative structure-activity relationships, Tubulin

Contents

Abbreviations

TMP	trimethoxyphenyl
CA4	combretastatin A-4
CSI	colchicine site inhibitors
DAMA-colchicine	(*N*-deacetyl-*N*-(2-mercaptoacetyl)colchicine)
EPO	epothilone
MSAA	microtubule stabilizing antimitotic agents
MD	molecular dynamics
MIF	molecular interaction field
PTX	paclitaxel

1 Molecular Modeling on Microtubule Destabilizing Agents

Microtubule destabilizing compounds act by inhibiting microtubule polymerization and include several agents, such as colchicine (**1**), combretastatin A-4 (**2**), podophyllotoxin (**3**), vinca alkaloids (vinblastine (**4**), vincristine (**5**) and others) (Chart 1) and a number of structurally unrelated small molecules [1]. Two different binding sites on tubulin are known for microtubule destabilizing agents, namely the colchicine and the vinca alkaloid site. The location of both sites was uncertain for a long time, until the crystallographic structures of tubulin complexed with colchicine or podophyllotoxin (colchicine binding site [2] and vinblastine (vinca alkaloid binding site [3] were reported. These structures revealed that, differently from microtubule stabilizers, interacting with a straight conformation of tubulin (characteristic of stable microtubules), microtubule destabilizers bind to a curved conformation of tubulin (characteristic of rings or depolymerizing microtubules) [4]. The changes detected in tubulin subunits in the switch from a straight to a curved conformation accounted for the loss of lateral contacts between protofilaments and, consequently, for the inhibitory effect on tubulin polymerization.

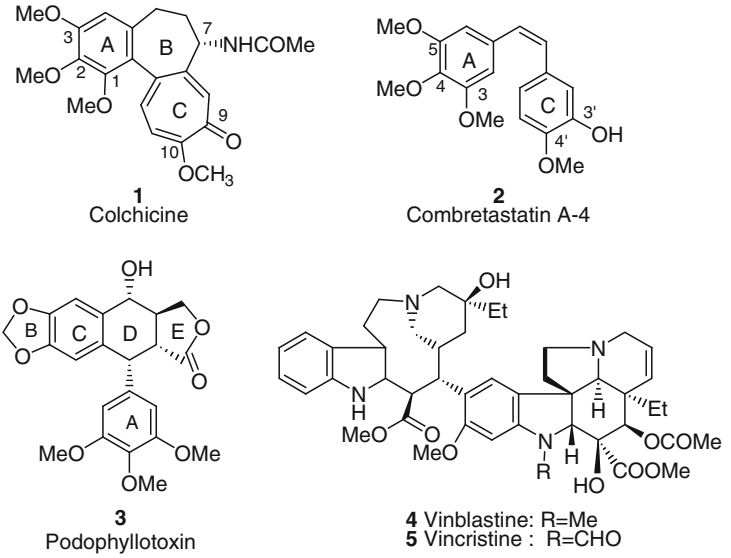

Chart 1 Chemical structures of colchicine (**1**), combretastatin A-4 (**2**), podophyllotoxin (**3**), vinblastine (**4**) and vincristine (**5**)

The identification of the binding site location within tubulin, together with the clarification of the binding mode for some representative destabilizing compounds, opened new perspectives to modeling studies in this field, making the application possible not only of ligand-based, but also structure-based approaches.

It is worth noting that molecular modeling studies in the field of microtubule destabilizing agents are substantially limited to compounds targeting the colchicine site, whereas there are only a few modeling studies involving drugs binding to the vinca domain. This can be ascribed, on the one hand, to the intensive efforts focused on discovering more potent and less toxic agents able to bind the colchicine pocket, which generated a huge number of compounds spanning several chemical classes [5–7], and, on the other hand, to the large size and structural complexity of agents interacting with the vinca alkaloid site [7, 8].

1.1 Molecular Modeling on Compounds Targeting the Colchicine Binding Site

1.1.1 Colchicine Site Inhibitors

The natural compound colchicine (**1**) was extracted from the poisonous meadow saffron *Colchicum autumnale L.* and was the first antimitotic destabilizing agent to be discovered [9]. It consists of three rings: a trimethoxyphenyl (TMP, ring A), a

methoxytropone (ring C) and a seven-membered ring (ring B) bearing an acetamido substituent at its C7 position. Structure-activity relationship (SAR) studies indicated the TMP and the tropone rings as crucial for colchicine-tubulin binding, whereas ring B, although important, did not emerge as essential for the activity, and substitutions at its C7 position were usually tolerated [10].

Noteworthy, neither colchicine nor other colchicine site inhibitors (CSI) have yet found significant clinical application in tumor treatment, mainly due to their high toxicity [11]. As a consequence, until now, only molecules binding to taxoid and vinca alkaloid domains have been extensively used in cancer chemotherapy [7, 12]. However, several CSI are now under investigation for tumor treatment [5]. Many of them are derived from natural products such as the combretastatins. Combretastatins, obtained from the South African tree *Combretum caffrum* [13–16], constitute an important class of CSI. Among them, combretastatin A–4 (CA4, **2**) became one of the most interesting antitubulin agents targeting the colchicine site and was considered for clinical trials, although poor water solubility hampered its development as drug [17]. The clinical potential of CA4 along with its structural simplicity stimulated intensive efforts over the years in the synthesis of a sizeable number of CA4 analogues [18–23]. Extensive SAR studies pointed out the importance of the trimethoxy substitution on the A ring and the *cis*-olefin configuration of the linkage; the ring B was shown to be tolerant to structural modifications at position 3′, where the hydroxy group was not essential, while the 4′-methoxy group seemed crucial for cytotoxicity [18, 24].

The colchicine binding site was identified in 2004, when Ravelli and co-workers reported the X-ray structure of tubulin in complex with DAMA-colchicine (*N*-deacetyl-*N*-(2-mercaptoacetyl)-colchicine) and with the RB3 protein stathmin-like domain (PDB entry: 1SA0) [2]. The structure showed the exact binding site of colchicine on tubulin, thus shedding light onto the mechanism of action and the binding mode of the destabilizing compound. The same paper also reported the structure of tubulin in complex with podophyllotoxin (**3**) and with the stathmin-like domain of RB3 (PDB entry: 1SA1), revealing that podophyllotoxin shares with colchicine a common binding site and locates the TMP moiety in the same region of the binding pocket as colchicine. In both structures, tubulin is in a curved conformation and the colchicine site is located at the a/β intradimer interface (Fig. 1a). It is mostly buried in the intermediate domain of the β-tubulin subunit, whereas the B ring side chain mainly interacts with residues of the a subunit. Once bound to the colchicine pocket, colchicine and the other CSI prevent curved tubulin from assuming a straight conformation, thus resulting in microtubule disassembly.

1.1.2 Ligand-Based Approaches to Colchicine Site Inhibitors

All ligand-based molecular modeling studies focusing on agents able to bind the colchicine site were performed before the determination of the X-ray structure of the tubulin-colchicine complex (see below). Computational tools in this field were mainly used to derive three-dimensional QSARs (through comparative molecular field analysis (CoMFA) and other original approaches), but CSI also constituted useful

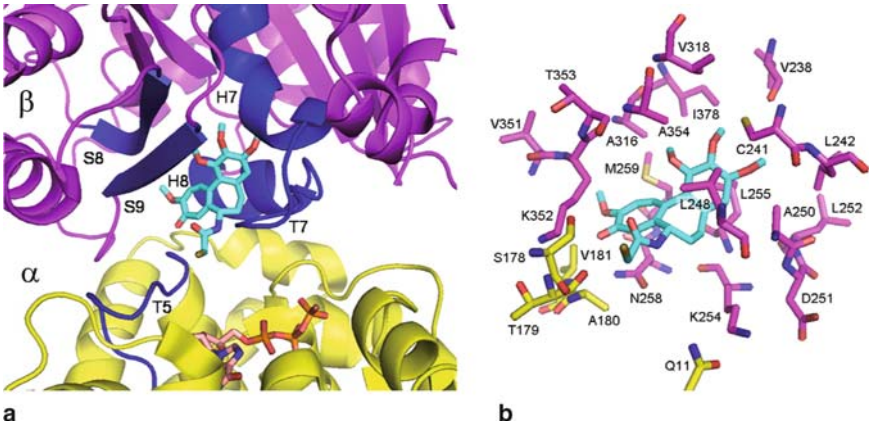

Fig. 1 **a** Location of the colchicine binding site in tubulin (1SA0 structure). α- and β-tubulin are represented as *yellow and magenta ribbons*, respectively; secondary structure elements contacting DAMA-colchicine (*cyan sticks*) are colored *blue*. Non-exchangeable GTP bound to the α subunit is represented as *pink sticks*. **b** Overall view of residues constituting the colchicine binding site (1SA0 structure) and proposed to interact with CSI by distinct structure-based molecular modeling studies (Sect. 1.1.3). Residues of α and β subunits are represented as *yellow and magenta sticks*, respectively. DAMA-colchicine is represented as *cyan sticks*

datasets for testing and applying newly developed methods in different fields of computer-aided drug design. Consistent with a common aspect of ligand-based approaches, all such analyses were primarily aimed at identifying chemical and structural features of molecules that are responsible for their affinity toward the colchicine binding site and consequently for their destabilizing activity. Therefore, they constitute an interesting example of how different computational tools can be applied to derive information about the binding mode of compounds under analysis.

In 1996, Day and co-workers reported a QSAR study on a wide set of tubulin polymerization inhibitors binding to the colchicine site [25]. The authors collected 536 chemicals along with their biological activities from several literature sources. The dataset compounds encompassed a number of chemical classes, including colchicinoids and allocolchicinoids, podophyllotoxins, chalcones, benzylbenzodioxoles, steroids, stilbenes, combretastatins, phenylquinolones, styrylquinazolinones, phenanthrenes, benzylanilines and miscellaneous agents. The statistical analysis led to the identification of several biophores, which are substructural features statistically correlated with the biological activity. Among them, the authors presented and discussed the biophores contained in colchicinoids, podophyllotoxins and combretastatins (reported in Chart 2), making some important SAR considerations and speculating about the relative orientation of colchicine and podophyllotoxin within the colchicine binding site.

The biophores present in colchicinoids highlighted the relevant role of the C1 and C10 methoxy groups and suggested that the size of the substituent at C7 scarcely influenced the interaction of colchicinoids with tubulin, as it was not included in any biophore.

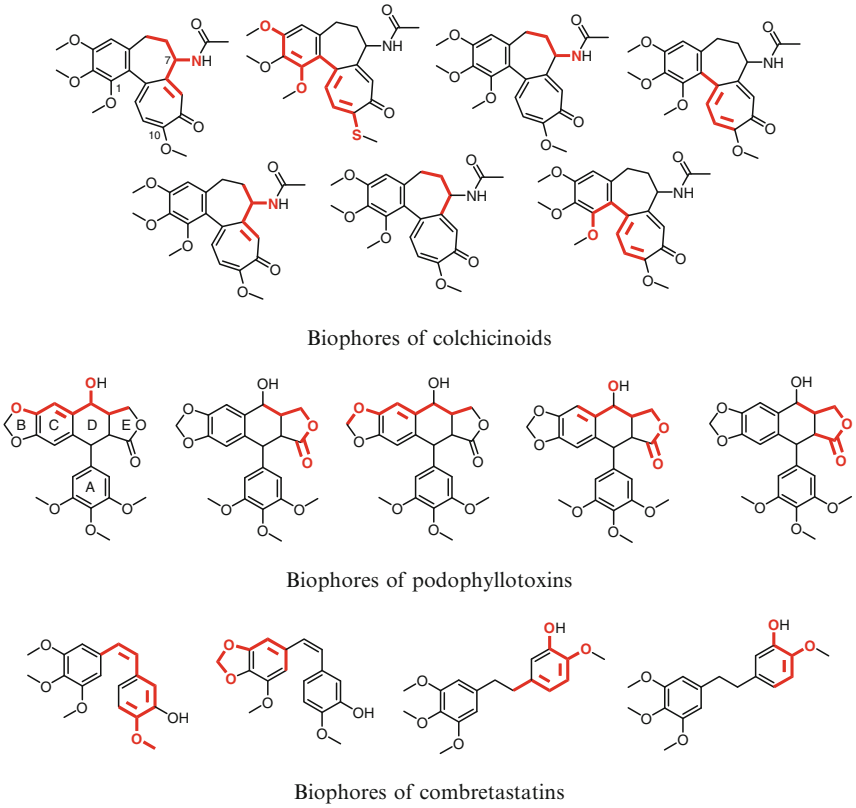

Chart 2 Biophores present in colchicinoids, podophyllotoxins and combretastatins among those identified as relevant for the activity of CSI

The biophores for podophyllotoxins included the lactone ring E and parts of the B, C and D rings, thus indicating them as important for the interaction between podophyllotoxins and tubulin. The A ring was not present in podophyllotoxin fragments, probably due to the fact that only a few analogues of the learning set were characterized by structural modification of the TMP moiety.

Concerning combretastatins, the biophores involving dihydrocombretastatins and combretastatin A–2 analogues mainly indicated the importance of the two carbon bridge, whereas the single CA4 biophore was unable to efficiently describe the activity of CA4 analogues.

Besides identifying the structural features crucial for the activity of different classes of compounds, in the same report the biophores were also used to explore the relative orientation of colchicine and podophyllotoxin within the colchicine binding pocket. As a result, the TMP rings of the two ligands were located in different regions of the binding site, near orthogonal to each other, suggesting that these moieties should interact with different regions of tubulin. Unfortunately, this hypothesis was denied by the recently determined complexes of tubulin with colchicine and

podophyllotoxin [2], which showed that the two TMP rings lie in the same region of the colchicine binding pocket.

In 2000, Macdonald and co-workers reported CoMFA-based 3D-QSAR models able to describe the binding of different structural types of combretastatins to the colchicine binding site [26]. The study resulted in the first significantly predictive models for the class of combretastatins.

CoMFA models were built starting from a training set of 22 combretastatin analogues (including CA4) collected from literature along with their activity data. The lowest energy conformers of each compound obtained from conformational analysis were aligned overlapping their A ring to the A ring of CA4, for which the X-ray structure was used. Colchicine, phenstatin and podophyllotoxin, included in a test set of ten compounds together with other combretastatins, were used in their X-ray conformation and were also aligned to CA4 by superposition of the TMP moiety. The developed CoMFA models were endowed with good statistical parameters, but poorly predicted the activity of test set compounds not belonging to the combretastatin class (i.e., colchicine, phenstatin and podophyllotoxin). This aspect led the authors to hypothesize a different pharmacophore for these compounds with respect to combretastatins, though a substantial overlapping of the TPM ring of different ligands has also been suggested by other subsequent studies.

An interesting CoMFA study was conducted by Weigt and Wiese on a set of 58 variously substituted 2-phenyl-4-quinolone and 2-phenyl-1,8-naphthyridin-4-one CSI (Chart 3) [27].

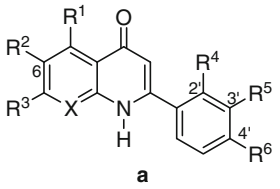

a

Chart 3 General structure of 2-phenyl-4-quinolones (X=CH) and 2-phenyl-1,8-naphthyridin-4-ones (X=N) used by Weigt and Weise to generate their CoMFA model

Two different alignment criteria were investigated (namely, the so-called atom-based database and the CoMFA field alignment). In the first case, compounds were aligned by superposition of atoms belonging to a common template; in the second case, they were aligned so as to achieve the best match of their CoMFA fields. In both cases, the final models showed good internal and external predictive power. CoMFA contour maps corresponding to different alignments provided similar information. On the basis of such plots, substituents at position 6 were expected to increase the activity, whereas R^3 substituents should have the opposite effect. Greater electronegativity at 3′ position was correlated with increased activity, and less electron withdrawing substituents were favorable at 2′ and 4′ positions. Remarkably, the importance of these structural features was further confirmed by a classical QSAR model built by the same authors on the naphthyridine set using the Free-Wilson approach [27]. As a whole, the computational analysis pointed out the importance of electrostatic interactions for

the activity of quinolone and naphthyridine CSI under study, and suggested the existence of a complex relationship between substitution pattern and inhibitory potency.

A third CoMFA model in this field was elaborated by Lee and co-workers [28]. The authors used a wide set of CSI synthesized in house and belonging to different structural classes. In detail, the 3D-QSAR model was developed using 104 colchicine site agents, including thiocolchicinoids, allocolchicinoids, 2-phenyl-quinolones and 2-aryl-naphthyridinones (the last two classes also included the compounds used by Weigt and Wiese in the study described above). Both a conventional and a q^2-guided region selection (GRS) CoMFA approach were applied. Each approach was combined with two different alignment rules, both based on the superposition of the diaryl system shared by all CSI under analysis. The most interesting model was obtained using a conventional CoMFA and an alignment rule based not only on topological aspects, but also taking into account the different dihedral angles of the aryl rings and the different direction of the side chain between *aR*,7*S* (the configuration of colchicine and of most dataset compounds) and *aS*,7*R* configurations of colchicinoids [29, 30]. This criterion involved the alignment of *aR*,7*S* and *aS*,7*R* compounds so as to overlap the aromatic rings of the diaryl system and to locate the side chains at C7 in the same region of space. Most of the steric and electrostatic fields provided by the CoMFA model surrounded the A ring of thiocolchicinoids and allocolchicinoids, and the 2-aryl ring of quinolones and naphthyridinones, which were all superimposed by the alignment procedure. As a consequence, these groups emerged as fundamental in modulating the affinity of analyzed CSI toward the colchicine binding site. Conversely, the B ring and the side chain of colchicinoids were surrounded by few fields, suggesting that these moieties, though important to keep the A and C rings in a suitable conformation, should not be involved (or should play a marginal role) in interactions with tubulin.

An original ligand-based approach aimed at predicting the activity of tubulin destabilizing agents and getting deeper insight into the structural basis of their binding to the colchicine site was proposed in more recent years by Ducki and co-workers, who developed a 5D-QSAR model for a series of combretastatin analogues [31]. Compared with the more common 3D-QSAR, 5D-QSAR attempts to reduce the bias associated with the choice of the bioactive conformation and the induced-fit model [32]. Accordingly, the fourth dimension allows the representation of each molecule by a set of conformations, orientations, protonation states and/or enantiomers, whereas the fifth dimension refers to the option of considering an ensemble of induced-fit models. The fields resulting from 5D-QSAR consist of color-coded 3D maps describing specific regions where the various atomistic descriptors (such as hydrophobic, hydrogen bond acceptor or donor, salt bridge, etc.) are found to be significantly correlated with the biological activity. The maps can therefore be considered as a model of the receptor where the ligands exert their action. All the 47 compounds selected for the study were characterized by two aromatic rings (corresponding to rings A and C of CA4) linked by various fragments such as an enone (chalcones), alkene (stilbenes), or ether (represented Chart 4 by structures **b**, **c** and **d**, respectively). Individual models were initially generated for the chalcone and the stilbene classes (19 and 18 ligands, respectively), then all 47 derivatives were grouped to build a more general model. In a first step, CA4, a chalcone derivative and colchicine were aligned each other (though the latter was not included in the dataset), resulting in the superposition of their TMP and C ring

moieties. The conformations so obtained were then taken as template for the alignment of the other dataset compounds, which were aligned by superimposing the corresponding oxygen atoms of the A rings tightly, and the oxygen atoms of the C rings with less constraint. QSAR analysis on the chalcone, stilbene and combined series resulted in models overall endowed with good predictive power. Color-coded surfaces were quite complex to interpret. Nevertheless, they highlighted the importance of polar substituents at position 3′ of C rings for increasing the biological activity. Moreover, the methoxy groups and the overall hydrophobic character of the ligands emerged as crucial in determining the potency of combretastatin-like compounds.

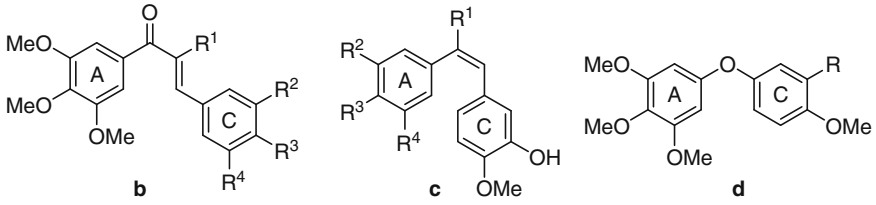

Chart 4 Representative structures of chalcone (**b**), stilbene (**c**) and ether (**d**) CSI constituting the dataset on which Ducki and co-workers developed a 5D-QSAR model

Interesting information in this context was also provided by the work of Feher and Schmidt, who proposed two possible alignments between CA4 and other important CSI, including colchicine [33]. The represented a test for the newly developed MultiSEAL procedure, which allows the application of the steric and electrostatic alignment (SEAL) [34] method to multiple conformations of multiple molecules. It should be emphasized that, when robust, an alignment method can be profitably used not only to prepare compounds for a 3D-QSAR analysis, but also to identify and locate potential pharmacophoric groups in a set of structurally diverse molecules. The CSI used by Feher and Schmidt were colchicine, CA4, allocolchicine (**6**), 2-methoxy-5-(2′,3′,4′-trimethoxyphenyl)-tropone (MTC) (**7**) and 2-methoxyestradiol (**8**) (Chart 5).

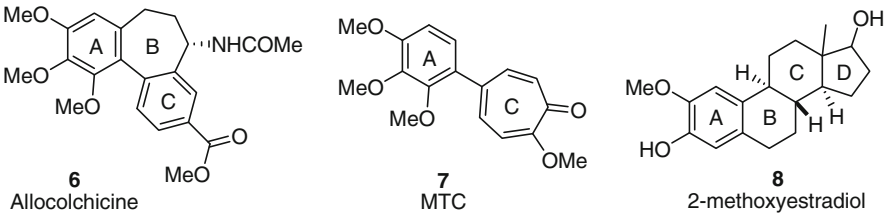

Chart 5 Chemical structures of allocolchicine (**6**), 2-methoxy-5-(2′,3′,4′-trimethoxyphenyl)-tropone (MTC) (**7**) and 2-methoxyestradiol (**8**), analyzed together with colchicine and CA4 through the MultiSEAL alignment procedure

As regards the first four molecules (those supposed to interact most similarly with the binding pocket), two basic alignments were identified. In both, colchicine, allocolchicine and MTC overlapped in a similar fashion, whereas combretastatin assumed two different orientations. In the first superposition, considered more likely

to occur according to the program, the A and C rings of combretastatin and colchicine were aligned with each other (an overlay similar to that proposed by Ducki and co-workers, as described above); in the second one, the A and C rings of combretastatin were aligned, respectively, to the C and A rings of colchicine and of the other molecules. Concerning 2-methoxyestradiol, two possible overlaps were found with respect to colchicine, though considerably worse than that of the other compounds. In fact, in both cases, only for the A ring of 2-methoxyestradiol, a good alignment with A or C ring of colchicine was found. As a consequence, the authors proposed that the ligand could interact favorably only with a portion of the colchicine site, but it was expected to be unable to well fit the entire binding pocket. This was in agreement with the weak antimitotic activity of 2-methoxyestradiol. Since the substitution pattern of the A ring of 2-methoxyestradiol is similar to that of the A ring of colchicine, this could be a key element for the inhibition of tubulin polymerization exerted by both compounds. However, a higher efficacy of binding should require the proper overlap of functional groups at both ends of the molecules.

The results achieved by ligand-based approaches described in this section are summarized in Table 1.

Table 1 Summary of ligand-based molecular modeling studies in the field of CSI

Study	CSI	Main results	References
QSAR	CSI encompassing several structural classes	Biophores for colchicinoids, podophyllotoxins and combretastatins, indicating the main structural features responsible for the activity of compounds	[25]
CoMFA	CA4 analogues	Hypothesis of a different pharmacophore for combretastatins and the other CSI colchicine, podophyllotoxin and phenstatin	[26]
CoMFA	Quinolones, naphthyridinones	Analysis of the effects of substituents at different positions of the quinolone/naphthyridinone scaffold	[27]
CoMFA	Thiocolchicinoids, allocolchicinoids, quinolones, naphthyridinones	Identification of the portions of the scaffolds playing a key role on the activity of compounds	[28]
5D-QSAR	CA4 analogues	Receptor models highlighting the regions where atomistic properties are significantly correlated with the activity of compounds	[31]
Alignment	Colchicine, CA4, allocolchicine, 2-methoxy-5-(2′,3′,4′-trimethoxyphenyl)-tropone, 2-methoxyestradiol	Alignment models for compounds under analysis	[33]

1.1.3 Structure-Based Approaches to Colchicine Site Inhibitors

With the exception of Hamel's work, the first described below, structure-based modeling studies in the field of CSI started after the determination of the tubulin–colchicine complex, reported by Ravelli and co-workers in 2004 [2]. Since then, the crystallographic structures of tubulin bound to colchicine (PDB entry: 1SA0) and, to a less extent, to podophyllotoxin (PDB entry: 1SA1) were used to dock a huge variety of tubulin polymerization inhibitors, especially analogues of CA4, within the colchicine site. In most cases, docking analyses were aimed at understanding the underlying SARs for a given class of destabilizing compounds, but they were also applied either for the design of novel antimitotic agents or for the elaboration of a structure-based pharmacophoric model codifying the essential structural features responsible for the activity of CSI, as reported in the final part of this section.

Taken together, structure-based studies on distinct classes of CSI resulted in the identification of several residues and interactions (summarized in Fig. 1b and Table 2) which were supposed to be involved in the binding process.

Table 2 Summary of hydrogen bond interactions that modeling studies suggested to occur between different CSI and residues of the colchicine binding site

Compound or class	Residue	Ligand-tubulin interaction	References
Colchicine	Ser α178	Amide C=O ---- side chain OH[a]	[35]
	Thr α179	Amide NH ---- backbone C=O[b]	[35]
	Val α181	C=O ---- backbone NH	[36–38]
	Cys β241	2-MeO ---- side chain SH	[38, 39]
	Lys β352	C=O ---- side chain NH_3^+	[35]
CA4	Thr α179	3′-OH ---- backbone C=O	[36, 37]
	Val α181	3′-OH ---- backbone NH	[37, 38]
	Cys β241	4-MeO ---- side chain SH	[38, 40]
Imidazoles (**e**)	Val α181	3′-F ---- backbone NH	[40]
	Cys β241	4-MeO ---- side chain SH	
Arylcoumarins (**f**)	Thr α179	3′-OH ---- backbone C=O	[36]
Triazoles (**g**)	Cys β241	3- and 4-MeO ---- side chain SH	[41]
Arylthioindoles (**h**)	Thr α179	Indole NH ---- backbone C=O	[35, 42, 43]
	Lys β352	Ester C=O ---- side chain NH_3^+	[35]
Benzoylthiophenes (**i**)	Leu β252	C=O ---- backbone NH	[44]
	Asn β258	2-NH_2 ---- side chain C=O	
9	Thr α179	3′-OH ---- backbone C=O	[37]
	Val α181	3′-OH ---- backbone NH	
MDL-27048	Cys β241	5-MeO ---- side chain SH	[39]
CSI[c]	Thr α179	D1[d] ---- backbone C=O	[38]
	Val α181	A1[d] ---- backbone NH	
	Cys β241	A2[d] ---- side chain SH	
	Ala β250	A3[d] ---- backbone NH	
	Asp β251	A3[d] ---- backbone NH	
	Leu β252	A3[d] ---- backbone NH	

[a]Formed during molecular dynamics simulation
[b]Lost during molecular dynamics simulation
[c]CSI belonging to different chemical classes
[d]Features of the common pharmacophore for CSI proposed by Nguyen and co-workers [38]

The study published in 2000 by Hamel and co-workers, describing an attempt to find a potential binding site for colchicinoids on tubulin by means of biochemical and molecular modeling techniques, can be considered the first structure-based approach in the field of molecular modeling of compounds targeting the colchicine site [45]. The structure of the tubulin–colchicine complex, and thus the exact location of the colchicine binding site, was reported a good 4 years later, but this aspect constitutes only an apparent discrepancy, since the Hamel's study was carried out using the straight structure of tubulin in complex with docetaxel, available since 1998 (PDB entry: 1TUB) [46]. The authors found that 2CTC and 3CTC, two chemically reactive colchicine analogues bearing a chloroacetyloxy group in place of the methoxy group at position 2 and 3 of the A ring, respectively, reacted covalently with β-tubulin, forming adducts with Cys β241 and Cys β356. Such biochemical information was used to assess the reliability of results obtained from molecular modeling studies which were aimed at identifying a putative binding site for colchicine and its structural analogues. Two potential binding sites, both located near the Cys β241/Cys β356 region of β-tubulin, emerged from the first part of the computational procedure as the most suitable: one site, labeled as "site A," was entirely contained within β-tubulin, whereas the other, referred to as "site B," was located at the α/β interface. However, subsequent docking analyses did not provide fully convincing results for both of the two proposed binding sites. Such findings led the authors to postulate that the colchicine binding site should undergo significant conformational changes that may occur either in the transition from the polymerized (straight tubulin) to the unpolymerized (curved tubulin) state, or as a consequence of ligand binding. This hypothesis was confirmed by the crystallographic structure of the tubulin–colchicine complex [2], which revealed that the movement of several secondary structure elements involved in the binding of colchicine is required with respect to the straight conformation of tubulin in order to make space available for the ligand (Fig. 2). The observed differences between the straight and curved conformation of tubulin are a reason that the colchicine binding pocket, although located at the α/β interface, differed from sites A and B, proposed by Hamel and co-workers on the basis of the straight 1TUB structure.

In 2006, Bellina and co-workers reported some docking studies on a series of novel imidazole-based CA4 analogues (**e** in Chart 6) [40]. The imidazole ring was one of the numerous alternative bridge groups (also including pyrazoles, tetrazoles, triazoles, etc.) introduced into CA4 to replace the double bond without losing the *cis*-olefin configuration. The authors combined molecular mechanics, rigid docking and molecular dynamics to investigate the interactions of a set of 1,5- and 1,2-diaryl-1*H*-imidazoles with the colchicine binding site. All the imidazole ligands showed the same orientation within the binding pocket, and the proposed binding models strongly resembled that proposed for CA4, with the A and C rings and the two carbon bridge of all ligands tightly superimposed each other. The TMP moieties were all located within the same hydrophobic pocket as the TMP ring of colchicine; their 4-methoxy groups were in hydrogen bond distance from the Cys β241 side chain and established favorable

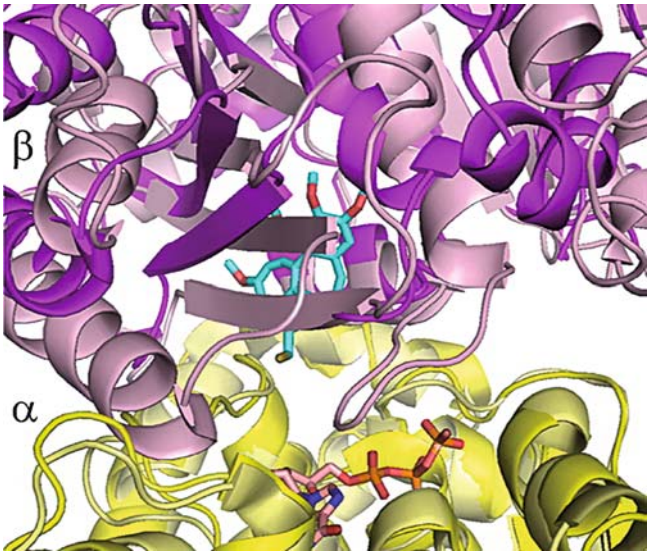

Fig. 2 Superposition of the straight (1TUB structure, *light colors*) and curved (1SA0 structure, *bright colors*) conformation of tubulin. As in Fig. 1, α- and β-tubulin are represented as yellow and magenta ribbons, respectively; DAMA-colchicine and GTP are still represented as *sticks*. In the straight conformation, the colchicine binding site is partially buried by secondary structure elements of β-tubulin and by residues of the α subunit. This is the structural reason accounting for the fact that the colchicine binding site can not properly be identified in the straight conformation and that curved tubulin cannot adopt a straight conformation when colchicine or another CSI is bound

hydrophobic interactions with Val β238, Leu β242, Leu β248, Ala β250, Leu β255 and Ala β354, constituting the hydrophobic pocket mentioned above. The C rings were found to favorably interact with the Asn β258 methylene and Ala β316 methyl groups, which are part of a large pocket also occupied by the C ring of colchicine. One of the most interesting ligands (**e1**, labelled as *2g* in [37]) involved the fluorine atom at position 3′ of the C ring in a hydrogen bond with the backbone NH of Val α181 (Chart 7).

In a study published by Barbier and co-workers, the X-ray structure of the tubulin-colchicine complex was used to establish a structure-activity relationship for a restricted set of 4-arylcoumarin analogues of CA4, (**f** in Chart 6) [36]. **f1** and **f2** showed an interesting activity, comparable to that of CA4, whereas compound **f3**, despite the close structural similarity, was found completely inactive. Complexes were generated by simple superposition of ligands on colchicine in the colchicine binding site, resulting in the location of the A ring 7-methoxy group of arylcoumarins, which was superimposed on the TMP moiety of DAMA colchicine, in front of Cys β241 (Chart 7). The C rings at the opposite end of ligands, although located in a similar region of the binding site, showed a very poor overlap. The authors highlighted the relevance of hydrogen bond interactions between the ligands under analysis (and, more generally, all CSI) and two residues of the tubulin subunit

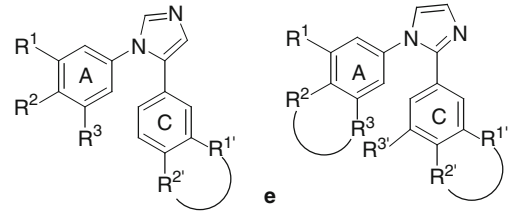

e1: R^1=R^2=R^3=$R^{2'}$=OMe
$R^{1'}$=F

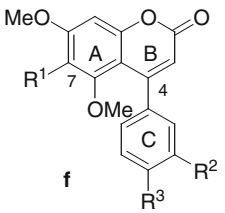

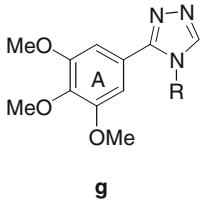

f1: R^1=H, R^2=OH, R^3=OMe
f2: R^1=OMe, R^2=OH, R^3=OMe
f3: R^1=OMe, R^2=OMe, R^3=OH

g1: R=*N*-CH_3-indol-5-yl

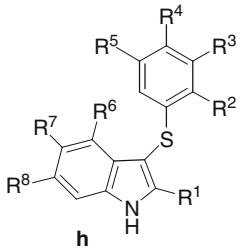

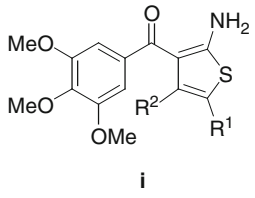

h1: R^1=COOEt,
R^2=R^6=R^8=H,
R^3=R^4=R^5=R^7=OMe

i1: R^1=*p*-F-C_6H_4, R^2=H

Chart 6 Representative structures of CSI used in different structure-based molecular modeling studies: imidazole-based (**e**), 4-arylcoumarin (**f**) and triazole-based (**g**) CA4 analogues; arylthioindoles (**h**) and benzoylthiophenes (**i**)

(namely, Thr α179 and Val α181) for the binding to the colchicine pocket. In fact, the carbonyl group of colchicine could form a hydrogen bond with the backbone NH of Val α181, whereas the hydroxy group at 3′ position of compounds **f1**, **f2** and CA4 could establish a hydrogen bond with the backbone carbonyl of Thr α179. The reasons for the inactivity of compound **f3** were not explicitly discussed, though they seemed to lie in the lack of a hydrogen bond donor group at 3′ position, that could prevent the ligand from establishing a key hydrogen bond interaction with the colchicine site.

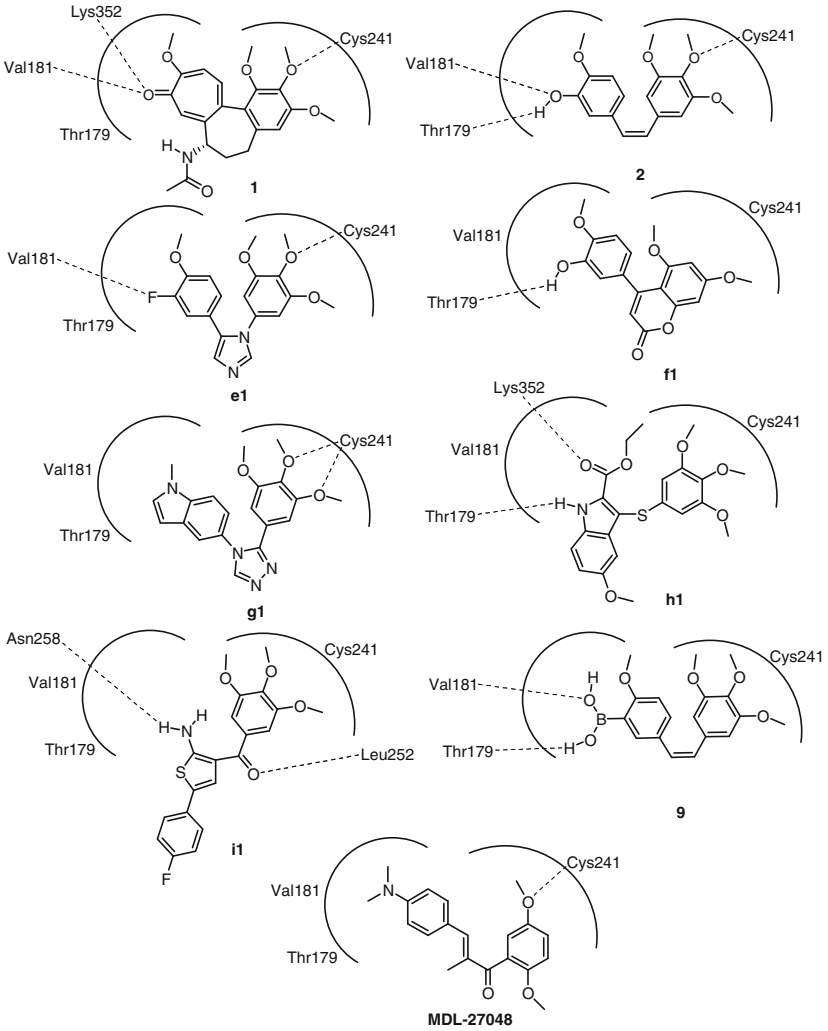

Chart 7 Schematic representation of the colchicines binding mode and of the binding models proposed for different classes of CSI on the basis of docking studies. The pocket embedding the A ring of colchicine is entirely located within the β-tubulin subunit, whereas the pocket interacting with the C ring consists of residues belonging to both α- and β-tubulin. All the hydrogen bond interactions proposed by different studies for colchicines and CA4 are displayed (see also Table 2)

A detailed analysis of interactions with the colchicine binding site was recently reported for a series of triazole-based analogues of CA4 (**g** in Chart 6), where the 1,2,4-triazole ring was selected to retain the *cis*-olefin configuration of the parent compound [41]. Docking and molecular dynamics simulations were performed on the most potent compound (**g1**, labelled as 7 in [39]) of the series to investigate its binding mode. Analysis of the resulting complex revealed that **g1** mostly interacted

with β-tubulin, but also some residues of the a subunit participated to the ligand binding. In detail, the TMP ring was embedded in the hydrophobic pocket occupied by the A ring of colchicine (van der Waals contact with Leu β248, Val β318, Thr β353 and Ile β378) and the methoxy oxygen atoms at position 3 and 4 resulted located at hydrogen bond distances from the SH group of Cys β241. The indole ring occupied a second hydrophobic region (bounded by Ala α180, Val α181, Lys β254, Asn β258, Met β259, Val β351 and Lys β352), whereas the triazole N2 atom was found to interact with the Lys β254 side chain.

In recent years [35, 42, 43], Silvestri and co-workers reported the synthesis and the biological evaluation of different series of arylthioindoles (whose general structure **h** is reported in Chart 6), as inhibitors of tubulin polymerization. The rationale behind the synthesis of such compounds was that the indole nucleus and the sulfur atom were separately contained in a large number of tubulin destabilizing agents, but no arylthioindoles had been reported to inhibit tubulin polymerization until then. Remarkably, several of the newly synthesized derivatives exhibited significant biological activities, and the trimethoxy substitution ($R^3 = R^4 = R^5 = OMe$) emerged as a key structural element. The binding model at the colchicine site, proposed on the basis of preliminary docking studies, involved the location of the TMP moiety in close contact with Cys β241, with an orientation very similar to that of the corresponding ring of DAMA-colchicine [42]. On the other edge of the molecule, the benzene ring of the indole nucleus occupied the same region of the tropone ring of colchicine, while the indole NH was found to establish a hydrogen bond with the backbone carbonyl of Thr α179.

This binding mode was partially revised by subsequent molecular modeling studies performed on a second series of arylthioindoles and involving both docking and molecular dynamics simulations [35]. In the new pose, exemplified by compound **h1**, the TMP moiety tightly overlapped with that of the previously proposed conformation in proximity to Cys β241, and the indole NH still established a hydrogen bond with Thr α179 (Chart 7). However, the indole ring was nearly flipped, thus directing the ester function at the opposite side with respect to the old pose, at hydrogen bond distance from Lys β352. The interaction with Cys β241 and the hydrogen bond with Thr α179 appeared crucial for binding, since a derivative unable to establish them was found (and predicted) to possess decreased biological activity. The same computational procedure was also applied to colchicine: the TMP ring resulted embedded within the hydrophobic pocket already described, establishing strong interactions with Leu β248 and Leu β255, while its methoxy group at C3 was in close proximity to Cys β241. The ligand was also engaged in two hydrogen bonds, the first between the carbonyl group of ring C and Lys β352, and the second between the amide NH group and Thr α179 (the same residues supposed to interact with arylthioindoles, as shown in Chart 7 and Table 2). However, during the simulation this hydrogen bond was lost and replaced by a similar interaction between the amide carbonyl group and the hydroxyl group of Ser α178.

The putative binding model of arylthioindoles described above was further confirmed by docking simulations on a third series of compounds synthesized by the same group [43].

Docking simulations were also performed to explore the possible binding modes for a series of 2-amino-3-(3′,4′,5′-trimethoxybenzoyl)-thiophenes (**i** in Chart 6), reported in 2006 as a novel class of CSI [44]. The most active compound of the series, namely **i1**, was docked into the colchicine site of tubulin (1SA0 structure) and its orientation was compared to that of DAMA-colchicine. The TMP moiety of the ligand superimposed well on the corresponding ring of the reference compound and shared with it the same hydrophobic pocket. Interestingly, the other molecular edge was directed at the opposite side of the binding pocket with respect to the C ring of DAMA-colchicine (up to interact with Gln α11), in a region that has been poorly involved so far in the binding of CSI. The complex was stabilized by two hydrogen bonds between the C2 amino group and the Asn β258 side chain, and between the carbonyl group and the backbone NH of Leu β252 (Chart 7).

As anticipated, the crystallographic structure of the colchicine binding site was also used for the in silico evaluation and rational design of novel CSI. In 2005, Brown and co-workers reported the discovery of a boronic acid bioisostere of CA4 by means of structure-based molecular modeling studies [37]. Using the 1SA0 structure as template, the authors initially proposed a potential binding model for CA4 and compared it with the pose of the co-crystallized DAMA-colchicine. As a result, the binding modes of the two agents were found very similar, in good agreement with the alignments proposed by ligand- and structure-based approaches previously described [31, 33, 40]. In fact, both TMP and phenyl rings in the putative binding model of CA4 adopted an orientation very similar to that of the A and C rings of DAMA-colchicine, respectively, and the position of the methoxy substituent on ring C closely resembled that of the corresponding group of the reference compound. The hydroxy group of CA4 was located in close proximity to the carbonyl oxygen of colchicine, both groups being able to form a hydrogen bond with the backbone NH of Val α181. Moreover, the hydroxy group of CA4 was involved in a second hydrogen bond with the backbone carbonyl of Thr α179, though with a sub-optimal geometry in terms of distance. Subsequently, structure-based modeling was also used to hypothesize that a boronic acid moiety could mimic the 3′-hydroxy group of CA4 very well. More precisely, docking analysis of the 3′-substituted boronic acid bioisostere of CA4 (**9** in Chart 8) suggested a binding mode analogous to that described above for CA4, with one of the hydroxy groups of the boronic acid located in a position very similar to that of the hydroxy group of CA4 and still able

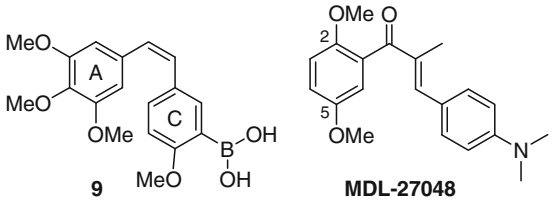

Chart 8 Chemical structures of the CA4 boronic acid bioisostere (**9**) and of MDL-27048. The former was proposed by a structure-based molecular modeling study, the latter was used to elaborate a virtual screening protocol for the identification of novel chalcone CSI

to establish a hydrogen bond with the backbone NH of Val α181 (Chart 7). The second hydroxy group of the boronic acid formed a hydrogen bond with the backbone carbonyl of Thr α179. Taken together, modeling studies suggested that **9** could be a potent CSI, and these findings were actually confirmed by biological assays, in which **9** exhibited a potency comparable to CA4, thus representing a new class of potent CA4 analogues.

An interesting structure-based molecular modeling approach for the design of novel CSI was described in 2006 by Seong and co-workers [39]. Authors proposed a binding model for the chalcone derivative MDL-27048 (a competitive inhibitor for colchicine and podophyllotoxin, Chart 8) and applied the model for the design of novel antimitotic agents. Binding of MDL-27048 to the colchicine site, as resulting from docking experiments, involved several amino acid residues, mostly through van der Waals interactions, similarly to colchicine and podophyllotoxin. In detail, the 2,5-dimethoxyphenyl moiety was placed in the hydrophobic pocket occupied by the TMP ring of colchicine, in contact with residues Cys β241, Leu β242, Leu β248, Ala β250, Leu β255, Ala β316, Val β318, and Ile β378. On the other hand, the 4′-dimethylamino phenyl moiety was located in the same region as

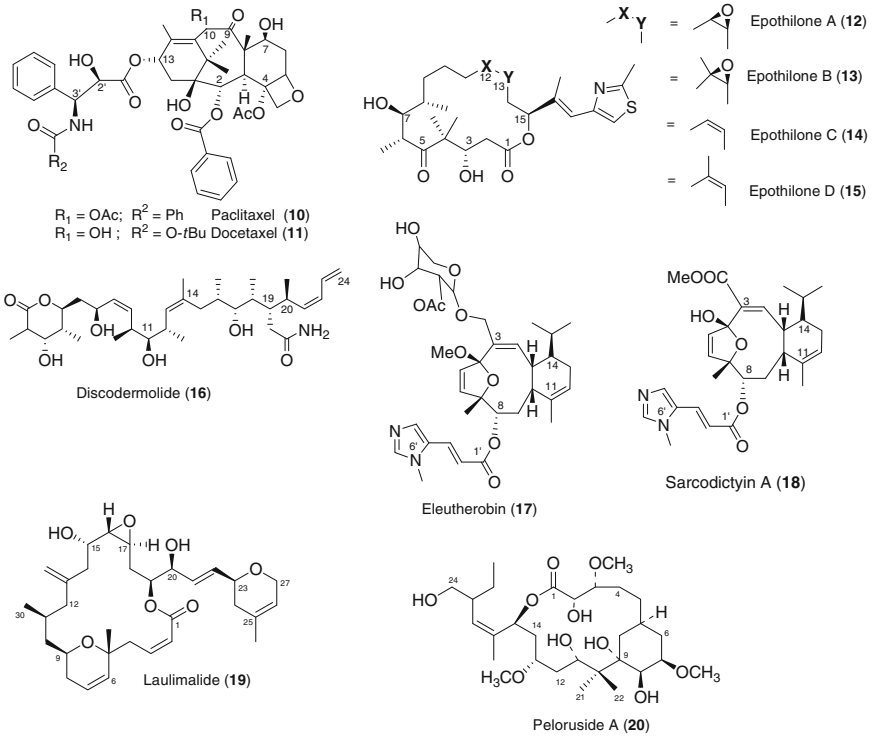

Chart 9 Schematic representation of the principal microtubule stabilizing agents (MSAA): paclitaxel (**10**) and docetaxel (**11**), epothilones A–D (**12–15**), discodermolide (**16**), eleutherobin (**17**) and sarcodictyin (**18**), laulimalide (**19**) and peloruside A (**20**)

the tropone ring of colchicine, interacting with Met β259, Ala β316, and with the alkyl portion of the Lys β352 side chain. The C5-methoxy group corresponded to the C2-methoxy substituent of the A ring of colchicine, and likewise established a polar interaction with Cys β241 (Chart 7 and Table 2). The binding model proposed for MDL-27084 properly matched a simple pharmacophoric model derived from the analysis of colchicine and podophyllotoxin interactions with tubulin (1SA0 and 1SA1 structures, respectively), consisting of two hydrophobic centers and one polar interaction site. The hydrophobic features of the pharmacophore corresponded to the A and C rings of the template ligands, while the polar interaction feature represented the interaction between the C2-oxygen of the A ring of colchicine and Cys β241. The analysis of complexes between tubulin and MDL-27084, colchicine and podophyllotoxin revealed the presence of an additional cavity within the colchicine binding site, mainly defined by residues Val β238, Leu β242 and Leu β255. The proposed pharmacophore was combined with such receptor shape information and used for the virtual screening of a 3D small molecule database consisting of 9720 chalcone compounds. The screening resulted in the selection of 24 candidates, among which 5 interesting agents emerged. Interestingly, a proper fit into the additional binding pocket emerged as crucial in modulating the activity of chalcones under study, the most potent compounds being characterized by a more thorough occupation of this region. These findings led the authors to suggest that for the design of novel CSI careful consideration should be given to the size of the moiety fitting the newly identified binding pocket.

Both ligand- and structure-based studies described here give an idea of the wide structural variety which characterizes CSI. As anticipated above, this aspect arises the crucial question what are the essential molecular determinants for binding to the colchicine site and thus what are the relevant interactions accounting for the activity of microtubule destabilizing agents. The most important attempt to answer this question has been made by Nguyen and co-workers, who used the X-ray structure of the tubulin–colchicine complex to determine the binding models for a set of structurally different CSI. From such models they derived a common, structure-based pharmacophore which delineated the key structural and functional features for inhibition [38]. This work is reported at the end of this section as a sort of summary, since differently from most studies in this field, it involved a number of structurally diverse CSI and identified most of the molecular features and interactions separately described by the studies previously reported.

Authors selected a representative set of fifteen CSI, including colchicine, podophyllotoxin and CA4, and proposed a binding model for all of them, using the crystallographic structures of colchicine and podophyllotoxin bound to tubulin as templates. Analysis of putative binding models revealed that all CSI were characterized by a biplanar conformation and occupied a similar space within the colchicine site, the TMP moieties being buried in the β-tubulin subunit. The binding mode proposed for CA4 was very similar to that of colchicine, with the TMP and phenyl rings of the former closely overlapped to the A and C rings of the latter.

The binding models of the 15 ligands were used to derive a 7-point pharmacophore connecting the different structural classes of CSI, based on consistent structural features and recurring tubulin–ligand interactions. As shown in Fig. 3a, the common

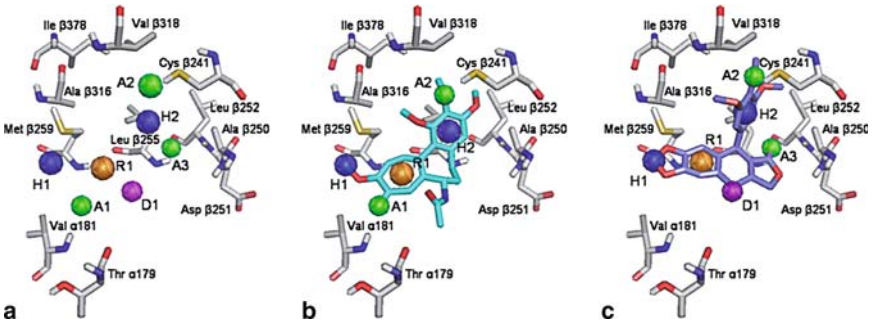

Fig. 3a,b Common seven-point pharmacophore for CSI. **a** Pharmacophoric points within the colchicine binding site together with the most important residues involved in interactions with them. **b** Colchicine is able to map five features, while podophyllotoxin (**c**) matches six points. The figure has been generated from the 1SA0 and 1SA1 structures of PDB, using the information provided by the paper of Nguyen and co-workers [38]

pharmacophore consisted of three hydrogen bond acceptors (labelled as A1, A2 and A3), one hydrogen bond donor (D1), two hydrophobic centers (H1 and H2) and one planar group (R1). H2 and R1 points represented the rigid portion of the molecular scaffold, while features A1, A2, A3, D1 and H1 represented critical interactions with the protein (Figs. 4b and 4c), thus being responsible for binding specificity. Due to their very high frequency in all binding models, A2, H1, H2, and R1 emerged as essential features for inhibitory activity at the colchicine site. It should also be noted that, while all 15 CSI were characterized by 5 or 6 pharmacophoric points, none possessed all of them, suggesting that the discovery of more potent tubulin destabilizing agents could be a feasible task. Fig. 3 also displays the interactions of the pharmacophoric points with tubulin. The hydrophobic point H1 (usually corresponding to a methoxy carbon atom) was at van der Waals contact with the side chains of Val α181 and Met β259. H2 (often matched by the TMP ring) was located within the hydrophobic pocket interacting with the TMP moiety of colchicine and podophyllotoxin, and established hydrophobic contacts with the side chains of Leu β255, Ala β316, Val β318 and Ile β378. The planar group feature R1 was embedded into a second hydrophobic pocket in correspondence of ring C of colchicine and podophyllotoxin. Hydrogen bond acceptor and donor points represented hydrogen bonds with the backbone NH of Val α181 (A1), SH of Cys β241 (A2), backbone NH of either Ala β250, Asp β251 or Leu β252 (A3), carbonyl backbone of Thr α179 (D1).

Most of the interactions codified by the seven-point pharmacophore were consistent with those found to be involved in the binding of CSI by the studies described above, thus confirming the key role they are expected to play in determining the potency of this class of antimitotic drugs. Finally, it should be emphasized that, besides constituting an important contribution to the understanding of interactions relevant to the binding process, this study also provided valuable insights for the rational design and modification of tubulin destabilizing agents targeting the colchicine site.

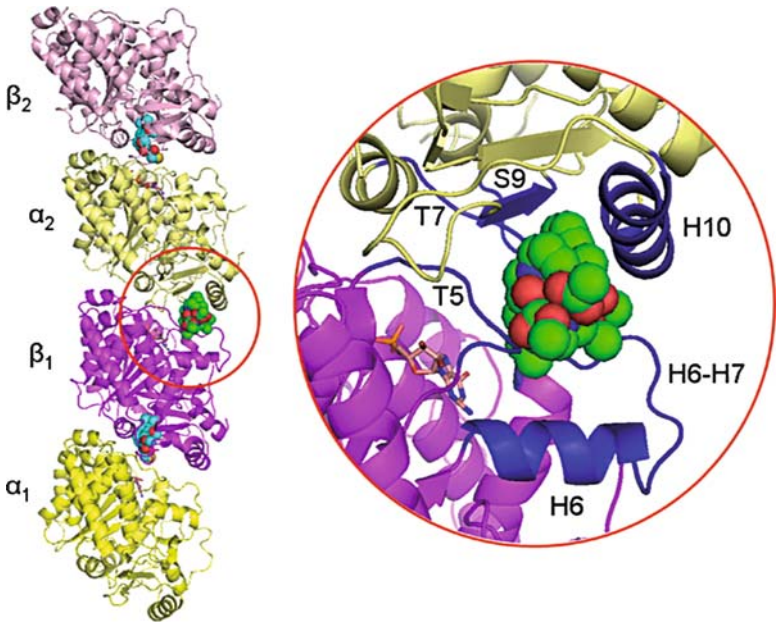

Fig. 4 *Left*, location of the vinblastine and colchicine binding sites in tubulin (1Z2B structure). α- and β-tubulin are represented as *yellow and magenta ribbons*, respectively; vinblastine and DAMA-colchicine are represented as *green and cyan spheres*, respectively; GTP and GDP are represented as *pink sticks*. Vinblastine binds at the interdimer interface, whereas colchicine binds at the intradimer interface. *Right*, zoom on the vinblastine binding site. Secondary structure elements contacting vinblastine are *colored blue*

1.2 Molecular Modeling on Compounds Targeting the Vinca Alkaloid Binding Site

Vinblastine (**4** in Chart 1) and its congeners are dimeric indole alkaloids derived from *Catharanthus (Vinca) roseus*. Nowadays, the vinca alkaloids constitute an important class of widely and successfully used anticancer agents that inhibit tubulin polymerization [8].

The exact binding site of vinca alkaloids remained unknown until 2005, when the crystal structure of vinblastine bound to tubulin complexed with colchicine and with the stathmin-like domain of RB3 was determined (PDB entry: 1Z2B) [3]. The structure revealed that vinblastine binds to curved tubulin at the interface between two α/β-tubulin heterodimers (interdimer interface, Fig. 4), introducing a wedge that interferes with tubulin assembly. The vinblastine binding site is defined by loop T7, helix H10 and strand S9 in the α subunit of the first heterodimer, and by helix H6 and loops T5 and H6–H7 in the β subunit of the second heterodimer. In microtubules, this region is located toward the inner lumen and is

involved in longitudinal contacts between protofilaments. Vinblastine interacts to a similar extent with both tubulin heterodimers and it is oriented so that both its catharanthine and vindoline moieties are in contact with them. It is worth noting that, differently from the colchicine (and also paclitaxel) binding site, which are mainly embedded within a tubulin heterodimer, the vinca alkaloid site is located between two different heterodimers. However, despite binding at a different site with respect to colchicine, vinblastine as well introduces curvature into tubulin and tubulin assemblies whose final outcome is the inhibition of tubulin polymerization to microtubules.

The number of molecular modeling studies on vinca domain inhibitors is extremely restricted, presumably due to the high structural complexity of such compounds. To the best of our knowledge, the only modeling studies reported in this field focused on the localization of the binding site of antimitotic peptides and depsipeptides targeting the peptide site of the vinca domain [47].

A combination of molecular dynamics simulations and docking experiments was used by Sept and Mitra to identify the tubulin binding site for peptides cryptophycin 1, cryptophycin 52, dolastatin 10, hemiasterlin and phomosin A, all targeting the vinca domain [48]. These compounds exhibited mutual competitive inhibition in binding to β-tubulin, while noncompetitively inhibiting the binding of vinblastine and vincristine. Molecular dynamics simulations were first performed on the 1JFF structure [49], extracting representative conformations of β-tubulin at regular intervals to capture the flexibility of the protein. Blind docking experiments were then carried out for all peptides under analysis on all sampled structures, resulting in the identification of a consensus high-affinity site in β-tubulin, bounded by residues Ser β174, Lys β176, Val β177, Asp β179, Asn β206, Glu β207, Tyr β210, Asp β211, Phe β214, Pro β222 and Tyr β224. Interestingly, a similar result has been obtained a few years before also by Barbier and co-workers, who used molecular modeling tools to identify a putative binding site for cryptophycin 52 on tubulin [50]. Docking experiments in this case were focused on a specific region of the 1TUB [46] heterodimer (not on the entire macromolecule), and located the synthetic peptide in a binding pocket containing residues 206–227 of β-tubulin. The identification of a common binding site for all the peptides was in good agreement with experimental data, showing that the compounds competitively inhibited each other. Further, this binding site also accounted for the observed resistance to some vinca domain drugs associated with the Ser172Ala point mutation, since docking experiments on the Ser172Ala mutant tubulin indicated a significant decrease of affinity toward the proposed binding site. Figure 5 displays the residues supposed to be involved in the binding of peptides relative to the vinblastine binding site (1Z2B structure). It can be seen that the predicted binding pocket for peptides was located at the interface with α-tubulin, similarly to the vinblastine site. As hypothesized by the authors, the binding of peptides to β-tubulin could interfere with the addition of tubulin heterodimers at the end of straight protofilaments due to steric clashes, or could induce a curvature in the protofilaments with consequent loss of lateral interactions and, ultimately, microtubule destabilization.

2 Molecular Modeling on Microtubule Stabilizing Agents

Microtubule stabilizing (Chart 9) antimitotic agents (MSAA) interact with tubulin with a peculiar mechanism of action, different from that of microtubule destabilizing agents. MSAA are often referred to as mitotic spindle poisons, because of their ability to block cells during the mitosis process [51]. The class of stabilizing agents collects molecules with a very different chemical structure, and all of them are natural compounds or semi-synthetic derivatives. The first compound found to stabilize microtubules was paclitaxel (**10**, PTX, Taxol®). In the early 1960s, the antileukemic and cytotoxic activity of taxus (*Taxus brevifolia*) extracts were reported [52], and in 1979 Horwitz discovered the mechanism of action of paclitaxel consisting in promoting tubulin assembly in microtubules [53]. The paclitaxel binding site was identified in a specific location on the β-subunit of tubulin dimer.

After the identification of the paclitaxel mechanism of action, several additional microtubule stabilizing agents were discovered from natural sources (Chart 9). Among them, epothilones (**12**–**15**) are the most studied and characterized. Epothilones A and B (**12**, **13**) were first isolated by Höfle and coworkers [54] from a myxobacterium (*Sorangium cellulosum* strain 90) in 1993, while their activity in stabilizing microtubule similarly to paclitaxel was reported for the first time by Bollag and co-workers in 1995 [55]. Experiments with radio-labeled paclitaxel

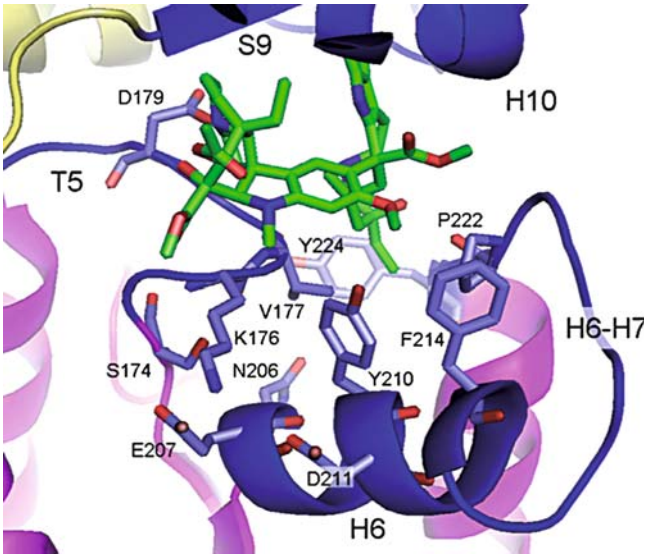

Fig. 5 Interaction of antimitotic peptides and depsipeptides with the vinca domain with respect to the vinblastine binding site (1Z2B structure). Residues supposed to interact with the peptides are represented as *blue sticks*, vinblastine is represented as *green sticks*. Tubulin ribbons are *colored* as in Fig. 4

confirmed that both molecular classes compete for the same binding site in the β-tubulin subunit. In 1996, discodermolide (**16**) was isolated from a marine sponge (*Discodermia dissoluta*) and it was found to act with a mechanism of action similar to paclitaxel [56], being more potent at nucleating tubulin assembly [57]. Other classes of stabilizing agents were isolated from different marine species. Eleutherobins (**17**) were extracted from a soft coral from Indian Ocean (gen. *Eleutherobia*), while sarcodictyins (**18**) from a coral from Mediterranean sea (*Sarcodictyon roseum*) [58, 59]. Moreover, a marine sponge (*Cacospongia mycofijiensis*) from Pacific Ocean provided laulimalide (**19**). Finally, the last molecule to be identified with a similar mechanism of action was peloruside A (**20**), a secondary metabolite isolated from a New Zealand marine sponge (*Mycale hentscheli*). While sharing the same mechanism of action, all these molecules differ by pharmacological profile as well as relative potency against P-gp resistant cell lines [60].

The structures of most important MSAA are reported in Chart 9.

2.1 Molecular Modeling on Paclitaxel and Taxanes

Paclitaxel was object of intense investigations focused on its chemical properties (i.e., the structural complexity and the low water solubility), as well as the induced resistance acquired by some cell lines upon treatment [61–63] of different cancer types (mainly ovarian [64], breast [65] and lung [66] carcinomas). Activity of paclitaxel was proved to be related both to the baccatin core and to the side chains, with a major role played by the C–13 and C–2 benzoyl moieties. In particular, the baccatin scaffold was suggested to be involved in holding in place and correctly pointing substituents and chains [63]. Many theoretical (from molecular modeling to ab initio [67, 68]) and experimental (NMR, X-ray crystallography) structural studies were performed to explore the taxoid conformational space, in order to obtain information on the behavior of ligands into the binding cavity. The first experimental information on the 3D structure of taxoids and their conformations was obtained by X-ray diffraction of docetaxel (**2**) [69]. However, all the ligand-based approaches on taxanes were unable to clarify their binding mode. The NMR approaches as well as in silico conformational studies were found to be insufficient to account for possible conformations of taxanes because of numerous degrees of freedom associated to their side chains. Moreover, the mainly hydrophobic properties of the side chains influenced their conformational behavior in different solvents. All the NMR data for paclitaxel and docetaxel, indeed, led to the hypothesis of a single or few strongly dominant conformations [70]. Suc h conformations were obtained by application of a variant of restrained molecular dynamics (r-MD) [71, 72] to find results that satisfy experimental coupling constants. The most important conformations of paclitaxel proposed as bioactive (Chart 10) are referred to as: (1) *polar*: this conformation corresponds to the paclitaxel crystal structure [73] and was also obtained by NMR experiments performed in polar solvents [74, 75] – this conformation is characterized by hydrophobic interaction between the C–3′ phenyl group and the benzoyl

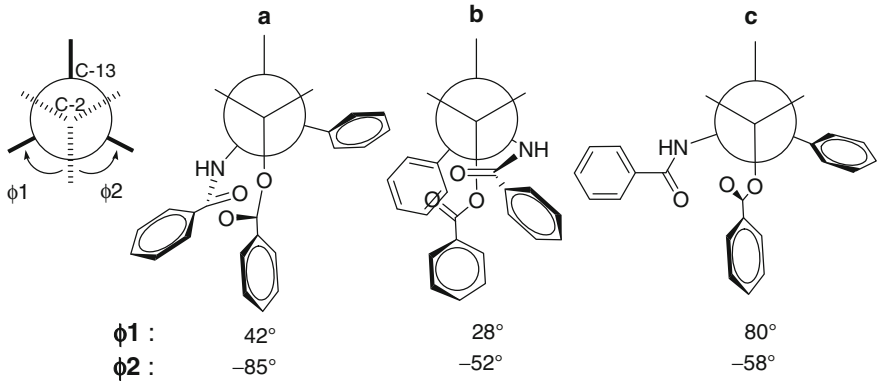

Chart 10 Three main paclitaxel conformations as reported by Snyder and co-workers: (**a**) polar conformation; (**b**) apolar conformation; (**c**) T-shape. The angles ϕ1 and ϕ2 correspond to the improper torsion angles O–C2–C3′-N(Bz) and O–C2–C3′–C(Ph), respectively

group at C–2; (2) *non-polar*: this conformation is found in the docetaxel crystal structure [76] and in NMR experiments performed in apolar solvents [77, 78] – in this conformation, apolar groups at the NH C–3′ apolar substituent are in close contact with the group at C–2 position; (3) *T-shape*: this conformation, also known as "butterfly structure" [79] is different from the previous ones because of the peculiar arrangement of the two C–3′ apolar substituents lying approximately at same distance from the C–2 benzoyl group, which is placed between of them (therefore the T-like shape).

Aromatic groups are suggested to interact with each other: both polar and non-polar conformation, indeed, can undergo to hydrophobic collapse of C2 and one of C3′- phenyl rings [70].

The T-shape conformation was initially hypothesized as one of the possible paclitaxel conformations in chloroform, obtained by clusterization of a Monte Carlo conformational search [36], but no ultimate conclusion about the bioactive form could be obtained solely from the ligand-based studies. Eventually, this conformation was identified as the most promising one to fit into the electron crystallography (EC) density map of paxlitaxel-bound structure [79].

In 1994, Erickson and co-workers [80] performed a 2 ns molecular dynamics (MD) simulation combined with NOE data [70, 71], investigating the conformational space of paclitaxel. Using the Discovery software [81], the Feedback-Restrained MD (FRMD) protocol was designed, implementing a multistage simulated annealing composed by a short heating stage (from 50 to 2000 K), a main restrained MD (NOE armonic restraints), and a short cooling stage (from 2000 to 50 K). The two most representative conformations were identified by the alignment of the C–13 chain with respect of the baccatin core, referred to as CI and CII. The former was a quasi-linear conformation stabilized by a hydrogen bond between the 2′–OH and the 3′-amide carbonyl oxygen atom, and believed to be the most similar to the binding conformation. In the latter, the 2′–OH

interacted by hydrogen bond with the 4-OAc oxygen atom, in a collapsed form preferred in solution state.

When more paclitaxel derivatives were available, it was possible to apply QSAR approaches. On the basis of conformational studies and biological data, in 1999 Snyder and co-workers, designed a semi-qualitative model [82] applying the minireceptor approach [83]. A series of 12 paclitaxel derivatives were overlapped in the non-polar conformation, forming the template on which the model was built. This template (also referred to as a training set) also included several epothilone derivatives, recently reported at that time. The low energy conformation of epothilone B (**13**), obtained from a Monte Carlo conformational search in water as the solvent, was used to model all the epothilone derivatives, which were in turn aligned on paclitaxel structure by a steric and electrostatic alignment approach (SEAL [34]). By means of PrGen software [83], the QSAR minireceptor model was built around the training set, surrounding it by 20 aminoacids selected from photoaffinity labeling data [84, 85]. Biological data necessary to build the model were obtained adapting different biological data from literature [82]. A further set of molecules constituted the test set on which predictivity of the QSAR model was tested. Both training and test set comprised a total of 26 taxanes and epothilones. Accordingly to the minireceptor protocol [83], the ligand–amino acids complex was optimized with a multistep equilibration process, to maximize the correlation function between biological data and 3D structural information of the model. The resulting model provided a good correlation ($r = 0.99$) and a low ΔG rms (0.2 kcal mol^{-1}), with good predictive results toward the test set. It was also able to account for many of SAR data available at that time. Essentially, the model aligned the two molecular cores in such a way as the epoxide ring of epothilones overlapped the oxetane ring of paclitaxel, while the thiazole ring of epothilones matches the C–2′ phenyl ring on the C–13 chain of paclitaxel.

In the same year, the team of Viterbo and co-workers [68] performed a conformational study on the C–13 side chain, by employing Hartree-Fock ab initio and PM3 semiemipirical calculations, evaluating both aqueous and non-aqueous solution conformations previously reported [75]. The apolar gas-phase conformation was found to be in agreement with the NMR and molecular mechanics data [75], and compatible with the recently reported structure from electron crystallography [46]. Stabilization of that conformation was ascribed to a potential hydrogen bond between NH and OH groups on the C–13, as well as the minimization of the steric repulsions, while the C3′ bulky hydrophobic group (i.e., the phenyl of paclitaxel **10** and *t*-butyl of docetaxel **11**) lies between the polar groups on the remaining part of side chain and the apolar solvent molecules.

2.1.1 The First Electron Crystallography Structure of α,β-Tubulin/ Paclitaxel Complex

A great step forward was made in 1999 when Nogales and co-workers published the first structure of the complex between paclitaxel and tubulin heterodimer, obtained by EC [46]. On this basis, the interactions between the ligand molecule

and the protein receptor could be investigated with sufficient level of detail. In spite of the insight in clarifying the molecular complementarity and alignment of paclitaxel in respect to the binding site, this model suffered from a series of limitations admitting a certain degree of uncertainty about fine details. The major limitation was the low resolution (3.7 Å) of the structure. Another issue was the presence of docetaxel (**11**) in place of paclitaxel **(10)**. In fact, docetaxel was not determined by experimental methods, but was obtained by fitting the crystal structure of docetaxel directly into the electron density of paclitaxel [46]. Therefore, many research groups designed computational protocols to refine structural data from the EC model, in particular to identify the exact conformation of the bound ligand [79, 80, 86, 87] by also analyzing various bridged paclitaxel derivatives [76, 88–91].

In 2001, Snyder and co-workers performed molecular modeling simulations combining the experimental data available at that time on the paclitaxel conformation, and the EC density data of the tubulin structure [79]. A set of paclitaxel conformers derived from X-ray crystal structures, NOE data and a large number of computer-generated conformers of paclitaxel and derivatives [74, 75, 77, 78, 92–96] were fitted into the ligand EC density map of protein complex. This conformer ensemble included the polar and non-polar conformations. The most promising pose was refined within the protein coordinates reported in the structure deposited at the Brookhaven Protein Data Bank entry 1TUB [61] by restricted low-temperature MD and force-field optimization to fit within the experimental density. The final result provided evidence that the T-shape conformation was the most reliable to fit into the density map, confirming the stabilizing role of the Hisβ229 [46, 79] (accordingly to the 1JFF residue number) placed among the two aromatic C–2 benzoyl and C–3′ benzamido groups (Chart 11). As a protocol validation, a random conformation of paclitaxel was docked by the DOCK program [97] into the binding pocket, obtaining a lowest energy conformation very close to the T-shape. The model proposed that the ligand–protein complex involves hydrophobic interactions and hydrogen bonds, identifying residues accountable for ligand stabilization.

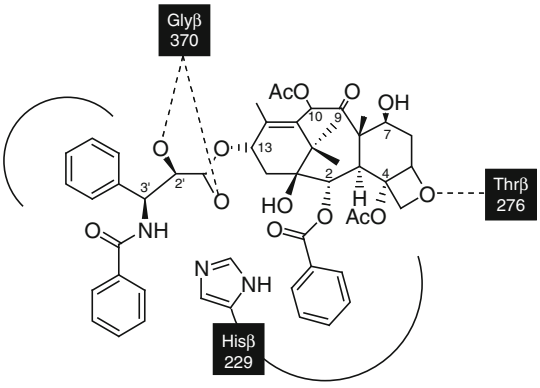

Chart 11 Potential interaction pattern of PTX in the β-tubulin binding site. *Dashed lines* represent potential hydrogen bonds between the ligand and the protein residues [46]

The 3′-benzamido, 3′-phenyl and 2-benzoyl groups engaged corresponding hydrophobic pockets formed by helices H1, H6, H7, and the loop between H6 and H7. The C–4 acetate was placed in a relatively large cleft formed by hydrophobic residues (Leuβ230, Alaβ233, Pheβ272, Proβ274, Thrβ276, Leuβ286, Leuβ291, Proβ360, Leuβ371, and Serβ374). The baccatin core interacted with Proβ360 and Leuβ371 of the B9–B10 loop.

2.1.2 The Oxetane Issue

In the past years, the role of the oxetane ring of paclitaxel has been the object of debate and different hypotheses were proposed to account for biological data which were sometimes in apparent contradiction. Due to uncertainty related to the low resolution of the EC model, modeling studies played a major role in investigating the influence on activity of this peculiar chemical moiety of paclitaxel. Before the availability of reliable atomic coordinates of paclitaxel–tubulin complex, the oxetane oxygen was considered as a main feature in the very first minireceptor model [82] because of its ability to be a hydrogen bond acceptor in the QSAR model. Experimental data proved that the oxetane oxygen is able to engage hydrogen bonds with both acetone solvent molecule and C–3′ hydroxy group of another paclitaxel molecule when packed in the solid state crystal [98]. But in the first tubulin structure (1TUB) [46], solved at 3.7 Å, the oxetane ring was located in a very unfavorable position with respect to the Thrβ276, with its oxygen atom at 4.6 Å from the backbone nitrogen. Molecular modeling simulation performed by Snyder and co-workers [99] on this structure led to the conclusion that the role of this ring could be considered as marginal in the overall binding of the baccatin core into the receptor cavity. According to the docking results on compound **21** (Chart 12), its main function is limited to rigidify conformation of remaining rings in the baccatin macrocycle, correctly pointing the C–2, C–4 and C–3′ side chains toward receptor surface [99]. Docking calculations of compounds bearing NH (**22**) or sulfur (**23**) atoms in place of the hydrogen bond acceptor oxygen (Chart 12) showed no significant differences in the predicted binding mode, but these compounds were found to be inactive. Estimation of both binding and solvation energies and QSAR minireceptor model predictions seemed to suggest that the presence of the oxygen atom does not favor the interaction with tubulin. Moreover, considering that the substitution of the oxetane with a cyclopropane ring led to a compound as active as paclitaxel [100], it may be summarized that the oxetane ring could contribute profitably to the interactions of a ligand with tubulin, while it is not absolutely required. Limitations of the minireceptor model required further modifications [99, 101] to compensate the errors in activity estimation of oxetane-derivatives and a series of D-seco paclitaxel analogues (**24–26**).

Derivatives designed to lack the oxetane by opening the D ring, indeed, led to an increased unfavorable steric hindrance between ligands and protein, that minireceptor was not able to account for, overestimating their activities. This steric effect was included in the minireceptor by means of the implementation of additional

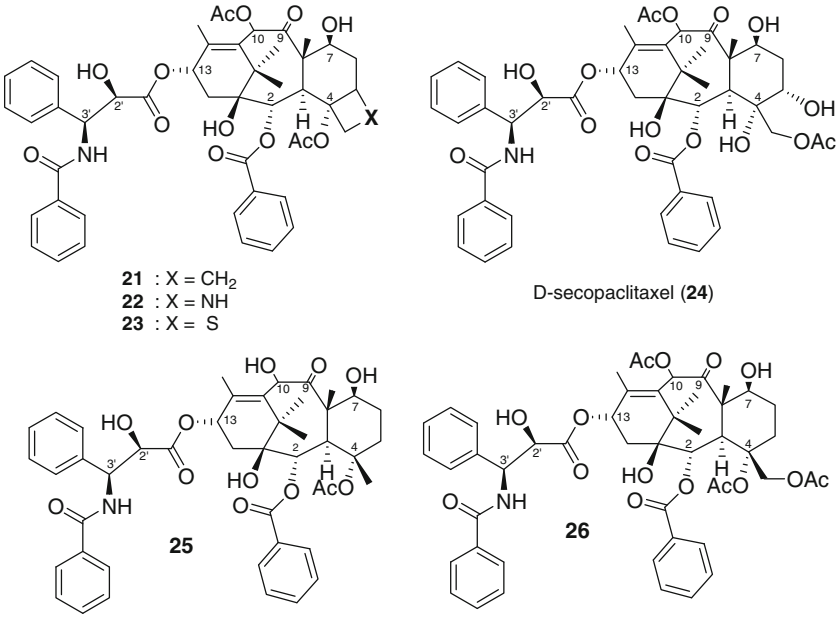

Chart 12 D-ring modified and D-secopaclitaxel derivatives investigated by Snyder and co-workers [98]

aminoacids in the region responsible for the overestimation. Results from MD simulations performed in the refinement suggested that the C–4 acetyl group could also play an important role in stabilizing the overall baccatin core.

In 2000, Zamir and Wu investigated on the binding mode of other D-seco analogues, taxuspine D and derivatives [75], a series of paclitaxel-like structures lacking both the D ring and the C–13 side chain (Chart 13). They determined that not only was the paclitaxel C–13 side chain not essential, but also that oxetane D ring could be replaced by opportune side chain, leading to a slight decrease of activity

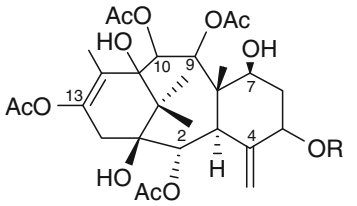

27 : R= CO-C=CHPh (Taxuspine D)

28 : R= H(Decinnamoyltaxuspine D)

29 : R= CO-CH=C[$(CH_2)_9$-Ph]-Ph

Chart 13 Taxuspine D and derivatives investigated by Zamir and co-workers

of tubulin polymerization [102]. The β-tubulin subunit from the 3.7 Å resolution dimer structure [46] was used as the starting point for docking calculations. Complex between the β-subunit and docetaxel was refined by a progressive relaxing protocol in explicit solvent model with the Discovery/InsightII suite [81]. The bound docetaxel (**11**) conformation from the final structure was used as template to build taxuspine D (**27**), 5-decinnamoyltaxuspine D (**28**), and a novel compound (**29**). These molecules were rigidly docked by means of DOCK, together with paclitaxel (**10**) as reference.

Complexes with the best intermolecular energy scores were chosen for further flexible refinement by MD simulations, using the Discovery software, allowing all the residues within 10 Å from the ligand to move freely. The simulation was performed for 6 ps at 350 K. As a result of calculations, the 5-cinnamoyl side chain of taxuspine D (**27**) should mimic the C–13 side chain of paclitaxel, resulting in a completely different alignment with respect to the baccatin core. The structural effect of oxetane D ring could be replaced by the C–12–C–13 double bond. The interaction energy trend derived from this alignment was in agreement with the biological activity, decreasing from paclitaxel to taxuspine D and 5-decinnamoyltaxuspine D.

At present, the controversial role of the oxetane in taxanes is considered not to be so essential as supposed in the past, due to the increase in biological data availability for paclitaxel derivatives, especially taxuspine and derivatives lacking this feature. Its main role is suggested to be the structural effect exerted in defining the bioactive conformation and the arrangement of the baccatin core, while an electrostatic effect could not be excluded.

2.1.3 The Paclitaxel Binding Mode

In 2001, Nogales and co-workers published a refined model of paclitaxel/tubulin complex [49], raising the resolution to 3.5 Å and reporting the conformation of paclitaxel bound in the binding site, allowing better identification of residues involved in interactions stabilizing the complex. Paclitaxel binds to microtubules (but does not bind strongly to heterodimers [103, 104]) in proximity of H1, H7 and H9 helices, B9 and B10 sheets and the loop connecting strands B9–B10 and M loop, stabilizing lateral contacts between protofilaments (Fig. 6). Moreover, it also influences the GTP binding by interacting with H7: paclitaxel binding induces structural changes to the protein domains which result in destabilizing the GTP hydrolysis [105].

The C–2 benzoyl group is stabilized within the hydrophobic pocket by a ring stacking with the Hisβ229 side chain. This refined model suggests that the backbone NH of Glyβ370 (B9–B10 loop) makes a hydrogen bond with the 2 –OH, in place of the Argβ369. The oxetane D ring is close to Thrβ276 in a more favorable position to establish a hydrogen bond interaction. The distance found between the oxygen and the NH group of the amino acid is reduced to 2.92 Å [49], and aminoacid backbone is oriented in a more favorable conformation with respect to the ligand oxygen. This allowed one to hypothesize that a hydrogen bond can likely

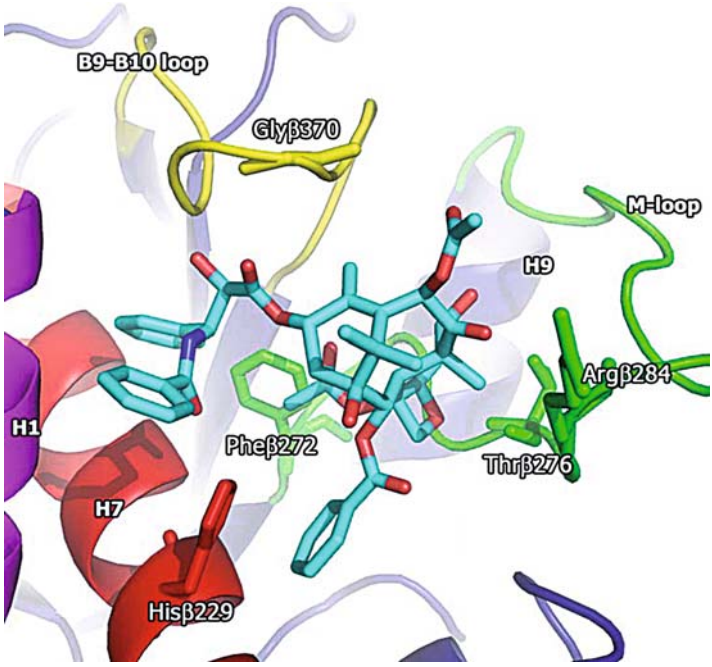

Fig. 6 Binding mode of paclitaxel into the refined structure of tubulin (entry 1JFF, from Nogales and co-workers [49]). *Magenta*: H1 helix; *red*: H7 helix; *yellow*: B9–B10 loop; *green*: M loop. Essential residues and paclitaxel are shown as *sticks*

occur and stabilize the molecule into the binding cavity. As a consequence of this alignment, the 7-hydroxy group, previously close to the Thrβ276, is now exposed to the solvent, accordingly to the SAR of taxanes suggesting that it is not involved in any direct interaction with the protein [106, 107].

To summarize, the paclitaxel and its derivatives was the first class of molecules showing the microtubule stabilizing activity. Due to this, all the initial efforts were focused on searching for information about the binding mode in order to rationalize the increasing amount of biological data. Initial efforts to identify the binding mode, as well as the possible binding conformation of paclitaxel, were unsuccessful until the first X-ray structure was available. This was due to both the structural complexity of the molecule and the conformational modifications induced by the interaction with the β-tubulin protein structure. The atomic resolution of the complex structure strongly simplified the rationalization of the structure-activity relationships, providing a strong experimental basis on which many computational simulations have been performed. Novel paclitaxel derivatives are now designed on the basis of the binding mode of paclitaxel and results are used to strongly increase the accuracy of model predictions.

2.2 Epothilones

The combination of structural simplicity of epothilones with respect to paclitaxel, together with their very interesting activity profile appealed different research teams, interested to overcome limitations of taxanes (poor solubility, multi drug-resistance – MDR [61–63]). Investigations on epothilones were focused on the interaction between the ligands and the paclitaxel binding site (as well as the possible similar portions between epothilones and taxanes) in order to find common pharmacopores to be used in activity improvement and design of novel molecules.

In 2001, Lee and Briggs performed a CoMFA study on a large set of epothilones and their polymerization activity data, obtaining a model for this class of compounds [108]. The model was built on 166 epothilone derivatives synthesized by Nicolaou et al. [109, 110], on which a conformational analysis has been performed. Since no information was available on the bioactive conformation of epothilones, the global minimum of epothilone B (**13**), the most active molecule of the entire set, was used as template. Remaining compounds were aligned on this conformation, with an automatic procedure (MCSG, Maximum Common Sub Group method [57]). Analysis of molecular interaction fields (MIFs) between ligands and a selected molecular probe has been applied to identify pharmacophoric regions of active molecules. In this work, authors have chosen the OH probe to describe epothilone molecular interactions and, in particular, to map hydrogen bond donor/acceptor properties of different derivatives. Once MIFs were calculated, a genetic function algorithm (GFA [81]) was used to sample descriptors and generate a multiple QSAR equation set. GFA is based on the iterative evolutionary refinement of models by means of a fitness function. After the generation of 4000 equations, the lack of fit (LOF) score on the biological activity was used as fitness function, that is the driving force to evolve toward the most predictive QSAR model. The best-scored QSAR equation presented good statistical properties, with a correlation coefficient R = 0.863, and an F value of 10.9.

The pharmacophore resulting from the model (Chart 14) identified two main regions responsible for the activity of epothilones, namely the thiazole ring region) and the C3–C5 portion in agreement with the work of Ojima et al. [51]. Besides, the model improves this pharmacophore by accounting for the contribution

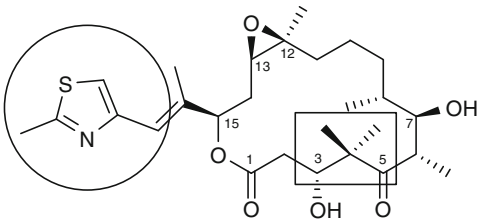

13

Chart 14 Essential regions responsible for epothilone activity on the structure of epothilone B, according to CoMFA results of Lee and Briggs [108]

of the epoxide ring to the activity, allowing rationalization of the difference of activity between epothilone A (**12**) and B (**13**).

2.3 Common Pharmacophores

Epothilones and taxanes share the same binding site, although their structural similarity is very low, being epothilones (**12**–**15**, Chart 9), 16-membered macrocyclic lactones. Many efforts have been made to build common pharmacophoric models able to find shared features among the two classes and to exploit the advantages related to epothilones (more affordable total synthesis approaches, activity toward MDR, higher solubility) which encouraged many efforts to find a common pharmacophore. The goal was to allow the rational design of novel hybrid derivatives, assuming that similar parts of the two molecular scaffold could overlap in some way. Initially, most of these efforts were focused on taxanes and epothilones, because of the high availability of derivatives and the corresponding amount of SAR data with respect to other MSAA. Nevertheless, derivatives did not sample uniformly modifications on all features of the entire scaffold, often focusing on the side chain or few chemical groups (i.e., epoxide region). This limitation was reduced during the years with the design of a large number of derivatives.

The first attempt to provide a common pharmacophore for taxanes and epothilones was made by Winkler and Axelsen [111] in 1996. Due to the complete lack of information about the SAR of epothilones recently discovered at that time, common portions were identified by search for steric and chemical similarity in the 3D conformational space of the two molecular classes. The resulting pharmacophore (Chart 15) proposed the following common regions between taxanes and epothilones. The C–2 benzoyl ring was superposed to the C–8–C–12 segment of epothilones; the C–13 side chain corresponded to the C–1–C–6 segment of epothilones; the C–10

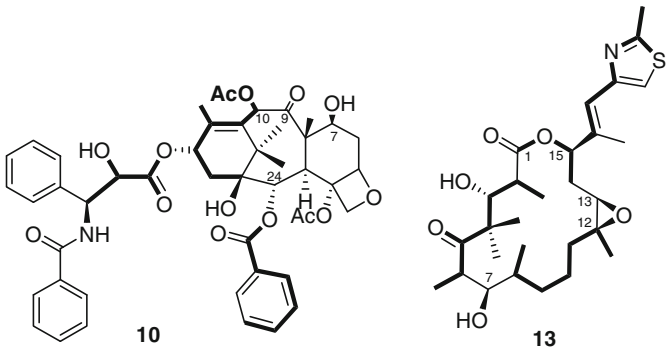

Chart 15 The first common pharmacophore proposed by Winkler and co-workers for taxanes and epothilones [111]

acetyl group was fitted to the C–15 thiazole ring. Due to activity retention of docetaxel lacking the C–10 acetyl group [46], the thiazole ring was then considered not essential, but eventual SAR confuted this assumption.

In 1999, Ojima et al. [51] proposed another pharmacophore model for taxanes, epothilones, eleutherobin and discodermolide on the basis of NMR conformational studies. The starting point to build the pharmacophore was a non-aromatic derivative of paclitaxel, nonantaxel (**30**, Chart 16), lacking the C–13 *N*-benzoylphenylisoserine and C–2 benzoyl ring. A distance-restrained conformational analysis (based on 2D-NOE spectroscopy results) of nonantaxel provided a low energy conformation as superimposition template. Low energy conformations of epothilone B, eleutherobin and discodermolide (obtained by sampling a 100 ps high temperature 1000 K MD simulation) were superposed on the template. The best fit criterion was the agreement with SAR data of the molecules (see Chart 16).

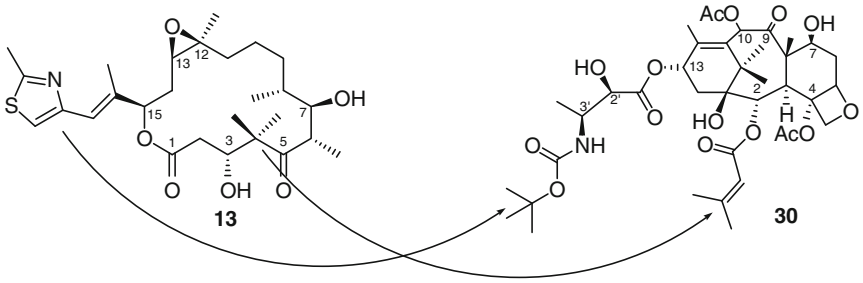

Chart 16 The common pharmacophore proposed by Ojima and co-workers, showing overlapping portions between epothilone B (**13**) and nonantaxel (**30**) [51]

The model recognized the thiazole ring as an essential feature for the activity, corresponding to the C–13 region of taxanes. As a consequence of the alignment, the epoxide ring points away from the superposed regions of the two molecules, in agreement with biological data reporting the better activity profile of 12,13-desoxy epothilone B (epothilone D) [112]. The C–3 hydroxy group of epothilone B was proposed as an important factor stabilizing the macrocyclic conformation by a hydrogen bond interaction with the C–1 carbonyl group [87].

The model also accounted for potential common regions between taxanes, discodermolide and eleutherobins that will be discussed further in the article (see Sects. 2.4.1 and 2.4.2, respectively).

In 2000, Giannakakou et al. [86] proposed another common pharmacophore for taxanes and epothilones, based on biological activity and resistance data related to β-tubulin mutations. In particular, the study focused on β276Thr->Ile, β284Arg->Gln and β272Phe->Val mutations, affecting both paclitaxel and epothilones ability to induce tubulin polymerization and inhibition of cell proliferation [113]. To identify patterns of epothilone to be superposed to taxanes, the authors sampled 100

low energy conformations from MD simulation. From the analysis of conformer population of epothilones, it was found that the centroid of 3–OH, 7–OH and 4-gem-dimethyl group is located at a stable mean distance (6.93 Å) from the epoxide oxygen atom. Therefore, this pattern was superposed to a similar pattern identified on paclitaxel, represented by the centroid of 1–OH, 9-carbonyl and 15-gem-dimethyl group and oxetane ring oxygen. Two epothilone conformations (Chart 17, a and b, respectively) were found to satisfy the pattern alignment, with a major difference on the thiazole ring placement. In the binding mode I, this portion corresponds to the C–2 benzoyl group, while in the binding mode II, it corresponds to the C–3′ phenyl ring.

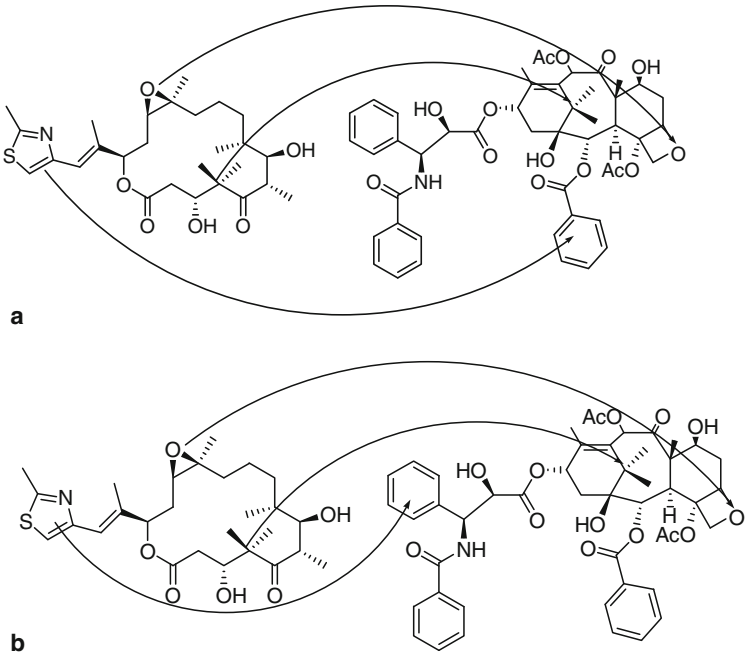

Chart 17 Two possible overlapping modes suggested by Giannakakou and co-workers: binding mode I (**a**) and binding mode II (**b**) [86]

According to this pharmacophore, epothilones were docked into the binding site of an energy-refined model of the tubulin EC coordinates [46]. Analysis of docking results allowed one to evaluate how single mutations affect the binding mode of ligands. The β284Arg->Gln mutation is located on the M loop and at that time was not believed to affect the binding directly. Remaining mutations were directly related to the interactions between residues and epothilones. In particular, accordingly to the model, the β276Thr->Ile was supposed to destabilize epothilone binding because of the disruption of a possible hydrogen bond network with 7–OH of epothilones. This hypothesis was further tested by simulations of interactions with explicit water molecules.

On the other hand, activity of epothilone derivatives bearing a pyridine ring instead of the thiazole was found to be more sensitive to the β272Phe->Val mutation present in 1A9 cells. [86] This result supported the hypothesis that a pyridine ring (thus the thiazole ring of natural epothilones) could be arranged in such a region. Therefore, the binding mode II was proposed as the most reliable [86]. Moreover, this binding mode relates the increased activity of epothilones bearing C–12 substituents (such as the methyl group of epothilone B, **13**) or derivatives where the epoxide was replaced by a double bond (i.e., epothilone C, **14**, and D, **15**) to the interaction with the hydrophobic pocket formed by Leuβ275, Leuβ217, Leuβ230 and Pheβ272.

In the same year, He et al. [87] presented a study on a baccatin derivative lacking the C–13 side chain and bearing a 2-*m*-azido benzoyl ring. Even if less active, this derivative showed an activity profile similar to that of paclitaxel. This result was related to the presence of the azido group, supposed to compensate partially the decrease of activity corresponding to the C–13 deletion. The docking of this molecule in the Nogales model [46] confirmed a binding mode very similar to that of docetaxel, where the 2-*m*-azido benzoyl ring was placed at close contact with Hisβ229 and Aspβ226. According to this binding model, the loss of activity of the 2-*p*-azido derivative was related to clashes occurring with this hydrophobic pocket. Assuming that the C–2 benzoyl group was sufficient to the alignment of the baccatin core into the binding site, He and co-workers proposed a common pharmacophoric model (Chart 18), in which the C–2 aromatic moiety corresponds to the thiazole ring of epothilones. This was in agreement with SAR of compounds bearing modifications at the thiazole ring [109, 110]. Similarly to Ojima and co-workers, they also included eleutherobin in their work (see Sect. 2.4.2).

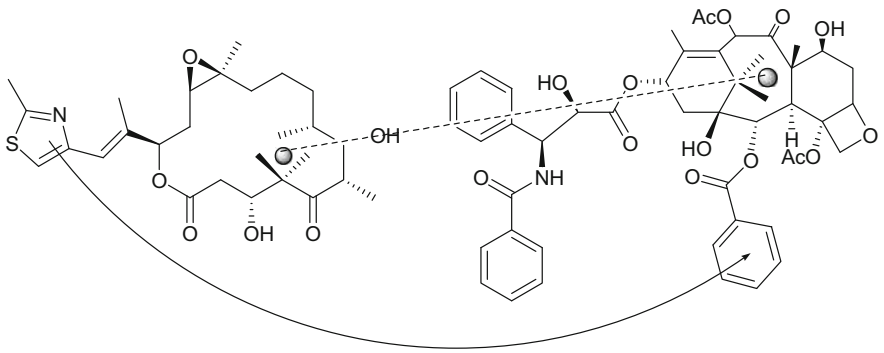

Chart 18 Common pharmacophore proposed by He and co-workers [87]

One of the last attempt to propose a common pharmacophoric model was made in 2001 by some of us, building a new pseudoreceptor for taxanes and epothilones [114] to account for the amount of new structural and biological information available since the first attempt of the minireceptor work [82]. A set of 12 taxanes and epothilones was used as training set on which the model was built. The small

number of compounds was a consequence of the difficulty in finding binding affinity data required by this approach [114, 115]. Unlike the first work, the residues used to built the pseudoreceptor binding site were obtained from the refined structure of tubulin published by Nogales et al.[46], as well as from alignment of paclitaxel with respect to the binding site. Following the standard refinement protocol already validated with PrGen software [82], all taxanes were overlapped to the EC structure of paclitaxel, while epothilones were aligned accordingly to all the common pharmacophores already proposed [51, 82, 86, 87, 111]. Since none of the alignments allowed one to obtain a QSAR equation with satisfying correlation, we coded the interaction pattern between paclitaxel and tubulin [49] into a pharmacophoric model in turn used to screen a multiconformational model (250 low energy conformations) of epothilone B. As a result, we chose a conformer of epopothilone B able to map all the known pharmacophoric features of paclitaxel.

The 7–OH group (Region A), the oxygen atom of the carbonyl group at C–1 (Region B), and the thiazole ring of epothilone B (Region C) were superposed to the oxetane oxygen atom, to the C–1′ carbonyl and the C–3′ phenyl ring of paclitaxel (Chart 19).

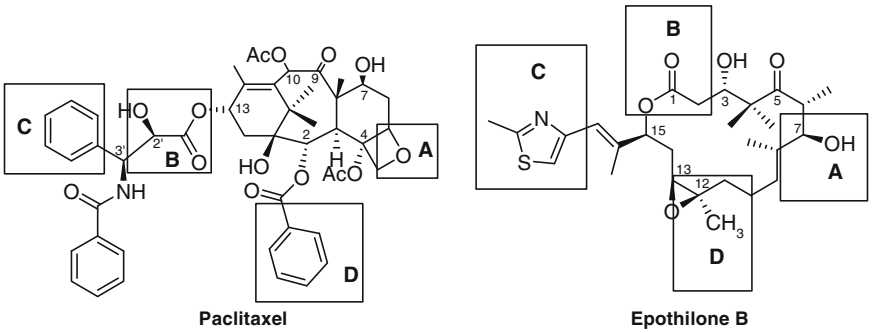

Chart 19 Alignment proposed by Botta and co-workers in the pseudoreceptor model for taxanes and epothilones [114], represented on paclitaxel (**10**) and epothilone B (**13**)

This alignment was in good agreement with available SARs of epothilones [114, 115] and mutagenesis studies from Giannakakou and co-workers. Moreover, this overlap allowed one to correlate the role of the substituent in C–12 of epothilones (Region D) to the region corresponding to the C–2 benzoyl group of paclitaxel [114], in the pocket identified by Hisβ229 and Aspβ226.

At the end of the equilibration protocol, a 3D-QSAR equation with a good correlation (r = 0.81) and a low root mean square deviation (rmsd 0.85) on the estimated interaction energies were derived. The predictive power of the model was evaluated with a test set of 11 taxanes and epothilones, obtaining a prediction coefficient of 0.78.

In 2004, Snyder, Downing and co-workers [116] presented the results of a study based on a combined approach of the EC crystallography and NMR-based

conformational analysis on the binding mode of epothilone A on the α,β-tubulin dimer (PDB id: 1TVK). Their results debated the hypothesis of a common pharmacophore for epothilones and taxanes, proposing that the two molecular classes engage the binding site in a unique and independent manner (see Fig. 7). In particular, the thiazole ring, previously considered to play the role of one of aromatic moieties of paclitaxel [51, 86, 87, 114], is found within a region unoccupied by any paclitaxel portion. The only common portion seems to be the C–7 hydroxy group of both molecules, occupying the same region, while remaining parts of the molecules interact with different portion of the binding site. Nevertheless, the macrolide ring conformation found from the EC study is different from that of the NMR-derived structure [117], in disagreement with some SAR data available [86, 87, 117].

In 2007, Carlomagno and co-workers re-opened the challenge of a common pharmacophore by publishing results of a NMR study of the complex between epothilone A (**12**) and non-polymerized tubulin in solution [118]. The model was built by combining the NMR-based pharmacophore mapping (INPHARMA, [119]) with the HADDOCK docking protocol, sampling the conformational states of the binding site against a rigid ligand structure. The resulting structure shows a pose of epothilone A that is stabilized by a partial movement of the M-loop, in comparison to the paclitaxel-tubulin complex, (see Chart 20). This model is able to explain the

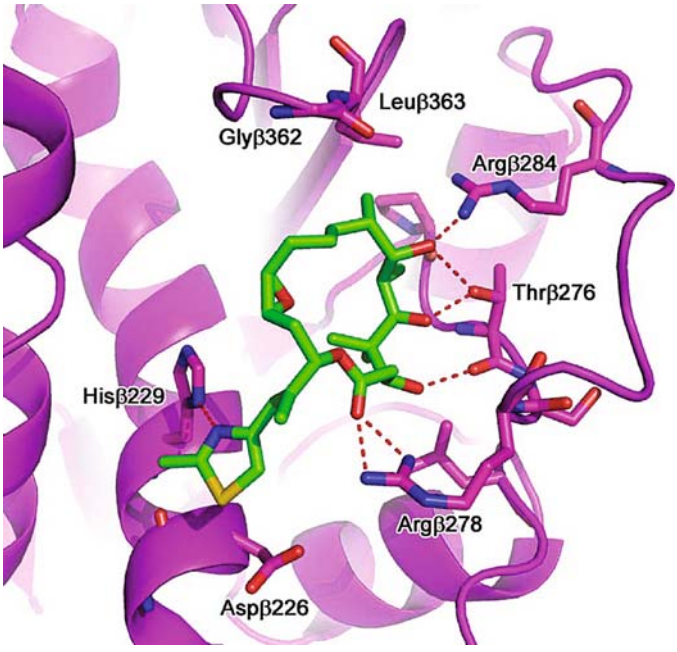

Fig. 7 The binding mode of epothilone A in 1TVK structure, as reported by Snyder and co-workers. The β-tubulin subunit is represented as *purple ribbons* (binding residues are represented as *sticks*) [106]

SAR data available for epothilone derivatives as well as tubulin mutants, providing a binding mode in strong disagreement with the EC crystallography study. Accordingly to these findings, the epothilones interact with the same residues in a similar fashion than taxanes, mimicking the paclitaxel itself while bound into the binding site. In particular, the thiazole ring is close to the receptor region occupied by the C–3′ benzamido group of paclitaxel, establishing a face-to-face interaction with Hisβ229. Moreover, the C–7 hydroxy oxygen interacts with Argβ284 and Thrβ276 by a network of hydrogen bonds (Chart 20).

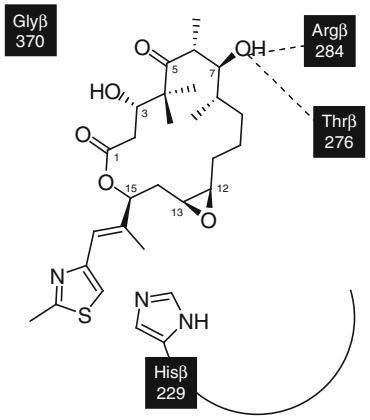

Chart 20 Schematic representation of the binding mode of epothilone A as proposed by Carlomagno and co-workers [118]

The findings of Carlomagno's team were in partial agreement with the common pharmacophore proposed by us [114], also supporting our recent results [120] on epothilone derivatives synthesized by Altmann and co-workers [121]. The binding conformations from the QSAR model and the NMR-derived model show some differences. In particular, the thiazole ring is overlapped on the C3′ phenyl ring or on the C3′ benzyl region, for the QSAR model and the NMR-derived structure (*purple* rings in Fig. 8). Despite these differences, they show the remaining pharmacophoric features accommodated within the same receptor regions. Both models, indeed, show that hydrogen bonds can be established by the epothilone C–7 hydroxy group in the region of the Thrβ276 (*blue* spheres, Fig. 8) and by the C–1 carbonyl oxygen in the region of the Glyβ370 (*yellow* spheres, Fig. 10). Moreover, the QSAR model relates the C–13 substituent of epothilones to the C–2 benzoyl group of paclitaxel, while the NMR-model places the former closer to the C–4 acetyl group, but always within the hydrophobic groove defined by Pheβ272, Leuβ217, Leuβ275 and Alaβ233 (*red* spheres, Fig. 8). In a very recent paper, Snyder and co-workers reported the activity of rigidified epothilone derivatives designed on the basis of their EC-derived structure. Due to the apparent disagreement between resulting activities and the model, the authors advised that previously proposed epothilone–tubulin complex structure should be re-examined [122].

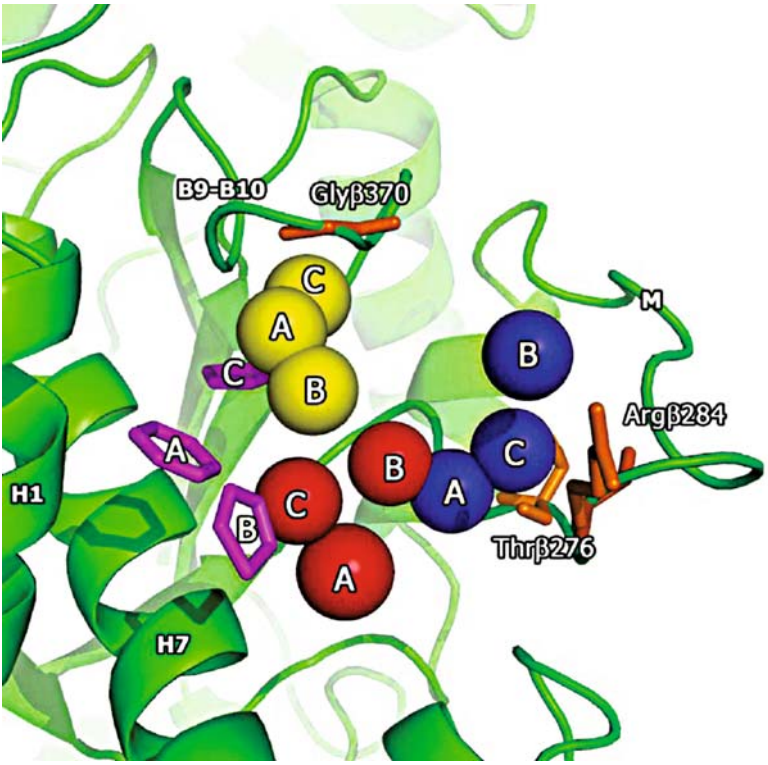

Fig. 8 Overlap of the three pharmacophores representing the interactions found for paclitaxel in the 1JFF structure (*A*), epothilone A in the NMR-derived structure (*B*), and epothilone A in the QSAR model from Botta and co-workers (*C*), respectively. *Blue*: C7-OH (epothilones); oxetane ring (paclitaxel); *red*: C13 carbon (epothilones); phenyl ring (paclitaxel); *yellow*: C1 carbonyl oxygen (epothilones); C1 carbonyl oxygen (paclitaxel); *purple*: thiazole ring (epothilone); C3 benzamide (paclitaxel). β-tubulin monomer is represented as a *green cartoon* and residues involved in hydrogen bonds are in *orange* (hydrogens are omitted for sake of clarity)

To summarize, besides taxanes, epothilones are the most studied microtubule stabilizing agents. The identification of a dramatically different class of molecules showing a mechanism of action similar to that of taxanes encouraged many efforts to identify molecular portions responsible for the activity of epothilones. Moreover, many studies were performed to find structural similarity between the two classes and many common pharmacophores were proposed to arrange the molecules into the binding site. Most of the supposed similarities on which the models were built have been disproved by the recently proposed EC structure of epothilone–tubulin complex. Nevertheless, there are still unclarified disagreements between this structure and other experimental and theoretical results, as well as the available SAR. Therefore, studies on the binding mode of epothilones seems to be still an open challenge.

2.4 Other Stabilizing Agents

2.4.1 Discodermolide and Dictyostatin

Polyketide molecule discodermolide (**16**, Chart 9) acts in a way similar to that of paclitaxel, by interfering with microtubule dynamics [55]. While radiolabeled experiments reported the displacement of bound paclitaxel in competitive assays [123], an allosteric mechanism has not been excluded [119, 124]. Since the clarification of its mechanism of action, many attempts have been made to correlate the linear structure of the discodermolide to paclitaxel, in order to identify similar molecular portions between the two molecules. In particular, the conformation of the discodermolide was studied by means of a detailed density functional study (DTF) by Ballone and Marchi [67] in 1999. Their findings evidenced the high flexibility of the ligand, as well as the electronic similarity with respect to paclitaxel and epothilone. In the same year, Ojima et al. [51] included discodermolide in the common pharmacophoric study they performed. Low energy conformations were obtained by sampling a high temperature MD simulation (100 ps at 1000 K) in a 10 kcal mol^{-1} range. Conformers were minimized and overlapped on the taxane structure. Beside epothilones and other molecules which are significantly rigid, discodermolide is extremely flexible; therefore the overlapping procedure was performed by manually selecting the conformation to be superposed. Results of the alignment highlighting the common chemical features, are depicted in Chart 21.

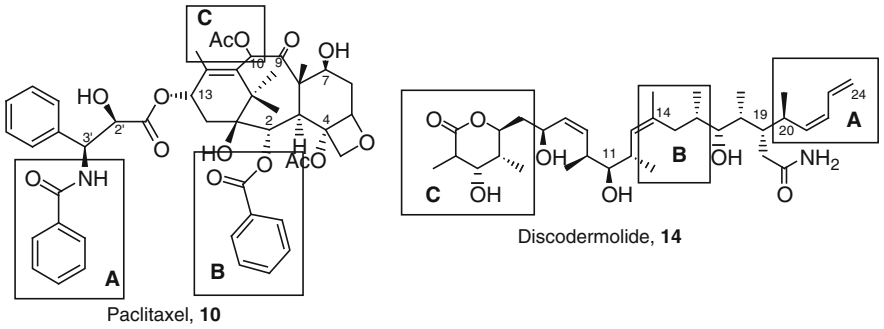

Chart 21 The common pharmacophoric regions proposed by Ojima et al. for paclitaxel and discodermolide

The two benzoyl moieties of paclitaxel were compared to two unsaturated hydrophobic regions of discodermolide (regions A and B), while the 10-acetyl group superposed the oxygen-rich region of the δ-lactone (region C).

On the other hand, a structural approach was followed by Horwitz and coworkers [123], which exploited the structural information available on solid and

solution state of discodermolide [125]. The linear structure of the molecule was reported to be folded in a U-shaped conformation with the δ-lactone and the C–19 chain at a very close distance. Dockings of the U-shaped conformation into the binding site of tubuline [46] identified to two possible orientations of discodermolide. These two alignments, referred to as model I and model II, are essentially characterized by the arrangement of the δ-lactone and the C–19 side chain. In the first model, the lactone is overlapped to the C–3′ phenyl ring, while the C–19 amide group matches the hydrophobic pocket formed by the Hisβ229, accommodating the C–2 benzoyl group of paclitaxel. In the model II, molecular portions mutually exchanged, the C–19 amide group of **16** being superposed to the 3′ benzoyl of paclitaxel and the lactone ring to the 2-benzoyl moiety. Evaluation of discodermolide derivatives led the authors to chose the model I as the most compatible with the SAR and the docking findings. In 2006, Carlomagno and co-workers determined the bound conformation of discodermolide in solution, by NMR structural analysis [124]. Furthermore, by the INPHARMA protocol [119] Authors supported the hypothesis that discodermolide binds the paclitaxel binding site and proposed a common pharmacophore between epothilones and discodermolide. The pharmacophoric model is based on NMR structural evidences that discodermolide main carbon chain adopt a helical folding which can mimic the macrocyclic core of epothilones. This folded conformation is very similar to the solution structure of dictyostatin **28**, a 22-membered macrocyclic lactone strictly related to discodermolide (from a structural and biogenetical point of view), with an inhibition activity similar to that of discodermolide [126, 127] (Chart 22).

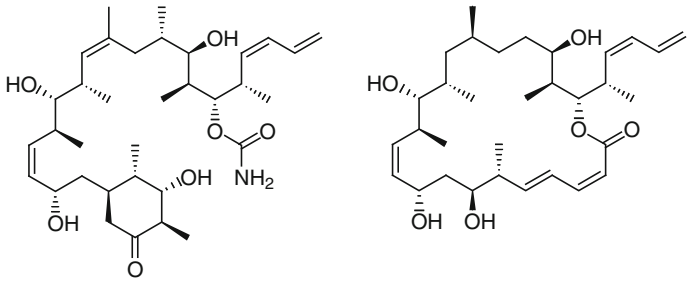

Discodermolide, **16** Dictyostatin, **28**

Chart 22 Comparison of linear structure of discodermolide **16** and dictyostatin **28**

The discodermolide conformation by Carlomagno's team overlaps epothilones in the proposed common pharmacophore (Chart 23) as follows: the C–1–C–11 oxygen-rich portion of discodermolide overlaps the thiazole nitrogen and oxygens of C–1–C–5 region of epothilones, in such way as C–1 carbonyl oxygen superposes the C–3 hydroxy group of epothilones (region A); the carbamate side chain of discodermolide overlaps the C–7 hydroxy group of epothilones (region B); the C–20–C-24 hydrophobic tail of discodermolide overlaps the C–10–C–13 hydrophobic region of epothilone A (region C).

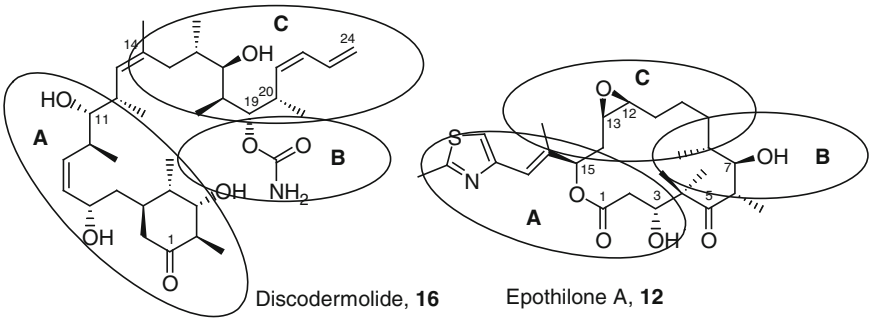

Chart 23 Common pharmacophore for discodermolide, **16** epothilone A, **12**

2.4.2 Sarcodictyins and Eleutherobins

Despite their different source, sarcodictyins (**18**) and eleutherobins (**17**) are structurally very similar (Chart 9). The former, indeed, are the sugar-free derivatives of the latter [58, 59], sharing the same diterpene core structure. This class of molecules was first investigated with the minireceptor approach [82], while the scarce availability of SAR data limited the possibility of detailed studies. The pharmacophoric model proposed by Ojima et al. [51] provided evidence of the similarity between the tricyclic core of paclitaxel and eleutherobin structure, that is supposed to fit in the main pocket between the baccatin core and the C–2 benzoyl group (Chart 24, region B), accordingly to its highly hydrophobic character. The C–8

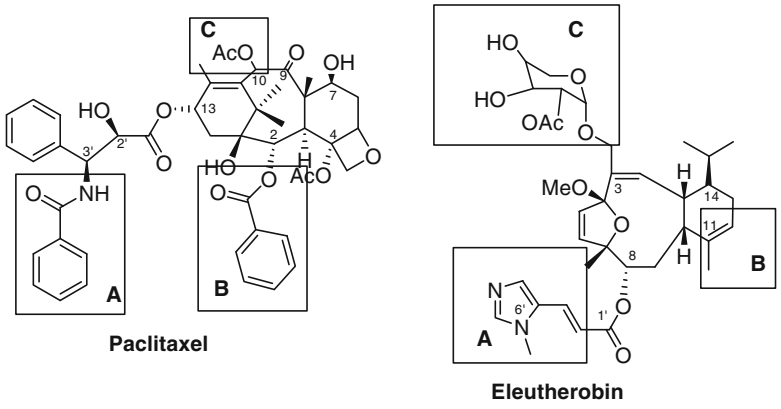

Chart 24 The common regions between paclitaxel and eleutherobin as proposed by Ojima et al.

urocanic acid chain is supposed to overlap the 3-benzammido hydrophobic substituent of taxanes (region A), while the potentially non essential sugar moiety could overlap the C–10 region of taxanes (region C). In the attempt to propose a common pharmacophore, sarcodictyins were studied by Giannakakou and co-workers

[86]. The conformational space of the ligands was investigated with high-temperature MD (1000 K) and ligands were docked into the α,β-tubulin dimer (1TUB). To take into account the role of the solvent, docking calculations were performed in the presence of different explicit water molecules. In the context of the common pharmacophoric model (Chart 25), the C–14 *i*-propyl group of sarcodictyins is overlapped to the *gem*-dimethyl group of paclitaxel and epothilones; the ether oxygen between C–4 and C–7 of sarcodictyins corresponds to the C–13 epoxide of epothilones and the oxetane ring of paclitaxel and it was supposed to act as hydrogen bond acceptor with a water molecule in the region of Thrβ276 residue. The aromatic moiety of methylimidazole side chain at C–8, overlapping the C–13 side chain of paclitaxel, makes hydrophobic interactions with the aromatic ring of Pheβ272. Due to the alignment, the C–7 methyl group could result in steric clashes with the Thrβ276 side chain, which is unfavorable but tolerated. Mutagenesis studies, correlating the decrease of activity of sarcodictyins in 1A9/A8 cells with the β276Thr->Ile mutation, which increases the bulkiness of the amino acid side chain, are in agreement with the previous hypothesis [86].

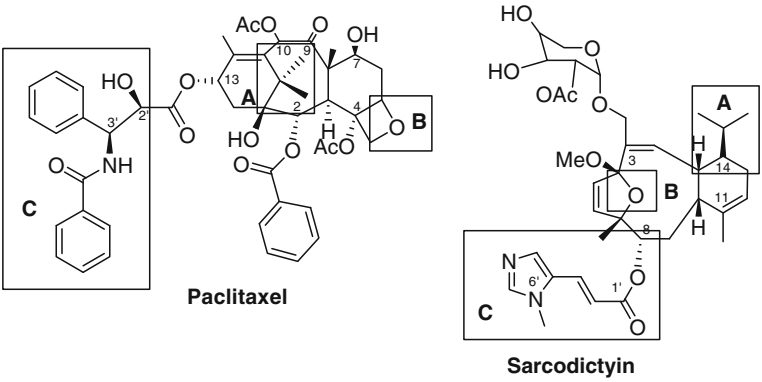

Chart 25 The common regions between paclitaxel and eleutherobin as proposed by Giannakakou et al. [86]

2.4.3 Laulimalide and Peloruside

Laulimalide (**19**) enhances the tubulin assembly and it is comparable to paclitaxel [128]. Laulimalide is also active in P-glycoprotein overexpressing cells [129]. Despite these similarities, laulimalide does not bind the paclitaxel binding site [129] and it shows a synergistic effect [130]. Likewise, peloruside A (**20**) interacts with the microtubule dynamics by stabilizing protofilaments [128] without directly competing with paclitaxel binding [131]. Since laulimalide appears to displace the bound peloruside A [132], it was hypothesized that they could share the same binding site.

To provide insights on the possible binding region of these molecules within the tubulin structure, Vilarrasa et al. [133] performed a detailed docking study on the entire protein surface. On the basis of biological evidence suggesting a possible allosteric site, the docking calculations were focused on tubulin regions different from the β-subunit. The flexibility of the B9–B10 loop in the α-subunit, (in correspondence of the paclitaxel binding site [79]) was tested by MD simulations and manual modifications, reporting a possible open conformation with low conformational energy (Fig. 9).

By means of AutoDock [134] and Gold software [135], laulimalide, peloruside and paclitaxel were docked in this structure, but only the former two compounds were able to give profitable interactions, mainly because of the overall size of the ligands. Nevertheless, the calculated binding energies for laulimalide and peloruside into the paclitaxel binding site were favorable to interaction, as well as the binding predictions performed with the pseudoreceptor model [133].

To overcome the intrinsic limitation of the pseudoreceptor built on the basis of paclitaxel binding site, a 5D-QSAR [83] model was built, further suggesting a preference for the β-subunit binding site. Results suggest that a multi-site binding is possible, indicating that laulimalide and peloruside can secondarily bind the paclitaxel binding site.

To summarize, since paclitaxel's discovery, many molecules with a similar mechanism of action have been identified from different natural sources. Amazingly, the structural similarities among them were very low despite the common target. This stimulated many computational efforts directed to the study of their binding modes and to the implementation of these molecules into interclass-wide pharmacophores. Up to now, there have been very promising results obtained by computational modeling, but contribution from experimental data is still an essential base on which to test and, often, correct the hypotheses, and to overcome the limitations arising from the management of both interaction patterns and structural complexity of target and ligands.

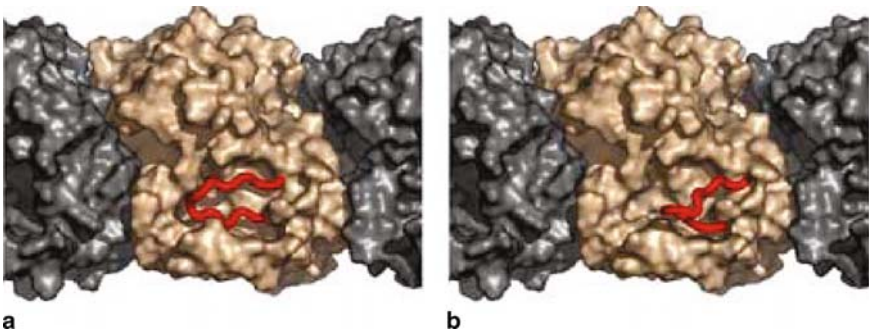

Fig. 9 The putative allosteric binding site where laulimalide and peloruside could bind: the moving αB9–B10 loop is represented in *red*; the tubulin subunits are represented in *gold* (α) and *silver* (β)

3 Conclusions

The widespread use of the vinca alkaloids and the relevant success of taxanes in clinical oncology account for the considerable interest generated by antimitotic compounds in the field of cytotoxic agents. Accordingly, over the years intensive efforts have been made both to develop novel and more efficacious tubulin stabilizing or destabilizing agents, and to get an exhaustive comprehension of the mechanism of action and binding mode of such compounds. This large amount of work involved various research fields, encompassing chemistry, crystallography, biochemistry and modeling, and resulted, on the one hand, in the discovery of several new classes of antitubulin agents from which a number of interesting drug candidates emerged and, on the other hand, in the identification of three distinct binding sites on tubulin for tubulin targeting agents, as well as the experimental definition of the binding mode for the most representative of them. In this context, molecular modeling approaches provided a fundamental contribution to the study of interactions between antimitotic agents and tubulin, and to the development of models able to explain the structure-activity relationships of several classes of compounds. However, computational studies were hampered for a long time by the absence of a crystallographic structure of tubulin and of the binding site location on it. In addition, the structural complexity of many tubulin targeting compounds constituted a further obstacle to modeling approaches. This gave rise to a fragmentary and quite confusing scenario, in which modeling studies often focused on a single structural class of molecules and sometimes also provided conflicting results. Nevertheless, in recent years, computational tools have allowed to identify some structural determinants responsible for efficacious binding of antimitotic agents to tubulin, and to propose suitable binding models for agents for which, despite the increasing importance as potential antitumor drugs, no crystallographic data are available. Especially in this research area, structural biology represent an essential source of data for molecular modeling, and the determination of more accurate structures of tubulin in microtubules and of its complexes with candidate drugs is expected to constitute in future years a valuable starting point to further increase the contribution of molecular modeling in the field of tubulin targeting agents.

References

1. Jordan MA, Wilson L (2004) *Nat Rev Cancer* 4:253
2. Ravelli RB, Gigant B, Curmi PA, Jourdain I, Lachkar S, Sobel A, Knossow M (2004) *Nature* 428:198
3. Gigant B, Wang C, Ravelli RB, Roussi F, Steinmetz MO, Curmi PA, Sobel A, Knossow M (2005) *Nature* 435:519
4. Downing KH, Nogales E (1998) *Curr Opin Cell Biol* 10:16
5. Prinz H (2002) *Exp Rev Anticancer Ther* 2:695
6. Li Q, Sham HL (2002) *Exp Opin Ther Patents* 12:1663
7. Checchi PM, Nettles JH, Zhou J, Snyder JP, Joshi HC (2003) *Trends Pharmacol Sci* 24:361

8. Gupta S, Bhattacharyya B (2003) *Mol Cell Biochem* 253:41
9. Hastie SB (1991) *Pharmacol Ther* 51:377
10. Bhattacharyya B, Panda P, Gupta S, Banerjee M (2008) *Med Res Rev* 28:155
11. Nakagawa-Goto K, Chen CX, Hamel E, Wu CC, Bastow KF, Brossi A, Lee KH (2005) *Bioorg Med Chem Lett* 15:235
12. Beckers T, Mahboobi S (2003) *Drugs Fut* 28:767
13. Pettit GR, Singh SB, Hamel E, Lin CM, Alberts DS, Garcia-Kendall D (1989) *Experientia* 45:680
14. Pettit GR, Cragg GM, Singh SB (1987) *J Nat Prod* 50:386
15. Pettit GR, Cragg GM, Herald DL, Schmidt JM, Lohavanijaya P (1982) *Can J Chem* 60:1374
16. Lin CM, Ho HH, Pettit GR, Hamel E (1989) *Biochemistry* 28:6984
17. Jordan A, Hadfield JA, Lawrence NJ, McGown AT (1998) *Med Res Rev* 18:259
18. Nam NH (2003) *Curr Med Chem* 10:1697
19. Ohsumi K, Nakagawa R, Fukuda Y, Hatanaka T, Morinaga Y, Nihei Y, Ohishi K, Suga Y, Akiyama Y, Tsuji T (1998) *J Med Chem* 41:3022
20. Pettit GR, Temple C Jr, Narayanan VL, Varma R, Simpson MJ, Boyd MR, Rener GA, Bansal N (1995) *Anticancer Drug Res* 10:299
21. Nihei Y, Suzuki M, Okano A, Tsuji T, Akiyama Y, Tsuruo T, Saito S, Hori K, Sato Y (1999) *Jpn J Cancer Res* 90:1387
22. Wang L, Woods KW, Li Q, Barr KJ, McCroskey RW, Hannick SM, Gherke L, Credo RB, Hui YH, Marsh K, Warner R, Lee JY, Zielinski-Mozng N, Frost D, Rosenberg SH, Sham HL (2002) *J Med Chem* 45:1697
23. Lin CM, Singh SB, Chu PS, Dempcy RO, Schmidt JM, Pettit GR, Hamel E (1988) *Mol Pharmacol* 34:200
24. Tron GC, Pirali T, Sorba G, Pagliai F, Busacca S, Genazzani AA (2006) *J Med Chem* 49:3033
25. Ter Haar E, Rosekranz HS, Hamel E, Day BW (1996) *Bioorg Med Chem* 4:1659
26. Brown ML, Rieger JM, Macdonald TL (2000) *Bioorg Med Chem* 8:1433
27. Weigt M, Weise M (2000) *QSAR J* 19:142
28. Zhang SX, Feng J, Kuo SC, Brossi A, Hamel E, Tropsha A, Lee KH (2000) *J Med Chem* 43:167
29. Berg U, Bladh H (1999) *Helv Chim Acta* 82:323
30. Brossi A, Lee KH, Yeh HJC (1999) *Helv Chim Acta* 82:1223
31. Ducki S, Mackenzie G, Lawrence NJ, Snyder JP (2005) *J Med Chem* 48:457
32. Vedani A, Dobler M (2002) *J Med Chem* 45:2139
33. Feher M, Schmidt JM (2000) *J Chem Inf Comput Sci* 40:495
34. Kearsley SK, Smith GM (1990) *Tetrahedron Comput Methods* 3:615
35. De Martino G, Edler MC, La Regina G, Coluccia A, Barbera MC, Barrow D, Nicholson RI, Chiosis G, Brancale A, Hamel E, Artico M, Silvestri R (2006) *J Med Chem* 49:947
36. Rappl C, Barbier P, Bourgarel-Rey V, Grégoire C, Gilli R, Manon C, Combes S, Finet JP, Peyrot V (2006) *Biochemistry* 45:9210
37. Kong Y, Grembecka J, Edler MC, Hamel E, Mooberry SL, Sabat M, Rieger J, Brown ML (2005) *Chem Biol* 12:1007
38. Nguyen TL, McGrath C, Hermone AR, Burnett JC, Zaharevitz DW, Day BW, Wipf P, Hamel E, Gussio R (2005) *J Med Chem* 48:6107
39. Kim DY, Kim KH, Kim ND, Lee KY, Han CK, Yoon JH, Moon SK, Lee SS, Seong BL (2006) *J Med Chem* 49:5564
40. Bellina F, Cauteruccio S, Monti S, Rossi R (2006) *Bioorg Med Chem Lett* 16:5757
41. Zhang Q, Peng Y, Wang XI, Keenan SM, Arora S, Welsh WJ (2007) *J Med Chem* 50:749
42. De Martino G, La Regina G, Coluccia A, Edler MC, Barbera MC, Brancale A, Wilcox E, Hamel E, Artico M, Silvestri R (2004) *J Med Chem* 47:6120
43. La Regina G, Edler MC, Brancale A, Kandil S, Coluccia A, Piscitelli F, Hamel E, De Martino G, Matesanz R, Diaz JF, Scovassi AI, Prosperi E, Lavecchia A, Novellino E, Artico M, Silvestri R (2007) *J Med Chem* 50:2865

44. Romagnoli R, Baraldi PG, Pavani MG, Tabrizi MA, Preti D, Fruttarolo F, Piccagli L, Jung MK, Hamel E, Borgatti M, Gambari R (2006) *J Med Chem* 49:3906
45. Bai R, Covell DG, Pei XF, Ewell JB, Nguyen NY, Brossi A, Hamel E (2000) *J Biol Chem* 275:40443
46. Nogales E, Wolf SG, Downing KH (1998) *Nature* 391:199
47. Bai R, Pettit GR, Hamel E (1990) *J Biol Chem* 265:17141
48. Mitra A, Sept D (2004) *Biochemistry* 43:13955
49. Löwe J, Li H, Downing KH, Nogales E (2001) *J Mol Biol* 313:1045
50. Barbier P, Gregoire C, Devred F, Sarrazin M, Peyrot V (2001) *Biochemistry* 40:13510
51. Ojima I, Chakravarty S, Inoue T, Lin S, He L, Horwitz SB, Kuduk SD, Danishefsky SJ (1999) *Proc Natl Acad Sci U S A* 96:4256
52. Suffness M, Wall ME Suffness M(ed.) Taxol: science and applications. CRC Press, Boca Ranton, FL, (1995)In:pp 3–25.
53. Schiff PB, Fant J, Horwitz SB (1979) *Nature* 277:665
54. Höfle G, Bedorf N, Gerth K, Reichenbach H (1993), (GBF) DE-4138042 1993; Chem Abstr
55. Bollag DM, McQueney PA, Zhu J, Hensens O, Koupal L, Liesch J, Goetz M, Lazarides E, Woods CM (1995) *Cancer Res* 55:2325
56. Hung DT, Chen J, Schreiber SL (1996) *Chem Biol* 3:287
57. Longley RE, Gunasekera SP, Faherty D, McLane J, Dumont F (1993) *Ann NY Acad Sci* 696:94
58. Long BH, Carboni JM, Wasserman AJ, Cornell LA, Casazza AM, Jensen PR, Lindel T, Fenical W, Fairchild CR (1998) *Cancer Res* 58:1111–1115
59. Hamel E, Sackett DL, Vourloumis D, Nicolaou KC (1999) *Biochemistry* 38:5490
60. He L, Jagtap PG, Kingston DG, Shen HJ, Orr GA, Horwitz SB (2000) *Biochemistry* 39:3972
61. Wilson L, Jordan MA (2004) *Chemotherapy* 16:83
62. Jordan MA, Wendell K, Gardiner S, Derry WB, Copp H, Wilson L (1996) *Cancer Res* 56:816
63. Nuijen B, Bouma M, Schellens JH, Beijnen JH (2001) *Invest New Drugs* 19:143
64. Aversa SM, Cattelan AM, Salvagno L, Crivellari G, Banna G, Trevenzoli M, Chiarion-Sileni V, Monfardini S (2005) *Crit Rev Oncol Hematol* 53:235
65. Mekhail TM, Markman M (2002) *Exp Opin Pharmacother* 3:755
66. Zhao J, Kim JE, Reed E, Li QQ (2005) *Int J Oncol* 27:247
67. Ballone P, Marchi M (1993) *J Phys Chem* 103:3097
68. Milanesio M, Ugliengo P, Viterbo D (1999) *J Med Chem* 42:291
69. Guéritte-Voegelein F, Guénard D, Mangatal K, Poitier P, Guilhem J, Césario M, Pascard C (1990) *Acta Crystallogr Sect C* 46:781
70. Jiménez-Barbero J, Amat-Guerri F, Snyder JP (2002) *Curr Med Chem Anticancer Agents* 2:91
71. Brünger AT, Karplus M (1991) *Acc Chem Res* 24:54
72. Leach AR (1996) Molecular modelling, principles and applications. Longman, London, pp 436–442
73. Mastropaolo D, Camerman A, Luo Y, Brayer GD, Camerman N (1995) *Proc Natl Acad Sci U S A* 92:6920
74. Vander Velde DG, Georg GI, Grunewald GL, Gunn CW, Mitscher LA (1993) *J Am Chem Soc* 115:11650
75. Williams HJ, Scott AI, Dieden RA, Swindell CS, Chirlian LE, Francl MM, Heerding JM, Krauss NE (1993) *Tetrahedron* 49:6545
76. Boge TC, Wu ZJ, Himes RH, Vander Velde DG, Georg GI (1999) *Bioorg Med Chem Lett* 9:3047
77. Dubois J, Guénard D, Guéritte-Voegelein F, Guedira N, Potier P, Gillet B, Beloeil JC (1993) *Tetrahedron* 49:6533
78. Snyder JP, Nevins N, Cicero DO, Jansen JJ (2000) *Am Chem Soc* 122:724
79. Snyder JP, Nettles JH, Cornett B, Downing KH, Nogales E (2001) *Proc Natl Acad Sci U S A* 98:5312

80. Cachau RR, Gussio R, Beutler JA, Chmurny GN, Hilton BD, Muschik GM, Erickson JW (1994) *Supercomput Appl High Performance Comput* 8:24
81. Discovery/InsightII was a software formerly distributed by Accelrys Inc.: San Diege, CA.
82. Wang M, Xia X, Kim Y, Hwang D, Jansen JM, Botta M, Liotta DC, Snyder JP (1999) *Org Lett* 15:43–46
83. Zbinden P, Max D, Folkers G, Vedani A (1998) *QSAR* 17:112
84. Rao S, Krauss NE, Heerding JM, Swindell CS, Ringel I, Orr GA, Horwitz SB (1994) *J Biol Chem* 269:3132
85. Rao S, Orr GA, Chaudray AG, Kingston DGI, Horwitz SB (1995) *J Biol Chem* 35:20235
86. Giannakakou P, Gussio R, Nogales E, Downing KH, Zaharevitz D, Bollbuck B, Poy G, Sacket D, Nicolaou KC, Fojo T (2000) *Proc Natl Acad Sci U S A* 6:2904
87. He L, Jagtap PG, Kingston DG, Shen HJ, Orr GA, Horwitz SB (2000) *Biochemistry* 39:3972
88. Barboni L, Lambertucci C, Appendino G, Vander Velde DG, Himes RH, Bombardelli E, Wang M, Snyder JP (2001) *J Med Chem* 44:1576
89. Querolle O, Dubois J, Thoret S, Roussi F, Montiel-Smith S, Guéritte F,Guénard D (2003) *J Med Chem* 46:3623
90. Ganesh T, Guza RC, Bane S, Ravindra R, Shanker N, Lakdawala AS, Snyder JP, Kingston DG (2004) *Proc Natl Acad Sci U S A* 101:10006
91. Shanker N, Kingston DG, Ganesh T, Yang C, Alcaraz AA, Geballe MT, Banerjee A, McGee D, Snyder JP, Bane S (2007) *Biochemistry* 46:11514
92. Gao Q, Wei JM, Chen SH (1995) *Pharm Res* 12:337
93. Gao Q, Chen SH (1996) *Tetrahedron Lett* 37:3425
94. Paloma LG, Guy RK, Wrasidlo W, Nicolaou KC (1994) *Chem Biol* 1:107
95. Ojima I, Kuduk SD, Chakravarty S, Ourevitch M, Bégue JP (1997) *J Am Chem Soc* 119:5519
96. Jiménez-Barbero J, Souto AA, Abal M, Barasoain I, Evangelio JA, Acuña AU, Andreu JM, Amat-Guerri F (1998) *Biorg Med Chem* 6:1857
97. Ewing TJA, Kuntz ED (1997) *J Comp Chem* 18:1175
98. Barboni L, Datta A, Dutta D, Georg G, Velde DG, Himes RH, Wang M, Snyder JP (2001) *J Org Chem* 66:3321
99. Wang M, Cornett B, Nettles J, Liotta DC, Snyder JP (2000) *J Org Chem* 65:1059
100. Gueritte F (2001) *Curr Pharm Des* 7:1229
101. Barboni L, Giarlo G, Riccutelli M, Ballini R, Georg G, VanderVelde DG, Himes RH, Wang M, Lakdawala A, Snyder JP (2004) *Org Lett* 6:461
102. Wu JH, Zamir LO (2000) *Anticancer Drug Des* 15:73
103. Nogales E, Whittaler M, Milligan RA, Downing KH (1999) *Cell* 96:79
104. Buey RM, Díaz FJ, Andreu JM, O'Brate A, Giannakakou P, Nicolaou KC, Sasmal PK, Ritzén A, Namoto K (2004) Chem Biol 11:225
105. Nogales E (1999) *Cel Mol Life Sci* 56:133
106. Miller ML, Ojima I (2001) *Chem Rec* 1:195
107. Mastalerz H, Zhang G, Kadow J, Fairchild C, Long B, Vyas DM (2001) *Org Lett* 3:1613
108. Lee KW, Briggs JM (2001) *J Comput Aided Mol Des* 15:41
109. Nicolaou KC, Vourloumis D, Li T, Pastor J, Wissinger N, He Y, Ninkovic S, Sarabaia F, Vallberg H, Roschangar F, King NP, Finlay MRV, Giannakakou P, Verdier-Pinard P, Hamel E (1997) *Angew Chem Int Ed Engl* 36:2093
110. Nicolaou KC, Roschangar F, Vourloumis D (1998) *Angew Chem Int Ed Engl* 37:2014
111. Winkler JD, Axelsen PH (1996) *Bioorg Med Chem Lett* 6:2963
112. Chou T, Zhang X, Balog A, Su D, Meng D, Savin K, Bertino JR, Danishefsky SJ (1997) *Proc Natl Acad Sci U S A* 95:9642
113. Rao S, Krauss NE, Heerding JM, Swindell CS, Ringel I, Orr GA, Horwitz SB (1994) *J Biol Chem* 269:3132
114. Manetti F, Forli S, Maccari L, Corelli F, Botta M (2001) *Il Farmaco* 58:375
115. Manetti F, Maccari L, Corelli F, Botta M (2004) *Curr Topics Med Chem* 4:203

116. Nettles JH, Li H, Cornett B, Krahn JM, Snyder JP, Downing KH (2004) *Science* 305:866
117. Carlomagno T, Blommers MJ, Meiler J, Jahnke W, Schupp T, Petersen F, Schinzer D, Altmann KH, Griesinger C (2007) *Angew Chem* 115:2615
118. Reese M, Sánchez-Pedregal VM, Kubicek K, Meiler J, Blommers MJ, Griesinger C, Carlomagno T (1997) *Angew Chem Int Ed Engl* 46:1864
119. Sánchez-Pedregal VM, Reese M, Meiler J, Blommers MJ, Griesinger C, Carlomagno T (2005) *Angew Chem Intl Ed Engl* 44:4172
120. Botta M, Forli S, Altmann K-H (unpublished results)
121. Bold G, Wojeik S, Caravatti G, Lindauer R, Stierlin C, Gertsch J, Wartmann M, Altmann KH (2006) *ChemMedChem* 1:37
122. Zhan W, Jiang Y, Brodie PJ, Kingston DI, Liotta DC, Snyder JP (2008) *Org Lett* 10:1565
123. Martello L, LaMarche MJ, He L, Beauchamp TJ, Smith AB, Hotwitz SB (2001) *Chem Biol* 8:843
124. Sánchez-Pedregal VM, Kubicek K, Meiler J, Lyothier I, Paterson I, Carlomagno T (2006) *Angew Chem Int Ed Engl* 45:7388
125. Smith ABI, LaMarche MJ, Falcone-Hindley M (2001) *Org Lett* 5:695
126. Petitt GR, Chichacz ZA, Gao F, Boyd MR, Schmidt JM (1994) *J Chem Soc Chem Commun* 1:1111
127. Madiraju C, Edker MC, Hamel E, Raccor BS, Balachandran R, Zhu G, Giuliano KA, Vogt A, Shin Y, Fournier JH, Fukui Y, Bruckner AM, Curran DP, Day BW (2005) *Biochemistry* 44:15053
128. Mooberry SL, Tien G Hernandez AH, Plubrukar A, Davidson BS (1999) *Cancer Res* 59:653
129. Pryor DE, O'Brate A, Bilcer G, Diaz JF, Wang Y, Wang Y, Kabaki M, Jung MK, Andreu JM, Ghosh AK, Giannakakou P, Hamel E (2002) *Biochemistry* 41:9109
130. Gapud EJ, Bai R, Ghosh AK, Hamel E (2004) *Mol Pharmacol* 66:113
131. Gaitanos TN, Buey RM, Diaz JF, Northcote PT, Teesdale-Spittle P, Andreu JM, Miller JH (2004) *Cancer Res* 64:5063
132. Miller JH, Rouwe B, Gaitanos TN, Hood KA, Crume KP, Backstrom BT, La Flamme AC, Berridge MV, Northcote PT (2004) *Apoptosis* 9:785
133. Pineda O, Farràs J, Maccari L, Manetti F, Botta M, Vilarrasa J (2004) *Bioorg Med Chem Lett* 14:4825
134. Morris GM, Goodsell DS, Halliday RS, Huey R, Hart WE, Belew RK, Olson AJ (1998) *J Comput Chem* 19:1639
135. Jones G, Willet P, Glen RC, Leach AR, Taylor J (1997) *J Mol Biol* 267:727

Index